MAGMATIC-HYDROTHERMAL EVOLUTION OF THE HOIDAS LAKE REE DEPOSIT, NORTHERN SASKATCHEWAN, CANADA

A Thesis Submitted to the College of
Graduate Studies and Research
in Partial Fulfillment of the Requirements
for the Degree of Doctor of Philosophy
in the Department of Geological Sciences
University of Saskatchewan
Saskatoon

By

KRISZTINA PANDUR

PERMISSION TO USE

In presenting this thesis in partial fulfillment of the requirements for a Postgraduate degree from the University of Saskatchewan, I agree that the Libraries of this University may make it freely available for inspection. I further agree that permission for copying of this thesis in any manner, in whole or in part, for scholarly purposes may be granted by the professor or professors who supervised my thesis work or, in their absence, by the Head of the Department of Geological Sciences or the Dean of the College of Graduate Studies and Research, in which my thesis work was done. It is understood that any copying or publication or use of this thesis or parts thereof for financial gain shall not be allowed without my written permission. It is also understood that due recognition shall be given to me and to the University of Saskatchewan in any scholarly use which may be made of any material in my thesis.

Requests for permission to copy or to make other uses of materials in this thesis in whole or part should be addressed to:

Head of the Department of Geological Sciences
University of Saskatchewan
114 Science Place
Saskatoon, Saskatchewan, S7N 5E2
CANADA

ABSTRACT

The Hoidas Lake rare earth element (REE) deposit in northern Saskatchewan, Canada, was investigated through field observations, detailed petrographic studies, scanning electron microscopy coupled with energy dispersive X-ray spectrometry (SEM-EDS) and electron microprobe analyses (EMPA), fluid inclusion microthermometry and in situ U-Pb, Lu-Hf and Sm-Nd isotopic studies, in order to unravel the magmatic-hydrothermal evolution of the deposit. The main aims were to evaluate the source and chemical variations of the fluids and melts that formed the mineralization and to provide constraints on the age of the deposit.

The structurally controlled mineralization consists of diopside-allanite veins and apatite breccia veins emplaced along the Hoidas-Nisikkatch Fault. In the diopside-allanite veins the allanites, commonly intergrown with hyalophane, titanite and diopside, show chemical variations that reflect relative REE-depletion in the melt during allanite crystallization, and subsequent REE-enrichment, possibly due to open system behavior and a new influx of melt/fluid into the vein system. The later apatite breccia veins show multiple phases of crystallization and a shift from Ce-dominance in the earlier red and green apatite phases to Nd-dominance in the latest coarse red apatite phase, which reflects a transition from magmatic to hydrothermal growth. Interaction with hydrothermal fluids resulted in chlorite-hematite alteration, irregular REE zonation in allanite and apatite, and local redistribution of the REEs into secondary monazite, REE-carbonates and REE-Sr-carbonates. Late quartz-carbonate veins that represent this hydrothermal overprint occasionally contain allanite, interpreted to have formed through hydrothermal remobilization of the REEs. The paragenetic relationships of the REE veins with hyalophane-bearing pegmatite dikes and late lamprophyre dikes and the mineral chemistry of the REE-bearing phases indicate a mantle-derived, most probably carbonatitic source for the melts and fluids responsible for the mineralization. The various vein generations formed due to repeated influxes of the mineralizing melts and fluids into the vein system, and caused limited Ba-metasomatism and albitization in the wall rocks.

Unusual LREE-rich primary graphic-textured inclusions in the apatite of the Hoidas Lake deposit were studied through integrated EMPA and SEM-EDS imaging, and show variable compositions between Ce_2O_3+SiO_2(+ThO_2)-dominant and La_2O_3+Nd_2O_3(+F)-dominant end members. These inclusions indicate rapid apatite growth and contemporaneous crystallization of

REE-enriched phases from the boundary-layer melt phase at the apatite-melt interface or alternatively, trapping of a melt phase during apatite growth due to melt-melt immiscibility. The fluid inclusion microthermometric data and evaporate mound analysis of the apatite breccia veins and related hyalophane-bearing pegmatites and quartz-carbonate veins suggest that entrapment of the hydrothermal fluids at Hoidas Lake occurred below 310°C, and pressure was transient between 0.5 and 2 kbars. Evolution of the Hoidas Lake mineralization involved early entrapment of a carbonic fluid followed by introduction of mixed Na-Ca-K-(Ba-Mn-Mg-Fe-Sr) aqueous fluids that were responsible for the late alteration of the mineralized veins and local redistribution of the REEs into secondary phases. Combination of the aforementioned studies indicates that the Hoidas Lake REE mineralization is a distal magmatic-hydrothermal counterpart of the hidden carbonatitic or alkaline igneous source.

Geological relationships and laser ablation inductively coupled plasma mass spectrometry (LA-ICP-MS) U-Pb geochronology of various mineral phases indicate that the REE-bearing veins formed after peak metamorphism in the Hoidas Lake area, which occurred at ca. 1.9 Ga. However, zircon crystals with concordant U-Pb dates of ca. 2350 Ma are interpreted to be inherited from granitoids that formed during the Arrowsmith Orogeny, also reported from other parts of the southern Rae Subprovince. Zircon rims that show concordant U-Pb ages around 1905 Ma represent new zircon growth during the emplacement of the REE mineralization and have considerably different Hf isotopic compositions, compared to the inherited zircon cores. Concordia ages of titanite from two distinct samples are ca. 1900 Ma and 1830 Ma and two monazite U-Pb date groups were observed at ca. 1910 Ma and 1845 Ma. The U-Pb dates correspond to the estimated period of tectonic activity of the Black Bay Fault System. The Sm-Nd isotopic systematics of titanite, green apatite and monazite are comparable to those previously reported for the Martin Group alkali basalts in the Beaverlodge Domain and the ultrapotassic rocks of the Christopher Island Formation in the Baker Lake Basin, both of which also yielded similar U-Pb ages to those of the Hoidas Lake veins. These regionally occurring alkali units likely originated from a similar source, most probably an ancient enriched lithospheric mantle reservoir.

ACKNOWLEDGEMENTS

First and foremost, I would like to express my gratitude to my graduate supervisor, Dr. Kevin Ansdell for his guidance throughout this Ph.D. degree. I am truly grateful for his insightful advice, encouragement and endless patience during our numerous discussions.

I owe a huge amount of gratitude to John Pearson who provided valuable insight and Kimberley Halpin for always being available for discussion. I am immensely thankful to Daniel Kontak for sharing his scientific expertise and providing me with eye-opening conversations on several aspects of my Ph.D, and Charlie Harper for contributing his incredible knowledge to the project. I greatly benefitted from the contributions of Dr. Chris McFarlane and Dr. John Hanchar, and I appreciate their willingness to accommodate my needs during my visits to their research laboratories. I owe special thanks to Dr. Bruce Eglington for his support and encouragement, and to my external examiner, Dr. Anton Chakhmouradian for his constructive comments to improve the thesis. I am thankful to the members of my advisory committee, Dr. Yuanming Pan, Dr. Chris Holmden, Dr. Derek Peak and Dr. Jim Merriam

I would like to thank Rylan Elliott, Bobby Janvier, Morris McKenzie and Mark McKenzie for their assistance during field work and Blaine Novakovski for preparing my samples. Steven Creighton, Robert Millar and Lucy Hunt from the Saskatchewan Research Council, as well as Wanda Aylward and Rebecca Lam from Memorial University of Newfoundland are thanked for analytical assistance, and I am grateful for the technical help I received from Jim Rosen at the University of Saskatchewan. Special thanks go out to Tim Prokopiuk for sharing the most spectacular petrographic phenomena with me. Finally, I would like to thank Balázs Törő, my family and friends for their presence and all the encouragement I got from them during the past years.

I am grateful to the former Great Western Minerals Ltd. for giving me the opportunity to work on this project and their financial and logistical support in organizing my field work at Hoidas Lake. I gratefully acknowledge the Natural Science and Engineering Research Council of Canada, for financial support through research grants to Dr. Kevin Ansdell, and the University of Saskatchewan for the Dean’s Graduate Scholarship I received. Additional funds for this research, which include travel and research grants from the Mineralogical Association of Canada and the Society of Economic Geologists, were also greatly appreciated.

TABLE OF CONTENTS

PERMISSION TO USE i

ABSTRACT ii

ACKNOWLEDGEMENTS iv

TABLE OF CONTENTS v

LIST OF TABLES ix

LIST OF FIGURES xi

1. INTRODUCTION 1
    - 1.1 Overview 1
        - 1.1.1 The Hoidas Lake REE deposit 1
        - 1.1.2 The importance of hydrothermal processes in REE mineralization 2
    - 1.2 Thesis outline 3
    - 1.3 Clarification of terms used in the thesis 4
    - 1.4 Research objectives 5
    - 1.5 Contributions of co-authors to the manuscripts included in the thesis 6
2. HYDROTHERMAL EVOLUTION IN THE HOIDAS LAKE VEIN-TYPE REE DEPOSIT, SASKATCHEWAN, CANADA: CONSTRAINTS FROM FLUID INCLUSION MICROTHERMOMETRY AND EVAPORATE MOUND ANALYSIS 7
    - 2.1 Abstract 7
    - 2.2 Introduction 8
    - 2.3 Geological Setting 10
        - 2.3.1 Regional geology 10
        - 2.3.2 Local geology 12
        - 2.3.3 Mineralogy, REE mineralization and paragenesis of the Hoidas Lake vein system 13
    - 2.4 Sampling and analytical procedures 19
    - 2.5 Analytical results 21
        - 2.5.1 Fluid inclusion petrography: types of inclusions and timing of entrapment 21
        - 2.5.2 Fluid inclusion microthermometry 25
        - 2.5.3 Chemistry of evaporate mounds 31
    - 2.6 Discussion 34

2.6.1 Preamble 34

2.6.2 Connection between fluids and melts in the Hoidas Lake REE mineralized system 35

2.6.3 Salinity, chemistry and evolution of the fluid system 36

2.6.4 Comparison to fluid inclusions in other carbonatite systems 38

2.6.5 P-T conditions of fluid entrapment 39

2.6.6 Implications of the fluid inclusion study for the nature and origin of the Hoidas Lake REE deposit and other REE mineralized systems 43

2.7 Conclusions 45

2.8 Relationship of manuscript to thesis 46

3. GRAPHIC-TEXTURED INCLUSIONS IN APATITE: EVIDENCE FOR PEGMATITIC GROWTH IN A REE ENRICHED CARBONATITIC SYSTEM 47

3.1 Abstract 47

3.2 Introduction 47

3.3 The Hoidas Lake LREE mineralization 48

3.4 Samples and methodology 50

3.5 Textural and chemical relationships of the graphic-textured inclusions 50

3.6 Discussion and summary 54

3.7 Relationship of manuscript to thesis 57

4. PETROGRAPHIC AND MINERAL CHEMICAL CHARACTERISTICS OF THE HOIDAS LAKE DEPOSIT, NORTHERN SASKATCHEWAN, CANADA: CONSTRAINTS ON THE ORIGIN OF A DISTAL MAGMATIC-HYDROTHERMAL REE SYSTEM 58

4.1 Abstract 58

4.2 Introduction 59

4.3 Geological setting 60

4.3.1 Regional geology 60

4.3.2 Local geology in the Hoidas Lake area 61

4.4 Sampling and analytical procedures 65

4.5 Results 66

4.5.1 Petrology and textural relationships of the REE mineralization 66

4.5.2 Mineral chemistry of the diopside-allanite veins 74
4.5.2.1 Allanite 74
4.5.2.2 Titanite 77
4.5.2.3 Feldspars 78
4.5.2.4 Diopside, amphibole and biotite 79
4.5.2.5 REE-carbonates 80
4.5.3 Mineral chemistry of the apatite breccia veins 81
4.5.3.1 Apatite 81
4.5.3.2 Monazite 83
4.5.3.3 Thorite 85
4.5.3.4 Apatite breccia matrix 85
4.5.4 Chemistry of the late allanite in quartz-carbonate veins 87
4.5.5 Inclusions representing a melt phase in the apatite breccia 89
4.6 Discussion 92
4.6.1 Formation of the Hoidas Lake REE mineralization – magmatic vs. hydrothermal processes 92
4.6.2 Origin of the melts and fluids responsible for the formation of the Hoidas Lake REE mineralization 94
4.6.3 Chemical variations in the REE-bearing minerals: implications for changing source composition 98
4.6.4 Chemical variations in the REE-bearing minerals: the role of hydrothermal fluids 100
4.7 Conclusions 105
4.8 Relationship of manuscript to thesis 105
5. IN SITU U-Pb GEOCHRONOLOGY, Lu-Hf AND Sm-Nd ISOTOPE SYSTEMATICS OF THE HOIDAS LAKE REE DEPOSIT, NORTHERN SASKATCHEWAN, CANADA 107
5.1 Abstract 107
5.2 Introduction 108
5.3 Geological background 109
5.3.1 Regional tectonic environment 109

5.3.2 Lithological and structural units of the Hoidas Lake area 111

5.3.3 Textural relationships, mineral chemistry and structural position of the REE mineralization at Hoidas Lake 112

5.4 Analytical techniques 117

5.4.1 Imaging of samples 117

5.4.2 Laser ablation ICP-MS U-Pb geochronology 118

5.4.3 Laser ablation ICP-MS Lu-Hf isotope characteristics 120

5.4.4 Laser ablation ICP-MS Sm-Nd isotope characteristics 120

5.5 Analytical results 121

5.5.1 U-Pb geochronology 121

5.5.1.1 Zircon 121

5.5.1.2 Titanite 124

5.5.1.3 Apatite 125

5.5.1.4 Monazite 126

5.5.2 Zircon Hf isotopic systematics 127

5.5.3 Sm-Nd isotopic systematics of titanite, monazite and apatite 128

5.6 Discussion 131

5.6.1 Age of the Hoidas Lake mineralization 131

5.6.2 The relationship of REE vein emplacement to the tectonic evolution of the Hoidas Lake area 134

5.6.3 Implications of Lu-Hf and Sm-Nd isotopic systematics for the source of the Hoidas Lake REE mineralization 137

5.7 Summary 140

5.8 Relationship of manuscript to thesis 142

6. SUMMARY 143

LIST OF REFERENCES 146

APPENDIX A. FLUID INCLUSION MICROTHERMOMETRY AND EVAPORATE MOUND ANALYSIS 163

APPENDIX B. ELECTRON MICROPROBE ANALYSIS 179

APPENDIX C. ADDITIONAL DATA FOR LASER ABLATION ICP-MS ANALYSIS 241

APPENDIX D. COPYRIGHT PERMISSIONS 245

LIST OF TABLES

Table 4.1 Representative electron microprobe analyses of early allanite and titanite from the Hoidas Lake diopside-allanite veins 75

Table 4.2 Representative electron microprobe analyses of hyalophane, potassium feldspar, zeolite, diopside, actinolite, hornblende and biotite from the Hoidas Lake diopside-allanite veins 79

Table 4.3 Representative electron microprobe analyses of REE-carbonate from the Hoidas Lake diopside-allanite veins 80

Table 4.4 Representative electron microprobe analyses of red apatite, green apatite and coarse red apatite from the Hoidas Lake apatite breccia veins 82

Table 4.5 Representative electron microprobe analyses of monazite and thorite from the Hoidas Lake apatite breccia veins 86

Table 4.6 Representative electron microprobe analyses of REE-carbonate, REE-Sr-carbonate, barite and calcite from the Hoidas Lake apatite breccia veins 87

Table 4.7 Representative electron microprobe analyses of late allanite from the Hoidas Lake quartz-carbonate veins 88

Table 5.1 Concordant U-Pb isotopic data for zircon from the Hoidas Lake REE deposit 123

Table 5.2 Concordant U-Pb isotopic data for titanite from the Hoidas Lake REE deposit 125

Table 5.3 U-Pb isotopic data for apatite from the Hoidas Lake REE deposit 126

Table 5.4 Concordant U-Pb isotopic data for monazite from the Hoidas Lake REE deposit 127

Table 5.5 Lu-Hf isotopic data for zircon from the Hoidas Lake REE deposit 128

Table 5.6 Sm-Nd isotopic data for titanite from the Hoidas Lake REE deposit 129

Table 5.7 Sm-Nd isotopic data for apatite from the Hoidas Lake REE deposit 130

Table 5.8 Sm-Nd isotopic data for monazite from the Hoidas Lake REE deposit 131

Table A.1 Summary of thermometric data for fluid inclusions from the Hoidas Lake rare earth element deposit. 163

Table A.2 Fluid inclusion microthermometry data 166

Table A.3 Evaporate mound SEM-EDS data 178

Table B.1 Composition of the inclusions displaying graphic texture in apatite 179

Table B.2 Composition of apatite containing graphic-textured inclusions 185

Table B.3 Composition of zircon in diopside-allanite veins 187
Table B.4 Composition of early allanite in diopside-allanite veins 189
Table B.5 Composition of titanite in diopside-allanite veins 195
Table B.6 Composition of zeolite in diopside-allanite veins.. 197
Table B.7 Composition of hyalophane, potassium feldspar and albite in diopside-allanite veins 198
Table B.8 Composition of diopside and green amphibole in diopside-allanite veins 199
Table B.9 Composition of biotite, epidote, barite and calcite in diopside-allanite veins 200
Table B.10 Composition of chlorite in diopside-allanite veins 201
Table B.11 Composition of REE-carbonate in diopside-allanite veins 203
Table B.12 Composition of red apatite in apatite breccia veins 205
Table B.13 Composition of green apatite in apatite breccia veins 208
Table B.14 Composition of coarse red apatite in apatite breccia veins 210
Table B.15 Composition of apatite of undeterminable stage in apatite breccia veins 212
Table B.16 Composition of monazite in apatite breccia veins 215
Table B.17 Composition of thorite in apatite breccia veins 220
Table B.18 Composition of chlorite in apatite breccia veins.. 222
Table B.19 Composition of calcite in apatite breccia veins 224
Table B.20 Composition of barite in apatite breccia veins... 226
Table B.21 Composition of REE-carbonates in apatite breccia veins 227
Table B.22 Composition of REE-Sr-carbonate and strontianite in apatite breccia veins............. 229
Table B.23 Composition of late allanite in quartz-carbonate veins 230
Table B.24 Composition of hyalophane, potassium feldspar and albite in hyalophane-bearing pegmatites 239
Table B.25 Average and range of detection limits for electron microprobe analyses 240
Table C.1 Discordant U-Pb isotopic data for zircon from the Hoidas Lake REE deposit 241
Table C.2 Discordant U-Pb isotopic data for titanite from the Hoidas Lake REE deposit 243
Table C.3 Discordant U-Pb isotopic data for monazite from the Hoidas Lake REE deposit 244

LIST OF FIGURES

Figure 2.1 Maps showing the regional geology and location of the Hoidas Lake REE deposit..... 11

Figure 2.2 Photographs, photomicrographs and back-scattered electron images of samples from the Hoidas Lake REE deposit showing the mineral paragenesis 16

Figure 2.3 A composite mineral paragenesis for the different vein types of the Hoidas Lake rare earth element deposit 18

Figure 2.4 Photomicrographs of the different fluid inclusion types, melt inclusions and monazite inclusions in quartz, calcite and apatite from the Hoidas Lake REE deposit 22

Figure 2.5 Schematic diagram showing the different paragenetic stages that were studied for fluid inclusions 25

Figure 2.6 Summary of thermometric data for fluid inclusions from Hoidas Lake 26

Figure 2.7 Histograms summarizing results for homogenization temperature measurements for type 1 quartz-hosted carbonic inclusions from Hoidas Lake 27

Figure 2.8 Binary plot of temperature of vapor disappearance vs. temperature of halite dissolution for type 3 L-V-H aqueous inclusions 28

Figure 2.9 Histograms summarizing results for homogenization temperature measurements of type 4 L-V aqueous inclusions 29

Figure 2.10 Histogram summarizing salinity data for individual type 4 L-V and type 3 L-V-H aqueous inclusions 30

Figure 2.11 Summary of melting temperatures of ice and hydrohalite in individual type 4 L-V aqueous inclusions 30

Figure 2.12 Back-scattered electron images of evaporate mounds hosted in quartz...................... 31

Figure 2.13 Ternary diagram of Ca-Na-K concentrations for evaporate mounds 32

Figure 2.14 Frequency plot for elemental concentrations detected in evaporate mounds 33

Figure 2.15 Schematic cross-section that summarizes the important geological relationships at Hoidas Lake 35

Figure 2.16 P-T diagrams that show isochoric projections for types 1 and 3 quartz-hosted fluid inclusions 40

Figure 3.1 Location of Hoidas Lake area, including location of brecciated apatite dike/vein with graphic-textured inclusions 49

Figure 3.2 Petrography of the graphic-textured inclusions 51

Figure 3.3 Ternary plots summarizing the chemistry of graphic inclusions 53

Figure 3.4 Chemical variations of the graphic-textured inclusions.. 54

Figure 3.5 Schematic diagram illustrating two possible models for the formation of graphic inclusions in apatite of the Hoidas Lake REE deposit 56

Figure 4.1 Regional lithotectonic assemblage map for parts of northern Alberta, Saskatchewan and Manitoba and contiguous Northwest Territories and Nunavut 61

Figure 4.2 Geological map of the Hoidas Lake area 62

Figure 4.3 Outcrop photographs of the distinct host rock units of the Hoidas Lake area 64

Figure 4.4 Outcrop photographs, sample photographs and photomicrographs of diopside-allanite veins from the Hoidas Lake deposit.. 68

Figure 4.5 Outcrop photographs, sample photographs and photomicrographs of apatite breccia veins from the Hoidas Lake deposit.. 70

Figure 4.6 Sample photographs, photomicrographs and back-scattered electron images of apatite breccia veins and late quartz-carbonate veins from the Hoidas Lake deposit 72

Figure 4.7 Outcrop photographs to demonstrate the abundance of hyalophane in the vicinity of the mineralized veins at Hoidas Lake 73

Figure 4.8 Chondrite-normalized REE distribution of the REE-enriched phases of the Hoidas Lake deposit 76

Figure 4.9 Back-scattered electron images of diopside-allanite vein samples 77

Figure 4.10 Composition of alkali feldspars in the diopside-allanite veins of Hoidas Lake deposit 78

Figure 4.11 Variations in average rare earth element contents among the distinct apatite generations in the Hoidas Lake deposit.. 83

Figure 4.12 Back-scattered electron images of apatite breccia samples...................................... 84

Figure 4.13 Back-scattered electron images of late allanite from the late quartz-carbonate veins 88

Figure 4.14 Graphic-textured inclusions in the apatite breccia 89

Figure 4.15 Non-graphic inclusions in the apatite breccia 90

Figure 4.16 Back-scattered electron image, X-ray element map and element profiles of complex non-graphic inclusion next to a barite crystal in apatite.. 90

Figure 4.17 Back-scattered electron images and X-ray element map of secondary vug-filling phases in apatite 91

Figure 4.18 Schematic diagram summarizing the paragenetic relationships of the Hoidas Lake REE deposit 92

Figure 4.19 Schematic cross-section of the geological relationships of the Hoidas Lake deposit 95

Figure 4.20 Trace element composition of the Hoidas Lake apatite 97

Figure 4.21 Rare earth element distributions of the REE-bearing phases of the Hoidas Lake deposit 99

Figure 4.22 Alteration of the hyalophane-bearing pegmatites 101

Figure 5.1 Regional and local geology of the Hoidas Lake REE mineralization 110

Figure 5.2 Schematic diagram summarizing the paragenetic relationships of the Hoidas Lake REE deposit 113

Figure 5.3 Photomicrographs and back-scattered electron images of zircon, titanite, green apatite and monazite crystals from the Hoidas Lake deposit 115

Figure 5.4 Complex zonation in zircon of the Hoidas Lake diopside-allanite veins 122

Figure 5.5 Conventional concordia diagrams and ^{207}Pb/^{206}Pb diagram showing the results of in situ U-Pb geochronology 124

Figure 5.6 Histogram and probability density plot of ^{207}Pb/^{206}Pb dates 132

Figure 5.7 Schematic diagram summarizing the local and regional age relationships of the Hoidas Lake mineralization 136

Figure 5.8 Hf isotopic data for the Hoidas Lake zircon grains 138

Figure 5.9 Sm-Nd isotopic data for the Hoidas Lake titanite, green apatite and monazite 141

CHAPTER 1
INTRODUCTION

1.1 Overview

Rare earth elements (REEs) are significant constituents for a number of high-technology applications, including wind power generation, hybrid cars, automotive catalytic converters, high-strength permanent magnets and visual display devices (Castor and Hedrick, 2006; Guanming et al. 2007; Walters et al. 2010; Chakhmouradian and Wall 2012; Hatch 2012), and the demand for these appliances, and thus for the REEs is expected to multiply in the future. China's continuing dominance over REE production and the global REE markets (Hedrick, 2010; Hatch, 2012) has raised concerns regarding the future of REE industry, and this resulted in increased interest for new REE resources. Therefore, scientific research on the origin and evolution of different REE mineralization styles, with the aim of expanding our knowledge on the constraints of REE mobilization and economic REE enrichment, has become essential in providing tools for future REE exploration and production.

1.1.1 The Hoidas Lake REE deposit

The Hoidas Lake deposit, located in northern Saskatchewan, Canada, is one of the most significant undeveloped LREE (light rare earth element) resources in North America with reserves of 2.6 million tonnes at 2.43% TREO (total rare earth oxides) (Pearson, 2006; Billingsley, 2010). The deposit has extremely high proportions of Nd (22% of the total REEs), which makes it a particularly important target for the permanent magnet industry for which this element is an essential component (Billingsley, 2010).

The Hoidas Lake deposit consists of multiple vein generations, emplaced along structures of the Hoidas-Nisikkatch Fault and the related regional Black Bay Fault System (Halpin, 2010). The mineralogy and chemistry of the REE-enriched veins is complex and unusual when compared to other REE deposits globally, e.g., the dominant REE-hosts are allanite and apatite, as opposed to monazite and bastnäsite which are more typical in other REE deposits. As an addition, the REE-enriched veins appear to be unrelated to the bulk of their strongly metamorphosed host rocks, and at present there is no known direct spatial or temporal relationship to a magmatic source, which hinders classification of the REE mineralization and understanding of its geodynamic position. Various authors have provided detailed field descriptions of the REE-enriched vein system, discussed its structural position within the strongly deformed Archean and Proterozoic host rocks of the southern Rae Subprovince, and proposed tentative models for its origin and emplacement (Hogarth, 1957; Harvey et al., 2002; Gunning and Card, 2005; Normand et al., 2009; Rogers 2011; Harper, 2012). Recently, the complex vein paragenesis and chemistry of the Hoidas Lake deposit was described in detail by Halpin (2010), who provided evidence for magmatic-hydrothermal origin for the REE mineralization, and proposed that the Black Bay Fault and its subsidiary, the Hoidas-Nisikkatch Fault provided the pathways for the REE-bearing fluids from an enigmatic buried magmatic body. However, the exact composition and characteristics of the hydrothermal fluids affecting the REE mineralization have not been determined and the potential source of the REE-bearing veins has not been constrained. Furthermore, the age relationships and geodynamic position of the vein system have not been studied in detail.

1.1.2 The importance of hydrothermal processes in REE mineralization

Historically, REEs were considered to be relatively immobile in hydrothermal fluids, and the main focus of REE exploration has traditionally been on deposits associated with carbonatites and alkaline intrusive complexes (e.g., Mountain Pass – Mariano 1989; Nechalacho deposit at Thor Lake – Sheard et al. 2012). However, the immobility of REEs has been argued by a number of workers, and both theoretical and experimental studies (Samson and Wood, 2005; Williams-Jones et al., 2012), and the discovery that deposits previously classified as magmatic in origin have experienced significant REE enrichment through interaction with late- to post-magmatic fluids (e.g., Strange Lake – Salvi and Williams-Jones, 1990; Nechalacho – Sheard et. al., 2012) provided evidence for hydrothermal REE mobilization, thus enhancing the general interest in hydrothermally related REE deposits.

The new models for REE mineralization take into account that REEs can be mobilized and transported in hydrothermal fluids in the form of carbonate, chloride, fluoride, sulphate, phosphate or hydroxide complexes, depending on temperature, pressure and the composition and pH of the fluid (Gieré 1996; Henderson 1996; Williams-Jones et al. 2012). Precipitation of hydrothermal rare earth minerals can be induced by a number of processes, such as changes in temperature or pressure, fluid mixing, fluid-wall-rock interaction or crystallization of gangue minerals (Gieré, 1996), and the zonation of REE-bearing mineral phases reflects these processes. It has also become apparent that hydrothermal processes can result in significant spatial fractionation of individual REEs, even within the same deposit (e.g., Bayan Obo – Smith et al., 2000). Furthermore, the magmatic-hydrothermal mobilization of REEs from their source region, via transport along available structural pathways can lead to economic REE mineralization in areas distal from their source.

Therefore, understanding the role of hydrothermal processes in the concentration of REEs to economic levels is important. However, there have only been a few detailed studies of REE deposits that are not directly related to a known magmatic source (e.g., Snowbird Deposit – Metz et al., 1985). The Hoidas Lake deposit of northern Saskatchewan is one such deposit, and the detailed study of the hydrothermal processes in this deposit is expected to add to our understanding of hydrothermal REE transportation and remobilization.

1.2 Thesis outline

The thesis is organized into six chapters. Chapter 1 provides an introduction to the thesis, including background information on magmatic and hydrothermal REE mineralization and the significance of understanding the magmatic-hydrothermal evolution, source and age relationships of the Hoidas Lake REE deposit. Chapter 1 provides the purpose and overview of the thesis, as well as the thesis organization and the main thesis objectives. The four discussion chapters (Chapters 2 to 5) each represent a separate manuscript focusing on different aspects of the project, written in peer-review publication format. Chapter 2 describes the fluid inclusion characteristics of the Hoidas Lake REE veins, obtained from microthermometry and evaporate mound analysis, and provides a model for the hydrothermal evolution of the deposit. The entirety of the chapter was recently published in the *Canadian Mineralogist* (Pandur et al., 2014), and the manuscript was reformatted for inclusion in the thesis. Chapter 3 reports on inclusions in the Hoidas Lake apatite breccia which display unique graphic textures, and discusses their implications for the nature and fine-scale processes during the evolution of the REE mineralization. This chapter was recently published in *Geology* (Pandur et al., 2015). Chapter 4 focuses on the mineral chemical characteristics of the various REE-bearing phases of the Hoidas Lake diopside-allanite veins and apatite breccia veins, in order to examine the effects of the magmatic-hydrothermal evolution of the system on the chemistry of vein-forming minerals. This chapter stems from a manuscript that was submitted for publication to *Economic Geology*. Chapter 5 reports on the results of in situ U-Pb geochronology, Lu-Hf and Sm-Nd isotopic systematics of the Hoidas Lake allanite, titanite, apatite and monazite, in order to constrain the age of the REE mineralization, as well as to provide isotopic constraints for the source of the deposit. This manuscript is in preparation for submission to *Precambrian Research*. Background information about samples and analytical techniques, as well as abbreviations used throughout the project, are provided within each respective discussion chapter. Chapter 6 discusses the relationship of individual discussion chapters to the entirety of the thesis and provides a summary of the major conclusions obtained. Appendices can be found at the end of the thesis, including additional data for fluid inclusion microthermometry and evaporate mound scanning electron microscopy coupled with energy dispersive X-ray spectroscopy (SEM-EDS), electron microprobe analyses (EMPA) and laser ablation inductively coupled plasma mass spectrometry (ICP-MS) and multi-collector inductively coupled plasma mass spectrometry (MC-ICP-MS) analyses, most of which are discussed in the four discussion chapters and are part of supplementary data files in the manuscript/publication versions.

1.3 Clarification of terms used in the thesis

The rare earth elements (REEs), as used in the thesis, denote the elements of the periodic table from La to Lu (atomic numbers from 57 to 71) and Y (atomic number: 39), according to the nomenclature of Henderson (1984). Among these, the light rare earth elements (LREEs) comprise La, Ce, Pr, Nd, Sm and Eu, and the heavy rare earth elements (HREEs) comprise Gd, Tb, Dy, Ho, Er, Tm, Yb, Lu and Y.

Pegmatite, according to London (2008), "is an essentially igneous rock, commonly of granitic composition, that is distinguished from other igneous rocks by its extremely coarse but variable grain-size, or by an abundance of crystals with skeletal, graphic, or other strongly directional growth-habits. Pegmatite occurs as sharply bounded homogeneous to zoned bodies within igneous or metamorphic host rocks". The terms "pegmatite" and "pegmatitic" in the thesis are dominantly used to describe textural features (e.g., coarse grain size of hyalophane-bearing pegmatite dikes, diopside-allanite veins and apatite breccia veins), and not to imply a genetic model. However, similarly to granitic pegmatites, the pegmatitic textures observed at the Hoidas Lake deposit indicate certain evolutionary features, like possible undercooling and rapid crystal growth, and thus the terms “pegmatitic growth” and “pegmatitic system” were used in instances in the published manuscripts (Chapter 2 and Chapter 3).

Carbonatites are igneous (intrusive or extrusive) rocks that contain more than 50% of carbonate minerals. In the thesis, the possible relation to a hidden carbonatitic source for the REE mineralization is assumed based on the chemistry and mineralogy of the diopside-allanite veins and apatite breccia veins, and the characteristics of hydrothermal fluids in the system. The statements regarding a “carbonatitic source” refer to an inferred magmatic source likely of mixed silicic-carbonatitic origin characterized by complex evolution, which resulted in the presence of early silicic diopside-allanite veins and later apatite-dominated breccia phases. Therefore, “a source with carbonatitic affinity” is used in parts of the thesis, although, in light of the information available, a definitive solution regarding the exact nature of the hidden magmatic source has not been reached yet.

1.4 Research objectives

The ultimate aim of this Ph.D. thesis is to gain a more detailed understanding of the paragenetic relationships and mineral chemical variations of the Hoidas Lake REE deposit, as well as to unravel the magmatic-hydrothermal evolution of the deposit. As an addition, in situ radiogenic isotopic studies were performed to constrain the age of the emplacement of the REE mineralization and to provide isotopic indications for the enigmatic source of the REE enriched melts and fluids. The four discussion chapters (Chapters 2 to 5) in this thesis aim to address different scientific aspects of the Hoidas Lake REE mineralization, and eventually enhance our understanding on how and when the Hoidas Lake mineralization formed, what factors controlled its emplacement, and thus to provide more insight into the late magmatic and hydrothermal processes affecting REEs. The main research aim of Manuscript I (Chapter 2) is to provide the first detailed constraints on the characteristics of hydrothermal fluids involved in the REE mineralization and determine how they evolved through time. Manuscript II (Chapter 3) documents the textural and chemical characteristics of a possibly unique set of primary graphic-textured inclusions in the apatite breccia of the Hoidas Lake mineralization, and aims to explain their formation with indications towards the nature of the REE mineralization, and to provide an understanding of fine-scale magmatic processes in apatite-rich melts. Manuscript III (Chapter 4) utilizes the properties of hydrothermal fluids present during the deposit evolution, obtained from Manuscript I, in order to evaluate the effect of hydrothermal processes on the chemical variations of the mineral phases present in the vein system. These studies were used to provide the appropriate framework for radiogenic isotope analyses, presented in Manuscript IV (Chapter 5), with the aim of constraining the age and duration of the REE mineralization, and providing isotopic tracers for the possible source of the REE mineralization.

1.5 Contributions of co-authors to the manuscripts included in the thesis

The discussion chapters (Chapters 2 to 5) were prepared in collaboration with various co-authors. The author of this thesis was the lead author in each of these manuscripts, and interpretation of the data was based on literature reviews and the author's ideas, further guided by the thesis supervisor, Kevin Ansdell. For the first manuscript (Chapter 2), the author of the thesis performed the analyses and wrote the manuscript, and Daniel Kontak and Kevin Ansdell contributed comments and suggestions. For the second manuscript (Chapter 3), electron microprobe analyses were performed by the author of the thesis, and Daniel Kontak performed the X-ray spectrometry analyses at Laurentian University. Interpretation of the data and completion of the manuscript were done by the thesis author, followed by commentary from Kevin Ansdell and Daniel Kontak. For the third manuscript (Chapter 4), Steven Creighton provided access to the facilities at the Saskatchewan Research Council, and the author of the thesis performed the electron microprobe analyses. Daniel Kontak performed the X-ray spectrometry analyses at Laurentian University. The manuscript was written by the thesis author, and commentary and suggestions were provided by Kevin Ansdell, Daniel Kontak, Kimberley Halpin and Steven Creighton. For the fourth manuscript (Chapter 5), John Hanchar and Christopher McFarlane provided access to the facilities at Memorial University and the University of New Brunswick, respectively. Analyses were performed by the author of the thesis; Christopher McFarlane and Rebecca Lam provided analytical assistance. The manuscript was completed by the author of the thesis, and Kevin Ansdell, Bruce Eglington, Charlie Harper, John Hanchar and Christopher McFarlane provided commentary.

CHAPTER 2

HYDROTHERMAL EVOLUTION IN THE HOIDAS LAKE VEIN-TYPE REE DEPOSIT, SASKATCHEWAN, CANADA: CONSTRAINTS FROM FLUID INCLUSION MICROTHERMOMETRY AND EVAPORATE MOUND ANALYSIS

The chapter is published as "Pandur, K., Kontak, D.J., and Ansdell, K.M. (2014) Hydrothermal evolution in the Hoidas Lake vein-type REE deposit, Saskatchewan, Canada: Constraints from fluid inclusion microthermometry and evaporate mound analysis. *Canadian Mineralogist* **52**, 717-744, DOI: 10.3749/canmin.1400005.", and reviews were provided by Dr. Iain Samson and Dr. Stefano Salvi.

2.1 Abstract

The Hoidas Lake rare earth element (REE) deposit, located in northern Saskatchewan, Canada, is a structurally controlled vein-type LREE deposit with allanite-(Ce) and fluorapatite as the main REE carriers. The mineralized veins cut Archean and Paleoproterozoic orthogneisses and supracrustal rocks of the southern Rae Subprovince. The paragenesis includes hyalophane-bearing pegmatite dikes, REE-mineralized allanite-, diopside-, hornblende-, hyalophane- and titanite-bearing veins and later breccia veins that contain several stages of apatite. The mineralized veins record hydrothermal alteration with nucleation of monazite and REE-carbonate inclusions in apatite and allanite, respectively. Barren quartz-, carbonate- and hematite-rich veins represent the latest stage of hydrothermal activity. Samples from the hyalophane-bearing pegmatites, apatite breccia veins and quartz-carbonate veins, used for fluid inclusion petrography and microthermometry, indicate four distinct fluid inclusion assemblages (FIAs): (1) carbonic inclusions showing L_{CO2} (liquid CO_2) + V_{CO2} (CO_2 vapor) phase composition with 20-40 vol.% V_{CO2} at 0°C; (2) aqueous inclusions showing L (liquid H_2O) + V (H_2O vapor) phase composition with 90-100 vol.% V at 20°C; (3) aqueous inclusions showing L + V + H (halite) phase composition with 15 vol.% V at 20°C; and (4) aqueous L + V inclusions with 15-20 vol.% V at 20°C. Type 1 inclusions homogenize to liquid CO_2 with Th(CO_2) from 3.3° to 30.5°C. Type 2 V-rich inclusions have high salinities and contain salts other than NaCl. Type 3 L-V-H inclusions have different homogenization behavior in quartz of the hyalophane-bearing pegmatites (L+V+H

→ L+V → L) compared to quartz-carbonate veins (L+V+H → L+H → L), and Th (total homogenization) values range from 180 to 315°C with salinities of 30-40 wt.% eq. NaCl. In type 4 inclusions Th ranges from 90° to 290°C, but for specific samples and FIAs (fluid inclusion assemblages) there is a more limited spread (from 5° to 25°C). Salinities range from 8 to 24 wt.% eq. NaCl, and the inclusions have variable Na/(Na+Ca). Evaporate mound analysis shows average normalized (to 100%) cation contents of 48% Na, 24% Ca, 6% K, 5% Ba, 4% Mn, 2% Fe, 2% Mg, 9% Sr for quartz-hosted inclusions in quartz-carbonate veins and 61% Na, 32% Ca, 7% K for quartz-hosted inclusions in hyalophane-bearing pegmatite dikes. The thermometric and chemical data suggest that evolution of the Hoidas Lake mineralization involved two fluid types with early entrapment of a carbonic fluid followed by introduction of a mixed Na-Ca-K-(Ba-Mn-Mg-Fe-Sr) aqueous fluid with variable salinities that was responsible for the late alteration of the mineralized veins. Furthermore, the inclusion data provide constraints on entrapment temperature (<310°C) and also indicate that pressure was transient (0.5 to 2 kbars) based on the homogenization temperature data for the carbonic (type 1) and aqueous L-V-H (type 3) inclusions.

2.2 Introduction

Rare earth elements (REEs) are significant constituents for a number of high-technology applications, including automotive catalytic converters, hybrid cars, wind power generation, high-strength permanent magnets, and visual display devices, the demand for which is expected to increase in the future (Castor and Hedrick, 2006; Guanming et al., 2007; Walters et al., 2010; Chakhmouradian and Wall, 2012; Hatch, 2012).

The main focus of REE exploration has traditionally been on deposits associated with carbonatites and alkaline intrusive complexes (e.g., Mountain Pass – Mariano, 1989; Nechalacho deposit at Thor Lake – Sheard et al., 2012), because the REEs have generally been considered to be relatively immobile in hydrothermal fluids. However, there has been renewed interest in hydrothermally related REE mineralization, as many deposits originally thought to be magmatic are now considered to be of hybrid origin, due to significant upgrading of the REEs related to interaction with late- to post-magmatic fluids (Salvi and Williams-Jones, 2005; Samson and Wood, 2005; Sheard et al., 2012; Williams-Jones et al., 2012). This latter model now accommodates the fact that REEs can be mobilized and transported in hydrothermal fluids in the form of carbonate, chloride, fluoride, sulphate, phosphate or hydroxide complexes, depending on temperature, pressure and the composition and pH of the fluid (Gieré, 1996; Henderson, 1996; Williams-Jones et al., 2012). Precipitation of hydrothermal rare earth minerals can be induced by a number of processes, such as changes in temperature or pressure, fluid mixing, fluid-wall-rock interaction or crystallization of gangue minerals (Gieré, 1996), and these processes can be reflected by zoning of REE-bearing mineral phases.

The potential importance of REE mobility in hydrothermal processes is supported by recent experimental research (Williams-Jones et al., 2012) and studies of magmatic REE deposits that were subsequently affected by hydrothermal processes (e.g., Sheard et al., 2012). However, there have only been a few detailed studies of hydrothermal REE deposits that are not directly related to a known magmatic source. The Hoidas Lake deposit of northern Saskatchewan is one such deposit and, like other REE deposits, represents an example of complex REE mineralization. Our detailed study of the hydrothermal processes in this deposit is expected to add to our understanding of hydrothermal REE transportation and remobilization.

The Hoidas Lake deposit, located 56 kilometers northeast of Uranium City in Saskatchewan, Canada, consists of a ca. 8 km long, light rare earth element (LREE)-enriched mineralized trend along Hoidas Lake and Nisikkatch Lake. The deposit is one of the most significant undeveloped LREE resources in North America, with an indicated resource of 2.6 million tonnes of 2.43 wt.% total rare earth oxides (TREOs), with extremely high proportions of Nd (22% of the total REEs), which makes it a particularly important target for the permanent magnet industry for which this element is an essential component (Billingsley, 2010). A magmatic-hydrothermal origin for this REE mineralization is suggested by Halpin (2010), however, the nature and origin of the causative fluids remain uncertain. Thus, the aims of this study are to provide more insight into the hydrothermal processes affecting REE enrichment in this system through a detailed fluid inclusion study which incorporates fluid inclusion petrography, microthermometry and SEM-EDS analysis of evaporate mounds. This work complements our detailed mineralogical and mineral chemical data obtained on the same samples (Pandur et al., 2013a, b) which are incorporated into the discussion of the results of the fluid inclusion work to further advance our understanding of the genesis of the Hoidas Lake REE deposit.

2.3 Geological setting

2.3.1 Regional geology

The Hoidas Lake area is located in the southern Rae Subprovince, which is part of the northwestern Churchill Province of the Canadian Precambrian Shield (Fig. 2.1a). The Rae Subprovince extends from the Taltson-Thelon Orogen in the west to the Snowbird tectonic zone (Baldwin et al., 2003; Flowers et al., 2006) in the east, which separates the Rae Subprovince from the Hearne Subprovince. The Rae and Hearne subprovinces formed the central area to which the Slave and Superior cratons were welded during the assembly of Laurentia (Hoffman, 1988; Aspler et al., 2002).

In northern Saskatchewan, the Rae Subprovince consists mainly of Archean granite-greenstone belts that are overlain by supracrustal units, the oldest of which is the Murmac Bay Group (Hartlaub et al., 2005; Ashton et al., 2009). The Archean units are overprinted by the 2.4 to 2.26 Ga Arrowsmith Orogen, which was accompanied by extensive arc magmatism along the western margin of the Rae Subprovince (Berman et al., 2005), and was largely obscured by younger thermo-tectonic episodes (Hartlaub et al., 2007). On its northwestern margin the Rae Subprovince is separated from the Slave Craton by the Taltson-Thelon Orogen which consists of the Thelon Orogen, the Great Slave Lake Shear Zone and the Taltson Magmatic Zone from northeast to southwest. These zones were formed by a 2.0 to 1.9 Ga subduction system which evolved into a collisional orogen (McNicoll et al., 2000; Ross, 2002; Ross and Eaton, 2002), and resulted in peak metamorphic conditions up to granulite grade in the Rae Subprovince (Grover et al., 1997). To the east the Churchill Province is separated from the Superior Craton by the 1.92 to 1.83 Ga Trans-Hudson Orogen which formed as a result of the collision between the Churchill and Superior provinces (Hoffman, 1988; Ansdell, 2005). The evolution of the Taltson-Thelon and the Trans-Hudson orogens resulted in intensive Paleoproterozoic reworking of the Archean rocks of the Rae Subprovince, including the development of numerous supracrustal units that often contain volcanic successions. Several lamprophyre dike suites were emplaced during this time along structures (Peterson et al., 2002).

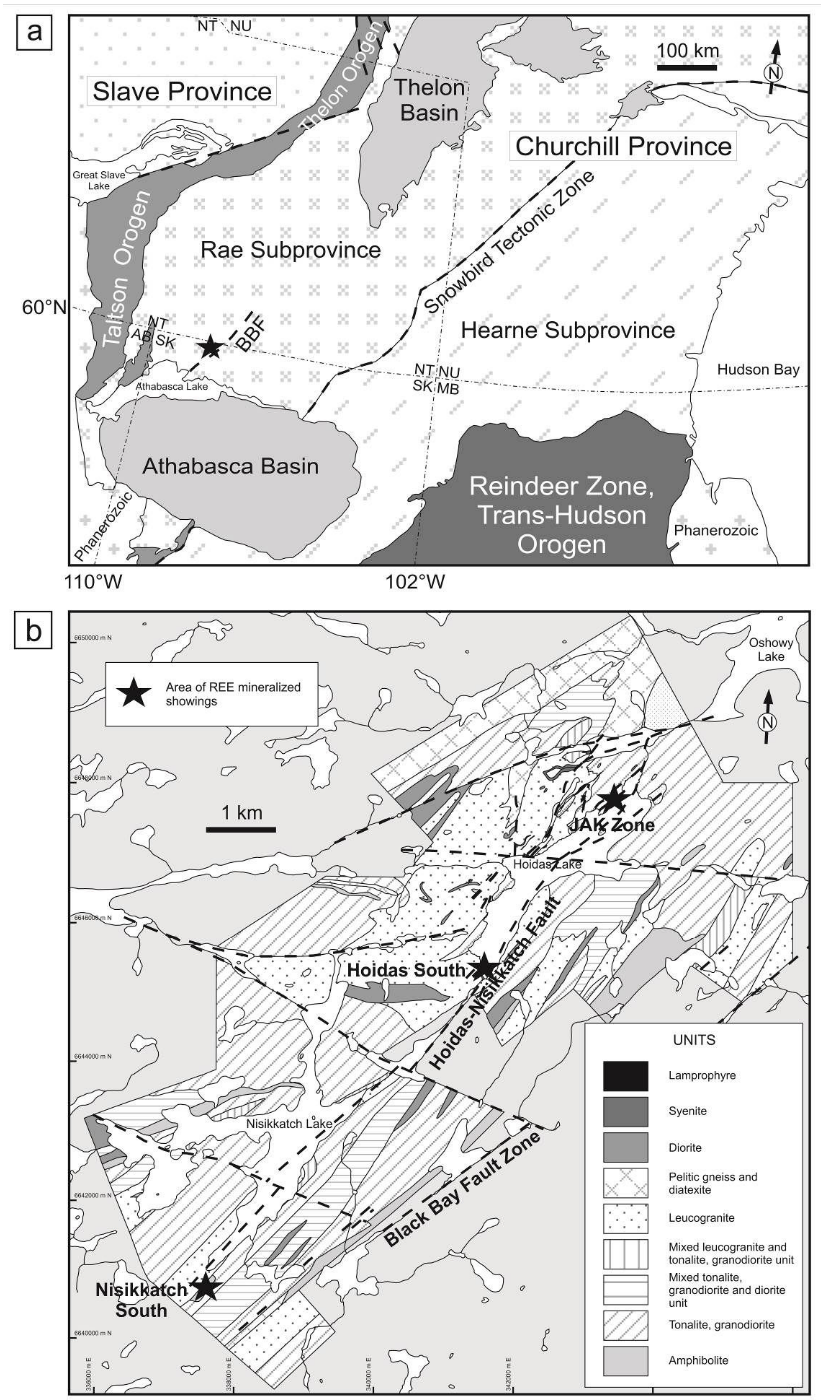

Figure 2.1 Maps showing the regional geology and location of the Hoidas Lake REE deposit. (a) Regional lithotectonic assemblage map for parts of northern Saskatchewan and Alberta and contiguous Northwest Territories and Nunavut and location of the Hoidas Lake REE deposit denoted by a black star (modified from Ashton et al., 2012), BBF = Black Bay Fault. (b) Local geology map of the Hoidas Lake area, showing the dominant lithological and structural units, and the location of the main mineralized showings (modified from Normand et al., 2009; Harper, 2012). UTM N and E coordinates denote the location of the area in the UTM 13V zone. The faults are represented by dashed lines on the maps.

A major structural unit of the southern Rae Subprovince is the Black Bay Fault (Fig. 2.1a), a northeast-trending, brittle-ductile structure with a prolonged and complex deformational history (Gunning and Card, 2005). The fault is superimposed on a belt of mylonitic gneisses named the "Black Bay Shear Zone" (Kraus and Ashton, 2000). Although the exact timing of the movement along the Black Bay Shear Zone is not well constrained, the entire deformation history is believed to have occurred between 2.3 and 1.7 Ga (Bergeron, 2001).

2.3.2 Local geology

The dominant host rock units in the Hoidas Lake area are Archean tonalitic to granodioritic gneisses containing amphibolite and diorite xenoliths, and Archean to Paleoproterozoic granitic gneisses (Harvey et al., 2002; Gunning and Card, 2005; Normand et al., 2009; Fig. 2.1b). Abundant pelitic gneisses are invaded by pink leucogranite sheets (Harper, 2012). Late intrusive bodies include syenite, diorite and mafic-ultramafic (amphibolite, gabbro, pyroxenite) dikes (Harvey et al., 2002; Normand et al., 2009; Fig. 2.1b). All these rocks were metamorphosed to upper amphibolite-lower granulite grade at approximately 1.9 Ga (Harvey et al., 2002; Gunning and Card, 2005; Ashton et al., 2009). Small intrusions of granitic pegmatite, likely of different ages, occur either as dikes or amoeboid bodies. Some of these pegmatitic bodies contain abundant hyalophane, and appear to postdate peak metamorphism. The youngest magmatic phase in the area is a suite of undeformed lamprophyre dikes that postdate peak metamorphism (Normand et al., 2009).

Multiple deformation stages are recognized in the area (Harvey et al., 2002; Gunning and Card, 2005; Normand et al., 2009; Harper, 2012). The D1 and D2 events resulted in a northwest-southeast-oriented composite S1-S2 foliation, and peak metamorphism occurred at this time. The D3 deformation resulted in formation of a northeast-southwest-trending S3 foliation which is heterogeneous in the area, with increasing levels of strain from northwest to southeast towards the Black Bay Fault. Kinematic indicators suggest dextral movement in the ductile shear zones, consistent with previous findings that there was early dextral ductile movement along the Black Bay Shear Zone (Ashton et al., 2001). The D4 deformation is expressed as gently undulating open folds with north-northwest-oriented steeply dipping axial planes. Late fractures and faults can be observed in east, northeast and southeast directions. Overall, the mineralized veins, described in more detail below, are spatially associated with the northeast-southwest oriented Hoidas-Nisikkatch Fault (Fig. 2.1b), which is parallel to, and likely shares the complex deformation history of, the Black Bay Fault, including several periods of reactivation and deformation (Halpin, 2010).

2.3.3 Mineralogy, REE mineralization and paragenesis of the Hoidas Lake vein system

The Hoidas Lake vein system consists of hyalophane-bearing pegmatites, diopside-allanite veins, apatite breccia veins and quartz-carbonate veins. The main mineralized zones of the Hoidas Lake deposit are emplaced along northeast-trending faults and fractures. The veins are characterized by anastomosing geometry and vary from 1 to 11 m width, but average around 3 m. The drilling programs of Great Western Minerals Group showed that the vein system continues to at least 300 m depth and is open both down dip and along strike (Halpin, 2010).

The hyalophane-bearing pegmatite bodies include dikes with sharp margins (Fig. 2.2a, b) and amoeboid pods that show diffuse contacts towards the host rocks. In some cases irregular, patchy clusters of hyalophane crystals (1-10 cm) can be observed in the host rocks, in the vicinity of hyalophane-bearing pegmatite dikes. The dikes contain quartz, hyalophane, K-feldspar, and lesser diopside, hornblende and magnetite. In most of the hyalophane-bearing pegmatites the hyalophane crystals are strongly altered and transformed into K-feldspar along the margins and clusters of barite appear along the contact between the hyalophane and K-feldspar (Fig. 2.2c). In the most altered hyalophane-bearing pegmatites albite replaces hyalophane and K-feldspar, and rare anhedral allanite crystals appear.

The diopside-allanite veins generally cross-cut the hyalophane-bearing pegmatites (Fig. 2.2a), but in some cases they are also cross-cut by hyalophane-bearing pegmatite dikes (Fig 2.2b). The contacts of the diopside-allanite veins with the surrounding host rocks are either sharp or diffuse. In the latter case the diopside-allanite veins are surrounded by a <25 cm thick monomineralic hyalophane-rich pegmatitic rim (Fig. 2.2d). The diopside-allanite veins are typically coarse grained (up to 10-30 cm), and the main REE carrier, allanite, occurs in variable amount, from a few percent to almost 100% in massive allanite-dominant intervals. The allanite crystals are generally anhedral to subhedral, and vary in color from black through brown and yellowish brown to red (Fig. 2.2e). They display irregular or concentric color zonation, and the cores are metamict and isotropic (Fig. 2.2f), whereas the rims can sometimes show optical properties similar to those of epidote. Subhedral to euhedral large (up to 1 cm) titanite crystals are found intergrown with allanite, forming irregular masses in the diopside-allanite veins. Some of the smaller titanite crystals show concentric color zonation. Hyalophane is abundant in the diopside-allanite veins, generally in the interstitial space between the allanite and titanite grains, but often in the outermost zones where coarse hyalophane crystals are intergrown with diopside. Allanite and diopside are also locally intergrown with dark red apatite and zircon. Less commonly, calcite, epidote and scapolite also appear in the veins, and coarse-grained irregular biotite-rich intervals also occur inside the veins. The allanite crystals are replaced by a mixture of REE-carbonates (Fig. 2.2f), REE-Sr-carbonates and chlorite in the crystal cores and along fractures. Hornblende replaces diopside in the veins. Brecciation of this vein generation is not common, but occurs locally, and sub-angular up to 10 cm clasts of the hyalophane-rich pegmatitic rims, and diopside and allanite can be observed in the apatite breccia phase.

The apatite breccia veins commonly appear as irregularly shaped intervals within diopside-allanite veins, with relatively sharp (Fig. 2.2g) or brecciated contacts between them. The breccia ranges from clast-supported to matrix-supported, and contains sub-angular to rounded apatite grains of variable size (up to 6 cm). Three dominant apatite generations were discovered: red apatite breccia (Fig. 2.2h), green apatite breccia (Fig. 2.2h) and a coarse red apatite phase. The contacts between the individual apatite breccia generations are commonly gradational and subtle (Fig. 2.2h). The red apatite phase is volumetrically the most significant portion of all the vein generations. The apatite crystals of this phase are dull red in color and strongly enriched in solid inclusions, particularly in the crystal cores. Most of these inclusions are finely dispersed hematite, and hematite also occurs along fracture planes in the apatite grains. Green apatite rims around the red apatite and small green apatite crystals in the matrix of the red apatite breccia are common. The apatite crystals of the green apatite breccia phase are clear, show a lustrous green color, and they contain fewer hematite inclusions. The late coarse red apatite phase is not brecciated, although the apatite crystals are fractured with the resulting fragments not rotated relative to each other. In all of the apatite breccia generations (especially the red apatite breccia) there are abundant monazite inclusions in the apatite crystals. These monazite crystals occur in irregular disseminated masses in the apatite crystals or along secondary fractures that cross-cut the apatite breccia, and in some cases also along grain boundaries in the fine-grained apatite in the matrix. Rare thorite inclusions can also be observed in the apatite crystals, surrounded by radial fractures. The matrix of all the apatite breccia phases consists of fine-grained apatite, lesser calcite, quartz (Fig. 2.2i) and hornblende, and in some cases chlorite, minor amounts of REE-carbonates and monazite, and sub-angular clasts of allanite, diopside and hyalophane. Very coarse-grained biotite (up to 5 cm), similar to the biotite of the diopside-allanite veins, can form up to 30 cm wide margins around the apatite breccia veins.

Quartz-rich, and calcite-, epidote-, chlorite- and hematite-containing veins cross-cut the mineralized diopside-allanite veins and apatite breccia veins. In some of these 2-3 mm wide calcite-rich veins that cross-cut the red apatite breccia (Fig. 2.2j), late euhedral allanite crystals (<5 mm) were observed. These allanite crystals exhibit oscillatory zonation in their cores with irregularly zoned margins.

Figure 2.2 (on next page) Photographs, photomicrographs and back-scattered electron (BSE) images of samples from the Hoidas Lake REE deposit showing the mineral paragenesis. (a) Hyalophane-bearing pegmatite dike of 3-4 cm width cross-cut by diopside-allanite vein, that in turn is cross-cut by a lamprophyre dike of similar orientation in granite, Di-Aln vein = diopside-allanite vein, Hy peg = hyalophane-bearing pegmatite. (b) Hyalophane-bearing pegmatite dike cross-cutting diopside-allanite vein in granite, Di-Aln vein = diopside-allanite vein, Hy peg = hyalophane-bearing pegmatite. (c) BSE image showing early hyalophane that is replaced along its border by Ba-containing K-feldspar ($Or_{89-90}Ab_{11-10}$ composition from EMPA data) and then replaced by albite. Note the presence of fine-grained disseminated barite at the contact between the hyalophane and the K-feldspar which likely formed due to the reaction of a S-bearing fluid with the hyalophane. (d) Outcrop photograph showing a diopside-allanite vein surrounded by a hyalophane-rich pegmatitic rim that shows diffuse contact towards the host granite, Di-Aln vein = diopside-allanite vein. (e) Strongly altered diopside-allanite vein sample with irregularly shaped large allanite crystal that shows concentric zonation, and the outer zone encompasses zircon and titanite crystals. (f) Thin section photomicrograph (cross polarized light) of close-up of area in green rectangle in (e), showing allanite crystal with clear rim and metamictized isotropic core, that encompasses late REE-carbonate, and is surrounded by strongly altered and fractured diopside. (g) Outcrop photograph showing an irregularly shaped red apatite breccia vein that formed by reopening of a former diopside-allanite vein, the remnants of which can be observed at the margin, Di-Aln vein = diopside-allanite vein. (h) Sample of red apatite breccia with gradational contacts towards green apatite breccia intervals, and calcite filling the vugs in the breccia and encompassing breccia clasts. (i) Thin section photomicrograph (cross polarized light) of fine-grained apatite, quartz, calcite and monazite crystals in the matrix of the green apatite breccia. (j) Coarse red apatite vein sample cross-cut by calcite veins that contain euhedral allanite crystals.

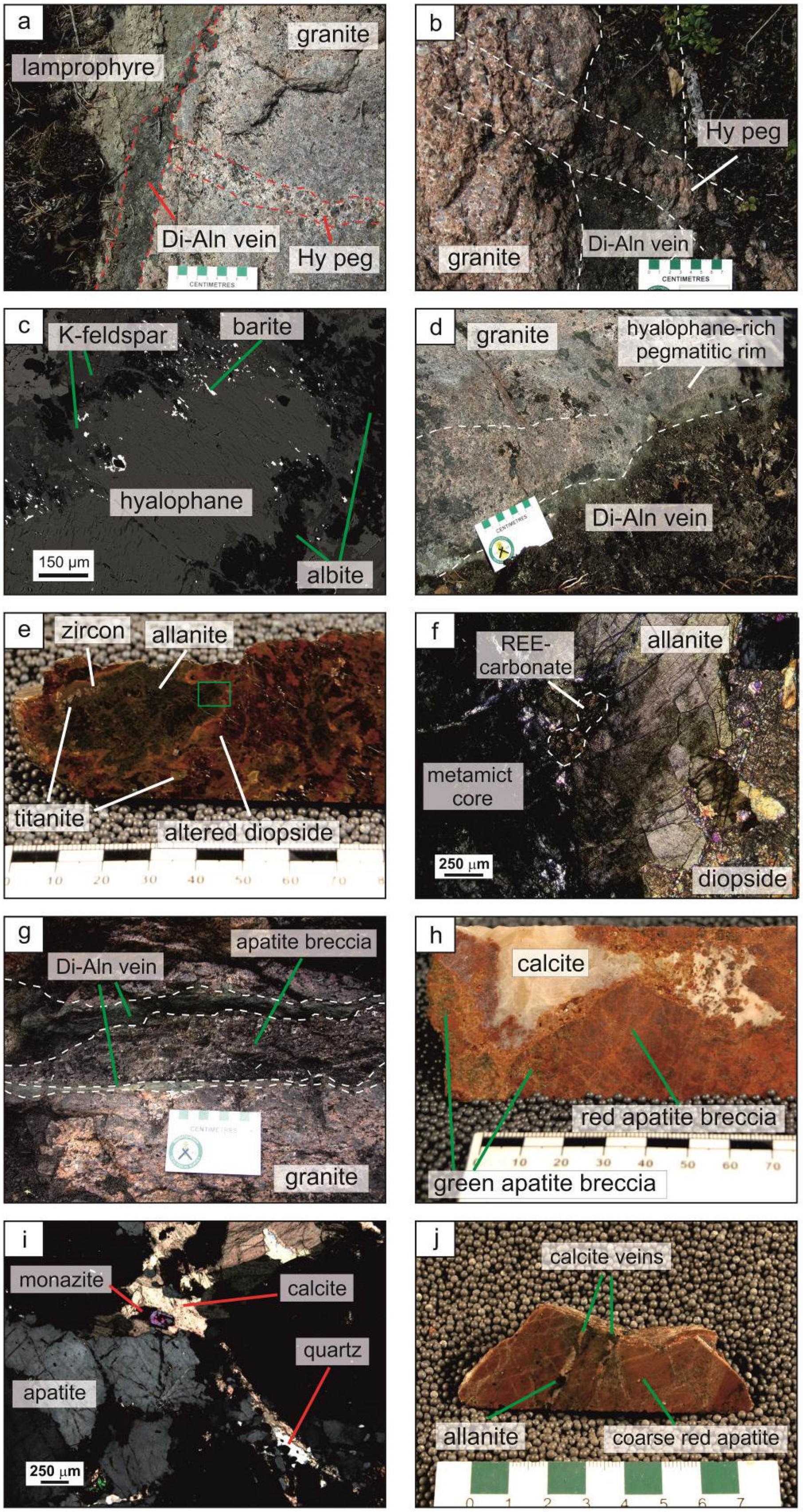
a
lamprophyre
granite
Di-Aln vein
Hy peg
CENTIMETRES
b
Hy peg
granite
Di-Aln vein
CENTIMETRES
c
K-feldspar
barite
hyalophane
150 μm
albite
d
granite
hyalophane-rich pegmatitic rim
Di-Aln vein
CENTIMETRES
e
zircon
allanite
titanite
altered diopside
10 20 30 40 50 60 70
f
REE-carbonate
allanite
metamict core
250 μm
diopside
g
Di-Aln vein
apatite breccia
CENTIMETRES
granite
h
calcite
red apatite breccia
green apatite breccia
10 20 30 40 50 60 70
i
monazite
calcite
quartz
apatite
250 μm
j
calcite veins
allanite
coarse red apatite
0 1 2 3 4 5 6 7

The paragenetic relationships of the Hoidas Lake vein system, including the hyalophane-bearing pegmatite dikes, the diopside-allanite veins, apatite breccia veins and quartz-carbonate veins, are summarized in Figure 2.3, to complement the description of these vein phases. The emplacement of hyalophane-bearing pegmatites likely occurred through multiple events, as identical hyalophane-bearing pegmatite dikes are cross-cut by, and cross-cut the diopside-allanite veins. This, as well as the common occurrence of hyalophane in pegmatitic rims around the diopside-allanite veins and in the diopside-allanite veins and the occurrence of allanite in the hyalophane-bearing pegmatites themselves, suggests that the emplacement of the hyalophane-bearing pegmatites and diopside-allanite veins likely overlapped in time. Furthermore, the hyalophane-bearing pegmatites are the only rock unit in the Hoidas Lake area that show elevated bulk Sr (up to 3500 ppm), Ba (up to 5000 ppm) and REE (up to 1200 ppm) contents, which are similar to the values observed in the diopside-allanite and apatite breccia veins (Halpin, 2010). The secondary phases in the hyalophane-bearing pegmatite dikes (K-feldspar, barite, albite and allanite) appear in greater abundance in the dikes that are in the immediate vicinity of the diopside-allanite and apatite breccia veins. These likely reflect alteration of the hyalophane-bearing pegmatites by interaction with the melts/fluids responsible for the formation of the mineralized diopside-allanite veins and the apatite breccia veins. The diopside-allanite veins were also likely emplaced in multiple stages, as they are sometimes zoned from hyalophane-diopside-rich zones, through diopside-rich zones with minor allanite, to allanite-rich internal zones. The diopside-allanite veins also show the effect of hydrothermal alteration that resulted in precipitation of chlorite and REE-carbonate phases. The emplacement of the various apatite breccia veins is related to reopening of the older structures that hosted the diopside-allanite veins, which explains the presence of apatite breccia intervals inside larger diopside-allanite veins and the common occurrence of diopside-allanite vein clasts in the apatite breccia. The oldest red apatite breccia phase was followed by green apatite breccia, and the latest phase in these veins is a coarse red apatite. All of the distinct apatite zones rarely appear together in the same vein. The presence of green apatite rims around the red apatite and small green apatite crystals in the matrix of the red apatite breccia indicate an overlap between these generations. The apatite breccia veins also reflect the effect of hydrothermal alteration which resulted in hematite and monazite precipitation. The quartz-, carbonate- and chlorite-filled intervals in the matrix surround resorbed apatite grains, indicating that these interstitial phases precipitated from hydrothermal fluids that infiltrated the apatite breccia. The late quartz-carbonate veins likely represent a hydrothermal event that affected the area, and this event might be responsible for the alteration of the hyalophane-bearing pegmatites, diopside-allanite veins and apatite breccia veins. The presence of allanite in the quartz-carbonate veins might indicate hydrothermal mobilization of the REEs.

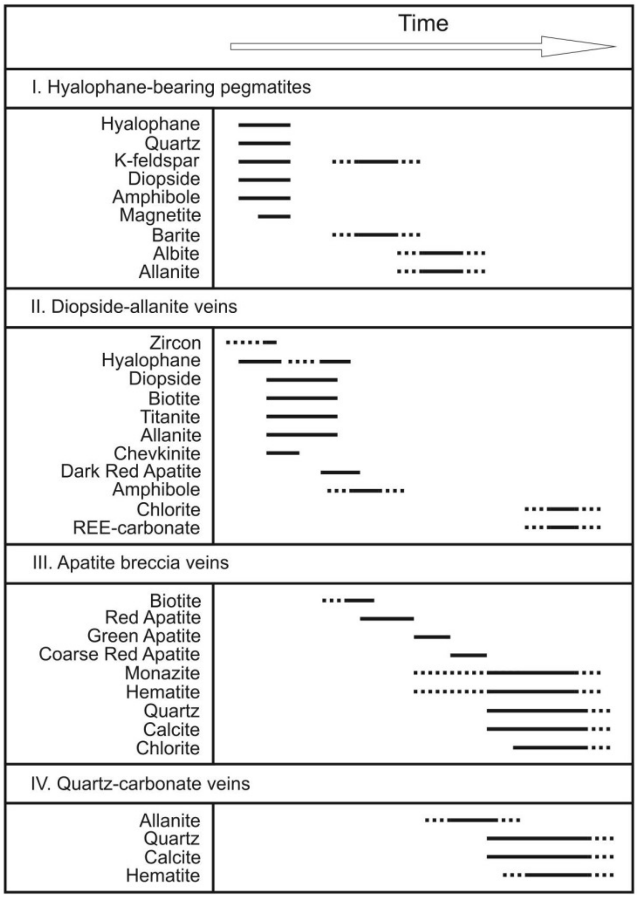

Figure 2.3 A composite mineral paragenesis for the different vein types (i.e., hyalophane-bearing pegmatite, diopside-allanite vein, apatite breccia vein, quartz-carbonate vein) of the Hoidas Lake rare earth element deposit (modified from Halpin, 2010). See the text for a detailed discussion of the mineral paragenesis.

In the diopside-allanite veins and apatite breccia veins there are multiple indications for both magmatic origin (e.g., complex mineralogy of the diopside-allanite veins, presence of primary melt inclusions in the apatite breccia, as discussed below) and hydrothermal origin (e.g., sharp contacts between different phases, brecciation, presence of hydrothermal REE-bearing phases). These REE-enriched veins most probably represent a transition between magmatic/pegmatitic and hydrothermal systems (see the discussion below). Therefore, the term ‘vein’ in the case of the diopside-allanite veins and apatite breccia veins is not used in the strict sense of the word, indicating a solely hydrothermal origin.

The REE-enriched veins were emplaced sub-parallel to the S3 foliation and the Hoidas-Nisikkatch Fault. The veins are variably affected by the heterogeneously developed D3 event, but cross-cut the composite S1-S2 foliation (Harvey et al., 2002; Normand et al., 2009). Thus, the mineralization is younger than the high-grade metamorphism in the region (1.911 to 1.903 Ga; Ashton et al., 2009). Monazite crystals from the apatite breccia yield a U-Pb age of ca. 1870 Ma (SHRIMP age, reported in Gunning and Card, 2005), whereas zircon crystals from the diopside-allanite veins gave U-Pb ages ranging from about 2380 Ma to 2290 Ma (reported in Normand, 2010). The geological relationships suggest that these zircon crystals must be inherited. An ongoing study by the authors (Chapter 5) is aiming to determine the absolute age and duration of the REE mineralizing system.

2.4 Sampling and analytical procedures

Samples were collected from surface exposures of the Hoidas Lake deposit and drill core from the drilling programs of Great Western Minerals Group. For the fluid inclusion petrography, forty-five doubly polished thick sections (200-250 μm) were prepared at the University of Saskatchewan. These were studied in transmitted light using an Olympus BX 51 microscope equipped with a Lumenera Infinity 2 camera at the University of Saskatchewan, Department of Geological Sciences. Detailed fluid inclusion petrography of quartz crystals from hyalophane-bearing pegmatites, apatite, quartz and carbonate crystals from apatite breccia veins, and quartz and carbonate crystals from quartz-carbonate veins was carried out. The early diopside-allanite veins do not contain mineral phases transparent enough for detailed petrographic study of fluid inclusions. Inclusion populations within sections were classified following Roedder’s rules (1979; in Goldstein, 2003). Based on examination of these samples, a subset of material was selected for detailed fluid inclusion thermometric study: one sample of the hyalophane-bearing pegmatite adjacent to mineralization, one sample of the hyalophane-bearing pegmatite distal to the mineralization, three red apatite breccia samples, one green apatite breccia and one coarse red apatite sample, and two samples of quartz-carbonate veins. These samples were then dismounted by immersion in acetone with subsequent washing with acetone and polishing on paper if needed, to remove any residual epoxy.

Fluid inclusion microthermometry was carried out on nine samples in the Fluid Inclusion Laboratory of the Department of Earth Sciences at Laurentian University. Areas containing fluid inclusions with similar phase proportions and located within fluid inclusion assemblages (FIAs; Goldstein and Reynolds, 1994) were selected for microthermometry. Heating and cooling of the inclusions was performed on a Linkam TMS600 heating-freezing stage attached to an Olympus BX 51 microscope equipped with a QImaging MicroPublisher 5.0 RTV camera. Calibration of the stage was monitored using synthetic fluid inclusions for pure CO_2 (Tm(CO_2) at -56.6°C), pure water (Tm(ice) at 0°C), and critical point of water (Tc(H_2O) at 374°C). Repeat measurements of these provide an accuracy of 0.1°C for Tm(CO_2) and Tm(ice) and 2°C for Tc(H_2O). The temperature limits of the stage are -200°C and 600°C. Measurements of fluid inclusion phase changes were made within FIAs (a total of fifty-four FIAs) and included final ice melting (Tm(ice)), dissolution of halite (Th(H)), homogenization of V (Th(L-V)) and total homogenization temperature (Th) for aqueous inclusions, and CO_2 melting (Tm(CO_2)), CO_2 homogenization (Th(CO_2)) and clathrate melting (Tm(clath)) for carbonic inclusions. The fluid inclusion studies provided constraints on the characteristics of the hydrothermal fluids present in the system (temperature, pressure of entrapment and composition of hydrothermal fluids). Salinity calculations for aqueous inclusions were based on the equations of Bodnar (2003) and Steele-MacInnis et al. (2012).

Analysis of evaporate salt mounds was carried out according to the method of Kontak (2004), in order to define fluid compositions. The term ‘evaporate’ analysis was suggested by Roedder and Bodnar (1997), and the term ‘mound’ is used to indicate what is being analyzed. Three samples of quartz chips hosting an abundance of all inclusion types from hyalophane-bearing pegmatites and quartz-carbonate veins were selected for this aspect of the study. The apatite breccia veins were not used for evaporate mound analysis because in the host apatite crystals there would have been interference with the Ca and Sr using the SEM-EDS analysis, and in the quartz and calcite in the matrix the studied fluid inclusions were small and much less abundant, and consequently, there would have been no evaporate mounds large enough for analysis. The fluid inclusions in the studied quartz chips were heated at 65°C/min to about 450°C to induce decrepitation. Following carbon coating of the quartz chips, the evaporate mounds were examined using a JEOL 6400 scanning electron microscope (SEM) equipped with back-scattered detector and an INCA Energy-Dispersive X-ray Spectrometer (EDS) at Laurentian University. The operating conditions were 10 s counting time, 20 kV accelerating voltage, and a 1.00 nA beam current. Mound analyses were done using raster mode in order to guarantee homogeneity of analysis and several mounds per area were analyzed to check for uniformity. The results were normalized (to 100%) free of SiO_2 from the substrate, and data are presented in a ternary plot of major cations (Na, K, Ca).

2.5 Analytical results

2.5.1 Fluid inclusion petrography: types of inclusions and timing of entrapment

In the early diopside-allanite veins, due to the lack of transparent mineral phases, only some observations could be made. A few barely visible fluid inclusions (<10 μm) occur along secondary planes in titanite crystals, and the titanite appears to be altered around these inclusions.

In the hyalophane-bearing pegmatites, the different apatite breccia phases and the quartz-carbonate veins four distinct types of carbonic and aqueous FIAs are present in the studied samples and are described below. Type 1 are carbonic fluid inclusions that have equant to elongate shapes, range from 3 to 35 μm in diameter, and are mono-phase at room temperature (20-25°C), thus they were examined at 0°C where they have L_{CO2}-V_{CO2} (liquid CO_2 + CO_2 vapor) phase composition with 20-40 vol.% V_{CO2} (Fig. 2.4a). Some of these type 1 inclusions contain up to 15 vol.% liquid H_2O, restricted to certain areas in the host quartz crystals (as discussed later in this chapter) (Fig. 2.4b). Type 2 are vapor-rich aqueous inclusions that have round to irregular shapes, are <50 μm in size, and at room temperature have L-V (liquid H_2O + H_2O vapor) phase composition with 90-100 vol.% V (Fig. 2.4c). The variability of observed phase proportions in some of these FIAs might be due to the morphology of the inclusions, or might suggest that in some cases necking of inclusions occurred. Type 3 are aqueous L-V-H (L + V + halite) inclusions that are <15 μm in diameter. At room temperature these inclusions have approximately 15 vol.% V and halite (a transparent cubic solid phase that and reacts to form hydrohalite upon freezing and reheating) occupies around 10-15% of the inclusion (Fig. 2.4d).

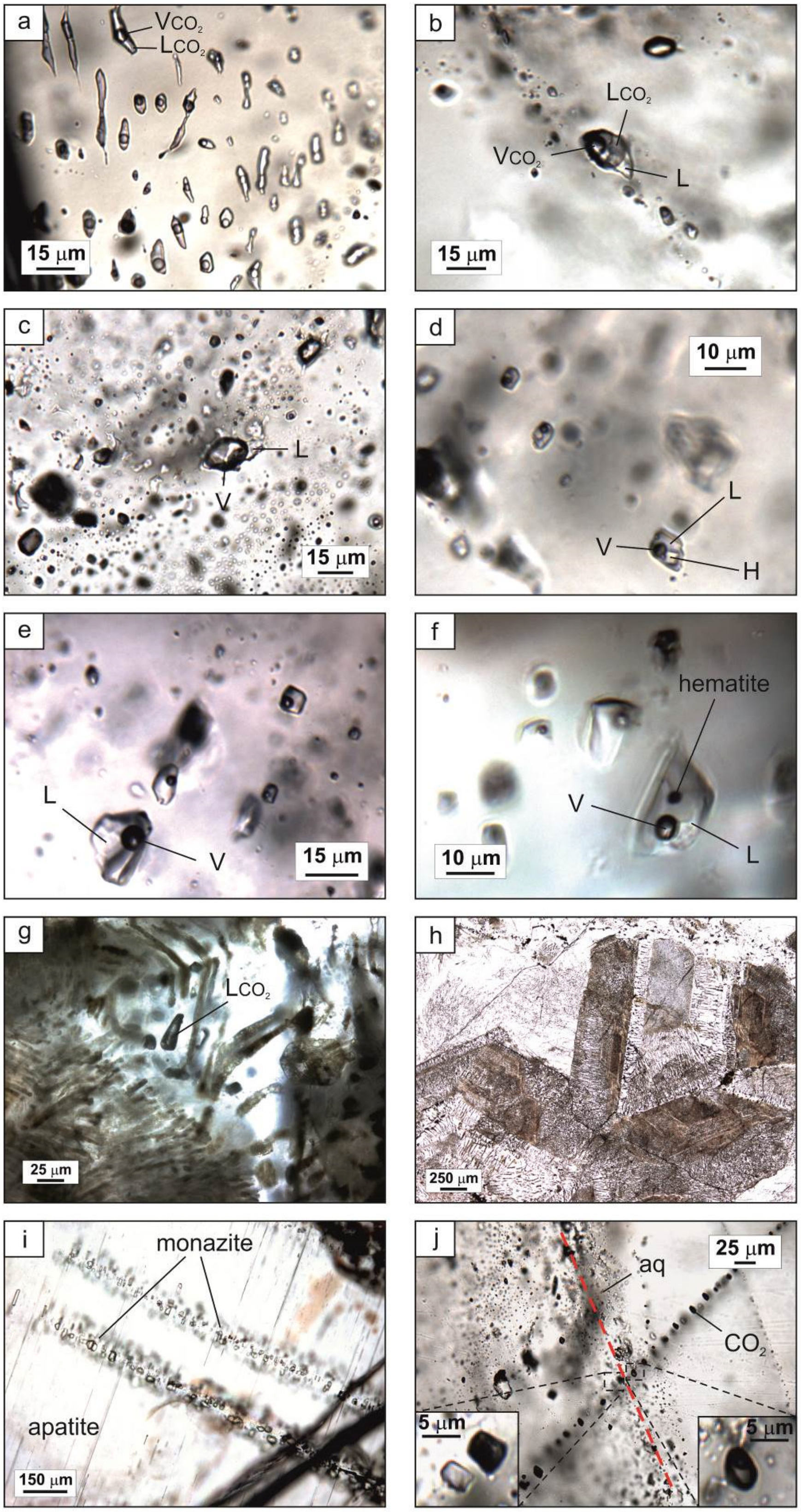
a
VCO₂
LCO₂
15 µm
b
LCO₂
VCO₂
L
15 µm
c
L
V
15 µm
d
10 µm
L
V
H
e
L
V
15 µm
f
hematite
V
L
10 µm
g
LCO₂
25 µm
h
250 µm
i
monazite
apatite
150 µm
j
25 µm
aq
CO₂
5 µm
5 µm

Figure 2.4 (on previous page) Photomicrographs (plane polarized light) of the different fluid inclusion types, melt inclusions and monazite inclusions in quartz, calcite and apatite from the Hoidas Lake REE deposit. (a) Type 1 fluid inclusion assemblage (FIA) of CO_2 inclusions in quartz from a hyalophane-bearing pegmatite distal to the REE mineralization (photo taken at -10°C). (b) Type 1 CO_2 inclusion that is wetted with some H_2O in quartz crystal from a hyalophane-bearing pegmatite adjacent to the REE mineralization (photo taken at -10°C). (c) Type 2 FIA showing V-rich aqueous inclusions along a shallow dipping secondary plane in a quartz crystal from a hyalophane-bearing pegmatite distal to the REE mineralization (photo taken at 22°C). (d) Type 3 FIA showing L-V-Halite aqueous inclusions in quartz from a quartz-carbonate vein (photo taken at 22°C). (e) Type 4 FIA showing L-V aqueous inclusions in quartz from a quartz-carbonate vein (photo taken at 22°C). Note that for one inclusion the L_{H2O} and V_{H2O} phases are labelled. (f) Type 4 aqueous L-V inclusion with accidentally trapped hematite crystal in apatite grain from a coarse red apatite breccia (photo taken at 22°C). (g) Abundant, elongate, primary melt inclusions in apatite grain from a sample of red apatite breccia. Note the presence of L_{CO2} attached to one of the melt inclusions (photo taken at 22°C). (h) Photomicrograph of multiple grains of apatite that are inundated with oriented, elongate melt inclusions which display growth zones. (i) Photomicrograph (plane polarized light) of parallel planes of monazite inclusions cutting apatite in a sample of the green apatite breccia. (j) Plane of secondary type 2 V-rich aqueous inclusions cross-cutting a plane of type 1 CO_2 inclusions in quartz from a sample of hyalophane-bearing pegmatite distal to the REE mineralization (photo taken at 0°C). The inset photos show enlargements of the fluid inclusion types present.

Type 4 are aqueous L-V inclusions <30 µm in diameter and at room temperature have L-V phase composition with 15-20 vol.% V (Fig. 2.4e). In some of these type 4 fluid inclusion assemblages a small number of inclusions contain halite (<10 vol.%), a transparent cubic solid phase that reacts to form hydrohalite, which suggests that this FIA has salinities near halite saturation. The type 4 inclusions often occur around the strongly altered, hematite-rich parts of apatite crystals and may contain hematite crystals, which are interpreted to be accidentally trapped phases (Fig. 2.4f). The latter observation suggests that type 4 fluids might be responsible for the late hematite alteration of the mineralized veins. A small group of aqueous inclusions <15 µm in diameter and having L-V-S1-S2 phase composition were observed in matrix quartz of the apatite breccia. The S1 solid phase ranges in shape from rounded to square, in the latter case it is similar to halite, however, it does not react to form hydrohalite upon freezing and reheating. This solid phase shows different phase proportions from 10 to 20 vol.%. The S2 solid is opaque with an irregular shape, and it forms ≤10 vol.% of the inclusions. At room temperature these L-V-S1-S2 inclusions have 15 vol.% V which is similar to the type 3 inclusions.

The absence of growth bands in the host phases and lack of appropriate alignment of the fluid inclusions along such features precludes classification of the inclusions as primary. Thus, given that in many cases the inclusions occur along secondary features (i.e., healed fractures) or isolated groups, the time of entrapment of the inclusions is inferred to be secondary or, in the latter case, indeterminate. Importantly, this does not necessarily imply that the inclusions are not cotemporal with the mineralizing event, but that it is not possible to determine this based on petrographic and textural criteria. However, a group of inclusions observed in the apatite crystals appears to be cogenetic with the emplacement of the red apatite breccia veins. These crystals contain some isolated, dark-rimmed, type 1 mono-phase CO_2 inclusions, and less commonly two-phase CO_2 inclusions with 20-30 vol.% V_{CO2} (<25 μm) at room temperature. Significantly, some of these CO_2 inclusions are closely associated with or attached to melt inclusions in the red apatite crystals (Fig. 2.4g). These melt inclusions are characterized by a graphic-like texture (Fig. 2.4h) and their spatial distribution outlines primary growth zones in individual apatite grains, which strongly suggests that the melt inclusions and related CO_2 inclusions may be of primary origin. In addition, based on the presence of accidentally entrapped hematite crystals in the type 4 L-V inclusions, we can infer that the entrapment of type 4 inclusions is likely coincident with the hematite-forming event. Monazite inclusions that often appear along secondary planes in the apatite breccia (indicating hydrothermal origin) are closely associated with the hematite-rich altered apatite intervals (Fig. 2.4i), which suggests that they are related to the same aqueous fluid that led to hematite alteration of the veins.

The secondary planes of type 1 CO_2 inclusions in quartz from the hyalophane-bearing pegmatite dikes and quartz-carbonate veins are cross-cut by secondary planes of all aqueous inclusion populations, and the inclusions at the intersection of these planes are fully or partially filled with aqueous fluid, which indicates that the carbonic fluids were entrapped first (Fig. 2.4j). In many cases, the planes populated by aqueous inclusions are approximately perpendicular to the planes of carbonic inclusions. The H_2O content of some of the carbonic inclusions is, therefore, interpreted to be the result of re-opening of those inclusions, and partial refilling by the later aqueous fluids, rather than heterogeneous trapping of two coexisting fluids. This conclusion is supported by the variable amount of L_{H2O} attached to type 1 inclusions and the lack of coexisting type 2 inclusions with type 1 inclusions.

The relative abundances of the fluid inclusion populations present in each of the three main stages of vein emplacement (i.e., hyalophane-bearing pegmatite, apatite breccia, quartz-carbonate vein formation) are summarized in Figure 2.5. Quartz crystals from hyalophane-bearing pegmatites contain secondary planes of type 1 carbonic inclusions that are cut by planes of all other inclusion types (2, 3, 4), with type 2 L-V aqueous inclusions being the second most abundant after type 1. In the apatite breccia the apatite crystals are much less enriched in inclusions and only a few isolated type 1 carbonic inclusions were observed, whereas type 4 inclusions are abundant in the quartz and carbonate crystals of the matrix. The quartz in the quartz-carbonate veins is mostly populated by type 1 carbonic inclusions, similarly to the quartz from hyalophane-bearing pegmatites, followed by type 3 L-V-H inclusions. Also present, but in lesser abundance, are types 2 and 4 aqueous inclusions which occur along secondary planes.

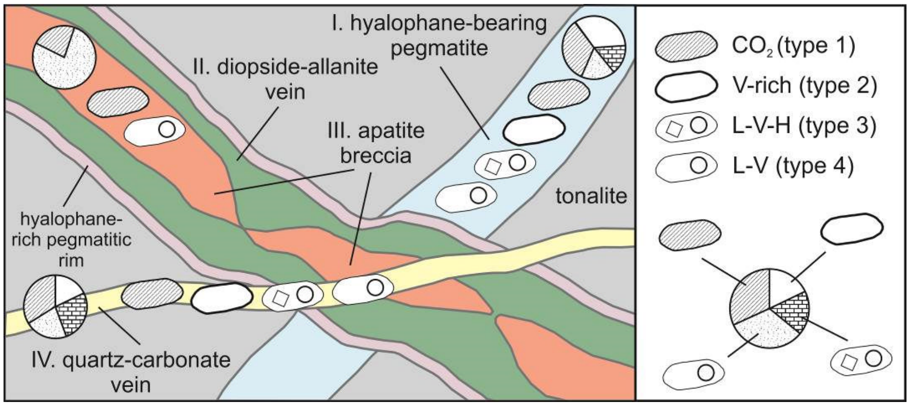

Figure 2.5 Schematic diagram showing the different paragenetic stages (i.e., hyalophane-bearing pegmatite, apatite breccia, quartz-carbonate vein) that were studied for fluid inclusions, with both the types and relative abundances (represented by pie charts) of the different fluid inclusion assemblages (FIAs) present in the Hoidas Lake rare earth element deposit. Diagram is not drawn to scale.

2.5.2 Fluid inclusion microthermometry

The results of microthermometric measurements of fluid inclusions hosted in quartz, carbonate and apatite are summarized in Table A.1 (available from the MAC Depository of Unpublished Data, document CM52-4_10.3749/canmin.0.0.00005) and Figure 2.6.

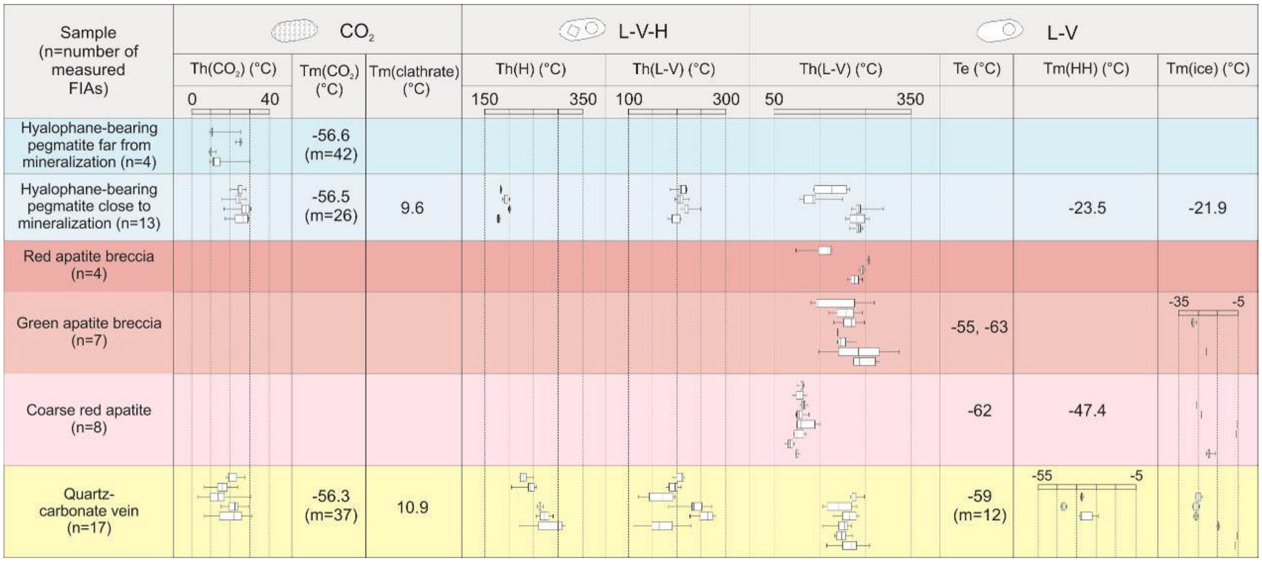

Figure 2.6 Summary of thermometric data for fluid inclusions from Hoidas Lake (see Table A.1 for complete list of data). Figure shows the data in boxplots, subdivided according to both vein types (hyalophane-bearing pegmatite far from mineralization, hyalophane-bearing pegmatite close to mineralization, red apatite breccia, green apatite breccia, coarse red apatite and quartz-carbonate vein) and fluid inclusion types (1, 3, 4). Note that there are no data for type 2 V-rich inclusions in the diagram, but data for these inclusions are discussed in the text. For each inclusion the data are presented for fluid inclusion assemblages (FIAs; n = number of measured FIAs for each vein type). In the boxplots the beginning and the end of the box are the first and third quartiles of the data, while the band inside the box is the median value. The ends of the whiskers represent the minimum and maximum of all the data (covering the whole range of measurements). Note that where only singular or a few measurements could be made, or the measurements all gave the same value (i.e., Tm(CO_2), Tm(clath), Te, Tm(HH), Tm(ice)) these data are provided as the values measured (m = number of individual measurements, if not 1).

Type 1 FIAs were analyzed in quartz in hyalophane-bearing pegmatite and quartz-carbonate veins, but not in the apatite breccia veins, as only a few isolated type 1 inclusions, but no observable FIAs, were found. Type 1 carbonic inclusions homogenize (i.e., Th(CO_2)) to the liquid phase over a large range of temperatures from 3.3° to 30.5°C (Fig. 2.7a, b), but the data can be separated into populations based on different samples and FIAs (Fig. 2.7a, b). Thus, quartz from hyalophane-bearing pegmatite far from REE mineralization (4 FIAs, Fig. 2.7a) has two dominant populations at 9° to 13°C and 24° to 26°C, whereas quartz from hyalophane-bearing pegmatite adjacent to the mineralization (4 FIAs, Fig. 2.7a) has values ranging from 16° to 30.5°C, with most between 19° and 30.5°C. Type 1 inclusions in a given FIA record uniform Th(CO_2) values in the hyalophane-bearing pegmatites, as seen in the summary of data in Table A.1. For example, the FIA displayed in Figure 2.4a includes 45 inclusions with a range of

Th(CO_2) values between 22.7 and 25.7°C. For quartz-carbonate veins, Th(CO_2) values range from 3.3° to 30.5°C (Fig. 2.7b). Importantly, subdivision of all the Th(CO_2) data into their respective FIAs, which have both narrow (3-4°C) and broad (10-20°C) ranges, indicates that there are distinct differences in fluid densities for FIAs (Fig. 2.7b). The results for Tm(CO_2) indicate that all values, regardless of sample or vein type, are near -56.6°C, hence the CO_2 is relatively pure, with little, if any, impurities (e.g., CH_4, N_2) present (Fig. 2.6). Finally, Tm(clath) values, which occurred in the presence of both L_{CO2} and V_{CO2}, were only obtained for a few inclusions that had a small amount of L_{H2O} wetting the inclusions. For such inclusions (n=2) very low salinities (<1 wt.% eq. NaCl) are indicated, using the equations of Diamond (1992).

Only a few type 2 inclusions were analyzed and the following points are noted: (1) homogenization of these V-rich inclusions was not observed when heated up to 450°C; and (2) some Tm(ice) values (from -34° to -35°C) were recorded from inclusions where a thin rim of L_{H2O} was observed, which indicate the fluid has both a high salinity, and contains salts other than NaCl.

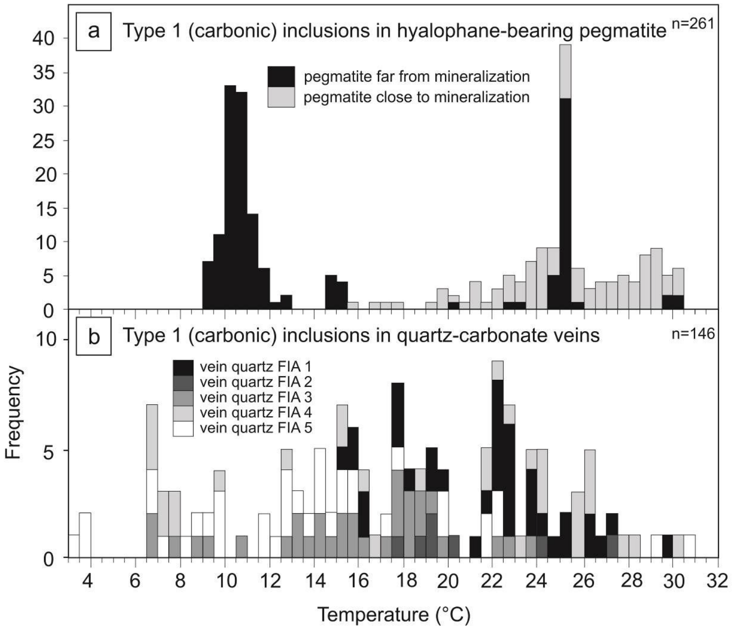

Figure 2.7 Histograms summarizing results for homogenization temperature measurements for type 1 quartz-hosted carbonic inclusions from Hoidas Lake. Note that in (a) the data for individual inclusions are divided into sample type, but in (b) individual data divided into FIAs are presented. (a) Summary of Th(CO_2) for type 1 inclusions from hyalophane-bearing pegmatites far from and close to the REE mineralized veins. (b) Summary of Th(CO_2) for type 1 inclusions in quartz-carbonate veins sorted by FIAs (n = number of individual measurements plotted in the diagram).

Type 3 L-V-H inclusions displayed two types of homogenization behavior that is specific to the vein type. Thus, for hyalophane-bearing pegmatites homogenization occurred by vapor phase disappearance in the sequence L+V+H → L+V → L, whereas in the quartz-carbonate veins homogenization occurred by halite disappearance in the sequence L+V+H → L+H → L. With reference to Figure 2.8, a plot of Th(H) versus Th(L-V) for these inclusions, it is noted that for hyalophane-bearing pegmatite samples the data define a more restricted range, whereas for the quartz-carbonate vein samples the data define a larger spread, which indicates a larger salinity range. For quartz from hyalophane-bearing pegmatites Th(L-V) values show a range from 180° to 250°C, and for quartz from quartz-carbonate veins Th(H) values range between 200° and 315°C (Fig. 2.8).

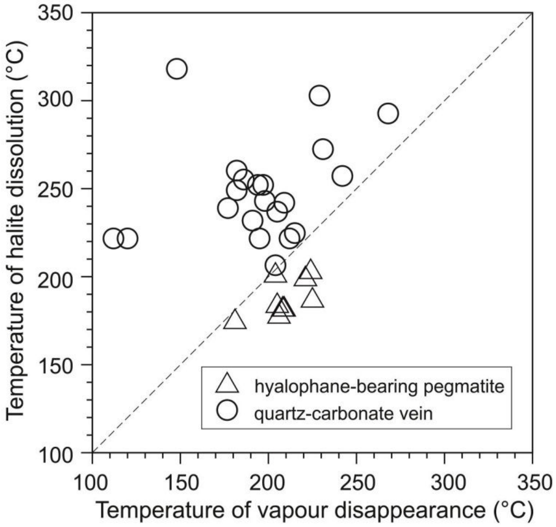

Figure 2.8 Binary plot of temperature of vapor disappearance vs. temperature of halite dissolution for type 3 L-V-H aqueous inclusions hosted by quartz from hyalophane-bearing pegmatite (denoted by triangles) and quartz-carbonate veins (denoted by circles). Note that the dashed line represents a 1:1 slope.

Type 4 L-V inclusions homogenized by vapor disappearance and there is a large range for Th values (from 75° to 290°C; Fig. 2.9), however, for specific samples and FIAs there is a more limited spread of data from 5-10° to 20-25°C (Fig. 2.6 and Table A.1). Examining these data by vein type shows: (1) 5 FIAs for hyalophane-bearing pegmatite adjacent to mineralization show a Th range from 100° to 290°C (Fig. 2.9a); (2) 19 FIAs from the apatite breccia record a Th range from 75° to 280°C, and there is a distinct separation of data for inclusions in early-stage red apatite breccia and green apatite breccia versus late-stage coarse red apatite (Fig. 2.9b); and (3) 6

FIAs from quartz of quartz-carbonate veins show a more restricted Th range from 155° to 260°C (Fig. 2.9c).

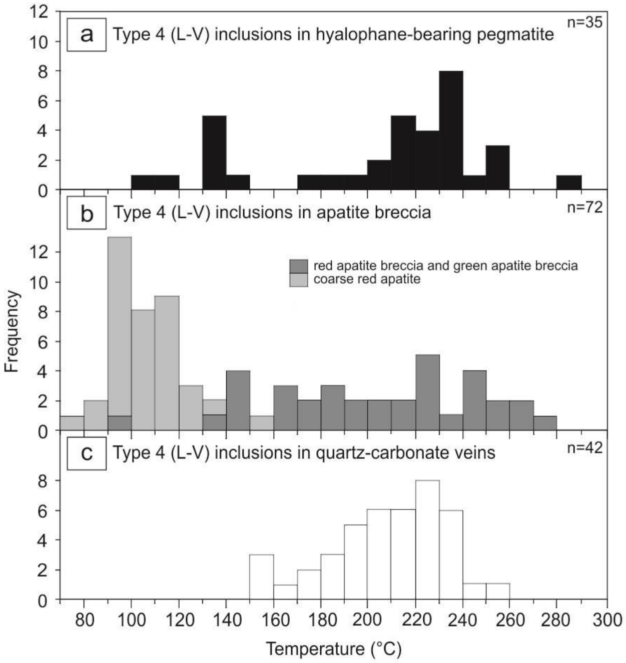

Figure 2.9 Histograms summarizing results for homogenization temperature measurements of type 4 L-V aqueous inclusions hosted by (a) quartz from hyalophane-bearing pegmatite; (b) apatite and calcite from red apatite breccia and green apatite breccia versus coarse red apatite; and (c) quartz from quartz-carbonate veins (n = number of individual measurements plotted in the diagram).

Using dissolution temperatures for halite (from 175° to 315°C) and the equation of Bodnar (2003), salinities for type 3 inclusions range between 30 and 32 wt.% eq. NaCl for the hyalophane-bearing pegmatites and between 31.5 and 40 wt.% eq. NaCl for the quartz-carbonate veins (Table A.1 and Fig. 2.10). The fluid composition and salinities for type 4 inclusions are inferred from eutectic (Te) and ice melting (Tm(ice)) temperatures. The observation of low Te values (from -65° to -55°C) for type 4 inclusions in apatite breccia and quartz-carbonate vein samples indicate the presence of divalent cations, likely Ca^{2+}, which is confirmed from the evaporate mound analysis, discussed below. Ice melting temperatures (Tm(ice)) range from -28° to -5°C for all type 4 inclusions (Table A.1). For the different vein types, the Tm(ice) data are summarized as follows: (1) the hyalophane-bearing pegmatite adjacent to mineralization has one FIA with values of -21.9°C; (2) late-stage apatite in the apatite breccia has 7 FIAs with values from -5° to -28°C; and (3) the quartz-carbonate veins have 6 FIAs with values from -6° to -28°C.

The calculated salinities for these inclusions range from 8 to 24 wt.% eq. NaCl, but with distinct groupings at 8-10 wt.% and 17-24 wt.% eq. NaCl (Fig. 2.10).

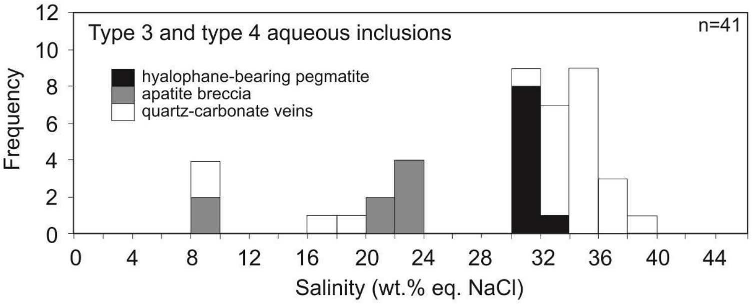

Figure 2.10 Histogram summarizing salinity data for individual type 4 L-V and type 3 L-V-H aqueous inclusions hosted by quartz from hyalophane-bearing pegmatite, apatite breccia and quartz-carbonate veins (n = number of individual measurements plotted in the diagram).

Where both hydrohalite and ice melting temperatures were noted, estimates of both salinity and Na:Ca ratio can be made with reference to the H_2O-NaCl-$CaCl_2$ ternary (Bodnar, 2003; Fig. 2.11). In these cases, the salinity was estimated to be 22.5 wt.% NaCl+$CaCl_2$ with X_{NaCl} (weight fraction of NaCl) = 0.3.

The previously mentioned L-V-S1-S2 multi-solid inclusions in the quartz matrix of the apatite breccia showed Th(L-V) values from 125° to 230°C (n=9). The dissolution of halite (the S1 phase) occurred between 308° and 370°C, which indicates salinities around 40-45 wt.% eq. NaCl.

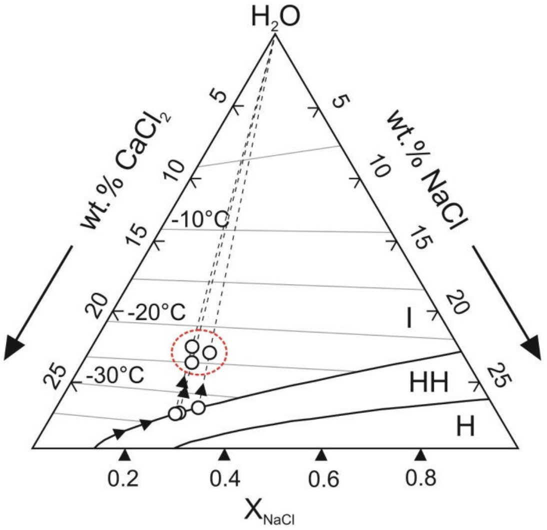

Figure 2.11 Summary of melting temperatures of ice and hydrohalite in individual type 4 L-V aqueous inclusions hosted by quartz from quartz-carbonate veins, plotted in the H_2O-NaCl-$CaCl_2$ ternary diagram of Oakes et al. (1990).

2.5.3 Chemistry of evaporate mounds

Representative images of evaporate mounds hosted in quartz from a hyalophane-bearing pegmatite dike adjacent to mineralization and two quartz-carbonate veins are shown in Figure 2.12, and results of SEM-EDS analysis of evaporate mounds are summarized in a Ca-Na-K ternary plot in Figure 2.13.

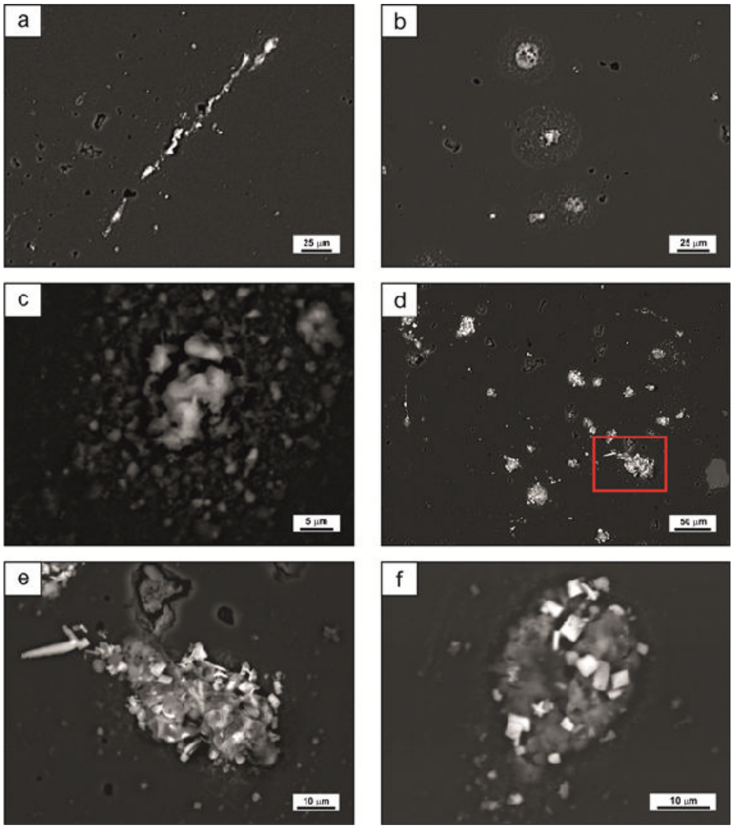

Figure 2.12 Back-scattered electron (BSE) images of evaporate mounds hosted in quartz. (a) An elongate mound formed due to leakage of secondary fluid inclusions along a fracture. (b) Series of isolated mounds that may represent an FIA. Note the presence of the round pits which represent evacuated fluid inclusions that were just beneath the quartz surface. Also note the splattered material about some of the mounds. (c) Close up of a mound surrounded by splatter or debris material. (d) Example of a mine field made up of many large mounds that may represent an FIA. Note that the bright acicular phases present in most of the mounds are a $SrCl_2$ phase. The mound in the lower right in the red rectangle is enlarged in the next image. (e) Close-up of area in red rectangle in (d) showing a large mound with an abundance of bright acicular grains with $SrCl_2$ composition. Note the uniform grey scale of the rest of the mound which indicates it has a uniform and homogeneous composition. (f) Another example of the same type of mound as in the previous image, but here the $SrCl_2$ phase has an equant habit.

The mounds occur as elongate features (Fig. 2.12a), likely due to fluid migrating from planes with abundant secondary inclusions, or more commonly as rounded shapes (Fig. 2.12b, c) of variable size (i.e., 10 to 100 µm) that can either be isolated (Fig. 2.12c) or form mound fields (Fig. 2.12b, d). Debris or splatter fields occur around mounds (Fig. 2.12b, c), but in such cases >90% of the mass of the mounds is in the core area. In some cases in situ fractionation of the mounds was noted (see Kontak (2004) for discussion of this feature) and we note, in particular, that this resulted in the rare formation of an elongate or equant, euhedral crystal phase with a stoichiometry of $SrCl_2$ (Fig. 2.12e, f). As noted earlier, the mounds were analyzed using a raster mode rather than point analysis to ensure representative and homogeneous bulk compositions. The fact that in BSE mode the mounds have a uniform grey scale (e.g., Fig. 2.12c) indicates that the phase is chemically uniform, which was also checked by doing multiple analyses of some of the larger mounds.

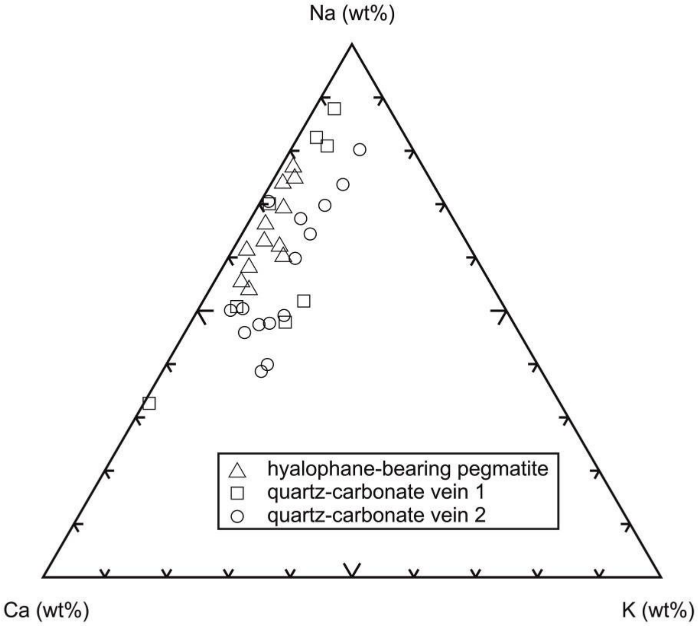

Figure 2.13 Ternary diagram of Ca-Na-K concentrations (wt.%) for evaporate mounds for quartz-hosted fluid inclusions from hyalophane-bearing pegmatite and quartz-carbonate vein (quartz-carbonate vein 1 and 2) samples.

With respect to the compositional data in Figure 2.13, the following points are noted: (1) in general, Na is the dominant solute in the mounds with Na/(Na+Ca+K) = 32-90%; (2) Ca can also be abundant with Ca/(Na+Ca+K) = 10-68%; (3) K is also present, but in lower abundance (K/(Na+Ca+K) = 0-15%); and (4) there is complete overlap of the data for the different samples, thus in terms of Na-Ca-K chemistry these samples cannot be discriminated. However, minor components in the mounds discriminate the hyalophane-bearing pegmatite versus quartz-carbonate vein samples. F and P were detected in mounds generated in quartz of the hyalophane-bearing pegmatite sample with abundances of <10 wt.% and 6 wt.% (values normalized to 100 wt.%), respectively, and S was also detected (<8 wt.%). The mounds generated in quartz from the quartz-carbonate veins, in contrast, contain Ba (2 to 4 wt.%), Mn (1 to 5 wt.%), Fe (1 to 2 wt.%), Mg (1 to 2 wt.%), Sr (<6 wt.%), besides S (<10 wt.%).

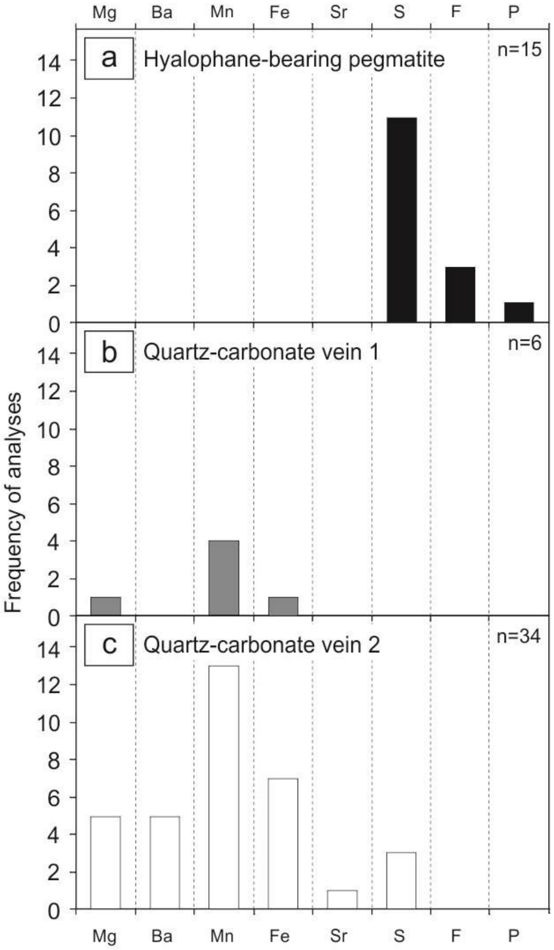

Figure 2.14 Frequency plot for elemental concentrations (Mg, Ba, Mn, Fe, Sr, S, F, P) detected in evaporate mounds determined by SEM-EDS analyses in (a) hyalophane-bearing pegmatite; (b) quartz-carbonate vein 1; and (c) quartz-carbonate vein 2.

Plotting the frequency of analyses of these less abundant elements highlights the distinction between the different samples (Fig. 2.14). Figure 2.14 shows that in the quartz from the hyalophane-bearing pegmatite S appears in greatest frequency, followed by F and P, and none of the other elements were detected. In contrast, for the two quartz-carbonate vein samples, the mounds show detectable amounts of Mn in most analyses, followed by the occurrence of Fe, Mg, Ba, S analyses, and there was only one mound where Sr appeared to have a concentration above the detection limit using raster analysis (Fig. 2.14), although individual $SrCl_2$ crystals were detected using point analysis in some of the mounds (Fig. 2.12e, f).

2.6 Discussion

2.6.1 Preamble

The Hoidas Lake REE mineralization occurs as a complex vein system that is focused along brittle-ductile structures parallel to the northeast-southwest trending Hoidas-Nisikkatch Fault. The combined magmatic (i.e., intrusive) and hydrothermal nature of the mineralized veins was first recognized by Hogarth (1957). The source(s) of the mineralizing melt and fluids has, however, not yet been identified. Halpin (2010) suggested, based on both vein mineralogy and geochemical data, that the mineralization might be related to a mantle-derived carbonatitic or alkalic magmatic body at depth (Fig. 2.15). In support of this model is the presence of lamprophyre dikes that occur along the same structural trend as the REE mineralization (Elliott et al., 2013). Thus, even though these dikes may not be genetically or temporally related to the mineralization, they indicate that channel ways for deeply derived magmas and fluids existed near the boundary of the Zemlak and Train Lake domains (Normand et al., 2009). The Hoidas Lake diopside-allanite veins and apatite breccia veins probably formed, therefore, from magmatic-hydrothermal fluids that used structural pathways associated with the development of the Hoidas-Nisikkatch Fault, a subsidiary of the Black Bay Fault System (Halpin, 2010), as shown schematically in Figure 2.15.

The results of recent and ongoing studies (Pandur et al., 2013a, b) are consistent with the above theory, and suggest that the initial magmatic-hydrothermal fluid responsible for mineralization was probably a pegmatitic melt derived from a mantle-derived magma that became enriched in REEs, Sr, Ba, F, S, CO_2 and PO_4 through fractionation (cf. London, 2005). The inferred presence of this early melt is represented by the hyalophane-bearing pegmatites that are closely related to the REE mineralization (Fig. 2.2a, b). In addition, the primary melt inclusions in red apatite crystals have a graphic-like texture (Fig. 2.4h) reminiscent of the graphic textures observed in granitic pegmatites, a feature that is interpreted as being due to rapid, non-equilibrium crystal growth in pegmatitic environments (London, 2009). These melt inclusions are currently being studied by the authors (Chapter 3), and are enriched in REEs, Ba, Sr and CO_2, which also indicates a connection to a REE-enriched carbonatitic or alkalic melt. The results of the current fluid inclusion study are discussed below in the context of addressing the nature, origin and evolution of the observed fluids, and also the P-T conditions that can be inferred from these data and that constrain emplacement of the mineralized vein system.

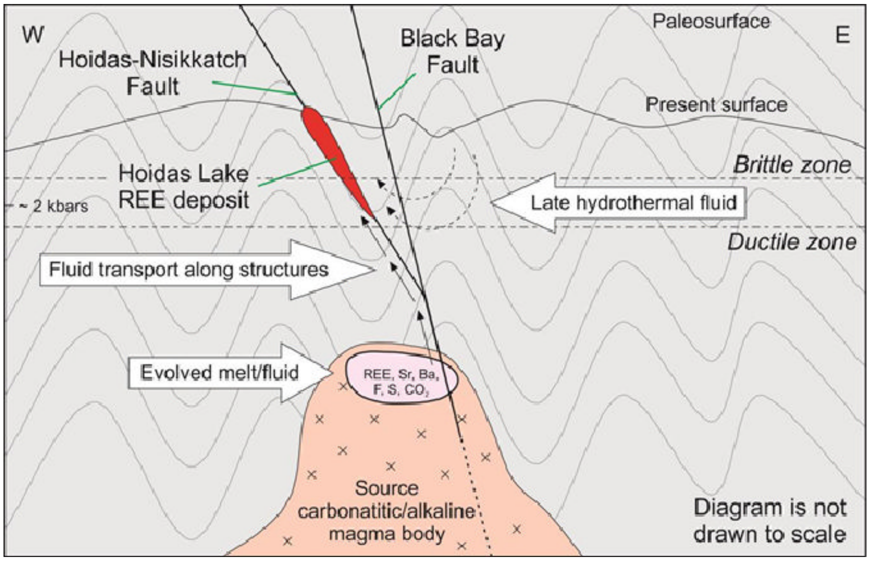

Figure 2.15 Schematic cross-section that summarizes the important geological relationships at Hoidas Lake and integrates this with a possible model for the origin of the mineralizing melt/fluid that is responsible for the rare earth element mineralization (modified from Halpin, 2010). Note that the chemical phases highlighted (REE, Sr, Ba, F, S, CO_2) have been identified in fluid and melt inclusions in vein samples from the mineralized zone, as discussed in the text. The arrows represent the transportation paths of the magmatic-hydrothermal fluids present in the system.

2.6.2 Connection between fluids and melts in the Hoidas Lake REE mineralized system

The Hoidas Lake REE mineralization is related to the carbonic and variably saline, aqueous fluid inclusions present in the vein system. Although the nature of the fluids is discussed in more detail below, it is first important to address the relationship of these fluids to their hosts and the mineralization. Despite the difficulty of constraining the timing of fluid entrapment (i.e., primary versus secondary), given the lack of obvious relationships of fluid inclusions and growth zones in their host phases, the chemistry of the fluids, as determined using microthermometry and evaporate mound analysis, provides a strong case that the fluids do in fact relate to the mineralization. In this regard, we first note that, from petrographic and SEM observations in the hyalophane-bearing pegmatites (Fig. 2.2c), there is a close association of REE mineralization and alteration of hyalophane (transformation into K-feldspar and sodic overprinting resulting in albite alteration) that mobilized the Ba to form barite, which indicates that S was introduced at this time. Thus, both the high salinity and enrichment of the aqueous inclusions in Na, Ca, K, Ba, Mn, Fe, Mg, Sr, S and F suggest that these fluids relate to the alteration in the hyalophane-bearing pegmatites. Furthermore, the nature of these fluids and similarity to fluids in carbonatites, as discussed below with reference to the carbonatite-related fluids (cf. Rankin, 2005), provide evidence that these fluids relate to the possible source of the Hoidas Lake REE mineralization implied by previous work in the area (cf. previous section). A final note is that the chemistry of melt inclusions in apatite of the apatite breccia veins indicates enrichment in REEs, Ba and Sr, thus further establishing that these rocks likely originate from a carbonatitic magma.

2.6.3 Salinity, chemistry and evolution of the fluid system

The thermometric data for both the carbonic and aqueous fluid inclusions, along with the evaporate mound data, permit evaluation of the chemical nature and evolution of the fluid system at Hoidas Lake, and comparison to other carbonatitic systems. The first two points are addressed before comparing these results to other systems.

With regards to the carbonic inclusions, two important features are noted: (1) type 1 inclusions represent entrapment of a purely carbonic fluid with the presence of some aqueous component (Fig. 2.4b) considered to represent infiltration of the aqueous fluid at some later time; and (2) the $Tm(CO_2)$ data for type 1 inclusions near -56.6°C indicate these are pure CO_2 inclusions with little, if any, other dissolved gas component (e.g., CH_4, N_2). Thus, the carbonic inclusions reflect derivation of this fluid from an oxidized source with little, if any, interaction with a source of reduced carbon.

The aqueous inclusions provide insight into fluid chemistry in terms of both salinity, thus total dissolved solutes, and also the nature of the solutes, the latter being inferred from ice and hydrohalite melting, eutectic measurements and evaporate mound data. In terms of salinity, temperatures of ice melting and halite dissolution indicate a large range, with the data falling into three distinct groupings (Fig. 2.10): (1) 8-10 wt.% eq. NaCl for hyalophane-bearing pegmatites and the apatite breccia; (2) 17-24 wt.% eq. NaCl in the apatite breccia and the late quartz-carbonate veins; and (3) 30-40 wt.% eq. NaCl in the hyalophane-bearing pegmatites and the quartz-carbonate veins. In terms of the nature of the solutes, the following is noted: (1) evaporate mound data indicate the bulk compositions are multi-component with abundant Na, Ca, K and lesser, but still appreciable amounts of Ba, Mn, Fe, Mg, Sr, S, F and P (Fig. 2.14); (2) low eutectic values (i.e., from -66° to -55°C, Table A.1) in type 2 and 4 inclusions in the hyalophane-bearing pegmatite, apatite breccia and quartz-carbonate veins are consistent with the presence of divalent cations, like Ca^{2+}; and (3) ice and hydrohalite melting indicate $X_{NaCl} = 0.3$ (Fig. 2.11). The evaporate mound data also show that only quartz from the hyalophane-bearing pegmatite contains detectable F and P, whereas Ba, Mn, Fe, Mg and Sr only occur in quartz-carbonate veins (Fig. 2.14). The differences in the abundance of F and P in the hyalophane-bearing pegmatites vs. Mg, Mn, Ba, Fe and Sr enrichment in the quartz-carbonate veins might be explained by some change in the evolution of the fluids or fluid/rock interaction, for which we have no definitive solution at present.

Further characterization of the fluid can be made by integrating the evaporate mound data and fluid inclusion salinity inferred from microthermometry. Given the range of salinities for type 3 (30-40 wt.%) and type 4 (avg. 20 wt.%) fluids, the calculations were done using 20 and 30 wt.% eq. NaCl salinities, and the average contents of solutes from mound analyses from the quartz-carbonate vein samples, based on normalization to 100%: Na (48%), Ca (24%), K (6%), Ba (5%), Mn (4%), Fe (2%), Mg (2%), Sr (9%). The results of these calculations, rounded to the nearest hundred for 20 and 30 wt.% eq. NaCl, respectively, provide the estimates of the compositions (in ppm) of the fluids: Na=37100/55600, Ca=17500/26200, K=6300/9500, Ba=6600/9900, Mn=3500/5300, Fe=1800/2700, Mg=1000/1500, Sr=10000/15000. Based on these results, the fluids are quite elevated in Ba, Sr and Mn in addition to Na, Ca and K.

Integration of the above compositional data and the presence of the different fluid inclusion types (type 1 to 4) allow evaluation of the evolution of the fluids at Hoidas Lake. Firstly, the presence of CO_2 inclusions in all vein stages is noted, along with the fact that saline aqueous fluids are found in hyalophane-bearing pegmatites adjacent to the mineralization, in addition to the apatite breccias and quartz-carbonate veins. These observations suggest that both the carbonic and saline aqueous fluids are an integral part of the mineralized system. In addition, the fact that the fluid inclusions are generally inferred to be of secondary origin suggests that fluid infiltration, particularly with respect to the hyalophane-bearing pegmatites, followed an earlier magmatic stage in the evolution of the Hoidas Lake system. Finally, there are two possible explanations for the presence of lower salinity inclusions (i.e., 8-10 wt.% eq. NaCl): (1) the evolution of the system from an early high salinity stage to a later lower salinity stage; or (2) dilution of the more saline fluid due to infiltration and possibly mixing with lower salinity fluids of meteoric or metamorphic origin. The absence of additional data, in particular, stable isotopes, does not allow at present a definitive answer in regards to these models, and further work is required.

2.6.4 Comparison to fluid inclusions in other carbonatite systems

The presence of abundant carbonic inclusions in the Hoidas Lake deposit and their similarities to those described in carbonatite complexes indicate that this mineralization might indeed be related to a distal carbonatitic source or a mixed carbonate-rich magmatic system. Previous fluid inclusion studies of mineralized carbonatites have shown that the most characteristic inclusion types are both CO_2-rich with >90 vol.% CO_2, and aqueous with L-V and L-V-H types (Rankin, 2005). The inclusions present in these settings often display extreme variations in phase proportions, thus indicating that necking and/or heterogeneous entrapment occurred (Nesbitt and Kelly, 1977). The aqueous inclusions studied in carbonatitic systems have large ranges for both homogenization temperatures (from <100° to 630°C) and salinities (from 0 to 50 wt.% eq. NaCl; Rankin, 2005), which indicates a complex fluid system that likely involves fluid unmixing, presence of different reservoirs (i.e., fluid mixing), and a protracted evolution. The lower temperatures recorded for Hoidas Lake contrast with the higher temperatures for some of these other settings, which is consistent with Hoidas Lake being more distal from its fluid source.

The composition of the hydrothermal fluids in carbonatite systems have been addressed by a few studies, and the results of these studies are summarized in Rankin (2005). In these systems, the presence of cations, such as K and Ca, in addition to Na has been inferred from measured eutectic temperatures (Bühn and Rankin, 1999; Samson et al., 1995a, b; Rankin, 2005). The analysis of both leachates and evaporate mounds of saline aqueous inclusions from the Oka carbonatite in Canada indicated that fluids were Cl^- and SO_4^{2-}-rich brines with Na as the dominant cation, but that K, Mg and Fe were also present (Samson et al., 1995a; b). The presence of Ca and Sr was also noted for the Kalkfeld igneous complex in Namibia, based on synchrotron-XRF (X-ray fluorescence) analysis (Bühn and Rankin, 1999). For the Amba Dongar igneous complex, India, Williams-Jones and Palmer (2002) attributed some of this elemental enrichment to the presence of accidentally trapped solid phases. In several of these studies, Ba, Fe and REEs have also been reported as dissolved phases within the fluid inclusions.

In regard to these former observations, we note that the estimates made for the Hoidas Lake fluids presented above are similar to those summarized by Rankin (2005) for fluids from the Namibian carbonatites mentioned above.

2.6.5 P-T conditions of fluid entrapment

The fluid inclusion data have been used to infer the P-T conditions of fluid entrapment for the hyalophane-bearing pegmatites and the quartz-carbonate veins (Fig. 2.16). The presence of fluid inclusions (i.e., carbonic and aqueous) with highly divergent isochoric projections in P-T space, provide an ideal opportunity to constrain the conditions of fluid entrapment. Before further discussion, it is noted, however, that petrographic observations do not suggest that these fluid types coexisted, inclusion types 1, 3 and 4 occur along different healed fracture planes. Having noted this, the chemistry of the fluids, that is carbonic and highly saline aqueous with Na-Ca-K-S-F-P in the hyalophane-bearing pegmatites and Na-Ca-K-Ba-Mn-Fe-Mg-Sr-S in the quartz-carbonate veins, is consistent with these two fluids being derived from the same evolving carbonatitic or alkalic magmatic system, which is discussed in more detail below. The assumption is made that there was no substantial time lapse between the trapping of types 1 and 3 fluids, and their different isochoric trajectories are used in Figure 2.16 to infer the conditions of fluid entrapment.

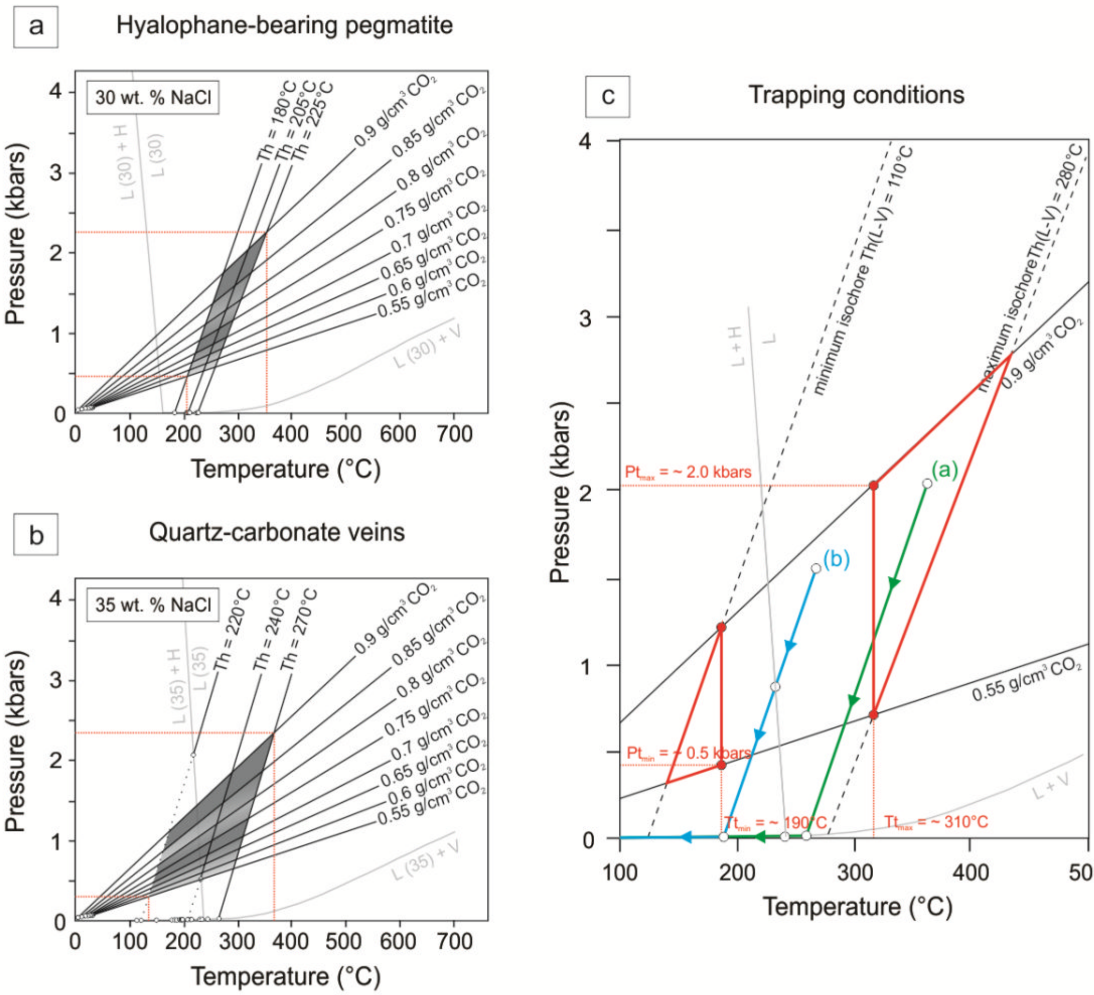

Figure 2.16 P-T diagrams that show isochoric projections for types 1 and 3 quartz-hosted fluid inclusions for samples from (a) hyalophane-bearing pegmatite; and (b) quartz-carbonate vein settings. The isochores were calculated using the results of microthermometry (Th, Tm(CO_2) and salinity), estimates of phase proportions for carbonic inclusions, and the software programs of Steele-MacInnis et al. (2012) and Hansteen and Klügel (2008). The phase boundaries (i.e., L+V–L+V+H, L+V surfaces) in the diagrams for 30 and 35 wt.% NaCl (in light grey lines) are from Bodnar (2003). Note that the grey area represents the intersection area of the measured isochores and the darker grey areas represent the maximum concentration of homogenization data for Th(CO_2) in the histogram plots (see Figure 2.6). (c) P-T diagram showing the entrapment conditions of type 1 carbonic and type 3 aqueous L-V-H fluids (after eliminating the effect of overpressure by disregarding the area in P-T space denoted by the red triangles), with the maximum and minimum pressures and temperatures of entrapment written in red. Note the trends labelled a (green) and b (blue) represent the cooling of type 3 L-V-H fluids in hyalophane-bearing pegmatite and quartz-carbonate vein settings, respectively. See text for discussion and interpretation of the diagrams.

With the aforementioned assumptions stated, we note the following thermometric properties of the fluid inclusions that together can be used to constrain the P-T conditions of fluid entrapment.

1. The large range in Th(CO_2) for the carbonic inclusions in both hyalophane-bearing pegmatite and quartz-carbonate vein types (Table A.1 and Fig. 2.7) translates into a large range for the density of these inclusions.

2. The small range in Th(CO_2) values for individual FIAs (i.e., 3-4°C) indicate that carbonic fluids of very different densities were trapped, due to varying pressures as discussed below, and that their densities were not modified by post-entrapment processes.

3. The restricted range for both homogenization temperatures (Th) and salinities for aqueous FIAs (Table A.1) also reflects entrapment of discrete fluids and that post-entrapment changes have not modified the inclusions.

4. The nature of homogenization of type 3 L-V-H inclusions, that is by either dissolution of halite or disappearance of the vapor phase (Fig. 2.8), reflects a difference in the trapping conditions for fluids of similar salinity (Becker et al., 2008).

The above features of the fluid inclusions along with the P-T plots in Figure 2.16 indicate that: (1) pressure was transient during entrapment of the carbonic inclusions (Fig. 2.16a, b); (2) the estimated maximum possible range of entrapment pressure for hyalophane-bearing pegmatites is between 0.5 and 2.3 kbars (Fig. 2.16a), and in the quartz carbonate veins the maximum possible range of entrapment pressure is between 0.3 and 2.4 kbars (Fig. 2.16b); and (3) the fluids, both aqueous and carbonic, were probably trapped over a range of temperatures, and the maximum possible range of entrapment temperatures is between 130°C and 370°C.

The range in pressures recorded by type 1 carbonic inclusions was probably due in part to repeated reactivation along the fault structure that focused the fluids and hosted the vein system. Pressure may have fluctuated between lithostatic and hydrostatic, and thus the highest pressures record $P_{lithostatic}$, whereas the lower pressures reflect periods when $P_{hydrostatic}$ prevailed. The fact that there is a continuous range in Th(CO_2) and, therefore, density for the carbonic fluids indicates that some combination of these two end member conditions occurred at various times. Such fluctuation in pressures is not uncommon in natural settings, thus, we note that similar transient conditions have been recorded in other deposit settings, such as porphyry (e.g., Redmond et al., 2004) and orogenic gold deposits (Chi et al., 2006). In the Hoidas Lake system the quartz-carbonate veins show the lower minimum pressures (300 bars) which indicates that these veins were trapped in a system with a larger component of hydrostatic pressure (Fig. 2.16b), likely consistent with the brecciation of mineralized veins.

The difference in the behavior of type 3 L-V-H inclusions (i.e., final homogenization by halite versus vapor disappearance) can be explained with an example of two fluid inclusions and their isochoric trajectories, one from the quartz of the hyalophane-bearing pegmatites and one from the quartz of quartz-carbonate veins, with reference to Figure 2.16c. The entrapment of fluids in the hyalophane-bearing pegmatite with subsequent cooling on the isochoric trajectory labelled (a) will result first in the appearance of vapor on the L-V curve followed by halite appearance once the fluid cools past the halite liquidus. In contrast, entrapment of fluids in the quartz-carbonate vein with cooling along the trajectory labelled (b) will result in the appearance of first halite and then vapor in such inclusions. As the fluid inclusions of the quartz-carbonate veins show a range of Th that reaches higher temperatures, compared to the fluid inclusions of the hyalophane-bearing pegmatites, the difference in behavior of these L-V-H inclusions must be due to different position of the isochoric trajectory with respect to the halite liquidus for each individual inclusion. As the salinity of the inclusion determines the position of the halite liquidus, the position of the isochoric trajectories with respect to the halite liquidus has to be the function of slightly different salinities for the individual inclusions. The difference in estimated salinities for the type 3 inclusions in hyalophane-bearing pegmatites versus quartz-carbonate veins (Fig. 2.10) supports this distinction.

The homogenization data for type 4 L-V inclusions also indicate that fluids were trapped over a range of temperatures. Importantly, this data set shows that the early and late stages of apatite yield distinctly different homogenization temperatures. The early red apatite breccia and green apatite breccia show higher homogenization temperatures (from 100° to 280°C) that overlap with those inferred from the hyalophane-bearing pegmatite and quartz-carbonate vein types, and the late-stage coarse red apatite shows lower homogenization temperatures (from 75° to 150°C). Thus, even though the inclusions in these samples appear to be secondary, they must have been trapped shortly after the time of apatite formation to record a cooling history consistent with their relative paragenesis.

In order to narrow the maximum possible range of entrapment pressure and temperature of the Hoidas Lake hydrothermal system, the effect of overpressure was eliminated, by disregarding the red-rimmed triangles on Figure 2.16c. The minimum aqueous isochore in this estimation is approximated from the lowest observed Th(L-V) for type 3 inclusions in the dataset, for an inclusion in the quartz-carbonate veins with Th(L-V) = 110°C at 35 wt.% salinity. The maximum isochore is approximated from the highest observed Th(L-V) for type 3 inclusions in the dataset, for an inclusion in the quartz-carbonate veins with Th(L-V) = 280°C at 35 wt.% salinity. The range of entrapment is defined by the intersection of these isochores with the carbonic isochores of 0.55 g/cm^3 and 0.9 g/cm^3. Thus, if the effect of over-pressure is eliminated, the maximum possible pressure of fluid entrapment was approximately 2 kbars, whereas the minimum possible pressure of entrapment was approximately 500 bars, and the maximum range of temperature of entrapment was 190° to 310°C (Fig. 2.16c). Considering lithostatic conditions (density of 2.8 g/cm^3), these pressures equate to 5.6 km and 1.4 km depth, respectively, whereas for hydrostatic conditions (density of 1 g/cm^3) the pressures equate to a depth of 2 km to 500 m. Even though the regional geological history of the area and the duration of mineralization are poorly understood at present, there is no evidence to suggest that there were significant changes in the depth during vein emplacement. In addition, given the assumption that there was no significant time lapse between the entrapment of type 1 and type 3 fluids, the complex and transient fluctuations in pressure between lithostatic and hydrostatic conditions are interpreted to be the result of multiple episodes of fluid pressure increase and subsequent release. Thus, entrapment at depths between about 1.4 km and 2 km may explain the observed pressure variations.

2.6.6 Implications of the fluid inclusion study for the nature and origin of the Hoidas Lake REE deposit and other REE mineralized systems

Previous work done on the Hoidas Lake REE deposit has provided a variety of models to account for the origin of the mineralization in the context of the geological setting, which includes the juxtaposition of hyalophane-bearing granitic pegmatites, apatite breccias and lamprophyre dikes. Harvey et al. (2002) suggested that the REE mineralization relates to calcium metasomatism of a pre-existing, pyroxene-rich ultramafic to lamprophyric vein-system. Gunning and Card (2005) suggested that the mineralized setting reflects mixing of two melts, one of granitic composition and the other a mantle-derived lamprophyric melt. Finally, Rogers (2011) appealed to metamorphism and metasomatism of alkaline intrusions to explain the nature of this type of mineralization. The Hoidas Lake system appears to be very similar to deposits in the Visakhapatnam district of eastern India, where allanite is associated with apatite in the core of zoned clinopyroxene-, biotite- and hyalophane-bearing dikes (Choudhuri and Banerji, 1976). Choudhuri and Banerji (1976) suggested these pegmatitic bodies formed from magmatic fluids, derived from an alkali syenite with a possible carbonatite association.

We propose that the generation of melts, which ultimately crystallized to form the hyalophane-bearing pegmatites and the carbonic and saline aqueous fluids, requires a carbonatitic or alkaline source. In addition, the spatial and temporal association with lamprophyre dikes also indicates that the regional-scale fault system was able to access an appropriate mantle source. Even though the absolute age of the mineralization and associated rocks is poorly known, there is evidence of compositionally distinct mantle-derived rocks in this part of the Canadian Shield that suggests that a suitable mantle source is available. Examples include the 1818 Ma alkali basalts of the Martin Group near Uranium City (Morelli et al., 2009), the ca. 1830 Ma minettes and ultrapotassic volcanic rocks in the Dubawnt Supergroup in Nunavut (Cousens et al., 2001; Peterson et al., 2002), and the post-Trans-Hudson Orogen Eden Lake carbonatite in northern Manitoba (Chakhmouradian et al., 2008). In all cases, the magmatic systems were generated and emplaced in intracontinental tectonic settings, and originate from a subcontinental mantle lithosphere that had likely undergone earlier metasomatic enrichment.

The maximum temperature of entrapment of the hydrothermal fluids related to the REE mineralization is 310°C (Fig. 2.16c). The temperatures of these fluids are significantly lower than the temperature of any magmatic source, and thus, they must have originated at depth and have cooled from higher temperatures. The nature and origin of the studied carbonic fluids and Na-Ca-K-rich saline aqueous fluids with enrichment in Ba, Mn, Fe, Mg, Sr, S and F are attributed to exsolution from an evolving alkali melt, and, in this context, our model, summarized in Figure 2.15, shares some aspects with the above mentioned models for the formation of the Hoidas Lake REE deposit, that is, the involvement of fluids, metasomatism and felsic melts. However, in our proposed model there is also an affinity with carbonatites, which is not part of the previous models, except that of Halpin (2010). The introduction of the mixed, high-salinity aqueous fluids into a pre-existing vein system, in particular the hyalophane-bearing pegmatites and apatite breccias, and the observation that this resulted in hydrothermal alteration, local redistribution of the REEs from earlier magmatic mineralization, and formation of a new generation of REE mineralization, has parallels with suggestions of others regarding the Hoidas Lake deposit.

As summarized by Salvi and Williams-Jones (2005), Rankin (2005) and most recently Williams-Jones et al. (2012), REE mineralization involving both carbonatitic and peralkaline granitic/syenitic settings is hybrid in nature with an early magmatic component that is overprinted by a later hydrothermal stage, the latter being critical in producing economic concentrations. At Hoidas Lake, this latter stage is well exemplified by the alteration of hyalophane concurrent with allanite formation, the presence of various REE-carbonate phases in allanite concurrent with crystallization of hydrothermal chlorite, and formation of monazite along secondary fractures (Fig. 2.4i) in magmatic apatite associated with hematite alteration. In the latter case, the presence of accidentally entrapped hematite crystals in the late aqueous type 4 inclusions (Fig. 2.4f) indicates that these fluids were able to locally redistribute the REE contents of the primary mineralization. As an addition, the monazite inclusions in the apatite crystals are often surrounded by irregular apatite zones that show relative depletion in REEs, which provides further evidence for the role of fluids in redistribution of REEs in the system. Thus, this study has both contributed to and further advanced this model by clearly documenting the nature and origin of such fluids in a similar hybrid setting.

2.7 Conclusions

The Hoidas Lake REE mineralization appears to be a unique example of a pegmatitic system related to an inferred carbonatite body at depth. The REE-rich veins were probably deposited from a pegmatitic melt enriched in Sr, Ba, F, PO_4, and CO_2 that ascended from its deep magmatic source along structures of the Hoidas-Nisikkatch Fault system. The entrapment of CO_2-rich fluids in the mineralized apatite breccia veins represents the first stage of hydrothermal activity in the system. The evolution of the Hoidas Lake mineralization involved two fluid types, represented by carbonic and aqueous inclusions. Cross-cutting relationships of secondary inclusion planes indicate that the entrapment of carbonic fluids was followed by introduction of mixed Na-Ca-K-(Ba-Mn-Fe-Mg-Sr) aqueous fluids showing a range of salinities (8-25 wt.% eq. NaCl and 22.5 wt.% $NaCl+CaCl_2$). These aqueous fluids are likely responsible for alteration of the mineralized veins and redistribution of their REE content. The estimated composition of the aqueous fluid using data from evaporate mound chemistry is generally similar to that calculated for fluids in known carbonatitic settings, thus, providing further support that these fluids are in fact derived from such source. The maximum possible range of entrapment pressures of the carbonic and aqueous L-V-H inclusions is between 0.5 and 2 kbars, and the pressure during entrapment was transient which supports a structural model in which conditions varied between lithostatic and hydrostatic.

2.8 Relationship of manuscript to thesis

The manuscript summarizes the first detailed classification of the hydrothermal fluids that were present during the formation of the Hoidas Lake REE deposit, and proposes a model for the chemical evolution of these fluids. This provides the groundwork for understanding some of the observed chemical variations in the REE-bearing phases in the diopside-allanite and apatite breccia veins (discussed in detail in Chapter 4). In addition, the possible constraints on the temperature and pressure of the entrapment of these hydrothermal fluids and emplacement of the mineralization are inferred in the manuscript, and therefore indications are provided on the hydrothermal conditions in which REEs can be mobilized in similar systems. Furthermore, the characteristics of the observed hydrothermal fluids are compared with fluid inclusions previously reported from carbonatitic systems, and the results of this comparison complement the suggestions for the possible source of the REE mineralization based on mineral chemical and isotopic characteristics (discussed in Chapter 4 and Chapter 5, respectively). Thus, the manuscript adds to our understanding of the nature, hydrothermal evolution and source of the Hoidas Lake REE deposit. The next manuscript (Chapter 3) focuses on the graphic-textured inclusions in the apatite breccia, mentioned in this chapter.

CHAPTER 3

GRAPHIC-TEXTURED INCLUSIONS IN APATITE: EVIDENCE FOR PEGMATITIC GROWTH IN A REE-ENRICHED CARBONATITIC SYSTEM

The chapter is published as “Pandur, K., Ansdell, K.M., and Kontak, D.J. (2015) Graphic-textured inclusions in apatite: Evidence for pegmatitic growth in a REE-enriched carbonatitic system. *Geology* **43**, 547-550, DOI: 10.1130/G36613.1.”, and reviews were provided by Dr. Rainer Thomas and two anonymous reviewers.

3.1 Abstract

Graphic texture, most common in felsic pegmatites, is documented here in an unusual setting, within apatite of the Hoidas Lake light rare earth element (LREE) deposit, an inferred distal pegmatitic-hydrothermal counterpart of a carbonatite in northern Saskatchewan, Canada. The graphic texture is displayed by vermicular and cuneiform LREE-rich inclusions which define primary growth zones in apatite. Integrated electron microprobe analysis and scanning electron microscope–energy dispersive X-ray spectroscopy imaging document the unusual and heterogeneous compositions of the inclusions, which vary between Ce2O3 + SiO2 (+ ThO2)–dominant and La2O3 + Nd2O3 (+ F)–dominant end members. Here we discuss the formation of these graphic-textured inclusions in the context of models suggested for the formation of graphic quartz–K-feldspar intergrowths in granitic pegmatites, based on the similarity of these features.

3.2 Introduction

Pegmatitic rocks with textures of graphic mineral intergrowths occur primarily in felsic intrusions. Graphic intergrowths of quartz and K-feldspar arranged in vermicular to cuneiform patterns are considered to form through rapid and simultaneous crystallization of quartz and feldspar from a melt (Fenn, 1986; London, 2008). Pegmatitic textures, such as coarse mineral intergrowths, are also found, albeit in lower abundance, in ultramafic, syenitic, and carbonatitic systems (Viljoen and Scoon, 1985; Horváth and Gault, 1990; Bowden et al., 2000). Pegmatites in carbonatites are characterized by their unusual mineralogy (e.g., calcite, calcic pyroxenes, amphiboles, apatite, fluorite) and coarse grain size, but examples of graphic-textured intergrowths are lacking, which is attributed to the lower viscosity of carbonatitic melts compared to granitic melts (London, 2008).

The Hoidas Lake (Saskatchewan, Canada) light rare earth element (LREE) deposit contains allanite and apatite as the main REE hosts. Although a progenitor magmatic reservoir remains enigmatic, a possible source, based on mineralogical and chemical characteristics, is a carbonatitic or alkaline magmatic body (Pandur et al., 2014). An unusual and, as far as we are aware, possibly unique feature of the setting is the spectacular occurrence of graphic-textured inclusions in apatite. Here we document the textural and chemical variations of these graphic-textured inclusions and aim to provide possible explanations for their formation by comparison with the classic graphic intergrowths observed in granitic pegmatites.

3.3 The Hoidas Lake LREE mineralization

The Hoidas Lake mineralization consists of multiple diopside-allanite dikes and brecciated apatite dikes/veins, with pegmatitic crystal sizes (up to 30 cm), that cross-cut deformed Archean and Paleoproterozoic metamorphic rocks in the southern Rae Subprovince of Canada (Fig. 3.1). The earliest diopside-allanite dikes consist mainly of allanite-(Ce), intergrown with hyalophane [$(K,Ba)Al(Si,Al)_3O_8$], titanite, and diopside, and minor amounts of dark red apatite, zircon, and calcite. These dikes are locally zoned from hyalophane-rich pegmatitic rims through diopside-allanite-rich zones to allanite-rich cores. The brecciated apatite dikes/veins commonly cross-cut the diopside-allanite dikes and may contain <10 cm diopside-allanite dike clasts. The apatite in the apatite dikes/veins crystallized in multiple stages. The lanthanide oxide (Ln_2O_3) values increase from 1.5 wt.% in early red apatite to 5.5 wt.% in later green apatite, both dominated by Ce. The latest apatite generation, the coarse red apatite phase, contains ~1 wt.% Ln_2O_3 and is Nd-dominant (Pandur et al., 2013b). The breccia matrix typically contains fine-grained apatite, minor calcite, quartz, green amphibole, REE-carbonate, monazite, and chlorite.

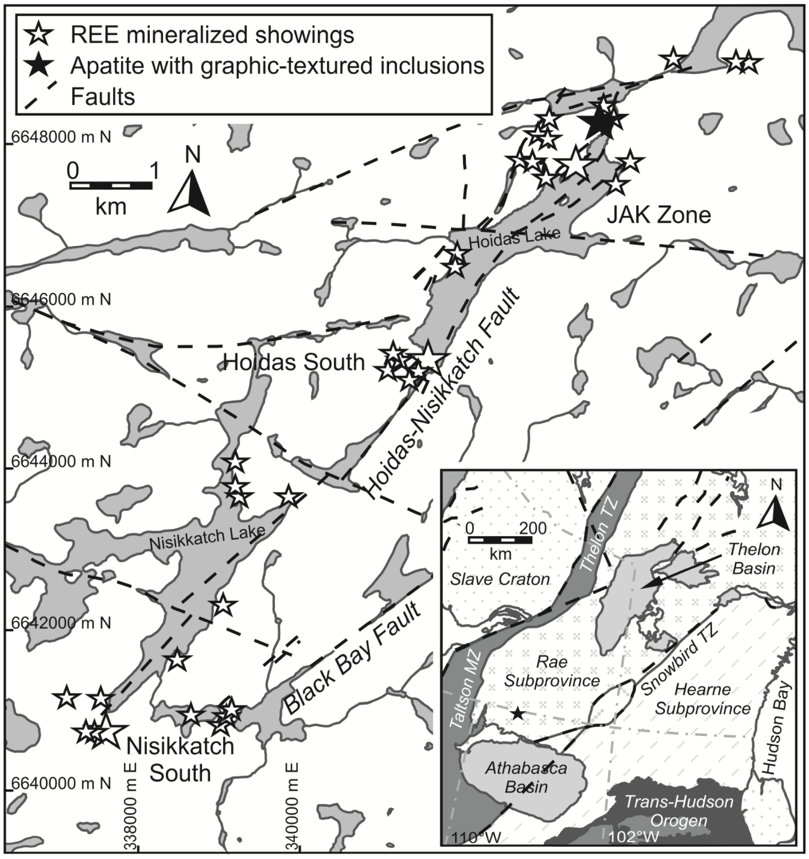

Figure 3.1 Location of Hoidas Lake area (Saskatchewan, Canada), including location of brecciated apatite dike/vein with graphic-textured inclusions used in this study (modified from Normand et al., 2009). Large stars represent main mineralized zones and small stars represent smaller mineralized showings in the area. North and east coordinates are in Universal Transverse Mercator Zone 13V. Inset shows regional lithotectonic domains for parts of northern Alberta, Saskatchewan, and Manitoba, and contiguous Northwest Territories and Nunavut (modified from Pehrsson et al., 2010); star denotes location of Hoidas Lake area. REE—rare earth element; TZ—tectonic zone; MZ—magmatic zone.

The Hoidas Lake mineralization was emplaced along structures sub-parallel to the Hoidas-Nisikkatch fault, a subsidiary of the regional Black Bay fault system (Halpin, 2010; Fig. 3.1) which focused melts and fluids. The dike/vein system represents a shift from an early magmatic stage, through a REE-enriched hydrothermal stage, to a late hydrothermal stage with REE remobilization. This is indicated by the transition from an early Ce-dominant to a later Nd-dominant stage during apatite crystallization, the presence of fluid inclusions (Pandur et al., 2014), and secondary monazite, REE-carbonate, and allanite, that formed through local hydrothermal REE redistribution. The mineralogy and trace element chemistry of the REE dikes/veins, the presence of related Ba- and Sr-rich hyalophane-bearing pegmatite dikes and lamprophyre dikes, and our fluid inclusion studies suggest a mantle-derived, likely carbonatitic or alkaline magmatic source for the melts and fluids (Halpin, 2010; Pandur et al., 2014).

3.4 Samples and methodology

The red apatite contains abundant graphic-textured inclusions throughout the main mineralized zones of the Hoidas Lake area, but primary textures are commonly masked by intense hematite alteration. However, a number of samples lacking hematite alteration, which are light red to greyish green in color, from one of the historic trenches of the JAK Zone (UTM Zone 13V, 343706 E, 6648184 N; Fig. 3.1) allow observation of the original inclusion textures.

Polished thin sections were studied in transmitted and reflected light using an Olympus BX 51 microscope. Quantitative microanalyses of the graphic-textured inclusions and encompassing apatite grains were carried out at the Saskatchewan Research Council Advanced Microanalysis Centre, using a CAMECA SX-100 electron probe microanalyzer with five wavelength-dispersive spectrometers. Beam conditions were set at 20 kV accelerating potential, 20 nA beam current, and 100 nm beam diameter. Representative analyses of the inclusions and the encompassing apatite are provided in Tables B.1 and B.2, respectively (Tables DR1 and DR2 in the GSA Data Repository). Qualitative X-ray element maps and element distribution profiles (La, Ce, Nd, Pr, Si, F, Ba, Th, C) for inclusions were constructed at the Central Analytical Facilities at Laurentian University (Ontario, Canada), using a JEOL 6400 scanning electron microscope with back-scattered detector and an INCA EDS detector, with 20 kV accelerating voltage, 20 nA beam current, and 1–3 μm beam diameter.

3.5 Textural and chemical relationships of the graphic-textured inclusions

The light red to greyish green apatite in the studied samples contains abundant light brown solid inclusions, with either vermicular (Fig. 3.2a) or rectangular and cuneiform (Fig. 3.2b) shapes, arranged in graphic texture (Fig. 3.2a). Distinct mineral phases cannot be distinguished within the inclusions; however, the inclusions are commonly cloudy in appearance, and in some cases have irregular darker and lighter sectors in transmitted light (Fig. 3.2a). Inclusion size and abundance vary between apatite domains, and these variations outline primary growth zones in the apatite. The contacts between zones with distinctly different graphic features are either sharp (Fig. 3.2a) or subtle (Fig. 3.2b). Generally, clusters of euhedral apatite crystals with the graphic textures are surrounded by inclusion-free apatite (Figs. 3.2a–d). The inclusions near apatite rims show a continuous transition into the material coating the surfaces of apatite (Fig. 3.2b), which indicates that this phase was present during the late stages of apatite crystallization. In rare cases, these surface coatings follow the shape of resorbed apatite, and the voids in the resorbed intervals are infilled by the later, inclusion-free apatite generation (Fig. 3.2c).

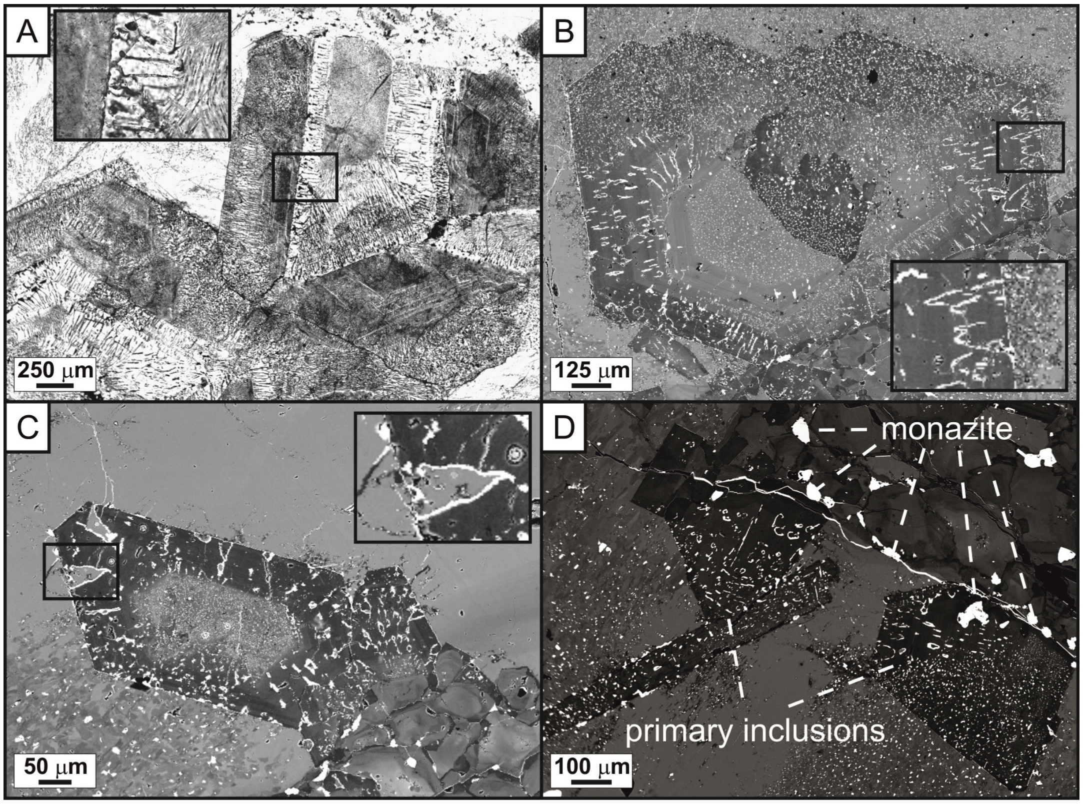

Figure 3.2 Petrography of the graphic-textured inclusions. (a) Photomicrograph (plane polarized light) of zoned euhedral apatite grains displaying variably oriented, light brown graphic inclusions. Inset shows enlargement of area in black rectangle. (b) Back-scattered electron (BSE) image of euhedral apatite that shows concentric compositional zonation and contains elongated inclusions that appear as pockets around euhedral apatite intervals. Inset is enlargement of the area in the black rectangle and shows inclusions that display continuous transition into the same phase that coats the apatite surface. (c) BSE image of euhedral apatite containing graphic inclusions that has resorption features along the rim. Inset shows enlargement of area in the black rectangle, where a resorbed void in apatite is filled with later inclusion-free apatite and its surface is coated by the late-stage inclusion phase. (d) BSE image of graphic inclusions in apatite, and secondary monazite inclusions along a prominent crack and at apatite rims.

Post-entrapment modification of the inclusions cannot be completely disregarded, especially in hematite-altered intervals where the graphic-textured inclusions are darker and reddish in color. These altered apatite zones also contain abundant secondary solid inclusions, commonly localized along fractures (Fig. 3.2d), and include monazite, barite, and REE-carbonates. These same phases, together with chlorite and hematite, commonly fill vugs in the breccia matrix. In the light red to greyish green apatite, this alteration is absent and fewer of the secondary phases are observed, which suggests that the hematite alteration is restricted to fractures in the apatite and grain boundaries and did not affect the grain interiors, hence the contained graphic inclusions likely remained chemically intact. In addition, the secondary mineral inclusions in the apatite are commonly surrounded by irregularly shaped REE-depleted zones, as opposed to the concentric zonation observed in areas around the graphic-textured inclusions. Thus, there are pronounced differences between areas with primary graphic-textured inclusions and those with secondary mineral inclusions (Fig. 3.2d).

The compositions of the graphic-textured inclusions (Table B.1) indicate a continuous compositional range between at least two end members, one with elevated Ce_2O_3 and SiO_2 and one with high $La_2O_3 + Nd_2O_3$ (Fig. 3.3a). Inclusions of the former end member have >6 wt.% SiO_2 and 16–46 wt.% Ce_2O_3, whereas the latter inclusions have 12–22 wt.% La_2O_3 and 19–26 wt.% Nd_2O_3. The lower analytical totals (~80 wt.%) for the latter suggest the presence of CO_2. The inclusions contain up to 2.7 wt.% F, with slightly higher F detected in the ($La_2O_3 + Nd_2O_3$)–rich inclusions (Fig. 3.3b). Regardless of the variations in SiO_2 (and Ce_2O_3) content, the ratio of La_2O_3 and Nd_2O_3 remains constant at ~4:6 (Fig. 3.3c). The inclusions also have up to 12 wt.% ThO_2, which increases slightly with SiO_2. The CaO and P_2O_5 contents of the inclusions range from 1 to 31 wt.% and 0.1 to 19 wt.%, respectively, and additional elemental enrichments include U (≤1.6 wt.% UO_2), Y (≤3.7 wt.% Y_2O_3), Fe (≤12.2 wt.% FeO), Mn (≤2.2 wt.% MnO), Mg (≤2.3 wt.% MgO), and Ba (≤4.5 wt.% BaO); however, these concentrations show no consistent relationship with Ce_2O_3 or $La_2O_3 + Nd_2O_3$.

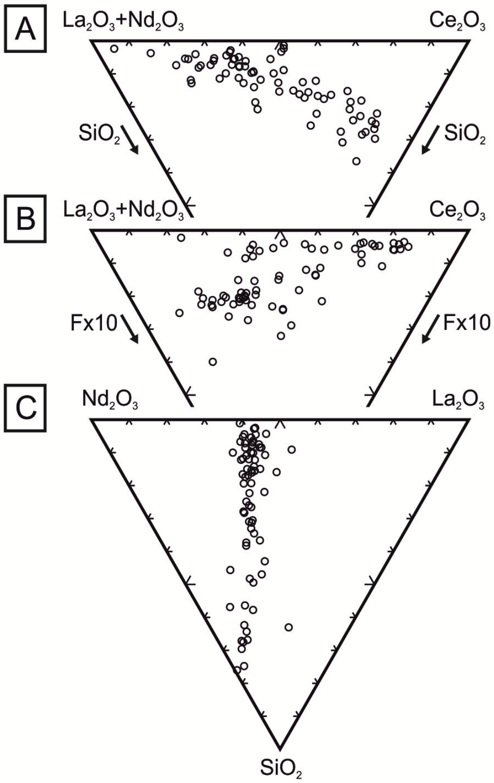

Figure 3.3 Ternary plots summarizing the chemistry of graphic inclusions (wt.%) in the Hoidas Lake (Saskatchewan, Canada) apatite, based on electron microprobe analyses. (a) Ce_2O_3–(La_2O_3 + Nd_2O_3)–SiO_2. (b) Ce_2O_3–(La_2O_3 + Nd_2O_3)–F x 10. (c) La_2O_3–Nd_2O_3–SiO_2.

X-ray element maps and chemical profiles show that individual graphic-textured inclusions can be chemically heterogeneous (Fig. 3.4). Irregular Ce- and La-dominant intervals are distinguished in certain inclusions, and the late-stage coatings along apatite rims are generally Ce-dominant (Fig. 3.4a). The Nd contents of inclusions are consistent in both their Ce- and La-dominant intervals (Fig. 3.4b), and relative enrichment of Pr occurs in the La-rich domains. The Si contents are higher in the Ce-rich intervals, whereas F is higher in the La-rich domains (Fig. 3.4c); C is also consistently higher in the La-rich domains and decoupled from Si (Fig. 3.4d), however the amount of CO_2 cannot be quantified with the techniques used. In addition, slightly higher Th was also detected in the Ce-rich domains of the inclusions.

Some apatite crystals displaying multiple growth zones with elongated graphic inclusions show variations in REE contents (from 0.9 to 5.9 wt.% Ln_2O_3; Table B.2; Fig. 3.2b) that accompany changes in the spacing and abundance of the inclusions. However, these chemical variations in apatite are not reflected by consistent variation in the compositions of the inclusions.

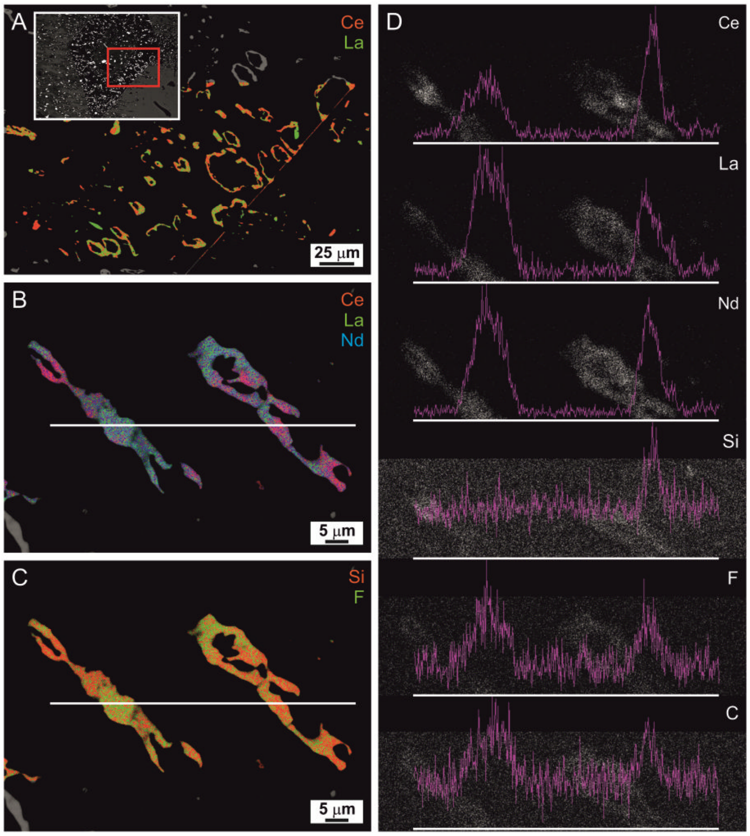

Figure 3.4 Chemical variations of the graphic-textured inclusions. (a) False-colored X-ray element map of graphic inclusions superimposed on back-scattered electron (BSE) image showing heterogeneous compositions, where red denotes Ce-rich and green denotes La-rich domains. Inset shows BSE image of the whole apatite crystal with red rectangle denoting the enlarged area. (b) False-colored Ce (red)–La (green)–Nd (blue) X-ray map for elongated graphic inclusions. White line represents traverse for chemical profiles shown in (d). (c) False-colored Si (red)–F (green) X-ray map for elongated graphic inclusions. White line represents traverse for chemical profiles in (d). (d) Chemical profiles for Ce, La, Nd, Si, F, and C for traverse shown in (b) and (c).

3.6 Discussion and summary

The graphic-textured inclusions lack recognizable crystalline phases, are cloudy in appearance, and do not show detectable phase changes upon heating to 800 °C. The presence of these inclusions in a graphic distribution indicates that they formed during apatite crystallization. These graphic textures are most similar in appearance to quartz–K-feldspar intergrowths observed in granitic pegmatites.

Multiple models have been suggested for the formation of graphic intergrowths in granitic pegmatites. According to Fenn (1986) and London (2008, 2009), these features form through kinetic processes at the boundary layer adjacent to the rapidly growing feldspar crystals, where ridges of the irregular growth surface of K-feldspar protrude beyond the mean growth-surface and drain the feldspar-forming components (Al, K) from the boundary-layer melt. This causes the melt to become oversaturated in silica, resulting in quartz precipitation between the ridges of K-feldspar. Subsequent quartz growth depletes the boundary-layer melt in silica, which restores feldspar-saturated growth; the process is repeated episodically to produce the rhythmic quartz-feldspar intergrowths (Lentz and Fowler, 1992). An alternative explanation for graphic textures, based on studies of natural melt and fluid inclusions (Thomas et al., 2012; Thomas and Davidson, 2012) and experimental work (Thomas and Veksler, 2002), is melt-melt immiscibility, which causes the formation of conjugate melt fractions from an exceptionally hydrous and flux-rich primary melt. During this process, droplets of a second melt are attracted to the growing crystal due to surface tension and subsequently trapped and overgrown to form graphic texture.

We suggest that, by analogy to the quartz–K-feldspar intergrowths, the formation of the graphic-textured inclusions in apatite of the Hoidas Lake REE deposit can be similarly explained. At the time of apatite growth, REE-rich phases may have precipitated on the growth surface of the apatite from a boundary-layer melt that contained REEs, Si, F and CO_2, and these phases were then overgrown by rapidly nucleating apatite ridges to form tube-shaped inclusions (Fig. 3.5, model 1). As these inclusions would then represent local saturation of REE-rich phases along the apatite growth front, they reflect the composition of a modified boundary-layer melt and not the bulk composition of the original melt from which apatite crystallized (London, 2008, 2009).

Even though the crystallinity of the graphic-textured inclusions has not been confirmed, it is possible that these inclusions represent melts trapped and overgrown by rapid apatite crystallization. We speculate that the demonstrated consistent chemical variations within and among these inclusions may reflect melt-melt immiscibility (Fig. 3.5, model 2), as has been documented in hydrous felsic melts (Thomas and Davidson, 2012). Therefore, the two compositional end members of the Hoidas Lake graphic-textured inclusions may represent two different melts that were trapped in melt pools, and the phase separation of which was not complete. The enrichment of fluxing components, in this case primarily F, in the melt likely played a role in the formation of the graphic textures.

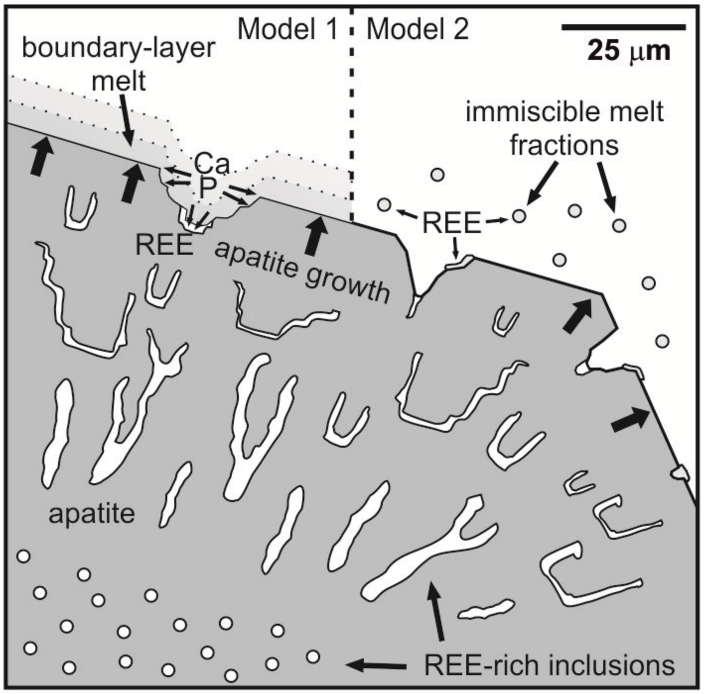

Figure 3.5 Schematic diagram illustrating two possible models for the formation of graphic inclusions in apatite of the Hoidas Lake (Saskatchewan, Canada) rare earth element (REE) deposit.

The observed abrupt changes in the size and density of inclusions among distinct apatite growth zones (Figs. 3.2a and b) are attributed to variation in crystal growth rates or diffusivity of the apatite-forming constituents in the melt (Ca, P). Coarser inclusions with wider spacing formed when the lateral diffusion of Ca and P toward the growing crystal surface was more effective due to either slower crystal growth or an increase in flux contents of the melt.

The Hoidas Lake REE deposit is most likely related to a carbonatitic or alkaline magma source, and is inferred to be the distal pegmatitic part of this system. As the brecciated apatite dikes/veins consist almost entirely of REE-bearing apatite, we are likely dealing with a highly fractionated REE-Ca–rich carbonate-phosphate melt with variable amounts of Si and inferred CO_2. The graphic-textured inclusions range from a Ce-Th–rich silicic end member to a La-Nd-F–rich end member. Within individual inclusions, there is heterogeneous separation of the Ce- versus La-dominant areas, although complete unmixing of the two phases was rarely observed.

The possible triggering factors for rapid apatite nucleation and formation of the inclusions include undercooling of the pegmatitic melt, changing melt composition (enrichment of fluxing components), and sudden pressure variations. The presence of graphic textures in pegmatites related to a carbonatitic system, like those observed at Hoidas Lake, indicates that such processes occur during the evolution of carbonatitic melts.

3.7 Relationship of manuscript to thesis

The manuscript reports on textural and chemical analysis of primary inclusions which display spectacular graphic texture in the Hoidas Lake apatite breccia. Such features have not previously been observed in carbonatitic or alkaline magmatic systems. The manuscript provides detailed description of the chemical variations in these inclusions, and two possible models for their formation. The results of this study indicate that fine-scale processes at the interface of the rapidly crystallizing apatite and the adjacent melt probably occurred in a similar way to those in granitic systems. The next chapter focuses on the chemical variations and magmatic-hydrothermal evolution of the mineralized vein phases, in view of the information obtained on the characteristics of fluids and melts in the Hoidas Lake deposit (from Chapter 2 and this chapter).

CHAPTER 4

PETROGRAPHIC AND MINERAL CHEMICAL CHARACTERISTICS OF THE HOIDAS LAKE DEPOSIT, NORTHERN SASKATCHEWAN, CANADA: CONSTRAINTS ON THE ORIGIN OF A DISTAL MAGMATIC-HYDROTHERMAL REE SYSTEM

The chapter was submitted as “Pandur, K., Ansdell, K.M., Kontak, D.J., Halpin, K.M., and Creighton, S. Petrographic and mineral chemical characteristics of the Hoidas Lake deposit, northern Saskatchewan, Canada: Constraints on the origin of a distal magmatic-hydrothermal REE system.” to *Economic Geology*, and is currently under review.

4.1 Abstract

The diopside-allanite and apatite breccia veins of the Hoidas Lake LREE (light rare earth element) deposit in northern Saskatchewan, Canada represent a complex magmatic-hydrothermal system unrelated to its strongly deformed Archean and Paleoproterozoic host rocks in the Rae Subprovince. The veins were emplaced along the Hoidas-Nisikkatch Fault, a subsidiary of the deeply-rooted Black Bay Fault System which likely provided the pathways for the melts and fluids. Allanite in the diopside-allanite veins shows concentric zonation, reflecting relative REE-depletion in the source melt, followed by REE-enrichment. The later apatite breccia veins consist of multiple apatite generations. Graphic-textured inclusions in the earliest red apatite phase indicate a magmatic origin. The average total rare earth oxide (TREO) content increases from 1.5 wt.% in the red apatite to 5.5 wt.% in the green apatite, both dominated by Ce. In contrast, the latest generation, coarse red apatite contains around 1 wt.% TREO, and is Nd-dominant. This shift from Ce- to Nd-dominance reflects transition from magmatic to hydrothermal growth. Interaction with hydrothermal fluids resulted in chlorite-hematite alteration and REE redistribution into secondary monazite, REE-carbonates, REE-Sr-carbonates and allanite, the latter occurring in late quartz-carbonate veins and showing TREO up to 32.9 wt.%. The chemistry of the REE-bearing phases and their connection with hyalophane-bearing pegmatites and lamprophyre dikes indicate a mantle-derived, most probably carbonatitic source for the mineralizing melts and fluids.

4.2 Introduction

Rare earth element (REE) deposits were previously considered to be dominantly of magmatic origin, due to the precept that the REEs are relatively immobile in hydrothermal fluids. The assumption of REE immobility, however, has been challenged for some time. For example, the origin of the Strange Lake (Salvi and Williams-Jones, 1990), Thor Lake (Sheard et. al., 2012) and Bokan Mountain (Dostal et al., 2014) REE deposits have been reinterpreted based on petrological observations. Thus, based on these aforementioned studies, and theoretical and experimental data (Samson and Wood, 2005; Williams-Jones et al., 2012), it is now generally accepted that many magmatic REE deposits have been significantly affected, and in some cases upgraded, by interaction with late-stage hydrothermal fluids of either magmatic origin or mixed provenance, regardless of the type of magmatic source. It has also become apparent that hydrothermal processes can lead to significant spatial fractionation of individual REEs, even within the same deposit (e.g., Bayan Obo – Smith et al., 2000), which relates to variable uptake of the REEs by the hydrothermal fluids (Williams-Jones et al., 2012). Furthermore, and of particular relevance to exploration and ore deposit vectoring, the magmatic-hydrothermal mobilization of REEs from their source region, via transport along available structural pathways can lead to economic REE mineralization in areas distal from their source.

The Proterozoic Hoidas Lake REE deposit, which has reserves of 2.56 million tonnes at 2.43 wt.% TREO (total rare earth oxides) (Billingsley, 2010), is located within the southern Rae Subprovince in northern Saskatchewan, Canada, and it is one such example of a distal deposit, since no direct spatial or temporal relationship to a magmatic source has been recognized. Our studies to date suggest that the complex LREE (light rare earth element)-rich vein system was focused along local structures related to the regional Black Bay Fault System (Halpin, 2010; Pandur et al., 2014). The nature and origin of the Hoidas Lake REE mineralization highlight, therefore, the importance of major structural pathways in REE mobilization and deposition.

The increasing scientific interest in the behavior of the REEs in hydrothermal fluids and the role of hydrothermal processes in the formation of economic REE deposits have provided the basis to study the various mineralized phases of the Hoidas Lake deposit and evaluate the mineral chemical evolution of the system in context of the hydrothermal fluids present. In our earlier study of the hydrothermal fluids preserved in the deposit (Pandur et al., 2014), the evolution of the mineralizing fluids was constrained. In this work, the results of fluid inclusion studies are integrated with detailed petrographic and mineral chemical data of REE-bearing vein minerals obtained by electron microprobe analysis, to evaluate both the chemical variations in the system and the effect of hydrothermal fluids on the distribution of REEs in the mineralized veins. The alteration characteristics of graphic-textured primary inclusions and secondary REE-enriched phases in apatite are also used to infer the transition from late-magmatic to hydrothermal conditions in the Hoidas Lake deposit. Furthermore, the chemical characteristics of the REE-enriched phases are used to provide constraints on the possible source of the mineralization.

4.3 Geological setting

4.3.1 Regional geology

The Rae Subprovince, which hosts the Hoidas Lake REE deposit, and the adjacent Hearne Subprovince form part of the Churchill Province of the Canadian Shield (Fig. 4.1). These subprovinces consist of Archean and Paleoproterozoic intrusive and supracrustal rocks, many of which have been multiply deformed and metamorphosed. Much of the thermal and structural overprint on the rocks developed during amalgamation with the Slave and Superior cratons during the assembly of Laurentia in the Paleoproterozoic (Hoffman, 1988; Aspler et al., 2002). The oldest Paleoproterozoic event, the Arrowsmith Orogeny, resulted in extensive arc magmatism along the western margin of the Rae Subprovince and widespread deformation and metamorphism at approximately 2.3 Ga (Berman et al., 2013). However, evidence for this thermo-tectonic episode was mostly concealed by the effects of younger events. The 2.0 to 1.9 Ga Taltson-Thelon Orogeny (Hartlaub et al., 2007) formed as a result of the collision between the Slave Craton and the Rae Subprovince, which was associated with magmatism in the western part of the Rae Subprovince (Taltson Magmatic Zone) and granulite facies peak metamorphic conditions, followed by amphibolite and greenschist facies retrograde metamorphism (Grover et al., 1997; McNicoll et al., 2000; Ross, 2002; Ross and Eaton, 2002). The younger Trans-Hudson Orogen developed between 1.92 and 1.8 Ga, resulting from the complex accretion of juvenile Paleoproterozoic rocks and older microcontinents along the southeastern margin of the Churchill Province, and eventual collision with the Superior Province (Hoffman, 1988; Ansdell, 2005, Corrigan et al., 2009). Within the Rae and Hearne subprovinces there are numerous fault-bounded sedimentary basins indicating extension coeval with the various orogenic episodes, and in some locations in these basins, mantle-derived magmas were emplaced (Peterson et al., 1994, 2002; Morelli et al., 2009; Ashton et al., 2009; Rainbird et al., 2010). The supracrustal rocks are variably deformed and metamorphosed, whereas the youngest (<1.75 Ga) sedimentary sequences, preserved in the intracontinental Athabasca and Thelon basins, are unmetamorphosed.

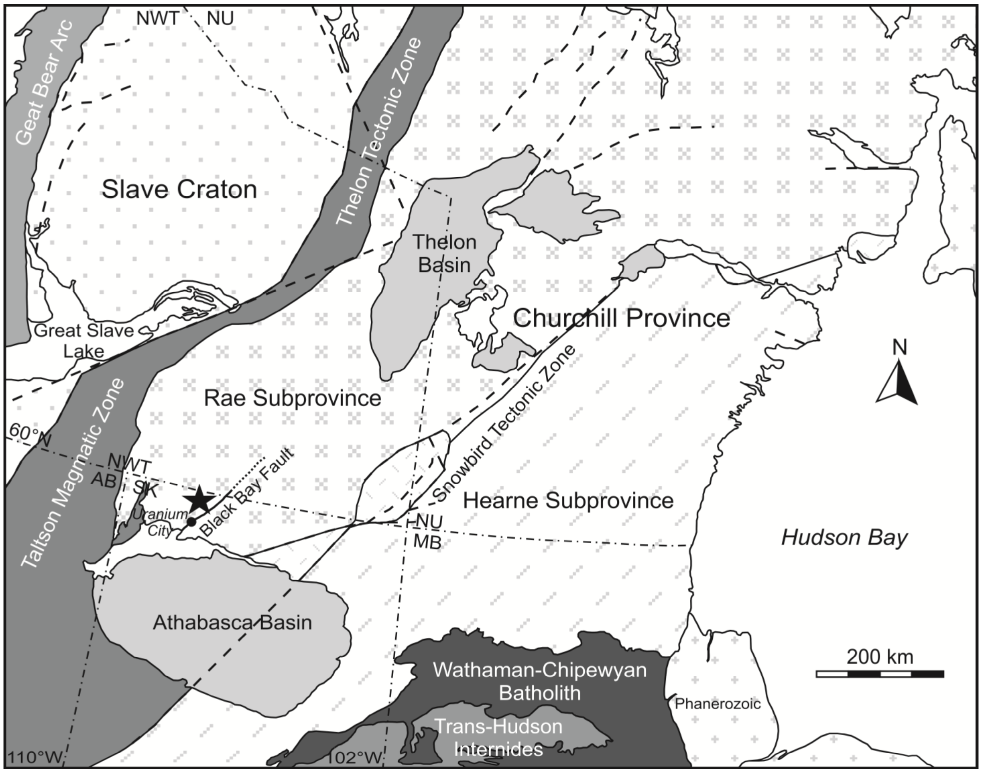

Figure 4.1 Regional lithotectonic assemblage map for parts of northern Alberta, Saskatchewan and Manitoba and contiguous Northwest Territories and Nunavut (modified from Pehrsson et al., 2010). A black star denotes the location of the Hoidas Lake REE deposit. The dashed lines represent faults.

4.3.2 Local geology in the Hoidas Lake area

The host rocks of the Hoidas Lake area consist of Archean to Paleoproterozoic tonalitic to granodioritic gneisses and leucogranitic gneisses (Fig. 4.2). Less extensive units in the area include amphibolites, metasedimentary gneisses, and younger diorite intrusions, syenites and quartz syenites, and lamprophyre dikes (Fig. 4.2; Harvey et al., 2002; Gunning and Card, 2005; Normand et al., 2009). The presence of amphibolite xenoliths in the tonalitic to granodioritic gneiss indicates that older supracrustal and/or earlier intrusive phases existed (Fig. 4.3a). The tonalitic to granodioritic gneiss complex (Fig. 4.3a) is intruded by various granitic rocks (Fig. 4.3b). Metasedimentary gneisses (Fig. 4.3c) northwest of Hoidas Lake are invaded by pink leucogranite sheets, indicating that this area might represent the upper part of a leucogranite pluton that intruded and assimilated the metasedimentary rocks (Harper, 2012). Syenites are abundant in one area north of Hoidas Lake (Fig. 4.3d), and there appears to be a continuous transition from syenite through quartz syenite to granite. Late diorite dikes were also observed in the area (Fig. 4.3e; Harvey et al., 2002; Normand et al., 2009).

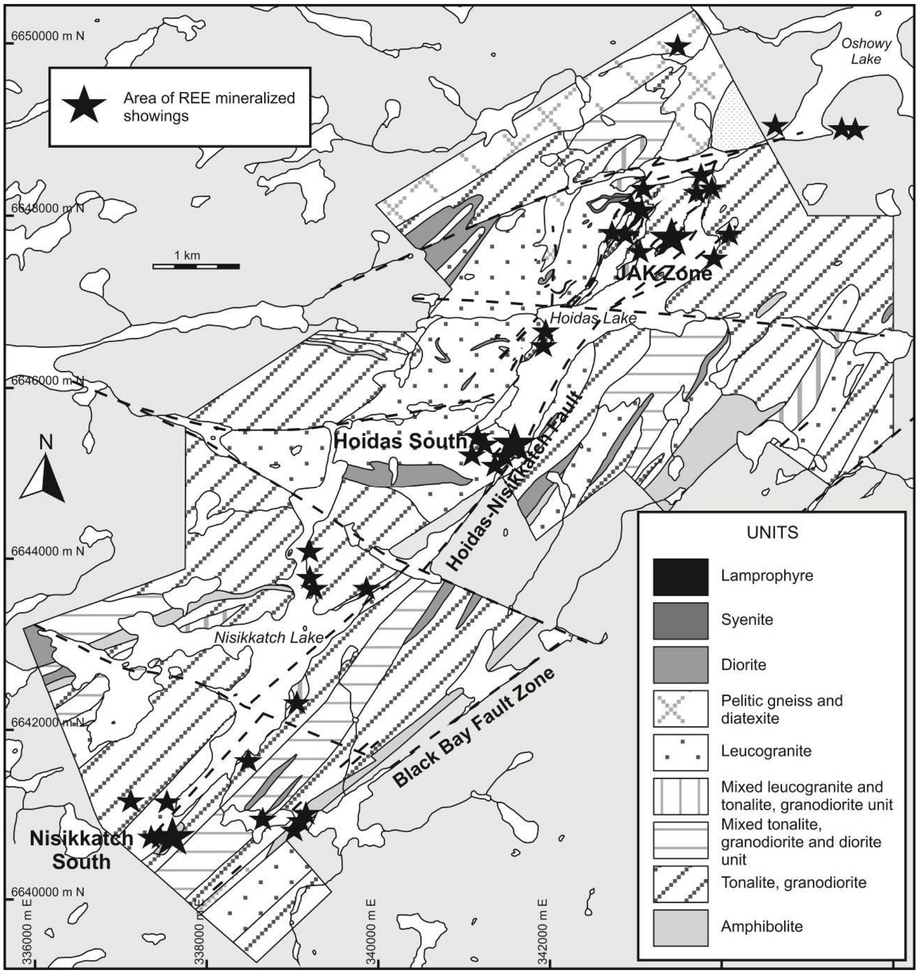

Figure 4.2 Geological map of the Hoidas Lake area, showing the dominant lithological and structural units, and the location of the mineralized showings (modified from Normand et al., 2009; Harper, 2012). The faults are represented by dashed lines on the map. N and E coordinates denote the location of the area in the UTM 13V zone.

All of the aforementioned rocks experienced upper amphibolite to lower granulite grade metamorphism at ca. 1.9 Ga (Harvey et al., 2002; Gunning and Card, 2005; Ashton et al., 2009).

Intrusions of granitic pegmatite, likely of different ages, have also been noted to occur in the area. A special type of pegmatite, and most relevant to the present study, is a suite of hyalophane-bearing pegmatites that occur as discrete dikes (Fig. 4.3f) and more irregular amoeboid bodies with diffuse contacts. These pegmatitic bodies are dominated by variable amounts of quartz, hyalophane, potassium feldspar with lesser diopside, hornblende and magnetite. Undeformed lamprophyre dikes represent the youngest magmatic event in the area (Fig. 4.3g), and are interpreted to postdate peak metamorphism (Normand et al., 2009). Quartz-, calcite-, epidote-, chlorite- and hematite-bearing veins, as well as hematite- and epidote-coated fractures, are abundant in the area (Fig. 4.3h). The quartz-carbonate veins are generally a few centimetres wide, but can coalesce to form zones of 1 m width. Some quartz flooded breccia occurrences with abundant epidote and hematite also occur in the area. The quartz-carbonate veins and quartz-flooded breccia cross-cut the mineralized veins, and the hematite- and epidote-coated fractures cross-cut the lamprophyre dikes. Detailed petrographic descriptions and whole-rock geochemical data of the host rocks in the area are given in Halpin (2010).

Successive deformation stages in the Hoidas Lake area resulted in the development of a northwest-southeast-oriented, composite S1-S2 foliation that is simultaneous with the upper amphibolite-lower granulite grade peak metamorphism (Ashton et al., 2009). These structural features are overprinted by a northeast-southwest-trending S3 foliation, related to shear zone development and reactivation along the Black Bay Fault, and later, gently undulating open F4 folds (Harvey et al., 2002; Gunning and Card, 2005; Normand et al., 2009; Harper, 2012). Late-stage development of east, northeast and southeast oriented fractures and faults were also observed in the area. The Black Bay Fault is a major, northeast-trending brittle structure in the southern Rae Subprovince (Fig. 4.1) superimposed on a belt of mylonitic gneisses. Overall, the Black Bay structure has a long-lived history, with ductile deformation being initiated at about 2.3 Ga and overprinted by brittle faults before 1.83 Ga and continuing to ca. 1.7 Ga (Kraus and Ashton, 2000; Bergeron, 2001). The northeast-southwest oriented Hoidas-Nisikkatch Fault is parallel to, and likely shares the complex deformation history of, the Black Bay Fault, including several periods of reactivation and deformation (Halpin, 2010).

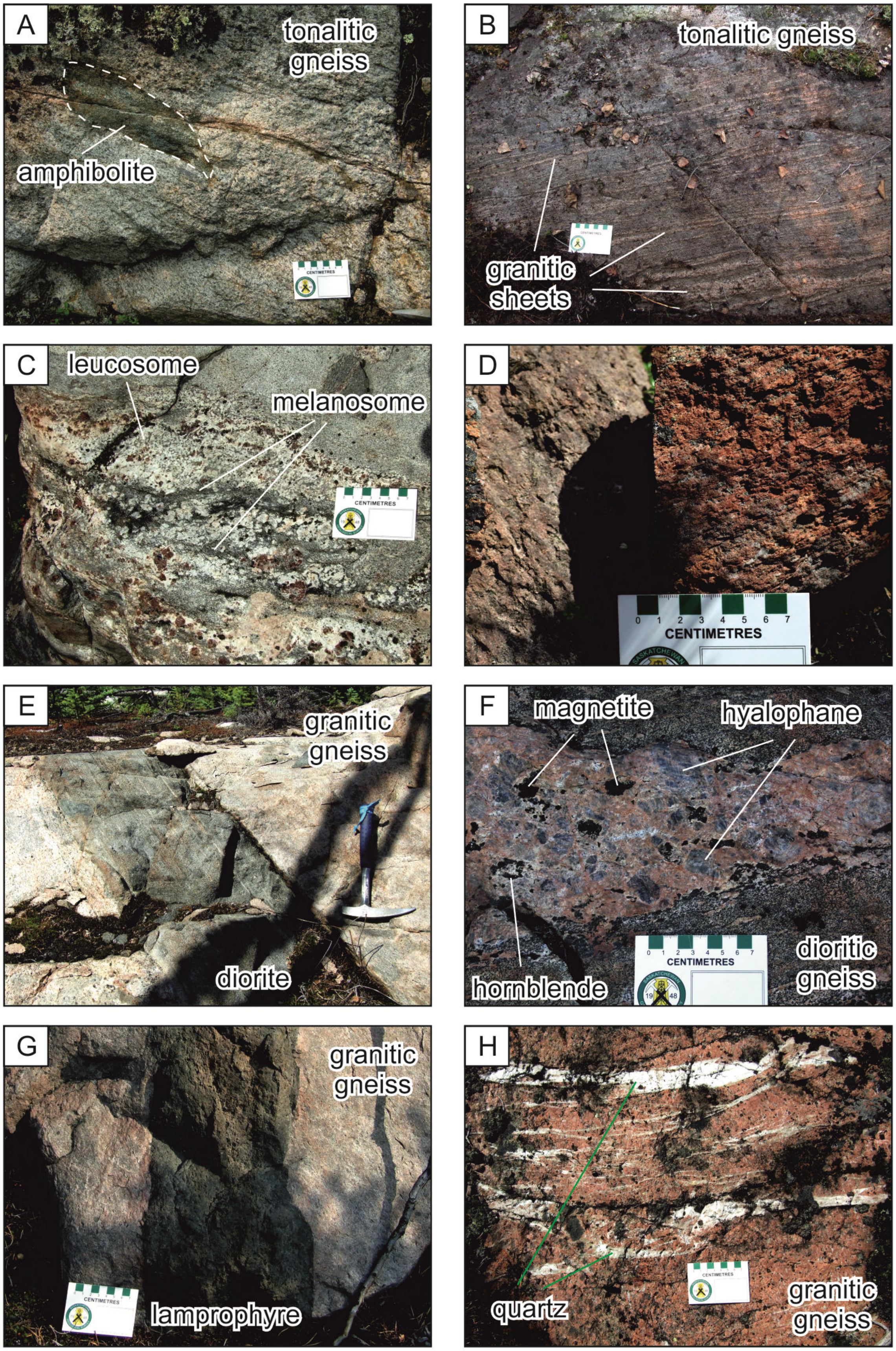
A
tonalitic gneiss
amphibolite
B
tonalitic gneiss
granitic sheets
C
leucosome
melanosome
D
0 1 2 3 4 5 6 7
CENTIMETRES
E
granitic gneiss
diorite
F
magnetite
hyalophane
hornblende
dioritic gneiss
G
granitic gneiss
lamprophyre
H
quartz
granitic gneiss

Figure 4.3 (on previous page) Outcrop photographs of the distinct host rock units of the Hoidas Lake area. (a) Tonalitic gneiss containing flattened amphibolite xenolith. (b) Tonalitic gneiss with abundant granitic sheets of variable thickness along the foliation. (c) Pelitic gneiss with segregated melanosome and leucosome layers, the latter containing up to 5 cm garnet porphyroblasts. (d) Syenite block with abundant potassium feldspar, amphibole and epidote. (e) Fine-grained diorite dike cross-cutting leucogranitic gneiss. (f) Hyalophane-bearing pegmatite dike with abundant magnetite and hornblende cross-cutting dioritic gneiss. (g) Lamprophyre dike cross-cutting leucogranitic gneiss. (h) Abundant quartz veins, showing variable thickness and similar orientation, cutting through foliated leucogranitic gneiss.

4.4 Sampling and analytical procedures

The samples used in this study were collected from surface exposures in the Hoidas Lake area and from drill core provided by Great Western Minerals Group. Polished thin sections from various host rock samples, hyalophane-bearing pegmatite dikes, quartz-carbonate veins/vugs and several generations of the REE mineralization were prepared at Vancouver Petrographics Ltd. and the Thin Section Laboratory in the Department of Geological Sciences at the University of Saskatchewan. The polished sections were studied in transmitted and reflected light using an Olympus BX 51 microscope equipped with a Lumenera Infinity 2 camera at the University of Saskatchewan.

Quantitative microanalyses of various mineral phases from pre-selected areas in 24 polished thin sections were carried out at the Saskatchewan Research Council (SRC) Advanced Microanalysis Centre, using a CAMECA SX-100 Electron Probe Micro-analyzer, equipped with five wavelength dispersive spectrometers. Each element was analyzed for 30 seconds on peak, and background intensity was calculated using a mean atomic number correction method (Donovan and Tingle, 1996). Beam conditions were set at 20 kV accelerating potential and 20 nA beam current. The calibration at SRC used a combination of pure element and mineral standards for the common elements and synthetic Ca-Al-Si-REE glasses for the REEs (J. Craven, pers. comm.). Peak overlaps were corrected for REEs based on observed interferences on the REE standards. Over 1400 spot analyses were performed, and many of these were from areas that are metamict or altered. The main focus of these analyses was on elemental variations of allanite and apatite, and the nature of inclusions present in these phases. However, other REE-bearing phases like titanite, monazite, REE-carbonates, REE-Sr-carbonates, thorite, zircon and various REE-barren minerals, like hyalophane, diopside and barite were also studied. Subsequent back-scattered electron (BSE) imaging was also carried out on these phases. Representative analyses are provided in Tables 4.1–4.7. Formulae of red apatite, green apatite, coarse red apatite, monazite, and thorite from the apatite breccia veins (expressed as atoms per formula unit, apfu) were calculated on the basis of empirical O or (O,OH,F,Cl) values and cation numbers. The OH component of the X-site anions for apatite was estimated from the calculated F and Cl atomic formula units. Chondrite-normalized REE plots for the REE-bearing phases were created. The slopes of the REE plots are represented by maximum $(La/Gd)_N$ ratios, as Gd was detected in most analyses, which enables comparison of the REE distributions of the distinct REE-bearing phases. The extent of derivation of the analyzed Eu abundances from those anticipated from the lanthanide contraction trend was quantified by calculating average Eu/Eu* values, where Eu* = $2xEu/(Sm_N+Gd_N)$.

In addition, back-scattered electron imaging of inclusions in the apatite breccia was done at the Central Analytical Facilities of Laurentian University, using a JEOL 6400 scanning electron microscope (SEM) equipped with a back-scattered electron detector and an INCA Energy-Dispersive X-ray Spectrometer (EDS). X-ray element maps for inclusions were acquired using 20 kV accelerating voltage, 20 nA beam current and 1-3 μm beam diameter.

4.5 Results

4.5.1 Petrology and textural relationships of the REE mineralization

The Hoidas Lake deposit consists of three main mineralized zones, the JAK Zone, the Hoidas South Showing and the Nisikkatch South Showing, and several other smaller showings along the same structural trend that passes through Hoidas Lake and Nisikkatch Lake (Fig. 4.2). The REE mineralization consists of up to 11 m wide diopside-allanite veins and apatite breccia veins. Hyalophane-bearing pegmatites and quartz-carbonate veins that seldom contain allanite are temporally and spatially associated with the mineralization, as discussed below. The most studied part of the vein system, the JAK Zone, is continuous to at least 300 m depth and at present remains open both down dip and along strike (Halpin, 2010). The diopside-allanite veins and apatite veins in all zones were emplaced along northeast-trending faults/fractures, sub-parallel to the dominant S3 foliation and the Hoidas-Nisikkatch Fault.

The diopside-allanite veins have sharp or diffuse contacts with the host rocks, and in the latter case they are surrounded by up to 25 cm thick, monomineralic hyalophane-rich pegmatitic margins (Fig. 4.4a). The diopside-allanite veins are typically coarse-grained (<10-30 cm), and allanite occurs in variable quantities from a few percent to almost 100% (i.e., intervals of massive allanite). The veins are sometimes zoned from hyalophane-rich pegmatitic margins, through hyalophane-diopside-rich zones, diopside-allanite rich zones, to allanite-rich internal zones. These veins generally cross-cut the hyalophane-bearing pegmatites (Fig. 4.4b) but, in some cases, they are cross-cut by the hyalophane-bearing pegmatites (Fig. 4.4c).

In the diopside-allanite veins, the allanite is anhedral to subhedral, varies in color from black through brown and yellowish brown to red, and often displays irregular or concentric color zonation (Fig. 4.4d, e). The rims of the allanite are occasionally characterized by distinctly different optical properties similar to those of epidote, and in such cases these epidote-like zones may extend into the internal parts of the allanite along fractures (Fig. 4.4e). The allanite cores are commonly metamict and isotropic, and surrounded by zones of fractured allanite. Coarse (<1 cm), subhedral to euhedral titanite occurs intergrown with allanite in these veins (Fig. 4.4f, g), which indicates their synchronous growth. Some of the smaller titanite grains show irregular, concentric color zonation. Hyalophane is abundant in the diopside-allanite veins, generally in the interstitial space between the allanite and titanite grains (Fig. 4.4g), but also in the outermost zones where hyalophane forms monomineralic intervals, or is intergrown with diopside. Diopside is commonly intergrown with allanite or fills interstitial space between allanite and titanite in the diopside-allanite veins, and is replaced by green amphibole (Fig. 4.4h). Dark red apatite, zircon, calcite, epidote, scapolite, magnetite and hematite also appear in the diopside-allanite veins along with coarse-grained biotite-rich intervals (Fig. 4.4g). In some of the brecciated diopside-allanite veins, euhedral tabular zeolite crystals occur in the vugs in the matrix, oriented perpendicular to the margin of the vugs. The diopside-allanite veins are often strongly altered, and in some cases even replaced by hematite- and chlorite-rich intervals. The less strongly altered allanite crystals are replaced by a mixture of REE-carbonates and chlorite in the crystal cores and along fractures (Fig. 4.4e), and in some cases by epidote along their rims.

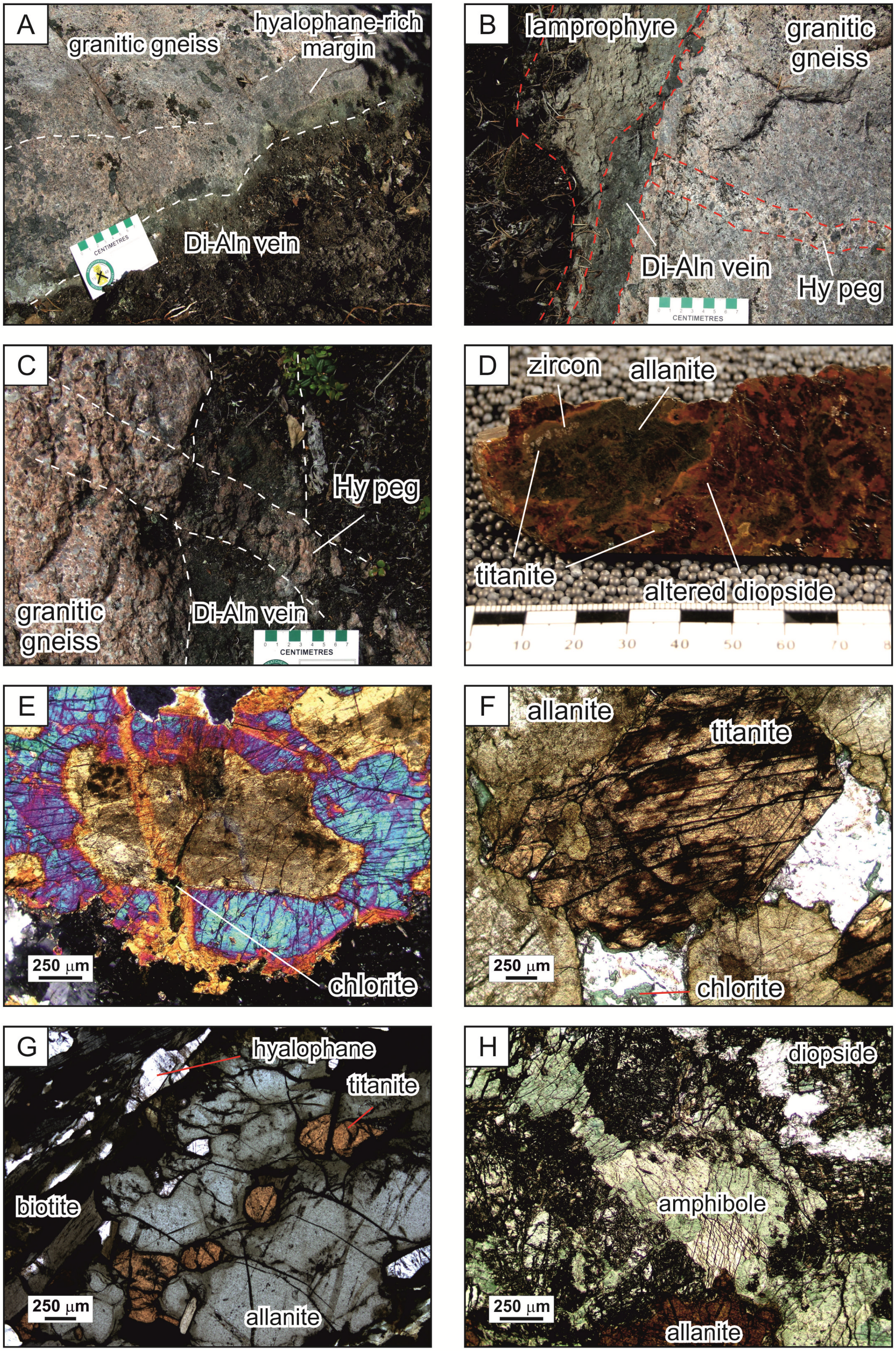
A
granitic gneiss
hyalophane-rich margin
Di-Aln vein
CENTIMETRES
B
lamprophyre
granitic gneiss
Di-Aln vein
Hy peg
CENTIMETRES
C
Hy peg
granitic gneiss
Di-Aln vein
CENTIMETRES
D
zircon
allanite
titanite
altered diopside
10
20
30
40
50
60
70
E
250 μm
chlorite
F
allanite
titanite
250 μm
chlorite
G
hyalophane
titanite
biotite
250 μm
allanite
H
diopside
amphibole
250 μm
allanite

Figure 4.4 (on previous page) Outcrop photographs, sample photographs and photomicrographs of diopside-allanite veins from the Hoidas Lake deposit. (a) Outcrop of diopside-allanite vein surrounded by up to 25 cm thick, irregular, hyalophane-rich pegmatitic margin that shows diffuse contact towards the surrounding leucogranitic gneiss, Di-Aln vein = diopside-allanite vein. (b) Outcrop of hyalophane-bearing pegmatite dike of 3-4 cm width cross-cut by diopside-allanite vein, that in turn is cross-cut by a lamprophyre dike in granitic gneiss, Di-Aln vein = diopside-allanite vein, Hy peg = hyalophane-bearing pegmatite. (c) Outcrop of hyalophane-bearing pegmatite dike cross-cutting diopside-allanite vein in granite, Di-Aln vein = diopside-allanite vein, Hy peg = hyalophane-bearing pegmatite. (d) Coarse-grained, strongly altered diopside-allanite vein sample with brown irregularly shaped allanite that shows concentric zonation, and encloses titanite and zircon crystals in its outermost zone. The allanite crystals are surrounded by diopside that was partially or in places fully replaced by hornblende, actinolite, chlorite, calcite and hematite. (e) Cross polarized light photomicrograph (XPL) of irregularly shaped allanite that shows concentric optical zonation, with the outer zone showing similar interference colors to those of epidote. The allanite is cross-cut by a fracture, along which it shows distinctive interference colors that extend to the rim of the crystal. Chlorite crystals also occur along the fracture. (f) Plane polarized light (PPL) photomicrograph of coarse titanite and allanite crystals in diopside-allanite vein. Chlorite appears in the interstitial space between the titanite and allanite. (g) PPL photomicrograph of diopside-allanite vein interval containing coarse-grained allanite enclosing finer-grained titanite crystals, and abundant hyalophane and biotite in the interstitial space. (h) PPL photomicrograph of diopside-allanite vein interval with abundant green amphibole replacing diopside.

The apatite breccia veins commonly appear as irregularly shaped intervals within the diopside-allanite veins, and have relatively sharp contacts (Fig. 4.5a). Brecciated, sub-angular clasts (<10 cm) of the diopside-allanite veins are observed locally in the apatite breccia (Fig. 4.5b).

The apatite breccia veins consist mainly of sub-angular to rounded apatite grains <6 cm across, and vary from clast-supported to matrix-supported. Three dominant apatite generations occur in the veins: (1) red apatite breccia (Fig. 4.5c); (2) green apatite breccia (Fig. 4.5c, d); and (3) coarse red apatite (Fig. 4.5e). The contacts between these different generations are often gradational and subtle. Multiple brecciation phases were detected, and in some cases, cross-cutting relationships of veins containing different apatite generations are observed. The red apatite phase, volumetrically the most significant among the apatite breccia veins, is dull red in color and strongly enriched in solid inclusions, particularly in the cores (Fig. 4.5f). Most of the solid inclusions are finely dispersed hematite, which also occurs along fracture planes in the apatite. The green apatite phase has a lustrous green color, and is less enriched in hematite inclusions, which are mostly restricted to crystal boundaries and fractures (Fig. 4.5g).

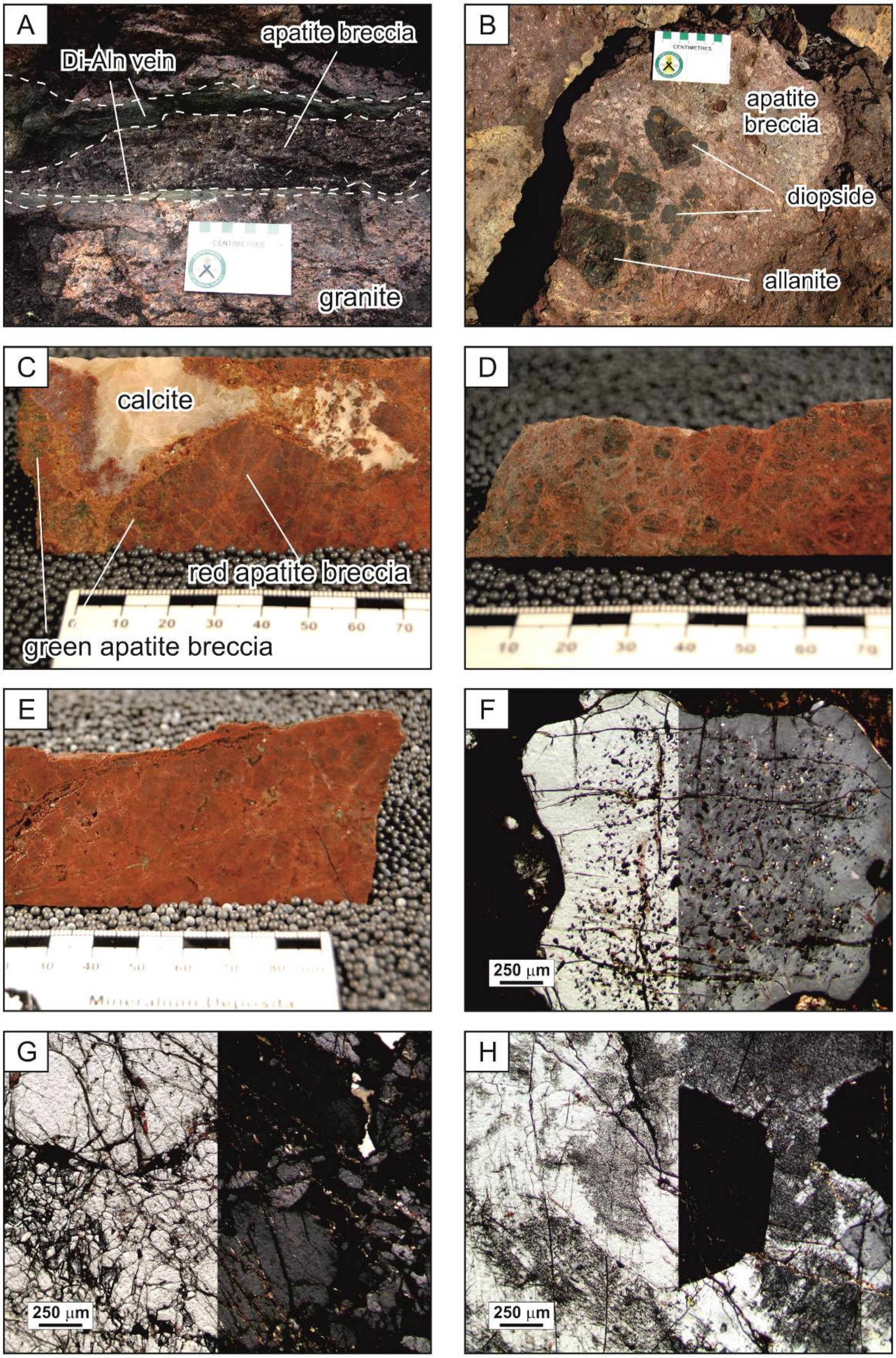
A
apatite breccia
Di-Aln vein
CENTIMETRES
granite
B
CENTIMETRES
apatite breccia
diopside
allanite
C
calcite
red apatite breccia
0 10 20 30 40 50 60 70
green apatite breccia
D
10 20 30 40 50 60 70
E
30 40 50 60 70 80
Mineralium Deposita
F
250 µm
G
250 µm
H
250 µm

Figure 4.5 (on previous page) Outcrop photographs, sample photographs and photomicrographs of apatite breccia veins from the Hoidas Lake deposit. (a) Outcrop with an irregularly shaped red apatite breccia vein that formed by reopening of a former diopside-allanite vein, the remnants of which can be observed at the margin, Di-Aln vein = diopside-allanite vein. (b) Outcrop of a red apatite breccia vein that contains up to 10 cm, sub-angular clasts of diopside-allanite veins. (c) Red apatite breccia with gradational contacts towards green apatite breccia intervals. Calcite fills the vugs in the breccia and encloses apatite clasts. (d) Green apatite breccia sample. (e) Coarse red apatite sample. (f) Plane polarized light (PPL – left) and cross polarized light (XPL – right) photomicrographs of red apatite breccia clast with hematite and monazite inclusions in the core and inclusion-free rims, and abundant hematite-coated fractures. (g) PPL (left) and XPL (right) photomicrographs of inclusion-free green apatite breccia clasts with abundant hematite-coated fractures, along which monazite inclusions can be observed. The matrix of the breccia consists mainly of fine-grained apatite, quartz, and minor monazite. (h) PPL (left) and XPL (right) photomicrographs of coarse red apatite breccia with abundant solid inclusions in the apatite crystals.

The presence of green apatite rims around the red apatite and small green apatite crystals in the matrix of the red apatite breccia indicate an overlap between the formation of these generations. The latest apatite phase, the coarse red apatite, is brecciated and fractured, although the crystal fragments did not undergo significant rotation (Fig. 4.5h). This generation of apatite is bright red and rich in hematite inclusions.

Monazite occurs as inclusions in all generations of apatite, and is more abundant in the earliest red apatite breccia, but can also be found in the later green apatite breccia and coarse red apatite. The monazite crystals, which occasionally contain thorite in their core (Fig. 4.6a, b), occur in irregular disseminated masses or along secondary fractures in the apatite (Fig. 4.6c), and along grain boundaries of the fine-grained apatite in the matrix. Rarely, thorite inclusions also occur in the apatite, in which case they are surrounded by radial fractures. Few barite inclusions were also detected along fractures in the apatite.

The matrix of the apatite breccia consists of fine-grained apatite, lesser calcite, quartz, green amphibole, minor amounts of REE-carbonate, REE-Sr-carbonate, monazite (Fig. 4.6d, e), chlorite, pyrite and some sub-angular clasts of allanite, diopside and hyalophane. The REE- and REE-Sr-carbonates commonly form euhedral, fibrous crystals that appear in clusters, closely related to chlorite. Very coarse-grained biotite (<5 cm), which is similar to the biotite of the diopside-allanite veins, is associated with the apatite breccia veins, and can form selvages (<30 cm) around the apatite veins.

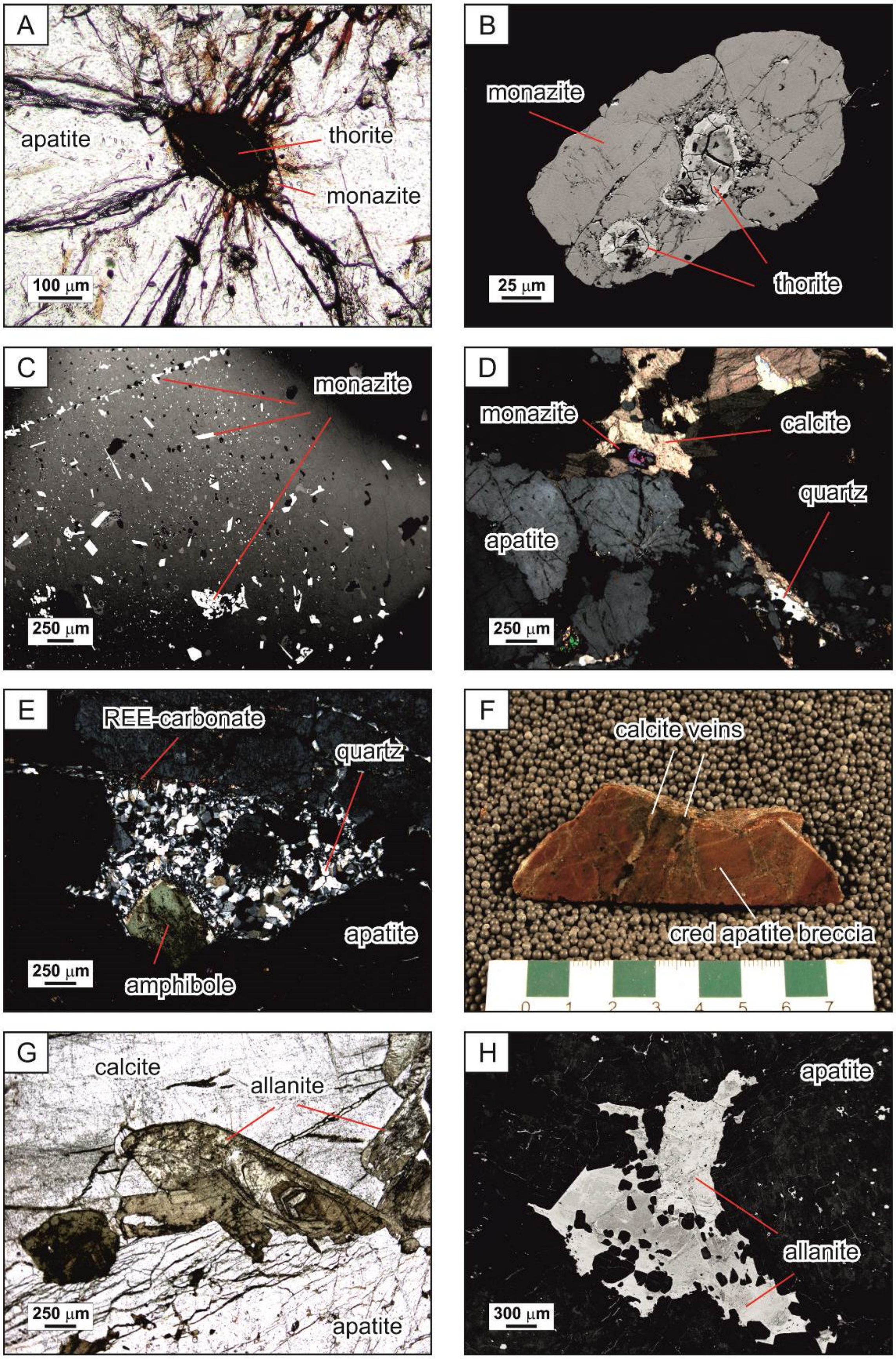
A
apatite
thorite
monazite
100 μm
B
monazite
thorite
25 μm
C
monazite
250 μm
D
monazite
calcite
quartz
apatite
250 μm
E
REE-carbonate
quartz
apatite
amphibole
250 μm
F
calcite veins
cred apatite breccia
0
1
2
3
4
5
6
7
G
calcite
allanite
apatite
250 μm
H
apatite
allanite
300 μm

Figure 4.6 (on previous page) Sample photographs, photomicrographs and back-scattered electron (BSE) images of apatite breccia veins and late quartz-carbonate veins from the Hoidas Lake deposit. (a) Plane polarized light (PPL) photomicrograph of monazite with thorite core in red apatite breccia, surrounded by radial, hematite-coated fractures. (b) BSE image of monazite inclusion in green apatite breccia, containing two thorite inclusions. (c) BSE image showing abundant monazite inclusions in green apatite breccia, some of them located along a fracture. (d) Cross polarized light (XPL) photomicrograph of fine-grained apatite, quartz, calcite and monazite in the matrix of the green apatite breccia. (e) XPL photomicrograph of quartz, green amphibole and REE-carbonate in the matrix of the green apatite breccia. (f) Coarse red apatite vein sample cross-cut by calcite veins that contain euhedral allanite crystals. (g) PPL photomicrograph of euhedral, zoned allanite crystals in calcite vein that cross-cuts the coarse red apatite vein. (h) BSE image of oscillatory zoned allanite in vug within the coarse red apatite vein containing resorbed apatite grains.

Some of the quartz-carbonate veins, which cross-cut the coarse red apatite phase, contain euhedral allanite crystals (<5 mm; Fig. 4.6f, g). These crystals are oriented at 20-50° to the vein walls, exhibit oscillatory color zonation in their cores, and have irregularly zoned margins. Similar allanite appears within vugs of the apatite breccia around the quartz-carbonate veins. In addition, this allanite generation is also observed along the contact of the apatite breccia and the host rocks, where it resorbs apatite (Fig. 4.6h).

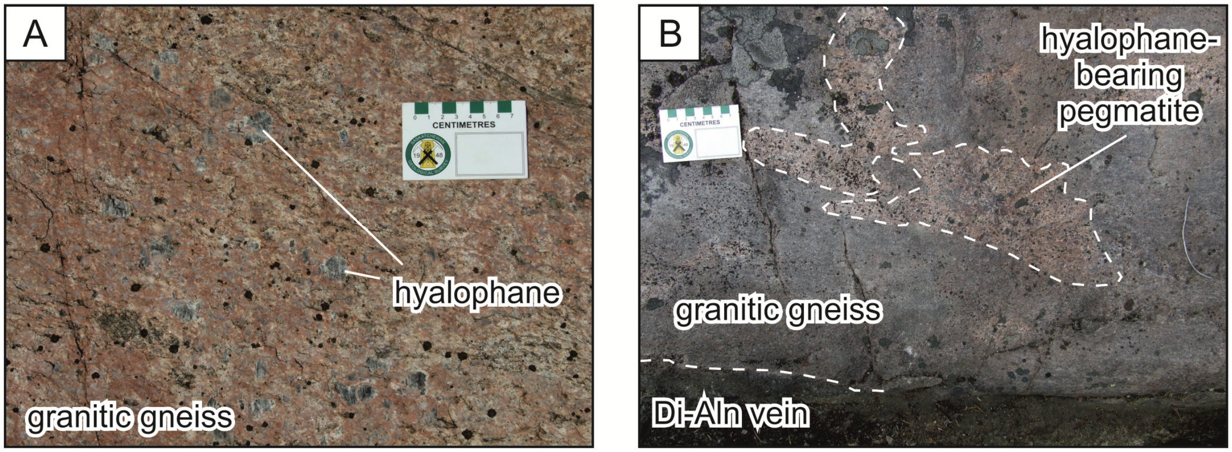

Figure 4.7 Outcrop photographs to demonstrate the abundance of hyalophane in the vicinity of the mineralized veins at Hoidas Lake. (a) Discrete hyalophane crystals and clusters of hyalophane crystals in granitic gneiss. (b) Irregular amoeboid hyalophane-bearing pegmatitic bodies in granitic gneiss.

Macroscopically very little visible alteration can be observed around the Hoidas Lake REE veins. However, the hyalophane-rich pegmatitic margins of the diopside-allanite veins often show diffuse contacts with the host rocks (Fig. 4.4a). In addition, there are abundant hyalophane clusters (<10 cm in diameter) and irregular amoeboid hyalophane-bearing pegmatitic bodies around the REE veins in the surrounding host rocks that otherwise contain no hyalophane (Fig. 4.7a, b). The diopside-allanite veins and apatite breccia veins, that cross-cut the hyalophane-bearing pegmatite dikes, are surrounded by albite- and calcite-rich thin (<4 mm) alteration haloes.

4.5.2 Mineral chemistry of the diopside-allanite veins

4.5.2.1 Allanite

The allanite grains from the diopside-allanite veins are compositionally closest to allanite-(Ce), although the strongly altered and metamict nature of these grains does not allow for formula calculation and precise classification within the epidote-group minerals (Table 4.1). The dominant REE in the early allanite is Ce (1.2 to 13.5 wt.% Ce_2O_3), and lesser La (0.6 to 6.8 wt.% La_2O_3), Nd (0.3 to 4.1 wt.% Nd_2O_3) Pr (0.1 to 1.3 wt.% Pr_2O_3), and trace amounts of Gd, Sm, Dy, Tb and Er were also detected. The chondrite-normalized REE plots for allanite (Fig. 4.8a) show a negative slope with $(La/Gd)_N$ ratios up to 57.5. Most of the allanites show irregular to roughly concentric compositional zones in BSE images that reflect a wide range of chemical variations, most pronounced in terms of the REE contents (Fig. 4.9a, b). The earliest allanite cores have TREO values from 16.9 to 23.7 wt.%, whereas the intermediate zones are less enriched in REEs, with TREO values from 6.9 to 21.7 wt.%. The outermost zones in the allanite are again enriched in the REEs, with TREO values from 12.6 to 22.6 wt.% (Fig. 4.9b). However, within these outermost zones the REE contents generally decrease slightly towards the rims. Thorium is detected in most allanites at values $\leq$1.2 wt.% ThO_2. The concentrations of Fe (3.5 to 18.0 wt.% FeO), Al (5.1 to 18.0 wt.% Al_2O_3), Ca (1.9 to 13.3 wt.% CaO) and Mn (<1.7 wt.% MnO) also vary among the different allanite zones. Allanite also contains minor amounts of Sr (up to 1.4 wt.% SrO), Ti (up to 1.3 wt.% TiO_2) and Cr (up to 0.2 wt.% Cr_2O_3), and the concentrations of these elements increase gradually towards the rim areas of the allanite. The MgO contents of the allanite crystals can be as high as 10.8 wt.%, especially in the most altered allanite intervals, and SiO_2 contents reach 37.0 wt.%, which, together with the low analytical totals, indicate that fine-grained alteration products of the allanite were also analyzed during the allanite analyses. Up to 5.2 wt.% BaO occurs in some of the allanites, and it is noted that the higher Ba contents (>2 wt.%) generally occur in altered samples that have lower analytical totals. The allanite grains show irregular, mottled texture in BSE images, which is likely of secondary origin, and reflect local variations in REE contents (Fig. 4.9a, b), with the irregular dark zones on the BSE images having the lowest TREO values (6.9 to 14.8 wt.%). The epidote sensu stricto that appears as an alteration product along the rims of some allanite contains up to 4.7 wt.% SrO.

Table 4.1 Representative electron microprobe analyses (wt.%) of early allanite and titanite from the Hoidas Lake diopside-allanite veins.

	Early allanite										Titanite				
SAMPLE	881179-4-537	881179-4-553	881179-4-563	881179-8-607	881187-3-628	881187-3-643	881187-3-647	881187-3-653	948521-3-230	948521-4-239	881179-3-507	881179-3-509	881187-9-747	948521-7-262	516674-4A-280
SiO_2	32.78	35.32	33.08	32.92	31.40	35.78	31.59	32.91	31.65	33.07	29.70	30.28	29.81	30.63	30.29
Al_2O_3	15.52	17.01	16.98	17.22	16.10	15.69	15.70	17.08	7.86	15.58	3.13	2.16	3.23	2.19	2.85
Na_2O	0.08	0.06	0.09	0.09	0.14	0.43	0.14	0.14	0.21	0.06	0.03	0.05	0.02	bdl	0.05
K_2O	0.02	0.09	bdl	bdl	bdl	0.14	bdl	bdl	bdl	bdl	bdl	0.02	bdl	bdl	0.02
CaO	8.75	6.32	10.93	13.28	11.05	5.92	10.88	8.00	9.05	11.84	26.29	26.43	27.07	26.07	25.43
MgO	1.10	0.75	0.63	0.49	1.09	1.57	1.06	0.90	0.73	1.23	0.14	0.66	0.12	0.04	0.12
FeO	8.33	5.98	10.01	10.62	7.92	10.40	9.81	6.29	17.27	10.31	1.76	1.11	1.86	1.39	2.01
MnO	0.84	0.71	0.48	0.47	0.75	1.45	0.53	1.53	0.70	0.35	0.10	0.05	0.09	0.07	0.11
BaO	0.37	1.26	0.99	0.43	bdl	4.03	0.18	0.68	0.40	bdl	0.16	0.29	0.12	0.18	0.18
SrO	0.68	0.53	1.33	1.44	0.82	0.90	0.92	1.16	0.29	0.70	0.12	0.07	0.11	bdl	0.06
TiO_2	0.79	0.66	0.24	0.18	0.70	0.86	0.42	0.70	0.92	0.60	30.62	32.70	30.85	33.28	31.80
Cr_2O_3	0.15	0.10	0.08	0.06	0.16	0.06	0.15	0.15	0.07	0.04	bdl	bdl	bdl	bdl	bdl
La_2O_3	5.08	5.76	3.96	3.47	5.70	2.85	5.35	5.57	6.81	5.41	0.15	0.09	0.14	0.12	0.15
Ce_2O_3	10.61	11.11	7.95	7.13	11.04	6.18	10.26	10.98	13.51	10.12	0.91	0.53	0.74	0.62	0.95
Pr_2O_3	1.05	1.07	0.82	0.69	1.08	0.61	0.91	1.01	1.07	1.03	0.21	0.07	0.12	0.18	0.23
Nd_2O_3	3.56	4.01	2.83	2.72	3.48	1.95	3.43	3.38	3.11	3.16	1.36	0.60	1.04	1.15	1.36
Sm_2O_3	0.26	0.25	0.19	0.17	0.27	0.13	0.25	0.23	0.17	0.23	0.33	0.15	0.21	0.32	0.34
Eu_2O_3	bdl*	bdl	bdl	bdl	bdl	bdl	bdl	bdl	bdl	bdl	0.07	0.07	0.06	0.07	0.05
Gd_2O_3	0.40	0.34	0.28	0.24	0.35	0.16	0.33	0.34	0.10	0.09	0.24	0.06	0.18	0.14	0.22
Tb_2O_3	bdl	bdl	bdl	bdl	bdl	bdl	bdl	bdl	0.12	0.07	bdl	bdl	bdl	bdl	0.05
Dy_2O_3	0.07	bdl	bdl	0.09	bdl	0.26	0.10	0.14	bdl	bdl	0.10	0.07	0.09	0.08	0.14
Y_2O_3	bdl	bdl	bdl	bdl	bdl	bdl	bdl	bdl	bdl	bdl	0.26	0.13	0.25	0.26	0.32
ZrO_2	bdl	bdl	bdl	bdl	bdl	bdl	bdl	bdl	bdl	bdl	0.06	0.10	bdl	bdl	0.05
Nb_2O_5	bdl	bdl	bdl	bdl	bdl	bdl	bdl	bdl	bdl	bdl	0.16	0.13	0.09	0.18	0.23
ThO_2	0.75	0.68	0.45	0.33	0.55	1.16	0.53	0.56	0.20	0.10	0.04	bdl	bdl	bdl	bdl
P_2O_5	bdl	bdl	bdl	bdl	bdl	bdl	bdl	bdl	bdl	bdl	0.05	bdl	bdl	bdl	bdl
SO_3	bdl	bdl	bdl	bdl	0.05	bdl	0.05	0.24	0.05	0.09	bdl	bdl	bdl	bdl	bdl
F	bdl	bdl	bdl	bdl	bdl	bdl	bdl	bdl	bdl	0.07	0.72	0.14	0.78	0.36	0.49
Cl	0.20	0.06	0.26	0.37	0.55	0.02	0.52	0.04	0.35	0.37	bdl	0.04	0.01	bdl	0.01
TOTAL	91.34	92.05	91.52	92.33	93.08	90.56	92.99	92.00	94.55	94.52	96.40	95.93	96.68	97.17	97.30
TREO	21.03	22.54	16.03	14.52	21.92	12.14	20.62	21.65	24.88	20.11	3.63	1.77	2.85	2.93	3.80

* below detection limit

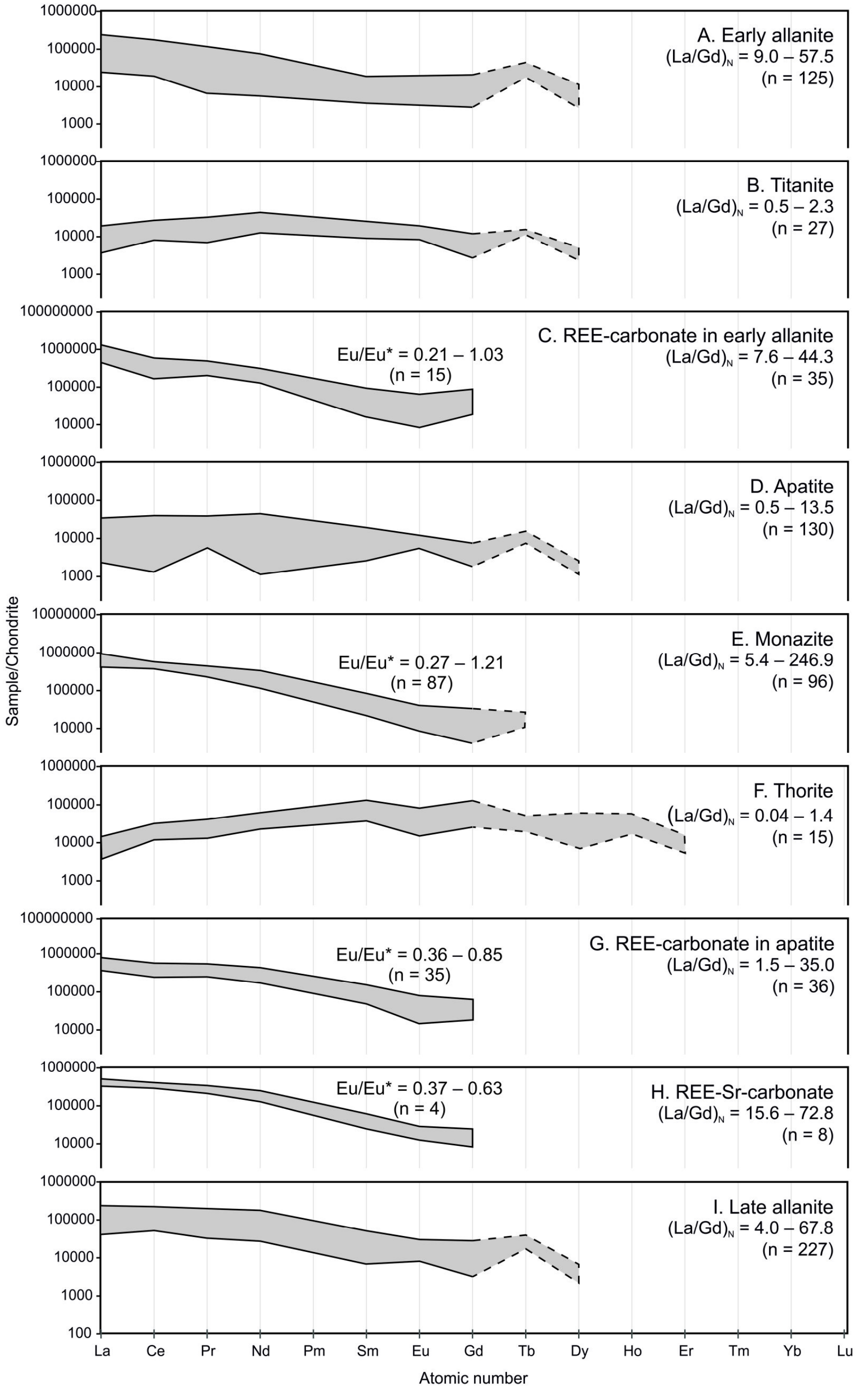

Figure 4.8 Chondrite-normalized REE (rare earth element) distribution of the REE-enriched phases of the Hoidas Lake deposit: (a) early allanite; (b) titanite; (c) REE-carbonate in early allanite; (d) apatite; (e) monazite; (f) thorite; (g) REE-carbonate in apatite; (h) REE-Sr-carbonate in apatite; and (i) late allanite. Only REE data that were above the detection limits from electron microprobe analyses were used to construct the plots. The chondritic REE values were used after McDonough and Sun (1995). The slopes of the REE plots are represented by the range of $(La/Gd)_N$ ratios, and Eu/Eu* values are displayed to quantify the Eu anomalies, where n is the number of analyses from which the $(La/Gd)_N$ values and Eu/Eu* values were calculated .

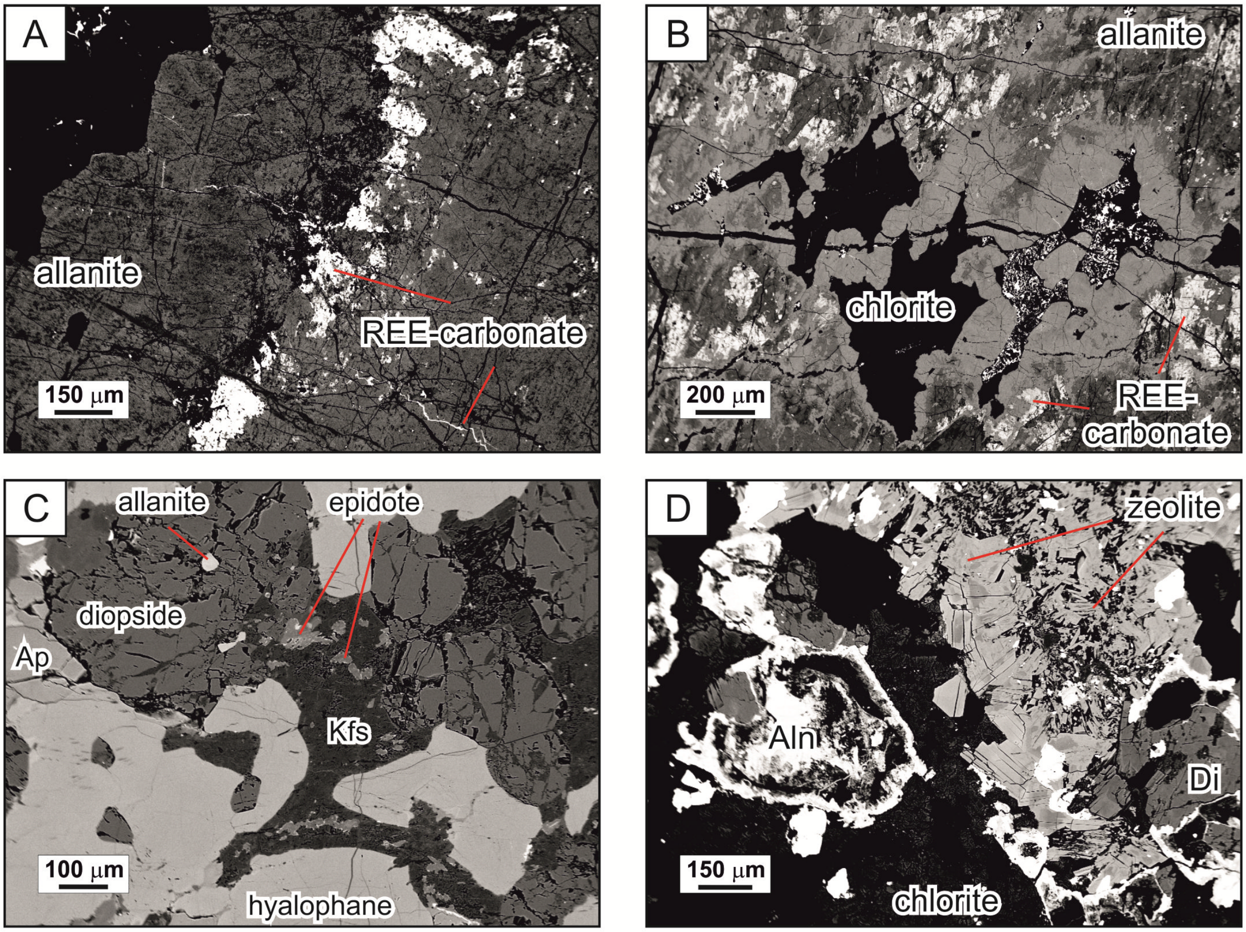

Figure 4.9 Back-scattered electron (BSE) images of diopside-allanite vein samples. (a) BSE image of allanite with two distinct concentric zones that have an irregular boundary between them. REE-carbonate inclusions are located along the contact of the concentric zones. The allanite has a rugged surface, and irregular mottled zonation within the growth zones. (b) BSE image of irregularly zoned allanite with abundant secondary REE-carbonate inclusions and a distinctive concentric compositional zone along the rim of the allanite around the vugs that shows elevated REE-contents (lighter color in the BSE image). The vugs in the allanite are filled with chlorite. (c) BSE image of diopside-rich interval of diopside-allanite vein with diopside, minor allanite and apatite, and interstitial space filled with hyalophane that is being replaced and resorbed in places by potassium feldspar. The potassium feldspar is partially replaced by epidote; Kfs = potassium feldspar, Ap = apatite. (d) BSE image of euhedral, tabular zeolite crystals in the interstitial space between allanite and diopside in a slightly brecciated diopside-allanite vein interval. The allanite crystals are partially replaced by chlorite; Aln = allanite, Di = diopside.

4.5.2.2 Titanite

The titanite in the diopside-allanite veins contains between 1.8 and 6.0 wt.% TREO (Table 4.1). As opposed to the other REE-bearing minerals in this vein generation, Nd is the dominant

REE (0.6 to 2.2 wt.% Nd_2O_3), followed by Ce (0.5 to 2.1 wt.% Ce_2O_3), Sm (0.2 to 0.4 wt.% Sm_2O_3), La (0.1 to 0.6 wt.% La_2O_3) and Y (0.1 to 0.4 wt.% Y_2O_3), and trace amounts of Pr, Gd, Dy, Eu and Tb. Titanite contains up to 4.7 wt.% FeO, up to 3.3 wt.% MgO, and up to 1.3 wt.% BaO, which might be a result of hydrothermal alteration. As titanite is less enriched in La compared to the allanite, the chondrite-normalized REE plots have $(La/Gd)_N$ ratios up to 2.3 (Fig. 4.8b). The titanite is fairly homogeneous, however, slight irregular zonation can be observed in some grains, especially towards their margins, where depletion in REEs occurs, and slightly elevated contents of Ti and Ba are detected.

4.5.2.3 Feldspars

The majority of the feldspar in the diopside-allanite veins is either hyalophane ($Cn_{27}Ab_{16-17}Or_{56-57}$, where Cn = Celsian component, Ab = albite component, Or = potassium feldspar component) or potassium feldspar with variable Ba-content ($Cn_{6-10}Ab_{6-10}Or_{80-88}$ to $Cn_{0-4}Ab_{1-6}Or_{91-99}$) (Fig. 4.10; Table 4.2). The hyalophane contains 2.4 to 2.5 wt.% SrO and trace amounts of Ca, whereas the Ba-containing potassium feldspar contains up to 1.5 wt.% SrO and up to 3 wt.% CaO.

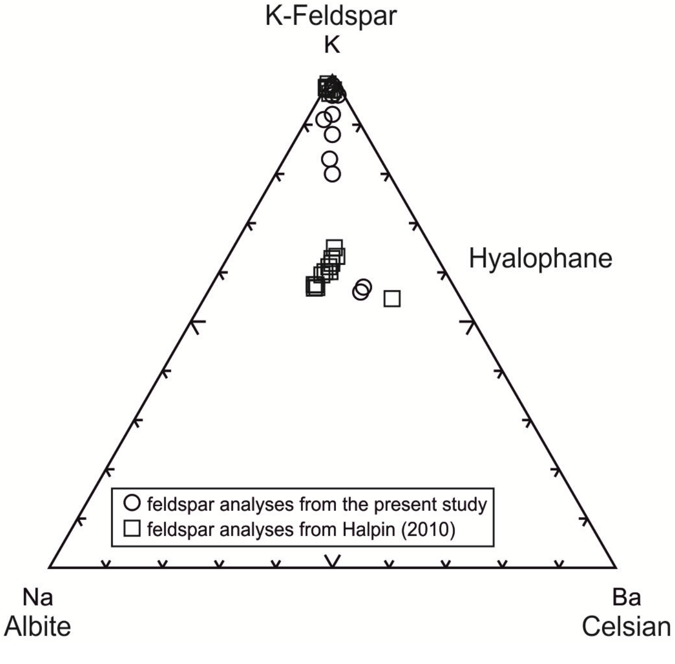

Figure 4.10 Composition of alkali feldspars (atomic proportions) in the diopside-allanite veins of Hoidas Lake deposit in the $NaAlSi_3O_8$–$KAlSi_3O_8$–$BaAl_2Si_2O_8$-ternary (n = 30), after Essene et al. (2005).

In some cases, hyalophane interstitial to allanite and diopside of the diopside-allanite veins is replaced by Ba-containing potassium feldspar, and this phase is then replaced by epidote containing up to 4.9 wt.% SrO (Fig. 4.9c). In rare cases, hyalophane is altered to barite or celestine along its edges (Halpin, 2010), where the former contains up to 1.3 wt.% SrO. Rare euhedral tabular zeolite crystals (likely heulandite-Ba) also occur as alteration products of hyalophane in brecciated diopside-allanite samples, and contain up to 0.5 wt.% SrO and up to 1.5 wt.% CaO (Fig. 4.9d).

Table 4.2 Representative electron microprobe analyses (wt.%) of hyalophane, potassium feldspar, zeolite, diopside, actinolite, hornblende and biotite from the Hoidas Lake diopside-allanite veins.

	Hyalophane		Potassium feldspar			Zeolite			Diopside		Actinolite		Hornblende	Biotite
SAMPLE	948521-6-257	948521-6-258	516647-4-307	881187-1-699	948521-6-254	881179-3-516	948521-3-235	948521-3-236	881179-6-588	948521-5-250	881187-5-692	948521-3-234	881187-6-716	516674-4A-276
SiO_2	53.50	54.08	61.32	63.39	64.69	55.88	64.17	64.27	50.83	51.01	52.92	56.09	41.56	36.97
Al_2O_3	22.44	22.45	19.46	19.29	19.02	16.81	14.53	15.37	2.58	2.44	2.95	0.04	11.36	13.34
Na_2O	1.59	1.51	0.89	0.37	0.11	bdl	0.26	0.21	0.75	0.41	0.90	bdl	1.81	0.15
K_2O	8.12	8.13	12.92	14.63	15.63	0.30	0.33	0.35	bdl	bdl	0.22	bdl	1.85	8.72
CaO	0.03	0.05	0.10	bdl	0.07	1.06	0.83	0.84	23.08	22.96	12.43	12.32	11.82	0.02
MgO	bdl*	bdl	bdl	bdl	bdl	bdl	0.01	bdl	11.53	12.05	16.13	14.06	11.01	16.36
FeO	0.05	0.07	0.03	0.03	0.09	0.16	bdl	bdl	8.98	9.68	10.36	13.84	14.74	13.68
MnO	bdl	bdl	bdl	bdl	bdl	bdl	bdl	bdl	0.54	0.53	0.57	0.33	0.40	0.30
BaO	12.53	12.50	4.24	1.79	1.51	15.02	10.58	11.37	bdl	bdl	bdl	bdl	0.25	3.41
SrO	2.47	2.36	1.24	0.09	bdl	0.41	0.44	0.45	0.12	bdl	bdl	bdl	0.16	bdl
TiO_2	0.10	0.11	0.03	0.04	bdl	0.09	0.06	0.07	0.25	0.22	0.19	bdl	0.65	2.49
Ce_2O_3	bdl	bdl	bdl	bdl	bdl	0.21	bdl	bdl	bdl	bdl	bdl	bdl	bdl	bdl
Tb_2O_3	bdl	bdl	bdl	bdl	bdl	bdl	bdl	bdl	0.15	0.09	0.09	0.13	0.16	0.08
Dy_2O_3	bdl	bdl	bdl	bdl	bdl	bdl	bdl	bdl	0.17	0.06	0.16	0.08	0.17	0.07
SO_3	bdl	bdl	bdl	bdl	bdl	bdl	0.20	0.14	bdl	bdl	bdl	bdl	bdl	0.05
F	bdl	bdl	bdl	bdl	bdl	bdl	bdl	bdl	bdl	bdl	0.53	bdl	0.71	1.42
Cl	bdl	bdl	bdl	bdl	bdl	bdl	bdl	bdl	bdl	bdl	0.14	bdl	0.25	0.43
TOTAL	100.82	101.27	100.22	99.62	101.13	89.94	91.43	93.08	98.99	99.43	97.32	96.88	96.64	96.79

* below detection limit

4.5.2.4 Diopside, amphibole and biotite

The diopside of the diopside-allanite veins is chemically homogeneous with 0.5 wt.% MnO, 0.2 to 0.3 wt.%. TiO_2, 2.3 to 2.8 wt.% Al_2O_3 and 0.4 to 0.8 wt.% Na_2O (Table 4.2). The majority of the amphibole, which occurs as an alteration product generally associated with diopside, ranges in composition from hornblende to actinolite (Table 4.2), and has Na_2O up to 1.8 wt.%, especially in close proximity to large zoned allanites. The biotite of the diopside-allanite veins, with FeO ranging from 13.1 to 13.7 wt.% and MgO ranging from 16.4 to 16.9 wt.%, has around 2.5 wt.% TiO_2, and up to 3.4 wt.% BaO (Table 4.2).

4.5.2.5 REE-carbonates

The secondary REE-carbonates, observed generally in areas of mottled or irregularly zoned allanites or along cross-cutting fractures (Fig. 4.9a, b), contain up to 2.6 wt.% F (Table 4.3). The TREO contents of these carbonates range from 63.0 to 77.8 wt.%, and in most of them Ce is the dominant REE (29.2 to 46.8 wt.% Ce_2O_3), with lesser La (12.7 to 29.7 wt.% La_2O_3), Nd (8.3 to 16.6 wt.% Nd_2O_3), Pr (2.3 to 4.7 wt.% Pr_2O_3), and trace amounts of Gd, Sm and Eu. However, some of these carbonates are most enriched in La (25.6 to 42.4 wt.% La_2O_3), with lesser Ce (11.2 to 23.9 wt.% Ce_2O_3), Nd (13.8 to 17.7 wt.% Nd_2O_3), Pr (4.3 to 5.9 wt.% Pr_2O_3), and trace amounts of Gd, Sm and Eu. The REE-carbonates also contain up to 3.2 wt.% CaO. The chondrite-normalized REE plots of the REE-carbonates show a negative slope with an average $(La/Gd)_N$ ratio of 17.5 (Fig. 4.8c). A negative Eu anomaly is observed with an average Eu/Eu* value of 0.48 ± 0.23.

Table 4.3 Representative electron microprobe analyses (wt.%) of REE-carbonate from the Hoidas Lake diopside-allanite veins.

	REE-carbonate					
SAMPLE	881179-1-456	881179-3-519	881179-6-590	881187-9-756	881187-9-758	881187-9-759
SiO_2	1.55	0.52	0.44	0.85	0.58	0.59
Al_2O_3	0.60	0.03	bdl	0.17	0.06	0.08
CaO	1.96	1.33	0.71	1.02	0.98	0.88
MgO	0.84	0.08	0.09	0.43	0.19	0.19
FeO	0.69	0.30	0.20	0.46	1.08	1.31
MnO	0.04	bdl	bdl	bdl	bdl	bdl
BaO	bdl*	bdl	bdl	0.09	bdl	bdl
SrO	0.08	0.11	bdl	0.09	bdl	0.09
Cr_2O_3	0.54	0.54	0.50	0.47	0.45	0.47
La_2O_3	17.13	19.51	16.50	13.13	14.53	14.07
Ce_2O_3	36.32	33.09	38.05	46.23	43.30	44.85
Pr_2O_3	3.77	3.58	3.55	2.78	2.68	2.53
Nd_2O_3	12.85	16.20	15.02	10.56	10.90	10.46
Sm_2O_3	0.62	1.64	1.18	0.81	0.78	0.84
Eu_2O_3	0.08	0.40	0.15	bdl	bdl	bdl
Gd_2O_3	1.27	1.79	1.37	1.29	1.29	1.21
Y_2O_3	bdl	0.26	bdl	bdl	bdl	bdl
SO_3	bdl	0.07	bdl	bdl	bdl	bdl
Cl	0.28	0.21	0.07	0.15	0.11	0.12
TOTAL	78.55	79.62	77.82	78.50	76.92	77.65
TREO	72.03	76.48	75.83	74.78	73.49	73.95

* below detection limit

4.5.3 Mineral chemistry of the apatite breccia veins

4.5.3.1 Apatite

The fluorapatite of the apatite breccia veins contains up to 7.3 wt.% TREO (Table 4.4), with a general dominance of Ce (0.1 to 2.9 wt.% Ce_2O_3), followed by Nd (0.1 to 2.5 wt.% Nd_2O_3), La (0.1 to 1.1 wt.% La_2O_3), Pr (0.1 to 0.5 wt.% Pr_2O_3), and minor Sm, Gd and Dy, as well as Y (<0.2 wt.% Y_2O_3). The REEs are incorporated via the coupled substitution: $(SiO_4)^{4-}$ + REE^{3+} = Ca^{2+} + $(PO_4)^{3-}$. The incorporation of Na in REE-rich apatite is another common mechanism of REE incorporation in the apatite structure, but the Na contents of the studied apatite grains are ≤0.2 wt.% Na_2O. Sr^{2+} also substitutes for Ca^{2+} in apatite (Pan and Fleet, 2002), and the SrO content of the studied apatites ranges from 0.1 to 1.6 wt.%. The apatite also contains Ba (<1.7 wt.% BaO), Mn (<0.3 wt.% MnO) and Th (<0.1 wt.% ThO_2). The chondrite-normalized REE plots of the apatite show a negative to relatively flat slope with $(La/Gd)_N$ up to 13.5 and no Eu anomaly (Fig. 4.8d).

Halpin (2010) divided the early red apatite generation, based on its chemical zonation (mainly variations in REE contents), into 4 distinct zones (Fig. 4.11). The Ce-dominant oldest apatite zone (Zone 1) has relatively low REE contents (typically around 1.5 wt.% TREO), is rich in monazite inclusions and has lesser amounts of thorite and REE-carbonate inclusions. It corresponds to the dark red apatite that can be found in the diopside-allanite veins. The apatite in Zone 2 is also Ce-dominant, shows an increase in REEs (to 2 wt.% TREO), and is also rich in solid inclusions (e.g., monazite, REE-carbonate). In Zone 3, the apatite is even more REE-enriched (up to 4 wt.% TREO), and is also Ce-dominant, but it lacks the solid inclusions of the previous apatite zones. Zone 4 apatite occurs as a narrow rim on many of the apatite clasts, and has the lowest REE contents (1 wt.% TREO). However, it is Nd-dominant, i.e. distinct from the other apatite zones. This apatite zone is chemically and visually equivalent to the coarse red apatite, the youngest apatite generation. The next apatite breccia generation, the Ce-dominant green apatite breccia, lacks the chemical zonation observed in the red apatite breccia and contains fewer solid inclusions. The green apatite phase is more enriched in REEs (up to 7.3 wt.%, with an average of 5.5 wt.% TREO). The last apatite generation, the coarse red apatite, also contains fewer solid inclusions. It is equivalent to Zone 4 in the red apatite breccias, it is Nd-dominant and displays the lowest overall TREO content (1 wt.%).

Table 4.4 Representative electron microprobe analyses (wt.% and apfu values) of red apatite, green apatite and coarse red apatite from the Hoidas Lake apatite breccia veins.

	Red apatite							Green apatite				Coarse red apatite		
SAMPLE	881344-3-284	881344-3-393	881344-3-405	948521-1-201	516665A-23A-77	516665B-14A-135	516665B-14A-136	881309A-1-109	881309A-3-163	881309A-4-212	881309A-5-242	517458-3-93	517458-3-100	517458-7-366
SiO_2	1.80	1.54	0.42	0.48	0.98	1.45	0.31	1.78	0.91	1.40	0.62	0.02	0.57	0.56
Al_2O_3	0.05	0.03	0.04	bdl	0.01	bdl	bdl	0.04	0.05	0.04	0.05	0.04	0.04	0.05
Na_2O	0.04	bdl	0.02	bdl	0.02	0.05	0.02	bdl	0.03	0.03	0.03	0.04	0.04	0.02
K_2O	bdl*	bdl	bdl	bdl	bdl	bdl	bdl	bdl	bdl	bdl	bdl	bdl	bdl	bdl
CaO	50.62	51.60	50.83	52.40	52.31	48.28	53.20	51.16	51.92	50.38	53.21	55.77	54.17	53.28
MgO	0.02	0.02	bdl	0.02	0.01	0.01	0.02	bdl	0.01	bdl	0.01	0.03	0.03	0.02
FeO	0.07	0.06	3.74	bdl	bdl	bdl	bdl	0.05	0.04	0.03	0.05	0.02	0.02	0.03
MnO	0.07	0.04	0.04	0.03	0.05	bdl	bdl	0.06	0.07	0.07	0.06	0.05	0.04	0.03
BaO	bdl	bdl	1.74	bdl	bdl	bdl	bdl	bdl	bdl	bdl	bdl	bdl	bdl	bdl
SrO	1.09	1.11	0.69	0.72	1.00	1.27	0.64	1.04	1.11	1.16	1.01	0.81	0.90	0.90
TiO_2	bdl	0.03	0.04	bdl	bdl	bdl	bdl	bdl	bdl	bdl	bdl	bdl	bdl	bdl
La_2O_3	0.98	0.76	0.19	0.15	0.36	0.58	0.13	0.58	0.39	0.47	0.21	bdl	0.16	0.08
Ce_2O_3	2.25	2.10	0.46	0.47	1.12	1.85	0.41	2.15	1.12	1.74	0.68	bdl	0.57	0.42
Pr_2O_3	0.41	0.20	0.06	0.11	0.15	0.27	0.06	0.41	0.23	0.33	0.10	bdl	0.12	0.09
Nd_2O_3	1.53	1.21	0.36	0.50	0.72	1.12	0.29	1.97	1.10	1.57	0.74	bdl	0.55	0.60
Sm_2O_3	0.14	0.14	0.06	0.07	0.12	0.15	0.04	0.32	0.16	0.24	0.12	bdl	0.13	0.13
Eu_2O_3	0.06	bdl	bdl	bdl	bdl	bdl	bdl	bdl	bdl	bdl	bdl	bdl	bdl	bdl
Gd_2O_3	0.10	0.11	bdl	0.08	0.06	0.07	bdl	0.10	0.10	0.10	0.07	bdl	bdl	0.12
Dy_2O_3	bdl	bdl	bdl	bdl	bdl	bdl	bdl	bdl	bdl	bdl	bdl	bdl	0.06	bdl
Y_2O_3	0.08	0.08	bdl	bdl	0.07	0.12	bdl	0.12	0.08	0.11	0.05	bdl	0.06	0.14
ZrO_2	0.11	0.10	0.12	0.15	0.13	0.12	0.15	0.12	0.09	0.15	0.10	0.12	0.14	0.10
Nb_2O_5	bdl	bdl	bdl	0.06	bdl	bdl	bdl	bdl	bdl	bdl	bdl	0.04	bdl	bdl
ThO_2	0.09	0.07	bdl	bdl	bdl	bdl	bdl	bdl	bdl	bdl	bdl	bdl	bdl	bdl
P_2O_5	37.24	38.20	39.46	42.05	37.31	36.53	39.07	37.34	39.15	37.45	39.23	42.28	40.65	40.76
SO_3	0.04	0.07	1.19	bdl	0.05	0.03	bdl	0.09	0.05	0.15	0.06	0.07	0.09	bdl
F	3.09	2.94	3.53	3.35	3.24	3.16	3.44	3.17	3.17	3.10	3.27	3.85	3.70	3.66
Cl	0.10	0.09	0.04	0.19	0.18	0.16	0.09	0.77	0.77	0.98	0.69	0.08	0.09	0.06
$O=(F_2,Cl_2)$	-1.32	-1.26	-1.50	-1.45	-1.40	-1.37	-1.47	-1.51	-1.51	-1.53	-1.53	-1.64	-1.58	-1.55
TOTAL	98.65	99.25	101.56	99.37	96.47	93.87	96.41	99.76	99.04	97.98	98.81	101.60	100.54	99.49
TREO	5.54	4.60	1.13	1.38	2.60	4.15	0.93	5.64	3.18	4.56	1.97	0.00	1.63	1.58
Si	0.16	0.13	0.04	0.04	0.08	0.13	0.03	0.15	0.08	0.12	0.05	0.00	0.05	0.05
Na	0.01	0.00	0.00	0.00	0.00	0.01	0.00	0.00	0.00	0.01	0.01	0.01	0.01	0.00
Ca	4.74	4.78	4.60	4.91	4.85	4.77	4.93	4.76	4.82	4.77	4.87	4.94	4.89	4.89
Fe^{2+}	0.01	0.00	0.26	0.00	0.00	0.00	0.00	0.00	0.00	0.00	0.00	0.00	0.00	0.00
Mn	0.01	0.00	0.00	0.00	0.00	0.00	0.00	0.00	0.01	0.01	0.00	0.00	0.00	0.00
Ba	0.00	0.00	0.06	0.00	0.00	0.00	0.00	0.00	0.00	0.00	0.00	0.00	0.00	0.00
Sr	0.06	0.06	0.03	0.04	0.05	0.07	0.03	0.05	0.06	0.06	0.05	0.04	0.04	0.04
La	0.03	0.02	0.01	0.00	0.01	0.02	0.00	0.02	0.01	0.02	0.01	0.00	0.00	0.00
Ce	0.07	0.07	0.01	0.02	0.04	0.06	0.01	0.07	0.04	0.06	0.02	0.00	0.02	0.01
Pr	0.01	0.01	0.00	0.00	0.00	0.01	0.00	0.01	0.01	0.01	0.00	0.00	0.00	0.00
Nd	0.05	0.04	0.01	0.02	0.02	0.04	0.01	0.06	0.03	0.05	0.02	0.00	0.02	0.02
Sm	0.00	0.00	0.00	0.00	0.00	0.00	0.00	0.01	0.00	0.01	0.00	0.00	0.00	0.00
Y	0.00	0.00	0.00	0.00	0.00	0.01	0.00	0.01	0.00	0.01	0.00	0.00	0.00	0.01
Zr	0.00	0.00	0.01	0.01	0.01	0.01	0.01	0.01	0.00	0.01	0.00	0.00	0.01	0.00
P	2.76	2.80	2.82	3.11	2.74	2.85	2.86	2.74	2.87	2.80	2.84	2.96	2.90	2.96
S	0.00	0.00	0.08	0.00	0.00	0.00	0.00	0.01	0.00	0.01	0.00	0.00	0.01	0.00
F	0.85	0.80	0.94	0.92	0.89	0.92	0.94	0.87	0.87	0.87	0.88	1.01	0.99	0.99
Cl	0.01	0.01	0.01	0.03	0.03	0.03	0.01	0.11	0.11	0.15	0.10	0.01	0.01	0.01
OH	-0.24	-0.11	-0.19	0.83	-0.79	0.02	-0.51	-0.41	-0.16	-0.27	-0.49	-0.17	-0.22	0.04
O	12.00	12.00	12.00	12.00	12.00	12.00	12.00	12.00	12.00	12.00	12.00	12.00	12.00	12.00

* below detection limit

The apatite, regardless of growth phase, often shows irregular or mottled zonation in the BSE images, which reflects abrupt variations in REE contents; in such cases, the REE-depleted zones have as little as 1 wt.% TREO, whereas the adjacent areas have higher TREO values (Fig. 4.12a). These REE-depleted zones are often closely associated with a greater abundance of secondary hematite, and the FeO content of apatite in these areas can be as high as 3.7 wt.%. Furthermore, these REE-depleted zones often surround secondary monazite and REE-carbonate inclusions in the apatite breccia (Fig. 4.12b), and the apatite locally shows faint oscillatory zonation around these inclusions.

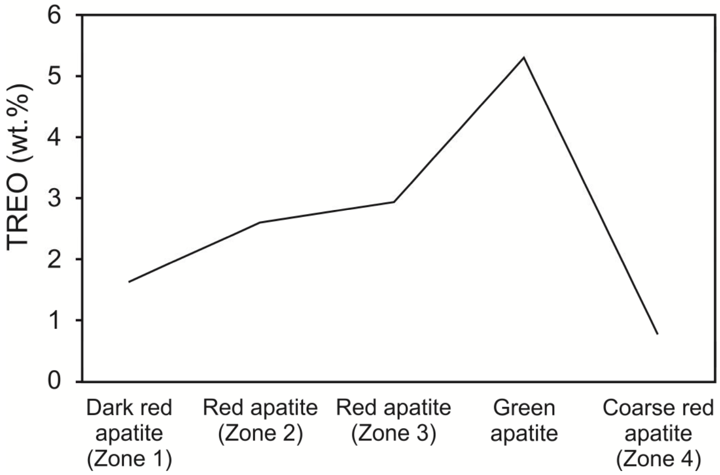

Figure 4.11 Variations in average rare earth element (REE) contents among the distinct apatite generations in the Hoidas Lake deposit, after Halpin (2010). The description of the different zones is given in the text.

4.5.3.2 Monazite

The monazite inclusions in the apatite, which are commonly elongated parallel to the c-axis of the host apatite, have TREO values from 59.2 to 80.5 wt.%, and are Ce-dominant (with 28.6 to 38.9 wt.% Ce_2O_3), followed by La (10.4 to 24.2 wt.% La_2O_3), Nd (6.9 to 19.8 wt.% Nd_2O_3), Pr (2.4 to 5.3 wt.% Pr_2O_3), Sm (0.4 to 2.8 wt.% Sm_2O_3) and lesser Gd, Dy, Eu and Tb (Table 4.5). Monazite has a negative slope in chondrite-normalized plots with $(La/Gd)_N$ ratios up to 247 (Fig. 4.8e), and displays a slight negative Eu anomaly, at an average Eu/Eu* value of 0.66 ± 0.21. The monazite contains minor amounts of Ca (<4 wt.% CaO), and Sr (<0.7 wt.% SrO), and the ThO_2 content is occasionally as high as 10.2 wt.%. Higher concentrations of Ca, Sr and Th are observed in samples with lower TREO content. Slight concentric zonation is not uncommon in the monazite, as revealed by BSE images (Fig. 4.12c), and the cores of these zoned grains are often slightly more enriched in Th and La and depleted in Ce, Nd, Pr, Sm and Eu, compared to the rims. In rare cases, monazite can be found in the matrix of the apatite breccia, more specifically at the margins of the late-phase apatite crystals. These matrix monazite grains have slightly higher REE, and slightly lower Th and Sr contents, compared to the monazite that occurs as inclusions in the apatite.

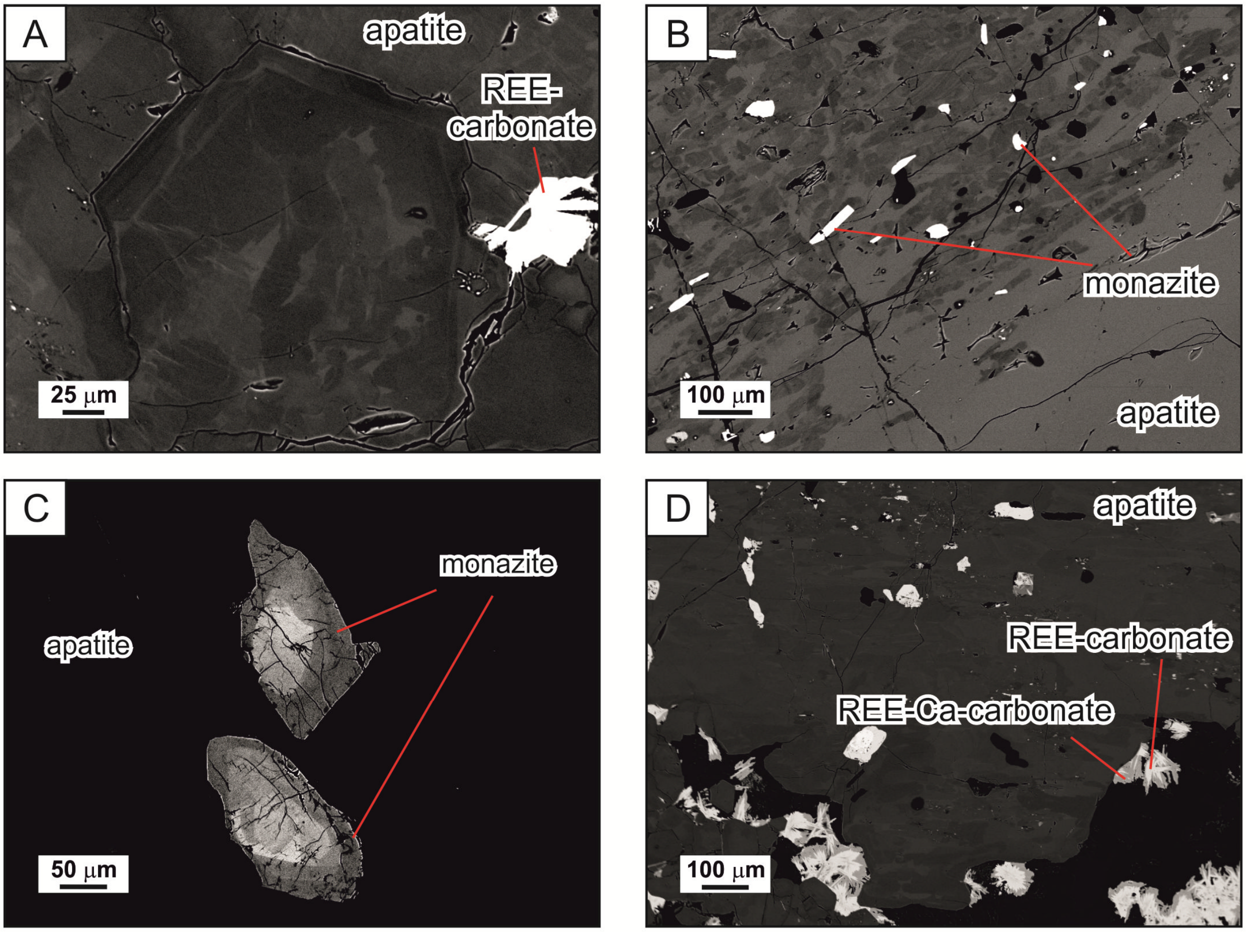

Figure 4.12 Back-scattered electron images of apatite breccia samples. (a) Euhedral apatite grain which shows irregular zonation from a red apatite breccia sample. The lighter and darker colors in the BSE image reflect variations in REE contents. (b) Red apatite breccia grain that shows irregular, mottled zonation and abundant monazite inclusions in the irregularly zoned interval. The lighter and darker colors in the BSE image reflect variations in REE contents. (c) Monazite inclusions in apatite that show concentric compositional zonation, with Th- and La-enriched cores, and rims enriched in other LREEs. (d) Clusters of fibrous REE-carbonate crystals overgrown by REE-Ca-carbonate in vugs within apatite crystals.

4.5.3.3 Thorite

Thorite, which is occasionally encapsulated in monazite, shows TREO values from 4.7 to 13.9 wt.%, and is most enriched in Ce (0.9 to 4.4 wt.% Ce_2O_3) and Nd (1.3 to 3.3 wt.% Nd_2O_3), but is notably depleted in La (up to 1.6 wt.% La_2O_3), compared to the other REE-bearing phases (Table 4.5). Thorite also contains up to 3.2 wt.% Gd_2O_3, up to 2.4 wt.% Sm_2O_3, up to 1.8 wt.% Dy_2O_3 and up to 4.9 wt.% Y_2O_3. On chondrite-normalized REE plots, thorite shows uniform enrichment in Pr, Nd, Sm, Eu, Gd and depletion in La, with $(La/Gd)_N$ ratios ≤ 1.4 (Fig. 4.8f).

4.5.3.4 Apatite breccia matrix

The fine-grained apatite of the matrix of the apatite breccia is generally of the latest apatite generation (coarse red apatite, generally equivalent to Zone 4 of the red apatite breccia) that exhibits TREO contents around 1 wt.%. Quartz crystals in the apatite breccia matrix often contain monazite, anhydrite and barite inclusions (the latter containing up to 0.9 wt.% SrO; Table 4.6). The calcite has up to 1.6 wt.% FeO, 3.0 wt.% MgO, 1.1 wt.% MnO and 1.2 wt.% SrO (Table 4.6). Abundant secondary REE-carbonate and REE-Sr-carbonate phases occur in the matrix of the apatite breccia and infilling vugs and fractures in apatite (Fig. 4.12d).

The REE-carbonates have F contents from 0.2 to 3.1 wt.%, and can have up to 18.0 wt.% CaO (Table 4.6). The Ca-rich variety contains 45.4 to 54.9 wt.% TREO, whereas the relatively Ca-poor variety contains 60.1 to 86.2 wt.% TREO. Cerium is the dominant REE (17.3 to 56.5 wt.% Ce_2O_3), followed by 8.1 to 29.9 wt.% Nd_2O_3, 3.0 to 21.5 wt.% La_2O_3, 1.1 to 7.2 wt.% Pr_2O_3, up to 3.1 wt.% Sm_2O_3, 1.6 wt.% Gd_2O_3, and trace amounts of Eu, Tb and Y. The chondrite-normalized REE plots of these REE-carbonates show a negative slope with $(La/Gd)_N$ ratios up to 35 (Fig. 4.8g) and a slight negative Eu anomaly (average $Eu/Eu^*=0.64 \pm 0.13$). In rare instances, the fibrous crystals of REE-carbonates in the matrix of the apatite breccia are overgrown by REE-Ca-carbonates (Fig. 4.12d).

The REE-Sr carbonates contain 49.0 to 57.5 wt.% TREO and SrO ranging from 13.6 to 22.5 wt.% (Table 4.6). They have 22.8 to 29.6 wt.% Ce_2O_3, 10.2 to 15.4 wt.% La_2O_3, 6.9 to 13.7 wt.% Nd_2O_3, 2.5 to 4.0 wt.% Pr_2O_3, up to 1.2 wt.% Sm_2O_3 and trace amounts of Gd, Eu and Y. The REE-Sr carbonates show a negative slope on chondrite-normalized REE plots, with an average $(La/Gd)_N$ ratio of 30, and have a slight negative Eu anomaly (average Eu/Eu*=0.52 ± 0.12) (Fig. 4.8h).

Table 4.5 Representative electron microprobe analyses (wt.% and apfu values) of monazite and thorite from the Hoidas Lake apatite breccia veins.

	Monazite							Thorite			
SAMPLE	517458-2-75	881344-3-396	881375B-2-54	881375B-2-56	948521-1-212	516665B-26A-164	516658-1A-197	881309A-3-175	881309A-X-101	517458-8-38	517458-8-47
SiO_2	3.70	1.72	1.64	2.20	1.91	1.98	1.30	15.68	18.01	15.53	14.83
Al_2O_3	0.55	bdl	bdl	bdl	bdl	bdl	bdl	bdl	0.03	0.21	0.15
Na_2O	0.04	bdl	bdl	0.05	bdl	0.05	0.05	bdl	bdl	bdl	bdl
CaO	1.32	0.90	0.19	0.29	0.45	0.66	0.43	1.98	2.36	2.34	2.00
MgO	0.21	bdl	bdl	0.04	0.03	0.03	0.03	0.11	0.19	0.20	0.18
FeO	1.31	0.07	0.39	0.11	0.03	bdl	bdl	0.71	0.74	0.34	0.36
MnO	0.07	bdl	bdl	bdl	bdl	bdl	bdl	bdl	0.04	bdl	bdl
BaO	0.19	bdl	bdl	bdl	bdl	bdl	bdl	1.42	1.70	0.67	0.66
SrO	0.56	bdl	0.14	bdl	bdl	bdl	bdl	0.07	0.12	0.13	0.13
Cr_2O_3	0.47	0.57	0.19	0.19	0.20	0.25	0.21	bdl	bdl	bdl	bdl
La_2O_3	12.58	17.39	15.27	17.87	11.85	20.07	19.34	bdl	0.12	0.14	0.15
Ce_2O_3	30.03	34.39	35.52	34.43	34.03	35.04	35.48	2.20	1.62	1.34	1.34
Pr_2O_3	3.96	3.40	3.71	3.21	4.08	3.07	3.15	0.41	0.20	0.38	0.29
Nd_2O_3	14.68	12.41	12.84	10.54	16.20	9.11	10.34	2.84	1.94	3.32	3.28
Sm_2O_3	1.17	0.92	0.83	0.69	1.34	0.51	0.63	1.61	1.05	2.40	2.41
Eu_2O_3	0.16	0.11	0.12	0.07	0.30	0.08	0.07	0.42	0.28	0.54	0.56
Gd_2O_3	0.51	1.34	0.31	0.32	0.36	0.17	0.06	1.53	1.07	3.17	3.12
Tb_2O_3	bdl*	bdl	bdl	0.09	0.11	0.09	0.08	bdl	bdl	0.22	0.22
Dy_2O_3	bdl	bdl	bdl	bdl	bdl	bdl	bdl	0.94	0.81	1.77	1.77
Ho_2O_3	bdl	bdl	bdl	bdl	bdl	bdl	bdl	bdl	bdl	0.29	0.38
Er_2O_3	bdl	bdl	bdl	bdl	bdl	bdl	bdl	0.17	0.24	0.30	0.28
Y_2O_3	bdl	bdl	bdl	0.09	0.11	bdl	bdl	3.10	3.49	4.92	4.79
ZrO_2	bdl	bdl	bdl	bdl	bdl	0.14	0.10	1.23	12.40	bdl	bdl
ThO_2	4.52	2.38	1.16	2.07	2.12	1.21	0.57	52.65	44.95	50.23	52.11
UO_2	bdl	bdl	bdl	0.07	bdl	bdl	bdl	bdl	0.06	2.51	1.28
P_2O_5	23.54	27.50	24.36	23.12	27.49	26.25	27.26	4.54	2.66	4.71	4.63
SO_3	0.48	0.73	1.17	1.34	0.92	1.22	0.86	0.15	bdl	bdl	0.06
F	bdl	bdl	0.15	0.23	0.26	0.30	0.33	bdl	bdl	bdl	bdl
Cl	0.07	0.06	0.12	0.12	0.07	0.04	0.04	bdl	0.02	0.12	0.14
TOTAL	100.11	103.86	98.03	97.01	101.74	100.14	100.18	91.75	94.10	95.75	95.07
TREO	63.10	69.96	68.61	67.31	68.38	68.14	69.15	13.21	10.83	18.79	18.58
Si	0.14	0.06	0.07	0.09	0.07	0.08	0.05	0.77	0.80	0.73	0.72
Al	0.02	0.00	0.00	0.00	0.00	0.00	0.00	0.00	0.00	0.01	0.01
Ca	0.05	0.04	0.01	0.01	0.02	0.03	0.02	0.10	0.11	0.12	0.10
Mg	0.01	0.00	0.00	0.00	0.00	0.00	0.00	0.01	0.01	0.01	0.01
Fe^{2+}	0.04	0.00	0.01	0.00	0.00	0.00	0.00	0.03	0.03	0.01	0.01
Ba	0.00	0.00	0.00	0.00	0.00	0.00	0.00	0.03	0.03	0.01	0.01
Sr	0.01	0.00	0.00	0.00	0.00	0.00	0.00	0.00	0.00	0.00	0.00
Cr	0.01	0.02	0.01	0.01	0.01	0.01	0.01	0.00	0.00	0.00	0.00
La	0.18	0.24	0.23	0.27	0.17	0.29	0.28	0.00	0.00	0.00	0.00
Ce	0.42	0.47	0.53	0.52	0.48	0.50	0.51	0.04	0.03	0.02	0.02
Pr	0.06	0.05	0.05	0.05	0.06	0.04	0.04	0.01	0.00	0.01	0.01
Nd	0.20	0.17	0.19	0.16	0.22	0.13	0.14	0.05	0.03	0.06	0.06
Sm	0.02	0.01	0.01	0.01	0.02	0.01	0.01	0.03	0.02	0.04	0.04
Eu	0.00	0.00	0.00	0.00	0.00	0.00	0.00	0.01	0.00	0.01	0.01
Gd	0.01	0.02	0.00	0.00	0.00	0.00	0.00	0.02	0.02	0.05	0.05
Dy	0.00	0.00	0.00	0.00	0.00	0.00	0.00	0.01	0.01	0.03	0.03
Y	0.00	0.00	0.00	0.00	0.00	0.00	0.00	0.08	0.08	0.12	0.12
Zr	0.00	0.00	0.00	0.00	0.00	0.00	0.00	0.03	0.27	0.00	0.00
Th	0.04	0.02	0.01	0.02	0.02	0.01	0.01	0.59	0.45	0.54	0.57
U	0.00	0.00	0.00	0.00	0.00	0.00	0.00	0.00	0.00	0.03	0.01
P	0.76	0.88	0.84	0.81	0.90	0.86	0.90	0.19	0.10	0.19	0.19
S	0.01	0.02	0.04	0.04	0.03	0.04	0.03	0.01	0.00	0.00	0.00
F	0.00	0.00	0.02	0.03	0.03	0.04	0.04	0.00	0.00	0.00	0.00
Cl	0.00	0.00	0.01	0.01	0.00	0.00	0.00	0.00	0.00	0.01	0.01
O	4.00	4.00	4.00	4.00	4.00	4.00	4.00	4.00	4.00	4.00	4.00

* below detection limit

Table 4.6 Representative electron microprobe analyses (wt.%) of REE-carbonate, REE-Sr-carbonate, barite and calcite from the Hoidas Lake apatite breccia veins.

	REE-carbonate					REE-Sr-carbonate		Barite				Calcite	
SAMPLE	881309A-3-188	881344-2-271	517458-2-77	517256-3-190	517256-4-194	517458-8-51	948521-2-225	881344-1-257	516665A-26A-86	516665A-20A-116	516665B-T-6A-179	881309A-4-226	881309A-4-229
SiO_2	0.37	0.54	0.49	1.89	0.62	0.22	0.52	0.16	bdl	0.11	bdl	bdl	bdl
Al_2O_3	bdl*	bdl	bdl	1.23	0.15	bdl	0.03	0.93	0.88	0.63	0.88	bdl	bdl
Na_2O	bdl	bdl	bdl	bdl	0.11	bdl	bdl	0.24	0.18	0.13	0.20	bdl	bdl
K_2O	bdl	bdl	bdl	bdl	bdl	bdl	bdl	0.04	bdl	bdl	bdl	bdl	bdl
CaO	2.27	1.45	4.26	17.57	17.96	1.48	2.09	bdl*	0.71	1.34	0.27	47.48	50.70
MgO	0.06	0.06	0.10	1.06	0.16	0.02	0.12	0.03	bdl	bdl	bdl	bdl	bdl
FeO	0.10	0.22	0.07	1.34	1.63	bdl	0.04	0.65	bdl	bdl	bdl	bdl	bdl
MnO	bdl	0.04	bdl	bdl	bdl	bdl	bdl	bdl	bdl	bdl	bdl	0.33	0.37
BaO	bdl	bdl	bdl	bdl	bdl	bdl	bdl	63.49	59.57	44.80	59.35	bdl	bdl
SrO	bdl	0.16	0.08	bdl	bdl	13.57	22.49	0.90	4.91	13.79	3.88	bdl	bdl
TiO_2	bdl	bdl	bdl	bdl	bdl	bdl	0.05	0.51	0.47	0.32	0.48	bdl	bdl
Cr_2O_3	0.49	0.46	0.45	bdl	bdl	0.34	bdl	bdl	bdl	bdl	bdl	bdl	bdl
La_2O_3	16.83	18.42	13.05	12.64	11.39	11.40	10.88	bdl	bdl	2.26	bdl	bdl	bdl
Ce_2O_3	36.87	26.44	31.32	17.29	19.60	26.70	22.84	0.12	0.13	1.00	bdl	bdl	bdl
Pr_2O_3	5.26	7.16	4.90	2.75	2.78	3.97	2.69	bdl	bdl	0.71	bdl	bdl	bdl
Nd_2O_3	21.39	29.94	21.41	10.34	10.47	13.70	10.35	bdl	bdl	2.75	bdl	bdl	bdl
Sm_2O_3	1.98	2.33	2.44	1.18	1.27	1.12	1.22	bdl	bdl	0.16	bdl	bdl	bdl
Eu_2O_3	0.36	0.40	0.48	0.21	0.27	bdl	0.20	bdl	bdl	bdl	bdl	bdl	bdl
Gd_2O_3	0.81	1.02	1.13	0.74	0.83	0.60	0.58	bdl	bdl	bdl	bdl	bdl	bdl
Yb_2O_3	bdl	bdl	bdl	bdl	bdl	bdl	bdl	0.48	bdl	bdl	bdl	bdl	bdl
Y_2O_3	0.35	0.49	0.25	0.72	0.83	bdl	0.23	bdl	bdl	bdl	bdl	bdl	bdl
ThO_2	bdl	bdl	bdl	0.12	0.85	bdl	bdl	bdl	bdl	bdl	bdl	bdl	bdl
P_2O_5	bdl	0.12	0.09	bdl	1.00	bdl	bdl	bdl	0.10	0.12	bdl	bdl	bdl
SO_3	0.07	bdl	bdl	bdl	bdl	bdl	bdl	34.96	34.44	31.62	33.80	bdl	bdl
F	bdl	bdl	0.22	2.82	3.07	bdl	0.90	bdl	bdl	bdl	bdl	bdl	bdl
Cl	0.24	0.14	0.20	0.05	0.15	0.04	0.04	bdl	bdl	0.02	bdl	bdl	bdl
TOTAL	87.41	89.36	80.79	70.75	71.81	73.14	74.88	102.50	101.39	99.77	98.86	47.80	51.06
TREO	83.86	86.21	74.98	45.87	47.44	57.48	48.98						

* below detection limit

4.5.4 Chemistry of the late allanite in quartz-carbonate veins

The rare euhedral allanite crystals that occur in the late-stage quartz-carbonate veins and vugs display oscillatory compositional zoning in their cores, and the cores are overgrown by irregularly zoned rims (Fig. 4.13a, b). The late allanites generally contain 4.2 – 22.5 wt.% FeO, 7.5 – 18.6 wt.% Al_2O_3, 2.9 – 14.6 wt.% CaO and up to 1.0 wt.% MnO (Table 4.7). They also contain Sr (up to 5.3 wt.% SrO), and minor amounts of Ti (up to 0.6 wt.% TiO_2) and Cr (up to 0.2 wt.% Cr_2O_3). The TREO contents of the allanites range from 7.1 to 33.0 wt.% with Ce as the dominant REE (3.6 to 16.0 wt.% Ce_2O_3), La (1.2 to 6.1 wt.% La_2O_3), Nd (1.6 to 8.6 wt.% Nd_2O_3), Pr (<2.2 wt.%, Pr_2O_3), and lesser Sm, Gd, Eu, Dy, Tb and Y. The chondrite-normalized REE plot of these late-stage allanites shows a negative slope with $(La/Gd)_N$ ratios up to 68 (Fig. 4.8i). The oscillatory zonation in the cores of allanite reflects distinct changes in REE contents among adjacent zones (from 7.1 to 33.0 wt.% TREO). The rims of the allanites show TREO varying from 14.0 to 28.2 wt.%, and contain slightly less Ti, Ba and Th, compared to the cores. Similarly to the early allanite from the diopside-allanite veins, the elevated Mg contents of the late allanites (up to 9.2 wt.% MgO), as well as elevated Ba contents (up to 3.3 wt.% BaO), reflect the effect of hydrothermal alteration. The presence of abundant chlorite in the late allanites also reflects this alteration. Few secondary REE-Sr-carbonates, the same phase that is present in the coarse red apatite, were detected replacing the allanite.

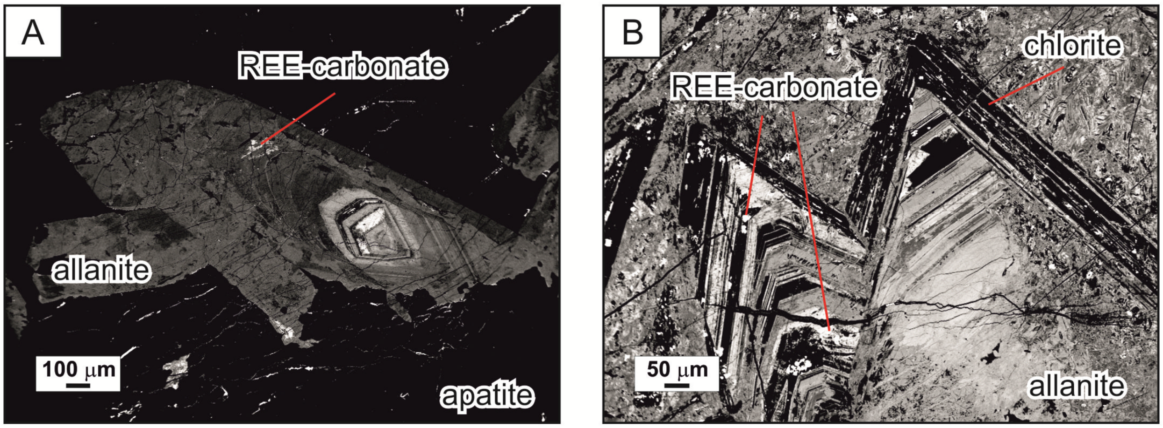

Figure 4.13 Back-scattered electron images of late allanite from the late quartz-carbonate veins. (a) Euhedral allanite with oscillatory zoned core surrounded by irregularly zoned rim. Secondary REE-carbonate partially replaces the allanite. (b) Strongly altered euhedral allanite showing oscillatory zonation, overgrown by allanite that has irregular mottled compositional zonation. Secondary REE-carbonate and chlorite replaces the allanite.

Table 4.7 Representative electron microprobe analyses (wt.%) of late allanite from the Hoidas Lake quartz-carbonate veins.

	Late allanite									
SAMPLE	517458-2-78	517458-2-79	517458-3-106	517458-3-163	517458-3-182	517458-3-203	517458-3-205	517458-3-213	517458-3-225	517458-7-371
SiO_2	28.34	28.31	28.91	28.49	25.23	29.50	29.61	29.13	26.30	29.85
Al_2O_3	7.51	8.59	8.31	12.29	11.36	12.07	12.50	10.82	11.75	11.53
Na_2O	0.21	0.15	bdl	0.03	0.02	0.13	0.06	0.10	0.04	0.08
K_2O	bdl*	bdl	bdl	0.12	0.07	bdl	0.06	bdl	bdl	bdl
CaO	8.86	9.10	9.55	5.91	4.81	10.34	8.55	9.76	5.39	9.89
MgO	0.73	0.82	0.47	0.93	1.70	0.66	1.16	0.77	0.59	0.88
FeO	18.88	18.74	21.66	6.87	5.05	15.00	12.23	16.14	4.59	13.26
MnO	0.77	0.74	0.76	0.66	0.50	0.53	0.69	0.52	0.58	0.44
BaO	bdl	bdl	bdl	2.36	1.95	bdl	0.98	bdl	1.78	bdl
SrO	0.20	0.18	0.06	3.36	5.16	0.52	0.72	0.43	4.69	0.34
TiO_2	0.25	0.28	bdl	0.24	0.19	0.20	0.25	0.09	0.23	0.09
Cr_2O_3	0.22	0.22	0.18	0.10	0.11	0.14	0.12	0.15	0.10	0.13
La_2O_3	5.59	5.82	6.04	4.64	5.63	4.99	4.12	5.65	5.20	4.91
Ce_2O_3	14.37	14.09	14.14	12.26	14.72	11.92	10.71	12.96	15.02	13.22
Pr_2O_3	1.79	1.69	1.72	1.65	1.98	1.62	1.50	1.68	1.60	1.49
Nd_2O_3	5.70	5.26	5.61	5.64	6.28	5.57	5.31	5.62	6.25	6.06
Sm_2O_3	0.40	0.39	0.36	0.49	0.43	0.46	0.48	0.32	0.44	0.45
Gd_2O_3	0.17	0.10	0.14	0.19	0.17	0.20	0.15	0.07	0.62	0.53
Tb_2O_3	bdl	bdl	0.16	bdl	bdl	bdl	bdl	0.08	bdl	bdl
ThO_2	0.11	0.05	bdl	0.47	0.74	0.29	0.41	0.28	0.28	0.10
P_2O_5	0.06	0.05	0.15	bdl	bdl	bdl	bdl	bdl	bdl	bdl
SO_3	0.06	bdl	bdl	bdl	bdl	bdl	bdl	bdl	bdl	bdl
Cl	0.36	0.31	0.02	0.04	0.02	0.75	0.36	0.63	0.02	0.62
TOTAL	94.51	94.82	98.23	86.73	86.14	94.70	89.91	95.07	85.47	93.71
TREO	28.03	27.35	28.18	24.88	29.22	24.76	22.27	26.39	29.13	26.66

* below detection limit

4.5.5 Inclusions representing a melt phase in the apatite breccia

A suite of characteristic graphic-textured inclusions that outline primary growth zones in the apatite of the earliest apatite breccia generation (Fig. 4.14a, b) has been described, and a model for their formation was proposed in Pandur et al. (2015; Chapter 3). These likely represent crystallization from a melt phase that was present during apatite formation.

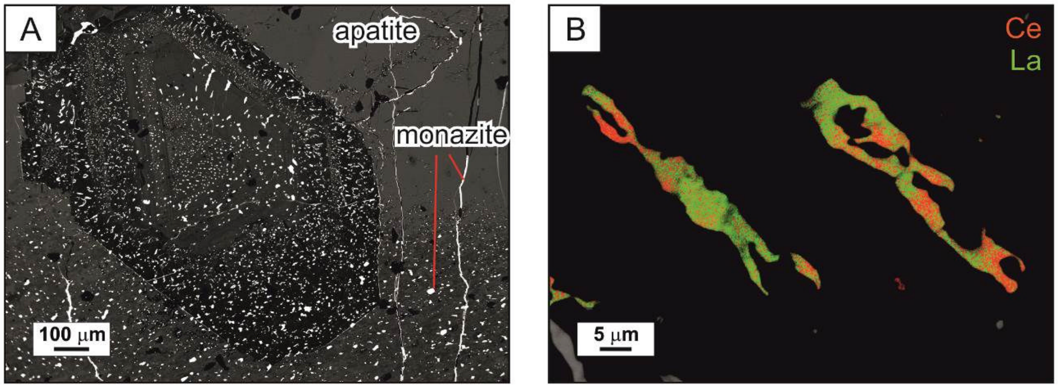

Figure 4.14 Graphic-textured inclusions in the apatite breccia. (a) BSE image of apatite with graphic-textured inclusions displaying euhedral apatite growth zones. (b) Ce (red) – La (green) X-ray map of graphic-textured inclusions.

Abundant non-graphic inclusions of similar chemistry also occur in the relatively unaltered samples of the red apatite breccia. These inclusions are commonly located along fractures in the apatite, and similarly to the graphic-textured inclusions, have irregular Ce-dominant and La-dominant intervals (Fig. 4.15a). The Ce-dominant and La-dominant inclusion intervals are occasionally separated into adjacent inclusions (Fig. 4.15b). X-ray element maps and element profiles of these inclusions have been used to illustrate that apart from the unambiguous decoupling of Ce and La, the relative enrichment of Pr can be observed in the La-dominant inclusions, and Nd shows homogeneous distribution across the individual inclusions (Fig. 4.15c). In addition, Si is more enriched in the Ce-dominant inclusions, whereas F-enrichment is tied to the La-dominant inclusions (Fig. 4.15c). The maps also show that Si and C are decoupled, indicating that the La-dominant phase has excess carbon, although we cannot quantify the amount of CO_2.

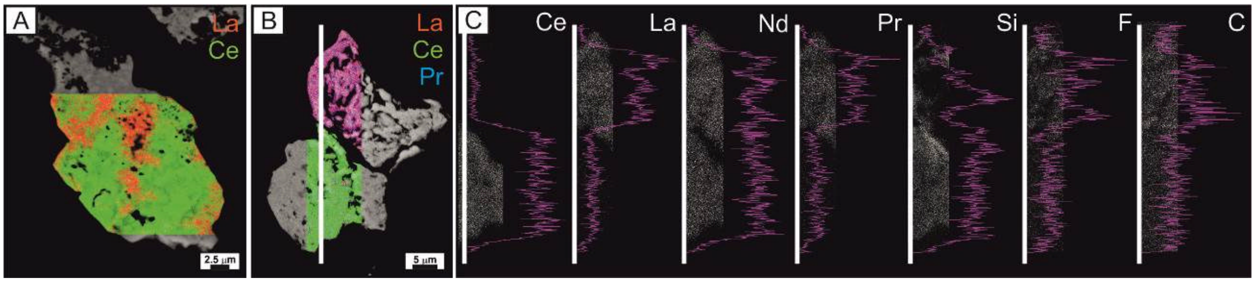

Figure 4.15 Non-graphic inclusions in the apatite breccia. (a) La (red) – Ce (green) X-ray map of non-graphic inclusion. (b) La (red) – Ce (green) – Pr (blue) X-ray map of two adjacent inclusions, where the white line represents the line along which the X-ray profiles were taken. (c) X-ray profiles (Ce, La, Nd, Pr, Si, F and C) of the inclusions on image b.

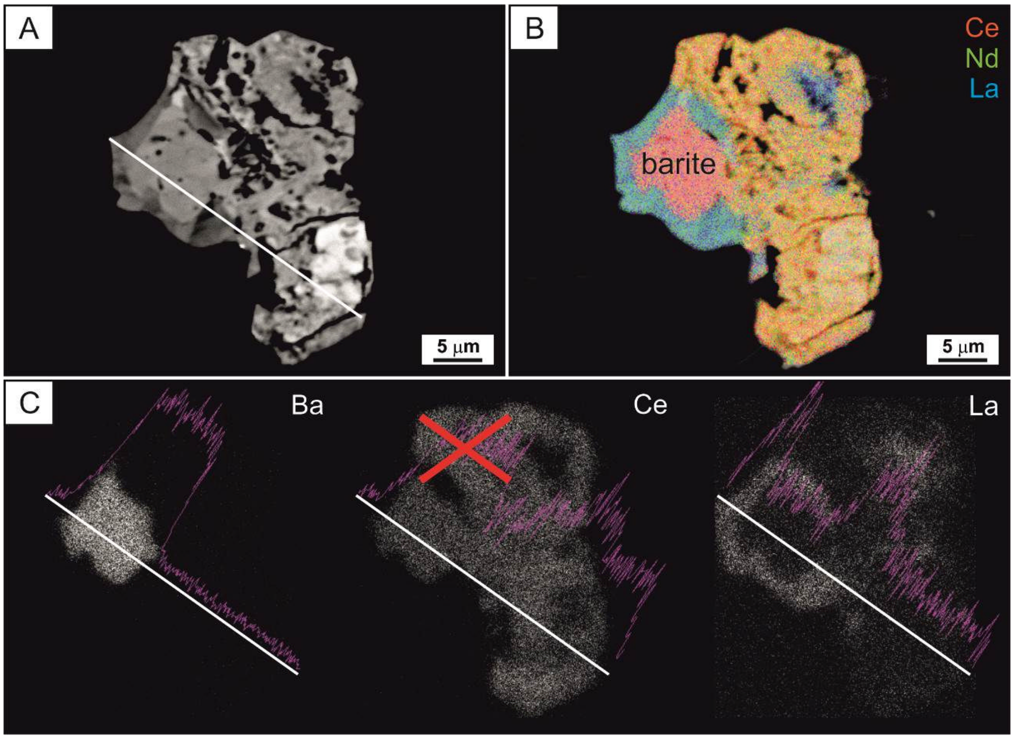

Figure 4.16 Back-scattered electron (BSE) image, X-ray element map and element profiles of complex non-graphic inclusion next to a barite crystal in apatite. (a) BSE image of non-graphic inclusion. The white line represents the line along which the X-ray profiles were taken. (b) Ce (red) – Nd (green) – La (blue) X-ray map of inclusion. (c) X-ray Ba, Ce and La profiles of the inclusion. The Ba and Ce peaks overlap on the X-ray spectra, so the Ce peak on the second profile with a red cross over it is not real.

In rare cases, barite (identification of which was based on the presence of a S peak because of the overlap of Ba and Ce peaks on the X-ray spectra; Fig. 4.16), was detected adjacent to the non-graphic inclusions, and might represent an unmixed phase in the melt or alternatively, an accidentally trapped crystal during apatite growth. However, in most cases, barite occurs along fractures in the apatite, along the contacts of apatite grains or infilling vugs in the breccia (Fig. 4.17a, b), similarly to other secondary phases like the monazite and thorite. These secondary barite inclusions are highly enriched in Sr, with up to 16.4 wt.% SrO (Table 4.6). Other post-entrapment alteration phases in the graphic-textured and non-graphic inclusions are hematite, a REE-silicate phase (with the semi-quantitative composition of 6.1-11.7 wt.% Si, 0.8-3.4 wt.% P, 0.4-2.3 wt.% Ca, 0.5-0.8 wt.% Fe, 1.0-3.1 wt.% Ba, 0.1-6.9 wt.% Th, 24.1-50.9 wt.% Ce, 1.0-7.5 wt.% Nd, <9.0 wt.% La) and REE-Sr-carbonate (Fig. 4.17b, c, d) which all resorb the aforementioned inclusions and the secondary thorite, monazite, barite inclusions.

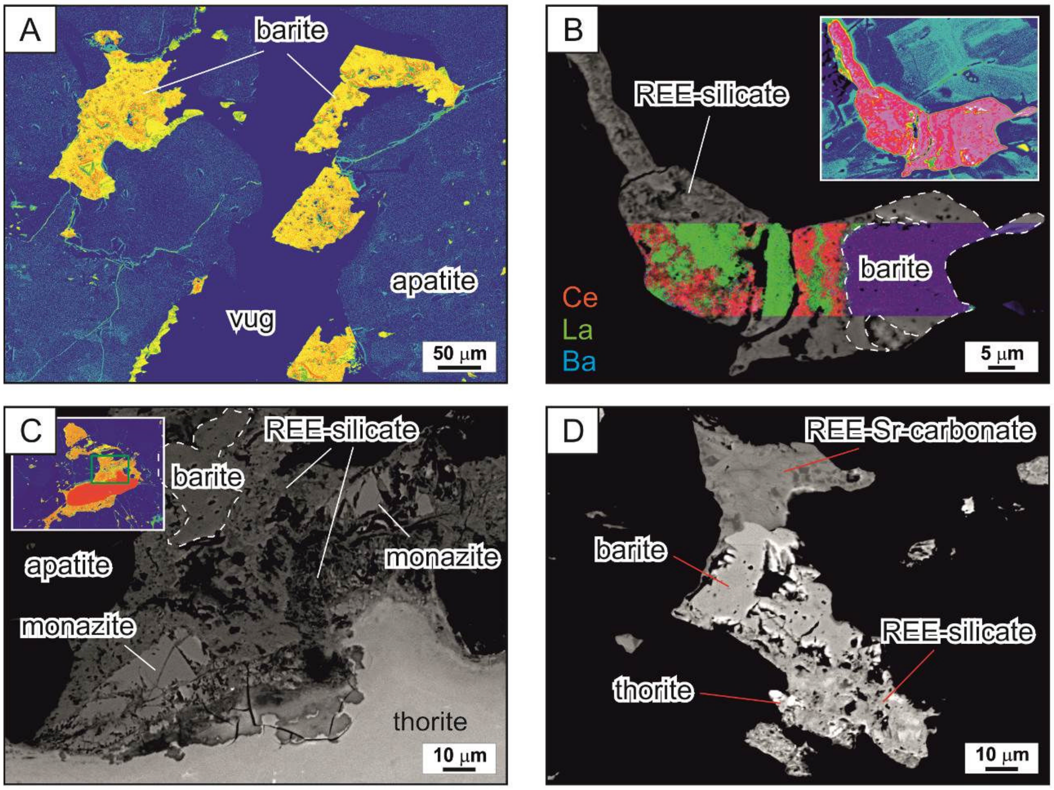

Figure 4.17 Back-scattered electron (BSE) images and X-ray element map of secondary vug-filling phases in apatite. (a) False color BSE image of barite crystals encrusting the rim of vugs in the apatite breccia. The apatite shows irregular patchy zonation around the vug. (b) Ce (red) – La (green) – Ba (blue) X-ray element map of inclusion, that consists of barite and a REE-silicate phase, in apatite overlain on BSE image. Inset is a false color BSE image of the same inclusion, showing irregular mottled zonation in the apatite surrounding the inclusion. (c) BSE image of vug in the apatite breccia, filled by thorite, monazite and barite which are resorbed by a REE-silicate phase. Inset is an enlarged, false color BSE image of the vug, where the green rectangle denotes the enlarged area. (d) BSE image of vug in the apatite breccia, filled by thorite and barite which are resorbed by a REE-silicate phase and REE-Sr-carbonate.

4.6 Discussion

4.6.1 Formation of the Hoidas Lake REE mineralization – magmatic vs. hydrothermal processes

Petrographic observations of the Hoidas Lake REE veins suggest that both magmatic and hydrothermal processes influenced the formation and evolution of the mineralized system, as has been suggested by Hogarth (1957). A schematic diagram summarizing the Hoidas Lake vein paragenesis is presented in Figure 4.18.

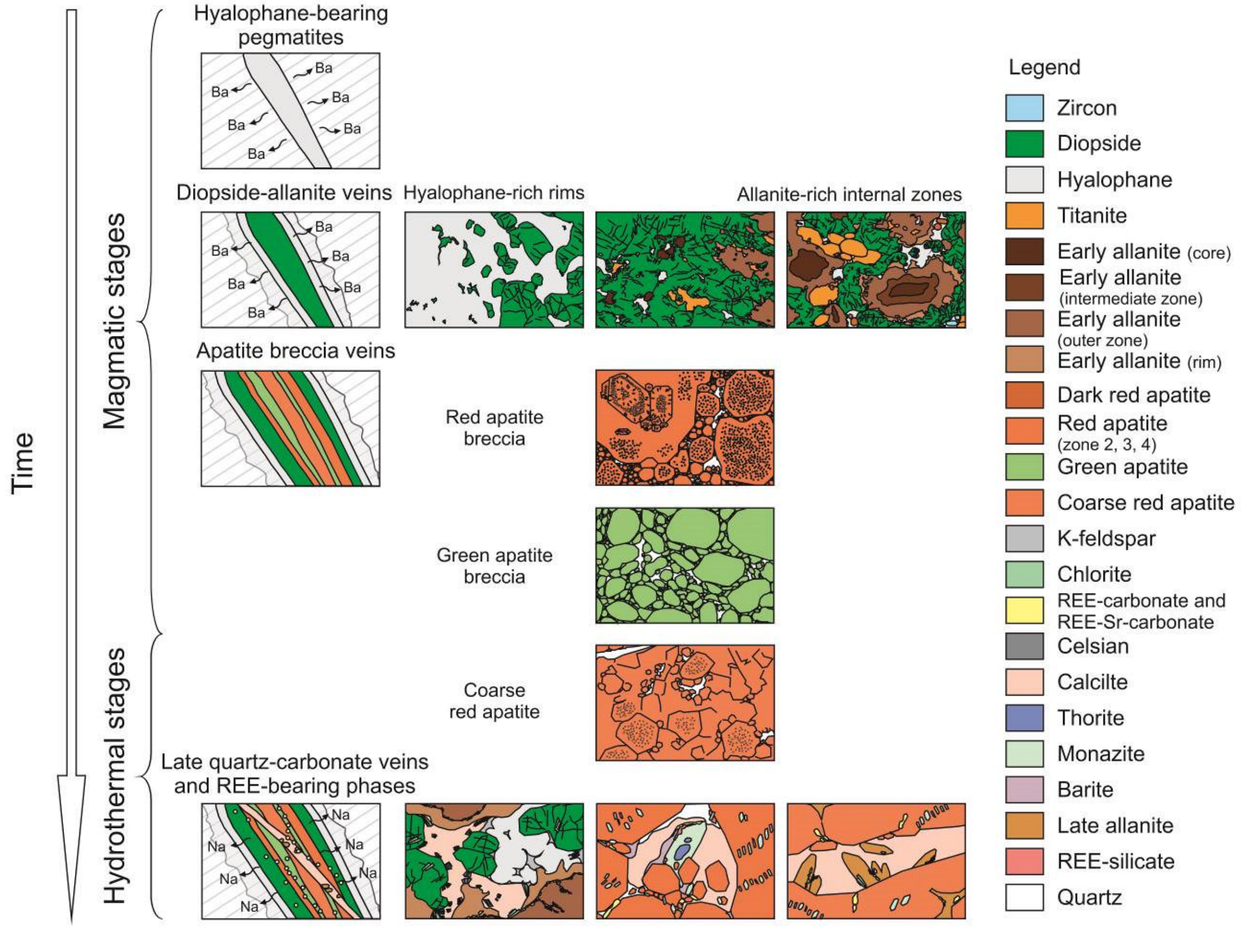

Figure 4.18 Schematic diagram summarizing the paragenetic relationships of the Hoidas Lake REE deposit, including hyalophane-bearing pegmatite dikes, diopside-allanite veins, apatite breccia veins and late quartz-carbonate veins and secondary phases.

One of the main lines of evidence for magmatic origin is that the Hoidas Lake diopside-allanite veins both cross-cut (Fig. 4.4b) and are cross-cut by the hyalophane-bearing pegmatites (Fig 4.4c). This observation, in addition to the common occurrence of hyalophane in both pegmatitic margins around the diopside-allanite veins and within the diopside-allanite veins (Fig. 4.4a), and the presence of allanite in the hyalophane-bearing pegmatites suggest that the diopside-allanite veins and the hyalophane-bearing pegmatites are both spatially and temporally related. The lamprophyre dikes of the Hoidas Lake area postdate the REE mineralization, although they commonly occur along the same structures as the REE veins (Fig. 4.4b). The spatial association of these rock types with the REE veins infer a magmatic origin for the early stages of the REE mineralization. The pegmatitic grain size of the mineralized veins and the presence of primary graphic-textured inclusions in the red apatite breccia indicate that there were episodes of rapid crystal growth under magmatic conditions in the vein system.

There are several indications for low-temperature hydrothermal origin of the mineralized veins, the most important of which being that the diopside-allanite veins and apatite breccia veins are relatively limited in extent, and there is no evidence for extensive metasomatism in the host rocks which would indicate magmatic formation temperatures. There are several features, like sharp contacts between the different vein phases (Fig. 4.5a), multiple phases of extensive brittle brecciation and the presence of hydrothermal REE-bearing phases, e.g., REE-carbonates, which indicate the presence of hydrothermal fluids during vein formation. Furthermore, towards the terminal stages of vein evolution, the presence of hydrothermal processes is indicated by: (1) the alteration of the primary vein minerals (Fig. 4.4d, e, h, 4.9a, b, 4.12a, b); (2) the abundance of secondary phases, such as monazite and REE-carbonates (Fig. 4.6c, 4.9a, b, 4.12a–d); (3) the presence of various generations of fluid inclusions (Pandur et al., 2014); and (4) the occurrence of hydrothermal quartz-, calcite-, epidote-, chlorite-, hematite-filled veins and vugs that are superimposed on the mineralized veins (Fig. 4.3h, 4.5c, 4.6f).

Therefore, the Hoidas Lake REE mineralization represents an example of a REE deposit that was influenced by both magmatic and hydrothermal processes during its evolution, and the veins are considered to represent a transition from an early magmatic stage, through a REE-enriched hydrothermal stage of vein formation, to a late REE-poor hydrothermal stage. Thus, the use of the term ‘vein’, as applied to the diopside-allanite veins and apatite breccia veins, is not used as an indicator of a strictly hydrothermal origin, as these units were affected by both magmatic and hydrothermal processes. The hydrothermal evolution of the Hoidas Lake vein system is discussed in more detail in our summary of the fluid inclusion characteristics (Pandur et al., 2014).

4.6.2 Origin of the melts and fluids responsible for the formation of the Hoidas Lake REE mineralization

The Hoidas Lake REE deposit is somewhat unique in the sense that in contrast to most REE deposits that have a direct relationship with their igneous host rocks (e.g., Mountain Pass, USA – Mariano, 1989; Ilimaussaq Complex, Greenland – Salvi and Williams-Jones, 2005; Rodeo de Los Molles, Argentina – Lira and Ripley, 1992), the studied diopside-allanite veins and apatite breccia veins cannot be related to coeval magmatic activity in the area, other than the early hyalophane-bearing pegmatite bodies. Furthermore, the REE veins are discordant to the prevailing S1-S2 deformation fabric of the wall rocks, which indicates that emplacement of the mineralization postdates the formation and subsequent deformation of the tonalitic to granodioritic gneisses and granitic gneisses of the area. In most cases, the mineralized veins have sharp contacts, excluding the presence of irregular hyalophane-rich margins (Fig. 4.4a), and there is evidence for Ba metasomatism in the host rocks adjacent to the veins (Fig. 4.7a, b). The limited spatial extent of these aforementioned features suggests that the melts and fluids that formed the mineralized veins had limited interaction with the wall rocks; hence, the melts and fluids must have been focused into actively dilating structures, and likely originate from a distal source.

Furthermore, the veins are enriched in REE-bearing phases, in contrast with the REE-deficient nature of the tonalitic to granodioritic and granitic gneisses that dominate the Hoidas Lake area, which indicates that any remobilization from the wall rocks is unlikely. Although the host gneisses occasionally contain trace amounts of allanite and apatite, their bulk Ca, Fe, Mg, P, Sr, Ba, and REE contents are relatively low (<1.4 wt.% CaO, <2.7 wt.% Fe_2O_3, <0.5 wt.% MgO, <0.08 wt.% P_2O_5, <1460 ppm Sr, <1150 ppm Ba, <0.04 wt.% TREE; Harper, 2012), compared to the enrichment of these same elements in the mineralized veins (<50.2 wt.% CaO, <11.2 wt.% Fe_2O_3, <11.2 wt.% MgO, <39.8 wt.% P_2O_5, 2260-11400 ppm Sr, 289-68000 ppm Ba, 0.025-16.166 wt.% TREE; Harper, 2012).

Of the rocks present in the Hoidas Lake area, only the hyalophane-bearing pegmatite dikes, the emplacement of which overlaps in time with the formation of the early diopside-allanite veins, and the later lamprophyre dikes that were emplaced along the same structures as the REE mineralized veins (Elliott et al., 2013) suggest a possible genetic link to the REE mineralization. These two intrusive units both show enrichment in Sr, Ba and REEs with the pegmatites having up to 3500 ppm Sr, 5000 ppm Ba and 1220 ppm TREE (Halpin, 2010), whereas the lamprophyres have up to 1150 ppm Sr, 4850 ppm Ba and 400 ppm TREE (Harper, 2012). These enrichment patterns are similar to, but not as strong as, those in the mineralized veins. The hyalophane-bearing pegmatites contain trace amounts of allanite and diopside, and hyalophane is a common constituent of the mineralized diopside-allanite veins. The presence of the hyalophane-bearing pegmatites and lamprophyre dikes along the same structural trend as the mineralization and the similarities in their bulk chemistry indicate that these units may be genetically related and derived from the same mantle-source as the REE mineralization.

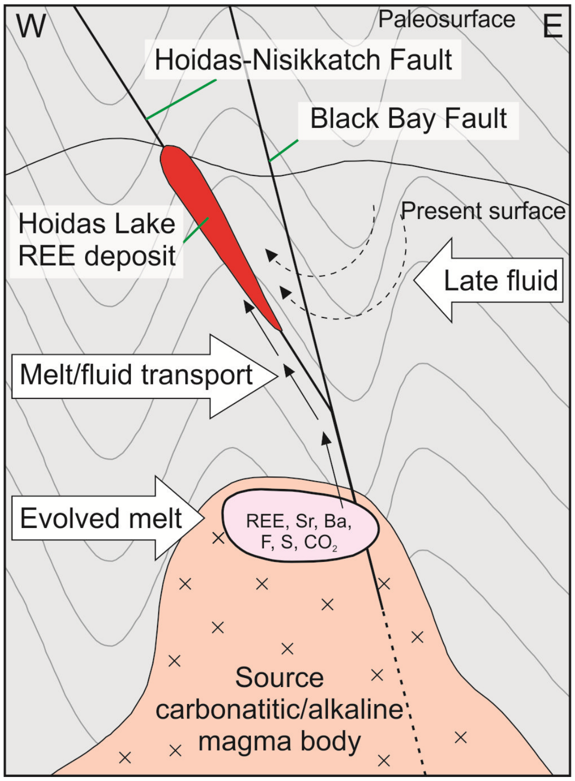

Figure 4.19 Schematic cross-section of the geological relationships of the Hoidas Lake deposit and a possible model for the origin of the mineralizing melts and fluids that are responsible for the REE mineralization (modified from Halpin, 2010). The black solid and dashed lines with arrows represent the likely transport paths of melts and magmatic-hydrothermal fluids present in the system. Diagram is not drawn to scale.

A mantle source for the veins was proposed by Harvey et al. (2002) and Gunning and Card (2005), whereas Halpin (2010) attributed the unique mineralogy and enrichment of the veins in LREEs, Ba and Sr to a hidden carbonatitic or alkaline source (Fig. 4.19). This latter model is consistent with our recent study of fluid inclusions (Pandur et al., 2014), in which it was concluded that the REE mineralization is attributed to fractionation of the unexposed magmatic source with carbonatitic affinity.

The occurrence of the Hoidas Lake mineralized veins along a structural trend parallel to the Hoidas-Nisikkatch Fault and to the long-lived regional Black Bay Fault System (Halpin, 2010; see Fig. 4.19) indicates that deeply-rooted structural pathways for melts and hydrothermal fluids existed in the area and possibly played a significant role in the transportation and localization of the REE mineralization.

Perhaps the most compelling evidence for the nature of the source of the mineralization relates to the apatite chemistry, several aspects of which suggest a relationship to an alkaline or carbonatitic melt: (1) the trace element composition of the apatites indicates that they are likely not derived from a highly fractionated granitic source, as apatites from such source generally have Sr concentrations below 100 ppm, whereas the Hoidas Lake apatites contain over 1000 ppm SrO; (2) the high Th and LREE concentrations (up to 0.1 wt.% ThO_2 and up to 7 wt.% LREO, respectively) of the apatite are also more typical of a carbonatitic or syenitic source (Belousova et al., 2002); (3) apatite from granitoids generally displays a relatively flat chondrite-normalized REE pattern with a pronounced negative Eu anomaly, however, the apatite from Hoidas Lake has more fractionated (i.e., steeper) REE pattern with no Eu anomaly (Fig. 4.8d) which is more typical of carbonatitic apatite (Belousova et al., 2002); and (4) the relatively high F contents of the apatite (2.4 to 4.4 wt.%) are also consistent with a carbonatitic origin (Bühn et al., 2001).

The chemical affinity of the Hoidas Lake apatite to a carbonatitic source is also suggested by the discrimination plots for apatites – Y (ppm) vs. Sr (ppm) and Mn (ppm) vs. Sr (ppm), as proposed by Belousova et al. (2002), as the data for the Hoidas Lake apatite grains plot close to the carbonatite field. We suggest that the slightly higher Y and Mn contents (Fig. 4.20a, b) of the Hoidas Lake apatite relate to their partly hydrothermal nature, similarly to carbonatitic fluorapatite grains studied by Bühn et al. (2001), where elevated Y contents were interpreted to indicate the coexistence of carbonatitic magma with aqueous fluids.

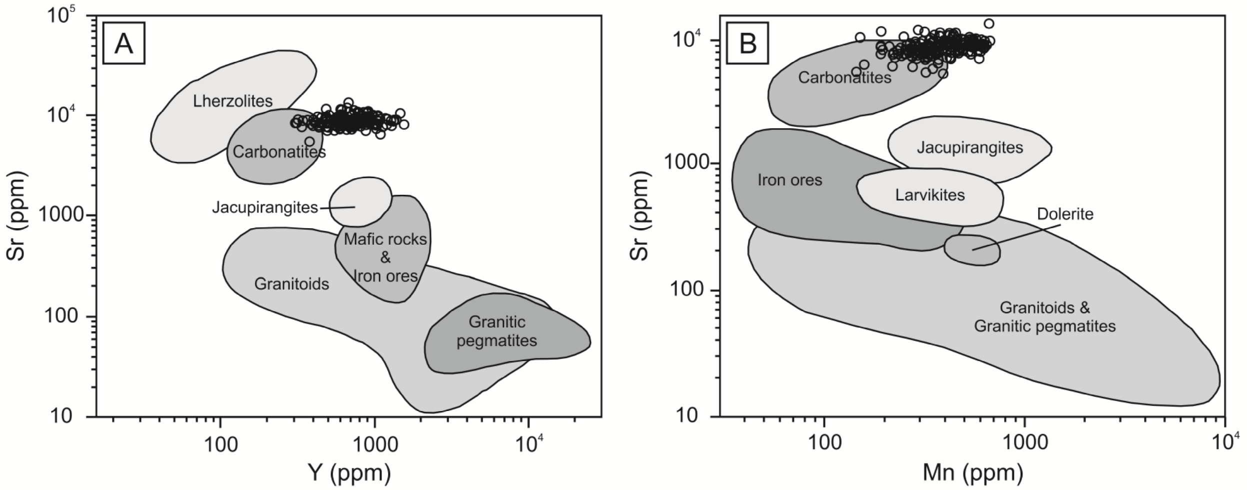

Figure 4.20 Trace element composition of the Hoidas Lake apatite (circles): (a) Y(ppm) vs. Sr (ppm), (n = 147); (b) Mn (ppm) vs. Sr (ppm), (n = 175). The fields of apatite compositions from different rock types were taken from Belousova et al. (2002).

The Hoidas Lake deposit is strikingly similar in its mineralogy and chemistry to the apatite-rich pegmatitic dikes in the Visakhapatnam District of eastern India (Choudhuri and Banerji, 1976; Rao, 1976). These latter pegmatitic dikes also display distinct zonation, with hyalophane-rich margins, clinopyroxene-, titanite-, then biotite-bearing layers, intermediate fluorapatite-dominated zones with minor zircon and magnetite, and allanite-rich cores. The pegmatites were interpreted to have formed from magmatic fluids, derived from an alkali syenite with a possible carbonatite association (Choudhuri and Banerji, 1976). Apatite from this setting has elevated Sr, Ba and REE contents (Narasayya and Sriramadas, 1974), and the allanite shows TREO of 24.6 wt.% and ThO_2 0.46 wt.% (Rao et al., 1969), which are similar to those of allanite from Hoidas Lake. A similar mineralogy has also been observed in the Khaluta Ba-Sr-LREE-rich carbonatite complex in the West Transbaikalia Carbonatite Province, Russia (Doroshkevich et al., 2010). In this locality, aegirine-diopside, apatite, phlogopite and allanite commonly occur in the fenites, whereas the alkaline syenite-shonkinite unit is enriched in aegirine-diopside, phlogopite, titanite and apatite, and the calcite and dolomite carbonatite dikes contain abundant magnetite, phlogopite, apatite and monazite linked to the apatite-rich zones. The Khaluta carbonatite complex is interpreted to have formed due to liquid immiscibility of a parental carbonate-saturated silicate melt with the subsequent silicate and carbonate melts evolving independently to form alkaline syenite-shonkinite and carbonatite suites, respectively. The Arshan REE-rich carbonatite complex, located in the same Carbonatite Province as the latter, is enriched in fluorite primarily, but allanite-, parisite- and bastnäsite-rich mineral assemblages are also common (Doroshkevich et al., 2008). The Hoidas Lake REE deposit may represent a distal magmatic-hydrothermal component of a similar magmatic system.

4.6.3 Chemical variations in the REE-bearing minerals: implications for changing source composition

The presence of the compositionally variable vein generations at Hoidas Lake indicates that the composition of the source melts may have changed during the evolution of the vein system. The evidence for this, namely, the zonation of the REE-bearing minerals, is explored below.

The early diopside-allanite veins were likely emplaced in multiple stages, as indicated by the fact that they consist of variable zones: hyalophane-rich pegmatitic margins (Fig. 4.4a), hyalophane-diopside-rich zones, diopside-allanite-rich zones with abundant titanite (Fig. 4.4d, e, f), and allanite-rich cores. This zonation records a progressive increase in REE contents in the mineralizing melt, although it is noted that the decrease in REE contents in the allanite of the diopside-allanite veins, from 16.9 to 23.7 wt.% TREO in the cores to 6.9 to 21.7 wt.% TREO in the intermediate zones, likely reflects relative REE depletion of the melt (Gieré and Sorensen, 2004), and the fractionation of the LREEs is considered to relate to closed-system growth of allanite in the veins (Gromet and Silver, 1983). In contrast, the relative enrichment of REEs in the outermost allanite zones (up to 22.6 wt.% TREO) might represent open system crystallization, and reflect an influx of new compositionally distinct melt into the vein system. The slope of the chondrite-normalized REE plots of synchronously crystallized allanite and titanite are distinctly different (Fig. 4.8a, b), more negative with enrichment of La and Ce for allanite, whereas the titanite exhibits enrichment in the heavier LREEs and relative depletion in La. This distinct fractionation among the LREEs between the two phases is also pronounced when comparing their compositions on the La+Ce+Pr(at.%)/TREE(at.%) vs. $(La/Nd)_N$ plot (Fig. 4.21a). The difference in their REE distributions can be explained by crystallographic factors, namely the difference in the sites available for REE in the structures of titanite ($^{[VII]}$Ca) and allanite ($^{[XI]}$A(2)), which results in preferential incorporation of the larger LREEs, like Ce and La, in allanite, whereas titanite has a preference for the smaller LREEs, like Nd (Seifert, 2005).

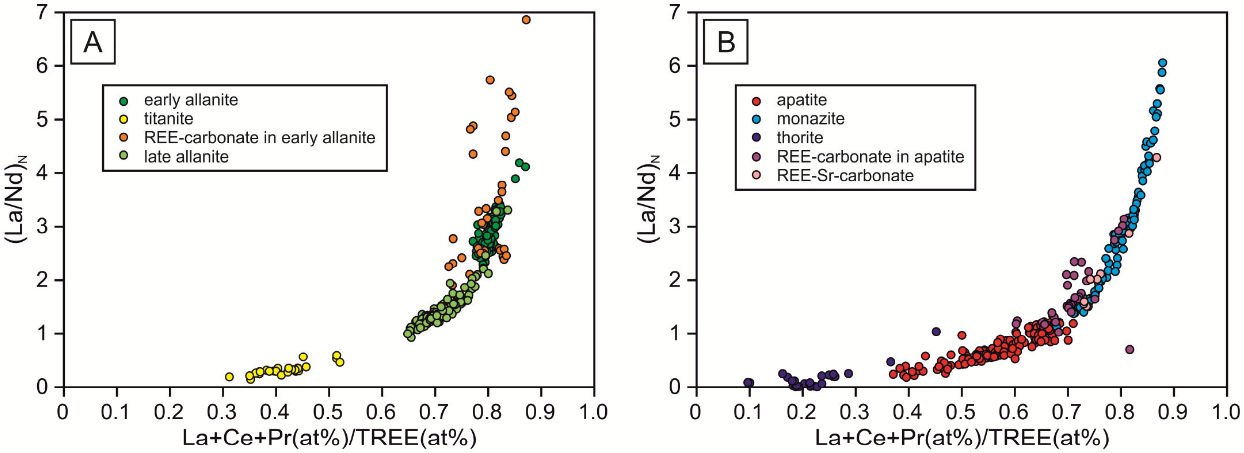

Figure 4.21 Rare earth element distributions of the REE-bearing phases of the Hoidas Lake deposit plotted on the La+Ce+Pr(at.%)/TREE(at.%) vs. $(La/Nd)_N$ diagram, based on Murata et al. (1953), Fleischer (1965), Gieré and Sorensen (2004). (a) Early allanite, titanite, REE-carbonate from the diopside-allanite veins and late allanite from the quartz-carbonate veins. (b) Apatite, thorite, monazite, REE-carbonate and REE-Sr-carbonates from the apatite breccia veins.

The emplacement of the various apatite breccia veins was accommodated by reopening of the early vein structures that hosted the diopside-allanite veins, which explains the presence of apatite breccia intervals and injections inside larger diopside-allanite veins (Fig. 4.5a) and the common occurrence of diopside-allanite vein clasts in the apatite breccia (Fig. 4.5b). The presence of graphic-textured inclusions (Fig. 4.14a, b), interpreted to have formed through rapid apatite crystallization (Pandur et al., 2015; Chapter 3), which delineate primary apatite growth zones, indicates that the dominant medium from which apatite crystallized was most likely an unusual phosphate-rich melt. The systematic compositional zoning in the Ce-dominant apatite generations, and increase in REE contents from the earliest dark red apatite (1.5 wt.% average TREO) to the green apatite breccia (5.5 wt.% average TREO) might reflect changes during fractional crystallization of this melt.

The non-graphic inclusions (Fig. 4.15) are strikingly similar in their chemistry to the graphic-textured inclusions, and likely represent the same residual melts in the system. These may represent migration of the melts from the apatite growth zone with subsequent entrapment along fractures in other apatite, thus they are considered secondary in origin. The presence of barite in some of these inclusions (Fig. 4.16) indicates that Ba may have been present in the melt, which is consistent with the occurrence of inferred primary barite as a solid phase in carbonatite-related melt inclusions, reported by Guzmics et al. (2011). However, given that no significant amounts of Ba were detected in the bulk analysis of most graphic-textured and non-graphic inclusions in the apatite breccia, and the majority of barite inclusions are associated with the most altered apatite intervals and fractures in the apatite, barite is suggested to be of secondary origin.

4.6.4 Chemical variations in the REE-bearing minerals: the role of hydrothermal fluids

Fluid inclusion studies (Pandur et al., 2014) suggest that carbonic fluids were present during formation of the red apatite breccia, and aqueous fluids subsequently infiltrated and affected the mineralized veins. These aqueous fluids have variable salinities (8 to 40 wt.% eq. NaCl), and have been characterized as containing Na, Ca and K, with lesser Ba, Mn, Fe, Mg and Sr. These fluids were interpreted to have originated from an evolving alkaline melt of carbonatitic affinity.

Introduction of these fluid types into the system resulted in the transformation of primary hyalophane ($Cn_{16-21}Ab_{15-18}Or_{63-73}$), via dissolution-reprecipitation reactions, to a Ba-rich potassium feldspar ($Cn_{9-10}Ab_{9-10}Or_{80-81}$) in both the hyalophane-bearing pegmatites and the diopside-allanite veins (Fig. 4.22a). There commonly is a sharp alteration front between these two phases (Fig. 4.22a), but in other instances, the alteration is localized along cleavage planes, fractures and grain boundaries of the hyalophane (Fig. 4.22b). In some cases, the transformation of hyalophane to potassium feldspar was accompanied by the precipitation of fine-grained disseminated barite at the contact between the two phases (Fig. 4.22a), which indicates local hydrothermal remobilization of Ba by a S-bearing fluid. The presence of high S contents (<6 wt.%) in evaporate mounds in these samples (Pandur et al., 2014) is consistent with this interpretation. At the contact of the cross-cutting REE veins and the early hyalophane-bearing pegmatite dikes, thin (up to 3-4 mm wide), irregular albite- and calcite-containing alteration haloes can be observed (Fig. 4.22b), and in these alteration haloes the hyalophane and potassium feldspar crystals are completely replaced by albite ($Ab_{92-96}An_{4-8}Or_{0-2}$).

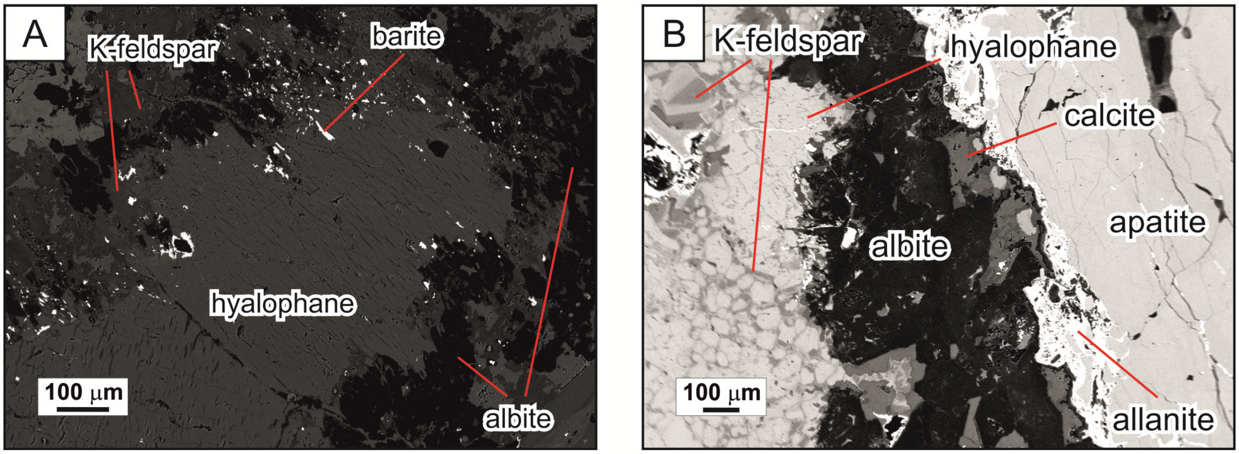

Figure 4.22 Alteration of the hyalophane-bearing pegmatites. (a) BSE image of hyalophane that is replaced along its margin by Ba-rich potassium feldspar and then by albite. Fine-grained disseminated barite crystals are present at the contact between the hyalophane and the potassium feldspar; these inclusions likely formed due to the reaction of a S-bearing fluid with the hyalophane. (b) BSE image of the contact of a red apatite breccia vein that cross-cuts a hyalophane-bearing pegmatite dike. The early hyalophane of the hyalophane-bearing pegmatite is invaded along cleavage by later Ba-free potassium feldspar and then is replaced by albite and calcite in the alteration halo related to the apatite breccia vein. Late allanite is present in the apatite breccia along the vein contact.

The latest apatite generation, the coarse red apatite and the equivalent Zone 4 apatite of the red apatite breccia, has the lowest average TREO (i.e., 1 wt.%; Fig. 4.11) and is Nd-dominant, in marked contrast to the earlier apatite generations. The Zone 4 apatite appears in BSE images as dark rims around the large apatite crystals and the fine-grained apatite in the breccia matrix, with irregular, mottled zonation. In some cases, these low-REE zones extend continuously into the larger apatite clasts along fractures, suggesting that these low-REE apatite zones might not represent a compositionally different apatite precipitation stage, but instead the effect of hydrothermal fluids along the more permeable intervals of apatite. The shift from dominance of Ce-dominant to Nd-dominant compositions also indicates that hydrothermal fluids affected the REE budget of this apatite phase (Smith et al., 2000).

The irregular, mottled zonation is not restricted to the latest apatite phase (Fig. 4.12a), as it is commonly observed in earlier apatite (Fig. 4.12b), allanite (Fig. 4.9a, b) and titanite, primarily in areas where the grains are fractured or along grain boundaries. The lowest TREO values (6.9 to 14.8 wt.%) and relatively high Mg and Ba contents of irregular, mottled allanite zones and the slight decrease in REE contents and increase in Sr, Ti and Cr towards the rims in the outermost allanite zones, as well as the rare REE-depleted rims of the titanite are interpreted to be the result of hydrothermal alteration and related REE remobilization. These features occur where there is a greater abundance of chlorite and hematite in the mineralized veins.

The irregularly zoned allanite and apatite often incorporate monazite, REE-carbonates, REE-Sr-carbonates and barite (Fig. 4.6a–c, 4.9a, b, 4.12a–d). As the occurrence of these phases is restricted to fractures (Fig. 4.6c) and vugs in the matrix of brecciated vein samples, they are suggested to have precipitated from the same hydrothermal fluids that affected the primary REE-bearing phases. The close association of these phases with the REE-depleted irregular zones of allanite and apatite indicates that the distribution of REEs, Ba and Sr in the primary minerals was locally affected by the hydrothermal fluids. Thus, the slight to prominent negative Eu anomaly observed in these secondary phases (Fig.4.8c, e, g, h) can be explained with Eu^{2+} preferentially partitioning into the aqueous fluid that was present during their formation, as reported in some granitic systems (Irber, 1999). In addition, the steeper chondrite-normalized REE plots of these phases, relative to those of primary REE-bearing minerals indicate that the hydrothermal processes responsible for their precipitation further fractionated the LREEs.

The secondary monazite inclusions in apatite formed through local hydrothermal redistribution of the REEs from apatite. Similar oriented monazite inclusions in apatite were described by Pan et al. (1993) from the Hemlo Au deposit, Ontario, and these were also interpreted to be of hydrothermal origin. Harlov et al. (2002) described similar features from the Kiirunavaara magnetite-apatite deposit in Sweden, where high temperature (700-800 °C), Cl-rich fluids are likely responsible for the dissolution-reprecipitation processes that led to monazite formation. Experiments by Harlov et al. (2005) suggest that REE redistribution from apatite into monazite is a local process; thus the REEs required to form the Hoidas Lake monazite were likely derived from the altered apatite zones surrounding these inclusions, and the original REE content of the apatite remained undisturbed in inclusion-free, unzoned regions. These processes might result in faint oscillatory zonation in the apatite surrounding the monazite inclusions, based on experimental monazite nucleation studies in fluorapatite (Harlov and Förster, 2003). Similar faint oscillatory zonation was observed in some of the Hoidas Lake apatite grains. Generally, the earlier apatite generations of the Hoidas Lake deposit have abundant monazite inclusions, whereas the later apatite generations are inclusion-poor (Fig. 4.5f–h). The possible explanation for this is that the earlier apatite generations were exposed to repeated influxes of hydrothermal fluids which triggered monazite precipitation. Experimental studies of Harlov and Förster (2003) showed that formation of the monazite inclusions is most common in apatite that has previously been metasomatized by dissolution-reprecipitation, as this process increases the microporosity of the affected areas.

The Hoidas Lake monazite commonly shows slight concentric zonation, with cores relatively enriched in Th and La, and rims enriched in Ce, Nd, Pr, Sm and Eu (Fig. 4.12c). The elevated Th contents in the core areas are consistent with the occasional appearance of thorite inclusions in the monazite, in which case monazite appears as an overgrowth around thorite (Fig. 4.17c). Thus, it is possible that these pre-existing thorite inclusions in the apatite provided the seeds for hydrothermal monazite growth, which resulted in the incorporation of the thorite by the growing monazite.

The origin of the thorite is less straightforward. Thorite may have already been in the melt as a crystalline phase prior to apatite growth, or it might have crystallized from the residual melt during apatite growth, or it might be the result of local hydrothermal Th and REE remobilization from the apatite, similarly to monazite. The thorite crystals show uniform enrichment in Pr, Nd, Sm, Eu, Gd and strong depletion in La.

The thorite, monazite and barite crystals in the mineralized veins all show intensively pitted surfaces in BSE images, and are partially resorbed and replaced by REE-carbonates, REE-Sr-carbonates and a REE-silicate phase (Fig. 4.17a–c). This observation indicates that they were further affected by hydrothermal fluids. The latest REE bearing phase in the matrix of the apatite breccia, the secondary REE-carbonate is overgrown by REE-Ca-carbonate (Fig. 4.12d), which suggests that the hydrothermal fluids responsible for the growth of these phases became progressively depleted in REEs.

The latest stage of hydrothermal fluid activity resulted in the formation of quartz-, calcite- and chlorite-filled vugs in the matrix of brecciated diopside-allanite veins and the apatite breccia, and these incorporate resorbed diopside, allanite and apatite (Fig. 4.6d, e). In addition, there are abundant quartz- and carbonate-rich veins that overprint the apatite breccia (Fig. 4.3h, 4.5c), and their origin likely relates to the same late-stage hydrothermal event. The rare occurrence of allanite in quartz- and carbonate-rich vugs and veins cross-cutting the coarse red apatite phase (Fig. 4.6f–h) indicates that the REEs were indeed remobilized by these late hydrothermal fluids (Fig. 4.6f, g). A hydrothermal origin for the late allanite is indicated by: (1) its confinement to veins and vugs with a negligible spatial extent; (2) its coexistence with such hydrothermal phases as calcite and quartz; and (3) the observation that this allanite replaces primary REE-rich phases, such as apatite (Fig. 4.6h).

The late allanite plots at lower La+Ce+Pr(at.%)/TREE(at.%) and $(La/Nd)_N$ values compared to the early allanites of the diopside-allanite veins (Fig. 4.21a). If it is assumed that the source for the constituents of the late allanite is the early allanite generation, then the hydrothermal remobilization resulted in a different degree of fractionation among the LREEs in the late allanite from that of the early allanite. Similar features are observed in the Bayan Obo Fe-REE-Nd deposit, where early-stage bastnäsite and monazite associated with high $X(CO_2)$ hydrothermal fluids show higher La/Nd ratios, whereas the later-stage REE-fluorocarbonates, which are inferred to have formed from dominantly aqueous fluids, show lower La/Nd ratios (Smith et al., 2000). This relationship is not observed in case of the Hoidas Lake REE-carbonate that formed through hydrothermal alteration of allanite (Fig. 4.21a) and monazite and REE-carbonate that formed through hydrothermal alteration of apatite (Fig. 4.21b), due to mineral chemical factors, namely, the preferential enrichment of the lightest LREEs in these phases, relative to allanite and apatite. On the other hand, in case of the thorite cores within the monazite inclusions (Fig. 4.21b), the lower La+Ce+Pr(at.%)/TREE(at.%) and $(La/Nd)_N$ values indicate preferential enrichment of the heavier LREEs in the thorite structure, similarly to titanite (Fig. 4.21a).

The late allanite displays oscillatory zonation, reflecting distinct changes in REE contents (Fig. 4.13a, b). This zonation pattern might be the result of fluctuating changes in the composition of the mineralizing fluid or the conditions under which crystallization took place. For example, during the precipitation of the allanite, the crystal growth rate might have exceeded the diffusion rate in the hydrothermal fluid, and thus, the concentration of REEs at the crystal growth surface would fluctuate. The growth of high-REE zones would deplete the adjacent fluid in REEs, resulting in the subsequent growth of low-REE zones, prior to re-enrichment of the fluid in REEs by diffusion to restart the cycle.

The compositional variations of the hydrothermal fluids that appear to be responsible for the late alteration, as inferred by fluid inclusion studies (Pandur et al., 2014), suggest that the REE transportation potential (i.e., presence of complexing agents) for these fluids is a function of both variations in the chemistry of the source from which the fluids were derived and interactions between the fluids and the early hyalophane-bearing pegmatite dikes and diopside-allanite veins.

Based on the composition of the minerals in the Hoidas Lake REE veins, the most important complexing agents were probably F^- and PO_4^{3-}, although minor amounts of either OH^- or CO_3^{2-} may have also had an effect (Jiang et al., 2003). The abundance of secondary hematite in the mineralized veins (Fig. 4.5f–h), the occurrence of allanite rims that show epidote-like chemistry (Fig. 4.4c) and the carbonic nature of the fluids that lack any CH_4 all indicate that the hydrothermal fluids affecting the REE veins were oxidizing.

4.7 Conclusions

The trace element chemistry and chemical variations of allanite, titanite, apatite, monazite, thorite, REE-carbonates and REE-Sr-carbonates were studied in detail, in order to complement our previous study of the hydrothermal fluids that were present during the formation of the Hoidas Lake REE deposit. The complex, multi-stage evolution of the LREE-enriched vein system is inferred to represent the combined effort of an initial magmatic system and a superimposed hydrothermal system, the evolution of which is reflected in the observed changes in vein paragenesis and mineral chemistry. Given the consistent sequence of crystallization stages, from apatite formation, through thorite and monazite, then barite precipitation (together with hematite and chlorite), to precipitation of REE-silicates and REE-Sr carbonates in close association with high salinity aqueous hydrothermal fluids, the apatite breccia veins likely represent a transition from a residual, highly evolved melt to a hydrothermal fluid that caused remobilization of the REEs. In addition, the mineralogy, chemistry, and extreme enrichment of the veins in REEs and other elements (i.e., Ba, Sr) indicate that the source of melts and fluids likely had a carbonatitic affinity.

4.8 Relationship of manuscript to thesis

This manuscript provides detailed description of the mineral chemical characteristics of the various REE-bearing phases of the diopside-allanite and apatite breccia veins of the Hoidas Lake deposit. The chemical variations of these minerals are discussed in view of the nature and characteristics of melts and hydrothermal fluids present in the vein system (discussed in Chapter 2 and 3), in order to relate the observed chemical variations to specific stages in the magmatic and hydrothermal evolution of the REE deposit. The effects of the emplacement of the mineralization on the host rocks of the area and potential relationships of the REE-rich veins with other alkaline rock types are discussed in order to better understand the nature of the mineralization. The manuscript places emphasis on understanding the formation of secondary REE-bearing phases in the mineralized veins, with focus on evidence for hydrothermal REE remobilization preserved in the chemical variations of vein phases. In addition, the trace element characteristics of the REE-bearing phases are used to provide further constraints on the evolution of the vein system, and to infer the nature of the magmatic source of the Hoidas Lake mineralization. This provides complementary evidence for the nature of the source of the REE mineralization, based on the fluid inclusion chemistry and radiogenic isotope characteristics of the Hoidas Lake deposit (discussed in Chapter 2 and Chapter 5, respectively). The chemical variations observed in the REE-bearing mineral phases are used to provide the background information for in situ laser ablation ICP-MS analyses, used to constrain the timing and evolution of the Hoidas Lake mineralization (Chapter 5).

CHAPTER 5

IN SITU U-Pb GEOCHRONOLOGY, Lu-Hf AND Sm-Nd ISOTOPE SYSTEMATICS OF THE HOIDAS LAKE REE DEPOSIT, NORTHERN SASKATCHEWAN, CANADA

5.1 Abstract

The diopside-allanite veins and apatite breccia veins of the Hoidas Lake light rare earth element deposit cross-cut the strongly deformed Archaean and Paleoproterozoic granitoid gneisses of the Rae Subprovince, in northern Saskatchewan, Canada. The timing and source of this unusual and complex REE deposit are not well constrained. Here we report on the results of laser ablation ICP-MS U-Pb geochronology of zircon and titanite from diopside-allanite veins and green apatite and monazite from apatite breccia veins, Hf isotopic data for zircon and Sm-Nd isotopic data for titanite, apatite and monazite, in an attempt to constrain the age and duration for the crystallization of REE-bearing phases, and provide implications on the hidden magmatic source of the mineralization.

Geological relationships and in situ U-Pb data indicate that the REE veins formed after peak metamorphism, which occurred at ca. 1.9 Ga. However, there are zircon crystals in the diopside-allanite veins with concordant U-Pb dates of ~2350 Ma which are interpreted to be inherited from granitoids that formed during the Arrowsmith Orogeny, also reported from other parts of the southern Rae Subprovince. Zircon rims show a concordant cluster of U-Pb dates around 1906 Ma, and these are interpreted to represent new zircon growth, based on textural features and their considerably different Hf isotopic compositions (initial εHf values of 26.9 and 34.3), compared to the inherited zircon cores (initial εHf values from -9.5 to -1.4). Concordia ages of titanite from two distinct samples are ca. 1900 Ma and 1830 Ma, two monazite U-Pb date groups were observed at ca. 1910 Ma and 1845 Ma, and preliminary discordant apatite ^{207}Pb/^{206}Pb dates average around 1845 Ma. This corresponds to the estimated period of tectonic activity of the Black Bay Fault System. The Sm-Nd isotopic characteristics of titanite, green apatite and monazite, and calculated initial εNd values (from -15.3 to -10.6) at the time of their formation are comparable to the εNd values previously reported for the Martin Group alkali basalts in the Beaverlodge Domain and the ultrapotassic rocks of the Christopher Island Formation in the Baker Lake Basin, both of which also yielded similar U-Pb dates to those of the

Hoidas Lake titanite, green apatite and monazite. These regionally occurring alkali units originated from a similar source, most probably an ancient enriched lithospheric mantle reservoir.

5.2 Introduction

The Hoidas Lake light rare earth element (LREE) deposit is located in northern Saskatchewan, Canada, and consists of multiple vein generations, including diopside-allanite veins and apatite breccia veins. The diopside-allanite veins consist mainly of allanite, hyalophane, diopside, green amphibole, titanite and lesser apatite and zircon. Among the apatite breccia veins early red apatite breccia, green apatite and late coarse red apatite stages are distinguished. The vein system is considered to have formed during the evolution of the major Black Bay Fault System and its subsidiary, the Hoidas-Nisikkatch Fault (Halpin, 2010); however, the potential source of the REE mineralization – a buried magmatic body with a carbonatitic affinity, is inferred solely from mineral chemical and fluid inclusion characteristics (Chapter 4; Pandur et al., 2014). The age and geodynamic position of the REE mineralization are not well constrained.

Recent advances in laser ablation inductively coupled plasma mass spectrometry (LA-ICP-MS) methods applied to in situ analyses for the U-Pb (Simonetti et al., 2006; Košler, 2007; Chew et al., 2011), the Lu-Hf (Fisher et al., 2011a) and the Sm-Nd (Foster and Vance, 2006; McFarlane and McCulloch, 2007; Fisher et al. 2011b) radiogenic isotope systems allow for accurate and precise measurements restricted to specific zones in complexly zoned zircon, titanite, apatite and monazite crystals for geochronological and radiogenic isotope tracer investigations. Furthermore, multiple LREE-enriched phases with well constrained petrographic relationships can be analyzed which allows for the tracking of Hf and Nd isotopic evolution of the mineralized system (Gregory et al., 2009).

This study aims to use in situ laser ablation inductively coupled plasma mass spectrometry techniques to provide a better understanding of the geology of the Hoidas Lake mineralization. U-Pb dating of zircon and titanite crystals from diopside-allanite veins, and green apatite and monazite crystals from apatite breccia veins were done, in order to constrain the age and duration for the crystallization of REE-enriched phases. The source of the REE mineralization was studied using radiogenic Hf isotope tracers for zircon and Nd isotope tracers for titanite, green apatite and monazite. Furthermore, the overview of the local geological features and Sm-Nd and Lu-Hf isotope systematics of the REE veins in the light of our knowledge on the regional geology of this part of the Rae Subprovince aims to resolve the Proterozoic tectonic environment of the REE mineralization.

5.3 Geological background

5.3.1 Regional tectonic environment

The Churchill Province is bounded by the Taltson-Thelon Orogen to the west and the Trans-Hudson Orogen to the east-southeast, and is divided into the Rae Subprovince in the northwest and the Hearne Subprovince in the southeast (Fig. 5.1a). The contact between these two subprovinces is the ca. 2000 km long Snowbird tectonic zone.

The Rae Subprovince, which hosts the Hoidas Lake REE deposit, is characterized by a protracted geological history and records the effects of four major Paleoproterozoic thermo-tectonic events: (1) the 2.5-2.3 Ga Arrowsmith Orogeny in the west (Berman et al., 2005, 2013); followed by (2) subduction, accretion and magmatism associated with the development of the Taltson magmatic zone (McDonough et al., 2000) which is inferred to represent the southern extension of the Thelon tectonic zone, defining the greater 1.99–1.92 Ga Taltson-Thelon Orogen (Hoffman, 1988, 1989; McNicoll et al., 2000; Ross, 2002; Ross and Eaton, 2002); (3) the 1.91-1.90 Ga tectonism along the Snowbird tectonic zone in the east (Baldwin et al., 2003; Flowers et al., 2006); and (4) the 1.87-1.80 Ga main stage of the Trans-Hudson Orogeny (Hoffman, 1988, 1989; Ansdell, 2005; Mahan and Williams, 2005). The Snowbird tectonic zone has been interpreted as a suture between the independent Rae and Hearne blocks during the early stage of the Trans-Hudson Orogeny (Berman et al., 2007) or as a long-lived intracontinental fault, initiated in the Archean and reactivated in multiple stages during the Paleoproterozoic (Hanmer et al., 1995; Mahan and Williams, 2005).

The Taltson-Thelon Orogeny and the Trans-Hudson Orogeny resulted in intense Paleoproterozoic reworking of the Archean rocks of the Rae Subprovince (Hoffman, 1989; Ashton et al., 2009), which led to the formation of siliciclastic basins, some of which contain mafic igneous rocks indicative of extensional magmatism (Ashton et al., 2009), such as the

Christopher Island Formation of the Baker Lake Basin in the east-central Rae Subprovince (Peterson et al., 2002), and the alkali basalts of the Martin Group in northwestern Saskatchewan (Ashton et al., 2001).

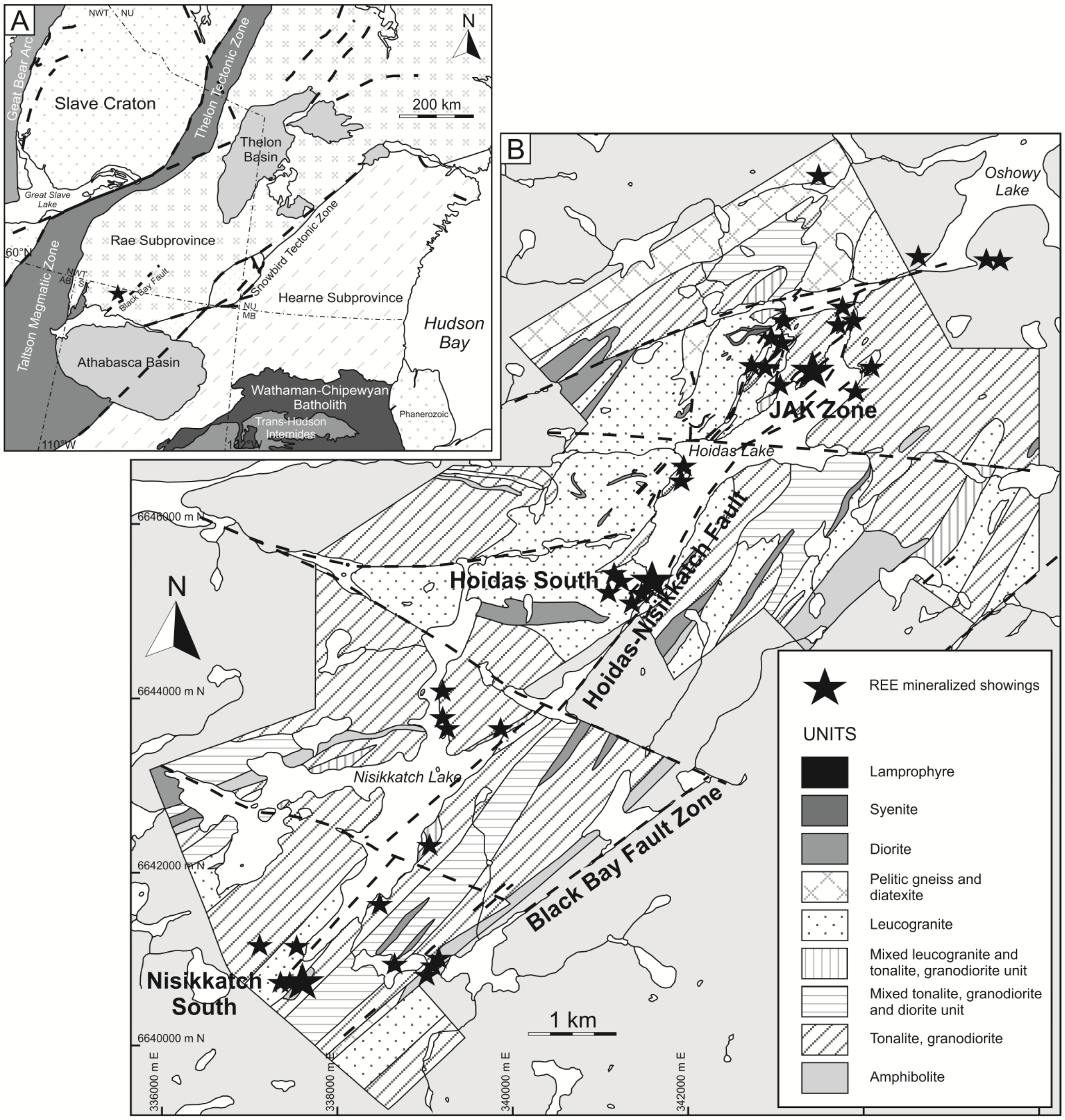

Figure 5.1 Regional and local geology of the Hoidas Lake REE mineralization. (a) Regional lithotectonic assemblage map for parts of northern Alberta, Saskatchewan and Manitoba and contiguous Northwest Territories and Nunavut (modified from Pehrsson et al., 2010). A black star denotes the location of the Hoidas Lake REE mineralization and Figure b. The dashed lines represent faults. (b) Local geology map of the Hoidas Lake area, showing the dominant lithological and structural units, and the location of the mineralized showings (modified from Normand et al., 2009; Harper, 2012). The faults are represented by dashed lines on the map. N and E coordinates denote the location of the area in the UTM 13V zone.

In northern Saskatchewan the Rae Subprovince consists of Archean to Paleoproterozoic granodioritic gneisses with minor amounts of more mafic gneisses, amphibolites and granitic gneisses, which are overlain by supracrustal units indicative of extensional environment (Hartlaub et al., 2005; Ashton et al., 2007). These rocks record the aforementioned tectonic events variably (Ashton et al., 2005, 2007, 2009; Hartlaub et al., 2007). The evolution of the Taltson-Thelon Orogen resulted in granulite facies peak metamorphic conditions, followed by amphibolite and greenschist facies retrograde metamorphism in the Rae Subprovince (Grover et al., 1997; Ashton et al., 2005).

5.3.2 Lithological and structural units of the Hoidas Lake area

The host rocks of the Hoidas Lake deposit are Archean tonalitic to granodioritic gneisses that contain amphibolite and diorite xenoliths, Archean to Paleoproterozoic granitic gneisses, less abundant metasedimentary gneisses, syenites, later garnetiferous dioritic gneisses and amphibolite dikes (Fig. 5.1b; Harvey et al., 2002; Gunning and Card, 2005; Normand et al., 2009; Harper, 2012). These units were metamorphosed to upper amphibolite-lower granulite grade related to peak metamorphism in the area at approximately 1.9 Ga (Ashton et al., 2009). There are also several generations of granitic pegmatite intrusions and late unmetamorphosed lamprophyre dikes.

Four main deformation stages have been described from the Hoidas Lake area (Harvey et al. 2002; Gunning and Card 2005; Normand et al. 2009; Harper 2012): Evidence for the D1 event is limited, as it was only locally preserved as foliation in amphibolite. However, the S1 foliation was folded during D2, resulting in tight to isoclinal F2 folds and strong northwest-southeast-oriented composite S1-S2 foliation. This S1-S2 foliation is defined by flattened or elongated mineral grains, alternating leucosome-melanosome and transposed primary compositional layering in amphibolites. The D2 deformation occurred during peak metamorphism in the Hoidas Lake area. The later D3 deformation is responsible for the regional northeast-southwest-trending structural fabric in the area. The S3 foliation is axial planar to F3 folds, dips steeply southeast or less commonly northwest, and is defined by parallel alignment of the long axes of mafic minerals. The development of this deformation stage is related to shear zone development and reactivation along the regional Black Bay Fault. The Black Bay Fault is a major northeast-trending brittle-ductile structure with prolonged, complex deformation history which extends over 100 km in strike length from the north shore of Lake Athabasca northeast into the Northwest Territories (Gunning and Card, 2005). The fault is superimposed on a several kilometers wide straight belt of mylonitic gneisses named the Black Bay Shear Zone (Kraus and Ashton, 2000). Although the exact timing of the movement along the Black Bay Shear Zone is not well constrained, the entire deformation history is believed to have occurred between 2.3 and 1.7 Ga (Bergeron, 2001). In the Hoidas Lake area the Hoidas-Nisikkatch Fault (Fig. 5.1b) is parallel to and likely shares the complex deformation history of the Black Bay Fault, including several periods of reactivation and deformation (Halpin, 2010). The intensity of S3 is heterogeneously developed in the area, with increasing levels of strain going from northwest to southeast, towards the Black Bay Fault. As a result of the variable strain, F3 folds vary from open to tight-isoclinal with steeply dipping northeast-trending axial planes. Kinematic indicators (ϭ- and δ-type porphyroclasts and back-rotated boudins) suggest dextral movement in the ductile shear zones. The D4 deformation event is reflected by gently undulating open F4 folds that have north-northwest-oriented steeply dipping axial planes, open interlimb angles, and lack axial planar foliation. Late east, northeast and southeast oriented fractures and faults can also be observed in the area.

5.3.3 Textural relationships, mineral chemistry and structural position of the REE mineralization at Hoidas Lake

The Hoidas Lake REE deposit consists of diopside-allanite veins and multiple stages of apatite breccia veins that occur in three main mineralized zones (JAK Zone, Hoidas South Showing and Nisikkatch South Showing), and several smaller showings along the Hoidas and Nisikkatch Lakes (Fig. 5.1b). In the JAK Zone, which is the most thoroughly studied part of the deposit, the width of the mineralized veins reaches 11 m, and the mineralization is continuous to at least 300 m depth and open both down dip and along strike (Halpin, 2010).

The paragenetic relationships of the Hoidas Lake REE veins are discussed in more detail in Pandur et al. (2014) and Chapter 4, and are summarized in a schematic diagram (Fig. 5.2). In this paper, we focus on the zircon and titanite crystals of the diopside-allanite veins and the green apatite and monazite crystals of the apatite breccia veins, hence, in this section the petrography and chemical characteristics of these phases are detailed and complemented by some general statements regarding the mineralogy of the veins.

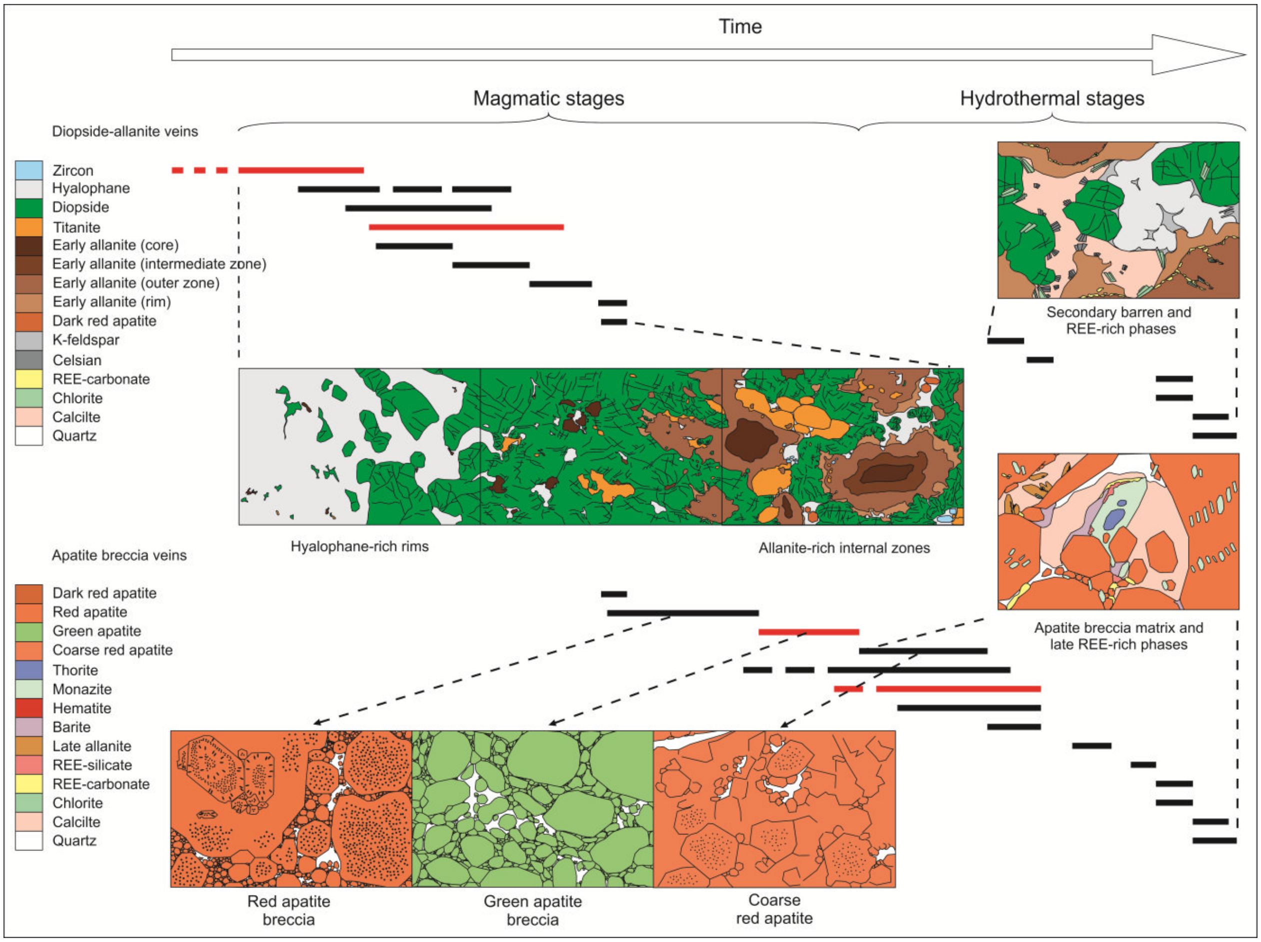

Figure 5.2 Schematic diagram summarizing the paragenetic relationships of the Hoidas Lake REE deposit: Paragenesis of the Hoidas Lake diopside-allanite veins divided into early hyalophane-rich margins, diopside-hyalophane-allanite-containing intervals and allanite-rich internal zones, the various apatite breccia vein phases (red apatite breccia, green apatite breccia and coarse red apatite phase), and their secondary phases. Magmatic and hydrothermal stages are distinguished among the vein-forming minerals.

The diopside-allanite veins are typically coarse grained (up to 30 cm), have sharp or diffuse contacts with the host rocks, and they are in some cases zoned from hyalophane-rich margins, through hyalophane-diopside-rich zones and diopside-allanite rich zones, to allanite-dominant cores (Fig. 5.2). In these veins, complexly zoned allanite-(Ce) crystals with TREO (total rare earth oxide) contents up to 24.9 wt.% are intergrown with diopside and hyalophane (Chapter 4). Zircon crystals in the diopside-allanite veins are euhedral or subhedral, strongly fractured and metamict (Fig. 5.3a, b), especially in their cores. Zircon also commonly occurs as inclusions within the outermost zones of the allanite crystals (Fig. 5.3a, c). The non-metamict areas of the zircon crystals are relatively homogeneous with some variations in ThO_2 (0.06 – 0.12 wt.%), HfO_2 (0.7 – 2.1 wt.%) and Y_2O_3 (0.07 – 0.2 wt.%) contents. The subhedral to euhedral, up to 1 cm titanite crystals in the diopside-allanite veins commonly occur adjacent to the outermost zones of allanite (Fig. 5.3a). Titanite occurs as inclusions within these allanite zones (Fig. 5.3c), and in some cases, titanite also contains inclusions of allanite, indicating synchronous growth. Rare zircon inclusions also occur in titanite (Fig. 5.3d). The TREO contents of titanite range from 1.8 wt.% to 6.0 wt.%, and Nd is the most dominant REE (Chapter 4). The titanite crystals are fairly homogeneous; however, irregular blotchy zonation can be observed in some grains (Fig. 5.3d), especially towards their margins, where depletion in REEs occurs, and slightly elevated contents of Ti and Ba are detected. The diopside-allanite veins also contain amphibole, biotite and minor amounts of apatite. The diopside-allanite veins are often strongly altered (hematite- and chlorite-alteration). This hydrothermal alteration is responsible for the irregular blotchy zonation in allanite and titanite, and resulted in precipitation of secondary REE-carbonates.

The apatite breccia veins commonly appear in irregularly shaped intervals within the diopside-allanite veins, and consist of sub-angular to rounded apatite grains <6 cm across (Fig. 5.3e). The apatite has up to 7.3 wt.% TREO, 0.1 to 1.6 wt.% SrO, <1.7 wt.% BaO, and <0.3 wt.% MnO (Chapter 4). Multiple brecciation phases were observed, and three dominant apatite generations occur in the veins: (1) red apatite breccia with 3 wt.% average TREO, dominated by Ce; (2) green apatite breccia with 5.5 wt.% average TREO, dominated by Ce; and (3) coarse red apatite with 1 wt.% average TREO, dominated by Nd (Fig. 5.2). The red apatite breccia and the coarse red apatite are strongly enriched in solid inclusions, whereas the green apatite breccia phase (Fig. 5.3e, f) is less enriched in inclusions. All apatite generations show irregular or mottled zonation in BSE images, which reflects differences in their REE content (Fig. 5.3g). These irregularly zoned regions in the apatite grains are often closely associated with a greater abundance of secondary hematite. The matrix of the apatite breccia contains fine-grained apatite, calcite, quartz, green amphibole, monazite, chlorite and sub-angular clasts of allanite, diopside and hyalophane.

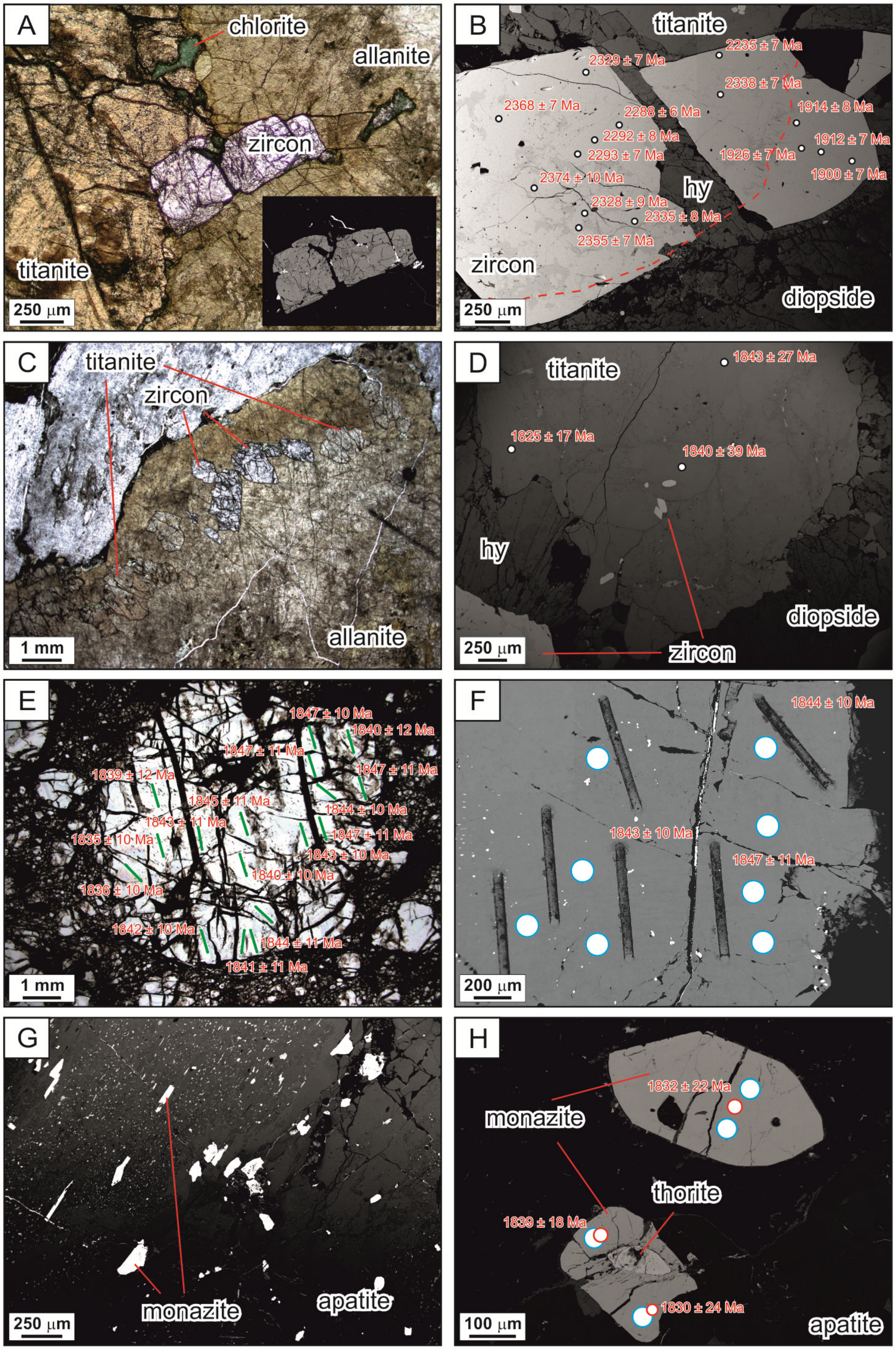
A
chlorite
allanite
zircon
titanite
250 µm
B
titanite
2235 ± 7 Ma
2329 ± 7 Ma
2338 ± 7 Ma
2368 ± 7 Ma
2288 ± 6 Ma
1914 ± 8 Ma
2292 ± 8 Ma
1912 ± 7 Ma
2293 ± 7 Ma
1926 ± 7 Ma
1900 ± 7 Ma
2374 ± 10 Ma
hy
2328 ± 9 Ma
2335 ± 8 Ma
2355 ± 7 Ma
zircon
diopside
250 µm
C
titanite
zircon
allanite
1 mm
D
titanite
1843 ± 27 Ma
1825 ± 17 Ma
1840 ± 39 Ma
hy
diopside
zircon
250 µm
E
1847 ± 10 Ma
1840 ± 12 Ma
1847 ± 11 Ma
1839 ± 12 Ma
1847 ± 11 Ma
1845 ± 11 Ma
1844 ± 10 Ma
1843 ± 11 Ma
1835 ± 10 Ma
1847 ± 11 Ma
1843 ± 10 Ma
1840 ± 10 Ma
1836 ± 10 Ma
1842 ± 10 Ma
1844 ± 11 Ma
1841 ± 11 Ma
1 mm
F
1844 ± 10 Ma
1843 ± 10 Ma
1847 ± 11 Ma
200 µm
G
monazite
apatite
250 µm
H
1832 ± 22 Ma
monazite
thorite
1839 ± 18 Ma
1830 ± 24 Ma
apatite
100 µm

Figure 5.3 (on previous page) Photomicrographs and back-scattered electron (BSE) images of zircon, titanite, green apatite and monazite crystals from the Hoidas Lake deposit. (a) Plane polarized light photomicrograph of euhedral zircon intergrown with titanite and allanite. The vugs in titanite and allanite are filled with chlorite. Inset shows BSE image of the same zircon crystals. (b) BSE image of fractured zircon, with a cross-cutting, hyalophane (hy) filled vein. The zircon is surrounded by titanite, diopside and hyalophane. Circles denote the locations of laser ablation spots for U-Pb zircon analyses that yielded concordant U-Pb dates, and the numbers are the $^{207}Pb/^{206}Pb$ dates for each spot. (c) Plane polarized light photomicrograph of allanite containing zircon and titanite inclusions along its rim. (d) BSE image of titanite containing zircon inclusions. The titanite is surrounded by diopside and hyalophane (hy). Circles denote the locations of laser ablation spots for U-Pb titanite analyses that yielded concordant U-Pb dates, and the numbers are the $^{207}Pb/^{206}Pb$ dates for each spot. (e) Plane polarized light photomicrograph of fractured green apatite. Green lines represent the locations of laser ablation raster lines for U-Pb apatite analyses, and the numbers are the uncorrected $^{207}Pb/^{206}Pb$ dates yielded. (f) BSE image of green apatite, with the U-Pb laser ablation raster line craters, and the numbers the uncorrected $^{207}Pb/^{206}Pb$ dates yielded. Blue circles denote the locations of laser ablation spots for Sm-Nd isotope analyses. (g) BSE image of red apatite with abundant monazite inclusions, and monazite along the apatite grain boundaries. (h) BSE image of monazite inclusions in red apatite. One of the monazite inclusions contains a thorite core. Red circles denote the locations of laser ablation spots for U-Pb monazite analyses that yielded concordant U-Pb dates, and the numbers are the $^{207}Pb/^{206}Pb$ dates for each spot. Blue circles denote the locations of laser ablation spots for Sm-Nd isotope analyses.

Monazite occurs as inclusions in all of the apatite breccia generations, in irregular disseminated masses or along secondary fractures in the apatite, as well as in the matrix of the apatite breccia (Fig. 5.3g, h). The monazite crystals are surrounded by REE-depleted irregular, mottled apatite zones. The monazite shows TREO values from 59.2 to 80.5 wt.%, and is Ce-dominant. The monazite contains minor amounts of Ca (<4 wt.% CaO), and Sr (<0.7 wt.% SrO), and has ThO_2 values up to 10.2 wt.% (Chapter 4). Higher concentrations of Ca, Sr and Th are observed in samples with lower TREO contents. Subtle concentric zoning is not uncommon in monazite, and the cores of the zoned monazite crystals are often slightly more enriched in Th and La and depleted in Ce, Nd, Pr, Sm and Eu, compared to their rims. The monazite grains occasionally contain inclusions of thorite in their cores (Fig. 5.3h). Hydrothermal alteration of the apatite breccia resulted in the formation of most of the monazite and hematite in the apatite breccia veins, as well as in the irregular, mottled zonation of the apatite clasts. Secondary REE-carbonates and REE-Sr-carbonates also occur in the matrix of the breccia.

The Hoidas Lake REE mineralization was influenced by both magmatic and hydrothermal processes during its evolution (Pandur et al., 2014; Chapter 4). The REE-enriched veins are interpreted to reflect a transition from (1) an early magmatic stage represented by the diopside-allanite veins and early apatite breccia veins; through (2) a REE-enriched hydrothermal stage represented by the apatite becoming Nd-dominant and the presence of secondary REE-bearing phases in the mineralized veins; to (3) a late REE-poor hydrothermal stage represented by the quartz-carbonate-rich veins that cross-cut the mineralization. Thus, the term ‘vein’ used in reference to the diopside-allanite rocks and apatite breccia, is not meant to reflect an exclusively hydrothermal origin.

The mineralized veins of the Hoidas Lake area were emplaced along northeast-trending structures, sub-parallel to the dominant S3 foliation and the Hoidas-Nisikkatch Fault (Fig. 5.1b). This indicates that the REE mineralization is related to shear zone development along the Black Bay Fault and its local subsidiary, the Hoidas-Nisikkatch Fault, and these structures provided the pathways for the mineralizing melts and fluids. The REE veins are unaffected by the D1 and D2 deformations, and they cross-cut the composite S1-S2 foliation, indicating that the mineralization is younger than peak metamorphism in the area. The mineralized veins were variably affected by the heterogeneously developed D3: in the JAK Zone the veins seem to be massive and undeformed, while at the Hoidas South showing the REE veins are folded, sheared, stretched and boudinaged with a strongly developed S3 fabric, which reflects the close proximity of the Hoidas-Nisikkatch Fault in this area (Normand et al., 2009; Halpin, 2010). Reactivation of the D3 structures is interpreted to be responsible for micro-faulting and brecciation of the mineralized veins, and grain size reduction of apatite in breccia veins (Harvey et al., 2002). The late lamprophyre dikes of the Hoidas Lake area postdate the earliest stages of REE mineralization, and they were emplaced along the same D3 structures (Normand et al., 2009).

5.4 Analytical techniques

5.4.1 Imaging of samples

The diopside-allanite veins and apatite breccia veins of the Hoidas Lake REE deposit were studied using laser ablation inductively coupled plasma mass spectrometry (LA-ICP-MS) for U-Pb, and laser ablation multi-collector inductively coupled plasma mass spectrometry (LA-MC-ICP-MS) for Lu-Hf and Sm-Nd analysis. Polished thin and thick sections (~30 μm and 200-250 μm in thickness, respectively) used for the U-Pb geochronology were prepared at the University of Saskatchewan, Department of Geological Sciences. The sections were then cut to 3-5 mm pieces and mounted on 1 inch diameter round-cut glass slides for the in situ Lu-Hf and Sm-Nd isotopic analyses. The sample selection included sections of the early diopside-allanite vein generation that contain zircon and titanite, and sections of the apatite breccia veins that contain green apatite and monazite. The complex chemical zonation of the grains studied necessitated the use of in situ techniques, and the regions to be analyzed were determined using back-scattered electron (BSE) imaging on a FEI QEMSCAN Quanta 650F field emission scanning electron microscope (SEM), equipped with two Bruker EDS detectors, at the Saskatchewan Research Council Advanced Microanalysis Centre, with the beam conditions set at 10 kV accelerating voltage, 3 μm spot size and 10-13 mm working distance. Cathodoluminescence (CL) images of zircon and apatite were acquired using a Deben CL detector attached to a JEOL 7100F field emission SEM at the Department of Earth Sciences at Memorial University of Newfoundland, to further investigate the zonation of these phases, and the beam conditions were set at 5 kV accelerating potential and 12 mm working distance. Zircon, titanite, apatite and monazite crystals from 9 samples were studied for the U-Pb geochronology and out of these, 2 were used for the Lu-Hf analyses of zircon, and 5 were used for Sm-Nd analysis of titanite, apatite and monazite.

5.4.2 Laser ablation ICP-MS U-Pb geochronology

In situ U-Pb geochronology of zircon, titanite, apatite and monazite was determined using a Resonetics M-50-LR 193 nm Excimer laser ablation system and Laurin Technic Pty. S-155 ablation cell coupled with an Agilent 7700x quadrupole ICP-MS at the University of New Brunswick, Department of Earth Sciences Laser Ablation ICP-MS Laboratory. Zircon crystals from 5 sections were analyzed using the ~1099 Ma FC1 zircon standard (Paces and Miller, 1993) as a primary external reference material and the ~1063 Ma 91500 zircon (Wiedenbeck et al., 1995) as a secondary standard. For zircon crystals the ablation lasted 40 seconds, with the laser conditions set at 36 μm spot size, 3 Hz repetition rate and 4 J/cm^2 laser fluence. Titanite crystals from 3 sections were analyzed using the ~520 Ma Khan Mine titanite as a primary standard using reference values from Heaman (2009) and the in-house ~28 Ma NM-1 titanite and the ~1015 Ma Otter Lake titanite (Kennedy et al., 2010) as secondary standards. For titanite the ablation lasted

40 seconds, with the laser conditions set at 48 μm spot size, 4 Hz repetition rate and 4 J/cm^2 laser fluence. Green apatite crystals from 2 sections were analyzed using the 91500 zircon as a primary external reference material and the in-house ~31 Ma Durango Apatite (McDowell et al., 2005) as a quality control standard. For apatite linear raster scans were programmed to run with a crater size of 48 μm and the ablation lasted 90 seconds. The laser conditions were set at 10 Hz repetition rate and 6 J/cm^2 laser fluence. Monazite crystals from 2 sections were analyzed using the ~500 Ma Geological Survey of Canada 8153 monazite standard (Williams et al., 2006) as a primary external reference material and the ~1766 Ma Thompson Mine monazite (Williams et al., 1996) as a secondary standard. For monazite the ablation lasted 30 seconds, with the laser conditions set at 14 μm spot size, 4 Hz repetition rate and 3 J/cm^2 laser fluence. The ablated material was transported out of the cell in carrier gas composed of 300 ml/min He, 930 ml/min Ar and 2 ml/min N_2. A total of 282 analyses were obtained, and offline data reduction was done using Iolite Trace Elements Data Reduction Scheme (Paton et al., 2011) and VizualAge for U-Pb geochronology (Petrus and Kamber, 2012). Common-Pb correction for the titanite data was implemented in VizualAge that minimizes inaccuracies associated with measuring low concentrations of ^{204}Pb and isobaric ^{204}Hg background interference (Kramers and Tolstikhin, 1997; Storey et al., 2006), using the correction routine described by Andersen (2002). During the analysis of the apatite grains, the possibility of issues with the interference of ^{204}Pb and ^{204}Hg and matrix-mismatch between the 91500 zircon we used for calibration and the unknown apatite can not be ruled out, and thus the accuracy of the ^{204}Pb correction of the strongly discordant apatite analyses is difficult to determine. Therefore, these data can only be considered preliminary at this point, and thus the weighted average of ^{207}Pb/^{206}Pb dates for the apatite analyses that did not require common Pb correction (n = 22) due to their unusually radiogenic nature was calculated and used in the interpretations. The results of U-Pb isotopic analyses are compiled in Tables 5.1-5.4 and Supplementary data Table C.1-C.3. Construction of concordia diagrams and calculation of concordia ages and intercept ages were done using Isoplot 4 (provided by Ken Ludwig, Berkeley Geochronological Center).

5.4.3 Laser ablation ICP-MS Lu-Hf isotope characteristics

In situ measurements of Lu and Hf isotopes were done using a GeoLas 193 nm laser ablation system connected to a Thermo Neptune multi-collector ICP-MS at the Memorial University of Newfoundland CREAIT Facility. The Lu-Hf isotope systematics of zircon crystals from 2 samples were analyzed using 59 µm spot size at a repetition rate of 10 Hz and a fluence of 5 J/cm^2, and the ablation lasted 60 seconds. The gas background was measured for 30 seconds at the beginning of each run. Throughout the zircon analyses, replicate analyses of b142 zircon (n = 5; Fisher et al., 2011a), R-33 zircon (n = 5; Vervoort, 2010) and Temora zircon (n = 5; Woodhead and Hergt, 2005) were used to correct for Hf and Yb mass bias and the ^{176}Yb and ^{176}Lu interference on ^{176}Hf (Fisher et al., 2011a). A total of 22 Lu-Hf analyses were obtained, and the data were processed offline using LAMTool-Hf (provided by Jan Kosler, University of Bergen). The results of Lu-Hf isotopic analyses for zircon are compiled in Table 5.5. The initial ^{176}Hf/^{177}Hf ratios were calculated using the present day ^{176}Hf/^{177}Hf and ^{176}Lu/^{177}Hf ratios, the λ^{176}Lu value of 1.865×10^{-11} year^{-1} from Scherer et al. (2001) and the previously obtained ^{207}Pb/^{206}Pb dates for each spot. Initial εHf (εHf(t)) values were calculated using ^{176}Hf/^{177}Hf(CHUR) = 0.282772 and ^{176}Lu/^{177}Hf(CHUR) = 0.0332 from Blichert-Toft and Albarède (1997).

5.4.4 Laser ablation ICP-MS Sm-Nd isotope characteristics

In situ measurements of Sm and Nd isotopes were done using a GeoLas 193 nm laser ablation system connected to a Thermo Neptune multi-collector ICP-MS at the Memorial University of Newfoundland CREAIT Facility. The Sm-Nd isotope systematics of titanite from one sample were analyzed using 89 µm spot size at a repetition rate of 6 Hz and a fluence of 5 J/cm^2 with ~65 second ablation time. For the in situ apatite analyses a 79 µm spot size was used at a repetition rate of 6 Hz and a fluence of 5 J/cm^2, and the ablation lasted ~65 seconds. For 2 samples of monazite 30 µm spot size was used at a repetition rate of 6 Hz and a fluence of 5 J/cm^2, and the ablation lasted ~65 seconds. The gas background was measured for 30 seconds at the beginning of each run. Replicate analyses of synthetic LREE-glass (n = 11) and the ~ 28 Ma Fish Canyon Tuff titanite (n = 10; Schmitz and Bowring, 2001) were used throughout the titanite measurements, replicate analyses of LREE glass (n = 15) and Durango apatite (n = 12) were used throughout the apatite measurements, and replicate analyses of LREE glass (n = 22) and the ~270 Ma Trebilcock monazite (n = 20; Tomascak et al., 1998) were used throughout the monazite analyses, to verify that the measured ^{143}Nd/^{144}Nd, and ^{145}Nd/^{144}Nd values for the standards were within error of the true values (Fisher et al., 2011b). The mass bias correction of ^{147}Sm/^{144}Nd was performed by external bracketing to replicate analyses of LREE glass with ^{147}Sm/^{144}Nd = 0.2451, with estimated error of 1% (2SE) for the corrected ^{147}Sm/^{144}Nd ratios. A total of 89 Sm-Nd analyses were obtained, and the data were processed offline using MCTool-Nd, an in-house data reduction macro modified from LAMTool-Hf. Corrections for instrumental mass bias followed the methodology outlined in Fisher et al. (2011b). The Sm-Nd isotopic systematics of the Durango apatite, the Trebilcock monazite, and the synthetic LREE glass doped with the internationally distributed JNdi-1 standard can be found in Fisher et al. (2011b). The results of Sm-Nd isotopic analyses for titanite, apatite and monazite are compiled in Tables 5.6, 5.7 and 5.8, respectively. The initial ^{143}Nd/^{144}Nd values were calculated on the basis of the previously obtained ^{207}Pb/^{206}Pb dates for titanite and monazite, and the weighted average of ^{207}Pb/^{206}Pb dates for apatite analyses that did not require common Pb correction, using the present day ^{143}Nd/^{144}Nd and ^{147}Sm/^{144} Nd ratios, the λ^{147}Sm decay constant of 6.54x10^{-12} year^{-1} from Lugmair and Marti (1978). Initial εNd (εNd(t)) values were calculated using ^{143}Nd/^{144}Nd(CHUR) = 0.512638 from Hamilton et al. (1983) and ^{147}Sm/^{144}Nd(CHUR) = 0.1967 from Jacobsen and Wasserburg (1980). Construction of Sm-Nd isochron diagram and calculation of Sm-Nd isochron age were done using Isoplot 4 (provided by Ken Ludwig, Berkeley Geochronological Center).

5.5 Analytical results

5.5.1 U-Pb geochronology

5.5.1.1 Zircon

The analyzed zircon crystals from the Hoidas Lake diopside-allanite veins are strongly fractured and commonly metamict. The zircon grains do not appear to have distinct compositional domains based on BSE images (Fig. 5.3b); however, CL imaging reveals some complexly zoned crystal cores (Fig. 5.4) that are not apparent in BSE. A total of 127 U-Pb spot analyses were done on 17 zircon grains. The zircon grains display a wide spectrum of ^{207}Pb/^{206}Pb dates from ~1878 to ~2431 Ma (Table 5.1; Table C.1), and there is a significant amount of discordant data from variable sectors of the zircon crystals (Fig. 5.5a). There are 43 zircon analyses that plot on concordia (less than 5% discordant date spots), with ^{207}Pb/^{206}Pb dates ranging from ~1890 to ~2374 Ma. Among these, two populations of dates with overlapping error ellipses were distinguished at ~2350 Ma (n = 23) and ~1900 Ma (n = 6), and there are a number of individual concordant dates in between the two populations (Fig. 5.5a). A discordia line laid between the two date populations yields an upper intercept age of 2348 ± 19 Ma and lower intercept age of 1906 ± 34 Ma (Fig. 5.5a). The measured variations among the ^{207}Pb/^{206}Pb dates do not correlate with the observed irregular zoning of the zircon crystals, except for two cases where the rims show consistently younger dates (Fig. 5.3b, 5.4).

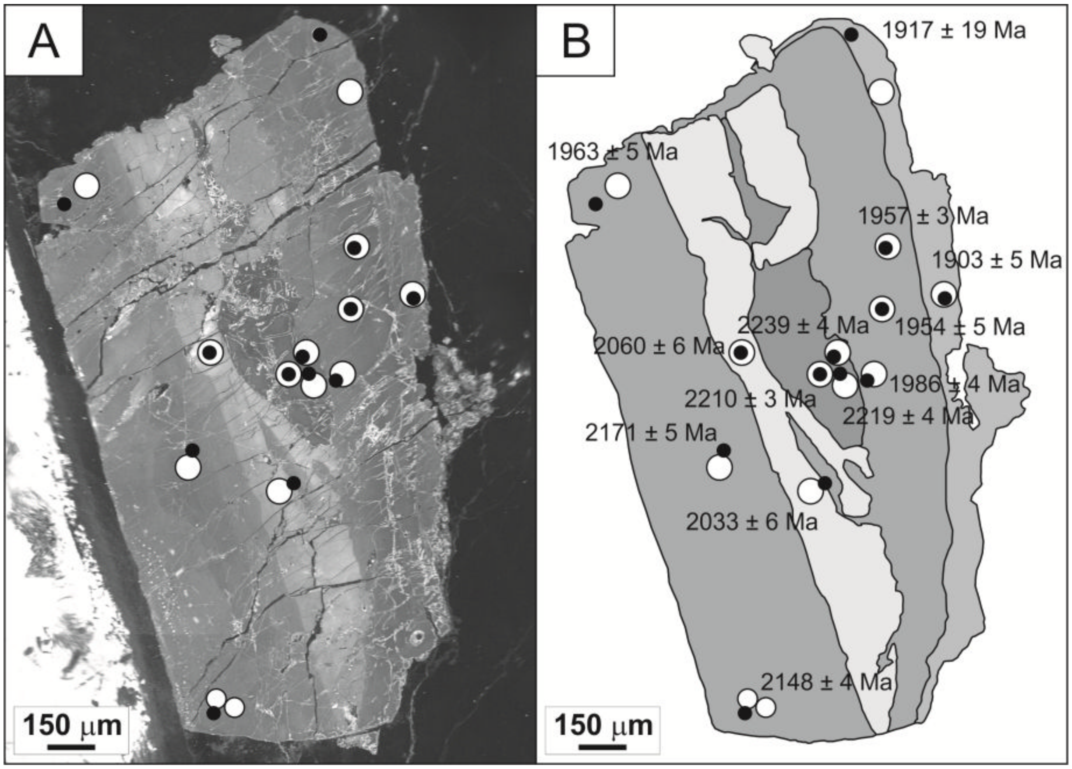

Figure 5.4 Complex zonation in zircon of the Hoidas Lake diopside-allanite veins. (a) Cathodoluminescence image of complexly zoned zircon with black dots denoting the locations of laser ablation spots for U-Pb zircon analyses and white circles denoting the locations of laser ablation spots for Hf isotope analyses. (b) Outline of the observable zones of the zircon crystal of A, with ^{207}Pb/^{206}Pb dates and 2σ error for each analyzed spot. Note the broken rim at the edge of the zircon that displays younger dates.

Table 5.1 Concordant U-Pb isotopic data for zircon from the Hoidas Lake REE deposit.

Sample	^{207}Pb/^{235}U	2σ	^{206}Pb/^{238}U	2σ	error correlation	^{207}Pb/^{206}Pb	2σ	^{207}Pb/^{235}U age (Ma)	2σ	^{206}Pb/^{238}U age (Ma)	2σ	^{207}Pb/^{206}Pb age (Ma)	2σ
881339-2	9.400	0.170	0.4453	0.0064	0.4163	0.1522	0.0012	2377	17	2374	29	2374	10
881339-4	9.191	0.130	0.4420	0.0046	0.4934	0.1510	0.0011	2357	13	2360	21	2355	7
881339-5	8.890	0.130	0.4345	0.0048	0.7827	0.1486	0.0012	2326	13	2326	22	2328	9
881339-6	9.040	0.130	0.4371	0.0048	0.5610	0.1492	0.0011	2342	13	2338	21	2335	8
881339-8	8.548	0.120	0.4264	0.0046	0.6221	0.1451	0.0010	2291	13	2290	21	2293	7
881339-9	8.610	0.110	0.4279	0.0044	0.5559	0.1455	0.0010	2297	12	2296	20	2292	8
881339-10	8.567	0.120	0.4265	0.0046	0.6786	0.1451	0.0010	2293	13	2290	21	2288	6
881339-12	8.952	0.120	0.4369	0.0044	0.4871	0.1484	0.0010	2333	12	2337	20	2329	7
881339-15	9.299	0.120	0.4432	0.0046	0.5492	0.1519	0.0010	2368	12	2365	21	2368	7
881339-23	5.694	0.076	0.3496	0.0037	0.5417	0.1180	0.0008	1930	11	1932	17	1926	7
881339-25	5.503	0.078	0.3429	0.0038	0.5788	0.1170	0.0008	1901	12	1902	18	1912	7
881339-27	5.433	0.078	0.3410	0.0037	0.7528	0.1161	0.0008	1890	12	1892	18	1900	7
881339-32	8.892	0.120	0.4355	0.0046	0.6793	0.1494	0.0010	2327	12	2330	21	2338	7
881339-34	7.966	0.120	0.4131	0.0048	0.8104	0.1408	0.0010	2227	13	2229	22	2235	7
881179-16	7.165	0.140	0.3912	0.0046	0.7311	0.1326	0.0018	2132	14	2128	21	2125	16
881179-19	8.961	0.120	0.4361	0.0049	0.6715	0.1480	0.0010	2335	13	2333	22	2323	7
881179-21	6.114	0.090	0.3620	0.0041	0.7579	0.1217	0.0009	1993	13	1991	19	1980	10
881179-28	8.606	0.130	0.4279	0.0047	0.6206	0.1451	0.0012	2297	12	2296	21	2289	8
881179-34	9.352	0.130	0.4442	0.0048	0.6078	0.1516	0.0010	2373	13	2370	22	2364	7
881179-39	8.700	0.130	0.4299	0.0058	0.8769	0.1461	0.0011	2305	14	2304	26	2302	9
881179-41	5.551	0.079	0.3443	0.0039	0.6310	0.1167	0.0009	1908	12	1907	19	1906	9
881179-43	8.591	0.130	0.4278	0.0055	0.8827	0.1454	0.0010	2295	14	2295	25	2289	7
881179-44	7.781	0.120	0.4085	0.0050	0.7927	0.1381	0.0009	2206	14	2208	23	2203	7
881179-T-1	7.290	0.140	0.3957	0.0057	0.5302	0.1341	0.0005	2147	18	2149	27	2148	4
881179-T-2	5.429	0.110	0.3401	0.0049	0.6971	0.1156	0.0005	1890	17	1887	24	1890	4
881179-T-3	6.388	0.140	0.3702	0.0061	0.8788	0.1254	0.0007	2028	20	2029	28	2033	6
881179-T-9	5.512	0.110	0.3431	0.0051	0.6723	0.1165	0.0005	1902	17	1901	24	1903	5
881179-T-11	6.570	0.130	0.3762	0.0056	0.6477	0.1270	0.0007	2057	18	2058	26	2060	6
881187-1	9.280	0.190	0.4430	0.0067	0.6561	0.1505	0.0006	2366	19	2365	30	2349	4
881187-2	9.258	0.190	0.4420	0.0068	0.8355	0.1508	0.0006	2364	19	2359	31	2357	3
881187-3	9.207	0.190	0.4417	0.0071	0.8515	0.1508	0.0006	2359	19	2358	31	2356	3
881187-4	9.204	0.180	0.4418	0.0065	0.7301	0.1500	0.0005	2358	18	2358	29	2345	3
881187-5	8.607	0.170	0.4281	0.0065	0.7953	0.1454	0.0005	2297	18	2297	29	2290	4
881187-6	8.972	0.180	0.4364	0.0067	0.8435	0.1485	0.0006	2334	19	2334	30	2332	4
881187-7	9.082	0.180	0.4387	0.0066	0.7919	0.1495	0.0006	2346	18	2345	30	2341	5
881187-8	8.985	0.180	0.4364	0.0065	0.7341	0.1487	0.0006	2336	18	2336	29	2331	4
881187-9	8.751	0.180	0.4311	0.0065	0.8376	0.1469	0.0005	2312	19	2310	29	2310	4
881187-12	8.883	0.180	0.4350	0.0067	0.6218	0.1491	0.0005	2326	18	2328	30	2336	4
881187-15	8.419	0.160	0.4251	0.0061	0.3559	0.1436	0.0007	2277	18	2284	28	2274	5
881187-30	9.077	0.190	0.4392	0.0067	0.7224	0.1498	0.0007	2345	19	2348	30	2346	5
881178-5	9.185	0.180	0.4420	0.0064	0.6869	0.1514	0.0006	2357	18	2359	29	2359	4
881178-6	9.134	0.190	0.4397	0.0071	0.8866	0.1500	0.0006	2351	20	2348	32	2345	4
881178-8	9.127	0.210	0.4414	0.0071	0.4842	0.1495	0.0011	2350	20	2357	31	2342	9

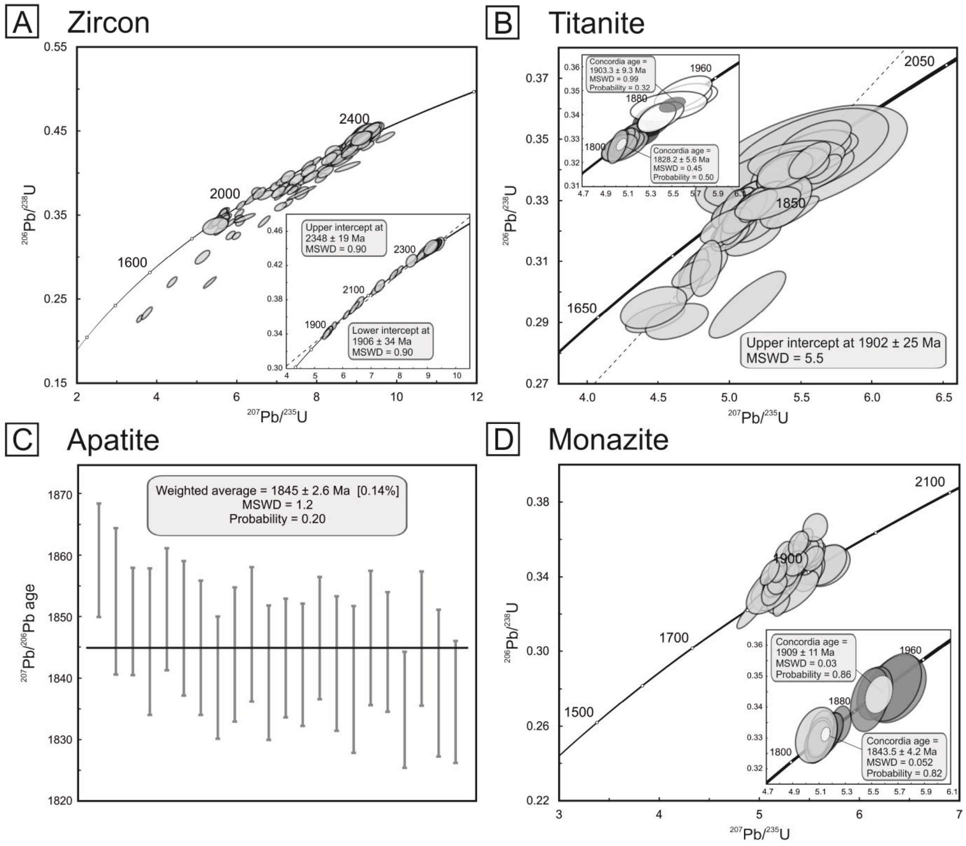

Figure 5.5 Conventional concordia diagrams and ^{207}Pb/^{206}Pb diagram showing the results of in situ U-Pb geochronology. (a) Zircon U-Pb data, where inset shows only the concordant analyses. Upper and lower intercept ages of a discordant line which connects two groups of dates with overlapping error ellipses are provided. (b) Titanite U-Pb data, where inset shows only the concordant analyses. Different shades of error ellipses in inset denote data from three distinct samples. For the oldest and youngest group a concordia age is provided and the group ellipses are framed by dashed lines. (c) Weighted average of ^{207}Pb/^{206}Pb dates that do not require common Pb correction. (d) Monazite U-Pb data, where inset shows only the concordant analyses. Different shades of error ellipses in inset denote data from two distinct samples. For the two groups of dates a concordia age is provided and the white group ellipses are framed by dashed lines. Error ellipses are 2σ confidence level.

5.5.1.2 Titanite

The Hoidas Lake titanite crystals are commonly closely associated with allanite, the main REE carrier phase in the diopside-allanite veins. The titanite is fractured and shows irregular zonation in BSE images (Fig. 5.3d), which commonly reflects REE-depleted zones adjacent to the fractures. Fifty U-Pb spot analyses were done, and out of these 16 are concordant (Fig. 5.5b;

Table 5.2; Table C.2). The titanite grains display a range of ^{204}Pb corrected ^{207}Pb/^{206}Pb dates from ~1785 to ~1988 Ma, and the concordant (less than 5% discordant) dates range from ~1825 to ~1931 Ma. The ^{204}Pb corrected concordant data for the three studied samples display three distinct populations on the ^{206}Pb/^{238}U vs. ^{207}Pb/^{235}U plot (Fig. 5.5b): (1) the data for titanite enclosed in the outer zone of allanite (together with zircon grains) cluster around 1900 Ma (n = 6) and yield a concordia age of 1903 ± 9 Ma; (2) larger titanite grains from an allanite-rich diopside-allanite vein cluster around 1860 Ma (n = 2); and (3) the data for titanite from a diopside-rich vein (adjacent to zircon and hyalophane and containing euhedral fine zircon inclusions) cluster around 1830 Ma (n = 8) and yield a concordia age of 1828 ± 6 Ma.

Table 5.2 Concordant U-Pb isotopic data for titanite from the Hoidas Lake REE deposit.

Sample	^{207}Pb/^{235}U	2σ	^{206}Pb/^{238}U	2σ	error correlation	^{207}Pb/^{206}Pb	2σ	^{207}Pb/^{235}U age (Ma)	2σ	^{206}Pb/^{238}U age (Ma)	2σ	^{207}Pb/^{206}Pb age (Ma)	2σ
881179-T-3	5.216	0.140	0.3318	0.0042	0.2952	0.1126	0.0023	1855	21	1847	21	1833	40
881179-T-7	5.324	0.140	0.3374	0.0054	0.3502	0.1152	0.0015	1873	24	1874	26	1880	23
881339-10	5.085	0.170	0.3267	0.0052	0.5727	0.1132	0.0016	1834	29	1823	25	1851	26
881339-12	5.125	0.130	0.3294	0.0059	0.6211	0.1137	0.0011	1840	22	1835	29	1857	18
881339-13	5.018	0.073	0.3266	0.0057	0.5480	0.1115	0.0010	1822	12	1822	28	1825	17
881339-14	5.084	0.140	0.3277	0.0044	0.4930	0.1126	0.0024	1832	24	1827	22	1840	39
881339-16	5.080	0.110	0.3284	0.0048	0.4964	0.1128	0.0017	1832	19	1831	23	1843	27
881339-17	5.051	0.054	0.3278	0.0049	0.5503	0.1122	0.0009	1827	9	1828	24	1833	14
881339-19	5.035	0.130	0.3262	0.0046	0.4601	0.1128	0.0018	1824	22	1820	22	1846	28
881339-21	5.080	0.077	0.3290	0.0045	0.6639	0.1124	0.0011	1832	13	1833	22	1838	17
881187-1	5.475	0.280	0.3434	0.0051	0.3677	0.1165	0.0027	1895	41	1903	24	1900	41
881187-6	5.604	0.210	0.3490	0.0059	0.5739	0.1170	0.0022	1916	37	1929	28	1910	32
881187-7	5.628	0.230	0.3472	0.0047	0.4089	0.1184	0.0029	1919	36	1921	23	1929	45
881187-9	5.615	0.200	0.3470	0.0050	0.4353	0.1182	0.0026	1917	31	1920	24	1931	39
881187-10	5.368	0.140	0.3387	0.0051	0.4728	0.1154	0.0019	1880	23	1880	24	1884	30
881187-13	5.401	0.170	0.3392	0.0050	0.5614	0.1159	0.0020	1884	27	1883	24	1892	30

5.5.1.3 Apatite

Among the various apatite phases, only the green apatite was free of solid inclusions to allow LA-ICP-MS U-Pb analyses. These apatite grains are homogeneous in BSE and CL images, but are strongly fractured. A total of 40 U-Pb raster analyses were carried out, and out of these 22 analyses did not require common Pb correction (Table 5.3), and thus were used for interpretation, although, due to the previously mentioned analytical issues, these are considered as preliminary. The ^{207}Pb/^{206}Pb dates of apatite from two different samples range from ~1835 to ~1859 Ma and all of the dates are discordant. The weighted average of these ^{207}Pb/^{206}Pb dates (1845 ± 3 Ma) was calculated using Isoplot 4.

Table 5.3 U-Pb isotopic data for apatite from the Hoidas Lake REE deposit.

Sample	^{207}Pb/^{235}U	2σ	^{206}Pb/^{238}U	2σ	error correlation	^{207}Pb/^{206}Pb	2σ	^{207}Pb/^{206}Pb age (Ma)	2σ
516665B-8	4.363	0.080	0.2867	0.0053	0.6005	0.1134	0.0011	1853	12
516665B-10	4.328	0.080	0.2852	0.0053	0.6789	0.1130	0.0011	1848	11
516665B-13	4.219	0.078	0.2840	0.0052	0.4889	0.1131	0.0012	1849	9
516665B-14	4.384	0.080	0.2871	0.0053	0.5896	0.1137	0.0011	1859	9
516665B-17	4.132	0.075	0.2828	0.0052	0.2128	0.1131	0.0012	1846	12
516665B-20	4.500	0.081	0.2892	0.0053	0.4689	0.1132	0.0012	1851	10
881011A-1	4.502	0.081	0.2906	0.0054	0.3000	0.1130	0.0012	1847	11
881011A-2	4.297	0.081	0.2868	0.0053	0.5963	0.1125	0.0012	1840	12
881011A-3	4.509	0.081	0.2907	0.0054	0.3169	0.1129	0.0012	1847	11
881011A-4	4.354	0.081	0.2871	0.0054	0.5837	0.1130	0.0012	1847	10
881011A-5	4.367	0.081	0.2870	0.0054	0.5926	0.1128	0.0012	1847	11
881011A-6	4.356	0.081	0.2868	0.0054	0.6286	0.1128	0.0012	1844	10
881011A-7	4.322	0.080	0.2839	0.0053	0.6675	0.1126	0.0011	1843	10
881011A-12	4.294	0.078	0.2809	0.0051	0.5109	0.1128	0.0011	1845	11
881011A-13	4.276	0.078	0.2815	0.0051	0.6343	0.1125	0.0012	1840	10
881011A-14	4.288	0.078	0.2814	0.0051	0.6566	0.1129	0.0012	1844	11
881011A-15	4.336	0.079	0.2844	0.0052	0.4466	0.1125	0.0012	1841	11
881011A-16	4.330	0.079	0.2840	0.0051	0.6465	0.1125	0.0011	1842	10
881011A-17	4.354	0.079	0.2847	0.0051	0.4936	0.1126	0.0011	1843	11
881011A-18	4.339	0.079	0.2845	0.0052	0.6771	0.1122	0.0011	1835	10
881011A-19	4.337	0.079	0.2838	0.0051	0.5844	0.1124	0.0011	1839	12
881011A-20	4.375	0.080	0.2857	0.0052	0.6125	0.1124	0.0011	1836	10

5.5.1.4 Monazite

The textural features of monazite in the apatite breccia veins indicate that it formed through alteration of the host apatite crystals that interacted with hydrothermal fluids. Monazite occurs in all apatite breccia phases, and there are likely multiple generations of monazite crystallization in the deposit, as the different parts of the vein system interacted with hydrothermal fluids at different times. A total of 65 U-Pb spot analyses were done on monazite crystals from two red apatite breccia samples (Table 5.4; Table C.3). These show a wide range of ^{207}Pb/^{206}Pb dates from ~1766 to ~1913 Ma. Out of these analyses, 15 fall on the concordia curve (less than 5% discordant), and these give a range of ^{207}Pb/^{206}Pb dates from ~1787 to ~1906 Ma. The concordant monazite data show two populations with overlapping error ellipses on the ^{206}Pb/^{238}U vs.

$^{207}Pb/^{235}U$ plot, distinguished using the 'Unmix ages' feature of Isoplot 4 and by the confinement of the two populations to the two samples (Fig. 5.5d). The two populations yielded concordia ages of 1844 ± 4 Ma (n = 11) and 1909 ± 11 Ma (n = 4) (Fig. 5.5d).

Table 5.4 Concordant U-Pb isotopic data for monazite from the Hoidas Lake REE deposit.

Sample	$^{207}Pb/^{235}U$	2σ	$^{206}Pb/^{238}U$	2σ	error correlation	$^{207}Pb/^{206}Pb$	2σ	$^{207}Pb/^{235}U$ age (Ma)	2σ	$^{206}Pb/^{238}U$ age (Ma)	2σ	$^{207}Pb/^{206}Pb$ age (Ma)	2σ
881253-2	5.143	0.066	0.3303	0.0049	0.2567	0.1120	0.0023	1842	11	1841	23	1832	22
881253-6	5.152	0.067	0.3307	0.0049	0.4487	0.1123	0.0023	1846	11	1842	24	1839	18
881253-7	5.074	0.069	0.3278	0.0049	0.2156	0.1124	0.0023	1831	11	1827	24	1830	24
881253-14	5.137	0.080	0.3299	0.0052	0.4329	0.1113	0.0025	1843	13	1837	26	1828	24
881253-21	5.184	0.072	0.3318	0.0053	0.4065	0.1113	0.0023	1849	12	1847	26	1830	21
881253-25	5.524	0.110	0.3445	0.0070	0.2980	0.1145	0.0024	1903	23	1908	35	1878	22
881253-35	5.261	0.067	0.3345	0.0048	0.2732	0.1119	0.0023	1863	11	1860	23	1834	22
881253-36	5.181	0.084	0.3319	0.0051	0.4639	0.1109	0.0024	1850	13	1847	24	1815	23
881253-40	5.486	0.120	0.3424	0.0084	0.3116	0.1140	0.0029	1898	24	1898	42	1852	38
881253-41	5.680	0.190	0.3459	0.0089	0.3206	0.1149	0.0044	1928	30	1913	43	1885	43
881253-42	5.670	0.170	0.3464	0.0089	0.4008	0.1175	0.0040	1925	26	1915	42	1906	37
881350B-7	5.099	0.071	0.3297	0.0049	0.3463	0.1098	0.0023	1839	12	1837	24	1803	19
881350B-9	5.109	0.077	0.3305	0.0050	0.2340	0.1106	0.0024	1837	13	1840	24	1805	22
881350B-10	5.081	0.130	0.3309	0.0074	0.2667	0.1100	0.0025	1832	19	1843	35	1800	21
881350B-14	5.122	0.076	0.3328	0.0050	0.2479	0.1094	0.0024	1838	13	1851	24	1787	26

5.5.2 Zircon Hf isotopic systematics

Lu-Hf spot analyses of 22 zircon domains were carried out (Table 5.5), with Lu-Hf laser spots positioned over or immediately adjacent to the U-Pb ablation pits, and yielded a range of measured $^{176}Hf/^{177}Hf$ ratios from 0.281165 to 0.282545. Out of these, 20 analyses range from 0.281165 to 0.281329 with $^{207}Pb/^{206}Pb$ dates ranging from ~1954 to ~2361 Ma, and only two analyses from the rim of a large zircon crystal showed higher $^{176}Hf/^{177}Hf$ values (0.282327 and 0.282545) and also younger $^{207}Pb/^{206}Pb$ dates of 1917.1 ± 19 and 1903 ± 5 Ma, respectively (Fig. 5.4). The initial $^{176}Hf/^{177}Hf$ ratios of the 20 older zircon domains, calculated based on the previously obtained $^{207}Pb/^{206}Pb$ dates for each spot, range from 0.281154 to 0.281324, and the εHf(t) values range from -9.5 to -1.4. The zircon rim spots have initial $^{176}Hf/^{177}Hf$ values of 0.282322 and 0.282537, and εHf(t) of 26.9 and 34.3, respectively.

Table 5.5 Lu-Hf isotopic data for zircon from the Hoidas Lake REE deposit.

Sample	^{207}Pb/^{206}Pb age (Ma)	2σ	^{176}Lu/^{177}Hf	2SE	^{176}Hf/^{177}Hf	2SE	initial ^{176}Hf/^{177}Hf	ε_{Hf}(t)
881179-T-b06	2148	4	0.000218	0.000019	0.281312	0.000044	0.281303	-4.0
881179-T-b07	2148	4	0.000218	0.000012	0.281259	0.000039	0.281250	-5.9
881179-T-b14	1963	5	0.000144	0.000001	0.281321	0.000018	0.281316	-7.8
881179-T-b15	2171	5	0.000099	0.000002	0.281306	0.000017	0.281302	-3.5
881179-T-b18	2060	6	0.000099	0.000003	0.281247	0.000027	0.281243	-8.1
881179-T-b19	2033	6	0.000082	0.000001	0.281225	0.000024	0.281222	-9.5
881179-T-b22	2210	3	0.000264	0.000003	0.281171	0.000028	0.281159	-7.7
881179-T-b23	2219	4	0.000271	0.000004	0.281165	0.000025	0.281154	-7.7
881179-T-b24	2239	4	0.000289	0.000007	0.281183	0.000031	0.281171	-6.6
881179-T-b28	1957	3	0.000167	0.000000	0.281317	0.000024	0.281311	-8.0
881179-T-b30	1954	5	0.000142	0.000000	0.281323	0.000020	0.281318	-7.9
881179-T-b31	1986	4	0.000152	0.000004	0.281329	0.000026	0.281324	-6.9
881179-T-b34	1903	5	0.000219	0.000013	0.282545	0.000028	0.282537	34.3
881179-T-b35	1917	19	0.000163	0.000003	0.282327	0.000024	0.282322	26.9
881178-c05	2359	4	0.000126	0.000001	0.281178	0.000027	0.281173	-3.8
881178-c06	2351	9	0.000133	0.000001	0.281250	0.000029	0.281244	-1.4
881178-c07	2361	12	0.000119	0.000003	0.281214	0.000024	0.281209	-2.4
881178-c09	2287	4	0.000143	0.000002	0.281189	0.000025	0.281183	-5.1
881178-c10	2334	5	0.000188	0.000002	0.281262	0.000021	0.281253	-1.5
881178-c13	2348	3	0.000109	0.000003	0.281213	0.000026	0.281208	-2.8
881178-c14	2345	4	0.000099	0.000003	0.281213	0.000029	0.281209	-2.8
881178-c15	2342	9	0.000295	0.000048	0.281232	0.000026	0.281219	-2.5

5.5.3 Sm-Nd isotopic systematics of titanite, monazite and apatite

A total of 13 Sm-Nd titanite spot analyses, adjacent to former U-Pb laser spots, yielded a range of measured ^{143}Nd/^{144}Nd ratios from 0.511135 to 0.511288 (Table 5.6). The initial ^{143}Nd/^{144}Nd ratios, calculated based on the previously obtained ^{207}Pb/^{206}Pb dates for each spot, range from 0.509472 to 0.509674, and εNd(t) values range from -13.4 to -11.6.

In green apatite 41 Sm-Nd spots were positioned adjacent to the U-Pb laser raster lines, and the measured ^{143}Nd/^{144}Nd ratios range from 0.510605 to 0.510846 (Table 5.7). The initial ^{143}Nd/^{144}Nd ratios range from 0.50963 to 0.50971, and the εNd(t) values range from -12.2 to -10.6.

A total of 35 Sm-Nd spots were analyzed in monazite, some adjacent to and some overlying the U-Pb laser spots, and the measured ^{143}Nd/^{144}Nd ratios range from 0.509979 to

0.510271 (Table 5.8). The initial ^{143}Nd/^{144}Nd ratios range from 0.509501 to 0.509659, and εNd(t) values range from -15.3 to -11.6.

Table 5.6 Sm-Nd isotopic data for titanite from the Hoidas Lake REE deposit.

Sample	^{207}Pb/^{206}Pb age (Ma)	2σ	^{147}Sm/^{144}Nd	^{143}Nd/^{144}Nd	2SE	initial ^{143}Nd/^{144}Nd	ε_{Nd}(t)
881179-T-a05	1889	47	0.1293	0.511201	0.000034	0.509594	-11.7
881179-T-a08	1822	32	0.1279	0.511192	0.000034	0.509659	-12.2
881179-T-a11	1824	35	0.1255	0.511143	0.000028	0.509637	-12.6
881179-T-a15	1833	40	0.1280	0.511187	0.000030	0.509643	-12.2
881179-T-a18	1863	36	0.1298	0.511153	0.000027	0.509561	-13.0
881179-T-a22	1949	27	0.1301	0.511155	0.000025	0.509486	-12.3
881179-T-a25	1880	23	0.1346	0.511204	0.000020	0.509539	-13.0
881179-T-a27	1869	29	0.1423	0.511288	0.000059	0.509537	-13.4
881179-T-a28	1895	30	0.1336	0.511182	0.000069	0.509516	-13.1
881179-T-a32	1857	46	0.1327	0.511219	0.000038	0.509598	-12.5
881179-T-a33	1791	55	0.1278	0.511179	0.000024	0.509674	-12.7
881179-T-a39	1988	42	0.1271	0.511135	0.000033	0.509472	-11.6
881179-T-a40	1909	29	0.1278	0.511152	0.000029	0.509547	-12.2

Table 5.7 Sm-Nd isotopic data for apatite from the Hoidas Lake REE deposit.

Sample	^{207}Pb/^{206}Pb age (Ma)	^{147}Sm/^{144}Nd	^{143}Nd/^{144}Nd	2SE	initial ^{143}Nd/^{144}Nd	ε_{Nd}(t)
516665B-b06	1845	0.0794	0.510652	0.000049	0.509688	-11.0
516665B-b07	1845	0.0803	0.510631	0.000053	0.509656	-11.6
516665B-b10	1845	0.0830	0.510659	0.000040	0.509651	-11.7
516665B-b13	1845	0.0824	0.510634	0.000015	0.509634	-12.1
516665B-b14	1845	0.0821	0.510639	0.000024	0.509643	-11.9
516665B-b17	1845	0.0809	0.510643	0.000053	0.509662	-11.5
516665B-b20	1845	0.0821	0.510654	0.000017	0.509658	-11.6
516665B-b22	1845	0.0812	0.510638	0.000055	0.509653	-11.7
516665B-b23	1845	0.0807	0.510633	0.000047	0.509654	-11.7
516665B-b27	1845	0.0806	0.510660	0.000042	0.509682	-11.1
516665B-b28	1845	0.0808	0.510650	0.000037	0.509669	-11.4
516665B-b29	1845	0.0812	0.510668	0.000040	0.509682	-11.1
516665B-b30	1845	0.0812	0.510639	0.000049	0.509654	-11.7
516665B-b31	1845	0.0812	0.510655	0.000043	0.509669	-11.4
516665B-a04	1845	0.0830	0.510646	0.000018	0.509639	-12.0
516665B-a05	1845	0.0821	0.510645	0.000014	0.509648	-11.8
516665B-a08	1845	0.0812	0.510643	0.000020	0.509658	-11.6
516665B-a11	1845	0.0803	0.510605	0.000045	0.509630	-12.2
516665B-a12	1845	0.0805	0.510645	0.000025	0.509668	-11.4
881011A-b03	1845	0.0945	0.510823	0.000066	0.509677	-11.2
881011A-b04	1845	0.0938	0.510819	0.000075	0.509680	-11.2
881011A-b06	1845	0.0934	0.510822	0.000048	0.509688	-11.0
881011A-b07	1845	0.0930	0.510831	0.000047	0.509703	-10.7
881011A-b11	1845	0.0924	0.510830	0.000044	0.509709	-10.6
881011A-b12	1845	0.0926	0.510815	0.000067	0.509690	-11.0
881011A-b13	1845	0.0931	0.510802	0.000058	0.509673	-11.3
881011A-b14	1845	0.0928	0.510786	0.000060	0.509659	-11.6
881011A-b17	1845	0.0929	0.510780	0.000038	0.509652	-11.7
881011A-b18	1845	0.0943	0.510817	0.000029	0.509672	-11.3
881011A-b19	1845	0.0944	0.510788	0.000042	0.509642	-11.9
881011A-b20	1845	0.0938	0.510782	0.000024	0.509643	-11.9
881011A-b25	1845	0.0964	0.510823	0.000018	0.509653	-11.7
881011A-b26	1845	0.0933	0.510804	0.000023	0.509672	-11.3
881011A-b27	1845	0.0970	0.510824	0.000016	0.509646	-11.8
881011A-b28	1845	0.0961	0.510846	0.000016	0.509678	-11.2
881011A-b31	1845	0.0945	0.510800	0.000020	0.509652	-11.7
881011A-b32	1845	0.0949	0.510834	0.000018	0.509682	-11.1
881011A-b33	1845	0.0947	0.510812	0.000020	0.509662	-11.5
881011A-b34	1845	0.0946	0.510824	0.000028	0.509676	-11.3
881011A-b39	1845	0.0955	0.510815	0.000018	0.509656	-11.7
881011A-b40	1845	0.0944	0.510788	0.000019	0.509642	-11.9

Table 5.8 Sm-Nd isotopic data for monazite from the Hoidas Lake REE deposit.

Sample	^{207}Pb/^{206}Pb age (Ma)	2σ	^{147}Sm/^{144}Nd	^{143}Nd/^{144}Nd	2SE	initial ^{143}Nd/^{144}Nd	ε_{Nd}(t)
881350B-c15	1804	24	0.0320	0.509979	0.000047	0.509599	-13.8
881350B-c18	1803	19	0.0376	0.510024	0.000090	0.509577	-14.3
881350B-c35	1811	21	0.0337	0.510012	0.000026	0.509611	-13.4
881350B-c36	1766	22	0.0353	0.510035	0.000035	0.509625	-14.3
881350B-c41	1790	24	0.0350	0.510019	0.000026	0.509607	-14.0
881350B-c42	1782	24	0.0359	0.510045	0.000028	0.509625	-13.9
881350B-c44	1810	24	0.0352	0.509988	0.000023	0.509569	-14.2
881253-d04	1816	25	0.0412	0.510080	0.000034	0.509588	-13.7
881253-d10	1819	22	0.0445	0.510120	0.000046	0.509587	-13.7
881253-d11	1811	22	0.0430	0.510134	0.000037	0.509621	-13.2
881253-d12	1831	21	0.0401	0.510105	0.000065	0.509622	-12.7
881253-d13	1806	23	0.0417	0.510098	0.000033	0.509602	-13.7
881253-d20	1819	23	0.0395	0.510072	0.000053	0.509599	-13.4
881253-d21	1832	22	0.0393	0.510082	0.000055	0.509608	-12.9
881253-d24	1832	22	0.0397	0.510107	0.000048	0.509629	-12.5
881253-d27	1818	21	0.0428	0.510165	0.000040	0.509653	-12.4
881253-d28	1839	18	0.0398	0.510084	0.000051	0.509602	-12.9
881253-d31	1830	24	0.0400	0.510085	0.000056	0.509604	-13.0
881253-d33	1875	21	0.0396	0.510073	0.000051	0.509584	-12.3
881253-d34	1816	21	0.0394	0.510105	0.000063	0.509634	-12.8
881253-d35	1822	20	0.0392	0.510089	0.000045	0.509620	-13.0
881253-d38	1825	21	0.0392	0.510046	0.000065	0.509575	-13.7
881253-d39	1808	26	0.0414	0.510113	0.000044	0.509620	-13.3
881253-d41	1815	23	0.0397	0.510089	0.000047	0.509615	-13.2
881253-d42	1809	23	0.0390	0.510096	0.000059	0.509632	-13.0
881253-d45	1834	22	0.0393	0.510103	0.000061	0.509629	-12.5
881253-d47	1827	21	0.0403	0.510080	0.000030	0.509595	-13.3
881253-d48	1798	25	0.0407	0.510089	0.000040	0.509608	-13.8
881253-d52	1878	22	0.0414	0.510125	0.000071	0.509613	-11.6
881253-d53	1829	20	0.0508	0.510233	0.000040	0.509621	-12.7
881253-d54	1810	24	0.0514	0.510271	0.000052	0.509659	-12.5
881253-d60	1830	21	0.0418	0.510144	0.000091	0.509641	-12.3
881253-d61	1820	24	0.0528	0.510133	0.000076	0.509501	-15.3
881253-d62	1816	25	0.0441	0.510174	0.000084	0.509647	-12.6
881253-d63	1817	22	0.0415	0.510081	0.000067	0.509585	-13.7

5.6 Discussion

5.6.1 Age of the Hoidas Lake mineralization

The ^{207}Pb/^{206}Pb dates of all concordant zircon, titanite and monazite analyses and the preliminary apatite analyses from the Hoidas Lake deposit are summarized in a probability density diagram (Fig. 5.6). The dominant REE-bearing phases of Hoidas Lake mineralization formed during and after peak metamorphism in the region at 1.911 to 1.903 Ga (Ashton et al., 2009), and there is a clear distinction between the early zircon ^{207}Pb/^{206}Pb dates at around 2.35 Ga and late zircon ^{207}Pb/^{206}Pb dates at around 1.9 Ga. These latter zircon dates, within the analytical uncertainty of the U-Pb data, coincide with the ^{207}Pb/^{206}Pb dates of the early stage of titanite and monazite growth in the Hoidas Lake REE veins, and a later growth stage is represented by ^{207}Pb/^{206}Pb dates from ca. 1.85 to 1.8 Ga for titanite, apatite and monazite.

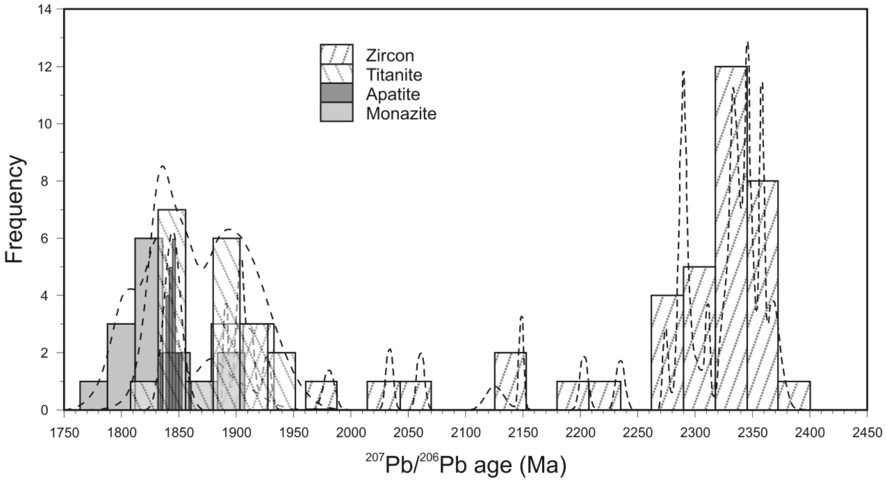

Figure 5.6 Histogram and probability density plot of ^{207}Pb/^{206}Pb dates. Diagram includes ^{207}Pb/^{206}Pb dates for zircon, titanite and monazite grains that yielded concordant U-Pb dates and preliminary apatite ^{207}Pb/^{206}Pb dates.

The U-Pb zircon dates presented here indicate that the oldest zircon grains in the Hoidas Lake REE deposit crystallized in the early Paleoproterozoic, with a group of 23 concordant U-Pb dates yielding a concordia intercept age of 2348 ± 19 Ma. Similar zircon U-Pb dates have previously been reported for the Hoidas Lake veins: (1) Gunning and Card (2005) reported a U-Pb date of ca. 2380 Ma for a zircon crystal in an apatite breccia vein; (2) Normand (2010) studied a euhedral zircon crystal from a diopside-allanite vein that showed a slightly discordant LA-ICP-MS U-Pb dataset with an upper intercept age of 2290 ± 7 Ma; and (3) Normand (2014) reported the results of further LA-ICP-MS U-Pb analyses of the zircon grain previously studied that yielded ^{207}Pb/^{206}Pb age of 2311 ± 7 Ma.

Based on structural features, the REE mineralization is considered to be younger than the peak metamorphism in the area, and therefore, the zircon crystals are interpreted to have been inherited from an early Paleoproterozoic source material, as has been discussed by Gunning and Card (2005), Normand (2010) and Harper (2012). However, Normand (2010, 2014) proposed that due to their euhedral habit and closely intergrown nature with allanite, the zircon crystals may be primary in the mineralized veins, indicating that the emplacement of the REE veins might have taken place during post-orogenic extensional events immediately following the 2.5-2.3 Ga Arrowsmith Orogeny (Normand, 2010; Hartlaub et al., 2007), and thus, the S1-S2 gneissic fabric in the host rocks of the mineralization might be an older, preserved fabric that was formed during the Arrowsmith Orogeny (Berman et al., 2005, 2013).

In this study, we propose that the zircon crystals in the mineralized veins are indeed inherited, as these zircon crystals show significantly older U-Pb dates than the titanite, green apatite and monazite crystals from the mineralized veins (Fig. 5.6). In addition, the zircon rims that yielded a concordant U-Pb date group with an intercept age of 1906 ± 34 Ma are inferred to have grown around the inherited zircon cores during the intrusion of the magmatic source of the REE mineralization or during the early stages of REE mineralization. The concordant U-Pb dates plotting in between the ca. 2350 Ma and ca. 1900 Ma date groups on the conventional concordia diagram (Fig. 5.5a) most probably reflect the effect of Pb loss related to this zircon re-equilibration event.

A large portion of the acquired zircon U-Pb data is discordant, and reflects single or multiple partial Pb-loss and/or new zircon growth followed by Pb loss (Fig. 5.5a). The possibility of late Pb diffusion processes altering the zircon crystals is also inferred from the strongly altered, metamict and fractured nature of the grains.

Textural evidence for the titanite crystals being coeval with the outermost allanite zones was observed, therefore, they are inferred to have crystallized during the allanite growth phase in the diopside-allanite veins. The titanite U-Pb data also reflect Pb loss, and the concordant portion of the data indicates a wide range of U-Pb dates from ca. 1931 Ma to 1825 Ma. The oldest sample with a group concordia age of 1903 ± 9 Ma include titanite crystals that are enclosed in the outer zone of allanite (together with zircon grains), which indicates that this titanite could have been inherited in the mineralized veins, similar to zircon. The younger titanite crystals that yielded a concordia age of 1828 ± 6 Ma may represent crystallization of the diopside-allanite veins.

The latest significant REE-enrichment stage is represented by the green apatite phase, and the weighted average of $^{207}Pb/^{206}Pb$ dates is 1845 ± 3 Ma, which coincides with the younger titanite and monazite ages.

An earlier SHRIMP (sensitive high-resolution ion microprobe) U-Pb study of the monazite from an apatite breccia vein in the Hoidas Lake deposit, reported by Gunning and Card (2005), indicated a monazite U-Pb date of 1870 Ma. Its recrystallized secondary nature was inferred by Halpin (2010) and further discussed by Normand (2014). Based on the U-Pb data acquired in this study, monazite growth in the earliest red apatite breccia veins appears to have occurred in at least two different periods, although there is no obvious petrographic difference between the two monazite generations. The oldest monazite crystals analyzed yielded a concordia age of 1909 ± 11 Ma, and might represent a primary monazite crystallization age in the earlier history of REE mineralization or inheritance from the source area. The younger monazite crystals, that yielded a concordia age of 1844 ± 4 Ma, represent monazite growth due to interaction of the red apatite with late hydrothermal fluids, as indicated by the textural features of the monazite. Based on textural features, monazite crystallization probably followed the formation of red apatite closely; however, as the secondary monazite crystals occur in all apatite generations, we can infer that multiple hydrothermal monazite growth phases were possible, due to interaction with multiple influxes of hydrothermal fluids.

5.6.2 The relationship of REE vein emplacement to the tectonic evolution of the Hoidas Lake area

The main metamorphic events affecting the Archean and Paleoproterozoic host rocks of the Hoidas Lake area, and the southern part of the Rae Subprovince, correspond to the 2.5-2.3 Ga Arrowsmith Orogeny and the 1.99-1.92 Ga Taltson-Thelon Orogeny (Ashton et al., 2009; Fig. 5.7a). Normand et al. (2009) compared the structural features of the Hoidas Lake area with those of the wider southern Rae Subprovince (Ashton et al., 2005, 2009), and suggested that the regional deformation history of the Hoidas Lake area includes: (1) peak metamorphism during the D1-D2 event, which was associated with partial melting and widespread leucogranite emplacement at ca. 1.94 to 1.92 Ga (Ashton et al., 2005, 2007, 2009), attributed to the Taltson-Thelon Orogeny; (2) the last high-grade metamorphic event during D3 at around 1.911 to 1.903 Ga, coincident with deformation associated with the Snowbird tectonic zone, which in the Hoidas Lake area is reflected by deformation along the Black Bay Fault; and (3) weak deformation during D4 (east-west shortening accompanying the final collision in the Trans-Hudson Orogen to the east) at 1.83 to 1.82 Ga (Fig. 5.7a). According to Normand et al. (2009) structural relationships indicate that the REE mineralization was emplaced during the latest stages of the D3 deformation, therefore, the monazite date of 1870 Ma (Gunning and Card, 2005) suggests that compressive deformation coaxial with D3 persisted for a long period, extending the previously estimated lower age limit of D3 by 30 Ma. If we assume for the concordant U-Pb dates obtained from this study to represent the crystallization ages of titanite and monazite, the lower age limit of D3 deformation is extended even further to younger ages.

The oldest concordant U-Pb age of the Hoidas Lake zircon crystals is coeval with some igneous rocks from the southern Rae Subprovince, which include (1) the ca. 2.32-2.29 Ga post-collisional granite suite related to the Murmac Bay Group in the Beaverlodge Domain (Yahyah Lake and Hayter Bay monzogranites; Hartlaub et al., 2007); (2) the 2330.3 ± 7.3 Ma porphyritic hornblende granite from the east side of Harper Lake in the Zemlak Domain which gave a 1925.3 ± 9.6 Ma metamorphic age (Ashton et al., 2007); (3) the 2325.1 ± 7.4 Ma Ena Lake granodiorite-tonalite gneiss in the Zemlak Domain which also gave a 1922 ± 16 Ma metamorphic age (Ashton et al., 2007); (4) an intermediate intrusive unit at Milliken Lake in the Beaverlodge Domain which gave a crystallization age of 2315.6 ± 0.6 Ma (Ashton et al., 2009); and (5) the 2343 ± 7 Ma zircon in the Dead Man granitic gneiss of the Beaverlodge Domain (Bethune et al., 2013) correlated with the 2.3 to 2.4 Ga D1 metamorphic event (Hartlaub et al., 2004, 2007). This granitoid intrusion event is interpreted to represent syn- to post-collisional magmatism near the end of Arrowsmith Orogeny (Hartlaub et al., 2007). The presence of these inherited zircon grains in the Hoidas Lake deposit might be related to assimilation of material from the 2.34-2.29 Ga granitoid intrusions by the REE-enriched melts.

Metamorphic dates around 1.9 Ga, similar to those of the younger concordant zircon U-Pb dates from the Hoidas Lake deposit, were also detected in other parts of the southern Rae Subprovince. These include: (1) a 1908 ± 1 Ma metamorphic age of a mafic dike that intrudes Zemlak orthogneiss; (2) metamorphic ages from amphibolite (1905 ± 3 Ma); (3) intermediate metavolcanic rocks (1903 ± 2 Ma); and (4) mafic metavolcanic rocks (1911 ± 10 Ma) from the Murmac Bay Group in the southern Beaverlodge Domain (Ashton et al., 2009; Hartlaub et al., 2009). These U-Pb dates at about 1.9 Ga reflect either the Taltson metamorphic event (Ashton et al., 2009) or deformation related to the development of the Snowbird Tectonic Zone.

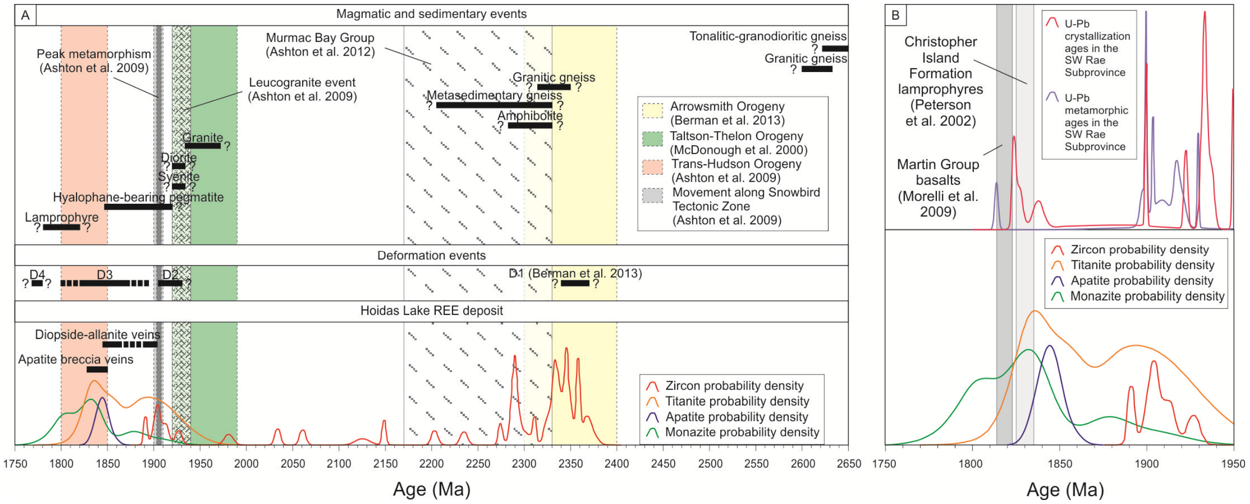

Figure 5.7 Schematic diagram summarizing the local and regional age relationships of the Hoidas Lake mineralization. (a) Summary of the inferred relative ages of the host rocks, deformation events and REE mineralization at Hoidas Lake, in context of the timing of regional deformation events and some of the discussed regionally significant stratigraphic units in the southwestern Rae Subprovince. The black bars represent relative ages and the ^{207}Pb/^{206}Pb probability density curves of zircon, titanite, apatite and monazite were created based on the present study. (b) Probability density curves of ^{207}Pb/^{206}Pb dates for the Hoidas Lake zircon, titanite, apatite and monazite grains compared to the inferred ages of the Christopher Island Formation ultrapotassic rocks, the Martin Group alkali basalts, and the U-Pb crystallization and metamorphic ages from the southwestern Rae Subprovince available in the DateView geochronological database.

The extended range of U-Pb dates of titanite, apatite and monazite in the Hoidas Lake mineralization from ca. 1.9 to 1.8 Ga overlaps with the evolution of the Snowbird Tectonic Zone and Trans-Hudson Orogen, and the estimated period of movement along the Black Bay Fault (Bergeron, 2001). The titanite, apatite and monazite U-Pb dates are also similar to other alkaline magmatic successions in the Rae Subprovince; including (1) the Martin Group alkali basalts in the Uranium City area to the south that are approximately 1818 ± 4 Ma (Ashton et al., 2009; Morelli et al., 2009; Fig. 5.7b); (2) the lamprophyre dikes in the Nevins Lake - Forsythe Lake area of the Beaverlodge Domain that yielded a U-Pb titanite date of 1780 Ma (Card, 2001), and a related syenite dike from the central Train Lake Domain with U-Pb titanite date of 1788 ± 3 Ma (Ashton et al., 2009); and (3) ultrapotassic rocks (minettes) of the Christopher Island Formation in the Baker Lake basin that are ~1.83 Ga (Cousens et al., 2001; Fig. 5.7b). The presence of these units and closely related basinal sedimentary successions likely represents localized extensional environments. Furthermore, the regional extent of these alkaline rock types of similar age indicates that the melts responsible for their formation might be related to a similar source, and the composition of these melts suggests that they were generated in the subcontinental mantle lithosphere.

5.6.3 Implications of Lu-Hf and Sm-Nd isotopic systematics for the source of the Hoidas Lake REE mineralization

Magmatic zircon crystals often yield discordant ^{238}U/^{206}Pb and ^{235}U/^{207}Pb dates, as they become metamict over time due to radiation damage induced by the decay of U and Th, and thus are particularly susceptible to thermal overprint, and/or fluid-driven dissolution-reprecipitation or diffusion-reaction processes (e.g., Pidgeon, 1992; Mezger and Krogstad, 1997; Geisler et al., 2001, 2007). This appears to have occurred in the Hoidas Lake zircon grains, as most of the zircon domains yield discordant dates (Fig. 5.5a), meaning they suffered single or multiple partial or total Pb loss (Gerdes and Zeh, 2009).

In contrast to the U-Pb isotope system, the zircon Lu-Hf system is less susceptible to alteration processes and metamictization (Patchett, 1983; Kinny and Maas, 2003; Zheng et al., 2005; Flowerdew et al., 2006; Wu et al., 2007; Zeh et al., 2007), since Hf is an essential element in the crystal structure (Patchett et al., 1981). In addition, zircon generally has low Lu/Hf ratios (<0.01) and thus, the Hf isotope composition of zircon corresponds closely to the isotope ratios of the magma at the time of zircon growth. Therefore, the combination of U-Pb zircon dating, which provides at least ^{207}Pb/^{206}Pb minimum formation dates, with Hf isotope signature of the same zircon grains provides a powerful tool to constrain the sources and evolution of a large variety of rocks (Patchett et al., 1981; Schärer et al., 1997; Amelin et al., 1999).

Among the 20 analyses of ca. 2.35 Ga zircon crystals from the Hoidas Lake deposit, the observed similarity in ^{177}Hf/^{176}Hf ratios (Fig. 5.8a) suggests that all zircon domains were formed from an isotopically homogeneous source, and they crystallized during a single magmatic event. The initial ^{176}Hf/^{177}Hf values of the inherited zircon cores range from 0.281154 to 0.281324, which correspond to εHf(t) values ranging from -9.5 to -1.4 (Fig. 5.8b), indicative of a strong crustal Hf contribution. Normand (2014) also reported similar preliminary values from the Hoidas Lake zircon grains. The two analyses of a zircon crystal rim with a concordant U-Pb age of ~1903 Ma (Fig. 5.4a, b) show higher initial ^{176}Hf/^{177}Hf and εHf(t) values (26.9 and 34.3), relative to the Depleted mantle evolution trend (Fig. 5.8a), indicating that they represent a new zircon growth event.

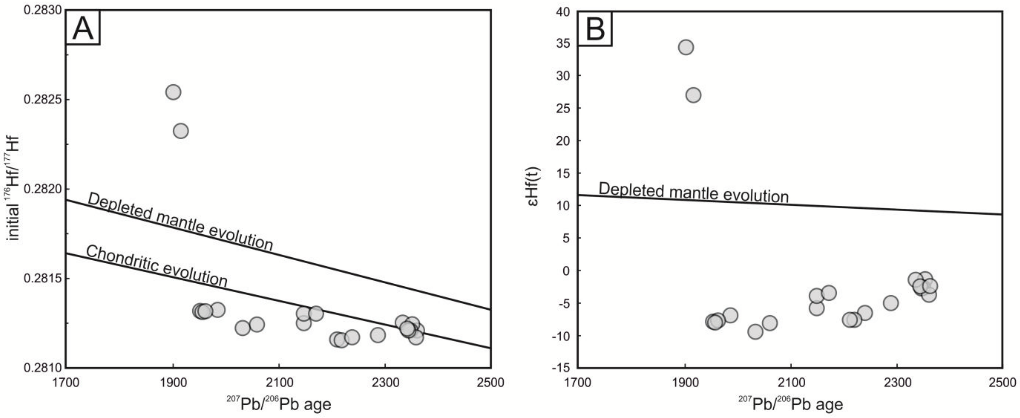

Figure 5.8 Hf isotopic data for the Hoidas Lake zircon grains. (a) ^{207}Pb/^{206}Pb date vs. initial ^{176}Hf/^{177}Hf plot of the analyzed zircon domains. (b) ^{207}Pb/^{206}Pb date vs. εHf(t) plot of the analyzed zircon domains. Initial ^{176}Hf/^{177}Hf and εHf(t) values were calculated using the ^{207}Pb/^{206}Pb dates of each spot. The chondritic evolution line was constructed using present-day ^{176}Hf/^{177}Hf(CHUR) = 0.282772, ^{176}Lu/^{177}Hf(CHUR) = 0.0332 and ^{176}Hf/ ^{177}Hf ratio of 0.279742 of the Solar System material 4.56 Ga ago from Blichert-Toft and Albarède (1997). The depleted mantle evolution line was constructed using present-day depleted mantle ^{176}Hf/^{177}Hf value of 0.2832 from Chauvel and Blichert-Toft (2001).

Similar extremely radiogenic εHf(t) values (as high as 40) were reported from hydrothermal zircon from the “Kiruna-type” magnetite-apatite deposits of the Adirondack Mountains in New York (Valley et al., 2010). Valley et al. (2010) proposed two models for the observed high εHf(t) values. One of these possible processes is the introduction of Zr and radiogenic Hf, following hydrothermal mobilization from earlier-formed magnetite-, apatite- and clinopyroxene-bearing ore bodies. The other process involved the crystallization of hydrothermal zircon from fluids that had interacted with Lu-rich garnet in the lower crust. At Hoidas Lake high εHf(t) values of the zircon rims could have developed through alteration or by crystallization from a melt which was derived from an unusual mantle source with a much higher Lu/Hf ratio than that of the depleted mantle. A more radiogenic Hf signature could have developed in this high Lu/Hf ratio mantle source over time, prior to generation of the melt.

Similar to the Hf isotope system, the Sm-Nd isotope system is also considered to be more resistant to modification by geologic reworking compared to the U-Pb system (e.g., Pearce et al., 1999), and thus, is a useful tool for identifying source regions. The Sm-Nd isotope data for titanite and monazite from the Hoidas Lake deposit were plotted on a Sm-Nd isochron plot (Fig. 5.9a), and the data clusters for the two different phases are situated along a linear array which could be interpreted as a quasi-isochron. The age for this linear array is 1847 ± 26 Ma with an initial ^{143}Nd/^{144}Nd = 0.509600 ± 0.000014. This age estimate overlaps with the age of the younger concordant monazite grains.

The Hoidas Lake titanite, green apatite and monazite crystals yielded similar initial ^{143}Nd/^{144}Nd values and εNd(t) values, ranging from 0.509472 to 0.509710 and -15.3 to -10.6, respectively. For comparison of the distinct phases, εNd(t) values were calculated using the concordant maximum of the ^{207}Pb/^{206}Pb dates for titanite and monazite and the weighted average of ^{207}Pb/^{206}Pb dates for apatite (Fig. 5.9b), and indicate initial εNd(t) values from -15 and -11.

These εNd values are close to those observed from whole rock Sm-Nd analyses of the ultrapotassic rocks of the Christopher Island Formation and the Martin Group alkali basalts. The ultrapotassic rocks of the Christopher Island Formation extend across the Snowbird Tectonic Zone, and have $\varepsilon\text{Nd}_{1830\text{Ma}}$ values that range from -11.5 to -6, with 80% of the data clustering between -9 and -7 (Cousens et al., 2001). There is no difference between the εNd values for the Christopher Island Formation rocks on either side of the Snowbird Tectonic Zone in the Rae and Hearne subprovinces, an thus Sandeman et al. (2000) and Cousens et al. (2001) interpreted these to have originated from a common lithospheric mantle source. Nd model ages of ca. 2.45 to 2.2 Ga indicate that this enriched lithospheric mantle source was probably created during an Archean metasomatic event, and remained isolated and isotopically closed until tapped during extension in the area related to the formation of the Wopmay and Trans-Hudson Orogens (Cousens et al., 2001). Cousens et al. (2001) suggested that the extensional structures provided mechanical pathways for rapid magma release. The Martin Group basalts have whole-rock $\varepsilon\text{Nd}_{1818\text{Ma}}$ values ranging from -4.1 to -6.3 (present-day ^{143}Nd/^{144}Nd values from 0.510901 to 0.511104; Morelli et al., 2009; Table 3). Morelli et al. (2009) interpreted these geochemical and isotopic features to be indicative of origin from a subcontinental lithospheric mantle source that experienced a complex enrichment history, including an ancient subduction-related contribution, similar to the source of the Christopher Island Formation.

The similarity of the U-Pb dates and Sm-Nd isotopic systematics of the Hoidas Lake vein minerals to the aforementioned alkali rock suites, and the U-Pb dates of the inherited zircon crystals indicate that the Hoidas Lake mineralizing melts may have also derived from the same metasomatized subcontinental lithospheric mantle reservoir beneath the Rae and Hearne subprovinces. Regional scale structures, such as the Black Bay Fault, provided conduits for the infiltration of these melts and related fluids into the Hoidas Lake area.

5.7 Summary

In situ U-Pb geochronology of zircon, titanite, green apatite and monazite crystals of the Hoidas Lake deposit indicates that the emplacement of the REE-rich veins formed after peak metamorphism in the area at ca. 1.9 Ga. Inherited zircon crystals in the diopside-allanite veins, with concordant U-Pb dates that cluster around 2.35 Ga, indicate their derivation from granitoids that formed during the Arrowsmith Orogeny. Zircon rims show a concordant cluster of U-Pb dates around 1.9 Ga, which suggests that new zircon growth occurred during the formation of early REE-bearing phases. This is also indicated by the considerable differences in Hf isotopic composition between the inherited zircon cores and zircon overgrowths (εHf(t) from -9.5 to -1.4 vs. εHf(t) around 25-30, respectively). Titanite from two distinct samples yielded concordia ages of 1903 ± 9 Ma and 1828 ± 6 Ma and two groups of monazite data yielded 1909 ± 11 Ma and 1844 ± 4 Ma concordia ages. These indicate that there might have been multiple vein emplacement events with significant time lapse between them, or alternatively, the youngest zircon generation and the early titanite and monazite grains might be inherited in the mineralized veins. The U-Pb dates coincide with the estimated period of movement along the Black Bay Fault, which further underlines the role of this deeply-rooted regional scale structure in the emplacement of the mineralization. The Sm-Nd isotopic systematics of titanite, apatite and monazite, and calculated εNd(t) values (from -15.3 to -10.6) are comparable to the εNd(t) values of alkali rocks of the Martin Group in the Beaverlodge Domain and the Christopher Island Formation in the Baker Lake Basin, both of which also yielded similar U-Pb dates to those of the Hoidas Lake veins. It is likely that these regionally occurring alkali units in the southern Rae Subprovince have a similar magmatic source, which is most probably an ancient enriched lithospheric mantle reservoir.

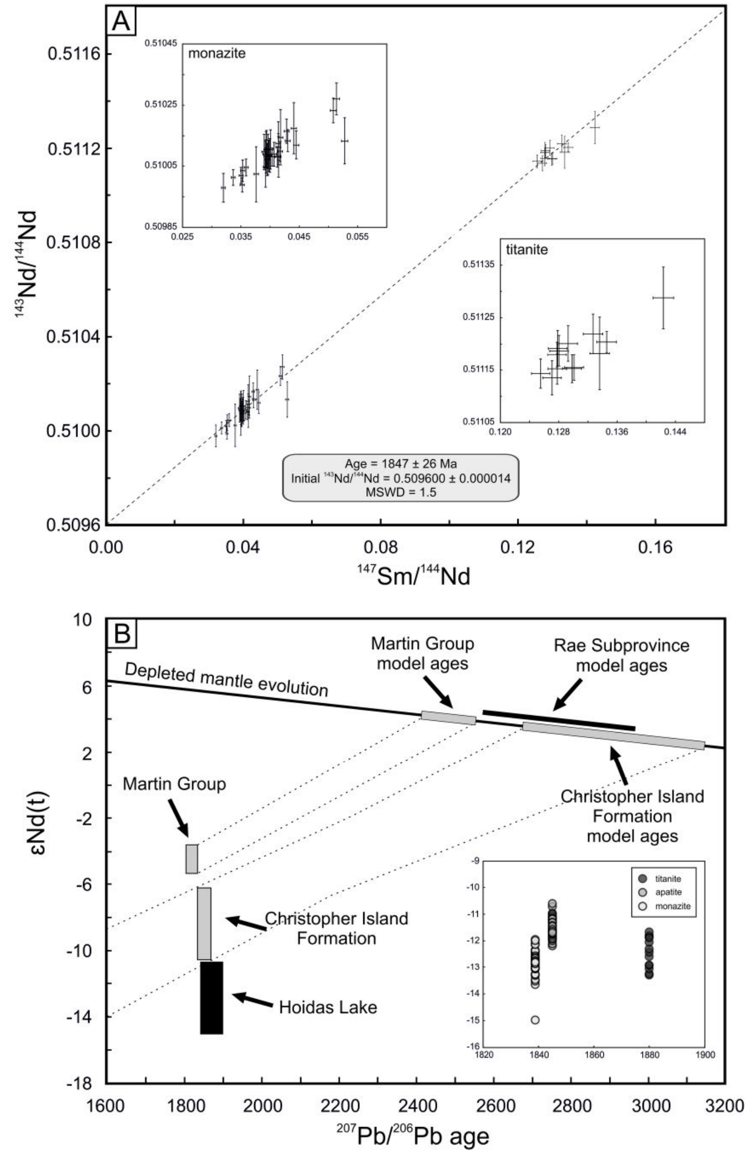

Figure 5.9 Sm-Nd isotopic data for the Hoidas Lake titanite, green apatite and monazite. (a) Sm-Nd isochron diagram where insets provide enlargements of the separate clusters of data for titanite and monazite analyses. Error crosses are 2σ confidence level. (b) ^{207}Pb/^{206}Pb age vs. εNd(t) plot. Nd isotopic data for the Christopher Island Formation (Cousens et al., 2001), the Martin Group (Morelli et al., 2009) and average Nd model ages for the Rae Subprovince (Cousens et al., 2001) are shown for comparison. Inset shows enlargement of the ^{207}Pb/^{206}Pb age vs. εNd(t) plot for the Hoidas Lake titanite, apatite and monazite. Out of the ^{207}Pb/^{206}Pb dates for each analyzed spot, the maximum concordant ^{207}Pb/^{206}Pb date was used for titanite and monazite (1880 Ma and 1839 Ma, respectively) and the weighted average of apatite ^{207}Pb/^{206}Pb dates (1845 Ma) were used to calculate εNd(t) values. The depleted mantle evolution trend was constructed, based on present-day depleted mantle ^{143}Nd/^{144}Nd of 0.513151 and ^{147}Sm/^{144}Nd of 0.2164 (Isnard and Gariépy, 2004).

5.8 Relationship of manuscript to thesis

In this manuscript the aim is to provide in situ radiogenic isotopic constraints on the age of the Hoidas Lake REE mineralization and the nature of its source region. The U-Pb isotopic characteristics of distinct mineral phases provide evidence for the duration and evolution of the mineralization. The temporal relationships of the analyzed phases are discussed in view of the paragenetic relationships and chemical evolution of the vein phases (detailed in Chapter 4). The position of the mineralization within the tectonic evolution of the area is detailed in this manuscript, and the Lu-Hf isotopic characteristics of the Hoidas Lake zircon crystals are used to infer isotopic evolution of the source for this phase over time. In addition, the Sm-Nd isotopic characteristics of the Hoidas Lake deposit are compared with those of other alkali units in the region, in order to contribute to the general understanding of the Paleoproterozoic tectonic evolution of the southern Rae Subprovince.

CHAPTER 6
SUMMARY

This Ph.D thesis was prepared with the aim of providing a case study for evaluating magmatic and hydrothermal processes responsible for the formation and evolution of a complex and unusual REE deposit, which is not directly related to a magmatic source. The four manuscripts presented in this thesis (Chapter 2 to 5) provide information on the characteristics of the melts and hydrothermal fluids, the magmatic-hydrothermal evolution of the mineralization and its effects on the chemical variations and alteration characteristics of the mineralized veins and their host rocks, the age relationships of the REE-bearing phases, and radiogenic isotopic implications for the source of mineralizing melts and fluids in the system. The aforementioned aims were addressed through field observations, detailed petrographic studies, scanning electron microscopy coupled with energy dispersive X-ray spectroscopy (SEM-EDS), electron microprobe analyses (EMPA), fluid inclusion microthermometry, laser ablation inductively coupled plasma mass spectrometry (LA-ICP-MS) U-Pb, and laser ablation multi-collector inductively coupled plasma mass spectrometry (LA-MC-ICP-MS) Lu-Hf and Sm-Nd isotopic studies.

The first manuscript (Chapter 2) provides the first constraints on the characteristics, including temperature, pressure and composition, of the hydrothermal fluids responsible for REE mobilization in the Hoidas Lake vein system, and thus allows evaluation of the observed mineral chemical variations (Chapter 4). The fluid inclusion study suggests that the first stage of hydrothermal activity is represented by CO_2-rich fluids entrapped in the apatite breccia veins, followed by the entrapment of mixed Na-Ca-K-(Ba-Mn-Fe-Mg-Sr)-containing aqueous fluids that show a range of salinities (8-40 wt.% eq. NaCl). These aqueous fluids are likely responsible for alteration of the mineralized veins and redistribution of their REE contents into secondary monazite and REE-carbonates. Entrapment of the hydrothermal fluids at Hoidas Lake occurred below 310°C, and the maximum possible range of entrapment pressures of the carbonic and aqueous L-V-H inclusions is between 0.5 and 2 kbars. The pressure during entrapment was transient and may have varied between lithostatic and hydrostatic during the emplacement of the REE mineralization. The estimated composition of the aqueous fluids, according to evaporate mound chemistry, is generally similar to those calculated for fluids in known carbonatitic settings, thus indicating that the fluids might have originated from a carbonatitic source.

A report on the petrography and chemistry of graphic-textured inclusions in the apatite of the Hoidas Lake deposit is provided in the second manuscript (Chapter 3). The formation of these inclusions is explained through two models: (1) oversaturation of the residual components in the boundary-layer melt immediately adjacent to the apatite growth surface, followed by precipitation of REE-enriched phases; or (2) entrapment of immiscible melt fractions from a flux-rich melt by the rapidly crystallizing apatite. The compositional variations of the inclusions and the presence of Ce-Th-rich silicic and La-Nd-F-rich compositional end members indicate that they are derived from an evolved melt. The possible triggering factors for rapid apatite nucleation and formation of the graphic-textured inclusions include undercooling of the melt, sudden pressure variations (also indicated by fluid inclusion characteristics and the presence of various breccia phases) and changing melt composition. The presence of these graphic textures in the apatite breccia at Hoidas Lake indicates that similar processes to those operating in granitic systems may occur in carbonatitic or alkaline melts.

The chemical variations of REE-bearing phases indicate that the multi-stage evolution of the deposit includes an initial magmatic stage and a superimposed hydrothermal system, as discussed in the third manuscript (Chapter 4). The evolution of magmatic and hydrothermal fluids is reflected in the vein paragenesis and the chemistry of REE-bearing phases. There was limited Ba-metasomatism and albitization in the wall rocks. The diopside-allanite veins likely formed from a highly evolved, chemically complex melt, showing progressive relative REE-depletion and subsequent REE-enrichment, possibly due to first closed then open system behavior. The apatite breccia veins represent a transition from a melt to a hydrothermal fluid that resulted in hydrothermal remobilization of the REEs. This is represented by a consistent sequence of crystallization stages, from apatite formation, through thorite and monazite, then barite precipitation (together with hematite and chlorite formation), and finally, precipitation of REE-silicates and REE-Sr carbonates from high salinity aqueous hydrothermal fluids. In addition, the mineralogy, chemistry, and extreme enrichment of the veins in REEs and other elements (i.e., Ba, Sr) indicate a source with carbonatitic affinity for the melts and fluids.

Precise knowledge of the chemical variations in REE-bearing phases allows for in situ measurement of radiogenic isotopic ratios, detailed in the fourth manuscript (Chapter 5), with the goal of constraining the age relationships of the mineralization. In situ U-Pb geochronology of the zircon, titanite, green apatite and monazite indicates that the Hoidas Lake deposit was emplaced after peak metamorphism in the southern Rae Subprovince, at ca. 1.9 Ga. Inherited zircon crystals, however, yield a ca. 2.35 Ga U-Pb age indicating their derivation from a granitoid source that formed during the older Arrowsmith Orogeny. Zircon rims with a concordant U-Pb age of around 1.9 Ga suggest that new zircon growth occurred during the emplacement of the REE mineralization, also indicated by the considerable difference between the Hf isotopic composition of the inherited zircon cores and zircon overgrowths (εHf(t) values from -9.5 to -1.4 vs. εHf(t) around 25-30, respectively). Concordia ages of titanite from two distinct samples are ca. 1900 Ma and 1830 Ma and two monazite U-Pb date groups were observed at ca. 1910 Ma and 1845 Ma, which coincide with the estimated period of movement along the Black Bay Fault. This supports the implication that the Black Bay Fault and subsidiary structures played an important role of in the emplacement of the mineralization. The Sm-Nd isotopic systematics of these phases, and calculated εNd(t) values (from -15.3 to -10.6) are comparable to the εNd(t) values of alkali rocks of the Martin Group in the Beaverlodge Domain and the Christopher Island Formation in the Baker Lake Basin, indicating that these regionally occurring alkali units and the Hoidas Lake melts and fluids were likely derived from a similar source region, most probably the ancient enriched sub-continental lithospheric mantle.

LIST OF REFERENCES

Amelin, Y., Lee, D.C., Halliday, A.N., and Pidgeon, R.T. (1999) Nature of the Earth's earliest crust from hafnium isotopes in single detrital zircons. *Nature* **399**, 252-255.

Andersen, T. (2002) Correction of common lead in U-Pb analyses that do not report ^{204}Pb. *Chemical Geology* **192**, 59-79.

Ansdell, K.M. (2005) Tectonic evolution of the Manitoba-Saskatchewan segment of the Paleoproterozoic Trans-Hudson Orogen, Canada. *Canadian Journal of Earth Sciences* **42**, 741-759.

Ashton, K.E., Boivin, D., and Heggie, G. (2001) Geology of the southern Black Bay Belt, west of Uranium City, Rae Province. *Saskatchewan Geological Survey, Saskatchewan Energy and Mines, Summary of Investigations* **2001-2**, *Miscellaneous Report* **2001-4.2**, 14 p.

Ashton, K.E., Card, C.D., and Modeland, S. (2005) Geological reconnaissance of the northern Tazin Lake map area (NTS 74N), including parts of the Ena, Nolan, Zemlak and Taltson domains, Rae Province. *Saskatchewan Geological Survey, Saskatchewan Industry and Resources, Summary of Investigations* **2005-2**, *Miscellaneous Report* **2005-4.2**, 24 p.

Ashton, K.E., Card, C.D., Davis, W., and Heaman, L.M. (2007) New U-Pb Zircon age dates from the Tazin Lake map area (NTS 74N). *Saskatchewan Geological Survey, Saskatchewan Ministry of Energy and Resources, Summary of Investigations* **2007-2**, *Miscellaneous Report* **2007-4.2**, 8 p.

Ashton, K.E., Hartlaub, R.P. Heaman, L.M. Morelli, R.M. Card, C.D., Bethune, K., and Hunter, R.C. (2009) Post-Taltson sedimentary and intrusive history of the southern Rae Province along the northern margin of the Athabasca Basin, Western Canadian Shield. *Precambrian Research* **175**, 16-34.

Ashton, K.E., Hartlaub, R.P., Bethune, K.M., Heaman, L.M., Rayner, N., and Niebergall, G.R. (2012) New depositional age constraints for the Murmac Bay group of the southern Rae craton, Canada. *Precambrian Research* **232**, 70-88.

Aspler, L.B., Chiarenzelli, J.R., and McNicoll, V.J. (2002) Paleoproterozoic basement-cover infolding and thick-skinned thrusting in Hearne domain, Nunavut, Canada: intracratonic response to Trans-Hudson orogen. *Precambrian Research* **116**, 331-354.

Baldwin, J.A., Bowring, S.A., and Williams, M.L. (2003) Petrological and geochronological constraints on high pressure high temperature metamorphism in the Snowbird tectonic zone, Canada. *Journal of Metamorphic Geology* **21**, 81-98.

Becker, S.P., Fall, A., and Bodnar, R.J. (2008) Synthetic fluid inclusions XVII. PVTX properties of high salinity H_2O-NaCl solutions (>30 wt.% NaCl): Application to fluid inclusions that homogenize by halite disappearance from porphyry copper and other hydrothermal ore deposits. *Economic Geology* **103**, 539-554.

Belousova, E.A., Griffin, W.L., O'Reilly, S.Y., and Fisher, N.I. (2002) Apatite as an indicator mineral for mineral exploration: trace-element compositions and their relationship to host rock type. *Journal of Geochemical Exploration* **76**, 45-69.

Berger, A., Gnos, E., Janots, E., Fernandez, A., and Giese, J. (2008) Formation and composition of rhabdophane, bastnäsite and hydrated thorium minerals during alteration: Implications for geochronology and low-temperature processes. *Chemical Geology* **254**, 238-248.

Bergeron, J. (2001) The deformational history of the Black Bay Structure near Uranium City, Northern Saskatchewan. *University of Saskatchewan Unpublished M.Sc. Thesis*, 269 p.

Berman, R.G., Sanborn-Barrie, M., Stern, R.A., and Carson, C.J. (2005) Tectonometamorphism at ca. 2.35 and 1.85 Ga in the Rae Domain, western Churchill Province, Nunavut, Canada: Insights from structural, metamorphic and in situ geochronological analysis of the southwestern Committee Bay Belt. *Canadian Mineralogist* **43**, 409-442.

Berman, R. G., Davis, W. J., and Pehrsson, S. (2007) Collisional Snowbird tectonic zone resurrected: Growth of Laurentia during the 1.9 Ga accretionary phase of the Hudsonian orogeny. *Geology* **35**, 911-914.

Berman, R.G., Pehrsson, S., Davis, W.J., Ryan, J.J., Qui, H., and Ashton, K.E. (2013) The Arrowsmith orogeny: Geochronological and thermobarometric constraints on its extent and tectonic setting in the Rae craton, with implications for pre-Nuna supercontinent reconstruction. *Precambrian Research* **232**, 44-69.

Bethune, K.M., Berman, R.G., Rayner, N., and Ashton, K.E. (2013) Structural, petrological and U-Pb SHRIMP geochronological study of the western Beaverlodge domain: Implications for crustal architecture, multi-stage orogenesis and the extent of the Taltson orogen in the SW Rae craton, Canadian Shield. *Precambrian Research* **232**, 89-118.

Billingsley, G. (2010) Focus on rare earths: Building the mine to market strategy. *Great Western Minerals Group Ltd. Speciality and Minor Metals Investment Summit*

Blichert-Toft, J., and Albarède, F. (1997) The Lu-Hf isotope geochemistry of chondrites and the evolution of the mantle-crust system. *Earth and Planetary Science Letters* **148**, 243-258.

Bodnar, R.J. (2003) Interpretation of data from aqueous-electrolyte fluid inclusions. In: Samson, I.M., Anderson, A., and Marshall, D. (Eds.): Fluid inclusions: Analysis and interpretation. *Mineralogical Association of Canada Short Course Volume* **32**, 81-99.

Bouvier, A., Vervoort, J.D., and Patchett, P.J. (2008) The Lu-Hf and Sm-Nd isotopic composition of CHUR: Constraints from unequilibrated chondrites and implications for the bulk composition of terrestrial planets. *Earth and Planetary Science Letters* **273**, 48-57.

Bowden, P., Wall, F., and Schurmann, L. (2000) 'Spinifex textured' pegmatitic crystallisation in carbonatites. In: Moutte, J., and Garcia, D. (Eds.): Carbonatite workshop. *Journal of African Earth Sciences* **32**, A11-A12.

Bühn, B., and Rankin, A.H. (1999) Composition of natural, volatile-rich Na-Ca-REE-Sr carbonatitic fluids trapped in fluid inclusions. *Geochimica et Cosmochimica Acta* **63**, 3781-3797.

Bühn, B., Wall, F., and Le Bas, M.J. (2001) Rare-earth element systematics of carbonatitic fluorapatites, and their significance for carbonatite magma evolution. *Contributions to Mineralogy and Petrology* **141**, 572-591.

Card, C. (2001) Geology and Tectonic Setting of the Oldman - Bulyea Shear Zone, Northern Saskatchewan, Canada. *University of Regina Unpublished M.Sc. Thesis*, 188 p.

Castor, S.B., and Hedrick, J.B. (2006) Rare earth elements. In: Kogel, J.E., Trivedi, N.C., Barker, J.M., and Krukowski S.T. (Eds.): Industrial minerals & rocks: Commodities, markets and uses, 7th edition. *Society for Mining, Metallurgy and Exploration Inc.*, 769-792.

Chakhmouradian, A.R., and Wall, F. (2012) Rare earth elements: Minerals, mines, magnets (and more). *Elements* **8**, 333-340.

Chakhmouradian, A.R., Mumin, A.H., Demeny, A., and Elliot, B. (2008) Postorogenic carbonatites at Eden Lake, Trans-Hudson Orogen (northern Manitoba, Canada): Geological setting, mineralogy and geochemistry. *Lithos* **103**, 503-526.

Chauvel, C., and Blichert-Toft, J. (2001) A hafnium isotope and trace element perspective on melting of the depleted mantle. *Earth and Planetary Science Letters* **190**, 137-151.

Chew, D.M., Sylvester, P.J., and Tubrett, M.N. (2011) U-Pb and Th-Pb dating of apatite by LA-ICP-MS. *Chemical Geology* **280**, 200-216.

Chi, G., Dubé, B., and Williamson, K. (2006) Formation of the Campbell-Red Lake gold deposit by H_2O-poor, CO_2-dominated fluids. *Mineralium Deposita* **40**, 726-741.

Choudhuri, R., and Banerji, K. C. (1976) On the occurrence, emplacement and origin of the apatite deposits of Kasipatnam in Visakhapatnam District, Andhra Pradesh. *Proceedings of the Indian National Science Academy* **42-A/5**, 387-406.

Corrigan, D., Pehrsson, S., Wodicka, N., and de Kemp, E. (2009) The Palaeoproterozoic Trans-Hudson Orogen: a prototype of modern accretionary processes. *Geological Society, London, Special Publications* **327**, 457-479.

Cousens, B.L., Aspler, L.B., Chiarenzelli, J.R., Donaldson, J.A., Sandeman, H., Peterson, T.D., and Lecheminant, A.N. (2001) Enriched Archean lithospheric mantle beneath western Churchill province tapped during Paleoproterozoic orogenesis. *Geology* **29**, 827-830.

Diamond, L.W. (1992) Stability of CO_2 clathrate hydrate + CO_2 liquid + CO_2 vapour + aqueous KCI-NaCl solutions: Experimental determination and application to salinity estimates of fluid inclusions. *Geochimica et Cosmochimica Acta* **56**, 273-280.

Donovan, J.J., and Tingle, T.N. (1996) An improved mean atomic number background correction for quantitative microanalysis. *Microscopy Society of America* **2**, 1-7.

Doroshkevich, A.G., Ripp, G.S., Viladkar, S.G., and Vladykin, N.V. (2008) The Arshan REE carbonatites, southwestern Transbaikalia, Russia: Mineralogy, paragenesis and evolution. *Canadian Mineralogist* **46**, 807-824.

Doroshkevich, A.G., Ripp, G.S., and Moore, K.R. (2010) Genesis of the Khaluta alkaline-basic Ba-Sr carbonatite complex (west Transbaikaila, Russia). *Mineralogy and Petrology* **98**, 245-268.

Dostal, J., Kontak, D.J., and Karl, S.M. (2014) The Early Jurassic Bokan Mountain peralkaline granitic complex (southeastern Alaska): Geochemistry, petrogenesis and rare-metal mineralization. *Lithos* **202-203**, 395-412.

Droop, G.T.R. (1987) A general equation for estimating Fe^{3+} concentrations in ferromagnesian silicates and oxides from microprobe analyses, using stoichiometric criteria. *Mineralogical Magazine* **51**, 431-435.

Elliott, R., Ansdell, K.M., Harper, C.T., Pandur, K., and Pearson, J. (2013) Field relationships, petrography and geochemistry of lamprophyre dykes from the Hoidas Lake Area, Ena Domain, Saskatchewan. *Geological Association of Canada - Mineralogical Association of Canada Conference Abstract, Winnipeg*

Essene, E.J., Claflin, C.L., Giorgetti, G., Mata, P.M., Peacor, D.R., Árkai, P., and Rathmell, M.A. (2005) Two-, three- and four-feldspar assemblages with hyalophane and celsian: implications for phase equilibria in $BaAl_2Si_2O_8$-$CaAl_2Si_2O_8$-$NaAlSi_3O_8$-$KAlSi_3O_8$. *European Journal of Mineralogy* **17**, 515-535

Fenn, P.M. (1986) On the origin of graphic granite. *American Mineralogist* **71**, 325-330.

Fisher, C.M., Hanchar, J.M., Samson, S.D., Dhuime, B., Blichert-Toft, J., Vervoort, J.D., and Lam, R. (2011a) Synthetic zircon doped with hafnium and rare earth elements: A reference material for in situ hafnium isotope analysis. *Chemical Geology* **286**, 32-47.

Fisher, C.M., McFarlane, C.R.M., Hanchar, J.M., Schmitz, M.D., Sylvester, P.J, Lam, R., and Longerich, H.P. (2011b) Sm-Nd isotope systematics by laser ablation-multicollector-inductively coupled plasma mass spectrometry: Methods and potential natural and synthetic reference materials. *Chemical Geology* **284**, 1-20.

Fleischer, M. (1965) Some aspects of the geochemistry of yttrium and the lanthanides. *Geochimica et Cosmochimica Acta* **29**, 755-772.

Flowerdew, M.J., Millar, I.L., Vaughan, A.P.M., Horstwood, M.S.A., and Fanning, C.M. (2006) The source of granitic gneisses and migmatites in the Antarctic Peninsula: a combined U-Pb SHRIMP and laser ablation Hf isotope study of complex zircons. *Contributions to Mineralogy and Petrology* **151**, 751-768.

Flowers, R.M., Bowring, S.A., and Williams, M.L. (2006) Timescales and significance of high pressure, high temperature metamorphism and mafic dike anatexis, Snowbird Tectonic Zone, Canada. *Contributions to Mineralogy and Petrology* **151**, 558-581.

Foster, G.L., and Vance, D. (2006) In situ Nd isotopic analysis of geological materials by laser ablation MC-ICP-MS. *Journal of Analytical Atomic Spectrometry* **21**, 288-296.

Geisler, T., Ulonska, M., Schleicher, H., Pidgeon, R.T., and van Bronswijk, W. (2001) Leaching and differential recrystallization of metamict zircon under experimental conditions. *Contributions to Mineralogy and Petrology* **141**, 53-65.

Geisler, T., Schaltegger, U., and Tomaschek, F. (2007) Re-equilibration of zircon in aqueous fluids and melts. *Elements* **3**, 43-50.

Gerdes, A., and Zeh, A. (2009) Zircon formation versus zircon alteration - New insights from combined U-Pb and Lu-Hf in-situ LA-ICP-MS analyses, and consequences for the interpretation of Archean zircon from the Central Zone of the Limpopo Belt. *Chemical Geology* **261**, 230-243.

Gieré, R. (1996) Formation of rare earth minerals in hydrothermal systems. In: Jones, A.P., Wall, F., and Williams, T. (Eds.): Rare earth minerals: Chemistry, origin and ore deposits. *The Mineralogical Society Series* **7**, 105-150.

Gieré, R., and Sorensen, S.S. (2004) Allanite and other REE-rich epidote-group minerals. *Reviews in Mineralogy and Geochemistry* **56**, 431-493.

Goldstein, R.H. (2003) Petrographic analysis of fluid inclusions. In: Samson, I.M., Anderson, A., and Marshall, D. (Eds.): Fluid Inclusions: Analysis and Interpretation. *Mineralogical Association of Canada Short Course Volume* **32**, 9-53.

Goldstein, R.H., and Reynolds, T.J. (1994) Systematics of fluid inclusions in diagenetic minerals. *Society for Sedimentary Geology Short Course Volume* **31**, 199 p.

Gregory, C.J., McFarlane, C.R.M., Hermann, J., and Rubatto, D. (2009) Tracing the evolution of calc-alkaline magmas: In-situ Sm-Nd isotope studies of accessory minerals in the Bergell Igneous Complex, Italy. *Chemical Geology* **260**, 73-86.

Gromet, L.P., and Silver, L. T. (1983) Rare earth element distributions among minerals in a granodiorite and their petrogenetic implications. *Geochimica et Cosmochimica Acta* **47**, 925-939.

Grover, T.W., Pattison, D.R.M., McDonough, M.R., and McNicoll, V.J. (1997) Tectonometamorphic evolution of the southern Taltson Magmatic Zone and associated shear zones, northeastern Alberta. *Canadian Mineralogist* **35**, 1051-1067.

Guanming, Q., Xikun, L., Tai, Q., Haitu, Z., Honghau, Y., and Ruiting, M. (2007) Application of rare earths in advanced ceramic materials. *Journal of Rare Earths* **25**, 281-285.

Gunning, M.H., and Card, C.D. (2005) Transects across the Black Bay Sear Zone and Hoidas-Nisikkatch Rare-element Trend, northwest Saskatchewan. *Saskatchewan Geological Survey, Saskatchewan Industry Resources, Open File Report* **2004-2**, 47 p.

Guzmics, T., Mitchell, R.H., Szabó, Cs., Berkesi, M., Milke, R., and Abart, R. (2011) Carbonatite melt inclusions in coexisting magnetite, apatite and monticellite in Kerimasi calciocarbonatite, Tanzania: melt evolution and petrogenesis. *Contributions to Mineralogy and Petrology* **161**, 177–196.

Halpin, K.M. (2010) The characteristics and origin of the Hoidas Lake REE deposit. *University of Saskatchewan Unpublished M.Sc. Thesis*, 173 p.

Hamilton, P.J., O'Nions, R.K., Bridgwater, D., and Nutman, A. (1983) Sm-Nd studies of Archaean metasediments and metavolcanics from West Greenland and their implications for the Earth's early history. *Earth and Planetary Science Letters* **62**, 263-272.

Hanmer, S., Williams, M., and Kopf, C. (1995) Striding-Athabasca mylonite zone: implications for the Archean and Early Proterozoic tectonics of the western Canadian Shield. *Canadian Journal of Earth Sciences* **32**, 178-196.

Hansteen, T.H., and Klügel, A. (2008) Fluid inclusion thermobarometry as a tracer for magmatic processes. *Reviews in Mineralogy and Geochemistry* **69**, 143-177.

Harlov, D.E., and Förster, H.-J. (2003) Fluid-induced nucleation of (Y+REE)-phosphate minerals within apatite: Nature and experiment. Part II. Fluorapatite. *American Mineralogist* **88**, 1209-1229.

Harlov, D.E., Andersson, U.B., Förster, H.-J., Nyström, J.O., Dulski, P., and Broman, C. (2002) Apatite-monazite relations in the Kiirunavaara magnetite-apatite ore, northern Sweden. *Chemical Geology* **191**, 47-72.

Harlov, D.E., Wirth, R., and Förster, H.-J. (2005) An experimental study of dissolution-reprecipitation in fluorapatite: fluid infiltration and the formation of monazite. *Contributions to Mineralogy and Petrology* **150**, 268-286.

Harper, C.T. (2012) Geology of the Hoidas Lake REE deposit and surrounding area, northwestern Saskatchewan. *Great Western Minerals Group Ltd. Report*, 72 p.

Hartlaub, R. P., Heaman, L. M., Ashton, K. E., and Chacko, T. (2004) The Archean Murmac Bay Group: evidence for a giant Archean rift in the Rae Province, Canada. *Precambrian Research* **131**, 345-372.

Hartlaub, R.P., Chacko, T., Heaman, L.M., Creaser, R.A., Ashton, K.E., and Simonetti, A. (2005) Ancient (Meso- to Paleoarchean) crust in the Rae Province, Canada: Evidence from Sm-Nd and U-Pb constraints. *Precambrian Research* **141**, 137-153.

Hartlaub, R.P., Heaman, L.M., Chacko, T., and Ashton, K.E. (2007) Circa 2.3 Ga Magmatism of the Arrowsmith Orogeny, Uranium City Region, Western Churchill Craton, Canada. *Journal of Geology* **115**, 181-195.

Harvey, S.E., Young, I., and Billingsley, G. (2002) Geology of the Hoidas Lake area, Ena domain, northwestern Saskatchewan. *Saskatchewan Geological Survey, Saskatchewan Industry and Resources, Summary of Investigations* **2002-2**, *Miscellaneous Report* **2002-4.2**, 13 p.

Hatch, G.P. (2012) Dynamics in the global market for rare earths. *Elements* **8**, 341-346.

Heaman, L.M. (2009) The application of U-Pb geochronology to mafic, ultramafic and alkaline rocks: An evaluation of three mineral standards. *Chemical Geology* **261**, 43-52.

Hedrick, J.B. (2010) Mineral Commodity Summaries – Rare Earths. *United States Geological Survey*, 128-129.

Henderson, P. (1996) The rare earth elements: introduction and review. In: Jones, A.P., Wall, F., and Williams, T. (Eds.): Rare earth minerals: Chemistry, origin and ore deposits. *The Mineralogical Society Series* **7**, 1-19.

Hoffman, P.F. (1988) The United Plates of America, The Birth of a Craton: Early Proterozoic Growth and Assembly of Laurentia. *Earth and Planetary Science Annual Review* **16**, 543-603.

Hoffman, P.F. (1989) Precambrian geology and tectonic history of North America. In: Bally, A.W., Palmer, A.R. (Eds.): The geology of North America - An overview. *Geological Society of America, Boulder, Colorado*, 447-512.

Hogarth, D.D. (1957) The apatite-bearing veins of Nisikkatch Lake, Saskatchewan. *Canadian Mineralogist* **6**, 140-150.

Horváth, L., and Gault R.A. (1990) The mineralogy of Mont Saint-Hilaire, Quebec. *Mineralogical Record* **21**, 282-359.

Irber, W. (1999) The lanthanide tetrad effect and its correlation with K/Rb, Eu/Eu*, Sr/Eu, Y/Ho and Zr/Hf of evolving peraluminous granite suites. *Geochimica et Cosmochimica Acta* **63**, 489-508.

Isnard, H., and Gariépy, C. (2004) Sm-Nd, Lu-Hf and Pb-Pb signatures of gneisses and granitoids from the La Grande belt: Extent of late Archean crustal recycling in the northeastern Superior Province, Canada. *Geochimica et Cosmochimica Acta* **68**, 1099-1113.

Jacobsen, S.B., and Wasserburg, G.J. (1980) Sm-Nd isotopic evolution of Chondrites. *Earth and Planetary Science Letters* **50**, 139-155.

Jiang, N., Sun, S., Chu, X., Mizuta, T., and Ishiyama, D. (2003) Mobilization and enrichment of high-field strength elements during late- and post-magmatic processes in the Shuiquangou syenitic complex, northern China. *Chemical Geology* **200**, 117-128.

Kennedy, A.K., Kamo, S.L., Nasdala, L., and Timms, N.E. (2010) Grenwille skarn titanite: Potential reference material for SIMS U-Th-Pb analysis. *Canadian Mineralogist* **48**, 1423-1443.

Kinny, P.D., and Maas, R. (2003) Lu-Hf and Sm-Nd isotope systems in zircon. In: Hanchar, J.M., Hoskin, P.W.O. (Eds.): Zircon, Reviews in Mineralogy & Geochemistry. *Mineralogical Society of America* **53**, 327-341.

Kontak, D.J. (2004) Analysis of evaporate mounds as a complement to fluid-inclusion thermometric data: Case studies from granitic environments in Nova Scotia and Peru. *Canadian Mineralogist* **42**, 1315-1329.

Košler, J. (2007) Laser ablation ICP-MS - a new dating tool in Earth science. *Proceedings of the Geologists' Association* **118**, 19-24.

Kramers, J.D., and Tolstikhin, I.N. (1997) Two terrestrial lead isotope paradoxes, forward transport modelling, core formation and the history of the continental crust. *Chemical Geology* **139**, 75-110.

Kraus, J., and Ashton, K.E. (2000) New insights into the structural geology and tectonic setting of the Uranium City area, northwestern Saskatchewan. *Saskatchewan Geological Survey, Saskatchewan Energy and Mines, Summary of Investigations* **2000-2**, *Miscellaneous Report* **2000-4.2**, 16-25.

Lentz, D.R., and Fowler, A.D. (1992) A dynamic model for graphic quartz-feldspar intergrowths in granitic pegmatites in the southwestern Grenville Province. *Canadian Mineralogist* **30**, 571-585.

Lira, R., and Ripley, E.M. (1992) Hydrothermal alteration and REE-Th mineralization at the Rodeo de Los Molles deposit, Las Chacras batholith, central Argentina. *Contributions to Mineralogy and Petrology* **110**, 370-386.

London, D. (2005) Geochemistry of alkali and alkaline earth elements in ore-forming granites, pegmatites and rhyolites. In: Linnen, R.L., and Samson, I.M. (Eds.): Rare earth element geochemistry and mineral deposits. *Geological Association of Canada Short Course Notes* **17**, 17-43.

London, D. (2008) Pegmatites. *Mineralogical Association of Canada Special Publication* **10**, 347 p.

London, D. (2009) The origin of primary textures in granitic pegmatites. *Canadian Mineralogist* **47**, 697-724.

Lugmair, G.W., and Marti, K. (1978) Lunar initial ^{143}Nd/^{144}Nd: Differential evolution of the lunar crust and mantle. *Earth and Planetary Science Letters* **39**, 349-357.

Mahan, K. H., and Williams, M. L. (2005) Reconstruction of a large deep-crustal terrane: Implications for the Snowbird tectonic zone and early growth of Laurentia. *Geology* **33**, 385-388.

Mariano, A.N. (1989) Economic geology of rare earth elements. In: Lipin, B.R., and McKay, G.A. (Eds.): Geochemistry and Mineralogy of Rare Earth Elements. *Reviews in Mineralogy* **21**, 309-337.

McDonough, M.R., McNicoll, V.J., Schetselaar, E.M., and Grover, T.W. (2000) Geochronological and kinematic constraints on crustal shortening and escape in a two-sided oblique-slip collisional and magmatic orogen, Paleoproterozoic Taltson magmatic zone, northeastern Alberta. In: Ross, G. (Ed.): The Lithoprobe-Alberta Basement Transect. *Canadian Journal of Earth Science* **37**, 1549-1573.

McDonough, W.F., and Sun, S.S. (1995) The composition of the Earth. *Chemical Geology* **120**, 223-253.

McDowell, F.W., McIntosh, W.C., and Farley, K.A. (2005) A precise ^{40}Ar-^{39}Ar reference age for the Durango apatite (U-Th)/He and fission-tract dating standard. *Chemical Geology* **214**, 249-263.

McFarlane, C.R.M., and McCulloch, M.T. (2007) Coupling of in-situ Sm-Nd systematics and U-Pb dating of monazite and allanite with applications to crustal evolution studies. *Chemical Geology* **245**, 45-60.

McNicoll, V.J., Thériault, R.J., and McDonough, M.R. (2000) Taltson basement gneissic rocks: U-Pb and Nd isotopic constraints on the basement to the Paleoproterozoic Taltson magmatic zone, northeastern Alberta. *Canadian Journal of Earth Sciences* **37**, 1575-1596.

Metz, M.C., Brookins, D.G., Rosenberg, P.E., and Zartman, R.E. (1985) Geology and geochemistry of the Snowbird Deposit, Mineral County, Montana. *Economic Geology* **80**, 394-409.

Mezger, K., and Krogstad, E.J. (1997) Interpretation of discordant U-Pb zircon ages: an evaluation. *Journal of Metamorphic Geology* **15**, 127-140.

Morelli, R., Hartlaub, R.P., Ashton, K.E., and Ansdell, K.M. (2009) Evidence for enrichment of subcontinental lithospheric mantle from Paleoproterozoic intracratonic magmas: Geochemistry and U-Pb geochronology of Martin Group igneous rocks, western Rae Craton, Canada. *Precambrian Research* **175**, 1-15.

Murata, K.J., Rose, H.J., and Carron, M.K. (1953) Systematic variation of rare earths in monazite. *Geochimica et Cosmochimica Acta* **4**, 292-800.

Narasayya, B.L., and Sriramadas, A. (1974) Apatite from apatite-magnetite deposits of Kasipatnam, Andhra Pradesh. *Proceedings of the Indian National Science Academy* **80**, 207-210.

Nesbitt, B.E., and Kelly, W.C. (1977) Magmatic and hydrothermal inclusions in carbonatite of the Magnet Cove Complex, Arkansas. *Contributions to Mineralogy and Petrology* **63**, 271-294.

Normand, C. (2010) Bedrock geology of the Oshowy Lake-Buchanan Lake area and investigation of the REE mineralization potential in the Ena Lake, Bear Lake, and Alces Lake areas, northeastern Zemlak and northern Beaverlodge domains. *Saskatchewan Geological Survey, Saskatchewan Ministry of Energy and Resources, Summary of Investigations* **2010-2**, *Miscellaneous Report* **2010-4.2**, 23 p.

Normand, C. (2014) Rare earths in Saskatchewan: Mineralization types, settings, and distributions. *Saskatchewan Ministry of the Economy, Saskatchewan Geological Survey Report* **264**, 105 p.

Normand, C., McEwan, B., and Ashton, K.E. (2009) Geology and REE mineralization of the Hoidas Lake-Nisikkatch Lake area revisited. *Saskatchewan Geological Survey, Saskatchewan Ministry of Energy and Resources, Summary of Investigations* **2009-2**, *Miscellaneous Report* **2009-4.2**, 17 p.

Oakes, C.S., Bodnar, R.J., and Simonson, J.M. (1990) The system NaCl-$CaCl_2$-H_2O: I. The ice liquidus at 1 atm total pressure. *Geochimica et Cosmochimica Acta* **54**, 603-610.

Paces, J.B., and Miller, J.D. (1993) Precise U-Pb ages of Duluth Complex and related mafic intrusions, northeastern Minnesota - Geochronological insights to physical, petrogenetic, paleomagnetic, and tectonomagmatic processes associated with the 1.1 Ga Midcontinent Rift System. *Journal of Geophysical Research-Solid Earth* **98**, 13997-14013.

Pan, Y., and Fleet, M.E. (2002) Compositions of the apatite-group minerals: Substitution mechanisms and controlling factors. *Reviews in Mineralogy and Geochemistry* **48**, 13-49.

Pan, Y., Fleet, M.E., and Macrae, N.D. (1993) Oriented monazite inclusions in apatite porphyroblasts from the Hemlo gold deposit, Ontario, Canada. *Mineralogical Magazine* **57**, 697-707.

Pandur, K., Ansdell, K.M., Kontak, D.J., Creighton, S., Harper, C.T, Pearson, J., and Halpin, K.M. (2013a) Allanites, melt and fluid inclusions in the Hoidas Lake REE deposit, Saskatchewan, Canada: constraints on a complex magmatic-hydrothermal system. *Geological Association of Canada - Mineralogical Association of Canada Conference Abstract, Winnipeg*

Pandur, K., Ansdell, K.M., and Creighton, S. (2013b) Allanite and apatite compositional variations and implications for the magmatic-hydrothermal evolution of the mineralized veins in the Hoidas Lake REE deposit, Saskatchewan. *Society of Economic Geologists & Canada Foundation Geoscience for Discovery Conference Abstract, Whistler*, Abstract P3.29, 99-100.

Pandur, K., Kontak, D.J., and Ansdell, K.M. (2014) Hydrothermal evolution in the Hoidas Lake vein-type REE deposit, Saskatchewan, Canada: Constraints from fluid inclusion microthermometry and evaporate mound analysis. *Canadian Mineralogist* **52**, 717-744.

Pandur, K., Ansdell, K.M., and Kontak, D.J. (2015) Graphic-textured inclusions in apatite: Evidence for pegmatitic growth in a REE-enriched carbonatitic system. *Geology* **43**, 547-550.

Patchett, P.J. (1983) Importance of the Lu-Hf isotopic system in studies of planetary chronology and chemical evolution. *Geochimica et Cosmochimica Acta* **47**, 81-91.

Patchett, P.J., Kouvo, O., Hedge, C.E., and Tatsumoto, M. (1981) Evolution of continental crust and mantle heterogeneity: evidence from Hf isotopes. *Contributions to Mineralogy and Petrology* **78**, 279-297.

Paton, C., Hellstrom, J.C., Paul, B., Woodhead, J.D., and Hergt, J.M. (2011) Iolite: Freeware for the visualisation and processing of mass spectrometric data. *Journal of Analytical Atomic Spectrometry* **26**, 2508-2518.

Pearce, J.A., Kempton, P.D., Nowell, G.M., and Noble, S.R. (1999) Hf-Nd element isotope perspective on the nature and provenance of mantle and subduction components in Western Pacific arc-basin systems. *Journal of Petrology* **40**, 1579-1611.

Pearson, J. (2006) Great Western Minerals Group Ltd. Saskatchewan Industry and Resources Assessment Report on the 2005-2006 Work Program, Hoidas Lake Rare Earth Project.

Pehrsson, S.J., Berman, R.G., Haijun, Q., Davis, W.J., and Ryan, J. (2010) Pre-Nuna supercontinent reconstruction: the role of the global Arrowsmith Orogeny and its impact in western Canada. *Geoscience Conference, Calgary, Extended Abstracts*, 4 p.

Peterson, T.D., Esperança, S., and LeCheminant, A.N. (1994) Geochemistry and origin of the Proterozoic ultrapotassic rocks of the Churchill Province, Canada. *Mineralogy and Petrology* **51**, 251-276.

Peterson, T.D., van Breemen, O., Sandeman, H., and Cousens, B. (2002) Proterozoic (1.85 to 1.75 Ga) igneous suites of the Western Churchill Province: granitoid and ultrapotassic magmatism in a reworked Archean hinterland. *Precambrian Research* **119**, 73-100.

Petrus, J.A., and Kamber, B.S. (2012) VizualAge: A novel approach to laser ablation ICP-MS U-Pb geochronology data reduction. *Geostandards and Geoanalytical Research* **36**, 247-270.

Pidgeon, R.T. (1992) Recrystallisation of oscillatory zoned zircon: some geochronological and petrological implications. *Contributions to Mineralogy and Petrology* **110**, 463-473.

Rainbird, R.H., Davis, W.J., Pehrsson, S.J., Wodicka, N., Rayner, N., and Skulski, T. (2010) Early Paleoproterozoic supracrustal assemblages of the Rae domain, Nunavut, Canada: Intracratonic basin development during supercontinent break-up and assembly. *Precambrian Research* **181**, 167-186.

Rankin, A.H. (2005) Carbonatite-associated rare earth metal deposits: Composition and evolution of ore-forming fluids: The Fluid Inclusion Evidence. In: Linnen, R.L., and Samson, I.M. (Eds.): Rare earth element geochemistry and mineral deposits. *Geological Association of Canada Short Course Notes* **17**, 299-314.

Rao, A.T. (1976) Study of the apatite-magnetite veins near Kasipatnam, Visakhapatnam District, Andhra Pradesh, India. *Tschermaks Mineralogische und Petrographische Mitteilungen* **23**, 87-103.

Rao, A.T., Rao, K.S.R., and Sriramadas, A. (1969) Allanite from apatite veins near Kasipatnam, Visakhapatnam District, Andhra Pradesh. *Proceedings of the Indian National Science Academy* **69**, 15-19.

Redmond, P.B., Einaudi, M.T., Inan, E.E., Landtwing, M.R., and Heinrich, C.A. (2004) Copper deposition by fluid cooling in intrusion-centered systems: New insights from the Bingham porphyry ore deposit, Utah. *Geology* **32**, 217-220.

Roedder, E., and Bodnar, R.J. (1997) Fluid inclusion studies of hydrothermal ore deposits. Barnes, H.L. (Ed.): Geochemistry of hydrothermal ore deposits. *John Wiley & Sons, New York*, 657-697.

Rogers, M.C. (2011) Saskatchewan descriptive mineral deposit models: Model number A-22: Hoidas Lake-type rare earth element. *Saskatchewan Geological Survey, Open File Report* **2011-57**, 53-54.

Ross, G.M. (2002) Evolution of Precambrian continental lithosphere in Western Canada: results from Lithoprobe studies in Alberta and beyond. *Canadian Journal of Earth Sciences* **39**, 413-437.

Ross, G.M., and Eaton, D.W. (2002) Proterozoic tectonic accretion and growth of western Laurentia: results from Lithoprobe studies in northern Alberta. *Canadian Journal of Earth Sciences* **39**, 313-329.

Salvi, S., and Williams-Jones, A. E. (1990) The role of hydrothermal processes in the granite-hosted Zr, Y, REE deposit at Strange Lake, Quebec/Labrador: evidence from fluid inclusions. *Geochimica et Cosmochimica Acta* **54**, 2403-2418.

Salvi, S., and Williams-Jones, A.E. (2005) Alkaline Granite-Syenite Deposits. In: Linnen, R.L., and Samson, I.M. (Eds.): Rare earth element geochemistry and mineral deposits. *Geological Association of Canada Short Course Notes* **17**, 315-341.

Samson, I.M., and Wood, S.A. (2005) The rare earth elements: behavior in hydrothermal fluids and concentration in hydrothermal mineral deposits, exclusive of alkaline settings. In: Linnen, R.L., and Samson, I.M. (Eds.): Rare earth element geochemistry and mineral deposits. *Geological Association of Canada Short Course Notes* **17**, 269-297.

Samson, I.M., Liu, W., and Williams-Jones, A.E. (1995a) The nature of orthomagmatic hydrothermal fluids in the Oka carbonatite, Quebec, Canada: Evidence from fluid inclusions. *Geochimica et Cosmochimica Acta* **59**, 1963-1977.

Samson, I.M., Williams-Jones, A.E., and Liu, W. (1995b) The chemistry of hydrothermal fluids in carbonatites: Evidence from leachate and SEM-decrepitate analysis of fluid inclusions from Oka, Quebec, Canada. *Geochimica et Cosmochimica Acta* **59**, 1979-1989.

Sandeman, H., Cousens, B.L., Peterson, T., Hemmingway, C., Davis, W.J., Hanmer, S., Tella, S., Ryan, J., and Aspler, L. (2000) Petrochemistry and Nd isotopic evolution of Proterozoic mafic rocks of the western Churchill Province, Nunavut, and their implications for the evolution of the lithospheric mantle. *Geocanada 2000 Meeting, Program with Abstracts*, 5 p.

Schärer, U., Corfu, F., and Demaiffe, D. (1997) U-Pb and Lu-Hf isotopes in baddeleyite and zircon megacrysts from the Mbuji-Mayi kimberlite: constraints on the subcontinental mantle. *Chemical Geology* **143**, 1-16.

Scherer, E., Münker, C., and Mezger, K. (2001) Calibration of the Lutetium-Hafnium Clock. *Science* **293**, 683-687.

Schmitz, M.D., and Bowring, S.A. (2001) U-Pb zircon and titanite systematics of the Fish Canyon Tuff: an assessment of high-precision U-Pb geochronology and its application to young volcanic rocks. *Geochimica et Cosmochimica Acta* **65**, 2571-2587.

Seifert, W. (2005) REE-, Zr-, and Th-rich titanite and associated accessory minerals from a kersantite in the Frankenwald, Germany. *Mineralogy and Petrology* **84**, 129-146.

Sheard, E.R., Williams-Jones, A.E., Heiligmann, M., Pederson, C., and Trueman, D.L. (2012) Controls on the Concentration of Zirconium, Niobium, and the Rare Earth Elements in the Thor Lake Rare Metal Deposit, Northwest Territories, Canada. *Economic Geology* **107**, 81-104.

Simonetti, A., Heaman, L.M., Chacko, T., and Banerjee, N.R. (2006) In situ petrographic thin section U-Pb dating of zircon, monazite, and titanite using laser ablation-MC-ICP-MS. *International Journal of Mass Spectrometry* **253**, 87-97.

Smith, M.P., Henderson, P., and Campbell, L.S. (2000) Fractionation of the REE during hydrothermal processes: Constraints from the Bayan Obo Fe-REE-Nd deposit, Inner Mongolia, China. *Geochimica et Cosmochimica Acta* **64**, 3141-3160.

Steele-MacInnis, M., Lecumberri-Sanchez, P., and Bodnar, R.J. (2012) HokieFlincs_H2O-NACL: A Microsoft Excel spreadsheet for interpreting microthermometric data from fluid inclusions based on the PVTX properties of H_2O-NaCl. *Computers and Geosciences* **49**, 334-337.

Storey, C.D., Jeffries, T.E., and Smith, M. (2006) Common lead-corrected laser ablation ICP-MS U-Pb systematics and geochronology of titanite. *Chemical Geology* **227**, 37-52.

Thomas, R., and Davidson, P. (2012) Water in granite and pegmatite-forming melts. *Ore Geology Reviews* **46**, 32-46.

Thomas, R., and Veksler, I. (2002) Formation of granite pegmatites in the light of melt and fluid inclusion studies and new and old experimental work. *Mineralogical Society of Poland Special Paper* **20**, 44-49.

Thomas, R., Davidson, P., and Beurlen, H. (2012) The competing models for the origin and internal evolution of granitic pegmatites in the light of melt and fluid inclusion research. *Mineralogy and Petrology* **106**, 55-73.

Tomascak, P.B., Krogstad, E.J., and Walker, R.J. (1998) Sm-Nd isotope systematics and the derivation of granitic pegmatites in southwestern Maine. *Canadian Mineralogist* **36**, 327-337.

Valley, P.M., Fisher, C.M., Hanchar, J.M., Lam, R., and Tubrett, M. (2010) Hafnium isotopes in zircon: A tracer of fluid-rock interaction during magnetite–apatite (“Kiruna-type”) mineralization. *Chemical Geology* **275**, 208-220.

Vervoort, J.D., 2010. Hf analysis in zircon by LA-MC-ICPMS: Promise and pitfalls. GSA Abstracts with Programs **42**, no. 5, p. 667 (paper no. 286–9)

Viljoen, M.J., and Scoon, R.N. (1985) The distribution and main geologic features of discordant bodies of iron-rich ultramafic pegmatite in the Bushveld Complex. *Economic Geology* **80**, 1109-1128

Walters, A., Lusty, P., Chetwyn, C., and Hill, A. (2010) Rare earth elements. *British Geological Survey Overview*, 45 p.

Wiedenbeck, M., Allé, P., Corfu, F., Griffin, W.L., Meier, F., Oberli, F., Von Quadt, A., Roddick, J.C., and Spiegel, W. (1995) Three natural zircon standards for U-Th-Pb, Lu-Hf, trace element and REE analyses. *Geostandards Newsletter* **19**, 1-23.

Williams, I.S., Buick, I.S., and Cartwright, I. (1996) An extended episode of early Mesoproterozoic metamorphic fluid flow in the Reynolds Range, central Australia. *Journal of Metamorphic Geology* **14**, 29-48.

Williams, M.L., Jercinovic, M.J., Goncalves, P., and Mahan, K. (2006) Format and philosophy for collecting, compiling, and reporting microprobe monazite ages. *Chemical Geology* **225**, 1-15.

Williams-Jones, A.E., and Palmer, D.A.S. (2002) The evolution of aqueous-carbonic fluids in the Amba Dongar carbonatite, India: implications for fenitisation. *Chemical Geology* **185**, 283-301.

Williams-Jones, A.E., Midgisov, A.A., and Samson, I.M. (2012) Hydrothermal Mobilisation of the Rare Earth Elements: A Tale of "Ceria" and "Yttria". *Elements* **8**, 355-360.

Woodhead, J.D., and Hergt, J.M. (2005) A preliminary appraisal of seven natural zircon reference materials for in situ Hf isotope determination. *Geostandards and Geolanalytical Research* **29**, 183-195.

Wu, Y.B., Zheng, Y.F., Zhang, S.B., Zhao, F.Y., Wu, F.Y., and Liu, X.M. (2007) Zircon U-Pb ages and Hf isotope compositions of migmatite from the North Dabie terrane in China: constraints on partial melting. *Journal of Metamorphic Geology* **25**, 991-1009.

Zeh, A., Gerdes, A., Klemd, R., and Barton Jr., J.M. (2007) Archean to Proterozoic crustal evolution in the Central Zone of the Limpopo Belt (South Africa/ Botswana): constraints from combined U-Pb and Lu-Hf isotope analyses of zircon. *Journal of Petrology* **48**, 1605-1639.

Zheng, Y.F., Wu, Y.B., Zhao, Z.F., Zhang, S.B., Xu, P., and Wu, F.Y. (2005) Metamorphic effect on zircon Lu-Hf and U-Pb isotope systems in ultrahigh-pressure eclogite-facies metagranite and metabasite. *Earth and Planetary Science Letters* **240**, 378-400.

APPENDIX A.

FLUID INCLUSION MICROTHERMOMETRY AND EVAPORATE MOUND ANALYSIS

Table A.1 Summary of thermometric data for fluid inclusions from the Hoidas Lake rare earth element deposit. For each inclusion the data are presented for fluid inclusion assemblages (FIAs) (i.e., range of measurements and mean value of measurements or number where only singular measurement could be made, i.e., Tm(clath), Te, Tm(HH), Tm(ice)). The data is subdivided according to both paragenetic stages (hyalophane-bearing pegmatite far from the mineralization and close to the mineralization, apatite breccia divided into red apatite, green apatite and coarse red apatite, and quartz-carbonate veins) and fluid inclusions (types 1, 2, 3, 4). Table A.1 can be found at MAC Depository of Unpublished Data, document CM52-4_10.3749/canmin.0.0.00005.

Sample (mineral hosting FIAs)	Fluid inclusion type	Phase compositions	Number of studied FIAs	FIA No.	Th(H) range (mean)	Th(L-V) range (mean)	$Th(CO_2)$ range (mean)	Te	Tm(HH) range (mean)	Tm(ice) range (mean)	$Tm(CO_2)$	Tm (clathrate)
Hyalophane-bearing pegmatite far from mineralization (quartz)	Type 1	LCO_2+VCO_2	4	1			9.5-25.2 (11.3)				-56.6	
				2			22.7-25.7 (25.0)				-56.6	
				3			9.2-12.8 (10.1)				-56.5	
				4			9.5-30.2 (13.8)				-56.6	
	Type 2	L+V	3	1				-61		-35-34 (-35)		
				2				-66		-35		
				3						-0.6		
Hyalophane-bearing pegmatite close to mineralization (quartz)	Type 1	LCO_2+VCO_2	4	1			20.0-28.0 (24.8)				-56.3	
				2			15.9-28.4 (24.2)				-56.5	9.6
				3			16.6-30.4 (27.0)				-56.6	
				4			17.3-29.5 (25.5)				-56.6	
	Type 3	L+V+halite	4	1	182-184 (183.0)	185-220 (207.2)						
				2	187-201 (194.0)	196-225 (208.3)						
				3	199-203 (201.0)	209-249 (222.8)						
				4	175-182 (178.3)	181-209 (197.4)						
	Type 4	L+V+(halite)+(hematite)	5	1		138-215 (176.0)						
				2	178	107-200 (138.5)						
				3	180-180 (180.0)	220-290 (240.9)			-23.5	-21.9		
				4	178	208-258 (232.5)						
				5		217-244 (233.7)						

Table A.1 cont.

Sample (mineral hosting FIAs)	Fluid inclusion type	Phase compositions	Number of studied FIAs	FIA No.	Th(H) range (mean)	Th(L-V) range (mean)	Th(CO_2) range (mean)	Te	Tm(HH) range (mean)	Tm(ice) range (mean)	Tm(CO_2)	Tm (clathrate)
Red apatite breccia (apatite)	Type 4	L+V+(halite)+ (hematite)	4	1		99-178 (155.2)						
				2		255-260 (257.5)						
				3		237-250 (243.5)						
				4		211-244 (227.5)						
Green apatite breccia (apatite)	Type 4	L+V+(halite)+ (hematite)	7	1		131-270 (183.4)						
				2		170-243 (207.0)						
				3		182-248 (216.2)		-55		-28.4-26.5 (-27.6)		
				4		190.0						
				5		190-230 (203.0)						
				6		148-325 (236.5)		-63		-21.0		
				7		224-280 (249.8)						
Coarse red apatite (calcite)	Type 4	L+V+(halite)+ (hematite)	8	1		100-116 (109.8)						
				2		92-122 (107.0)						
				3		108-124 (115.8)				-26.0		
				4		99-127 (108.7)				-18.0		
				5		100-152 (120.4)				-5.3		
				6		94-120 (104.9)		-62		-6.2		
				7		74-95 (85.5)						
				8	101	98-106 (101.0)			-47.4	-21.0-17.0 (-19.5)		

Table A.1 cont.

Sample (mineral hosting FIAs)	Fluid inclusion type	Phase compositions	Number of studied FIAs	FIA No.	Th(H) range (mean)	Th(L-V) range (mean)	Th(CO_2) range (mean)	Te	Tm(HH) range (mean)	Tm(ice) range (mean)	Tm(CO_2)	Tm (clathrate)
Quartz-carbonate vein (quartz)	Type 1	LCO_2+VCO_2	5	1			18.0-27.5 (21.3)				-56.3	
				2			6.8-23.7 (15.7)				-56.3	
				3			3.3-30.6 (14.1)				-56.3	10.9
				4			15.2-29.6 (21.7)				-56.4	
				5			6.7-30.1 (19.1)				-56.2	
	Type 3	L+V+halite	6	1	220-250 (231.6)	191-215 (206.0)						
				2	205-256 (241.1)	177-209 (193.3)						
				3	220-220 (220.0)	120-195 (163.8)						
				4	258-270 (264.0)	182-271 (234.2)						
				5	255-290 (272.5)	227-279 (258.9)						
				6	220-315 (278.3)	112-229 (168.6)						
	Type 4	L+V+(halite)+ (hematite)	6	1		218-248 (228.1)		-58	-33.0-32.0 (-32.5)	-26.0-23.0 (-24.8)		
				2		157-232 (193.4)		-59	-43.0-40.0 (-41.7)	-28.0-24.0 (26.0)		
				3		180-237 (213.3)		-60	-33.0-23.0 (-29.3)	-27.0-25.0 (-26.0)		
				4		158-220 (198.4)				-15.4-14.2 (-14.8)		
				5		183-223 (199.5)				-5.7		
				6		166-260 (215.8)				-6.4		

Table A.2 Fluid inclusion microthermometry data.

Sample	Vein generation	Mineral	Assemblage	Assemblage no. in sample	Th(H) (°C)	Th(L-V) (°C)	Th(S2) (°C)	Th(VCO$_2$) (°C)	Te (°C)	Tm(HH) (°C)	Tm(ice) (°C)	Tm(CO$_2$) (°C)	Tm (clathrate) (°C)
881400	pegmatite	quartz	Type 1	1				10.9					
881400	pegmatite	quartz	Type 1	1				10.9					
881400	pegmatite	quartz	Type 1	1				10.7				-56.6	
881400	pegmatite	quartz	Type 1	1				10.7				-56.6	
881400	pegmatite	quartz	Type 1	1				20.4				-56.6	
881400	pegmatite	quartz	Type 1	1				10.7					
881400	pegmatite	quartz	Type 1	1				9.6					
881400	pegmatite	quartz	Type 1	1				9.5					
881400	pegmatite	quartz	Type 1	1				9.5				-56.6	
881400	pegmatite	quartz	Type 1	1				25.2				-56.6	
881400	pegmatite	quartz	Type 1	1				10.5				-56.6	
881400	pegmatite	quartz	Type 1	1				10.9					
881400	pegmatite	quartz	Type 1	1				10.7					
881400	pegmatite	quartz	Type 1	1				10.5					
881400	pegmatite	quartz	Type 1	1				10.7					
881400	pegmatite	quartz	Type 1	1				10.8					
881400	pegmatite	quartz	Type 1	1				10.8					
881400	pegmatite	quartz	Type 1	1				10.8					
881400	pegmatite	quartz	Type 1	1				11.3					
881400	pegmatite	quartz	Type 1	1				10.8					
881400	pegmatite	quartz	Type 1	1				10.8					
881400	pegmatite	quartz	Type 1	1				10.8					
881400	pegmatite	quartz	Type 1	1				10.6				-56.6	
881400	pegmatite	quartz	Type 1	1				11				-56.6	
881400	pegmatite	quartz	Type 1	1				11					
881400	pegmatite	quartz	Type 1	1				11.3				-56.6	
881400	pegmatite	quartz	Type 1	1				10.3					
881400	pegmatite	quartz	Type 1	1				10.6				-56.6	
881400	pegmatite	quartz	Type 1	1				11				-56.6	
881400	pegmatite	quartz	Type 1	1				10.3					
881400	pegmatite	quartz	Type 1	1				10.7					
881400	pegmatite	quartz	Type 1	1				10.8					
881400	pegmatite	quartz	Type 1	1				10.8					
881400	pegmatite	quartz	Type 1	1				10.5					
881400	pegmatite	quartz	Type 1	1				10.5					
881400	pegmatite	quartz	Type 1	1				10.5					
881400	pegmatite	quartz	Type 1	1				10.1					
881400	pegmatite	quartz	Type 1	2				25.1					
881400	pegmatite	quartz	Type 1	2				25.1				-56.6	
881400	pegmatite	quartz	Type 1	2				25.2				-56.6	
881400	pegmatite	quartz	Type 1	2				25				-56.6	
881400	pegmatite	quartz	Type 1	2				25.1					
881400	pegmatite	quartz	Type 1	2				25.1					
881400	pegmatite	quartz	Type 1	2				25.1					
881400	pegmatite	quartz	Type 1	2				25.2				-56.6	
881400	pegmatite	quartz	Type 1	2				25.1					
881400	pegmatite	quartz	Type 1	2				25.1				-56.6	
881400	pegmatite	quartz	Type 1	2				25.1					
881400	pegmatite	quartz	Type 1	2				25.2				-56.6	
881400	pegmatite	quartz	Type 1	2				25.1					
881400	pegmatite	quartz	Type 1	2				25.1				-56.6	
881400	pegmatite	quartz	Type 1	2				25.1					
881400	pegmatite	quartz	Type 1	2				25.1					
881400	pegmatite	quartz	Type 1	2				25					
881400	pegmatite	quartz	Type 1	2				25.3					

Table A.2 cont.

Sample	Vein generation	Mineral	Assemblage	Assemblage no. in sample	Th(H) (°C)	Th(L-V) (°C)	Th(S2) (°C)	Th(VCO$_2$) (°C)	Te (°C)	Tm(HH) (°C)	Tm(ice) (°C)	Tm(CO$_2$) (°C)	Tm (clathrate) (°C)
881400	pegmatite	quartz	Type 1	2				23.2					
881400	pegmatite	quartz	Type 1	2				25.3					
881400	pegmatite	quartz	Type 1	2				25.2					
881400	pegmatite	quartz	Type 1	2				25.2					
881400	pegmatite	quartz	Type 1	2				22.7					
881400	pegmatite	quartz	Type 1	2				25					
881400	pegmatite	quartz	Type 1	2				24.9					
881400	pegmatite	quartz	Type 1	2				25.7					
881400	pegmatite	quartz	Type 1	2				25.2					
881400	pegmatite	quartz	Type 1	2				25					
881400	pegmatite	quartz	Type 1	2				25.1					
881400	pegmatite	quartz	Type 1	2				25.1					
881400	pegmatite	quartz	Type 1	2				25.2					
881400	pegmatite	quartz	Type 1	2				25.1					
881400	pegmatite	quartz	Type 1	2				25.2					
881400	pegmatite	quartz	Type 1	2				25.2					
881400	pegmatite	quartz	Type 1	2				25.1					
881400	pegmatite	quartz	Type 1	2				25.1					
881400	pegmatite	quartz	Type 1	2				25.4					
881400	pegmatite	quartz	Type 1	2				25.1					
881400	pegmatite	quartz	Type 1	3				9.6					
881400	pegmatite	quartz	Type 1	3				9.8					
881400	pegmatite	quartz	Type 1	3				9.6					
881400	pegmatite	quartz	Type 1	3				9.2					
881400	pegmatite	quartz	Type 1	3				9.2				-56.5	
881400	pegmatite	quartz	Type 1	3				9.6				-56.5	
881400	pegmatite	quartz	Type 1	3				9.5					
881400	pegmatite	quartz	Type 1	3				9.8					
881400	pegmatite	quartz	Type 1	3				9.2					
881400	pegmatite	quartz	Type 1	3				10.4				-56.5	
881400	pegmatite	quartz	Type 1	3				10.7				-56.5	
881400	pegmatite	quartz	Type 1	3				10.4					
881400	pegmatite	quartz	Type 1	3				10.1					
881400	pegmatite	quartz	Type 1	3				10.2				-56.5	
881400	pegmatite	quartz	Type 1	3				10.2				-56.5	
881400	pegmatite	quartz	Type 1	3				10.3				-56.5	
881400	pegmatite	quartz	Type 1	3				10.2					
881400	pegmatite	quartz	Type 1	3				10.1					
881400	pegmatite	quartz	Type 1	3				10.2				-56.5	
881400	pegmatite	quartz	Type 1	3				10.3					
881400	pegmatite	quartz	Type 1	3				9.8					
881400	pegmatite	quartz	Type 1	3				10.2					
881400	pegmatite	quartz	Type 1	3				10.1					
881400	pegmatite	quartz	Type 1	3				9.8					
881400	pegmatite	quartz	Type 1	3				9.8					
881400	pegmatite	quartz	Type 1	3				10.2					
881400	pegmatite	quartz	Type 1	3				10.2					
881400	pegmatite	quartz	Type 1	3				9.8					
881400	pegmatite	quartz	Type 1	3				9.8					
881400	pegmatite	quartz	Type 1	3				10.4					
881400	pegmatite	quartz	Type 1	3				10.2					
881400	pegmatite	quartz	Type 1	3				10.1					
881400	pegmatite	quartz	Type 1	3				10.5				-56.5	
881400	pegmatite	quartz	Type 1	3				10.4					
881400	pegmatite	quartz	Type 1	3				10.3					

Table A.2 cont.

Sample	Vein generation	Mineral	Assemblage	Assemblage no. in sample	Th(H) (°C)	Th(L-V) (°C)	Th(S2) (°C)	Th(VCO$_2$) (°C)	Te (°C)	Tm(HH) (°C)	Tm(ice) (°C)	Tm(CO$_2$) (°C)	Tm (clathrate) (°C)
881400	pegmatite	quartz	Type 1	3				10.2					
881400	pegmatite	quartz	Type 1	3				10.5					
881400	pegmatite	quartz	Type 1	3				10.1					
881400	pegmatite	quartz	Type 1	3				10.3				-56.5	
881400	pegmatite	quartz	Type 1	3				10.8				-56.5	
881400	pegmatite	quartz	Type 1	3				12.8				-56.5	
881400	pegmatite	quartz	Type 1	3				10.3					
881400	pegmatite	quartz	Type 1	4				11.2					
881400	pegmatite	quartz	Type 1	4				9.5					
881400	pegmatite	quartz	Type 1	4				14.6					
881400	pegmatite	quartz	Type 1	4				15.2				-56.6	
881400	pegmatite	quartz	Type 1	4				14.6				-56.6	
881400	pegmatite	quartz	Type 1	4				14.6					
881400	pegmatite	quartz	Type 1	4				15.2					
881400	pegmatite	quartz	Type 1	4				15.4					
881400	pegmatite	quartz	Type 1	4				14.6				-56.6	
881400	pegmatite	quartz	Type 1	4				30.1				-56.6	
881400	pegmatite	quartz	Type 1	4				10.9					
881400	pegmatite	quartz	Type 1	4				15					
881400	pegmatite	quartz	Type 1	4				10.9					
881400	pegmatite	quartz	Type 1	4				10.9					
881400	pegmatite	quartz	Type 1	4				30.2					
881400	pegmatite	quartz	Type 1	4				30					
881400	pegmatite	quartz	Type 1	4				11.8				-56.6	
881400	pegmatite	quartz	Type 1	4				11.2				-56.6	
881400	pegmatite	quartz	Type 1	4				11.1				-56.6	
881400	pegmatite	quartz	Type 1	4				11.6					
881400	pegmatite	quartz	Type 1	4				15.3					
881400	pegmatite	quartz	Type 1	4				11.5					
881400	pegmatite	quartz	Type 1	4				11.7					
881400	pegmatite	quartz	Type 1	4				11.5					
881400	pegmatite	quartz	Type 1	4				11.6					
881400	pegmatite	quartz	Type 1	4				10.6					
881400	pegmatite	quartz	Type 1	4				11.5					
881400	pegmatite	quartz	Type 1	4				10.9					
881400	pegmatite	quartz	Type 1	4				11.5				-56.6	
881400	pegmatite	quartz	Type 1	4				11.5				-56.6	
881400	pegmatite	quartz	Type 1	4				30				-56.6	
881400	pegmatite	quartz	Type 1	4				11.1					
881400	pegmatite	quartz	Type 1	4				11.6				-56.6	
881400	pegmatite	quartz	Type 1	4				11.5					
881400	pegmatite	quartz	Type 1	4				11.8					
881400	pegmatite	quartz	Type 1	4				12.2				-56.6	
881400	pegmatite	quartz	Type 1	4				12.6					
881400	pegmatite	quartz	Type 1	4				11.1					
881400	pegmatite	quartz	Type 1	4				10.8					
881400	pegmatite	quartz	Type 1	4				11.1					
881400	pegmatite	quartz	Type 1	4				10.6					
881400	pegmatite	quartz	Type 1	4				10.9					
881400	pegmatite	quartz	Type 2	1					-61		-35		
881400	pegmatite	quartz	Type 2	1							-34		
881400	pegmatite	quartz	Type 2	2					-66		-35		
881400	pegmatite	quartz	Type 2	3							-0.6		
881045	pegmatite	quartz	Type 1	1				25.9				-56.3	
881045	pegmatite	quartz	Type 1	1				20				-56.3	

Table A.2 cont.

Sample	Vein generation	Mineral	Assemblage	Assemblage no. in sample	Th(H) (°C)	Th(L-V) (°C)	Th(S2) (°C)	Th(VCO$_2$) (°C)	Te (°C)	Tm(HH) (°C)	Tm(ice) (°C)	Tm(CO$_2$) (°C)	Tm (clathrate) (°C)
881045	pegmatite	quartz	Type 1	1				24.9					
881045	pegmatite	quartz	Type 1	1				23.8					
881045	pegmatite	quartz	Type 1	1				24.3					
881045	pegmatite	quartz	Type 1	1				26.4				-56.3	
881045	pegmatite	quartz	Type 1	1				26.7				-56.3	
881045	pegmatite	quartz	Type 1	1				25					
881045	pegmatite	quartz	Type 1	1				24.4					
881045	pegmatite	quartz	Type 1	1				24.2					
881045	pegmatite	quartz	Type 1	1				23.5				-56.3	
881045	pegmatite	quartz	Type 1	1				22.8				-56.3	
881045	pegmatite	quartz	Type 1	1				23.9					
881045	pegmatite	quartz	Type 1	1				24.1					
881045	pegmatite	quartz	Type 1	1				27.5					
881045	pegmatite	quartz	Type 1	1				28					
881045	pegmatite	quartz	Type 1	1				24.5					
881045	pegmatite	quartz	Type 1	1				26.1					
881045	pegmatite	quartz	Type 1	2				28.4					
881045	pegmatite	quartz	Type 1	2				26.2					
881045	pegmatite	quartz	Type 1	2				25.7				-56.5	
881045	pegmatite	quartz	Type 1	2				25.3				-56.5	
881045	pegmatite	quartz	Type 1	2				23.1				-56.5	
881045	pegmatite	quartz	Type 1	2				23.1					
881045	pegmatite	quartz	Type 1	2				21.4					
881045	pegmatite	quartz	Type 1	2				25.8					
881045	pegmatite	quartz	Type 1	2				24.2					
881045	pegmatite	quartz	Type 1	2				23.8					
881045	pegmatite	quartz	Type 1	2				25.5					
881045	pegmatite	quartz	Type 1	2				25.2					
881045	pegmatite	quartz	Type 1	2				25.8					
881045	pegmatite	quartz	Type 1	2				15.9					
881045	pegmatite	quartz	Type 1	2				25.5					
881045	pegmatite	quartz	Type 1	2				25.5					
881045	pegmatite	quartz	Type 1	2				24				-56.5	
881045	pegmatite	quartz	Type 1	2				24.7				-56.5	9.6
881045	pegmatite	quartz	Type 1	2				21.5					
881045	pegmatite	quartz	Type 1	2				22.8					
881045	pegmatite	quartz	Type 1	2				22.4					
881045	pegmatite	quartz	Type 1	2				23.8					
881045	pegmatite	quartz	Type 1	2				24.1					
881045	pegmatite	quartz	Type 1	2				26.8					
881045	pegmatite	quartz	Type 1	3				29.6					
881045	pegmatite	quartz	Type 1	3				29.5				-56.6	
881045	pegmatite	quartz	Type 1	3				28.5					
881045	pegmatite	quartz	Type 1	3				25.4					
881045	pegmatite	quartz	Type 1	3				21.4				-56.6	
881045	pegmatite	quartz	Type 1	3				23				-56.6	
881045	pegmatite	quartz	Type 1	3				27.8					
881045	pegmatite	quartz	Type 1	3				27.5					
881045	pegmatite	quartz	Type 1	3				26.7				-56.6	
881045	pegmatite	quartz	Type 1	3				26.8				-56.6	
881045	pegmatite	quartz	Type 1	3				16.6					
881045	pegmatite	quartz	Type 1	3				21.4					
881045	pegmatite	quartz	Type 1	3				25.5					
881045	pegmatite	quartz	Type 1	3				29.2					
881045	pegmatite	quartz	Type 1	3				30					

Table A.2 cont.

Sample	Vein generation	Mineral	Assemblage	Assemblage no. in sample	Th(H) (°C)	Th(L-V) (°C)	Th(S2) (°C)	Th(VCO$_2$) (°C)	Te (°C)	Tm(HH) (°C)	Tm(ice) (°C)	Tm(CO$_2$) (°C)	Tm (clathrate) (°C)
881045	pegmatite	quartz	Type 1	3				30.4					
881045	pegmatite	quartz	Type 1	3				30.3					
881045	pegmatite	quartz	Type 1	3				29.6					
881045	pegmatite	quartz	Type 1	3				30.4					
881045	pegmatite	quartz	Type 1	3				19.2					
881045	pegmatite	quartz	Type 1	3				30.4					
881045	pegmatite	quartz	Type 1	3				29					
881045	pegmatite	quartz	Type 1	3				29				-56.6	
881045	pegmatite	quartz	Type 1	3				29.4					
881045	pegmatite	quartz	Type 1	3				27.7				-56.6	
881045	pegmatite	quartz	Type 1	3				27.6					
881045	pegmatite	quartz	Type 1	4				28.8					
881045	pegmatite	quartz	Type 1	4				29.3					
881045	pegmatite	quartz	Type 1	4				29					
881045	pegmatite	quartz	Type 1	4				28.6					
881045	pegmatite	quartz	Type 1	4				29					
881045	pegmatite	quartz	Type 1	4				27.6					
881045	pegmatite	quartz	Type 1	4				27.3				-56.6	
881045	pegmatite	quartz	Type 1	4				26				-56.6	
881045	pegmatite	quartz	Type 1	4				28.2				-56.6	
881045	pegmatite	quartz	Type 1	4				29.2					
881045	pegmatite	quartz	Type 1	4				28.8					
881045	pegmatite	quartz	Type 1	4				28.4					
881045	pegmatite	quartz	Type 1	4				29					
881045	pegmatite	quartz	Type 1	4				24.2					
881045	pegmatite	quartz	Type 1	4				29.4					
881045	pegmatite	quartz	Type 1	4				29.4					
881045	pegmatite	quartz	Type 1	4				29.4					
881045	pegmatite	quartz	Type 1	4				29.5					
881045	pegmatite	quartz	Type 1	4				25.4				-56.6	
881045	pegmatite	quartz	Type 1	4				22.8				-56.6	
881045	pegmatite	quartz	Type 1	4				23.7					
881045	pegmatite	quartz	Type 1	4				19.9					
881045	pegmatite	quartz	Type 1	4				22.1					
881045	pegmatite	quartz	Type 1	4				25					
881045	pegmatite	quartz	Type 1	4				22.5				-56.6	
881045	pegmatite	quartz	Type 1	4				19.9					
881045	pegmatite	quartz	Type 1	4				20.7					
881045	pegmatite	quartz	Type 1	4				20.3				-56.6	
881045	pegmatite	quartz	Type 1	4				17.8				-56.6	
881045	pegmatite	quartz	Type 1	4				21.6					
881045	pegmatite	quartz	Type 1	4				17.3					
881045	pegmatite	quartz	Type 1	4				23.9					
881045	pegmatite	quartz	Type 1	4				24.4					
881045	pegmatite	quartz	Type 1	4				27.4					
881045	pegmatite	quartz	Type 3	1		220							
881045	pegmatite	quartz	Type 3	1	184	205							
881045	pegmatite	quartz	Type 3	1	182	208							
881045	pegmatite	quartz	Type 3	1		218							
881045	pegmatite	quartz	Type 3	1		185							
881045	pegmatite	quartz	Type 3	2		> 250							
881045	pegmatite	quartz	Type 3	2		208							
881045	pegmatite	quartz	Type 3	2	187	225							
881045	pegmatite	quartz	Type 3	2	201	204							
881045	pegmatite	quartz	Type 3	2		196							

Table A.2 cont.

Sample	Vein generation	Mineral	Assemblage	Assemblage no. in sample	Th(H) (°C)	Th(L-V) (°C)	Th(S2) (°C)	Th(VCO$_2$) (°C)	Te (°C)	Tm(HH) (°C)	Tm(ice) (°C)	Tm(CO$_2$) (°C)	Tm (clathrate) (°C)
881045	pegmatite	quartz	Type 3	3		249							
881045	pegmatite	quartz	Type 3	3	203	224							
881045	pegmatite	quartz	Type 3	3	199	221							
881045	pegmatite	quartz	Type 3	3		209							
881045	pegmatite	quartz	Type 3	3		218							
881045	pegmatite	quartz	Type 3	3		216							
881045	pegmatite	quartz	Type 3	4		201							
881045	pegmatite	quartz	Type 3	4		190							
881045	pegmatite	quartz	Type 3	4	182	209							
881045	pegmatite	quartz	Type 3	4	178	206							
881045	pegmatite	quartz	Type 3	4	175	181							
881045	pegmatite	quartz	Type 4	1		213							
881045	pegmatite	quartz	Type 4	1		215							
881045	pegmatite	quartz	Type 4	1		184							
881045	pegmatite	quartz	Type 4	1		173							
881045	pegmatite	quartz	Type 4	1		208							
881045	pegmatite	quartz	Type 4	1		139							
881045	pegmatite	quartz	Type 4	1		138							
881045	pegmatite	quartz	Type 4	1		138							
881045	pegmatite	quartz	Type 4	2		143							
881045	pegmatite	quartz	Type 4	2		134							
881045	pegmatite	quartz	Type 4	2		200							
881045	pegmatite	quartz	Type 4	2		107							
881045	pegmatite	quartz	Type 4	2		111							
881045	pegmatite	quartz	Type 4	2	178	136							
881045	pegmatite	quartz	Type 4	3		240							
881045	pegmatite	quartz	Type 4	3		290							
881045	pegmatite	quartz	Type 4	3	180	235							
881045	pegmatite	quartz	Type 4	3	180	226							
881045	pegmatite	quartz	Type 4	3		235							
881045	pegmatite	quartz	Type 4	3		238							
881045	pegmatite	quartz	Type 4	3		220							
881045	pegmatite	quartz	Type 4	3		254							
881045	pegmatite	quartz	Type 4	3		230							
881045	pegmatite	quartz	Type 4	3						-23.5	-21.9		
881045	pegmatite	quartz	Type 4	4		237							
881045	pegmatite	quartz	Type 4	4	178	215							
881045	pegmatite	quartz	Type 4	4		224							
881045	pegmatite	quartz	Type 4	4		208							
881045	pegmatite	quartz	Type 4	4		258							
881045	pegmatite	quartz	Type 4	4		253							
881045	pegmatite	quartz	Type 4	5		217							
881045	pegmatite	quartz	Type 4	5		230							
881045	pegmatite	quartz	Type 4	5		231							
881045	pegmatite	quartz	Type 4	5		240							
881045	pegmatite	quartz	Type 4	5		240							
881045	pegmatite	quartz	Type 4	5		244							
881041	red apatite breccia	apatite	Type 4	1		166							
881041	red apatite breccia	apatite	Type 4	1		168							
881041	red apatite breccia	apatite	Type 4	1		142							
881041	red apatite breccia	apatite	Type 4	1		99							
881041	red apatite breccia	apatite	Type 4	1		178							
881041	red apatite breccia	apatite	Type 4	1		178							
881060	red apatite breccia	quartz	(L+V+H+S2)	1		134							
881060	red apatite breccia	quartz	(L+V+H+S2)	1	308	207							

Table A.2 cont.

Sample	Vein generation	Mineral	Assemblage	Assemblage no. in sample	Th(H) (°C)	Th(L-V) (°C)	Th(S2) (°C)	Th(VCO$_2$) (°C)	Te (°C)	Tm(HH) (°C)	Tm(ice) (°C)	Tm(CO$_2$) (°C)	Tm (clathrate) (°C)
881060	red apatite breccia	quartz	(L+V+H+S2)	1	345	211							
881060	red apatite breccia	quartz	(L+V+H+S2)	1		230							
881060	red apatite breccia	quartz	(L+V+H+S2)	1		126							
881060	red apatite breccia	quartz	(L+V+H+S2)	1	315	224							
881060	red apatite breccia	quartz	(L+V+H+S2)	1	370	207							
881060	red apatite breccia	quartz	(L+V+H+S2)	1		208							
881060	red apatite breccia	quartz	(L+V+H+S2)	1		214							
517430	red apatite breccia	apatite	Type 4	1		255							
517430	red apatite breccia	apatite	Type 4	1		260							
517430	red apatite breccia	apatite	Type 4	2		250							
517430	red apatite breccia	apatite	Type 4	2		237							
517430	red apatite breccia	apatite	Type 4	3		244							
517430	red apatite breccia	apatite	Type 4	3		211							
517423	green apatite breccia	apatite	Type 4	1		227							
517423	green apatite breccia	apatite	Type 4	1		270							
517423	green apatite breccia	apatite	Type 4	1		131							
517423	green apatite breccia	apatite	Type 4	1		146							
517423	green apatite breccia	apatite	Type 4	1		143							
517423	green apatite breccia	apatite	Type 4	2		243							
517423	green apatite breccia	apatite	Type 4	2		208							
517423	green apatite breccia	apatite	Type 4	2		170							
517423	green apatite breccia	apatite	Type 4	3		182			-55		-28.4		
517423	green apatite breccia	apatite	Type 4	3		220					-26.5		
517423	green apatite breccia	apatite	Type 4	3		228					-28		
517423	green apatite breccia	apatite	Type 4	3		203							
517423	green apatite breccia	apatite	Type 4	3		248							
517423	green apatite breccia	apatite	Type 4	3		> 250							
517423	green apatite breccia	apatite	Type 4	3		> 250							
517423	green apatite breccia	apatite	Type 4	4		190							
517423	green apatite breccia	apatite	Type 4	5		230							
517423	green apatite breccia	apatite	Type 4	5		200							
517423	green apatite breccia	apatite	Type 4	5		192							
517423	green apatite breccia	apatite	Type 4	5		190							
517423	green apatite breccia	apatite	Type 4	6		148							
517423	green apatite breccia	apatite	Type 4	6		325			-63		-21		
517423	green apatite breccia	apatite	Type 4	7		280							
517423	green apatite breccia	apatite	Type 4	7		225							
517423	green apatite breccia	apatite	Type 4	7		270							
517423	green apatite breccia	apatite	Type 4	7		224							
516680	coarse red apatite	calcite	Type 4	1		112							
516680	coarse red apatite	calcite	Type 4	1		116							
516680	coarse red apatite	calcite	Type 4	1		111							
516680	coarse red apatite	calcite	Type 4	1		100							
516680	coarse red apatite	calcite	Type 4	2		92							
516680	coarse red apatite	calcite	Type 4	2		122							
516680	coarse red apatite	calcite	Type 4	3		124							
516680	coarse red apatite	calcite	Type 4	3		112					-26		
516680	coarse red apatite	calcite	Type 4	3		108							
516680	coarse red apatite	calcite	Type 4	3		119							
516680	coarse red apatite	calcite	Type 4	3		116							
516680	coarse red apatite	calcite	Type 4	4		115							
516680	coarse red apatite	calcite	Type 4	4		127					-18		
516680	coarse red apatite	calcite	Type 4	4		100							
516680	coarse red apatite	calcite	Type 4	4		105							
516680	coarse red apatite	calcite	Type 4	4		99							

Table A.2 cont.

Sample	Vein generation	Mineral	Assemblage	Assemblage no. in sample	Th(H) (°C)	Th(L-V) (°C)	Th(S2) (°C)	Th(VCO$_2$) (°C)	Te (°C)	Tm(HH) (°C)	Tm(ice) (°C)	Tm(CO$_2$) (°C)	Tm (clathrate) (°C)
516680	coarse red apatite	calcite	Type 4	4		106							
516680	coarse red apatite	calcite	Type 4	5		140							
516680	coarse red apatite	calcite	Type 4	5		101							
516680	coarse red apatite	calcite	Type 4	5		109							
516680	coarse red apatite	calcite	Type 4	5		100							
516680	coarse red apatite	calcite	Type 4	5		152							
516680	coarse red apatite	calcite	Type 4	5							-5.3		
516680	coarse red apatite	calcite	Type 4	6		100							
516680	coarse red apatite	calcite	Type 4	6		120							
516680	coarse red apatite	calcite	Type 4	6		120			-62		-6.2		
516680	coarse red apatite	calcite	Type 4	6		94							
516680	coarse red apatite	calcite	Type 4	6		110							
516680	coarse red apatite	calcite	Type 4	6		95							
516680	coarse red apatite	calcite	Type 4	6		95							
516680	coarse red apatite	calcite	Type 4	7		89							
516680	coarse red apatite	calcite	Type 4	7		95							
516680	coarse red apatite	calcite	Type 4	7		84							
516680	coarse red apatite	calcite	Type 4	7		74							
516680	coarse red apatite	calcite	Type 4	8		99							
516680	coarse red apatite	calcite	Type 4	8							-19.9		
516680	coarse red apatite	calcite	Type 4	8	101	106				-47.4	-21		
516680	coarse red apatite	calcite	Type 4	8		98					-17		
516680	coarse red apatite	calcite	Type 4	8		101					-20		
517412	quartz-carbonate vein	quartz	Type 3	1	235	205							
517412	quartz-carbonate vein	quartz	Type 3	1	> 250	211							
517412	quartz-carbonate vein	quartz	Type 3	1	230	191							
517412	quartz-carbonate vein	quartz	Type 3	1		214							
517412	quartz-carbonate vein	quartz	Type 3	1	223	215							
517412	quartz-carbonate vein	quartz	Type 3	1	220	212							
517412	quartz-carbonate vein	quartz	Type 3	1	250	194							
517412	quartz-carbonate vein	quartz	Type 3	2	240	209							
517412	quartz-carbonate vein	quartz	Type 3	2	237	177							
517412	quartz-carbonate vein	quartz	Type 3	2	253	186							
517412	quartz-carbonate vein	quartz	Type 3	2	250	197							
517412	quartz-carbonate vein	quartz	Type 3	2	256								
517412	quartz-carbonate vein	quartz	Type 3	2	247	182							
517412	quartz-carbonate vein	quartz	Type 3	2	241	198							
517412	quartz-carbonate vein	quartz	Type 3	2	205	204							
517412	quartz-carbonate vein	quartz	Type 3	3	220	195							
517412	quartz-carbonate vein	quartz	Type 3	3	220	120							
517412	quartz-carbonate vein	quartz	Type 3	3		190							
517412	quartz-carbonate vein	quartz	Type 3	3		150							
517412	quartz-carbonate vein	quartz	Type 4	1		228			-58	-33	-26		
517412	quartz-carbonate vein	quartz	Type 4	1		236							
517412	quartz-carbonate vein	quartz	Type 4	1		222				-32			
517412	quartz-carbonate vein	quartz	Type 4	1		218			-58		-24		
517412	quartz-carbonate vein	quartz	Type 4	1		223							
517412	quartz-carbonate vein	quartz	Type 4	1		228							
517412	quartz-carbonate vein	quartz	Type 4	1		230			-58				
517412	quartz-carbonate vein	quartz	Type 4	1		220			-58		-26		
517412	quartz-carbonate vein	quartz	Type 4	1		248					-23		
517412	quartz-carbonate vein	quartz	Type 4	2		232			-59		-24		
517412	quartz-carbonate vein	quartz	Type 4	2		227			-59	-40			
517412	quartz-carbonate vein	quartz	Type 4	2		213			-59		-28		
517412	quartz-carbonate vein	quartz	Type 4	2		191			-59	-42			

Table A.2 cont.

Sample	Vein generation	Mineral	Assemblage	Assemblage no. in sample	Th(H) (°C)	Th(L-V) (°C)	Th(S2) (°C)	Th(VCO$_2$) (°C)	Te (°C)	Tm(HH) (°C)	Tm(ice) (°C)	Tm(CO$_2$) (°C)	Tm (clathrate) (°C)
517412	quartz-carbonate vein	quartz	Type 4	2		160			-59	-43			
517412	quartz-carbonate vein	quartz	Type 4	2		157							
517412	quartz-carbonate vein	quartz	Type 4	2		174							
517412	quartz-carbonate vein	quartz	Type 4	3					-65		-26		
517412	quartz-carbonate vein	quartz	Type 4	3		201			-60/-55	-32	-25		
517412	quartz-carbonate vein	quartz	Type 4	3		215				-33	-27		
517412	quartz-carbonate vein	quartz	Type 4	3		233			-57	-23			
517412	quartz-carbonate vein	quartz	Type 4	3		227							
517412	quartz-carbonate vein	quartz	Type 4	3		237							
517412	quartz-carbonate vein	quartz	Type 4	3		180							
517412	quartz-carbonate vein	quartz	Type 4	3		200							
881063	quartz-carbonate vein	quartz	Type 1	1				24.3				-56.4	
881063	quartz-carbonate vein	quartz	Type 1	1				19.5				-56.4	
881063	quartz-carbonate vein	quartz	Type 1	1				27.5				-56.3	
881063	quartz-carbonate vein	quartz	Type 1	1				19.5				-56.3	
881063	quartz-carbonate vein	quartz	Type 1	1				19				-56.3	
881063	quartz-carbonate vein	quartz	Type 1	1				18				-56.2	
881063	quartz-carbonate vein	quartz	Type 1	2				18.3					
881063	quartz-carbonate vein	quartz	Type 1	2				17.4				-56.3	
881063	quartz-carbonate vein	quartz	Type 1	2				18.9				-56.3	
881063	quartz-carbonate vein	quartz	Type 1	2				18.3					
881063	quartz-carbonate vein	quartz	Type 1	2				18.1					
881063	quartz-carbonate vein	quartz	Type 1	2				18.8				-56.3	
881063	quartz-carbonate vein	quartz	Type 1	2				19.7					
881063	quartz-carbonate vein	quartz	Type 1	2				16.4					
881063	quartz-carbonate vein	quartz	Type 1	2				13.9					
881063	quartz-carbonate vein	quartz	Type 1	2				20.5				-56.2	
881063	quartz-carbonate vein	quartz	Type 1	2				17.7					
881063	quartz-carbonate vein	quartz	Type 1	2				15					
881063	quartz-carbonate vein	quartz	Type 1	2				14.2				-56.3	
881063	quartz-carbonate vein	quartz	Type 1	2				14.2				-56.3	
881063	quartz-carbonate vein	quartz	Type 1	2				18					
881063	quartz-carbonate vein	quartz	Type 1	2				15.5					
881063	quartz-carbonate vein	quartz	Type 1	2				15.6					
881063	quartz-carbonate vein	quartz	Type 1	2				13.5					
881063	quartz-carbonate vein	quartz	Type 1	2				6.8					
881063	quartz-carbonate vein	quartz	Type 1	2				9.2					
881063	quartz-carbonate vein	quartz	Type 1	2				6.9					
881063	quartz-carbonate vein	quartz	Type 1	2				13.5				-56.2	
881063	quartz-carbonate vein	quartz	Type 1	2				22.8					
881063	quartz-carbonate vein	quartz	Type 1	2				7.7					
881063	quartz-carbonate vein	quartz	Type 1	2				22.1					
881063	quartz-carbonate vein	quartz	Type 1	2				8.7					
881063	quartz-carbonate vein	quartz	Type 1	2				17.6					
881063	quartz-carbonate vein	quartz	Type 1	2				16					
881063	quartz-carbonate vein	quartz	Type 1	2				19.2					
881063	quartz-carbonate vein	quartz	Type 1	2				11					
881063	quartz-carbonate vein	quartz	Type 1	2				23.7					
881063	quartz-carbonate vein	quartz	Type 1	2				15.1					
881063	quartz-carbonate vein	quartz	Type 1	2				12.6					
881063	quartz-carbonate vein	quartz	Type 1	3				14					
881063	quartz-carbonate vein	quartz	Type 1	3				15.7					
881063	quartz-carbonate vein	quartz	Type 1	3				19.8					
881063	quartz-carbonate vein	quartz	Type 1	3				3.3					
881063	quartz-carbonate vein	quartz	Type 1	3				6.8					

Table A.2 cont.

Sample	Vein generation	Mineral	Assemblage	Assemblage no. in sample	Th(H) (°C)	Th(L-V) (°C)	Th(S2) (°C)	Th(VCO$_2$) (°C)	Te (°C)	Tm(HH) (°C)	Tm(ice) (°C)	Tm(CO$_2$) (°C)	Tm (clathrate) (°C)
881063	quartz-carbonate vein	quartz	Type 1	3				3.6					
881063	quartz-carbonate vein	quartz	Type 1	3				3.9				-56.3	
881063	quartz-carbonate vein	quartz	Type 1	3				7.2				-56.3	
881063	quartz-carbonate vein	quartz	Type 1	3				13.2				-56.3	
881063	quartz-carbonate vein	quartz	Type 1	3				14.8					
881063	quartz-carbonate vein	quartz	Type 1	3				10				-56.3	
881063	quartz-carbonate vein	quartz	Type 1	3				12.7					
881063	quartz-carbonate vein	quartz	Type 1	3				15.8					
881063	quartz-carbonate vein	quartz	Type 1	3				9.4					
881063	quartz-carbonate vein	quartz	Type 1	3				19.9					
881063	quartz-carbonate vein	quartz	Type 1	3				12.5				-56.3	
881063	quartz-carbonate vein	quartz	Type 1	3				15.5				-56.3	
881063	quartz-carbonate vein	quartz	Type 1	3				13					
881063	quartz-carbonate vein	quartz	Type 1	3				15.5				-56.3	
881063	quartz-carbonate vein	quartz	Type 1	3				10					
881063	quartz-carbonate vein	quartz	Type 1	3				9.7					
881063	quartz-carbonate vein	quartz	Type 1	3				30.6					10.9
881063	quartz-carbonate vein	quartz	Type 1	3				22					
881063	quartz-carbonate vein	quartz	Type 1	3				22					
881063	quartz-carbonate vein	quartz	Type 1	3				> 60					
881063	quartz-carbonate vein	quartz	Type 1	3				8.7					
881063	quartz-carbonate vein	quartz	Type 1	3				11.9					
881063	quartz-carbonate vein	quartz	Type 1	3				7					
881063	quartz-carbonate vein	quartz	Type 1	3				11.9					
881063	quartz-carbonate vein	quartz	Type 1	3				22.3				-56.2	
881063	quartz-carbonate vein	quartz	Type 1	3				22.3				-56.2	
881063	quartz-carbonate vein	quartz	Type 1	3				17.9				-56.2	
881063	quartz-carbonate vein	quartz	Type 1	3				14.5					
881063	quartz-carbonate vein	quartz	Type 1	3				14.5					
881063	quartz-carbonate vein	quartz	Type 1	3				14.5					
881063	quartz-carbonate vein	quartz	Type 1	3				8.5					
881063	quartz-carbonate vein	quartz	Type 1	3				13					
881063	quartz-carbonate vein	quartz	Type 1	3				17.4					
881063	quartz-carbonate vein	quartz	Type 1	3				29.5					
881063	quartz-carbonate vein	quartz	Type 1	4				23					
881063	quartz-carbonate vein	quartz	Type 1	4				18.3					
881063	quartz-carbonate vein	quartz	Type 1	4				19.5					
881063	quartz-carbonate vein	quartz	Type 1	4				20.5					
881063	quartz-carbonate vein	quartz	Type 1	4				20.2					
881063	quartz-carbonate vein	quartz	Type 1	4				20.2					
881063	quartz-carbonate vein	quartz	Type 1	4				25.1				-56.5	
881063	quartz-carbonate vein	quartz	Type 1	4				26.3				-56.6	
881063	quartz-carbonate vein	quartz	Type 1	4				26.7					
881063	quartz-carbonate vein	quartz	Type 1	4				21.6				-56.3	
881063	quartz-carbonate vein	quartz	Type 1	4				22.8				-56.3	
881063	quartz-carbonate vein	quartz	Type 1	4				17.8				-56.3	
881063	quartz-carbonate vein	quartz	Type 1	4				22.4					
881063	quartz-carbonate vein	quartz	Type 1	4				21.2					
881063	quartz-carbonate vein	quartz	Type 1	4				22.8					
881063	quartz-carbonate vein	quartz	Type 1	4				15.2					
881063	quartz-carbonate vein	quartz	Type 1	4				16.2					
881063	quartz-carbonate vein	quartz	Type 1	4				22.2					
881063	quartz-carbonate vein	quartz	Type 1	4				16					
881063	quartz-carbonate vein	quartz	Type 1	4				17.6					
881063	quartz-carbonate vein	quartz	Type 1	4				24.6					

Table A.2 cont.

Sample	Vein generation	Mineral	Assemblage	Assemblage no. in sample	Th(H) (°C)	Th(L-V) (°C)	Th(S2) (°C)	Th(VCO$_2$) (°C)	Te (°C)	Tm(HH) (°C)	Tm(ice) (°C)	Tm(CO$_2$) (°C)	Tm (clathrate) (°C)
881063	quartz-carbonate vein	quartz	Type 1	4				22.9				-56.3	
881063	quartz-carbonate vein	quartz	Type 1	4				23.6					
881063	quartz-carbonate vein	quartz	Type 1	4				22.8					
881063	quartz-carbonate vein	quartz	Type 1	4				23.8					
881063	quartz-carbonate vein	quartz	Type 1	4				16				-56.3	
881063	quartz-carbonate vein	quartz	Type 1	4				22.5					
881063	quartz-carbonate vein	quartz	Type 1	4				19.4					
881063	quartz-carbonate vein	quartz	Type 1	4				19.9					
881063	quartz-carbonate vein	quartz	Type 1	4				27.3					
881063	quartz-carbonate vein	quartz	Type 1	4				24.3					
881063	quartz-carbonate vein	quartz	Type 1	4				17.6					
881063	quartz-carbonate vein	quartz	Type 1	4				22.3					
881063	quartz-carbonate vein	quartz	Type 1	4				23.6					
881063	quartz-carbonate vein	quartz	Type 1	4				25.2					
881063	quartz-carbonate vein	quartz	Type 1	4				22.1					
881063	quartz-carbonate vein	quartz	Type 1	4				26.2					
881063	quartz-carbonate vein	quartz	Type 1	4				29.6					
881063	quartz-carbonate vein	quartz	Type 1	4				16.1					
881063	quartz-carbonate vein	quartz	Type 1	5				16.5					
881063	quartz-carbonate vein	quartz	Type 1	5				20.5					
881063	quartz-carbonate vein	quartz	Type 1	5				26.1					
881063	quartz-carbonate vein	quartz	Type 1	5				26.1					
881063	quartz-carbonate vein	quartz	Type 1	5				20.5					
881063	quartz-carbonate vein	quartz	Type 1	5				20.4					
881063	quartz-carbonate vein	quartz	Type 1	5				28.5					
881063	quartz-carbonate vein	quartz	Type 1	5				19				-56.2	
881063	quartz-carbonate vein	quartz	Type 1	5				23.1				-56.2	
881063	quartz-carbonate vein	quartz	Type 1	5				24.2				-56.2	
881063	quartz-carbonate vein	quartz	Type 1	5				30.1				-56.2	
881063	quartz-carbonate vein	quartz	Type 1	5				25.6					
881063	quartz-carbonate vein	quartz	Type 1	5				> 55					
881063	quartz-carbonate vein	quartz	Type 1	5				26					
881063	quartz-carbonate vein	quartz	Type 1	5				26.4					
881063	quartz-carbonate vein	quartz	Type 1	5				24.2					
881063	quartz-carbonate vein	quartz	Type 1	5				27.6					
881063	quartz-carbonate vein	quartz	Type 1	5				26					
881063	quartz-carbonate vein	quartz	Type 1	5				22.6				-56.2	
881063	quartz-carbonate vein	quartz	Type 1	5				21.9				-56.2	
881063	quartz-carbonate vein	quartz	Type 1	5				6.9					
881063	quartz-carbonate vein	quartz	Type 1	5				8					
881063	quartz-carbonate vein	quartz	Type 1	5				6.9					
881063	quartz-carbonate vein	quartz	Type 1	5				9.6					
881063	quartz-carbonate vein	quartz	Type 1	5				22.3					
881063	quartz-carbonate vein	quartz	Type 1	5				15.4					
881063	quartz-carbonate vein	quartz	Type 1	5				23.8				-56.3	
881063	quartz-carbonate vein	quartz	Type 1	5				22					
881063	quartz-carbonate vein	quartz	Type 1	5				7.3					
881063	quartz-carbonate vein	quartz	Type 1	5				6.7					
881063	quartz-carbonate vein	quartz	Type 1	5				16.7					
881063	quartz-carbonate vein	quartz	Type 1	5				7.7					
881063	quartz-carbonate vein	quartz	Type 1	5				12.8					
881063	quartz-carbonate vein	quartz	Type 1	5				15.1					
881063	quartz-carbonate vein	quartz	Type 1	5				7.5					
881063	quartz-carbonate vein	quartz	Type 1	5				24.1					
881063	quartz-carbonate vein	quartz	Type 3	1	270	231							

Table A.2 cont.

Sample	Vein generation	Mineral	Assemblage	Assemblage no. in sample	Th(H) (°C)	Th(L-V) (°C)	Th(S2) (°C)	Th(VCO$_2$) (°C)	Te (°C)	Tm(HH) (°C)	Tm(ice) (°C)	Tm(CO$_2$) (°C)	Tm (clathrate) (°C)
881063	quartz-carbonate vein	quartz	Type 3	1		252							
881063	quartz-carbonate vein	quartz	Type 3	1		235							
881063	quartz-carbonate vein	quartz	Type 3	1		271							
881063	quartz-carbonate vein	quartz	Type 3	1	258	182							
881063	quartz-carbonate vein	quartz	Type 3	2	255	242							
881063	quartz-carbonate vein	quartz	Type 3	2		264	246						
881063	quartz-carbonate vein	quartz	Type 3	2		278	215						
881063	quartz-carbonate vein	quartz	Type 3	2		254							
881063	quartz-carbonate vein	quartz	Type 3	2		279							
881063	quartz-carbonate vein	quartz	Type 3	2		227	210						
881063	quartz-carbonate vein	quartz	Type 3	2	290	268	210						
881063	quartz-carbonate vein	quartz	Type 3	3		190							
881063	quartz-carbonate vein	quartz	Type 3	3	300	229							
881063	quartz-carbonate vein	quartz	Type 3	3	315	148							
881063	quartz-carbonate vein	quartz	Type 3	3	220	112							
881063	quartz-carbonate vein	quartz	Type 3	3		164							
881063	quartz-carbonate vein	quartz	Type 4	1		204							
881063	quartz-carbonate vein	quartz	Type 4	1		213					-14.2		
881063	quartz-carbonate vein	quartz	Type 4	1		158							
881063	quartz-carbonate vein	quartz	Type 4	1		220							
881063	quartz-carbonate vein	quartz	Type 4	1		187							
881063	quartz-carbonate vein	quartz	Type 4	1		197							
881063	quartz-carbonate vein	quartz	Type 4	1		210					-15.4		
881063	quartz-carbonate vein	quartz	Type 4	2		185					-5.7		
881063	quartz-carbonate vein	quartz	Type 4	2		196							
881063	quartz-carbonate vein	quartz	Type 4	2		223							
881063	quartz-carbonate vein	quartz	Type 4	2		183							
881063	quartz-carbonate vein	quartz	Type 4	2		201							
881063	quartz-carbonate vein	quartz	Type 4	2		209							
881063	quartz-carbonate vein	quartz	Type 4	3		231							
881063	quartz-carbonate vein	quartz	Type 4	3		208							
881063	quartz-carbonate vein	quartz	Type 4	3		232							
881063	quartz-carbonate vein	quartz	Type 4	3		260					-6.4		
881063	quartz-carbonate vein	quartz	Type 4	3		166							
881063	quartz-carbonate vein	quartz	Type 4	3		198							

Table A.3 Evaporate mound SEM-EDS data.

Sample	Vein generation	Analysis no.	Na (wt%)	Ca (wt%)	K (wt%)	Mg (wt%)	Ba (wt%)	Mn (wt%)	Fe (wt%)	Sr (wt%)	S (wt%)	F (wt%)	P (wt%)	Cl (wt%)
881045-E	pegmatite	1	9.1	28.2	21.4	bdl	bdl	bdl	bdl	bdl	7.9	bdl	6.4	26.9
881045-E	pegmatite	2	30.0	21.6	bdl	bdl	bdl	bdl	bdl	bdl	2.1	9.4	bdl	37.0
881045-E	pegmatite	3	35.7	13.1	bdl	bdl	bdl	bdl	bdl	bdl	2.9	bdl	bdl	48.3
881045-E	pegmatite	4	37.7	12.2	0.8	bdl	bdl	bdl	bdl	bdl	4.3	bdl	bdl	45.0
881045-E	pegmatite	5	34.0	15.6	bdl	bdl	bdl	bdl	bdl	bdl	4.0	bdl	bdl	46.4
881045-E	pegmatite	6	37.2	11.7	bdl	bdl	bdl	bdl	bdl	bdl	4.8	2.7	bdl	43.6
881045-E	pegmatite	7	31.1	14.3	1.3	bdl	bdl	bdl	bdl	bdl	2.9	1.3	bdl	49.2
881045-E	pegmatite	8	28.1	20.1	2.1	bdl	bdl	bdl	bdl	bdl	1.5	bdl	bdl	48.2
881045-E	pegmatite	9	31.9	20.4	2.2	bdl	bdl	bdl	bdl	bdl	1.7	bdl	bdl	43.8
881045-E	pegmatite	10	34.9	13.1	2.0	bdl	bdl	bdl	bdl	bdl	bdl	bdl	bdl	50.0
881045-E	pegmatite	11	28.5	14.5	4.0	bdl	bdl	bdl	bdl	bdl	bdl	bdl	bdl	53.0
881045-E	pegmatite	12	33.2	17.0	2.1	bdl	bdl	bdl	bdl	bdl	bdl	bdl	bdl	47.7
881045-E	pegmatite	13	28.6	20.8	3.3	bdl	bdl	bdl	bdl	bdl	bdl	bdl	bdl	47.3
881045-E	pegmatite	14	29.4	17.2	1.0	bdl	bdl	bdl	bdl	bdl	bdl	bdl	bdl	52.4
881045-E	pegmatite	15	38.2	10.3	0.9	bdl	bdl	bdl	bdl	bdl	bdl	bdl	bdl	50.7
881045-E	pegmatite	16	29.4	14.3	3.3	bdl	bdl	bdl	bdl	bdl	1.0	bdl	bdl	52.0
881045-E	pegmatite	17	36.4	10.4	1.5	bdl	bdl	bdl	bdl	bdl	1.3	bdl	bdl	50.4
881063-C	quartz-carbonate vein	18	36.1	14.6	0.8	bdl	bdl	bdl	bdl	bdl	bdl	bdl	bdl	48.5
881063-C	quartz-carbonate vein	19	32.8	19.3	bdl	bdl	bdl	bdl	bdl	bdl	bdl	bdl	bdl	47.9
881063-C	quartz-carbonate vein	20	29.7	27.0	bdl	bdl	bdl	bdl	bdl	bdl	bdl	bdl	bdl	27.0
881063-C	quartz-carbonate vein	21	42.1	12.9	bdl	bdl	bdl	bdl	bdl	bdl	bdl	bdl	bdl	45.0
881063-C	quartz-carbonate vein	22	37.8	16.3	bdl	bdl	bdl	bdl	bdl	bdl	bdl	bdl	bdl	45.9
881063-C	quartz-carbonate vein	23	37.6	6.6	1.4	bdl	bdl	bdl	bdl	bdl	bdl	bdl	bdl	54.4
881063-C	quartz-carbonate vein	24	25.8	15.9	8.1	bdl	bdl	2.2	bdl	bdl	bdl	bdl	bdl	48.1
881063-C	quartz-carbonate vein	25	22.1	17.0	7.1	bdl	bdl	3.7	bdl	bdl	bdl	bdl	bdl	50.2
881063-C	quartz-carbonate vein	26	44.1	bdl*	bdl	bdl	bdl	bdl	bdl	bdl	bdl	bdl	bdl	55.9
881063-C	quartz-carbonate vein	27	43.6	bdl	bdl	bdl	bdl	bdl	bdl	bdl	bdl	bdl	bdl	56.4
881063-C	quartz-carbonate vein	28	42.1	bdl	0.5	bdl	bdl	bdl	bdl	bdl	bdl	bdl	bdl	57.4
881063-C	quartz-carbonate vein	29	42.5	bdl	1.3	bdl	bdl	bdl	bdl	bdl	bdl	bdl	bdl	56.2
881063-C	quartz-carbonate vein	30	18.3	37.4	0.5	1.5	bdl	bdl	bdl	bdl	bdl	bdl	bdl	42.3
881063-C	quartz-carbonate vein	31	28.1	24.0	3.3	bdl	bdl	bdl	bdl	bdl	bdl	bdl	bdl	44.6
881063-C	quartz-carbonate vein	32	35.9	6.0	2.5	bdl	bdl	1.0	1.4	bdl	bdl	bdl	bdl	53.2
881063-C	quartz-carbonate vein	33	38.7	3.9	1.4	bdl	bdl	1.9	bdl	bdl	bdl	bdl	bdl	54.0
517412-I	quartz-carbonate vein	34	31.3	6.2	5.0	bdl	bdl	1.0	2.0	bdl	bdl	bdl	bdl	54.6
517412-I	quartz-carbonate vein	35	27.7	10.6	4.8	bdl	bdl	2.7	1.2	bdl	bdl	bdl	bdl	53.0
517412-I	quartz-carbonate vein	36	28.2	10.3	3.4	bdl	bdl	1.5	0.7	bdl	bdl	bdl	bdl	55.9
517412-I	quartz-carbonate vein	37	27.5	13.5	5.0	bdl	bdl	2.0	0.9	bdl	bdl	bdl	bdl	51.1
517412-I	quartz-carbonate vein	38	34.1	9.5	5.3	bdl	bdl	bdl	1.2	bdl	bdl	bdl	bdl	49.9
517412-I	quartz-carbonate vein	39	18.0	17.5	3.8	bdl	2.9	3.0	bdl	bdl	0.1	bdl	bdl	54.7
517412-I	quartz-carbonate vein	40	22.4	16.6	6.6	bdl	2.3	2.1	bdl	bdl	bdl	bdl	bdl	50.0
517412-I	quartz-carbonate vein	41	21.7	18.0	5.9	1.1	bdl	1.4	bdl	bdl	bdl	bdl	bdl	51.9
517412-I	quartz-carbonate vein	42	26.8	22.6	3.8	bdl	bdl	1.1	bdl	bdl	bdl	bdl	bdl	45.7
517412-I	quartz-carbonate vein	43	13.4	15.7	5.6	0.8	4.1	4.6	0.8	6.0	bdl	bdl	bdl	49.1
517412-I	quartz-carbonate vein	44	33.1	13.3	0.6	2.4	bdl	1.0	bdl	bdl	1.1	bdl	bdl	48.6
517412-I	quartz-carbonate vein	45	24.9	22.2	2.6	1.4	bdl	1.9	bdl	bdl	9.6	bdl	bdl	37.3
517412-I	quartz-carbonate vein	46	22.9	20.0	5.4	0.7	3.1	2.7	bdl	bdl	bdl	bdl	bdl	45.2
517412-I	quartz-carbonate vein	47	15.6	17.1	6.4	bdl	4.3	4.8	bdl	bdl	bdl	bdl	bdl	51.8
517412-I	quartz-carbonate vein	48	33.9	3.7	4.7	bdl	bdl	bdl	0.6	bdl	bdl	bdl	bdl	57.1

* below detection limit

APPENDIX B.
ELECTRON MICROPROBE ANALYSIS

Table B.1 Composition of the inclusions displaying graphic texture in apatite of the Hoidas Lake deposit. Table B.1 is available as Table DR1 online at www.geosociety.org/pubs/ft2015.htm, or on request from editing@geosociety.org or Documents Secretary, GSA, P.O. Box 9140, Boulder, CO 80301, USA.

Sample	516665 66 (wt.%)	516665 67 (wt.%)	516665 68 (wt.%)	516665 70 (wt.%)	516665 79 (wt.%)	516665 80 (wt.%)	516665 81 (wt.%)	516665 83 (wt.%)	516665 85 (wt.%)	516665 87 (wt.%)	516665 88 (wt.%)	516665 92 (wt.%)
SiO_2	5.34	0.47	9.55	6.67	7.88	1.65	3.18	10.12	2.39	11.88	15.40	11.38
Al_2O_3	0.11	bdl	0.02	0.04	0.59	0.03	0.11	0.41	bdl	0.17	0.07	0.10
Na_2O	0.20	0.05	0.05	bdl	0.05	0.03	0.03	0.13	0.05	0.05	0.03	0.06
K_2O	bdl*	bdl	bdl	bdl	0.03	bdl	bdl	0.05	bdl	bdl	bdl	bdl
CaO	8.90	5.99	13.10	22.49	3.79	4.92	31.06	3.90	4.51	3.59	2.67	2.94
MgO	0.07	0.05	0.12	0.10	2.30	0.04	0.11	0.37	0.07	0.19	0.07	0.07
FeO	0.06	bdl	0.72	0.06	1.36	bdl	0.12	0.30	bdl	0.16	0.36	0.15
MnO	0.88	bdl	0.07	0.23	0.34	0.09	bdl	1.73	0.48	0.67	0.66	1.42
BaO	1.99	4.46	0.47	0.55	0.56	1.05	0.64	1.14	0.55	2.51	0.70	0.96
SrO	1.65	11.96	0.42	0.52	0.54	0.86	0.53	0.57	0.50	0.36	1.72	0.35
Cr_2O_3	0.10	bdl	0.06	bdl	bdl	0.04	bdl	0.17	bdl	0.16	0.13	0.17
La_2O_3	12.06	16.70	5.74	6.31	16.95	14.30	17.04	5.80	17.58	4.39	2.25	8.53
Ce_2O_3	22.14	bdl	28.66	20.37	12.37	20.50	8.13	40.16	15.25	41.01	40.44	35.23
Pr_2O_3	4.58	6.46	2.11	2.35	5.89	4.89	3.75	2.43	6.25	1.95	1.70	3.42
Nd_2O_3	18.28	25.89	10.32	10.95	24.26	21.35	14.87	10.56	24.38	8.35	9.45	13.06
Sm_2O_3	1.73	1.75	2.14	1.52	2.08	2.29	0.87	1.73	1.72	1.83	2.80	1.92
Eu_2O_3	0.32	0.19	0.58	0.43	0.33	0.50	bdl	0.40	0.28	0.43	0.69	0.42
Gd_2O_3	0.52	0.27	1.48	0.76	0.57	0.86	bdl	0.87	0.45	1.02	1.62	1.04
Tb_2O_3	bdl	bdl	0.12	0.07	bdl	bdl	bdl	0.08	bdl	0.08	0.13	0.10
Dy_2O_3	0.07	bdl	0.43	0.16	bdl	bdl	bdl	0.26	bdl	0.30	0.39	0.20
Er_2O_3	bdl	bdl	bdl	bdl	bdl	bdl	bdl	bdl	bdl	bdl	bdl	bdl
Y_2O_3	0.17	bdl	2.12	1.22	0.18	0.76	0.08	0.84	0.12	1.57	2.43	1.11
ZrO_2	bdl	bdl	bdl	0.07	bdl	bdl	bdl	0.08	bdl	bdl	bdl	bdl
ThO_2	2.25	bdl	1.00	0.81	1.34	1.39	bdl	2.94	1.86	1.95	2.07	2.05
UO_2	0.08	bdl	0.30	0.14	bdl	bdl	bdl	0.32	bdl	0.51	0.74	0.34
P_2O_5	11.71	2.63	9.11	18.88	0.62	3.21	14.76	6.73	0.93	3.33	2.65	3.12
SO_3	0.19	2.28	0.14	0.06	0.06	0.56	0.08	0.30	0.10	0.09	bdl	0.32
F	0.45	0.15	1.22	1.53	1.56	1.48	2.66	0.33	1.74	0.27	0.26	0.73
Cl	0.15	0.07	0.10	0.07	0.28	0.17	0.12	0.24	0.24	0.08	0.18	0.19
O	-0.22	-0.08	-0.54	-0.66	-0.72	-0.66	-1.15	-0.20	-0.79	-0.13	-0.15	-0.35
TOTAL	93.85	79.31	89.64	95.77	83.23	80.38	97.06	92.78	78.73	86.80	89.47	89.05

* below detection limit

Table B.1 cont.

Sample	516665 96 (wt.%)	516665 99 (wt.%)	516665 102 (wt.%)	516665 103 (wt.%)	516665 104 (wt.%)	516665 107 (wt.%)	516665 108 (wt.%)	516665 109 (wt.%)	516665 110 (wt.%)	516665 112 (wt.%)	516665 113 (wt.%)	516665 114 (wt.%)
SiO_2	8.43	10.34	5.81	4.58	2.14	4.26	1.27	3.95	18.25	5.97	2.69	7.83
Al_2O_3	0.35	0.65	0.43	0.21	bdl	0.34	bdl	0.13	0.18	0.12	bdl	0.14
Na_2O	0.06	0.06	0.07	0.03	0.05	0.07	0.08	0.11	0.03	0.05	0.05	0.05
K_2O	bdl	bdl	bdl	bdl	bdl	bdl	bdl	bdl	bdl	bdl	bdl	bdl
CaO	3.30	2.97	4.13	4.82	4.47	8.90	20.83	8.49	2.50	4.40	10.11	4.13
MgO	0.11	0.86	0.84	0.25	0.06	0.85	0.05	0.48	0.07	0.07	0.03	0.30
FeO	0.25	0.47	0.49	0.10	0.03	bdl	bdl	bdl	0.15	0.19	bdl	0.06
MnO	1.42	0.04	0.57	0.65	0.24	0.37	0.12	0.25	0.89	0.99	0.31	0.89
BaO	0.75	1.71	0.96	0.75	0.55	1.18	1.21	0.89	0.99	1.01	1.17	1.31
SrO	0.23	1.48	0.40	0.54	0.56	0.81	0.58	2.91	0.10	0.49	0.50	0.79
Cr_2O_3	0.16	0.14	bdl	0.08	bdl	bdl	bdl	bdl	0.20	0.11	bdl	0.09
La_2O_3	9.33	9.31	14.72	17.19	22.07	16.20	7.90	12.04	1.76	13.54	14.66	10.81
Ce_2O_3	37.22	30.12	18.11	17.63	8.05	12.83	18.89	18.89	45.41	24.15	15.38	26.74
Pr_2O_3	3.53	3.04	4.87	5.84	6.59	4.83	2.27	4.17	1.21	4.65	4.19	3.96
Nd_2O_3	14.68	14.25	20.36	23.68	25.74	19.35	10.74	16.36	7.02	19.47	18.69	16.51
Sm_2O_3	1.78	2.45	2.13	2.23	2.02	1.76	1.00	1.65	2.26	1.91	1.84	2.01
Eu_2O_3	0.31	0.51	0.42	0.47	0.40	0.25	bdl	0.29	0.64	0.33	0.35	0.39
Gd_2O_3	0.69	1.26	0.76	0.72	0.55	0.55	bdl	0.57	1.61	0.75	0.59	0.82
Tb_2O_3	bdl	0.12	bdl	bdl	bdl	bdl	bdl	bdl	0.24	bdl	bdl	0.11
Dy_2O_3	0.10	0.26	bdl	bdl	bdl	bdl	bdl	bdl	0.68	bdl	bdl	0.17
Er_2O_3	bdl	bdl	bdl	bdl	bdl	bdl	bdl	bdl	0.12	bdl	bdl	bdl
Y_2O_3	0.51	1.69	0.38	0.30	0.21	0.28	0.38	0.28	3.10	0.46	0.38	1.00
ZrO_2	bdl	bdl	bdl	bdl	bdl	bdl	bdl	bdl	bdl	bdl	bdl	bdl
ThO_2	1.67	0.77	2.23	2.23	0.94	1.52	0.20	0.89	2.04	2.59	1.23	2.04
UO_2	0.20	0.14	0.05	bdl	bdl	bdl	bdl	bdl	0.74	0.05	bdl	0.14
P_2O_5	1.24	1.08	0.47	0.97	0.23	7.20	4.81	6.17	2.41	1.36	3.96	4.52
SO_3	bdl	0.22	bdl	bdl	0.09	0.25	bdl	0.51	0.08	bdl	bdl	0.55
F	0.95	1.19	1.54	1.62	1.87	1.42	1.77	0.44	0.33	1.27	1.73	0.95
Cl	0.19	0.15	0.27	0.22	0.12	0.15	0.03	0.12	0.11	0.22	0.07	0.18
O	-0.44	-0.53	-0.71	-0.73	-0.81	-0.63	-0.75	-0.21	-0.16	-0.58	-0.74	-0.44
TOTAL	87.08	84.81	79.41	84.58	76.16	82.75	71.38	79.41	93.04	83.65	77.28	86.08

Table B.1 cont.

Sample	516665 115 (wt.%)	516665 117 (wt.%)	516665 118 (wt.%)	516665 119 (wt.%)	516665 130 (wt.%)	516665 131 (wt.%)	516665 132 (wt.%)	516665 133 (wt.%)	516665 144 (wt.%)	516665 145 (wt.%)	516665 146 (wt.%)	516665 147 (wt.%)
SiO_2	12.78	11.91	10.70	11.78	5.69	3.36	19.14	15.56	9.39	1.97	3.97	17.51
Al_2O_3	0.98	0.04	0.65	0.04	0.20	0.04	0.08	0.54	0.16	bdl	bdl	0.05
Na_2O	0.04	0.06	0.24	0.06	0.08	0.06	0.08	0.08	0.13	0.07	0.04	bdl
K_2O	0.06	bdl	0.03	bdl	bdl	bdl	bdl	0.07	0.03	bdl	bdl	bdl
CaO	7.95	3.95	3.25	3.29	7.55	4.63	2.26	3.60	4.15	4.76	13.46	2.64
MgO	2.18	0.14	0.69	0.09	0.21	0.10	0.13	1.67	0.32	0.05	0.07	0.10
FeO	0.30	0.05	0.38	0.08	0.11	0.04	0.16	0.20	0.07	bdl	bdl	0.15
MnO	1.40	0.43	2.20	1.07	0.46	0.51	0.72	1.53	0.62	0.15	0.28	0.67
BaO	0.86	2.23	1.36	1.18	1.57	0.86	1.08	1.20	1.81	0.40	1.20	1.14
SrO	0.42	0.78	0.66	0.46	2.70	0.50	0.19	0.38	0.80	0.19	0.57	0.19
Cr_2O_3	0.13	0.15	0.15	0.15	0.05	0.07	0.18	0.14	0.14	bdl	bdl	0.11
La_2O_3	4.71	3.66	7.70	9.22	10.52	17.45	1.39	3.45	7.99	14.28	10.95	1.63
Ce_2O_3	35.82	38.28	36.18	32.79	25.09	13.99	44.16	37.06	30.02	20.44	17.77	37.26
Pr_2O_3	2.01	2.02	2.84	3.37	4.06	6.58	1.15	1.69	3.17	5.09	3.96	1.16
Nd_2O_3	8.36	10.54	10.82	14.69	16.55	26.21	6.99	8.59	12.98	21.74	17.70	6.94
Sm_2O_3	1.20	2.61	1.28	2.31	1.72	2.28	2.53	2.19	1.95	2.57	2.17	2.45
Eu_2O_3	0.19	0.70	0.19	0.52	0.32	0.42	0.63	0.55	0.39	0.66	0.42	0.68
Gd_2O_3	0.45	1.47	0.46	1.16	0.53	0.57	1.83	1.47	0.94	1.14	0.79	1.99
Tb_2O_3	0.09	0.17	bdl	0.11	bdl	bdl	0.19	0.15	0.13	bdl	0.07	0.20
Dy_2O_3	0.11	0.38	0.10	0.27	bdl	bdl	0.56	0.45	0.26	0.11	0.06	0.60
Er_2O_3	bdl	bdl	bdl	bdl	bdl	bdl	bdl	bdl	bdl	bdl	bdl	bdl
Y_2O_3	0.45	1.57	0.29	1.32	0.26	0.20	2.52	1.46	1.28	1.00	0.65	3.22
ZrO_2	0.06	bdl	bdl	0.06	bdl	bdl	bdl	bdl	bdl	bdl	0.06	0.07
ThO_2	1.91	2.19	3.28	1.90	1.18	1.31	2.17	3.00	2.39	0.38	0.80	7.66
UO_2	0.11	0.48	0.15	0.24	bdl	bdl	0.57	0.46	0.17	bdl	bdl	0.63
P_2O_5	5.72	1.68	6.19	2.66	1.28	0.80	2.41	4.52	9.07	0.81	7.80	2.54
SO_3	0.34	0.32	0.75	0.26	0.18	0.08	0.14	0.14	0.64	0.26	0.34	bdl
F	0.38	0.20	0.26	0.77	0.30	1.50	0.19	0.21	0.30	1.57	1.74	0.18
Cl	0.36	0.10	0.60	0.16	0.15	0.12	0.08	0.09	0.13	0.13	0.09	0.07
O	-0.24	-0.11	-0.25	-0.36	-0.16	-0.66	-0.10	-0.11	-0.16	-0.69	-0.75	-0.09
TOTAL	89.13	86.05	91.22	89.64	80.64	81.12	91.51	90.33	89.32	77.16	84.24	89.80

Table B.1 cont.

Sample	516665 148 (wt.%)	516665 149 (wt.%)	516665 151 (wt.%)	516665 152 (wt.%)	516665 153 (wt.%)	516665 154 (wt.%)	516665 155 (wt.%)	516665 156 (wt.%)	516665 157 (wt.%)	516665 158 (wt.%)	516665 159 (wt.%)	516665 160 (wt.%)
SiO_2	3.32	4.46	7.46	2.97	4.81	3.79	4.51	3.15	14.91	1.09	20.60	21.32
Al_2O_3	bdl	bdl	0.10	bdl	bdl	0.02	0.12	bdl	0.13	bdl	0.02	0.09
Na_2O	0.08	0.05	0.06	0.04	0.06	0.06	0.07	0.04	0.17	bdl	0.05	0.03
K_2O	bdl	bdl	bdl	bdl	bdl	bdl	bdl	bdl	bdl	bdl	bdl	bdl
CaO	5.54	6.62	5.36	4.46	4.72	4.20	4.94	4.74	3.17	3.75	1.74	2.18
MgO	0.08	0.06	0.14	0.05	0.08	0.08	0.39	0.06	0.22	bdl	0.08	0.17
FeO	bdl	bdl	0.05	bdl	0.04	bdl	0.19	bdl	0.48	bdl	0.87	0.26
MnO	0.31	0.51	0.88	0.33	0.49	0.29	0.35	0.38	0.50	0.07	0.19	0.45
BaO	0.66	1.51	1.93	1.30	1.44	0.82	1.32	1.63	1.04	0.09	0.88	1.18
SrO	0.34	0.57	1.67	0.53	0.43	0.37	0.63	0.66	0.73	18.68	bdl	bdl
Cr_2O_3	0.07	bdl	0.05	0.08	0.05	0.10	0.04	bdl	0.16	bdl	0.16	0.20
La_2O_3	10.81	12.96	8.60	14.92	14.34	14.39	16.88	17.95	8.49	18.51	2.46	0.88
Ce_2O_3	26.89	20.72	29.72	22.23	21.86	23.36	15.25	13.00	32.88	2.24	41.69	43.36
Pr_2O_3	4.33	4.59	3.51	4.90	4.95	5.06	5.58	5.91	2.67	6.17	1.21	0.94
Nd_2O_3	19.14	20.40	13.96	20.60	20.97	20.26	23.76	24.61	11.31	24.28	7.77	6.32
Sm_2O_3	2.53	2.31	1.76	2.24	2.05	2.25	2.01	2.07	2.12	1.37	3.07	2.62
Eu_2O_3	0.52	0.48	0.28	0.41	0.38	0.51	0.34	0.32	0.54	0.15	0.99	0.69
Gd_2O_3	1.13	0.77	0.61	0.79	0.68	0.85	0.50	0.47	1.33	0.17	2.48	2.13
Tb_2O_3	bdl	bdl	bdl	bdl	bdl	bdl	bdl	bdl	0.19	bdl	0.28	0.25
Dy_2O_3	0.17	bdl	0.07	bdl	bdl	0.08	bdl	bdl	0.33	bdl	0.67	0.73
Er_2O_3	bdl	bdl	bdl	bdl	bdl	bdl	bdl	bdl	bdl	bdl	0.12	0.16
Y_2O_3	0.97	0.41	0.26	0.38	0.35	0.63	0.15	0.12	1.70	bdl	3.71	3.58
ZrO_2	bdl	bdl	bdl	bdl	0.07	0.07	bdl	bdl	bdl	bdl	bdl	bdl
ThO_2	0.25	1.94	3.47	0.77	1.58	0.23	1.68	2.30	2.88	bdl	bdl	0.80
UO_2	bdl	bdl	bdl	bdl	0.06	bdl	bdl	bdl	0.42	bdl	0.64	0.72
P_2O_5	1.85	2.74	3.75	0.64	1.22	0.76	1.36	1.98	5.76	0.25	1.31	1.77
SO_3	0.09	bdl	0.08	0.16	0.07	0.09	bdl	bdl	0.86	bdl	bdl	bdl
F	1.71	1.37	0.23	1.55	1.41	1.70	1.50	1.27	0.33	bdl	0.64	0.27
Cl	0.15	0.09	0.08	0.13	0.08	0.15	0.09	0.08	0.11	0.05	0.05	0.05
O	-0.75	-0.60	-0.11	-0.68	-0.61	-0.75	-0.65	-0.55	-0.16	-0.01	-0.28	-0.12
TOTAL	80.22	82.11	84.10	78.79	81.62	79.41	81.04	80.29	93.26	76.90	91.51	91.15

Table B.1 cont.

Sample	516665 161 (wt.%)	516665 162 (wt.%)	516665 163 (wt.%)	516665 165 (wt.%)	516665 168 (wt.%)	516665 169 (wt.%)	516665 170 (wt.%)	516665 171 (wt.%)	516665 172 (wt.%)	516665 173 (wt.%)	516665 175 (wt.%)	516665 180 (wt.%)
SiO_2	5.66	2.19	4.39	6.04	7.93	12.33	9.60	3.28	3.41	24.65	3.74	7.37
Al_2O_3	0.18	bdl	bdl	bdl	0.06	0.03	0.42	0.05	0.06	0.18	0.05	bdl
Na_2O	0.16	0.11	0.05	0.07	0.06	0.10	0.07	0.03	0.06	bdl	0.05	0.06
K_2O	bdl	bdl	bdl	bdl	bdl	bdl	bdl	bdl	bdl	bdl	bdl	bdl
CaO	6.32	8.60	4.43	3.51	4.39	3.19	3.59	5.25	5.27	6.32	4.58	4.07
MgO	0.68	0.04	0.07	0.04	0.09	0.05	0.10	0.06	0.08	0.13	0.10	0.05
FeO	0.16	bdl	0.05	bdl	bdl	bdl	0.10	bdl	bdl	2.78	0.18	0.05
MnO	0.44	0.11	0.52	0.76	0.31	0.16	0.59	0.23	0.25	0.05	0.37	0.41
BaO	1.53	0.42	1.33	1.00	1.30	0.42	1.24	0.81	0.80	0.17	1.28	1.09
SrO	2.61	3.12	0.50	8.63	0.45	0.13	0.39	0.60	0.61	0.78	0.60	0.56
Cr_2O_3	0.06	bdl	0.10	bdl	0.08	0.09	0.13	0.07	bdl	0.17	0.07	0.09
La_2O_3	12.97	11.89	14.41	15.10	12.57	11.51	10.54	15.82	16.47	8.12	16.01	19.04
Ce_2O_3	21.97	16.61	20.51	10.39	21.03	22.60	26.31	21.32	21.60	40.94	18.23	18.27
Pr_2O_3	4.57	4.56	4.87	5.53	4.68	4.35	4.00	4.78	4.89	1.58	5.54	5.58
Nd_2O_3	17.87	18.81	21.63	19.37	20.46	19.77	16.06	20.06	20.46	6.34	24.08	19.89
Sm_2O_3	1.77	2.04	2.54	1.46	2.51	2.75	1.65	2.19	2.33	1.06	2.28	1.40
Eu_2O_3	0.35	0.40	0.46	0.23	0.54	0.62	0.24	0.42	0.41	0.25	0.42	0.23
Gd_2O_3	0.60	0.69	0.96	0.65	1.09	1.37	0.42	0.87	0.84	0.78	0.68	0.53
Tb_2O_3	bdl	bdl	0.07	bdl	0.06	0.09	bdl	bdl	bdl	0.13	bdl	bdl
Dy_2O_3	bdl	bdl	0.09	0.14	0.16	0.24	bdl	bdl	0.06	0.09	bdl	bdl
Er_2O_3	bdl	bdl	bdl	bdl	bdl	bdl	bdl	bdl	bdl	bdl	bdl	bdl
Y_2O_3	0.16	0.18	0.59	1.40	1.29	1.63	0.52	0.57	0.61	0.62	0.39	0.53
ZrO_2	bdl	0.08	bdl	bdl	bdl	0.08	bdl	bdl	bdl	bdl	bdl	bdl
ThO_2	1.03	1.18	1.73	bdl	1.27	0.39	4.44	0.83	0.81	bdl	1.07	1.36
UO_2	bdl	bdl	bdl	bdl	0.14	0.21	0.09	bdl	bdl	0.10	bdl	0.19
P_2O_5	7.62	1.20	0.81	1.09	1.50	1.68	2.48	1.14	1.10	0.50	1.32	2.51
SO_3	0.70	bdl	bdl	0.18	bdl	0.27	0.17	0.55	0.51	bdl	0.06	0.42
F	0.32	0.34	1.45	0.10	1.27	1.31	0.85	1.33	1.04	0.61	1.44	1.46
Cl	0.17	0.17	0.09	0.05	0.11	0.15	0.10	0.09	0.09	0.05	0.10	0.12
O	-0.17	-0.18	-0.63	-0.05	-0.56	-0.59	-0.38	-0.58	-0.46	-0.27	-0.63	-0.64
TOTAL	87.80	72.59	81.07	75.69	82.87	84.95	83.79	79.95	81.39	96.15	82.05	84.72

Table B.1 cont.

Sample	516665 181 (wt.%)	516665 182 (wt.%)	516665 183 (wt.%)	516665 184 (wt.%)	516665 186 (wt.%)	516665 187 (wt.%)	516665 188 (wt.%)	516665 190 (wt.%)	516665 191 (wt.%)	516665 192 (wt.%)	516658 193 (wt.%)	516658 205 (wt.%)
SiO_2	23.35	7.03	5.22	19.88	12.06	7.11	18.35	15.28	9.35	17.85	0.78	1.20
Al_2O_3	bdl	0.32	0.12	0.03	0.03	0.08	0.08	0.17	0.09	0.37	bdl	0.06
Na_2O	0.06	0.22	0.08	0.09	0.12	0.07	0.05	bdl	bdl	0.24	0.03	0.03
K_2O	bdl	0.07	bdl	bdl	bdl	bdl	bdl	bdl	bdl	0.07	bdl	bdl
CaO	1.02	5.63	6.78	2.13	2.77	3.62	1.72	2.78	3.66	2.68	2.16	1.70
MgO	0.04	0.48	0.06	0.07	0.17	0.09	0.24	0.11	0.06	0.33	0.08	0.25
FeO	bdl	0.05	0.09	0.75	bdl	0.07	0.72	0.09	0.20	0.72	3.66	12.16
MnO	0.22	0.85	0.41	0.24	bdl	0.56	0.15	1.01	0.41	0.75	bdl	bdl
BaO	0.89	1.97	1.34	0.77	0.83	1.20	1.26	1.20	1.14	0.83	0.07	bdl
SrO	bdl	1.98	2.62	2.55	7.26	0.55	0.13	0.23	0.43	bdl	bdl	bdl
Cr_2O_3	0.07	0.15	0.08	0.17	0.05	0.09	0.14	0.21	0.12	0.23	0.08	0.06
La_2O_3	0.18	11.95	10.04	4.82	10.37	13.97	8.48	2.29	14.88	2.50	12.02	10.95
Ce_2O_3	33.24	23.31	27.45	37.79	19.61	21.18	32.35	44.86	24.10	45.58	29.14	26.35
Pr_2O_3	0.66	4.32	4.01	2.12	4.26	4.78	2.62	1.37	4.60	1.45	3.73	3.41
Nd_2O_3	7.19	17.52	16.30	9.74	16.18	21.11	12.27	6.94	18.43	7.41	16.00	14.37
Sm_2O_3	3.13	1.84	1.94	2.71	1.64	2.34	3.05	1.82	1.99	2.14	1.93	1.74
Eu_2O_3	0.66	0.33	0.38	0.83	0.47	0.45	0.85	0.43	0.33	0.56	0.36	0.28
Gd_2O_3	1.79	0.60	0.54	2.01	0.78	0.99	2.32	0.89	0.74	1.42	0.77	0.66
Tb_2O_3	0.15	0.08	bdl	0.26	bdl	bdl	0.22	0.11	0.07	0.23	0.07	0.11
Dy_2O_3	0.34	bdl	bdl	0.48	0.21	0.11	0.50	0.20	0.05	0.44	0.06	0.09
Er_2O_3	bdl	bdl	bdl	0.08	bdl	bdl	0.06	bdl	bdl	0.06	bdl	bdl
Y_2O_3	2.01	0.33	0.21	3.23	2.12	0.79	3.31	1.42	0.72	1.72	0.57	0.48
ZrO_2	0.08	0.08	bdl	bdl	bdl	bdl	bdl	bdl	bdl	bdl	bdl	bdl
ThO_2	11.94	1.91	1.57	bdl	bdl	2.35	bdl	4.42	1.22	2.54	1.63	bdl
UO_2	1.59	0.08	0.05	0.39	0.13	0.14	0.38	0.33	0.11	0.46	bdl	bdl
P_2O_5	1.78	6.96	1.29	1.41	0.91	1.30	1.06	1.75	2.75	2.32	0.52	0.11
SO_3	bdl	0.53	bdl	bdl	0.32	0.13	bdl	0.19	0.15	0.16	bdl	bdl
F	0.25	0.35	0.21	0.22	0.21	1.46	0.84	0.24	1.04	0.35	1.80	1.65
Cl	0.04	0.17	0.13	0.07	0.05	0.11	0.07	0.08	0.12	0.07	0.18	0.17
O	-0.11	-0.19	-0.12	-0.11	-0.10	-0.64	-0.37	-0.12	-0.46	-0.16	-0.80	-0.73
TOTAL	90.59	88.93	80.88	92.75	80.50	84.08	90.91	88.34	86.34	93.42	74.94	75.25

Table B.2 Composition of apatite containing graphic-textured inclusions in the Hoidas Lake deposit. Table B.2 is available as Table DR2 online at www.geosociety.org/pubs/ft2015.htm, or on request from editing@geosociety.org or Documents Secretary, GSA, P.O. Box 9140, Boulder, CO 80301, USA.

Sample	516665 72 (wt.%)	516665 73 (wt.%)	516665 74 (wt.%)	516665 75 (wt.%)	516665 76 (wt.%)	516665 77 (wt.%)	516665 89 (wt.%)	516665 91 (wt.%)	516665 122 (wt.%)	516665 123 (wt.%)	516665 124 (wt.%)
SiO_2	1.08	1.58	1.31	1.28	1.50	0.98	1.37	1.30	1.33	1.20	0.49
Na_2O	bdl*	0.05	0.04	0.04	0.05	bdl	0.04	0.05	bdl	bdl	bdl
CaO	51.87	50.52	51.27	51.38	51.00	52.31	47.72	47.68	48.50	47.50	52.35
MgO	bdl	bdl	bdl	0.02	0.02	bdl	bdl	bdl	0.03	bdl	bdl
MnO	0.04	0.05	0.05	0.04	0.05	0.05	0.04	0.02	0.05	0.05	bdl
BaO	bdl	bdl	bdl	bdl	bdl	bdl	bdl	bdl	0.08	0.09	bdl
SrO	1.10	1.33	1.28	1.35	1.32	1.00	1.40	1.37	0.94	0.94	0.75
La_2O_3	0.40	0.71	0.52	0.49	0.61	0.36	0.59	0.52	0.98	0.68	0.20
Ce_2O_3	1.30	1.93	1.56	1.45	1.80	1.12	1.83	1.77	2.79	2.88	0.61
Pr_2O_3	0.15	0.24	0.24	0.23	0.26	0.15	0.21	0.27	0.35	0.33	0.09
Nd_2O_3	0.86	1.18	0.99	0.95	1.08	0.72	1.06	1.17	1.56	1.50	0.44
Sm_2O_3	0.11	0.17	0.14	0.12	0.14	0.12	0.14	0.10	0.21	0.16	0.05
Gd_2O_3	0.06	0.09	0.10	0.07	0.06	0.06	bdl	bdl	0.06	bdl	bdl
Y_2O_3	bdl	0.08	0.09	bdl	0.09	bdl	0.08	bdl	0.09	bdl	bdl
ZrO_2	0.18	0.16	0.13	0.13	0.13	0.13	0.12	0.13	0.13	0.14	0.11
P_2O_5	36.99	36.09	36.58	36.96	36.41	37.31	36.85	37.03	36.16	36.44	38.87
SO_3	bdl	0.06	bdl	bdl	0.08	0.05	0.06	0.05	0.06	bdl	bdl
F	3.28	3.28	3.26	3.34	3.30	3.24	2.98	3.14	2.91	2.96	3.38
Cl	0.19	0.23	0.18	0.21	0.18	0.18	0.06	0.09	0.12	0.07	0.12
O	-1.42	-1.43	-1.41	-1.46	-1.43	-1.40	-1.27	-1.34	-1.25	-1.26	-1.45
TOTAL	96.41	96.44	96.52	96.82	96.70	96.53	93.38	93.44	95.19	93.92	96.17
Ln_2O_3	2.89	4.31	3.55	3.32	3.94	2.53	3.83	3.83	5.95	5.54	1.40

* below detection limit

Table B.2 cont.

Sample	516665 125 (wt.%)	516665 134 (wt.%)	516665 135 (wt.%)	516665 136 (wt.%)	516665 137 (wt.%)	516665 138 (wt.%)	516665 139 (wt.%)	516665 140 (wt.%)	516665 141 (wt.%)	516665 142 (wt.%)
SiO_2	0.33	0.57	1.45	0.31	1.58	1.23	1.29	1.38	0.82	0.56
Na_2O	0.03	bdl	0.05	bdl	0.06	0.05	0.04	0.06	0.03	bdl
CaO	52.88	52.51	48.28	53.20	48.58	48.32	48.90	49.59	50.16	51.69
MgO	0.02	0.02	bdl	0.02	bdl	bdl	bdl	bdl	0.02	bdl
MnO	bdl	bdl	bdl	bdl	0.05	bdl	0.04	0.04	0.02	bdl
BaO	bdl	bdl	bdl	bdl	bdl	bdl	bdl	bdl	bdl	bdl
SrO	0.58	0.64	1.27	0.64	1.25	1.23	1.15	1.17	0.90	0.65
La_2O_3	0.15	0.26	0.58	0.13	0.79	0.67	0.60	0.58	0.32	0.22
Ce_2O_3	0.38	0.67	1.85	0.41	2.48	1.63	1.60	1.75	1.05	0.72
Pr_2O_3	0.06	0.10	0.27	0.06	0.28	0.21	0.21	0.28	0.13	0.11
Nd_2O_3	0.29	0.42	1.12	0.29	1.39	0.89	0.96	1.05	0.69	0.49
Sm_2O_3	bdl	bdl	0.15	bdl	0.16	0.12	0.14	0.11	0.09	0.07
Gd_2O_3	bdl	bdl	0.07	bdl	0.08	bdl	bdl	0.07	bdl	bdl
Y_2O_3	bdl	bdl	0.12	bdl	0.11	bdl	bdl	0.08	bdl	bdl
ZrO_2	0.15	0.15	0.12	0.15	0.13	0.14	0.11	0.13	0.11	0.15
P_2O_5	38.85	38.76	36.53	39.07	36.40	36.89	36.48	36.68	37.85	38.26
SO_3	bdl	bdl	bdl	bdl	0.07	bdl	0.06	0.05	bdl	bdl
F	3.46	3.68	3.16	3.44	3.16	3.30	3.01	3.18	3.25	3.25
Cl	0.10	0.14	0.16	0.09	0.12	0.15	0.18	0.18	0.15	0.12
O	-1.48	-1.58	-1.37	-1.47	-1.36	-1.42	-1.31	-1.38	-1.40	-1.40
TOTAL	95.98	96.63	93.92	96.54	95.51	93.60	93.60	95.03	94.36	95.08
Ln_2O_3	0.89	1.44	4.03	0.89	5.19	3.53	3.51	3.85	2.28	1.61

Table B.3 Composition of zircon (in wt.%) in diopside-allanite veins.

SAMPLE	881179-2-474	881179-2-475	881179-2-476	881179-2-477	881179-2-478	881179-2-479	881179-2-480	881179-2-481	881179-2-482	881179-2-483	881179-2-484	881179-2-485	881179-2-486	881179-2-487	881179-3-488	881179-3-489
SiO_2	31.99	32.01	32.07	31.97	32.08	31.93	31.91	31.92	32.06	32.01	30.60	30.47	31.95	29.78	32.12	32.00
Al_2O_3	0.05	bdl	bdl	bdl	bdl	bdl	bdl	0.06	bdl	0.08	0.03	0.04	bdl	bdl	0.01	0.02
Na_2O	bdl*	bdl	bdl	bdl	bdl	bdl	bdl	bdl	bdl	bdl	0.27	0.11	bdl	0.15	bdl	bdl
K_2O	bdl	bdl	bdl	bdl	bdl	bdl	bdl	bdl	bdl	bdl	bdl	bdl	bdl	bdl	bdl	bdl
CaO	0.02	bdl	bdl	bdl	0.04	0.11	bdl	0.05	0.02	bdl	0.25	1.32	0.03	1.91	bdl	bdl
MgO	0.03	bdl	bdl	bdl	bdl	bdl	bdl	0.01	bdl	0.05	bdl	0.04	bdl	0.03	bdl	bdl
FeO	0.10	0.04	0.03	bdl	0.06	0.06	0.06	0.11	0.05	0.06	0.41	0.69	0.02	0.74	0.21	0.05
MnO	bdl	bdl	bdl	bdl	bdl	bdl	bdl	bdl	bdl	bdl	0.09	0.09	bdl	0.30	bdl	bdl
BaO	bdl	bdl	bdl	bdl	bdl	bdl	bdl	bdl	bdl	bdl	bdl	bdl	bdl	bdl	bdl	bdl
SrO	0.12	0.13	0.11	0.10	0.11	0.11	0.13	0.11	0.14	0.14	0.11	0.13	0.10	0.15	0.12	0.12
TiO_2	bdl	bdl	bdl	bdl	0.08	0.16	bdl	bdl	bdl	bdl	bdl	bdl	bdl	bdl	bdl	bdl
Cr_2O_3	bdl	bdl	bdl	bdl	bdl	bdl	bdl	bdl	bdl	bdl	bdl	bdl	bdl	bdl	bdl	bdl
La_2O_3	bdl	bdl	bdl	bdl	bdl	bdl	bdl	bdl	bdl	bdl	bdl	bdl	bdl	bdl	bdl	bdl
Ce_2O_3	bdl	bdl	bdl	bdl	bdl	bdl	bdl	bdl	bdl	bdl	bdl	bdl	bdl	bdl	bdl	bdl
Pr_2O_3	bdl	bdl	bdl	bdl	bdl	bdl	bdl	bdl	bdl	bdl	bdl	bdl	bdl	bdl	bdl	bdl
Nd_2O_3	bdl	bdl	bdl	bdl	bdl	bdl	bdl	bdl	bdl	bdl	bdl	bdl	bdl	bdl	bdl	bdl
Sm_2O_3	bdl	bdl	bdl	bdl	bdl	bdl	bdl	bdl	bdl	bdl	bdl	bdl	bdl	bdl	bdl	bdl
Eu_2O_3	bdl	bdl	bdl	bdl	bdl	bdl	bdl	bdl	bdl	bdl	bdl	bdl	bdl	bdl	bdl	bdl
Gd_2O_3	bdl	bdl	bdl	bdl	bdl	bdl	bdl	bdl	bdl	bdl	bdl	bdl	bdl	bdl	bdl	bdl
Tb_2O_3	bdl	bdl	bdl	bdl	bdl	bdl	bdl	bdl	bdl	bdl	bdl	bdl	bdl	bdl	bdl	bdl
Dy_2O_3	bdl	bdl	bdl	bdl	bdl	bdl	bdl	bdl	bdl	bdl	bdl	bdl	bdl	bdl	bdl	bdl
Ho_2O_3	bdl	bdl	bdl	bdl	bdl	bdl	bdl	bdl	bdl	bdl	bdl	bdl	bdl	bdl	bdl	bdl
Er_2O_3	bdl	bdl	bdl	bdl	bdl	bdl	bdl	bdl	bdl	bdl	bdl	bdl	bdl	bdl	bdl	bdl
Tm_2O_3	bdl	bdl	bdl	bdl	bdl	bdl	bdl	bdl	bdl	bdl	bdl	bdl	bdl	bdl	bdl	bdl
Yb_2O_3	bdl	bdl	bdl	bdl	bdl	bdl	bdl	bdl	bdl	bdl	bdl	bdl	bdl	bdl	bdl	bdl
Lu_2O_3	bdl	bdl	bdl	bdl	bdl	bdl	bdl	bdl	bdl	bdl	bdl	bdl	bdl	bdl	bdl	bdl
Y_2O_3	bdl	bdl	bdl	bdl	bdl	bdl	bdl	bdl	bdl	bdl	0.19	0.11	bdl	0.09	bdl	bdl
ZrO_2	65.10	65.27	65.27	65.72	64.51	65.76	65.91	65.55	65.55	65.36	61.74	61.93	65.15	59.48	66.01	66.02
HfO_2	1.10	1.15	1.03	1.06	2.11	1.01	1.08	1.00	0.94	1.05	1.30	1.11	1.22	1.77	0.85	0.82
Nb_2O_5	0.10	0.09	0.10	0.10	0.08	0.10	0.08	0.10	0.08	0.07	0.06	0.07	0.11	0.08	0.09	0.07
Sc_2O_3	bdl	bdl	bdl	bdl	bdl	bdl	bdl	bdl	bdl	bdl	bdl	bdl	bdl	bdl	bdl	bdl
ThO_2	bdl	bdl	bdl	bdl	bdl	bdl	bdl	bdl	bdl	bdl	bdl	0.12	bdl	bdl	bdl	bdl
UO_2	bdl	bdl	bdl	0.06	bdl	bdl	bdl	bdl	bdl	bdl	0.11	0.07	bdl	0.13	bdl	bdl
P_2O_5	0.05	bdl	bdl	bdl	0.07	bdl	bdl	0.04	bdl	0.05	bdl	bdl	bdl	bdl	0.05	bdl
SO_3	bdl	bdl	bdl	bdl	0.05	bdl	bdl	0.05	bdl	bdl	bdl	bdl	bdl	0.06	0.05	bdl
F	bdl	bdl	bdl	bdl	bdl	bdl	bdl	bdl	bdl	bdl	bdl	bdl	bdl	bdl	bdl	bdl
Cl	bdl	bdl	bdl	bdl	bdl	bdl	bdl	bdl	bdl	bdl	0.02	0.14	bdl	0.18	bdl	bdl
TOTAL	98.67	98.68	98.61	99.01	99.20	99.24	99.16	99.01	98.83	98.86	95.17	96.40	98.59	94.81	99.51	99.09

* below detection limit

Table B.3 cont.

SAMPLE	881179-3-490	881179-3-491	881179-3-492	881179-3-493	881179-3-494	881179-3-495	881179-7-599	881179-7-600	881179-7-601	881179-7-602	881179-7-603	881179-7-604	881179-7-605	881179-7-606	881187-9-761	881187-9-762
SiO_2	31.94	30.47	31.87	32.05	32.04	32.08	32.20	31.98	29.59	31.84	31.88	31.97	31.98	31.80	32.21	30.71
Al_2O_3	bdl	0.06	bdl	bdl	0.01	bdl	bdl	bdl	bdl	bdl	0.01	bdl	bdl	bdl	0.02	0.04
Na_2O	bdl	0.17	bdl	bdl	bdl	bdl	bdl	bdl	0.13	bdl	bdl	bdl	bdl	bdl	bdl	0.10
K_2O	bdl	bdl	bdl	bdl	bdl	bdl	bdl	bdl	bdl	bdl	bdl	bdl	bdl	bdl	bdl	bdl
CaO	bdl	0.56	bdl	bdl	0.02	bdl	bdl	bdl	1.47	bdl	bdl	bdl	bdl	bdl	bdl	0.89
MgO	bdl	0.02	bdl	bdl	bdl	bdl	bdl	bdl	0.03	bdl	bdl	bdl	bdl	bdl	bdl	0.02
FeO	bdl	0.58	0.02	0.05	0.06	0.06	0.04	bdl	0.97	bdl	bdl	bdl	bdl	bdl	0.07	0.53
MnO	bdl	0.14	bdl	bdl	bdl	bdl	bdl	bdl	0.14	bdl	bdl	bdl	bdl	bdl	bdl	0.14
BaO	bdl	bdl	bdl	bdl	bdl	bdl	bdl	bdl	bdl	bdl	bdl	bdl	bdl	bdl	bdl	bdl
SrO	0.12	0.09	0.10	0.12	0.12	0.11	0.11	0.11	0.17	0.13	0.15	0.12	0.09	0.14	0.12	0.15
TiO_2	bdl	bdl	bdl	bdl	bdl	bdl	bdl	bdl	bdl	bdl	bdl	bdl	bdl	bdl	bdl	bdl
Cr_2O_3	bdl	bdl	bdl	bdl	bdl	bdl	bdl	bdl	bdl	bdl	bdl	bdl	bdl	bdl	bdl	bdl
La_2O_3	bdl	bdl	bdl	bdl	bdl	bdl	bdl	bdl	bdl	bdl	bdl	bdl	bdl	bdl	bdl	bdl
Ce_2O_3	bdl	bdl	bdl	bdl	bdl	bdl	bdl	bdl	bdl	bdl	bdl	bdl	bdl	bdl	bdl	bdl
Pr_2O_3	bdl	bdl	bdl	bdl	bdl	bdl	bdl	bdl	bdl	bdl	bdl	bdl	bdl	bdl	bdl	bdl
Nd_2O_3	bdl	bdl	bdl	bdl	bdl	bdl	bdl	bdl	bdl	bdl	bdl	bdl	bdl	bdl	bdl	bdl
Sm_2O_3	bdl	bdl	bdl	bdl	bdl	bdl	bdl	bdl	bdl	bdl	bdl	bdl	bdl	bdl	bdl	bdl
Eu_2O_3	bdl	bdl	bdl	bdl	bdl	bdl	bdl	bdl	bdl	bdl	bdl	bdl	bdl	bdl	bdl	bdl
Gd_2O_3	bdl	bdl	bdl	bdl	bdl	bdl	bdl	bdl	bdl	bdl	bdl	bdl	bdl	bdl	bdl	bdl
Tb_2O_3	bdl	bdl	bdl	bdl	bdl	bdl	bdl	bdl	bdl	bdl	bdl	bdl	bdl	bdl	bdl	bdl
Dy_2O_3	bdl	bdl	bdl	bdl	bdl	bdl	bdl	bdl	bdl	bdl	bdl	bdl	bdl	bdl	bdl	bdl
Ho_2O_3	bdl	bdl	bdl	bdl	bdl	bdl	bdl	bdl	bdl	bdl	bdl	bdl	bdl	bdl	bdl	bdl
Er_2O_3	bdl	bdl	bdl	bdl	bdl	bdl	bdl	bdl	bdl	bdl	bdl	bdl	bdl	bdl	bdl	bdl
Tm_2O_3	bdl	bdl	bdl	bdl	bdl	bdl	bdl	bdl	bdl	bdl	bdl	bdl	bdl	bdl	bdl	bdl
Yb_2O_3	bdl	bdl	bdl	bdl	bdl	bdl	bdl	bdl	bdl	bdl	bdl	bdl	bdl	bdl	bdl	bdl
Lu_2O_3	bdl	bdl	bdl	bdl	bdl	bdl	bdl	bdl	bdl	bdl	bdl	bdl	bdl	bdl	bdl	bdl
Y_2O_3	bdl	0.20	bdl	bdl	bdl	bdl	bdl	0.10	0.08	0.09	0.13	0.07	bdl	0.08	bdl	0.11
ZrO_2	65.95	61.68	65.23	65.83	65.51	65.41	65.75	65.33	61.47	65.61	65.44	65.18	65.50	65.67	65.70	62.47
HfO_2	0.94	0.99	1.11	1.06	0.99	1.63	1.15	0.75	0.72	0.76	0.73	0.81	0.89	0.96	0.96	0.79
Nb_2O_5	0.08	0.06	0.11	0.11	0.10	0.09	0.07	0.09	0.09	0.10	0.09	0.09	0.11	0.06	0.08	0.09
Sc_2O_3	bdl	bdl	bdl	bdl	bdl	bdl	bdl	bdl	bdl	bdl	bdl	bdl	bdl	bdl	bdl	bdl
ThO_2	bdl	0.07	0.10	bdl	bdl	bdl	bdl	bdl	bdl	bdl	0.06	bdl	bdl	bdl	bdl	bdl
UO_2	bdl	0.09	bdl	bdl	bdl	0.08	bdl	bdl	0.15	bdl	0.13	bdl	bdl	bdl	bdl	0.08
P_2O_5	0.06	0.04	bdl	bdl	bdl	bdl	bdl	bdl	0.05	bdl	bdl	0.05	bdl	bdl	bdl	bdl
SO_3	bdl	bdl	bdl	bdl	bdl	bdl	bdl	bdl	bdl	bdl	bdl	bdl	bdl	bdl	bdl	bdl
F	bdl	bdl	bdl	bdl	bdl	bdl	bdl	bdl	bdl	bdl	bdl	bdl	bdl	bdl	bdl	bdl
Cl	bdl	0.03	bdl	bdl	bdl	bdl	bdl	bdl	0.15	bdl	bdl	bdl	bdl	bdl	bdl	0.06
TOTAL	99.08	95.24	98.55	99.23	98.84	99.46	99.31	98.36	95.19	98.53	98.61	98.28	98.57	98.72	99.16	96.18

Table B.4 Composition of early allanite (in wt.%) in diopside-allanite veins.

SAMPLE	881179-1-459	881179-1-460	881179-1-465	881179-1-466	881179-1-467	881179-1-468	881179-4-534	881179-4-535	881179-4-536	881179-4-537	881179-4-538	881179-4-539	881179-4-543	881179-4-548	881179-4-549	881179-4-550	881179-4-553	881179-4-554	881179-4-555	881179-4-556	881179-4-557
SiO_2	33.06	34.57	32.92	31.97	32.22	32.30	30.32	31.36	31.85	32.78	32.81	33.16	35.75	36.28	35.37	36.99	35.32	32.86	32.79	32.79	32.36
Al_2O_3	15.04	16.32	15.85	15.49	15.47	14.52	14.02	14.55	14.71	15.52	15.36	15.32	16.27	17.05	16.47	16.67	17.01	16.10	15.87	16.26	15.39
Na_2O	0.07	0.04	0.06	0.06	0.08	0.09	0.08	0.08	0.07	0.08	0.08	0.04	bdl	0.03	bdl	bdl	0.06	0.04	0.07	0.09	0.05
K_2O	0.05	0.05	0.03	bdl	0.02	bdl	bdl	bdl	bdl	0.02	0.03	0.04	0.04	0.11	0.08	0.04	0.09	0.06	0.02	0.03	bdl
CaO	6.87	5.72	6.95	7.87	8.11	8.37	8.67	8.95	8.72	8.75	8.14	6.89	5.14	4.97	4.95	4.66	6.32	6.51	8.97	8.07	7.52
MgO	1.75	1.34	0.94	1.27	0.93	1.10	1.14	1.32	1.58	1.10	1.09	0.96	0.43	0.47	0.41	0.36	0.75	0.64	0.95	0.84	0.93
FeO	7.62	5.78	7.28	7.93	7.97	8.87	9.90	9.49	9.00	8.33	7.89	6.81	3.63	4.90	4.62	3.54	5.98	5.89	7.78	7.30	7.47
MnO	0.73	0.77	0.99	0.75	0.77	0.90	0.64	0.69	0.72	0.84	0.74	0.61	0.70	0.49	0.58	0.66	0.71	0.56	0.63	0.58	0.86
BaO	1.28	2.06	0.93	0.62	0.57	0.43	0.74	0.55	0.42	0.37	0.81	1.77	4.54	2.54	3.37	5.20	1.26	2.00	0.36	0.99	0.93
SrO	0.58	0.53	0.48	0.52	0.61	0.58	0.69	0.62	0.60	0.68	0.57	0.61	0.52	0.47	0.47	0.53	0.53	0.60	0.72	0.71	0.60
TiO_2	0.82	0.82	0.75	0.70	0.79	0.80	0.80	0.85	0.91	0.79	0.95	0.90	1.06	0.83	0.82	0.92	0.66	0.80	0.80	0.76	0.72
Cr_2O_3	0.14	0.08	0.12	0.10	0.15	0.14	0.12	0.13	0.12	0.15	0.13	0.09	0.09	0.09	0.10	0.08	0.10	0.11	0.13	0.10	0.12
La_2O_3	5.19	4.57	5.32	4.89	5.20	5.17	5.16	5.02	4.97	5.08	5.12	5.03	3.90	5.19	4.94	3.64	5.76	5.54	5.43	5.51	5.39
Ce_2O_3	10.43	11.38	11.49	10.70	11.39	10.88	10.88	10.63	10.59	10.61	10.69	10.54	9.49	10.95	10.54	8.87	11.11	11.17	10.88	11.04	11.32
Pr_2O_3	1.00	0.95	1.09	1.07	1.01	1.11	1.18	1.10	1.08	1.05	1.05	1.05	0.90	1.12	1.05	0.84	1.07	1.13	1.13	1.07	1.09
Nd_2O_3	3.75	3.46	3.90	3.88	4.03	3.90	3.91	3.85	3.77	3.56	3.85	3.73	3.21	4.13	3.67	3.05	4.01	3.91	3.81	3.82	3.98
Sm_2O_3	0.23	0.24	0.27	0.25	0.29	0.27	0.24	0.28	0.25	0.26	0.29	0.23	0.18	0.26	0.22	0.22	0.25	0.24	0.25	0.27	0.23
Eu_2O_3	bdl*	bdl	bdl	bdl	bdl	bdl	bdl	bdl	bdl	bdl	bdl	bdl	bdl	bdl	bdl	bdl	bdl	bdl	bdl	bdl	bdl
Gd_2O_3	0.39	0.32	0.40	0.38	0.36	0.41	0.36	0.38	0.39	0.40	0.41	0.34	0.29	0.32	0.37	0.25	0.34	0.39	0.36	0.36	0.35
Tb_2O_3	bdl	bdl	bdl	bdl	bdl	bdl	bdl	bdl	bdl	bdl	bdl	bdl	bdl	bdl	bdl	bdl	bdl	bdl	bdl	bdl	bdl
Dy_2O_3	bdl	bdl	0.07	bdl	0.09	bdl	bdl	bdl	0.08	0.07	bdl	bdl	bdl	bdl	bdl	bdl	bdl	bdl	bdl	bdl	bdl
Ho_2O_3	bdl	bdl	bdl	bdl	bdl	bdl	bdl	bdl	bdl	bdl	bdl	bdl	bdl	bdl	bdl	bdl	bdl	bdl	bdl	bdl	bdl
Er_2O_3	bdl	bdl	bdl	bdl	bdl	bdl	bdl	bdl	bdl	bdl	bdl	bdl	bdl	bdl	bdl	bdl	bdl	bdl	bdl	bdl	bdl
Tm_2O_3	bdl	bdl	bdl	bdl	bdl	bdl	bdl	bdl	bdl	bdl	bdl	bdl	bdl	bdl	bdl	bdl	bdl	bdl	bdl	bdl	bdl
Yb_2O_3	bdl	bdl	bdl	bdl	bdl	bdl	bdl	bdl	bdl	bdl	bdl	bdl	bdl	bdl	bdl	bdl	bdl	bdl	bdl	bdl	bdl
Lu_2O_3	bdl	bdl	bdl	bdl	bdl	bdl	bdl	bdl	bdl	bdl	bdl	bdl	bdl	bdl	bdl	bdl	bdl	bdl	bdl	bdl	bdl
Y_2O_3	bdl	bdl	bdl	bdl	bdl	bdl	bdl	bdl	bdl	bdl	bdl	bdl	bdl	bdl	bdl	bdl	bdl	bdl	bdl	bdl	bdl
ZrO_2	bdl	bdl	bdl	bdl	bdl	bdl	bdl	bdl	bdl	bdl	bdl	bdl	bdl	bdl	bdl	bdl	bdl	bdl	bdl	bdl	bdl
HfO_2	bdl	bdl	bdl	bdl	bdl	bdl	bdl	bdl	bdl	bdl	bdl	bdl	bdl	bdl	bdl	bdl	bdl	bdl	bdl	bdl	bdl
Nb_2O_5	bdl	bdl	bdl	bdl	bdl	bdl	bdl	bdl	bdl	bdl	bdl	bdl	bdl	bdl	bdl	bdl	bdl	bdl	bdl	bdl	bdl
Sc_2O_3	bdl	bdl	bdl	bdl	bdl	bdl	bdl	bdl	bdl	bdl	bdl	bdl	bdl	bdl	bdl	bdl	bdl	bdl	bdl	bdl	bdl
ThO_2	0.71	0.70	0.74	0.68	0.67	0.74	0.72	0.73	0.78	0.75	0.71	0.68	0.63	0.65	0.64	0.76	0.68	0.64	0.59	0.55	0.67
UO_2	bdl	bdl	bdl	bdl	bdl	bdl	bdl	bdl	bdl	bdl	bdl	bdl	bdl	bdl	bdl	bdl	bdl	bdl	bdl	bdl	bdl
P_2O_5	bdl	bdl	bdl	bdl	bdl	bdl	bdl	bdl	bdl	bdl	bdl	bdl	bdl	bdl	bdl	bdl	bdl	bdl	bdl	bdl	bdl
SO_3	bdl	0.05	bdl	bdl	bdl	bdl	bdl	0.05	0.05	bdl	bdl	bdl	bdl	bdl	bdl	bdl	bdl	bdl	bdl	bdl	bdl
F	bdl	bdl	bdl	bdl	bdl	bdl	bdl	bdl	bdl	bdl	bdl	bdl	bdl	bdl	bdl	bdl	bdl	bdl	bdl	bdl	bdl
Cl	0.08	0.04	0.06	0.13	0.10	0.13	0.11	0.15	0.17	0.20	0.17	0.13	0.02	0.03	0.03	0.01	0.06	0.07	0.23	0.18	0.10
TOTAL	89.78	89.80	90.63	89.23	90.81	90.69	89.64	90.76	90.78	91.34	90.84	88.90	86.78	90.86	88.69	87.28	92.05	89.25	91.69	91.27	90.06
TREO	21.00	20.94	22.53	21.17	22.37	21.74	21.73	21.26	21.13	21.03	21.40	20.92	17.97	21.95	20.79	16.87	22.54	22.38	21.84	22.06	22.37

* below detection limit

Table B.4 cont.

SAMPLE	881179-4-558	881179-4-559	881179-4-560	881179-4-561	881179-4-562	881179-4-563	881179-5-567	881179-5-568	881179-5-569	881179-5-570	881179-5-571	881179-5-574	881179-5-575	881179-5-576	881179-5-577	881179-5-578	881179-5-579	881179-5-580	881179-5-582	881179-5-583	881179-5-584
SiO_2	32.01	31.85	33.74	32.00	31.22	33.08	31.85	32.55	31.59	32.34	32.27	33.24	31.43	32.89	33.51	32.42	32.92	33.31	32.09	32.22	31.62
Al_2O_3	15.39	15.10	16.84	14.70	14.23	16.98	14.39	15.62	15.45	15.38	15.23	16.68	16.67	16.69	17.18	16.58	16.73	16.26	15.54	15.28	14.84
Na_2O	0.05	0.06	0.09	0.05	0.08	0.09	0.08	0.06	0.05	0.08	0.06	0.07	0.10	0.07	0.08	0.06	0.07	0.08	0.07	0.06	0.05
K_2O	bdl	bdl	0.03	bdl	bdl	bdl	0.02	bdl	bdl	bdl	bdl	0.03	0.02	0.03	0.02	bdl	0.03	0.02	bdl	bdl	bdl
CaO	8.03	9.08	9.74	8.55	8.28	10.93	8.73	8.95	9.61	8.54	9.60	7.18	7.85	7.22	7.66	8.60	7.26	7.29	8.48	7.10	7.82
MgO	1.20	0.98	0.85	1.21	1.20	0.63	1.28	1.23	0.85	1.12	1.53	0.75	0.84	1.14	0.84	0.80	0.84	1.11	1.29	1.30	1.73
FeO	7.74	8.62	9.03	8.52	9.29	10.01	9.63	8.02	8.82	8.60	8.48	5.89	6.43	6.31	6.42	7.02	6.18	6.58	7.91	7.86	8.25
MnO	0.81	0.66	0.65	0.90	0.84	0.48	0.74	0.71	0.64	0.68	0.78	1.07	1.20	1.14	1.19	1.15	1.19	0.93	0.87	0.89	0.84
BaO	0.29	0.57	1.40	0.36	0.62	0.99	1.04	0.09	0.09	0.86	bdl	1.15	0.91	0.66	0.59	0.17	1.25	1.33	0.27	0.88	0.64
SrO	0.63	0.67	1.05	0.58	0.60	1.33	0.76	0.61	0.75	0.65	0.76	0.53	0.54	0.52	0.62	0.64	0.48	0.58	0.68	0.52	0.59
TiO_2	0.84	0.77	0.22	0.86	0.79	0.24	0.81	0.81	0.63	0.81	0.73	0.82	0.81	0.77	0.81	0.93	0.81	0.88	0.74	0.80	0.90
Cr_2O_3	0.11	0.12	0.10	0.12	0.15	0.08	0.12	0.14	0.14	0.12	0.12	0.11	0.13	0.11	0.13	0.14	0.13	0.14	0.14	0.14	0.14
La_2O_3	5.37	5.19	4.08	5.36	5.55	3.96	5.15	5.15	5.32	5.17	5.04	4.86	5.07	5.02	5.05	4.93	4.99	5.20	5.29	5.22	5.38
Ce_2O_3	10.85	10.85	8.30	11.07	11.17	7.95	10.21	10.91	10.79	10.81	10.51	12.60	12.97	12.62	12.70	12.07	12.51	12.25	11.15	11.22	10.74
Pr_2O_3	1.09	1.07	0.88	1.09	1.14	0.82	1.12	1.16	1.00	1.09	1.07	1.05	1.23	1.15	1.09	1.12	1.13	1.19	1.02	1.15	1.08
Nd_2O_3	3.78	3.94	3.08	3.74	3.98	2.83	3.86	3.93	3.58	3.87	3.79	3.52	3.69	3.67	3.69	3.63	3.60	3.71	3.84	3.70	3.75
Sm_2O_3	0.25	0.23	0.23	0.27	0.26	0.19	0.27	0.24	0.21	0.25	0.25	0.26	0.26	0.25	0.25	0.29	0.27	0.26	0.31	0.26	0.28
Eu_2O_3	bdl	bdl	bdl	bdl	bdl	bdl	bdl	bdl	bdl	bdl	bdl	bdl	bdl	bdl	bdl	bdl	bdl	bdl	bdl	bdl	bdl
Gd_2O_3	0.30	0.34	0.36	0.38	0.47	0.28	0.39	0.34	0.40	0.36	0.34	0.44	0.34	0.35	0.41	0.36	0.42	0.37	0.37	0.36	0.32
Tb_2O_3	bdl	bdl	bdl	bdl	bdl	bdl	bdl	bdl	bdl	bdl	bdl	bdl	bdl	bdl	bdl	bdl	bdl	bdl	bdl	bdl	bdl
Dy_2O_3	0.08	bdl	0.10	bdl	bdl	bdl	bdl	bdl	bdl	bdl	0.08	0.10	0.10	0.11	0.13	0.08	0.12	bdl	0.07	bdl	bdl
Ho_2O_3	bdl	bdl	bdl	bdl	bdl	bdl	bdl	bdl	bdl	bdl	bdl	bdl	bdl	bdl	bdl	bdl	bdl	bdl	bdl	bdl	bdl
Er_2O_3	bdl	bdl	bdl	bdl	bdl	bdl	bdl	bdl	bdl	bdl	bdl	bdl	bdl	bdl	bdl	bdl	bdl	bdl	bdl	bdl	bdl
Tm_2O_3	bdl	bdl	bdl	bdl	bdl	bdl	bdl	bdl	bdl	bdl	bdl	bdl	bdl	bdl	bdl	bdl	bdl	bdl	bdl	bdl	bdl
Yb_2O_3	bdl	bdl	bdl	bdl	bdl	bdl	bdl	bdl	bdl	bdl	bdl	bdl	bdl	bdl	bdl	bdl	bdl	bdl	bdl	bdl	bdl
Lu_2O_3	bdl	bdl	bdl	bdl	bdl	bdl	bdl	bdl	bdl	bdl	bdl	bdl	bdl	bdl	bdl	bdl	bdl	bdl	bdl	bdl	bdl
Y_2O_3	bdl	bdl	bdl	bdl	bdl	bdl	bdl	bdl	bdl	bdl	bdl	bdl	bdl	bdl	bdl	bdl	bdl	bdl	bdl	bdl	bdl
ZrO_2	bdl	bdl	bdl	bdl	bdl	bdl	bdl	bdl	bdl	bdl	bdl	bdl	bdl	bdl	bdl	bdl	bdl	bdl	bdl	bdl	bdl
HfO_2	bdl	bdl	bdl	bdl	bdl	bdl	bdl	bdl	bdl	bdl	bdl	bdl	bdl	bdl	bdl	bdl	bdl	bdl	bdl	bdl	bdl
Nb_2O_5	bdl	bdl	bdl	bdl	bdl	bdl	bdl	bdl	bdl	bdl	bdl	bdl	bdl	bdl	bdl	bdl	bdl	bdl	bdl	bdl	bdl
Sc_2O_3	bdl	bdl	bdl	bdl	bdl	bdl	bdl	bdl	bdl	bdl	bdl	bdl	bdl	bdl	bdl	bdl	bdl	bdl	bdl	bdl	bdl
ThO_2	0.75	0.66	0.61	0.79	0.74	0.45	0.65	0.74	0.58	0.58	0.62	0.60	0.34	0.59	0.55	0.60	0.50	0.49	0.59	0.75	0.72
UO_2	bdl	bdl	bdl	bdl	bdl	bdl	bdl	bdl	bdl	bdl	bdl	bdl	bdl	bdl	bdl	bdl	bdl	bdl	bdl	bdl	bdl
P_2O_5	bdl	bdl	bdl	bdl	bdl	bdl	bdl	bdl	bdl	bdl	bdl	bdl	bdl	bdl	bdl	bdl	bdl	bdl	bdl	bdl	bdl
SO_3	0.06	0.08	0.06	0.05	bdl	bdl	0.06	bdl	0.08	bdl	bdl	0.09	0.11	0.08	0.13	bdl	0.16	bdl	bdl	bdl	bdl
F	bdl	bdl	bdl	bdl	bdl	bdl	bdl	bdl	bdl	bdl	bdl	bdl	bdl	bdl	bdl	bdl	bdl	bdl	bdl	bdl	bdl
Cl	0.11	0.16	0.15	0.11	0.10	0.26	0.12	0.14	0.13	0.15	0.19	0.04	0.06	0.05	0.05	0.06	0.05	0.06	0.12	0.07	0.10
TOTAL	89.71	90.96	91.57	90.69	90.69	91.52	91.26	91.38	90.68	91.41	91.42	91.08	91.09	91.42	93.10	91.63	91.64	92.04	90.83	89.77	89.76
TREO	21.71	21.62	17.04	21.91	22.57	16.03	21.01	21.73	21.30	21.55	21.10	22.83	23.65	23.16	23.33	22.48	23.05	22.97	22.06	21.91	21.55

Table B.4 cont.

SAMPLE	881179-5-585	881179-8-607	881179-8-608	881179-8-609	881179-8-610	881179-8-611	881179-8-612	881179-8-613	881179-8-614	881179-8-615	881187-3-626	881187-3-627	881187-3-628	881187-3-629	881187-3-630	881187-3-631	881187-3-632	881187-3-633	881187-3-635	881187-3-636	881187-3-637
SiO_2	32.17	32.92	32.49	32.40	32.99	34.43	35.42	35.11	34.54	35.87	31.98	31.62	31.40	34.74	32.44	32.20	32.77	32.85	33.31	31.55	32.48
Al_2O_3	15.56	17.22	15.35	15.29	16.05	17.03	18.00	17.69	17.53	17.63	16.17	15.75	16.10	17.18	17.71	16.58	16.07	15.89	16.46	16.26	16.08
Na_2O	0.05	0.09	0.06	0.09	0.08	0.03	0.06	0.05	0.08	0.05	0.14	0.13	0.14	0.17	0.12	0.13	0.18	0.21	0.28	0.10	0.12
K_2O	bdl	bdl	bdl	bdl	0.04	0.06	0.07	0.05	0.06	0.06	bdl	bdl	bdl	0.04	bdl	bdl	0.06	0.05	0.04	bdl	bdl
CaO	9.59	13.28	7.97	8.08	7.21	6.24	6.06	6.10	6.25	5.41	11.18	10.77	11.05	7.39	9.40	9.24	7.05	7.17	7.06	8.30	7.21
MgO	1.19	0.49	1.47	1.12	0.91	0.63	0.67	0.65	0.68	0.62	1.08	1.24	1.09	0.49	0.72	1.24	0.51	0.44	0.51	0.81	1.51
FeO	8.75	10.62	8.34	8.10	7.30	5.37	5.42	5.08	5.46	4.71	8.21	8.17	7.92	5.03	6.74	7.34	4.93	4.88	4.89	6.83	6.99
MnO	0.89	0.47	0.83	0.67	0.84	0.66	0.73	0.73	0.89	0.66	0.64	0.70	0.75	1.36	0.98	1.09	1.37	1.41	1.38	1.25	1.36
BaO	bdl	0.43	0.83	0.85	0.86	1.76	1.80	2.24	1.72	2.21	0.39	0.39	bdl	3.74	0.70	0.57	3.99	4.39	4.45	1.26	1.58
SrO	0.73	1.44	0.64	0.53	0.67	0.64	0.56	0.56	0.48	0.48	0.98	0.96	0.82	1.07	1.02	0.84	0.96	0.94	1.10	0.98	0.77
TiO_2	0.82	0.18	0.72	0.84	0.82	0.86	0.83	0.79	0.92	0.83	0.66	0.74	0.70	0.84	0.67	0.72	0.89	0.97	0.95	0.70	0.81
Cr_2O_3	0.13	0.06	0.14	0.16	0.13	0.08	0.11	0.11	0.13	0.12	0.13	0.16	0.16	0.09	0.09	0.11	0.10	0.11	0.10	0.11	0.12
La_2O_3	5.18	3.47	5.31	5.40	5.34	5.33	4.89	4.92	5.04	4.94	5.11	5.23	5.70	3.96	5.04	5.60	4.02	4.00	3.71	5.63	5.49
Ce_2O_3	10.88	7.13	10.61	11.17	11.38	11.49	10.83	11.53	11.86	11.43	10.28	10.20	11.04	9.51	10.13	10.71	9.14	8.58	8.42	10.80	10.14
Pr_2O_3	1.14	0.69	1.07	1.15	1.14	1.18	1.16	1.11	1.14	1.12	1.14	0.97	1.08	0.93	1.03	0.96	0.90	0.80	0.88	1.03	1.00
Nd_2O_3	3.81	2.72	3.88	4.03	4.02	3.79	3.75	3.76	3.73	3.87	3.45	3.34	3.48	2.82	3.38	3.50	2.71	2.72	2.65	3.57	3.18
Sm_2O_3	0.25	0.17	0.25	0.26	0.30	0.28	0.23	0.23	0.32	0.24	0.22	0.20	0.27	0.19	0.18	0.23	0.14	0.21	0.15	0.21	0.22
Eu_2O_3	bdl	bdl	bdl	bdl	bdl	bdl	bdl	bdl	bdl	bdl	bdl	bdl	bdl	bdl	bdl	bdl	bdl	bdl	bdl	bdl	bdl
Gd_2O_3	0.37	0.24	0.39	0.34	0.24	0.28	0.41	0.33	0.40	0.37	0.30	0.37	0.35	0.29	0.30	0.35	0.20	0.33	0.18	0.35	0.28
Tb_2O_3	bdl	bdl	bdl	bdl	bdl	bdl	bdl	bdl	bdl	bdl	bdl	bdl	bdl	bdl	bdl	bdl	bdl	bdl	bdl	bdl	bdl
Dy_2O_3	bdl	0.09	bdl	bdl	0.08	bdl	bdl	bdl	bdl	bdl	bdl	bdl	bdl	0.17	0.11	0.09	0.18	0.14	0.19	0.13	0.12
Ho_2O_3	bdl	bdl	bdl	bdl	bdl	bdl	bdl	bdl	bdl	bdl	bdl	bdl	bdl	bdl	bdl	bdl	bdl	bdl	bdl	bdl	bdl
Er_2O_3	bdl	bdl	bdl	bdl	bdl	bdl	bdl	bdl	bdl	bdl	bdl	bdl	bdl	bdl	bdl	bdl	bdl	bdl	bdl	bdl	bdl
Tm_2O_3	bdl	bdl	bdl	bdl	bdl	bdl	bdl	bdl	bdl	bdl	bdl	bdl	bdl	bdl	bdl	bdl	bdl	bdl	bdl	bdl	bdl
Yb_2O_3	bdl	bdl	bdl	bdl	bdl	bdl	bdl	bdl	bdl	bdl	bdl	bdl	bdl	bdl	bdl	bdl	bdl	bdl	bdl	bdl	bdl
Lu_2O_3	bdl	bdl	bdl	bdl	bdl	bdl	bdl	bdl	bdl	bdl	bdl	bdl	bdl	bdl	bdl	bdl	bdl	bdl	bdl	bdl	bdl
Y_2O_3	bdl	bdl	bdl	bdl	bdl	bdl	bdl	bdl	bdl	bdl	bdl	bdl	bdl	bdl	bdl	bdl	bdl	bdl	bdl	bdl	bdl
ZrO_2	bdl	bdl	bdl	bdl	bdl	bdl	bdl	bdl	bdl	bdl	bdl	bdl	bdl	bdl	bdl	bdl	bdl	bdl	bdl	bdl	bdl
HfO_2	bdl	bdl	bdl	bdl	bdl	bdl	bdl	bdl	bdl	bdl	bdl	bdl	bdl	bdl	bdl	bdl	bdl	bdl	bdl	bdl	bdl
Nb_2O_5	bdl	bdl	bdl	bdl	bdl	bdl	bdl	bdl	bdl	bdl	bdl	bdl	bdl	bdl	bdl	bdl	bdl	bdl	bdl	bdl	bdl
Sc_2O_3	bdl	bdl	bdl	bdl	bdl	bdl	bdl	bdl	bdl	bdl	bdl	bdl	bdl	bdl	bdl	bdl	bdl	bdl	bdl	bdl	bdl
ThO_2	0.66	0.33	0.67	0.64	0.72	0.70	0.79	0.50	0.61	0.62	0.49	0.57	0.55	0.65	0.53	0.56	0.61	0.63	0.72	0.57	0.63
UO_2	bdl	bdl	bdl	bdl	bdl	bdl	bdl	bdl	bdl	bdl	bdl	bdl	bdl	bdl	bdl	bdl	bdl	bdl	bdl	bdl	bdl
P_2O_5	bdl	bdl	bdl	bdl	bdl	bdl	bdl	bdl	bdl	bdl	bdl	bdl	bdl	bdl	bdl	bdl	bdl	bdl	bdl	bdl	bdl
SO_3	bdl	bdl	0.05	bdl	bdl	bdl	bdl	0.09	bdl	bdl	0.05	bdl	0.05	bdl	0.10	0.07	bdl	bdl	bdl	0.16	0.10
F	bdl	bdl	bdl	bdl	bdl	bdl	bdl	bdl	bdl	bdl	bdl	bdl	bdl	bdl	bdl	bdl	bdl	bdl	bdl	bdl	bdl
Cl	0.21	0.37	0.12	0.14	0.11	0.04	0.04	0.03	0.02	0.03	0.69	0.48	0.55	0.03	0.18	0.25	0.04	0.05	0.03	0.11	0.11
TOTAL	92.34	92.33	91.18	91.24	91.19	90.87	91.79	91.68	91.86	91.25	93.12	91.86	93.08	90.68	91.52	92.33	86.80	86.76	87.45	90.68	90.28
TREO	21.64	14.52	21.51	22.35	22.49	22.35	21.26	21.89	22.49	21.96	20.49	20.31	21.92	17.86	20.17	21.43	17.29	16.79	16.17	21.71	20.43

Table B.4 cont.

SAMPLE	881187-3-638	881187-3-640	881187-3-641	881187-3-642	881187-3-643	881187-3-645	881187-3-646	881187-3-647	881187-3-651	881187-3-653	881187-3-654	881187-3-655	881187-3-656	881187-3-657	881187-3-658	881187-3-659	881187-3-660	881187-3-661	881187-5-663	881187-5-664	881187-5-665
SiO_2	32.68	33.80	33.10	32.73	35.78	30.60	31.30	31.59	32.37	32.91	32.69	32.91	30.64	31.79	32.44	28.41	33.26	34.56	31.42	33.03	34.83
Al_2O_3	15.91	15.41	16.23	15.77	15.69	15.14	14.47	15.70	16.56	17.08	16.91	17.28	14.99	14.03	16.98	14.10	14.30	15.01	15.72	15.61	16.61
Na_2O	0.12	0.41	0.06	0.08	0.43	0.19	0.36	0.14	0.12	0.14	0.11	0.10	0.31	0.34	0.10	0.20	0.33	0.40	0.10	0.37	0.35
K_2O	bdl	0.12	bdl	0.03	0.14	0.05	0.11	bdl	bdl	bdl	bdl	bdl	0.04	0.15	bdl	0.04	0.35	0.17	bdl	0.08	0.06
CaO	6.91	6.24	6.81	6.77	5.92	6.63	6.06	10.88	9.02	8.00	7.14	7.90	6.48	5.22	8.77	6.41	5.23	5.56	9.99	6.76	7.22
MgO	0.80	1.19	0.63	0.69	1.57	0.49	1.75	1.06	0.76	0.90	0.82	0.81	0.92	2.55	0.82	0.47	2.58	2.03	1.08	1.27	0.55
FeO	6.61	8.78	6.43	6.30	10.40	4.57	8.36	9.81	7.71	6.29	5.87	6.27	5.97	10.18	6.92	4.62	11.06	11.47	8.12	6.75	5.24
MnO	1.44	1.38	1.29	1.21	1.45	1.33	1.31	0.53	1.29	1.53	1.49	1.44	1.38	1.33	1.48	1.26	1.35	1.46	0.86	1.56	1.51
BaO	2.27	4.27	2.76	2.90	4.03	4.50	3.86	0.18	0.70	0.68	2.20	1.65	4.20	3.93	0.46	4.37	3.72	3.80	0.19	3.94	4.21
SrO	0.90	0.88	0.88	1.09	0.90	0.98	0.84	0.92	1.22	1.16	0.85	1.06	0.98	0.74	1.09	1.00	0.75	0.75	0.95	0.90	0.96
TiO_2	0.75	0.86	0.84	0.62	0.86	1.03	0.90	0.42	0.34	0.70	0.69	0.67	0.94	0.79	0.38	0.89	0.74	0.77	0.59	0.99	1.05
Cr_2O_3	0.15	0.10	0.10	0.12	0.06	0.07	0.09	0.15	0.13	0.15	0.10	0.11	0.08	0.05	0.12	0.06	bdl	0.07	0.14	0.09	0.11
La_2O_3	5.69	3.02	5.33	5.44	2.85	3.79	3.01	5.35	5.54	5.57	5.61	5.77	3.51	2.61	5.60	3.72	2.55	2.66	5.80	3.38	4.34
Ce_2O_3	10.10	6.64	10.23	10.86	6.18	7.45	6.35	10.26	10.37	10.98	10.43	9.87	7.28	5.28	10.59	8.02	5.57	5.72	10.57	7.43	8.30
Pr_2O_3	0.98	0.64	0.91	0.98	0.61	0.71	0.67	0.91	1.04	1.01	0.99	1.04	0.78	0.48	1.01	0.78	0.56	0.63	1.02	0.77	0.89
Nd_2O_3	3.24	2.07	3.12	3.35	1.95	2.49	2.12	3.43	3.38	3.38	3.55	3.48	2.46	1.75	3.48	2.52	1.74	1.83	3.61	2.60	2.67
Sm_2O_3	0.16	0.14	0.19	0.17	0.13	0.18	0.13	0.25	0.19	0.23	0.19	0.23	0.19	0.10	0.21	0.12	0.10	0.12	0.21	0.19	0.17
Eu_2O_3	bdl	bdl	bdl	bdl	bdl	bdl	bdl	bdl	bdl	bdl	bdl	bdl	bdl	bdl	bdl	bdl	bdl	bdl	bdl	bdl	bdl
Gd_2O_3	0.29	0.21	0.28	0.32	0.16	0.16	0.18	0.33	0.36	0.34	0.26	0.28	0.14	0.11	0.30	0.14	0.13	0.16	0.37	0.20	0.24
Tb_2O_3	bdl	bdl	bdl	bdl	bdl	bdl	bdl	bdl	bdl	bdl	bdl	bdl	bdl	bdl	bdl	bdl	bdl	bdl	bdl	bdl	bdl
Dy_2O_3	0.11	0.23	0.12	0.12	0.26	0.10	0.14	0.10	0.14	0.14	0.19	0.12	0.16	0.18	0.12	0.10	0.21	0.30	bdl	0.21	0.20
Ho_2O_3	bdl	bdl	bdl	bdl	bdl	bdl	bdl	bdl	bdl	bdl	bdl	bdl	bdl	bdl	bdl	bdl	bdl	bdl	bdl	bdl	bdl
Er_2O_3	bdl	bdl	bdl	bdl	bdl	bdl	bdl	bdl	bdl	bdl	bdl	bdl	bdl	bdl	bdl	bdl	bdl	bdl	bdl	bdl	bdl
Tm_2O_3	bdl	bdl	bdl	bdl	bdl	bdl	bdl	bdl	bdl	bdl	bdl	bdl	bdl	bdl	bdl	bdl	bdl	bdl	bdl	bdl	bdl
Yb_2O_3	bdl	bdl	bdl	bdl	bdl	bdl	bdl	bdl	bdl	bdl	bdl	bdl	bdl	bdl	bdl	bdl	bdl	bdl	bdl	bdl	bdl
Lu_2O_3	bdl	bdl	bdl	bdl	bdl	bdl	bdl	bdl	bdl	bdl	bdl	bdl	bdl	bdl	bdl	bdl	bdl	bdl	bdl	bdl	bdl
Y_2O_3	bdl	bdl	bdl	bdl	bdl	bdl	bdl	bdl	bdl	bdl	bdl	bdl	bdl	bdl	bdl	bdl	bdl	0.07	bdl	bdl	bdl
ZrO_2	bdl	bdl	bdl	bdl	bdl	bdl	bdl	bdl	bdl	bdl	bdl	bdl	bdl	bdl	bdl	bdl	bdl	bdl	bdl	bdl	bdl
HfO_2	bdl	bdl	bdl	bdl	bdl	bdl	bdl	bdl	bdl	bdl	bdl	bdl	bdl	bdl	bdl	bdl	bdl	bdl	bdl	bdl	bdl
Nb_2O_5	bdl	bdl	bdl	bdl	bdl	bdl	bdl	bdl	bdl	bdl	bdl	bdl	bdl	bdl	bdl	bdl	bdl	bdl	bdl	bdl	bdl
Sc_2O_3	bdl	bdl	bdl	bdl	bdl	bdl	bdl	bdl	bdl	bdl	bdl	bdl	bdl	bdl	bdl	bdl	bdl	bdl	bdl	bdl	bdl
ThO_2	0.59	1.11	0.69	0.62	1.16	0.86	0.92	0.53	0.47	0.56	0.54	0.55	0.79	1.08	0.53	0.79	0.77	0.97	0.55	1.00	0.81
UO_2	bdl	bdl	bdl	bdl	bdl	bdl	bdl	bdl	bdl	bdl	bdl	bdl	bdl	bdl	bdl	bdl	bdl	bdl	bdl	bdl	bdl
P_2O_5	bdl	bdl	bdl	bdl	bdl	bdl	bdl	bdl	bdl	bdl	bdl	bdl	bdl	bdl	bdl	bdl	bdl	bdl	bdl	bdl	bdl
SO_3	0.07	bdl	0.08	0.06	bdl	bdl	bdl	0.05	0.19	0.24	0.29	0.23	bdl	bdl	0.27	bdl	bdl	bdl	0.11	bdl	bdl
F	bdl	bdl	bdl	bdl	bdl	bdl	bdl	bdl	bdl	bdl	bdl	bdl	bdl	bdl	bdl	bdl	bdl	bdl	bdl	bdl	bdl
Cl	0.08	0.03	0.04	0.06	0.02	0.04	0.03	0.52	0.07	0.04	0.04	0.04	0.03	0.03	0.07	0.02	0.04	0.02	0.25	0.05	0.04
TOTAL	89.82	87.53	90.12	90.28	90.56	81.35	82.95	92.99	91.96	92.00	90.94	91.79	82.29	82.71	91.70	78.03	85.32	88.54	91.60	87.18	90.36
TREO	20.56	12.96	20.18	21.24	12.14	14.87	12.60	20.62	21.03	21.65	21.22	20.78	14.54	10.51	21.31	15.39	10.85	11.50	21.59	14.78	16.81

Table B.4 cont.

SAMPLE	881187-5-666	881187-5-667	881187-5-668	881187-5-670	881187-5-671	881187-5-674	881187-5-675	881187-5-676	881187-5-677	881187-5-678	881187-5-679	881187-5-680	881187-5-681	881187-5-683	881187-5-684	881187-5-685	881187-5-686	881187-5-687	881187-5-688	881187-5-689	881187-5-690
SiO_2	32.71	33.94	34.98	33.33	35.25	32.37	33.98	34.25	32.32	33.02	32.42	31.86	32.28	31.93	31.42	31.60	31.62	31.51	32.29	32.33	31.79
Al_2O_3	17.21	14.14	14.16	13.74	14.64	15.10	15.56	15.19	14.84	15.95	16.90	16.05	16.30	16.00	15.03	15.01	15.38	15.20	13.96	13.30	14.09
Na_2O	0.10	0.35	0.21	0.16	0.20	0.13	0.07	0.41	0.26	0.27	0.11	0.13	0.13	0.11	0.16	0.15	0.14	0.14	0.12	0.19	0.20
K_2O	bdl	0.29	0.19	0.18	0.13	0.10	0.10	0.15	0.07	0.05	bdl	bdl	bdl	bdl	bdl	bdl	bdl	bdl	bdl	bdl	bdl
CaO	7.28	4.98	4.53	4.65	5.15	4.82	3.62	5.83	4.98	6.14	9.61	10.98	9.25	8.93	8.33	9.44	8.14	9.59	7.87	8.33	9.06
MgO	0.89	2.53	2.70	2.63	2.30	6.58	10.77	2.47	5.99	3.23	0.83	0.88	1.23	1.11	1.82	1.30	1.49	1.22	1.56	1.35	1.09
FeO	5.78	13.80	15.18	13.71	12.87	8.38	8.47	9.81	8.10	6.55	7.27	8.21	7.43	7.48	8.15	9.16	8.10	9.08	8.89	9.82	9.70
MnO	1.43	1.63	1.36	1.44	1.50	1.33	1.31	1.38	1.38	1.33	1.01	0.73	0.95	1.14	1.34	1.09	1.18	1.12	1.39	1.71	1.32
BaO	1.73	3.40	3.78	3.49	3.63	2.84	2.24	3.87	3.21	3.21	0.85	0.84	0.81	1.11	1.12	0.64	1.22	0.68	2.31	2.30	1.73
SrO	1.05	0.73	0.65	0.75	0.74	0.64	0.49	0.83	0.71	0.86	1.02	1.05	0.86	0.93	0.91	0.98	0.86	0.96	1.04	1.18	1.12
TiO_2	0.64	0.62	0.68	0.70	0.69	0.52	0.43	0.73	0.60	0.75	0.73	0.73	0.71	0.76	0.76	0.76	0.75	0.76	0.89	0.95	0.84
Cr_2O_3	0.12	0.06	0.06	0.05	0.08	0.05	bdl	0.05	0.06	0.07	0.11	0.12	0.10	0.14	0.13	0.14	0.15	0.14	0.15	0.12	0.13
La_2O_3	5.69	2.36	2.02	2.05	2.29	2.33	1.50	2.93	2.36	3.35	5.00	4.80	5.20	5.44	5.56	5.67	5.36	5.53	4.87	4.86	4.89
Ce_2O_3	10.30	4.93	4.33	4.56	5.15	5.04	3.63	6.19	5.48	7.53	10.14	9.55	10.42	10.68	10.57	10.09	10.36	10.23	9.90	10.05	10.13
Pr_2O_3	0.90	0.50	0.45	0.40	0.46	0.54	0.38	0.57	0.58	0.76	1.01	0.93	0.99	1.04	1.10	1.01	1.06	1.04	1.14	1.11	1.12
Nd_2O_3	3.29	1.49	1.42	1.49	1.53	1.66	1.07	1.88	1.51	2.31	3.36	3.35	3.28	3.50	3.12	3.44	3.29	3.32	2.99	3.18	3.62
Sm_2O_3	0.18	0.10	0.09	0.10	0.10	0.09	0.06	0.14	0.10	0.14	0.26	0.22	0.15	0.19	0.18	0.24	0.19	0.17	0.22	0.20	0.26
Eu_2O_3	bdl	bdl	bdl	bdl	bdl	bdl	bdl	bdl	bdl	bdl	bdl	bdl	bdl	bdl	bdl	bdl	bdl	bdl	bdl	bdl	bdl
Gd_2O_3	0.26	0.15	0.14	0.09	0.19	0.12	0.08	0.18	0.10	0.19	0.22	0.24	0.23	0.39	0.25	0.33	0.25	0.28	0.28	0.30	0.24
Tb_2O_3	bdl	0.08	0.10	bdl	0.08	bdl	bdl	bdl	bdl	bdl	bdl	bdl	bdl	bdl	bdl	bdl	bdl	bdl	bdl	bdl	bdl
Dy_2O_3	0.13	0.34	0.24	0.28	0.28	0.23	0.21	0.22	0.19	0.16	0.14	bdl	bdl	0.09	0.15	bdl	0.12	0.13	0.22	0.24	0.20
Ho_2O_3	bdl	bdl	bdl	bdl	bdl	bdl	bdl	bdl	bdl	bdl	bdl	bdl	bdl	bdl	bdl	bdl	bdl	bdl	bdl	bdl	bdl
Er_2O_3	bdl	bdl	bdl	bdl	bdl	bdl	bdl	bdl	bdl	bdl	bdl	bdl	bdl	bdl	bdl	bdl	bdl	bdl	bdl	bdl	bdl
Tm_2O_3	bdl	bdl	bdl	bdl	bdl	bdl	bdl	bdl	bdl	bdl	bdl	bdl	bdl	bdl	bdl	bdl	bdl	bdl	bdl	bdl	bdl
Yb_2O_3	bdl	bdl	bdl	bdl	bdl	bdl	bdl	bdl	bdl	bdl	bdl	bdl	bdl	bdl	bdl	bdl	bdl	bdl	bdl	bdl	bdl
Lu_2O_3	bdl	bdl	bdl	bdl	bdl	bdl	bdl	bdl	bdl	bdl	bdl	bdl	bdl	bdl	bdl	bdl	bdl	bdl	bdl	bdl	bdl
Y_2O_3	bdl	bdl	bdl	bdl	bdl	bdl	bdl	bdl	bdl	bdl	bdl	bdl	bdl	bdl	bdl	bdl	bdl	bdl	bdl	bdl	bdl
ZrO_2	bdl	bdl	bdl	bdl	bdl	bdl	bdl	bdl	bdl	bdl	bdl	bdl	bdl	bdl	bdl	bdl	bdl	bdl	bdl	bdl	bdl
HfO_2	bdl	bdl	bdl	bdl	bdl	bdl	bdl	bdl	bdl	bdl	bdl	bdl	bdl	bdl	bdl	bdl	bdl	bdl	bdl	bdl	bdl
Nb_2O_5	bdl	bdl	bdl	bdl	bdl	bdl	bdl	bdl	bdl	bdl	bdl	bdl	bdl	bdl	bdl	bdl	bdl	bdl	bdl	bdl	bdl
Sc_2O_3	bdl	bdl	bdl	bdl	bdl	bdl	bdl	bdl	bdl	bdl	bdl	bdl	bdl	bdl	bdl	bdl	bdl	bdl	bdl	bdl	bdl
ThO_2	0.63	0.72	0.67	0.71	0.72	0.56	0.55	1.10	0.67	0.69	0.54	0.49	0.70	0.65	0.56	0.57	0.69	0.65	0.73	0.77	0.55
UO_2	bdl	bdl	bdl	bdl	bdl	bdl	bdl	bdl	bdl	bdl	bdl	bdl	bdl	bdl	bdl	bdl	bdl	bdl	bdl	bdl	bdl
P_2O_5	bdl	bdl	bdl	bdl	bdl	bdl	bdl	bdl	bdl	bdl	bdl	bdl	bdl	bdl	bdl	bdl	bdl	bdl	bdl	bdl	bdl
SO_3	0.27	bdl	bdl	bdl	bdl	bdl	bdl	bdl	bdl	bdl	0.06	0.18	bdl	0.05	0.06	bdl	0.08	0.07	bdl	bdl	bdl
F	bdl	bdl	bdl	bdl	bdl	bdl	bdl	bdl	bdl	bdl	bdl	bdl	bdl	bdl	bdl	bdl	bdl	bdl	bdl	bdl	bdl
Cl	0.04	0.01	0.01	0.01	0.01	0.02	0.02	0.02	0.02	0.03	0.19	0.27	0.24	0.19	0.13	0.14	0.13	0.16	0.05	0.04	0.08
TOTAL	90.64	87.17	87.94	84.51	88.01	83.43	84.55	88.19	83.53	86.57	91.75	91.56	91.19	91.81	90.84	91.71	90.51	91.96	90.83	92.31	92.14
TREO	20.76	9.96	8.79	8.97	10.10	10.01	6.93	12.11	10.33	14.43	20.13	19.10	20.27	21.32	20.93	20.78	20.62	20.71	19.61	19.94	20.46

Table B.4 cont.

SAMPLE	881187-7-728	881187-7-729	881187-7-730	881187-7-731	881187-7-732	881187-7-733	881187-7-734	881187-7-735	881187-7-736	881187-7-740	881187-8-741	881187-8-742	881187-8-743	881187-8-744	881187-9-750	948521-3-226	948521-3-227	948521-3-228	948521-3-229	948521-3-230	948521-4-239	948521-4-240
SiO_2	30.37	33.49	31.85	31.23	32.02	31.58	32.60	31.35	31.69	31.67	31.19	31.20	31.34	31.82	30.60	32.93	27.27	25.24	32.06	31.65	33.07	32.86
Al_2O_3	12.35	12.36	13.45	13.35	14.08	13.57	14.02	12.86	13.40	13.35	14.04	14.51	14.68	13.91	12.55	13.57	5.12	9.94	8.66	7.86	15.58	15.80
Na_2O	0.31	0.22	0.26	0.19	0.21	0.15	0.19	0.16	0.17	0.26	0.15	0.14	0.21	0.16	0.27	0.08	0.22	0.31	0.21	0.21	0.06	0.16
K_2O	0.02	0.07	bdl	bdl	0.04	bdl	bdl	bdl	bdl	0.02	bdl	bdl	bdl	bdl	bdl	bdl	0.18	bdl	bdl	bdl	bdl	bdl
CaO	7.89	6.82	8.73	8.82	8.67	8.44	8.08	8.83	9.06	8.24	8.34	9.71	10.61	8.87	8.65	11.80	1.86	6.77	8.91	9.05	11.84	12.54
MgO	1.90	7.14	1.80	1.27	1.65	1.46	1.80	1.06	1.23	2.14	1.25	1.48	0.99	1.02	1.30	1.12	7.56	0.83	0.60	0.73	1.23	0.87
FeO	13.00	10.49	10.37	10.90	9.88	9.86	9.02	10.06	10.67	9.97	9.76	9.52	10.54	10.09	11.87	11.30	8.08	6.49	17.99	17.27	10.31	8.65
MnO	1.60	1.37	1.51	1.37	1.08	1.15	1.37	1.38	1.31	1.38	1.22	1.04	1.12	1.29	1.47	0.42	0.22	0.63	0.76	0.70	0.35	0.48
BaO	1.93	1.48	1.77	1.92	2.49	2.05	2.33	1.99	1.83	1.80	1.66	0.73	0.14	1.84	1.50	bdl	0.35	0.87	0.57	0.40	bdl	0.16
SrO	1.16	0.83	1.08	1.07	1.17	0.94	1.01	1.04	1.13	1.00	0.89	0.96	1.05	1.13	1.03	0.65	0.37	0.70	0.55	0.29	0.70	0.81
TiO_2	0.94	0.69	0.93	0.70	0.59	0.95	0.97	0.99	0.80	1.04	0.72	0.70	0.39	0.63	0.68	0.72	0.27	1.28	1.35	0.92	0.60	0.72
Cr_2O_3	0.12	0.11	0.14	0.10	0.10	0.16	0.12	0.14	0.17	0.14	0.14	0.16	0.16	0.13	0.13	0.05	bdl	bdl	0.06	0.07	0.04	bdl
La_2O_3	4.52	3.90	4.86	4.63	4.70	5.15	4.84	5.25	4.90	4.88	5.43	5.30	5.49	4.93	5.28	5.41	0.61	3.79	5.48	6.81	5.41	4.70
Ce_2O_3	9.31	8.98	10.17	10.02	9.34	10.49	9.99	11.18	10.51	10.66	10.37	10.62	10.31	10.23	11.07	10.72	1.24	6.91	12.50	13.51	10.12	9.43
Pr_2O_3	0.99	0.82	1.05	1.02	0.95	1.03	1.03	1.08	0.97	1.10	1.08	1.07	1.12	1.13	1.05	1.04	0.07	0.54	1.29	1.07	1.03	0.98
Nd_2O_3	2.79	2.37	3.02	3.03	2.95	3.16	3.03	3.10	3.06	3.14	3.31	3.26	3.18	3.34	3.01	3.22	0.28	1.87	4.13	3.11	3.16	2.99
Sm_2O_3	0.19	0.13	0.24	0.19	0.21	0.23	0.24	0.22	0.24	0.24	0.23	0.17	0.23	0.25	0.18	0.22	bdl	0.08	0.30	0.17	0.23	0.26
Eu_2O_3	bdl	bdl	bdl	bdl	bdl	bdl	bdl	bdl	bdl	bdl	bdl	bdl	bdl	bdl	bdl	bdl	bdl	bdl	bdl	bdl	bdl	bdl
Gd_2O_3	0.24	0.16	0.28	0.28	0.25	0.29	0.28	0.32	0.28	0.29	0.29	0.35	0.30	0.35	0.33	0.12	bdl	bdl	0.09	0.10	0.09	0.10
Tb_2O_3	0.07	0.07	bdl	bdl	bdl	bdl	bdl	bdl	bdl	bdl	bdl	bdl	bdl	bdl	bdl	0.09	bdl	bdl	0.20	0.12	0.07	0.08
Dy_2O_3	0.24	0.23	0.20	0.24	0.13	0.12	0.17	0.20	0.17	0.13	0.11	0.08	0.13	0.15	0.19	bdl	bdl	bdl	0.06	bdl	bdl	bdl
Ho_2O_3	bdl	bdl	bdl	bdl	bdl	bdl	bdl	bdl	bdl	bdl	bdl	bdl	bdl	bdl	bdl	bdl	bdl	bdl	bdl	bdl	bdl	bdl
Er_2O_3	bdl	bdl	bdl	bdl	bdl	bdl	bdl	bdl	bdl	bdl	bdl	bdl	bdl	bdl	bdl	bdl	bdl	bdl	0.09	bdl	bdl	bdl
Tm_2O_3	bdl	bdl	bdl	bdl	bdl	bdl	bdl	bdl	bdl	bdl	bdl	bdl	bdl	bdl	bdl	bdl	bdl	bdl	bdl	bdl	bdl	bdl
Yb_2O_3	bdl	bdl	bdl	bdl	bdl	bdl	bdl	bdl	bdl	bdl	bdl	bdl	bdl	bdl	bdl	bdl	bdl	bdl	bdl	bdl	bdl	bdl
Lu_2O_3	bdl	bdl	bdl	bdl	bdl	bdl	bdl	bdl	bdl	bdl	bdl	bdl	bdl	bdl	bdl	bdl	bdl	bdl	bdl	bdl	bdl	bdl
Y_2O_3	bdl	bdl	bdl	bdl	bdl	bdl	bdl	bdl	bdl	bdl	bdl	bdl	bdl	bdl	bdl	bdl	bdl	bdl	bdl	bdl	bdl	bdl
ZrO_2	bdl	bdl	bdl	bdl	bdl	bdl	bdl	bdl	bdl	bdl	bdl	bdl	bdl	bdl	bdl	bdl	bdl	bdl	bdl	bdl	bdl	bdl
HfO_2	bdl	bdl	bdl	bdl	bdl	bdl	bdl	bdl	bdl	bdl	bdl	bdl	bdl	bdl	bdl	bdl	bdl	bdl	bdl	bdl	bdl	bdl
Nb_2O_5	bdl	bdl	bdl	bdl	bdl	bdl	bdl	bdl	bdl	bdl	bdl	bdl	bdl	bdl	bdl	bdl	bdl	bdl	bdl	bdl	bdl	bdl
Sc_2O_3	bdl	bdl	bdl	bdl	bdl	bdl	bdl	bdl	bdl	bdl	bdl	bdl	bdl	bdl	bdl	bdl	bdl	bdl	bdl	bdl	bdl	bdl
ThO_2	0.67	0.51	0.59	0.63	0.60	0.65	0.64	0.52	0.51	0.57	0.58	0.55	0.43	0.51	0.48	0.12	0.04	0.38	0.14	0.20	0.10	0.26
UO_2	bdl	bdl	bdl	bdl	bdl	bdl	bdl	bdl	bdl	bdl	bdl	bdl	bdl	bdl	bdl	bdl	bdl	bdl	bdl	bdl	bdl	bdl
P_2O_5	bdl	bdl	bdl	bdl	bdl	bdl	bdl	bdl	bdl	bdl	bdl	bdl	bdl	bdl	bdl	bdl	bdl	bdl	bdl	bdl	bdl	bdl
SO_3	bdl	bdl	0.07	bdl	0.16	0.05	bdl	0.06	0.05	bdl	bdl	bdl	bdl	bdl	bdl	0.11	bdl	bdl	bdl	0.05	0.09	0.09
F	bdl	bdl	bdl	bdl	bdl	bdl	bdl	bdl	bdl	bdl	bdl	bdl	bdl	bdl	bdl	bdl	bdl	bdl	bdl	bdl	0.07	0.10
Cl	0.05	0.04	0.05	0.07	0.08	0.06	0.06	0.08	0.08	0.07	0.10	0.16	0.26	0.08	0.07	0.37	0.31	0.27	0.06	0.35	0.37	0.87
TOTAL	90.66	92.29	92.40	91.01	91.30	91.51	91.78	91.87	92.20	92.06	90.83	91.68	92.62	91.85	91.70	93.97	53.98	66.82	96.05	94.55	94.42	92.66
TREO	18.36	16.66	19.83	19.42	18.51	20.47	19.58	21.36	20.11	20.44	20.81	20.85	20.76	20.39	21.11	20.82	2.20	13.18	24.14	24.88	20.11	18.54

Table B.5 Composition of titanite (in wt.%) in diopside-allanite veins.

SAMPLE	881179-3-503	881179-3-504	881179-3-505	881179-3-506	881179-3-507	881179-3-508	881179-3-509	881179-3-510	881179-3-511	881179-3-512	881179-3-513	881187-9-747	881187-9-748	881187-9-749
SiO_2	29.32	29.23	29.35	29.35	29.70	30.08	30.28	30.06	29.70	29.61	29.74	29.81	29.87	29.98
Al_2O_3	3.39	3.39	3.39	3.37	3.13	2.72	2.16	2.91	3.08	3.07	3.18	3.23	3.67	3.29
Na_2O	0.04	0.03	0.03	0.03	0.03	0.09	0.05	0.12	0.10	bdl	bdl	0.02	bdl	bdl
K_2O	bdl*	bdl	bdl	bdl	bdl	0.02	0.02	0.02	0.02	bdl	0.02	bdl	bdl	bdl
CaO	25.08	25.03	25.12	25.32	26.29	25.28	26.43	24.10	25.15	26.52	26.13	27.07	26.74	27.29
MgO	0.17	0.16	0.17	0.16	0.14	0.96	0.66	1.28	0.19	0.12	0.14	0.12	0.14	0.13
FeO	1.77	1.70	1.82	1.82	1.76	1.88	1.11	2.10	1.68	1.79	1.75	1.86	1.67	1.79
MnO	0.10	0.08	0.09	0.10	0.10	0.07	0.05	0.09	0.12	0.08	0.09	0.09	0.10	0.09
BaO	0.17	0.14	0.12	0.14	0.16	0.29	0.29	0.37	0.32	0.17	0.15	0.12	0.18	0.16
SrO	0.13	0.14	0.10	0.11	0.12	0.07	0.07	0.12	0.11	0.15	0.14	0.11	0.12	0.10
TiO_2	29.32	29.36	29.42	29.67	30.62	31.73	32.70	30.27	30.87	30.72	30.76	30.85	30.29	30.83
Cr_2O_3	bdl	bdl	bdl	bdl	bdl	bdl	bdl	bdl	bdl	bdl	bdl	bdl	bdl	bdl
La_2O_3	0.33	0.44	0.35	0.38	0.15	0.12	0.09	0.15	0.23	0.17	0.20	0.14	0.13	0.14
Ce_2O_3	1.90	1.99	1.93	1.81	0.91	0.54	0.53	0.73	1.11	0.92	1.02	0.74	0.92	0.75
Pr_2O_3	0.31	0.31	0.40	0.29	0.21	0.11	0.07	0.08	0.27	0.19	0.14	0.12	0.22	0.17
Nd_2O_3	2.11	2.23	2.20	2.03	1.36	0.67	0.60	0.93	1.49	1.30	1.36	1.04	1.12	0.87
Sm_2O_3	0.44	0.41	0.43	0.38	0.33	0.20	0.15	0.24	0.30	0.30	0.34	0.21	0.26	0.24
Eu_2O_3	0.08	0.08	0.09	0.13	0.07	bdl	0.07	bdl	0.07	bdl	0.08	0.06	bdl	0.06
Gd_2O_3	0.28	0.22	0.29	0.23	0.24	0.09	0.06	0.13	0.20	0.23	0.18	0.18	0.14	0.14
Tb_2O_3	bdl	bdl	bdl	bdl	bdl	bdl	bdl	bdl	bdl	bdl	bdl	bdl	bdl	bdl
Dy_2O_3	0.10	0.07	0.10	0.12	0.10	0.08	0.07	0.08	0.11	0.09	0.12	0.09	0.07	0.11
Ho_2O_3	bdl	bdl	bdl	bdl	bdl	bdl	bdl	bdl	bdl	bdl	bdl	bdl	bdl	bdl
Er_2O_3	bdl	bdl	bdl	bdl	bdl	bdl	bdl	bdl	bdl	bdl	bdl	bdl	bdl	bdl
Tm_2O_3	bdl	bdl	bdl	bdl	bdl	bdl	bdl	bdl	bdl	bdl	bdl	bdl	bdl	bdl
Yb_2O_3	bdl	bdl	bdl	bdl	bdl	bdl	bdl	bdl	bdl	bdl	bdl	bdl	bdl	bdl
Lu_2O_3	bdl	bdl	bdl	bdl	bdl	bdl	bdl	bdl	bdl	bdl	bdl	bdl	bdl	bdl
Y_2O_3	0.24	0.25	0.27	0.23	0.26	0.12	0.13	0.18	0.26	0.28	0.26	0.25	0.24	0.27
ZrO_2	0.10	0.10	0.14	0.07	0.06	0.11	0.10	0.07	0.06	0.07	0.08	bdl	bdl	bdl
HfO_2	bdl	bdl	bdl	bdl	bdl	bdl	bdl	bdl	bdl	bdl	bdl	bdl	bdl	bdl
Nb_2O_5	0.18	0.18	0.17	0.16	0.16	0.13	0.13	0.16	0.11	0.16	0.13	0.09	0.05	0.07
Sc_2O_3	bdl	bdl	bdl	bdl	bdl	bdl	bdl	bdl	bdl	bdl	bdl	bdl	bdl	bdl
ThO_2	0.09	0.11	0.10	0.09	0.04	bdl	bdl	bdl	0.04	0.05	0.05	bdl	bdl	0.04
UO_2	bdl	0.04	bdl	bdl	bdl	bdl	bdl	bdl	bdl	bdl	bdl	bdl	bdl	bdl
P_2O_5	0.06	0.07	0.10	0.04	0.05	0.04	bdl	bdl	bdl	0.04	bdl	bdl	0.04	bdl
SO_3	bdl	bdl	bdl	bdl	bdl	bdl	bdl	bdl	bdl	bdl	bdl	bdl	bdl	bdl
F	0.64	0.65	0.67	0.58	0.72	0.23	0.14	0.25	0.51	0.74	0.74	0.78	0.86	0.73
Cl	bdl	bdl	bdl	bdl	bdl	0.04	0.04	0.06	0.01	bdl	bdl	0.01	bdl	bdl
TOTAL	96.08	96.13	96.54	96.37	96.40	95.56	95.93	94.38	95.88	96.45	96.48	96.68	96.45	96.91
TREO	5.79	6.00	6.04	5.60	3.63	1.93	1.77	2.52	4.04	3.48	3.70	2.85	3.10	2.73

* below detection limit

Table B.5 cont.

SAMPLE	948521-5-251	948521-7-260	948521-7-261	948521-7-262	948521-7-263	516674-4A-277	516674-4A-278	516674-4A-279	516674-4A-280	516674-5A-283	516674-5A-285	516674-5A-286	516674-5A-287
SiO_2	30.30	30.19	30.20	30.63	30.38	29.78	30.47	30.13	30.29	30.14	29.87	30.17	28.46
Al_2O_3	2.53	3.29	3.72	2.19	2.59	3.38	2.90	3.55	2.85	3.37	4.80	3.42	4.05
Na_2O	bdl	bdl	bdl	bdl	bdl	0.07	0.04	0.05	0.05	0.06	0.12	0.05	0.11
K_2O	bdl	bdl	bdl	bdl	bdl	bdl	bdl	bdl	0.02	bdl	0.02	bdl	0.07
CaO	25.73	24.65	24.59	26.07	25.53	24.67	25.45	24.63	25.43	24.46	18.71	24.63	19.69
MgO	0.05	0.09	0.10	0.04	0.09	0.21	0.12	0.19	0.12	0.21	3.29	0.19	1.81
FeO	1.57	1.63	1.66	1.39	1.65	2.13	1.85	2.05	2.01	2.15	3.47	2.19	4.69
MnO	0.10	0.10	0.10	0.07	0.10	0.12	0.11	0.12	0.11	0.13	0.21	0.11	0.21
BaO	0.16	0.14	0.16	0.18	0.20	0.15	0.16	0.16	0.18	0.17	1.26	0.14	0.70
SrO	0.10	0.19	0.14	bdl	0.13	0.09	0.09	0.10	0.06	0.08	0.12	0.08	0.10
TiO_2	32.52	30.54	30.11	33.28	32.22	30.25	31.53	30.20	31.80	30.08	28.34	30.32	28.37
Cr_2O_3	bdl	0.16	0.11	bdl	0.07	bdl	bdl	bdl	bdl	bdl	bdl	bdl	bdl
La_2O_3	0.19	0.49	0.43	0.12	0.26	0.28	0.10	0.29	0.15	0.27	0.58	0.32	0.34
Ce_2O_3	0.96	1.95	2.02	0.62	1.25	1.64	0.96	1.51	0.95	1.63	2.14	1.59	1.15
Pr_2O_3	0.20	0.29	0.39	0.18	0.26	0.30	0.28	0.35	0.23	0.34	0.35	0.30	0.21
Nd_2O_3	1.26	1.75	1.79	1.15	1.45	1.67	1.35	1.71	1.36	1.87	1.87	1.72	1.17
Sm_2O_3	0.35	0.34	0.26	0.32	0.29	0.44	0.37	0.42	0.34	0.38	0.38	0.41	0.32
Eu_2O_3	0.10	0.08	0.07	0.07	0.12	0.10	0.10	0.07	0.05	0.08	0.05	0.06	0.05
Gd_2O_3	0.19	0.18	0.16	0.14	0.17	0.24	0.18	0.20	0.22	0.23	0.22	0.26	0.16
Tb_2O_3	bdl	bdl	0.06	bdl	bdl	0.06	0.05	0.05	0.05	bdl	bdl	0.05	bdl
Dy_2O_3	0.08	bdl	0.06	0.08	bdl	0.10	0.10	0.11	0.14	0.10	0.08	0.14	0.13
Ho_2O_3	bdl	bdl	bdl	bdl	bdl	bdl	bdl	bdl	bdl	bdl	bdl	bdl	bdl
Er_2O_3	bdl	bdl	bdl	bdl	bdl	bdl	bdl	bdl	bdl	bdl	bdl	bdl	bdl
Tm_2O_3	bdl	bdl	bdl	bdl	bdl	bdl	bdl	bdl	bdl	bdl	bdl	bdl	bdl
Yb_2O_3	bdl	bdl	bdl	bdl	bdl	bdl	bdl	bdl	bdl	bdl	bdl	bdl	bdl
Lu_2O_3	bdl	bdl	bdl	bdl	bdl	bdl	bdl	bdl	bdl	bdl	bdl	bdl	bdl
Y_2O_3	0.32	0.24	0.21	0.26	0.22	0.26	0.34	0.29	0.32	0.42	0.29	0.35	0.26
ZrO_2	0.06	0.18	0.24	bdl	0.09	0.13	0.06	0.12	0.05	0.10	0.14	0.13	bdl
HfO_2	bdl	bdl	bdl	bdl	bdl	bdl	bdl	bdl	bdl	bdl	bdl	bdl	bdl
Nb_2O_5	0.12	0.19	0.21	0.18	0.19	0.24	0.24	0.24	0.23	0.33	0.23	0.28	0.16
Sc_2O_3	bdl	bdl	bdl	bdl	bdl	bdl	bdl	bdl	bdl	bdl	bdl	bdl	bdl
ThO_2	bdl	0.09	0.09	bdl	bdl	bdl	bdl	bdl	bdl	0.05	bdl	0.06	bdl
UO_2	0.04	bdl	bdl	bdl	bdl	0.05	0.05	0.06	bdl	0.05	0.06	0.04	0.05
P_2O_5	bdl	0.06	0.10	bdl	0.09	0.09	0.05	0.06	bdl	0.07	0.11	0.10	0.06
SO_3	bdl	bdl	bdl	bdl	bdl	bdl	bdl	bdl	bdl	bdl	bdl	bdl	bdl
F	0.46	0.53	0.62	0.36	0.39	0.61	0.59	0.68	0.49	0.72	0.31	0.68	0.33
Cl	bdl	bdl	bdl	bdl	bdl	0.01	bdl	bdl	0.01	bdl	0.01	bdl	0.05
TOTAL	97.19	97.09	97.34	97.17	97.57	96.79	97.29	97.03	97.30	97.21	96.89	97.51	92.56
TREO	3.65	5.30	5.46	2.93	4.02	5.08	3.82	5.00	3.80	5.33	5.96	5.21	3.78

Table B.6 Composition of zeolite (in wt.%) in diopside-allanite veins.

SAMPLE	881179-3-514	881179-3-515	881179-3-516	881179-3-517	881179-3-518	881179-8-622	948521-3-232	948521-3-233	948521-3-235	948521-3-236	948521-3-237
SiO_2	41.94	52.30	55.88	50.21	45.47	43.49	53.03	54.61	64.17	64.27	53.30
Al_2O_3	7.95	14.62	16.81	11.77	11.07	17.84	14.55	16.63	14.53	15.37	15.69
Na_2O	bdl*	bdl	bdl	bdl	bdl	0.20	bdl	0.18	0.26	0.21	0.08
K_2O	0.34	0.40	0.30	0.45	0.37	0.45	0.16	0.21	0.33	0.35	0.32
CaO	0.87	1.19	1.06	1.27	1.50	0.11	0.46	0.43	0.83	0.84	0.47
MgO	bdl	bdl	bdl	bdl	bdl	bdl	bdl	bdl	0.01	bdl	bdl
FeO	0.37	0.64	0.16	0.33	0.54	0.15	bdl	bdl	bdl	bdl	bdl
MnO	bdl	bdl	bdl	bdl	bdl	bdl	bdl	bdl	bdl	bdl	bdl
BaO	13.09	14.01	15.02	11.79	11.93	20.70	15.45	16.30	10.58	11.37	15.47
SrO	0.22	0.55	0.41	0.26	0.21	bdl	0.37	0.49	0.44	0.45	0.52
TiO_2	0.08	0.09	0.09	0.10	0.08	0.15	0.11	0.09	0.06	0.07	0.08
Cr_2O_3	bdl	bdl	bdl	bdl	bdl	bdl	bdl	bdl	bdl	bdl	bdl
La_2O_3	bdl	bdl	bdl	bdl	bdl	bdl	bdl	bdl	bdl	bdl	bdl
Ce_2O_3	0.07	0.14	0.21	0.09	0.12	0.20	bdl	bdl	bdl	bdl	bdl
Pr_2O_3	bdl	bdl	bdl	bdl	bdl	bdl	bdl	bdl	bdl	bdl	bdl
Nd_2O_3	bdl	bdl	bdl	bdl	bdl	bdl	bdl	bdl	bdl	bdl	bdl
Sm_2O_3	bdl	bdl	bdl	bdl	bdl	bdl	bdl	bdl	bdl	bdl	bdl
Eu_2O_3	bdl	bdl	bdl	bdl	bdl	bdl	bdl	bdl	bdl	bdl	bdl
Gd_2O_3	bdl	bdl	bdl	bdl	bdl	bdl	bdl	bdl	bdl	bdl	bdl
Tb_2O_3	bdl	bdl	bdl	bdl	bdl	bdl	bdl	bdl	bdl	bdl	bdl
Dy_2O_3	bdl	bdl	bdl	bdl	bdl	bdl	bdl	bdl	bdl	bdl	bdl
Ho_2O_3	bdl	bdl	bdl	bdl	bdl	bdl	bdl	bdl	bdl	bdl	bdl
Er_2O_3	bdl	bdl	bdl	bdl	bdl	bdl	bdl	bdl	bdl	bdl	bdl
Tm_2O_3	bdl	bdl	bdl	bdl	bdl	bdl	bdl	bdl	bdl	bdl	bdl
Yb_2O_3	bdl	bdl	bdl	bdl	bdl	bdl	bdl	bdl	bdl	bdl	bdl
Lu_2O_3	bdl	bdl	bdl	bdl	bdl	bdl	bdl	bdl	bdl	bdl	bdl
Y_2O_3	bdl	bdl	bdl	bdl	bdl	bdl	bdl	bdl	bdl	bdl	bdl
ZrO_2	bdl	bdl	bdl	bdl	bdl	bdl	bdl	bdl	bdl	bdl	bdl
HfO_2	bdl	bdl	bdl	bdl	bdl	bdl	bdl	bdl	bdl	bdl	bdl
Nb_2O_5	bdl	bdl	bdl	bdl	bdl	bdl	bdl	bdl	bdl	bdl	bdl
Sc_2O_3	bdl	bdl	bdl	bdl	bdl	bdl	bdl	bdl	bdl	bdl	bdl
ThO_2	bdl	bdl	bdl	bdl	bdl	bdl	bdl	bdl	bdl	bdl	bdl
UO_2	bdl	bdl	bdl	bdl	bdl	bdl	bdl	bdl	bdl	bdl	bdl
P_2O_5	bdl	bdl	bdl	bdl	bdl	bdl	bdl	bdl	bdl	bdl	bdl
SO_3	bdl	bdl	bdl	bdl	bdl	bdl	bdl	bdl	0.20	0.14	bdl
F	bdl	bdl	bdl	bdl	bdl	bdl	bdl	bdl	bdl	bdl	bdl
Cl	bdl	bdl	bdl	bdl	bdl	bdl	bdl	bdl	bdl	bdl	bdl
TOTAL	64.93	83.94	89.94	76.27	71.28	83.28	84.13	88.95	91.43	93.08	85.94

* below detection limit

Table B.7 Composition of hyalophane, potassium feldspar and albite (in wt.%) in diopside-allanite veins.

SAMPLE	948521-6-256	948521-6-257	948521-6-258	516647-4-305	516647-4-306	516647-4-307	881187-1-699	948521-5-245	948521-5-246	948521-6-253	948521-6-254	881328B-1A-242	881328B-1A-244	881179-3-528	881179-3-529	881179-8-620	881179-8-621
SiO_2	53.50	54.08	53.94	60.65	62.38	61.32	63.39	63.57	58.65	64.31	64.69	49.88	48.73	67.70	65.22	66.95	66.64
Al_2O_3	22.44	22.45	22.46	20.10	19.57	19.46	19.29	19.96	22.07	18.96	19.02	25.93	33.74	22.40	23.13	22.90	23.07
Na_2O	1.59	1.51	1.61	1.03	0.66	0.89	0.37	0.13	0.54	0.24	0.11	0.06	0.09	7.25	7.71	7.26	6.61
K_2O	8.12	8.13	7.97	12.38	13.70	12.92	14.63	13.62	11.66	15.19	15.63	9.92	10.80	0.03	0.02	bdl	0.02
CaO	0.03	0.05	0.06	bdl	0.02	0.10	bdl	1.16	3.11	0.12	0.07	0.08	0.05	bdl	0.04	0.04	0.05
MgO	bdl*	bdl	bdl	bdl	bdl	bdl	bdl	0.38	0.60	0.02	bdl	3.26	1.69	0.24	0.03	0.05	0.09
FeO	0.05	0.07	0.07	0.08	0.04	0.03	0.03	0.59	1.84	0.18	0.09	2.76	0.97	0.16	0.06	0.09	0.09
MnO	bdl	bdl	bdl	bdl	bdl	bdl	bdl	bdl	0.08	bdl	bdl	0.32	0.04	bdl	bdl	bdl	bdl
BaO	12.53	12.50	12.45	5.06	3.09	4.24	1.79	1.12	1.24	1.27	1.51	0.12	0.36	bdl	bdl	bdl	bdl
SrO	2.47	2.36	2.44	1.55	1.14	1.24	0.09	bdl	0.23	0.10	bdl	bdl	bdl	bdl	bdl	bdl	0.06
TiO_2	0.10	0.11	0.12	0.03	0.03	0.03	0.04	bdl	bdl	bdl	bdl	bdl	bdl	bdl	bdl	bdl	bdl
Cr_2O_3	bdl	bdl	bdl	bdl	bdl	bdl	bdl	bdl	bdl	bdl	bdl	bdl	bdl	bdl	bdl	bdl	bdl
La_2O_3	bdl	bdl	bdl	bdl	bdl	bdl	bdl	bdl	bdl	bdl	bdl	bdl	bdl	bdl	bdl	bdl	bdl
Ce_2O_3	bdl	bdl	bdl	bdl	bdl	bdl	bdl	bdl	bdl	bdl	bdl	bdl	bdl	bdl	bdl	bdl	bdl
Pr_2O_3	bdl	bdl	bdl	bdl	bdl	bdl	bdl	bdl	bdl	bdl	bdl	bdl	bdl	bdl	bdl	bdl	bdl
Nd_2O_3	bdl	bdl	bdl	bdl	bdl	bdl	bdl	bdl	bdl	bdl	bdl	bdl	bdl	bdl	bdl	bdl	bdl
Sm_2O_3	bdl	bdl	bdl	bdl	bdl	bdl	bdl	bdl	bdl	bdl	bdl	bdl	bdl	bdl	bdl	bdl	bdl
Eu_2O_3	bdl	bdl	bdl	bdl	bdl	bdl	bdl	bdl	bdl	bdl	bdl	bdl	bdl	bdl	bdl	bdl	bdl
Gd_2O_3	bdl	bdl	bdl	bdl	bdl	bdl	bdl	bdl	bdl	bdl	bdl	bdl	bdl	bdl	bdl	bdl	bdl
Tb_2O_3	bdl	bdl	bdl	bdl	bdl	bdl	bdl	bdl	bdl	bdl	bdl	bdl	bdl	bdl	bdl	bdl	bdl
Dy_2O_3	bdl	bdl	bdl	bdl	bdl	bdl	bdl	bdl	bdl	bdl	bdl	bdl	bdl	bdl	bdl	bdl	bdl
Ho_2O_3	bdl	bdl	bdl	bdl	bdl	bdl	bdl	bdl	bdl	bdl	bdl	bdl	bdl	bdl	bdl	bdl	bdl
Er_2O_3	bdl	bdl	bdl	bdl	bdl	bdl	bdl	bdl	bdl	bdl	bdl	bdl	bdl	bdl	bdl	bdl	bdl
Tm_2O_3	bdl	bdl	bdl	bdl	bdl	bdl	bdl	bdl	bdl	bdl	bdl	bdl	bdl	bdl	bdl	bdl	bdl
Yb_2O_3	bdl	bdl	bdl	bdl	bdl	bdl	bdl	bdl	bdl	bdl	bdl	bdl	bdl	bdl	bdl	bdl	bdl
Lu_2O_3	bdl	bdl	bdl	bdl	bdl	bdl	bdl	bdl	bdl	bdl	bdl	bdl	bdl	bdl	bdl	bdl	bdl
Y_2O_3	bdl	bdl	bdl	bdl	bdl	bdl	bdl	bdl	bdl	bdl	bdl	bdl	bdl	bdl	bdl	bdl	bdl
ZrO_2	bdl	bdl	bdl	bdl	bdl	bdl	bdl	bdl	bdl	bdl	bdl	bdl	bdl	bdl	bdl	bdl	bdl
HfO_2	bdl	bdl	bdl	bdl	bdl	bdl	bdl	bdl	bdl	bdl	bdl	bdl	bdl	bdl	bdl	bdl	bdl
Nb_2O_5	bdl	bdl	bdl	bdl	bdl	bdl	bdl	bdl	bdl	bdl	bdl	bdl	bdl	bdl	bdl	bdl	bdl
Sc_2O_3	bdl	bdl	bdl	bdl	bdl	bdl	bdl	bdl	bdl	bdl	bdl	bdl	bdl	bdl	bdl	bdl	bdl
ThO_2	bdl	bdl	bdl	bdl	bdl	bdl	bdl	bdl	bdl	bdl	bdl	bdl	bdl	bdl	bdl	bdl	bdl
UO_2	bdl	bdl	bdl	bdl	bdl	bdl	bdl	bdl	bdl	bdl	bdl	bdl	bdl	bdl	bdl	bdl	bdl
P_2O_5	bdl	bdl	bdl	bdl	bdl	bdl	bdl	bdl	bdl	bdl	bdl	bdl	bdl	bdl	bdl	bdl	bdl
SO_3	bdl	bdl	bdl	bdl	bdl	bdl	bdl	0.05	0.10	0.04	bdl	bdl	bdl	bdl	bdl	bdl	bdl
F	bdl	bdl	bdl	bdl	bdl	bdl	bdl	0.04	0.05	bdl	bdl	0.05	bdl	bdl	bdl	bdl	bdl
Cl	bdl	bdl	bdl	bdl	bdl	bdl	bdl	0.01	0.13	0.01	bdl	0.01	bdl	bdl	0.01	bdl	0.01
TOTAL	100.82	101.27	101.12	100.87	100.62	100.22	99.62	100.60	100.24	100.44	101.13	92.36	96.45	97.78	96.21	97.27	96.63

* below detection limit

Table B.8 Composition of diopside and green amphibole (actinolite and hornblende) (in wt.%) in diopside-allanite veins.

SAMPLE	881179-6-586	881179-6-587	881179-6-588	881179-6-589	948521-4-244	948521-5-249	948521-5-250	948521-6-255	881187-3-648	881187-5-662	881187-5-691	881187-5-692	881187-5-694	881187-1-695	881187-1-696	881187-1-708	881187-1-709	881187-6-715	881187-6-716	881187-6-717	881187-6-718	948521-3-234	948521-3-238
SiO_2	50.73	50.94	50.83	50.79	51.35	50.87	51.01	50.79	54.10	53.14	52.97	52.92	52.67	50.06	54.49	54.30	54.27	53.78	41.56	54.66	50.53	56.09	59.00
Al_2O_3	2.49	2.27	2.58	2.55	2.58	2.59	2.44	2.82	1.85	2.66	2.53	2.95	2.35	4.51	1.14	1.17	1.10	1.95	11.36	0.85	4.46	0.04	0.05
Na_2O	0.70	0.69	0.75	0.72	0.40	0.42	0.41	0.50	0.56	0.82	0.72	0.90	0.58	1.06	0.26	0.22	0.18	0.75	1.81	0.12	1.24	bdl	bdl
K_2O	bdl*	bdl	bdl	bdl	bdl	bdl	bdl	bdl	0.24	0.24	0.23	0.22	0.06	0.58	0.11	0.05	0.04	0.23	1.85	0.05	0.35	bdl	bdl
CaO	23.25	23.10	23.08	23.01	22.90	22.90	22.96	22.39	12.46	12.53	12.67	12.43	12.67	12.32	12.90	12.78	12.64	12.19	11.82	12.95	12.32	12.32	12.23
MgO	11.47	11.64	11.53	11.46	11.84	11.79	12.05	11.61	17.27	16.83	16.38	16.13	15.21	14.70	16.28	14.88	15.13	16.56	11.01	15.34	15.63	14.06	18.43
FeO	9.00	8.74	8.98	9.02	9.42	9.59	9.68	10.11	9.03	9.55	10.10	10.36	11.34	11.91	10.24	12.06	11.78	10.27	14.74	11.32	10.63	13.84	8.58
MnO	0.54	0.50	0.54	0.52	0.53	0.49	0.53	0.51	0.56	0.46	0.55	0.57	0.47	0.61	0.61	0.53	0.48	0.46	0.40	0.58	0.41	0.33	0.49
BaO	bdl	bdl	bdl	bdl	bdl	bdl	bdl	bdl	bdl	bdl	bdl	bdl	bdl	bdl	bdl	bdl	bdl	bdl	0.25	bdl	bdl	bdl	bdl
SrO	0.13	0.10	0.12	0.10	0.14	0.13	bdl	0.14	bdl	0.04	0.05	bdl	bdl	0.05	bdl	bdl	bdl	bdl	0.16	bdl	0.06	bdl	bdl
TiO_2	0.23	0.25	0.25	0.22	0.22	0.26	0.22	0.27	0.15	0.10	0.14	0.19	0.07	0.15	bdl	0.08	0.05	0.19	0.65	0.06	0.29	bdl	bdl
Cr_2O_3	bdl	bdl	bdl	bdl	bdl	bdl	bdl	0.05	bdl	bdl	bdl	bdl	bdl	bdl	bdl	bdl	bdl	bdl	bdl	bdl	bdl	bdl	bdl
La_2O_3	bdl	bdl	bdl	bdl	bdl	bdl	bdl	bdl	bdl	bdl	bdl	bdl	bdl	bdl	bdl	bdl	bdl	bdl	bdl	bdl	bdl	bdl	bdl
Ce_2O_3	bdl	bdl	bdl	bdl	bdl	bdl	bdl	bdl	bdl	bdl	bdl	bdl	bdl	bdl	bdl	bdl	bdl	bdl	bdl	bdl	bdl	bdl	bdl
Pr_2O_3	bdl	bdl	bdl	bdl	bdl	bdl	bdl	bdl	bdl	bdl	bdl	bdl	bdl	bdl	bdl	bdl	bdl	bdl	bdl	bdl	bdl	bdl	bdl
Nd_2O_3	bdl	bdl	bdl	bdl	bdl	bdl	bdl	bdl	bdl	bdl	bdl	bdl	bdl	bdl	bdl	bdl	bdl	bdl	bdl	bdl	bdl	bdl	bdl
Sm_2O_3	bdl	bdl	bdl	bdl	bdl	bdl	bdl	bdl	bdl	bdl	bdl	bdl	bdl	bdl	bdl	bdl	bdl	bdl	bdl	bdl	bdl	bdl	bdl
Eu_2O_3	bdl	bdl	bdl	bdl	bdl	bdl	bdl	bdl	bdl	bdl	bdl	bdl	bdl	bdl	bdl	bdl	bdl	bdl	bdl	bdl	bdl	bdl	bdl
Gd_2O_3	bdl	bdl	bdl	bdl	bdl	bdl	bdl	bdl	bdl	bdl	bdl	bdl	bdl	bdl	bdl	bdl	bdl	bdl	bdl	bdl	bdl	bdl	bdl
Tb_2O_3	0.07	bdl	0.15	0.09	0.09	0.10	0.09	0.09	0.07	0.08	0.09	0.09	0.09	0.09	0.10	0.10	0.11	0.10	0.16	0.08	0.11	0.13	0.07
Dy_2O_3	0.13	0.19	0.17	0.15	0.11	0.09	0.06	0.10	0.18	0.17	0.14	0.16	0.13	0.15	0.18	0.17	0.19	0.14	0.17	0.19	0.17	0.08	0.07
Ho_2O_3	bdl	bdl	bdl	bdl	bdl	bdl	bdl	bdl	bdl	bdl	bdl	bdl	bdl	bdl	bdl	bdl	bdl	bdl	bdl	bdl	bdl	bdl	bdl
Er_2O_3	bdl	bdl	bdl	bdl	bdl	bdl	bdl	bdl	bdl	bdl	bdl	bdl	bdl	bdl	bdl	bdl	bdl	bdl	0.09	bdl	bdl	bdl	bdl
Tm_2O_3	bdl	bdl	bdl	bdl	bdl	bdl	bdl	bdl	bdl	bdl	bdl	bdl	bdl	bdl	bdl	bdl	bdl	bdl	bdl	bdl	bdl	bdl	bdl
Yb_2O_3	bdl	bdl	bdl	bdl	bdl	bdl	bdl	bdl	bdl	bdl	bdl	bdl	bdl	bdl	bdl	bdl	bdl	bdl	bdl	bdl	bdl	bdl	bdl
Lu_2O_3	bdl	bdl	bdl	bdl	bdl	bdl	bdl	bdl	bdl	bdl	bdl	bdl	bdl	bdl	bdl	bdl	bdl	bdl	bdl	bdl	bdl	bdl	bdl
Y_2O_3	bdl	bdl	bdl	bdl	0.09	bdl	bdl	bdl	bdl	bdl	bdl	bdl	bdl	bdl	bdl	bdl	bdl	bdl	bdl	bdl	bdl	bdl	bdl
ZrO_2	bdl	bdl	bdl	bdl	bdl	bdl	bdl	bdl	bdl	bdl	bdl	bdl	bdl	bdl	bdl	bdl	bdl	bdl	bdl	bdl	bdl	bdl	bdl
HfO_2	bdl	bdl	bdl	bdl	bdl	bdl	bdl	bdl	bdl	bdl	bdl	bdl	bdl	bdl	bdl	bdl	bdl	bdl	bdl	bdl	bdl	bdl	bdl
Nb_2O_5	bdl	bdl	bdl	bdl	bdl	bdl	bdl	bdl	bdl	bdl	bdl	bdl	bdl	bdl	bdl	bdl	bdl	bdl	bdl	bdl	bdl	bdl	bdl
Sc_2O_3	bdl	bdl	bdl	bdl	bdl	bdl	bdl	bdl	bdl	bdl	bdl	bdl	bdl	bdl	bdl	bdl	bdl	bdl	bdl	bdl	bdl	bdl	bdl
ThO_2	bdl	bdl	bdl	bdl	bdl	bdl	bdl	bdl	bdl	bdl	bdl	bdl	bdl	bdl	bdl	bdl	bdl	bdl	bdl	bdl	bdl	bdl	bdl
UO_2	bdl	bdl	bdl	bdl	bdl	0.04	bdl	bdl	bdl	bdl	bdl	bdl	bdl	bdl	bdl	bdl	bdl	bdl	bdl	bdl	bdl	bdl	bdl
P_2O_5	bdl	bdl	bdl	bdl	bdl	bdl	bdl	bdl	bdl	bdl	bdl	bdl	bdl	bdl	bdl	bdl	bdl	bdl	bdl	bdl	bdl	bdl	bdl
SO_3	bdl	bdl	bdl	bdl	bdl	bdl	bdl	bdl	bdl	bdl	bdl	bdl	bdl	bdl	bdl	bdl	bdl	bdl	bdl	bdl	bdl	bdl	bdl
F	bdl	bdl	bdl	bdl	bdl	bdl	bdl	0.04	0.52	0.53	0.51	0.53	0.41	0.49	0.33	0.08	0.13	0.56	0.71	0.09	0.53	bdl	0.23
Cl	bdl	bdl	bdl	bdl	bdl	bdl	bdl	bdl	0.05	0.11	0.08	0.14	0.08	0.15	0.01	bdl	bdl	bdl	0.25	bdl	0.03	bdl	0.01
TOTAL	98.75	98.41	98.99	98.64	99.67	99.26	99.43	99.41	96.78	97.01	96.93	97.32	95.95	96.59	96.50	96.38	96.04	96.95	96.64	96.25	96.54	96.88	99.06

* below detection limit

Table B.9 Composition of biotite, epidote, barite and calcite (in wt.%) in diopside-allanite veins.

SAMPLE	516674-4A-275	516674-4A-276	948521-5-247	948521-5-248	881328B-1A-243	881328B-2A-248	881328B-2A-249	881179-6-592	881179-6-593	881179-6-594	948521-4-243
SiO_2	37.46	36.97	36.29	37.17	37.24	37.07	38.09	0.07	bdl	0.05	bdl
Al_2O_3	13.14	13.34	23.62	22.67	25.63	22.36	28.51	0.71	0.75	0.76	bdl
Na_2O	0.16	0.15	bdl	bdl	bdl	bdl	bdl	0.08	0.08	0.11	bdl
K_2O	8.85	8.72	bdl	bdl	bdl	bdl	bdl	bdl	bdl	bdl	bdl
CaO	bdl*	0.02	19.84	21.04	21.09	20.25	22.16	bdl	bdl	bdl	50.91
MgO	16.90	16.36	0.02	0.01	0.03	0.02	0.02	0.02	bdl	bdl	0.01
FeO	13.12	13.68	11.23	11.72	8.91	12.98	5.70	0.07	0.03	0.04	0.02
MnO	0.29	0.30	0.25	0.10	0.45	0.08	0.07	bdl	bdl	bdl	0.29
BaO	2.99	3.41	bdl	bdl	bdl	bdl	bdl	57.07	57.93	57.65	bdl
SrO	bdl	bdl	4.89	3.27	3.95	4.70	2.78	1.27	0.55	0.36	0.15
TiO_2	2.42	2.49	bdl	bdl	bdl	bdl	bdl	0.45	0.48	0.48	bdl
Cr_2O_3	bdl	bdl	bdl	bdl	bdl	bdl	bdl	bdl	bdl	bdl	bdl
La_2O_3	bdl	bdl	0.05	bdl	bdl	bdl	bdl	bdl	bdl	bdl	bdl
Ce_2O_3	bdl	bdl	bdl	bdl	bdl	bdl	bdl	0.90	0.86	0.79	bdl
Pr_2O_3	bdl	bdl	bdl	bdl	bdl	bdl	bdl	bdl	bdl	bdl	bdl
Nd_2O_3	bdl	bdl	bdl	bdl	bdl	bdl	bdl	bdl	bdl	bdl	bdl
Sm_2O_3	bdl	bdl	bdl	bdl	bdl	bdl	bdl	bdl	bdl	bdl	bdl
Eu_2O_3	bdl	bdl	bdl	bdl	bdl	bdl	bdl	bdl	bdl	bdl	bdl
Gd_2O_3	bdl	bdl	bdl	bdl	0.04	bdl	bdl	bdl	bdl	bdl	bdl
Tb_2O_3	0.08	0.08	0.07	0.11	0.06	0.08	bdl	bdl	bdl	bdl	bdl
Dy_2O_3	0.09	0.07	bdl	0.05	0.06	bdl	0.04	bdl	bdl	bdl	bdl
Ho_2O_3	bdl	bdl	bdl	bdl	bdl	bdl	bdl	bdl	bdl	bdl	bdl
Er_2O_3	bdl	bdl	bdl	bdl	bdl	bdl	bdl	bdl	bdl	bdl	bdl
Tm_2O_3	bdl	bdl	bdl	bdl	bdl	bdl	bdl	bdl	bdl	bdl	bdl
Yb_2O_3	bdl	bdl	bdl	bdl	bdl	bdl	bdl	bdl	bdl	bdl	bdl
Lu_2O_3	bdl	bdl	bdl	bdl	bdl	bdl	bdl	bdl	bdl	bdl	bdl
Y_2O_3	bdl	bdl	bdl	bdl	bdl	bdl	bdl	bdl	bdl	bdl	bdl
ZrO_2	bdl	bdl	bdl	bdl	bdl	bdl	bdl	bdl	bdl	bdl	bdl
HfO_2	bdl	bdl	bdl	bdl	bdl	bdl	bdl	bdl	bdl	bdl	bdl
Nb_2O_5	bdl	bdl	bdl	bdl	bdl	bdl	bdl	bdl	0.06	bdl	bdl
Sc_2O_3	bdl	bdl	bdl	bdl	bdl	bdl	bdl	bdl	bdl	bdl	bdl
ThO_2	bdl	bdl	bdl	bdl	bdl	bdl	bdl	bdl	bdl	bdl	bdl
UO_2	0.03	bdl	bdl	bdl	bdl	bdl	bdl	bdl	bdl	bdl	bdl
P_2O_5	bdl	bdl	bdl	0.08	bdl	bdl	bdl	bdl	bdl	bdl	bdl
SO_3	0.04	0.05	bdl	bdl	bdl	bdl	bdl	33.20	32.50	32.49	bdl
F	1.39	1.42	bdl	bdl	0.07	bdl	bdl	bdl	bdl	bdl	bdl
Cl	0.39	0.43	bdl	bdl	0.03	bdl	bdl	bdl	bdl	bdl	bdl
TOTAL	96.67	96.79	96.23	96.22	97.52	97.53	97.37	93.82	93.24	92.73	51.37

* below detection limit

Table B.10 Composition of chlorite (in wt.%) in diopside-allanite veins.

SAMPLE	881179-1-457	881179-1-458	881179-3-499	881179-3-500	881179-3-501	881179-3-502	881179-3-523	881179-3-524	881179-3-525	881179-3-530	881179-3-531	881179-3-532	881179-3-533	881179-8-618	881179-8-619	881187-3-652	881187-1-697	881187-1-702
SiO_2	28.60	28.61	27.29	27.31	27.79	27.61	28.44	28.64	27.47	41.35	34.16	35.23	27.53	28.90	28.99	39.22	42.25	21.56
Al_2O_3	14.95	14.63	16.16	15.99	15.94	15.36	15.66	15.95	16.10	11.60	12.51	12.45	9.95	15.19	15.21	19.50	11.42	4.16
Na_2O	bdl*	bdl	bdl	bdl	bdl	bdl	bdl	bdl	bdl	0.09	0.02	0.04	bdl	bdl	bdl	0.06	0.09	0.07
K_2O	0.02	bdl	0.02	bdl	bdl	bdl	bdl	0.02	bdl	0.93	0.03	0.02	bdl	bdl	bdl	1.34	1.82	0.07
CaO	0.14	0.25	0.39	0.43	0.42	0.37	0.31	0.23	0.37	1.05	0.23	0.21	0.34	0.19	0.21	0.24	0.71	0.66
MgO	15.70	14.72	9.67	9.54	10.72	10.66	12.99	13.86	10.35	19.36	24.46	26.66	22.29	15.12	15.35	12.66	17.25	11.07
FeO	22.43	22.57	28.75	28.78	26.89	27.88	25.69	24.54	28.20	5.43	11.64	8.26	6.57	23.28	23.03	13.04	12.04	38.47
MnO	0.37	0.48	0.70	0.76	0.73	0.66	0.51	0.41	0.67	0.24	0.09	0.07	0.08	0.50	0.51	0.28	0.35	0.56
BaO	bdl	bdl	bdl	bdl	bdl	bdl	bdl	bdl	bdl	0.68	bdl	bdl	bdl	bdl	bdl	0.20	0.26	0.35
SrO	bdl	bdl	bdl	bdl	bdl	bdl	bdl	bdl	bdl	0.06	bdl	bdl	bdl	bdl	bdl	bdl	0.07	0.06
TiO_2	0.12	0.03	bdl	bdl	bdl	bdl	0.04	0.02	bdl	0.03	bdl	bdl	bdl	bdl	0.03	bdl	bdl	0.03
Cr_2O_3	bdl	bdl	bdl	bdl	bdl	bdl	bdl	bdl	bdl	bdl	bdl	bdl	0.03	bdl	bdl	bdl	bdl	bdl
La_2O_3	bdl	bdl	bdl	bdl	bdl	bdl	bdl	bdl	bdl	bdl	bdl	bdl	3.47	bdl	bdl	bdl	bdl	bdl
Ce_2O_3	bdl	bdl	bdl	bdl	bdl	bdl	bdl	bdl	bdl	bdl	bdl	bdl	6.36	bdl	bdl	0.15	bdl	bdl
Pr_2O_3	bdl	bdl	bdl	bdl	bdl	bdl	bdl	bdl	bdl	bdl	bdl	bdl	0.60	bdl	bdl	bdl	bdl	bdl
Nd_2O_3	bdl	bdl	bdl	bdl	bdl	bdl	bdl	bdl	bdl	bdl	bdl	bdl	2.79	bdl	bdl	bdl	bdl	bdl
Sm_2O_3	bdl	bdl	bdl	bdl	bdl	bdl	bdl	bdl	bdl	bdl	bdl	bdl	0.10	bdl	bdl	bdl	bdl	bdl
Eu_2O_3	bdl	bdl	bdl	bdl	bdl	bdl	bdl	bdl	bdl	bdl	bdl	bdl	bdl	bdl	bdl	bdl	bdl	bdl
Gd_2O_3	bdl	bdl	bdl	bdl	bdl	bdl	bdl	bdl	bdl	bdl	bdl	bdl	0.14	bdl	bdl	bdl	bdl	bdl
Tb_2O_3	0.19	0.21	0.28	0.25	0.25	0.25	0.24	0.21	0.26	bdl	0.08	bdl	bdl	0.21	0.22	0.11	0.10	0.40
Dy_2O_3	0.18	0.21	0.26	0.28	0.27	0.29	0.20	0.23	0.27	0.06	bdl	bdl	bdl	0.20	0.22	0.09	0.12	0.26
Ho_2O_3	bdl	bdl	bdl	bdl	bdl	bdl	bdl	bdl	bdl	bdl	bdl	bdl	bdl	bdl	bdl	bdl	bdl	bdl
Er_2O_3	0.06	0.06	0.15	0.10	0.09	bdl	0.09	bdl	0.08	bdl	bdl	bdl	bdl	bdl	0.09	bdl	bdl	0.17
Tm_2O_3	bdl	bdl	bdl	bdl	bdl	bdl	bdl	bdl	bdl	bdl	bdl	bdl	bdl	bdl	bdl	bdl	bdl	bdl
Yb_2O_3	bdl	bdl	bdl	bdl	bdl	bdl	bdl	bdl	bdl	bdl	bdl	bdl	bdl	bdl	bdl	bdl	bdl	bdl
Lu_2O_3	bdl	bdl	bdl	bdl	bdl	bdl	bdl	bdl	bdl	bdl	bdl	bdl	bdl	bdl	bdl	bdl	bdl	bdl
Y_2O_3	bdl	bdl	bdl	bdl	bdl	bdl	bdl	bdl	bdl	bdl	bdl	bdl	bdl	bdl	bdl	bdl	bdl	bdl
ZrO_2	bdl	bdl	bdl	bdl	bdl	bdl	bdl	bdl	bdl	bdl	bdl	bdl	bdl	bdl	bdl	bdl	bdl	bdl
HfO_2	bdl	bdl	bdl	bdl	bdl	bdl	bdl	bdl	bdl	bdl	bdl	bdl	bdl	bdl	bdl	bdl	bdl	bdl
Nb_2O_5	bdl	bdl	bdl	bdl	bdl	bdl	bdl	bdl	bdl	bdl	bdl	bdl	bdl	bdl	bdl	bdl	bdl	bdl
Sc_2O_3	bdl	bdl	bdl	bdl	bdl	bdl	bdl	bdl	bdl	bdl	bdl	bdl	bdl	bdl	bdl	bdl	bdl	bdl
ThO_2	bdl	bdl	bdl	bdl	bdl	bdl	bdl	bdl	bdl	bdl	bdl	bdl	bdl	bdl	bdl	bdl	bdl	bdl
UO_2	bdl	bdl	0.05	bdl	bdl	0.07	0.05	bdl	0.06	bdl	bdl	bdl	bdl	0.06	bdl	bdl	bdl	0.08
P_2O_5	bdl	bdl	bdl	bdl	bdl	bdl	bdl	bdl	bdl	0.05	bdl	bdl	bdl	bdl	bdl	bdl	0.06	bdl
SO_3	bdl	bdl	bdl	bdl	bdl	bdl	bdl	bdl	bdl	bdl	bdl	bdl	bdl	bdl	bdl	bdl	bdl	bdl
F	bdl	bdl	bdl	bdl	bdl	bdl	bdl	bdl	bdl	bdl	bdl	bdl	0.38	bdl	bdl	bdl	bdl	bdl
Cl	bdl	0.01	0.01	0.01	0.01	0.01	0.01	0.02	0.01	0.16	0.02	0.04	0.03	bdl	bdl	0.02	0.14	0.10
TOTAL	82.74	81.79	83.73	83.44	83.11	83.16	84.23	84.13	83.84	81.06	83.23	82.97	80.50	83.65	83.86	86.92	86.62	78.05

* below detection limit

Table B.10 cont.

SAMPLE	881187-1-703	881187-1-704	881187-1-705	881187-1-706	881187-1-707	881187-1-710	881187-1-712	881187-6-719	881187-6-720	881187-6-726	881187-6-727	881187-7-737	881187-8-745	881187-8-746	881187-11-763	881187-11-764	881187-11-765	948521-3-231
SiO_2	45.32	24.91	24.71	43.90	40.02	48.52	39.19	43.99	45.63	45.57	47.77	37.81	45.19	42.96	36.57	37.50	31.92	44.04
Al_2O_3	13.71	2.98	4.60	13.06	10.93	5.21	14.75	7.72	7.07	6.34	6.08	11.94	11.92	11.79	15.46	13.34	13.70	5.71
Na_2O	0.06	0.21	0.09	0.04	0.04	0.30	0.03	0.24	0.25	0.24	0.16	0.02	0.03	0.04	bdl	bdl	0.12	0.09
K_2O	2.34	0.14	0.07	1.95	0.27	0.12	0.34	0.21	0.15	0.11	0.09	0.06	3.40	3.57	0.04	bdl	0.13	0.11
CaO	0.56	0.67	0.71	0.51	0.18	0.94	0.58	0.77	0.90	0.90	1.14	0.50	0.51	0.55	0.31	0.33	6.69	1.76
MgO	13.40	11.17	12.81	14.80	29.69	25.09	18.41	25.67	26.50	25.81	26.32	25.06	15.57	15.00	26.50	25.80	10.44	16.36
FeO	9.61	36.44	36.55	10.86	4.19	4.62	9.57	5.36	4.93	4.54	4.20	7.27	8.77	12.27	6.14	6.87	11.83	12.08
MnO	0.30	0.48	0.55	0.36	0.11	0.17	0.25	0.15	0.16	0.14	0.13	0.45	0.57	0.60	0.36	0.39	0.71	0.17
BaO	0.70	0.43	0.41	0.61	bdl	0.18	0.15	0.27	0.19	0.23	0.21	0.38	0.36	0.55	0.26	0.25	0.63	0.34
SrO	0.05	bdl	bdl	0.10	bdl	0.11	0.06	0.06	0.09	0.07	0.11	0.06	0.08	0.06	bdl	0.06	0.76	0.18
TiO_2	0.03	bdl	bdl	bdl	bdl	bdl	bdl	0.03	0.02	bdl	0.03	0.03	0.30	1.10	0.04	0.05	0.47	0.05
Cr_2O_3	bdl	bdl	bdl	bdl	bdl	bdl	bdl	bdl	bdl	bdl	bdl	bdl	bdl	bdl	bdl	bdl	0.11	bdl
La_2O_3	bdl	bdl	bdl	bdl	bdl	bdl	bdl	bdl	bdl	bdl	bdl	bdl	0.14	0.12	bdl	bdl	3.47	bdl
Ce_2O_3	bdl	bdl	bdl	bdl	bdl	bdl	bdl	bdl	bdl	bdl	bdl	0.05	0.32	0.18	bdl	bdl	5.99	bdl
Pr_2O_3	bdl	bdl	bdl	bdl	bdl	bdl	bdl	bdl	bdl	bdl	bdl	bdl	bdl	bdl	bdl	bdl	0.59	bdl
Nd_2O_3	bdl	bdl	bdl	bdl	bdl	bdl	bdl	bdl	bdl	bdl	bdl	bdl	0.10	0.05	bdl	bdl	1.59	bdl
Sm_2O_3	bdl	bdl	bdl	bdl	bdl	bdl	bdl	bdl	bdl	bdl	bdl	bdl	bdl	bdl	bdl	bdl	0.14	bdl
Eu_2O_3	bdl	bdl	bdl	bdl	bdl	bdl	bdl	bdl	bdl	bdl	bdl	bdl	bdl	bdl	bdl	bdl	bdl	bdl
Gd_2O_3	bdl	bdl	bdl	bdl	bdl	bdl	bdl	bdl	bdl	bdl	bdl	bdl	bdl	bdl	bdl	bdl	0.14	bdl
Tb_2O_3	bdl	0.28	0.35	0.06	bdl	bdl	bdl	bdl	bdl	bdl	bdl	bdl	bdl	0.07	bdl	bdl	bdl	0.05
Dy_2O_3	0.06	0.23	0.27	0.07	bdl	0.05	0.06	bdl	bdl	bdl	bdl	0.08	0.15	0.20	0.08	0.10	0.15	0.06
Ho_2O_3	bdl	bdl	bdl	bdl	bdl	bdl	bdl	bdl	bdl	bdl	bdl	bdl	bdl	bdl	bdl	bdl	bdl	bdl
Er_2O_3	bdl	0.16	0.14	bdl	bdl	bdl	bdl	bdl	bdl	bdl	bdl	bdl	bdl	bdl	bdl	bdl	bdl	bdl
Tm_2O_3	bdl	bdl	bdl	bdl	bdl	bdl	bdl	bdl	bdl	bdl	bdl	bdl	bdl	bdl	bdl	bdl	bdl	bdl
Yb_2O_3	bdl	bdl	bdl	bdl	bdl	bdl	bdl	bdl	bdl	bdl	bdl	bdl	bdl	bdl	bdl	bdl	bdl	bdl
Lu_2O_3	bdl	bdl	bdl	bdl	bdl	bdl	bdl	bdl	bdl	bdl	bdl	bdl	bdl	bdl	bdl	bdl	bdl	bdl
Y_2O_3	bdl	bdl	bdl	bdl	bdl	bdl	bdl	bdl	bdl	bdl	bdl	bdl	bdl	bdl	bdl	bdl	bdl	bdl
ZrO_2	bdl	bdl	bdl	bdl	bdl	bdl	bdl	bdl	bdl	bdl	bdl	bdl	bdl	bdl	bdl	bdl	bdl	bdl
HfO_2	bdl	bdl	bdl	bdl	bdl	bdl	bdl	bdl	bdl	bdl	bdl	bdl	bdl	bdl	bdl	bdl	bdl	bdl
Nb_2O_5	bdl	bdl	bdl	bdl	bdl	bdl	bdl	bdl	bdl	bdl	bdl	bdl	bdl	bdl	bdl	bdl	bdl	bdl
Sc_2O_3	bdl	bdl	bdl	bdl	bdl	bdl	bdl	bdl	bdl	bdl	bdl	bdl	bdl	bdl	bdl	bdl	bdl	bdl
ThO_2	bdl	bdl	bdl	bdl	bdl	bdl	bdl	bdl	bdl	bdl	bdl	bdl	0.34	bdl	bdl	bdl	0.22	bdl
UO_2	bdl	0.07	0.09	bdl	bdl	bdl	bdl	bdl	bdl	bdl	bdl	bdl	bdl	bdl	bdl	bdl	bdl	bdl
P_2O_5	0.05	0.15	0.09	bdl	bdl	0.14	bdl	bdl	bdl	bdl	bdl	bdl	bdl	bdl	bdl	bdl	bdl	bdl
SO_3	bdl	bdl	bdl	bdl	bdl	bdl	bdl	bdl	bdl	bdl	bdl	bdl	bdl	bdl	bdl	bdl	bdl	bdl
F	bdl	bdl	bdl	bdl	bdl	bdl	bdl	0.09	0.09	bdl	0.18	0.10	0.12	0.09	0.09	0.18	bdl	0.07
Cl	0.11	0.26	0.16	0.07	0.12	0.26	0.08	0.06	0.06	0.07	0.05	0.06	0.03	0.03	0.09	0.08	0.08	0.10
TOTAL	86.27	78.50	81.56	86.37	85.51	85.63	83.44	84.55	85.99	83.99	86.40	83.82	87.83	89.20	85.87	84.86	89.88	81.11

Table B.11 Composition of REE-carbonate (in wt.%) in diopside-allanite veins.

SAMPLE	881179-1-453	881179-1-455	881179-1-456	881179-2-470	881179-2-471	881179-2-472	881179-2-473	881179-3-496	881179-3-498	881179-3-519	881179-3-520	881179-3-521	881179-4-565	881179-4-566	881179-5-581	881179-6-591	881179-6-590
SiO_2	0.47	0.21	1.55	0.42	1.08	2.41	0.37	0.40	1.07	0.52	0.41	1.51	0.89	1.92	1.23	0.53	0.44
Al_2O_3	bdl*	bdl	0.60	0.06	0.27	0.68	bdl	0.03	0.37	0.03	bdl	0.35	0.04	0.21	0.42	0.03	bdl
Na_2O	bdl	bdl	bdl	bdl	bdl	bdl	bdl	bdl	bdl	bdl	bdl	bdl	bdl	bdl	bdl	bdl	bdl
K_2O	bdl	bdl	bdl	bdl	bdl	0.03	bdl	bdl	bdl	bdl	bdl	bdl	bdl	bdl	bdl	bdl	bdl
CaO	2.64	2.12	1.96	0.68	1.50	3.22	0.74	1.93	0.48	1.33	1.38	1.58	1.43	1.20	2.27	0.48	0.71
MgO	0.18	0.02	0.84	0.15	0.43	0.41	0.04	0.10	1.15	0.08	0.06	0.81	0.06	0.12	0.30	0.13	0.09
FeO	bdl	0.10	0.69	0.10	0.12	0.41	0.25	bdl	0.21	0.30	0.15	0.20	0.03	bdl	0.33	0.05	0.20
MnO	bdl	bdl	0.04	bdl	bdl	0.03	bdl	bdl	bdl	bdl	bdl	bdl	bdl	bdl	0.06	bdl	bdl
BaO	bdl	bdl	bdl	bdl	bdl	bdl	bdl	bdl	bdl	bdl	bdl	bdl	bdl	bdl	bdl	bdl	bdl
SrO	bdl	0.08	0.08	bdl	bdl	0.09	bdl	bdl	bdl	0.11	0.11	0.07	0.11	0.11	0.12	bdl	bdl
TiO_2	bdl	bdl	bdl	bdl	bdl	bdl	bdl	bdl	bdl	bdl	bdl	bdl	bdl	bdl	0.06	bdl	bdl
Cr_2O_3	0.72	0.62	0.54	0.79	0.59	0.48	0.72	0.61	0.72	0.54	0.54	0.57	1.03	0.82	0.60	0.62	0.50
La_2O_3	24.48	20.50	17.13	27.31	20.10	16.43	25.16	20.83	25.38	19.51	19.44	19.40	41.27	29.26	25.56	21.32	16.50
Ce_2O_3	33.40	36.38	36.32	34.20	37.36	35.16	34.69	37.23	35.67	33.09	31.98	32.42	16.95	30.77	23.85	35.49	38.05
Pr_2O_3	2.68	3.38	3.77	2.62	2.84	3.57	2.87	3.26	2.70	3.58	3.77	3.40	4.30	3.03	5.18	3.62	3.55
Nd_2O_3	9.32	11.26	12.85	9.62	10.22	12.57	10.28	10.95	9.47	16.20	16.56	15.40	13.79	10.17	17.68	12.95	15.02
Sm_2O_3	0.53	0.49	0.62	0.56	0.75	0.56	0.63	0.50	0.42	1.64	1.70	1.14	0.47	0.44	0.78	0.82	1.18
Eu_2O_3	bdl	bdl	0.08	0.07	0.09	0.11	bdl	bdl	bdl	0.40	0.31	0.16	0.08	0.08	0.13	bdl	0.15
Gd_2O_3	1.31	1.47	1.27	1.48	1.55	1.29	1.46	1.33	1.21	1.79	1.93	1.47	0.82	1.23	1.10	1.39	1.37
Tb_2O_3	bdl	bdl	bdl	bdl	bdl	bdl	bdl	bdl	bdl	bdl	bdl	bdl	bdl	bdl	bdl	bdl	bdl
Dy_2O_3	bdl	bdl	bdl	bdl	bdl	bdl	bdl	bdl	bdl	bdl	bdl	bdl	bdl	bdl	bdl	bdl	bdl
Ho_2O_3	bdl	bdl	bdl	bdl	bdl	bdl	bdl	bdl	bdl	bdl	bdl	bdl	bdl	bdl	bdl	bdl	bdl
Er_2O_3	bdl	bdl	bdl	bdl	bdl	bdl	bdl	bdl	bdl	bdl	bdl	bdl	bdl	bdl	bdl	bdl	bdl
Tm_2O_3	bdl	bdl	bdl	bdl	bdl	bdl	bdl	bdl	bdl	bdl	bdl	bdl	bdl	bdl	bdl	bdl	bdl
Yb_2O_3	bdl	bdl	bdl	bdl	bdl	bdl	bdl	bdl	bdl	bdl	bdl	bdl	bdl	bdl	bdl	bdl	bdl
Lu_2O_3	bdl	bdl	bdl	bdl	bdl	bdl	bdl	bdl	bdl	bdl	bdl	bdl	bdl	bdl	bdl	bdl	bdl
Y_2O_3	bdl	bdl	bdl	bdl	bdl	bdl	bdl	bdl	bdl	0.26	0.26	0.11	bdl	bdl	bdl	bdl	bdl
ZrO_2	bdl	bdl	bdl	bdl	bdl	bdl	bdl	bdl	bdl	bdl	bdl	bdl	bdl	bdl	bdl	bdl	bdl
HfO_2	bdl	bdl	bdl	bdl	bdl	bdl	bdl	bdl	bdl	bdl	bdl	bdl	bdl	bdl	bdl	bdl	bdl
Nb_2O_5	bdl	bdl	bdl	bdl	bdl	bdl	bdl	bdl	bdl	bdl	bdl	bdl	bdl	bdl	bdl	bdl	bdl
Sc_2O_3	bdl	bdl	bdl	bdl	bdl	bdl	bdl	bdl	bdl	bdl	bdl	bdl	bdl	bdl	bdl	bdl	bdl
ThO_2	bdl	bdl	bdl	bdl	bdl	bdl	bdl	bdl	bdl	bdl	bdl	bdl	bdl	bdl	0.51	bdl	bdl
UO_2	bdl	bdl	bdl	bdl	bdl	bdl	bdl	bdl	bdl	bdl	bdl	bdl	bdl	bdl	bdl	bdl	bdl
P_2O_5	bdl	bdl	bdl	bdl	bdl	bdl	bdl	bdl	bdl	bdl	bdl	bdl	bdl	bdl	bdl	bdl	bdl
SO_3	bdl	bdl	bdl	bdl	bdl	0.06	bdl	bdl	bdl	0.07	0.10	0.05	0.11	0.08	0.09	bdl	bdl
F	0.33	bdl	bdl	bdl	bdl	0.17	bdl	bdl	bdl	bdl	bdl	0.13	0.61	0.23	0.50	bdl	bdl
Cl	0.10	0.21	0.28	0.09	0.12	0.19	0.08	0.29	0.06	0.21	0.21	0.09	0.20	0.22	0.22	0.07	0.07
TOTAL	76.00	76.77	78.55	78.13	77.00	77.77	77.27	77.39	78.90	79.62	78.86	78.77	81.90	79.72	80.73	77.50	77.82
TREO	71.72	73.48	72.03	75.85	72.91	69.70	75.10	74.11	74.85	76.48	75.94	73.49	77.69	74.97	74.28	75.60	75.83

* below detection limit

Table B.11 cont.

SAMPLE	881179-6-595	881179-6-596	881179-8-616	881179-8-617	881187-1-700	881187-1-701	881187-9-752	881187-9-753	881187-9-754	881187-9-755	881187-9-756	881187-9-757	881187-9-758	881187-9-759	881187-9-760	881341-1C-234	881328B-1A-247	881328B-3A-255
SiO_2	0.68	0.37	0.22	0.20	1.83	1.14	0.95	0.49	0.93	0.49	0.85	0.78	0.58	0.59	1.05	0.61	3.81	1.74
Al_2O_3	bdl	bdl	bdl	bdl	0.17	0.07	0.03	0.03	0.17	0.04	0.17	0.13	0.06	0.08	0.21	0.10	1.33	0.82
Na_2O	bdl	bdl	bdl	bdl	bdl	bdl	bdl	bdl	bdl	bdl	bdl	bdl	bdl	bdl	bdl	0.07	0.07	0.06
K_2O	bdl	bdl	bdl	bdl	bdl	bdl	bdl	bdl	bdl	bdl	bdl	bdl	bdl	bdl	bdl	bdl	0.09	bdl
CaO	1.67	0.48	0.34	0.47	0.93	1.02	0.80	0.76	0.91	0.94	1.02	0.88	0.98	0.88	0.92	1.31	1.85	2.15
MgO	0.03	0.06	0.03	0.03	0.50	0.12	0.06	0.06	0.38	0.12	0.43	0.30	0.19	0.19	0.52	0.08	0.98	0.45
FeO	0.04	0.06	bdl	bdl	0.08	0.06	0.08	0.12	0.93	0.43	0.46	1.71	1.08	1.31	1.28	4.36	1.66	2.55
MnO	bdl	bdl	bdl	bdl	0.06	0.08	0.04	bdl	bdl	bdl	bdl	bdl	bdl	bdl	bdl	bdl	bdl	bdl
BaO	bdl	bdl	bdl	bdl	0.08	0.08	bdl	bdl	bdl	bdl	0.09	bdl	bdl	bdl	bdl	0.26	bdl	bdl
SrO	0.13	bdl	bdl	0.07	0.12	0.12	0.09	bdl	0.07	0.11	0.09	0.14	bdl	0.09	bdl	0.35	0.20	bdl
TiO_2	bdl	bdl	bdl	bdl	bdl	bdl	bdl	bdl	bdl	bdl	bdl	bdl	bdl	bdl	bdl	bdl	bdl	0.49
Cr_2O_3	0.94	0.66	0.74	0.83	0.68	0.69	0.86	0.97	0.48	0.62	0.47	0.48	0.45	0.47	0.45	0.06	0.06	0.08
La_2O_3	40.04	23.55	25.13	29.73	22.28	25.84	37.22	42.44	13.52	22.88	13.13	14.96	14.53	14.07	12.73	15.75	14.49	15.42
Ce_2O_3	13.24	34.98	35.80	34.76	33.99	29.94	17.32	11.16	45.83	33.45	46.23	42.66	43.30	44.85	46.79	31.33	29.22	31.03
Pr_2O_3	4.85	3.51	3.17	2.73	4.34	4.68	5.43	5.90	2.64	4.13	2.78	2.88	2.68	2.53	2.28	3.19	3.67	3.14
Nd_2O_3	15.73	13.53	10.95	8.31	14.05	15.06	16.40	16.89	10.61	14.29	10.56	11.06	10.90	10.46	9.93	11.63	14.58	11.79
Sm_2O_3	0.44	0.90	0.56	0.29	0.73	0.56	0.53	0.36	0.77	0.72	0.81	0.81	0.78	0.84	0.88	1.36	1.68	1.08
Eu_2O_3	0.11	bdl	bdl	bdl	bdl	bdl	bdl	bdl	bdl	bdl	bdl	bdl	bdl	bdl	bdl	0.22	0.41	0.20
Gd_2O_3	0.80	1.32	1.32	1.23	1.17	1.13	0.72	0.79	1.42	1.16	1.29	1.30	1.29	1.21	1.39	0.55	0.54	0.36
Tb_2O_3	bdl	bdl	bdl	bdl	bdl	bdl	bdl	bdl	bdl	bdl	bdl	bdl	bdl	bdl	bdl	bdl	bdl	bdl
Dy_2O_3	bdl	bdl	bdl	bdl	bdl	bdl	bdl	bdl	bdl	bdl	bdl	bdl	bdl	bdl	bdl	bdl	bdl	bdl
Ho_2O_3	bdl	bdl	bdl	bdl	bdl	bdl	bdl	bdl	bdl	bdl	bdl	bdl	bdl	bdl	bdl	bdl	bdl	bdl
Er_2O_3	bdl	bdl	bdl	bdl	bdl	bdl	bdl	bdl	bdl	bdl	bdl	bdl	bdl	bdl	bdl	bdl	bdl	bdl
Tm_2O_3	bdl	bdl	bdl	bdl	bdl	bdl	bdl	bdl	bdl	bdl	bdl	bdl	bdl	bdl	bdl	bdl	bdl	bdl
Yb_2O_3	bdl	bdl	bdl	bdl	bdl	bdl	bdl	bdl	bdl	bdl	bdl	bdl	bdl	bdl	bdl	bdl	bdl	bdl
Lu_2O_3	bdl	bdl	bdl	bdl	bdl	bdl	bdl	bdl	bdl	bdl	bdl	bdl	bdl	bdl	bdl	bdl	bdl	bdl
Y_2O_3	bdl	bdl	bdl	bdl	bdl	bdl	bdl	bdl	bdl	bdl	bdl	bdl	bdl	bdl	bdl	0.27	bdl	bdl
ZrO_2	bdl	bdl	bdl	bdl	bdl	bdl	bdl	bdl	bdl	bdl	bdl	bdl	bdl	bdl	bdl	bdl	bdl	bdl
HfO_2	bdl	bdl	bdl	bdl	bdl	bdl	bdl	bdl	bdl	bdl	bdl	bdl	bdl	bdl	bdl	bdl	bdl	bdl
Nb_2O_5	bdl	bdl	bdl	bdl	bdl	bdl	bdl	bdl	bdl	bdl	bdl	bdl	bdl	bdl	bdl	bdl	bdl	bdl
Sc_2O_3	bdl	bdl	bdl	bdl	bdl	bdl	bdl	bdl	bdl	bdl	bdl	bdl	bdl	bdl	bdl	bdl	bdl	bdl
ThO_2	bdl	bdl	bdl	bdl	bdl	bdl	bdl	bdl	bdl	bdl	bdl	bdl	bdl	bdl	bdl	0.11	bdl	0.58
UO_2	bdl	bdl	bdl	bdl	bdl	bdl	bdl	bdl	bdl	bdl	bdl	bdl	bdl	bdl	bdl	bdl	bdl	bdl
P_2O_5	bdl	bdl	bdl	bdl	bdl	bdl	bdl	bdl	bdl	bdl	bdl	bdl	bdl	bdl	bdl	bdl	bdl	bdl
SO_3	0.09	bdl	bdl	bdl	bdl	bdl	bdl	bdl	bdl	bdl	bdl	bdl	bdl	bdl	bdl	bdl	bdl	0.12
F	1.15	bdl	bdl	bdl	bdl	bdl	bdl	0.16	bdl	bdl	bdl	bdl	bdl	bdl	bdl	2.09	2.45	2.63
Cl	0.35	0.08	0.04	0.05	0.17	0.15	0.10	0.09	0.13	0.14	0.15	0.12	0.11	0.12	0.13	0.12	0.14	0.38
TOTAL	79.72	79.48	78.29	78.67	81.13	80.68	80.62	80.13	78.77	79.49	78.50	78.20	76.92	77.65	78.52	72.89	76.14	73.88
TREO	75.22	77.79	76.93	77.05	76.55	77.20	77.63	77.54	74.79	76.64	74.78	73.67	73.49	73.95	73.99	64.28	64.58	63.03

Table B.12 Composition of red apatite (in wt.%) in apatite breccia veins.

SAMPLE	881344-2-261	881344-2-262	881344-2-263	881344-2-264	881344-2-265	881344-2-266	881344-3-281	881344-3-282	881344-3-283	881344-3-284	881344-3-285	881344-3-286	881344-3-287	881344-3-288	881344-3-289	881344-3-290	881344-3-291	881344-3-292	881344-3-389	881344-3-390	881344-3-391	881344-3-392
SiO_2	1.02	1.12	0.97	1.09	1.21	0.63	1.98	1.72	1.58	1.80	1.11	0.82	1.12	1.75	0.83	1.59	1.70	0.90	1.67	1.67	1.47	1.82
Al_2O_3	0.05	0.04	0.05	0.05	0.04	0.05	0.04	0.05	0.05	0.05	0.05	0.05	0.04	0.04	0.05	0.04	0.04	0.05	0.04	0.03	0.04	0.03
Na_2O	0.04	bdl	0.04	0.03	bdl	0.03	0.02	0.04	bdl	0.04	bdl	bdl	bdl	0.04	0.03	0.04	0.03	0.05	0.03	0.03	0.02	0.03
K_2O	bdl*	bdl	bdl	bdl	bdl	bdl	bdl	bdl	bdl	bdl	bdl	bdl	bdl	bdl	bdl	bdl	bdl	bdl	bdl	bdl	bdl	bdl
CaO	51.81	51.48	52.32	51.71	51.87	52.93	50.00	50.53	50.99	50.62	52.69	53.36	52.42	50.97	52.41	50.06	50.61	51.59	52.52	52.75	53.22	52.77
MgO	0.03	0.01	0.02	0.02	0.02	0.02	0.02	0.01	0.01	0.02	0.02	0.02	bdl	0.01	0.01	0.01	0.02	0.02	0.01	0.02	0.02	0.02
FeO	0.05	0.03	0.05	0.04	bdl	0.03	0.09	0.04	0.07	0.07	0.10	0.11	0.05	0.12	0.08	0.03	0.05	1.01	0.03	0.03	0.03	0.04
MnO	0.04	0.05	0.03	0.04	0.04	0.03	0.05	0.04	0.04	0.07	0.04	0.03	0.04	0.05	0.04	0.04	0.03	0.03	0.05	0.05	0.05	0.02
BaO	bdl	bdl	bdl	bdl	bdl	bdl	bdl	bdl	bdl	bdl	bdl	bdl	bdl	bdl	bdl	bdl	bdl	bdl	bdl	bdl	bdl	bdl
SrO	0.90	0.98	0.93	0.97	0.93	0.91	1.10	1.13	1.03	1.09	1.03	1.00	0.89	0.98	0.87	1.21	0.98	0.89	1.12	1.16	1.14	1.05
TiO_2	0.03	bdl	0.03	0.03	0.03	0.04	0.03	bdl	bdl	bdl	bdl	bdl	0.04	0.03	0.04	bdl	bdl	0.03	bdl	bdl	0.03	0.03
Cr_2O_3	bdl	bdl	bdl	bdl	bdl	bdl	bdl	bdl	bdl	bdl	bdl	bdl	bdl	bdl	bdl	bdl	bdl	bdl	bdl	bdl	bdl	bdl
La_2O_3	0.36	0.49	0.46	0.60	0.56	0.17	1.09	0.94	0.89	0.98	0.63	0.37	0.53	0.87	0.30	0.93	0.93	0.47	0.70	0.69	0.62	0.78
Ce_2O_3	1.16	1.50	1.24	1.47	1.62	0.81	2.43	2.36	2.06	2.25	1.47	0.96	1.37	2.36	1.06	2.19	2.33	1.51	2.16	2.11	1.79	2.29
Pr_2O_3	0.24	0.21	0.20	0.22	0.22	0.13	0.36	0.35	0.33	0.41	0.27	0.10	0.23	0.36	0.16	0.29	0.35	0.18	0.27	0.27	0.26	0.26
Nd_2O_3	1.28	1.31	1.03	1.13	1.22	0.80	1.85	1.54	1.47	1.53	1.04	0.79	0.99	1.68	0.99	1.60	1.62	0.97	1.30	1.31	1.14	1.31
Sm_2O_3	0.17	0.19	0.12	0.18	0.17	0.13	0.25	0.22	0.16	0.14	0.13	0.10	0.11	0.17	0.17	0.22	0.17	0.12	0.17	0.17	0.15	0.18
Eu_2O_3	0.07	bdl	bdl	bdl	0.05	bdl	bdl	bdl	bdl	0.06	bdl	0.06	bdl	bdl	bdl	bdl	bdl	bdl	bdl	bdl	bdl	bdl
Gd_2O_3	0.08	0.14	0.07	bdl	0.08	0.09	0.10	0.08	0.09	0.10	0.06	0.06	0.10	0.13	0.08	0.08	0.12	0.08	0.15	0.15	0.13	0.16
Tb_2O_3	bdl	bdl	bdl	bdl	bdl	bdl	bdl	bdl	bdl	bdl	bdl	bdl	bdl	bdl	bdl	bdl	bdl	bdl	bdl	bdl	bdl	bdl
Dy_2O_3	bdl	bdl	bdl	bdl	bdl	bdl	bdl	bdl	bdl	bdl	bdl	bdl	bdl	bdl	bdl	bdl	bdl	bdl	bdl	bdl	bdl	bdl
Ho_2O_3	bdl	bdl	bdl	bdl	bdl	bdl	bdl	bdl	bdl	bdl	bdl	bdl	bdl	bdl	bdl	bdl	bdl	bdl	bdl	bdl	bdl	bdl
Er_2O_3	bdl	bdl	bdl	bdl	bdl	bdl	bdl	bdl	bdl	bdl	bdl	bdl	bdl	bdl	bdl	bdl	bdl	bdl	bdl	bdl	bdl	bdl
Tm_2O_3	bdl	bdl	bdl	bdl	bdl	bdl	bdl	bdl	bdl	bdl	bdl	bdl	bdl	bdl	bdl	bdl	bdl	bdl	bdl	bdl	bdl	bdl
Yb_2O_3	bdl	bdl	bdl	bdl	bdl	bdl	bdl	bdl	bdl	bdl	bdl	bdl	bdl	bdl	bdl	bdl	bdl	bdl	bdl	bdl	bdl	bdl
Lu_2O_3	bdl	bdl	bdl	bdl	bdl	bdl	bdl	bdl	bdl	bdl	bdl	bdl	bdl	bdl	bdl	bdl	bdl	bdl	bdl	bdl	bdl	bdl
Y_2O_3	0.09	0.07	0.08	0.08	0.10	0.09	0.08	0.07	0.06	0.08	0.07	0.05	0.06	0.09	0.08	0.08	0.06	0.06	0.06	0.08	bdl	0.10
ZrO_2	0.10	0.13	0.13	0.14	0.10	0.10	0.09	0.13	0.11	0.11	0.13	0.12	0.11	0.09	0.12	0.11	0.10	0.10	0.12	0.08	0.10	0.10
HfO_2	bdl	bdl	bdl	bdl	bdl	bdl	bdl	bdl	bdl	bdl	bdl	bdl	bdl	bdl	bdl	bdl	bdl	bdl	bdl	bdl	bdl	bdl
Nb_2O_5	bdl	bdl	bdl	bdl	0.04	bdl	bdl	bdl	bdl	bdl	bdl	bdl	bdl	bdl	bdl	bdl	bdl	bdl	bdl	bdl	bdl	bdl
Sc_2O_3	bdl	bdl	bdl	bdl	bdl	bdl	bdl	bdl	bdl	bdl	bdl	bdl	bdl	bdl	bdl	bdl	bdl	bdl	bdl	bdl	bdl	bdl
ThO_2	bdl	bdl	bdl	bdl	bdl	bdl	0.13	0.11	0.06	0.09	bdl	bdl	bdl	0.07	bdl	0.04	0.04	bdl	bdl	0.05	bdl	0.12
UO_2	bdl	bdl	bdl	bdl	bdl	bdl	bdl	bdl	bdl	bdl	bdl	bdl	bdl	bdl	bdl	bdl	bdl	bdl	bdl	bdl	bdl	bdl
P_2O_5	38.34	38.38	38.33	38.52	38.80	39.05	36.75	37.09	37.70	37.24	38.28	39.07	38.79	37.42	38.96	37.56	37.13	37.94	39.11	39.84	40.63	39.76
SO_3	0.05	0.06	0.08	bdl	0.05	bdl	0.07	0.06	0.06	0.04	0.09	0.05	0.06	0.06	0.05	0.06	0.05	0.07	0.07	0.06	0.04	0.05
F	4.16	3.29	3.44	3.82	3.50	3.29	2.97	3.01	3.69	3.09	3.16	4.07	3.21	3.47	3.35	3.27	3.14	4.40	2.91	2.87	3.07	3.42
Cl	0.08	0.09	0.08	0.08	0.09	0.07	0.11	0.10	0.09	0.10	0.07	0.06	0.06	0.09	0.07	0.10	0.09	0.10	0.10	0.08	0.08	0.09
$O=(F_2,Cl_2)$	-1.77	-1.41	-1.47	-1.63	-1.49	-1.40	-1.27	-1.29	-1.57	-1.32	-1.35	-1.73	-1.36	-1.48	-1.43	-1.40	-1.34	-1.88	-1.25	-1.23	-1.31	-1.46
TOTAL	98.38	98.14	98.25	98.58	99.25	98.01	98.35	98.34	98.95	98.65	99.08	99.52	98.85	99.36	98.31	98.15	98.26	98.70	101.36	102.28	102.73	102.99
TREO	3.45	3.90	3.21	3.68	4.01	2.23	6.16	5.57	5.05	5.54	3.67	2.48	3.40	5.65	2.83	5.38	5.58	3.38	4.81	4.78	4.09	5.08

* below detection limit

Table B.12 cont.

SAMPLE	881344-3-393	881344-3-394	881344-3-395	881344-3-405	881375B-2-65	881375B-2-66	881375B-2-67	881375B-2-68	881375B-2-69	881375B-4-78	881375B-4-79	881375B-4-80	948521-1-199	948521-1-200	948521-1-201	948521-1-202	948521-1-203	948521-1-217	948521-1-218	948521-1-219	948521-6-259	516665A-23A-72
SiO_2	1.54	1.71	1.63	0.42	1.37	0.43	0.44	0.81	1.22	1.48	0.18	1.56	0.53	0.74	0.48	0.61	0.70	0.18	0.70	1.12	0.39	1.08
Al_2O_3	0.03	0.05	0.04	0.04	bdl	bdl	bdl	bdl	bdl	bdl	bdl	bdl	bdl	bdl	bdl	0.01	bdl	bdl	bdl	bdl	0.02	bdl
Na_2O	bdl	0.02	0.04	0.02	0.07	0.07	0.06	0.10	0.10	0.09	0.06	0.08	0.02	0.02	bdl	bdl	bdl	bdl	0.03	0.02	bdl	bdl
K_2O	bdl	bdl	bdl	bdl	bdl	bdl	bdl	bdl	bdl	bdl	bdl	bdl	bdl	bdl	bdl	bdl	bdl	bdl	bdl	bdl	bdl	bdl
CaO	51.60	52.01	52.92	50.83	49.43	51.74	52.27	51.65	50.54	48.98	51.62	48.41	52.38	51.87	52.40	51.40	50.74	53.07	51.57	49.74	53.30	51.87
MgO	0.02	0.02	0.02	bdl	0.02	0.02	0.01	0.02	0.02	bdl	0.01	bdl	0.02	0.02	0.02	bdl	0.01	0.02	bdl	bdl	0.02	0.01
FeO	0.06	0.07	0.10	3.74	0.03	0.03	0.05	0.03	0.02	0.04	0.03	0.12	bdl	bdl	bdl	0.08	0.02	0.03	0.02	0.02	0.70	bdl
MnO	0.04	0.03	0.03	0.04	0.05	0.06	0.06	0.06	0.06	0.08	0.06	0.08	0.04	0.06	0.03	0.04	0.04	0.05	0.06	0.04	0.06	0.04
BaO	bdl	bdl	bdl	1.74	bdl	bdl	bdl	bdl	bdl	bdl	bdl	bdl	bdl	bdl	bdl	bdl	bdl	bdl	bdl	bdl	bdl	bdl
SrO	1.11	1.06	1.10	0.69	1.03	0.95	0.98	1.07	1.02	0.95	0.98	0.83	1.09	1.09	0.72	0.83	0.91	1.04	0.92	1.14	0.95	1.10
TiO_2	0.03	bdl	bdl	0.04	bdl	bdl	bdl	bdl	bdl	bdl	bdl	bdl	bdl	bdl	bdl	bdl	bdl	bdl	bdl	bdl	bdl	bdl
Cr_2O_3	bdl	bdl	bdl	bdl	bdl	bdl	bdl	bdl	bdl	bdl	bdl	bdl	bdl	bdl	bdl	bdl	bdl	bdl	bdl	bdl	bdl	bdl
La_2O_3	0.76	0.83	0.77	0.19	0.37	0.13	0.11	0.23	0.34	0.45	0.10	0.52	0.20	0.21	0.15	0.12	0.16	0.07	0.15	0.37	bdl	0.40
Ce_2O_3	2.10	2.28	2.03	0.46	1.50	0.52	0.46	0.87	1.35	1.63	0.34	1.80	0.64	0.76	0.47	0.51	0.65	0.17	0.67	1.23	0.16	1.30
Pr_2O_3	0.20	0.32	0.27	0.06	0.27	0.06	0.09	0.18	0.21	0.25	bdl	0.27	0.06	0.11	0.11	0.13	0.16	0.06	0.10	0.16	bdl	0.15
Nd_2O_3	1.21	1.36	1.28	0.36	1.23	0.43	0.42	0.71	1.05	1.18	0.19	1.21	0.47	0.75	0.50	0.60	0.71	0.22	0.75	0.99	0.28	0.86
Sm_2O_3	0.14	0.17	0.15	0.06	0.20	0.10	0.09	0.15	0.13	0.18	bdl	0.15	0.08	0.14	0.07	0.15	0.16	0.05	0.12	0.13	0.12	0.11
Eu_2O_3	bdl	bdl	bdl	bdl	bdl	bdl	bdl	bdl	0.05	0.05	bdl	bdl	bdl	bdl	bdl	bdl	bdl	bdl	bdl	bdl	bdl	bdl
Gd_2O_3	0.11	0.16	0.14	bdl	0.09	bdl	0.08	0.10	0.10	0.12	bdl	0.09	0.06	0.05	0.08	0.13	bdl	0.05	0.07	bdl	0.08	0.06
Tb_2O_3	bdl	bdl	bdl	bdl	bdl	bdl	bdl	bdl	bdl	bdl	bdl	bdl	bdl	bdl	bdl	bdl	bdl	bdl	bdl	bdl	0.05	bdl
Dy_2O_3	bdl	bdl	bdl	bdl	bdl	bdl	bdl	bdl	bdl	bdl	bdl	bdl	bdl	bdl	bdl	0.07	bdl	bdl	bdl	bdl	bdl	bdl
Ho_2O_3	bdl	bdl	bdl	bdl	bdl	bdl	bdl	bdl	bdl	bdl	bdl	bdl	bdl	bdl	bdl	bdl	bdl	bdl	bdl	bdl	bdl	bdl
Er_2O_3	bdl	bdl	bdl	bdl	bdl	bdl	bdl	bdl	bdl	bdl	bdl	bdl	bdl	bdl	bdl	bdl	bdl	bdl	bdl	bdl	bdl	bdl
Tm_2O_3	bdl	bdl	bdl	bdl	bdl	bdl	bdl	bdl	bdl	bdl	bdl	bdl	bdl	bdl	bdl	bdl	bdl	bdl	bdl	bdl	bdl	bdl
Yb_2O_3	bdl	bdl	bdl	bdl	bdl	bdl	bdl	bdl	bdl	bdl	bdl	bdl	bdl	bdl	bdl	bdl	bdl	bdl	bdl	bdl	bdl	bdl
Lu_2O_3	bdl	bdl	bdl	bdl	bdl	bdl	bdl	bdl	bdl	bdl	bdl	bdl	bdl	bdl	bdl	bdl	bdl	bdl	bdl	bdl	bdl	bdl
Y_2O_3	0.08	0.07	0.08	bdl	0.12	bdl	0.08	0.10	0.08	0.09	bdl	0.06	0.08	0.06	bdl	0.11	0.07	0.08	0.08	0.08	0.11	0.06
ZrO_2	0.10	0.11	0.11	0.12	0.13	0.14	0.16	0.16	0.13	0.11	0.16	0.10	0.15	0.14	0.15	0.12	0.13	0.14	0.15	0.15	0.08	0.18
HfO_2	bdl	bdl	bdl	bdl	bdl	bdl	bdl	bdl	bdl	bdl	bdl	bdl	bdl	bdl	bdl	bdl	bdl	bdl	bdl	bdl	bdl	bdl
Nb_2O_5	bdl	bdl	bdl	bdl	bdl	bdl	bdl	bdl	bdl	bdl	bdl	bdl	bdl	bdl	0.06	bdl	bdl	bdl	bdl	bdl	bdl	bdl
Sc_2O_3	bdl	bdl	bdl	bdl	bdl	bdl	bdl	bdl	bdl	bdl	bdl	0.03	bdl	bdl	bdl	bdl	bdl	bdl	bdl	bdl	bdl	bdl
ThO_2	0.07	0.05	0.07	bdl	bdl	bdl	bdl	bdl	bdl	bdl	bdl	bdl	bdl	bdl	bdl	bdl	bdl	bdl	bdl	bdl	bdl	bdl
UO_2	bdl	bdl	bdl	bdl	bdl	bdl	bdl	bdl	bdl	bdl	bdl	bdl	bdl	bdl	bdl	bdl	bdl	bdl	bdl	bdl	bdl	bdl
P_2O_5	38.20	39.34	39.59	39.46	33.05	35.57	36.06	35.20	33.84	31.49	34.49	30.50	41.00	39.79	42.05	40.03	39.46	38.25	37.82	35.89	38.23	36.99
SO_3	0.07	0.05	0.06	1.19	0.10	0.05	0.04	0.12	0.17	0.20	0.04	0.28	0.07	bdl	bdl	0.04	bdl	bdl	bdl	0.12	0.07	bdl
F	2.94	2.89	2.96	3.53	3.12	3.35	3.45	3.38	3.10	2.97	3.50	2.93	3.15	3.19	3.35	3.29	3.07	3.41	3.16	2.97	3.12	3.28
Cl	0.09	0.10	0.08	0.04	0.34	0.26	0.27	0.29	0.33	0.30	0.21	0.34	0.20	0.24	0.19	0.21	0.22	0.15	0.21	0.21	0.14	0.19
$O=(F_2,Cl_2)$	-1.26	-1.24	-1.27	-1.50	-1.39	-1.47	-1.51	-1.49	-1.38	-1.32	-1.52	-1.31	-1.37	-1.40	-1.45	-1.43	-1.34	-1.47	-1.38	-1.30	-1.35	-1.42
TOTAL	99.25	101.46	102.19	101.56	91.10	92.44	93.68	93.73	92.50	89.32	90.46	88.06	98.88	97.84	99.37	97.04	95.89	95.56	95.21	93.08	96.52	96.26
TREO	4.60	5.18	4.72	1.13	3.78	1.24	1.33	2.33	3.32	3.96	0.64	4.10	1.60	2.09	1.38	1.81	1.91	0.69	1.95	2.97	0.79	2.95

Table B.12 cont.

SAMPLE	516665A-23A-73	516665A-23A-74	516665A-23A-75	516665A-23A-76	516665A-23A-77	516665A-9A-89	516665A-9A-91	516665B-2A-122	516665B-2A-123	516665B-2A-124	516665B-2A-125	516665B-14A-134	516665B-14A-135	516665B-14A-136	516665B-14A-137	516665B-14A-138	516665B-14A-139	516665B-14A-140	516665B-14A-141	516665B-14A-142
SiO_2	1.58	1.31	1.28	1.50	0.98	1.37	1.30	1.33	1.20	0.49	0.33	0.57	1.45	0.31	1.58	1.23	1.29	1.38	0.82	0.56
Al_2O_3	bdl	bdl	bdl	bdl	0.01	bdl	bdl	bdl	bdl	bdl	bdl	0.01	bdl	bdl	bdl	bdl	bdl	bdl	bdl	0.01
Na_2O	0.05	0.04	0.04	0.05	0.02	0.04	0.05	bdl	0.02	0.03	0.03	0.02	0.05	0.02	0.06	0.05	0.04	0.06	0.03	0.02
K_2O	bdl	bdl	bdl	bdl	bdl	bdl	bdl	bdl	bdl	bdl	bdl	bdl	bdl	bdl	bdl	bdl	bdl	bdl	bdl	bdl
CaO	50.52	51.27	51.38	51.00	52.31	47.72	47.68	48.50	47.50	52.35	52.88	52.51	48.28	53.20	48.58	48.32	48.90	49.59	50.16	51.69
MgO	0.01	0.02	0.02	0.02	0.01	0.01	0.01	0.03	0.01	0.01	0.02	0.02	0.01	0.02	0.02	0.01	bdl	0.01	0.02	0.01
FeO	0.02	bdl	bdl	bdl	bdl	bdl	bdl	bdl	bdl	bdl	bdl	bdl	bdl	bdl	bdl	bdl	bdl	bdl	bdl	bdl
MnO	0.05	0.05	0.04	0.05	0.05	0.04	0.02	0.05	0.05	0.02	bdl	bdl	bdl	bdl	0.05	0.02	0.04	0.04	0.02	0.02
BaO	bdl	bdl	bdl	bdl	bdl	bdl	bdl	0.08	0.09	bdl	bdl	bdl	bdl	bdl	0.06	bdl	bdl	bdl	bdl	bdl
SrO	1.33	1.28	1.35	1.32	1.00	1.40	1.37	0.94	0.94	0.75	0.58	0.64	1.27	0.64	1.25	1.23	1.15	1.17	0.90	0.65
TiO_2	bdl	bdl	bdl	bdl	bdl	bdl	bdl	bdl	bdl	bdl	bdl	bdl	bdl	bdl	bdl	bdl	bdl	bdl	bdl	bdl
Cr_2O_3	bdl	bdl	bdl	bdl	bdl	bdl	bdl	bdl	bdl	bdl	bdl	bdl	bdl	bdl	bdl	bdl	bdl	bdl	bdl	bdl
La_2O_3	0.71	0.52	0.49	0.61	0.36	0.59	0.52	0.98	0.68	0.20	0.15	0.26	0.58	0.13	0.79	0.67	0.60	0.58	0.32	0.22
Ce_2O_3	1.93	1.56	1.45	1.80	1.12	1.83	1.77	2.79	2.88	0.61	0.38	0.67	1.85	0.41	2.48	1.63	1.60	1.75	1.05	0.72
Pr_2O_3	0.24	0.24	0.23	0.26	0.15	0.21	0.27	0.35	0.33	0.09	0.06	0.10	0.27	0.06	0.28	0.21	0.21	0.28	0.13	0.11
Nd_2O_3	1.18	0.99	0.95	1.08	0.72	1.06	1.17	1.56	1.50	0.44	0.29	0.42	1.12	0.29	1.39	0.89	0.96	1.05	0.69	0.49
Sm_2O_3	0.17	0.14	0.12	0.14	0.12	0.14	0.10	0.21	0.16	0.05	0.04	0.05	0.15	0.04	0.16	0.12	0.14	0.11	0.09	0.07
Eu_2O_3	bdl	bdl	bdl	bdl	bdl	bdl	bdl	bdl	bdl	bdl	bdl	bdl	bdl	bdl	bdl	bdl	bdl	bdl	bdl	bdl
Gd_2O_3	0.09	0.10	0.07	0.06	0.06	bdl	bdl	0.06	bdl	bdl	bdl	bdl	0.07	bdl	0.08	bdl	bdl	0.07	bdl	bdl
Tb_2O_3	bdl	bdl	bdl	bdl	bdl	bdl	bdl	bdl	bdl	bdl	bdl	bdl	bdl	bdl	bdl	bdl	bdl	bdl	bdl	bdl
Dy_2O_3	bdl	bdl	bdl	bdl	bdl	bdl	bdl	bdl	bdl	bdl	bdl	bdl	bdl	bdl	bdl	bdl	bdl	bdl	bdl	bdl
Ho_2O_3	bdl	bdl	bdl	bdl	bdl	bdl	bdl	bdl	bdl	bdl	bdl	bdl	bdl	bdl	bdl	bdl	bdl	bdl	bdl	bdl
Er_2O_3	bdl	bdl	bdl	bdl	bdl	bdl	bdl	bdl	bdl	bdl	bdl	bdl	bdl	bdl	bdl	bdl	bdl	bdl	bdl	bdl
Tm_2O_3	bdl	bdl	bdl	bdl	bdl	bdl	bdl	bdl	bdl	bdl	bdl	bdl	bdl	bdl	bdl	bdl	bdl	bdl	bdl	bdl
Yb_2O_3	bdl	bdl	bdl	bdl	bdl	bdl	bdl	bdl	bdl	bdl	bdl	bdl	bdl	bdl	bdl	bdl	bdl	bdl	bdl	bdl
Lu_2O_3	bdl	bdl	bdl	bdl	bdl	bdl	bdl	bdl	bdl	bdl	bdl	bdl	bdl	bdl	bdl	bdl	bdl	bdl	bdl	bdl
Y_2O_3	0.08	0.09	0.08	0.09	0.07	0.08	0.06	0.09	0.08	bdl	bdl	0.05	0.12	bdl	0.11	bdl	0.06	0.08	0.06	bdl
ZrO_2	0.16	0.13	0.13	0.13	0.13	0.12	0.13	0.13	0.14	0.11	0.15	0.15	0.12	0.15	0.13	0.14	0.11	0.13	0.11	0.15
HfO_2	bdl	bdl	bdl	bdl	bdl	bdl	bdl	bdl	bdl	bdl	bdl	bdl	bdl	bdl	bdl	bdl	bdl	bdl	bdl	bdl
Nb_2O_5	bdl	bdl	bdl	bdl	bdl	bdl	bdl	bdl	bdl	bdl	bdl	0.04	bdl	bdl	bdl	bdl	bdl	bdl	bdl	bdl
Sc_2O_3	bdl	bdl	bdl	bdl	bdl	bdl	bdl	bdl	bdl	bdl	bdl	bdl	bdl	bdl	bdl	bdl	bdl	bdl	bdl	bdl
ThO_2	bdl	bdl	bdl	bdl	bdl	bdl	bdl	bdl	0.04	bdl	bdl	bdl	bdl	bdl	bdl	bdl	bdl	bdl	bdl	bdl
UO_2	bdl	bdl	bdl	bdl	bdl	bdl	bdl	bdl	bdl	bdl	bdl	bdl	bdl	bdl	bdl	bdl	bdl	bdl	bdl	bdl
P_2O_5	36.09	36.58	36.96	36.41	37.31	36.85	37.03	36.16	36.44	38.87	38.85	38.76	36.53	39.07	36.40	36.89	36.48	36.68	37.85	38.26
SO_3	0.06	0.05	bdl	0.08	0.05	0.06	0.05	0.06	0.05	bdl	0.04	bdl	0.03	bdl	0.07	0.05	0.06	0.05	0.04	bdl
F	3.28	3.26	3.34	3.30	3.24	2.98	3.14	2.91	2.96	3.38	3.46	3.68	3.16	3.44	3.16	3.30	3.01	3.18	3.25	3.25
Cl	0.23	0.18	0.21	0.18	0.18	0.06	0.09	0.12	0.07	0.12	0.10	0.14	0.16	0.09	0.12	0.15	0.18	0.18	0.15	0.12
$O=(F_2,Cl_2)$	-1.43	-1.41	-1.46	-1.43	-1.40	-1.27	-1.34	-1.25	-1.26	-1.45	-1.48	-1.58	-1.37	-1.47	-1.36	-1.42	-1.31	-1.38	-1.40	-1.40
TOTAL	96.34	96.38	96.70	96.65	96.47	93.31	93.42	95.07	93.86	96.07	95.90	96.51	93.87	96.41	95.43	93.48	93.52	95.02	94.29	94.97
TREO	4.39	3.64	3.39	4.04	2.60	3.91	3.89	6.03	5.62	1.40	0.93	1.54	4.15	0.93	5.31	3.53	3.57	3.93	2.34	1.61

Table B.13 Composition of green apatite (in wt.%) in apatite breccia veins.

SAMPLE	881309A-1-103	881309A-1-104	881309A-1-105	881309A-1-106	881309A-1-108	881309A-1-109	881309A-1-120	881309A-1-121	881309A-1-122	881309A-3-163	881309A-3-164	881309A-3-165	881309A-3-166	881309A-3-167	881309A-3-168	881309A-3-169	881309A-3-170	881309A-3-171	881309A-3-172	881309A-3-173	881309A-4-208
SiO_2	2.01	2.14	1.20	1.23	2.36	1.78	1.67	1.52	0.74	0.91	1.36	1.84	1.21	0.87	1.49	0.74	1.01	0.44	1.12	1.14	0.58
Al_2O_3	0.04	0.04	0.05	0.04	0.04	0.04	0.04	0.04	0.05	0.05	0.04	0.04	0.04	0.04	0.05	0.05	0.05	0.04	0.05	0.04	0.05
Na_2O	0.03	bdl	0.03	0.02	bdl	bdl	0.03	0.02	bdl	0.03	0.03	0.03	0.03	0.03	0.04	0.02	0.04	0.02	0.03	0.02	0.04
K_2O	bdl*	bdl	bdl	bdl	bdl	bdl	bdl	bdl	bdl	bdl	bdl	bdl	bdl	bdl	bdl	bdl	bdl	bdl	bdl	bdl	bdl
CaO	50.14	50.63	52.18	52.27	50.03	51.16	50.14	50.19	52.94	51.92	50.46	49.43	51.11	51.88	50.17	52.11	51.83	52.95	51.45	50.78	52.89
MgO	0.02	0.01	0.02	0.02	0.02	bdl	0.02	0.01	0.01	0.01	0.02	0.01	0.02	0.02	0.02	0.02	bdl	0.02	0.01	0.01	0.01
FeO	0.04	0.05	0.06	0.05	0.05	0.05	0.02	0.02	0.03	0.04	0.02	0.05	0.03	0.04	0.04	0.06	0.05	0.09	0.10	0.05	0.02
MnO	0.07	0.08	0.07	0.06	0.08	0.06	0.06	0.07	0.05	0.07	0.08	0.08	0.07	0.06	0.07	0.07	0.05	0.05	0.07	0.08	0.05
BaO	bdl	bdl	bdl	bdl	bdl	bdl	bdl	bdl	bdl	bdl	bdl	bdl	bdl	bdl	bdl	bdl	bdl	bdl	bdl	bdl	bdl
SrO	1.04	1.03	0.90	1.06	1.09	1.04	1.10	1.05	1.06	1.11	1.07	1.06	1.07	1.11	1.18	1.05	1.00	0.99	1.09	1.15	1.07
TiO_2	bdl	bdl	0.03	0.03	bdl	bdl	bdl	bdl	bdl	bdl	0.03	bdl	bdl	0.03	bdl	bdl	0.04	0.03	0.03	0.04	bdl
Cr_2O_3	bdl	bdl	bdl	bdl	bdl	bdl	bdl	bdl	bdl	bdl	bdl	0.04	bdl	bdl	bdl	bdl	bdl	bdl	bdl	bdl	bdl
La_2O_3	0.74	0.76	0.33	0.37	0.82	0.58	0.55	0.59	0.32	0.39	0.46	0.61	0.41	0.37	0.48	0.26	0.35	0.10	0.40	0.40	0.22
Ce_2O_3	2.40	2.51	1.42	1.53	2.84	2.15	2.08	1.87	0.95	1.12	1.72	2.17	1.46	1.09	1.76	0.90	1.22	0.47	1.28	1.46	0.65
Pr_2O_3	0.43	0.43	0.29	0.27	0.42	0.41	0.40	0.33	0.12	0.23	0.33	0.40	0.27	0.15	0.35	0.15	0.23	0.09	0.23	0.25	0.08
Nd_2O_3	2.10	2.27	1.47	1.50	2.53	1.97	1.93	1.72	0.89	1.10	1.61	2.01	1.43	1.03	1.69	0.89	1.12	0.57	1.25	1.38	0.70
Sm_2O_3	0.32	0.31	0.25	0.21	0.37	0.32	0.23	0.26	0.14	0.16	0.25	0.31	0.21	0.15	0.24	0.17	0.18	0.08	0.23	0.21	0.10
Eu_2O_3	0.06	0.07	0.05	bdl	bdl	bdl	bdl	bdl	bdl	bdl	bdl	0.05	bdl	bdl	bdl	bdl	0.07	bdl	bdl	bdl	bdl
Gd_2O_3	0.19	0.17	0.15	0.10	0.17	0.10	0.08	0.12	0.08	0.10	0.08	0.17	0.08	0.07	0.11	bdl	0.08	bdl	0.10	0.08	0.08
Tb_2O_3	bdl	bdl	bdl	bdl	bdl	bdl	bdl	bdl	bdl	bdl	bdl	bdl	bdl	bdl	bdl	bdl	bdl	bdl	bdl	bdl	bdl
Dy_2O_3	bdl	bdl	bdl	bdl	bdl	bdl	bdl	bdl	bdl	bdl	bdl	bdl	bdl	bdl	bdl	bdl	bdl	bdl	bdl	bdl	bdl
Ho_2O_3	bdl	bdl	bdl	bdl	bdl	bdl	bdl	bdl	bdl	bdl	bdl	bdl	bdl	bdl	bdl	bdl	bdl	bdl	bdl	bdl	bdl
Er_2O_3	bdl	bdl	bdl	bdl	bdl	bdl	bdl	bdl	bdl	bdl	bdl	bdl	bdl	bdl	bdl	bdl	bdl	bdl	bdl	bdl	bdl
Tm_2O_3	bdl	bdl	bdl	bdl	bdl	bdl	bdl	bdl	bdl	bdl	bdl	bdl	bdl	bdl	bdl	bdl	bdl	bdl	bdl	bdl	bdl
Yb_2O_3	bdl	bdl	bdl	bdl	bdl	bdl	bdl	bdl	bdl	bdl	bdl	bdl	bdl	bdl	bdl	bdl	bdl	bdl	bdl	bdl	bdl
Lu_2O_3	bdl	bdl	bdl	bdl	bdl	bdl	bdl	bdl	bdl	bdl	bdl	bdl	bdl	bdl	bdl	bdl	bdl	bdl	bdl	bdl	0.07
Y_2O_3	0.16	0.17	0.09	0.10	0.14	0.12	0.15	0.11	0.05	0.08	0.13	0.17	0.08	0.07	0.12	0.04	0.10	0.06	0.10	0.10	0.04
ZrO_2	0.09	0.11	0.10	0.10	0.10	0.12	0.12	0.11	0.14	0.09	0.14	0.13	0.13	0.09	0.14	0.11	0.11	0.11	0.11	0.09	0.14
HfO_2	bdl	bdl	bdl	bdl	bdl	bdl	bdl	bdl	bdl	bdl	bdl	bdl	bdl	bdl	bdl	bdl	bdl	bdl	bdl	bdl	bdl
Nb_2O_5	bdl	bdl	bdl	bdl	bdl	bdl	bdl	bdl	bdl	bdl	bdl	bdl	bdl	bdl	bdl	bdl	bdl	0.04	bdl	bdl	bdl
Sc_2O_3	bdl	bdl	bdl	bdl	bdl	bdl	bdl	bdl	bdl	bdl	bdl	bdl	bdl	bdl	bdl	bdl	bdl	bdl	bdl	bdl	bdl
ThO_2	bdl	bdl	bdl	bdl	0.04	bdl	bdl	bdl	bdl	bdl	bdl	bdl	bdl	bdl	bdl	bdl	bdl	bdl	bdl	bdl	bdl
UO_2	bdl	bdl	bdl	bdl	bdl	bdl	bdl	bdl	bdl	bdl	bdl	bdl	bdl	bdl	bdl	bdl	bdl	bdl	bdl	bdl	bdl
P_2O_5	36.75	36.17	38.14	38.53	35.74	37.34	36.98	37.46	38.98	39.15	37.71	36.93	38.24	39.09	37.51	39.26	38.76	39.74	38.61	38.43	39.44
SO_3	0.16	0.11	bdl	bdl	0.16	0.09	0.09	0.07	bdl	0.05	0.10	0.18	0.06	0.05	0.16	bdl	0.07	0.04	0.07	bdl	0.06
F	2.94	2.67	3.00	3.16	2.96	3.17	2.65	2.97	3.21	3.17	3.04	2.86	3.10	3.13	2.89	3.23	3.17	3.53	3.10	3.10	3.50
Cl	0.82	0.91	0.74	0.73	0.90	0.77	0.66	0.60	0.40	0.77	0.82	0.91	0.78	0.71	0.86	0.60	0.67	0.48	0.78	0.79	0.74
$O=(F_2,Cl_2)$	-1.42	-1.33	-1.43	-1.49	-1.45	-1.51	-1.27	-1.39	-1.44	-1.51	-1.47	-1.41	-1.48	-1.48	-1.41	-1.49	-1.49	-1.59	-1.48	-1.48	-1.64
TOTAL	99.15	99.31	99.13	99.86	99.40	99.76	97.75	97.73	98.71	99.04	98.03	98.09	98.35	98.60	97.96	98.24	98.71	98.34	98.73	98.13	98.89
TREO	6.41	6.68	4.04	4.07	7.28	5.64	5.43	4.99	2.54	3.18	4.58	5.89	3.94	2.92	4.75	2.40	3.35	1.37	3.59	3.89	1.94

* below detection limit

Table B.13 cont.

SAMPLE	881309A-4-209	881309A-4-210	881309A-4-211	881309A-4-212	881309A-4-213	881309A-5-242	881309A-5-243	881309A-5-244	881011B-1-111	881011B-1-112	881011B-3-113	881011B-3-114	881011B-3-115	881011B-3-116	881011B-7-126	881011B-7-127	881011B-7-128	881011B-7-129	881011B-7-130	881011B-7-131
SiO_2	1.60	1.11	0.39	1.40	0.45	0.62	1.33	1.51	1.10	1.52	1.59	1.72	0.88	1.08	1.73	1.72	0.55	1.40	1.20	1.72
Al_2O_3	0.04	0.05	0.05	0.04	0.04	0.05	0.05	0.05	bdl	bdl	bdl	bdl	bdl	bdl	bdl	bdl	bdl	bdl	bdl	bdl
Na_2O	0.04	0.03	0.06	0.03	0.04	0.03	0.04	0.05	0.04	0.06	0.04	0.04	0.03	0.04	0.05	0.05	bdl	0.04	0.06	0.05
K_2O	bdl	bdl	bdl	bdl	0.01	bdl	bdl	bdl	bdl	bdl	bdl	bdl	bdl	bdl	bdl	bdl	bdl	bdl	bdl	bdl
CaO	50.49	51.62	53.37	50.38	53.06	53.21	51.69	51.16	51.39	50.21	49.76	49.45	51.17	49.98	49.10	49.31	52.41	49.82	50.17	49.24
MgO	0.02	0.01	0.02	bdl	0.03	0.01	0.03	0.02	0.02	0.01	bdl	0.02	0.01	0.02	0.02	0.01	0.02	0.01	0.01	0.02
FeO	0.03	0.04	0.04	0.03	0.04	0.05	0.04	0.04	bdl	bdl	bdl	bdl	0.03	0.02	bdl	bdl	bdl	bdl	bdl	bdl
MnO	0.07	0.07	0.06	0.07	0.06	0.06	0.07	0.07	0.04	0.03	0.06	0.05	0.04	0.05	0.04	0.04	bdl	0.06	0.04	0.05
BaO	bdl	bdl	bdl	bdl	bdl	bdl	bdl	bdl	bdl	bdl	bdl	bdl	bdl	bdl	bdl	bdl	bdl	bdl	0.06	bdl
SrO	1.07	1.09	1.03	1.16	1.07	1.01	1.07	1.20	1.02	1.02	0.93	0.76	0.86	0.85	0.87	0.92	0.32	0.96	0.99	1.09
TiO_2	bdl	0.03	0.03	bdl	0.03	bdl	bdl	bdl	bdl	bdl	bdl	bdl	bdl	bdl	bdl	bdl	bdl	bdl	bdl	bdl
Cr_2O_3	bdl	bdl	bdl	bdl	bdl	bdl	bdl	bdl	bdl	bdl	bdl	bdl	bdl	bdl	bdl	bdl	bdl	bdl	bdl	bdl
La_2O_3	0.48	0.34	0.16	0.47	0.17	0.21	0.42	0.48	0.35	0.52	0.45	0.47	0.20	0.33	0.54	0.49	bdl	0.50	0.41	0.63
Ce_2O_3	1.76	1.29	0.51	1.74	0.54	0.68	1.47	1.69	1.22	1.76	1.70	1.75	0.91	1.17	1.80	1.74	0.47	1.56	1.32	1.91
Pr_2O_3	0.29	0.17	0.06	0.33	0.10	0.10	0.27	0.29	0.20	0.27	0.23	0.30	0.16	0.18	0.27	0.28	0.08	0.21	0.19	0.30
Nd_2O_3	1.78	1.30	0.48	1.57	0.55	0.74	1.45	1.64	0.92	1.20	1.30	1.40	0.79	0.86	1.43	1.36	0.59	1.20	0.94	1.40
Sm_2O_3	0.29	0.20	0.10	0.24	0.08	0.12	0.20	0.22	0.13	0.18	0.22	0.23	0.14	0.09	0.21	0.21	0.10	0.15	0.15	0.20
Eu_2O_3	0.07	0.08	bdl	bdl	bdl	bdl	bdl	bdl	bdl	bdl	0.06	0.05	bdl	bdl	0.06	bdl	bdl	bdl	bdl	bdl
Gd_2O_3	0.12	0.11	bdl	0.10	bdl	0.07	0.17	0.12	0.06	0.10	0.10	0.13	0.09	0.10	0.08	0.09	0.06	0.08	0.10	0.09
Tb_2O_3	bdl	bdl	bdl	bdl	bdl	bdl	bdl	bdl	bdl	bdl	bdl	bdl	bdl	bdl	bdl	bdl	bdl	bdl	bdl	bdl
Dy_2O_3	bdl	bdl	bdl	bdl	bdl	bdl	bdl	bdl	bdl	bdl	bdl	bdl	bdl	bdl	bdl	bdl	bdl	bdl	bdl	bdl
Ho_2O_3	bdl	bdl	bdl	bdl	bdl	bdl	bdl	bdl	bdl	bdl	bdl	bdl	bdl	bdl	bdl	bdl	bdl	bdl	bdl	bdl
Er_2O_3	bdl	bdl	bdl	bdl	bdl	bdl	bdl	bdl	bdl	bdl	bdl	bdl	bdl	bdl	bdl	bdl	bdl	bdl	bdl	bdl
Tm_2O_3	bdl	bdl	bdl	bdl	bdl	bdl	bdl	bdl	bdl	bdl	bdl	bdl	bdl	bdl	bdl	bdl	bdl	bdl	bdl	bdl
Yb_2O_3	bdl	bdl	bdl	bdl	bdl	bdl	bdl	bdl	bdl	bdl	bdl	bdl	bdl	bdl	bdl	bdl	bdl	bdl	bdl	bdl
Lu_2O_3	bdl	bdl	bdl	bdl	bdl	bdl	bdl	bdl	bdl	bdl	bdl	bdl	bdl	bdl	bdl	bdl	bdl	bdl	bdl	bdl
Y_2O_3	0.18	0.09	bdl	0.11	0.05	0.05	0.12	0.09	0.09	0.10	0.16	0.14	0.08	0.08	0.13	0.08	0.09	0.10	0.08	0.16
ZrO_2	0.11	0.10	0.10	0.15	0.09	0.10	0.12	0.10	0.12	0.08	0.09	0.13	0.16	0.12	0.13	0.13	0.11	0.13	0.15	0.11
HfO_2	bdl	bdl	bdl	bdl	bdl	bdl	bdl	bdl	bdl	bdl	bdl	bdl	bdl	bdl	bdl	bdl	bdl	bdl	bdl	bdl
Nb_2O_5	bdl	bdl	bdl	bdl	bdl	bdl	bdl	bdl	0.06	bdl	bdl	bdl	bdl	bdl	bdl	bdl	bdl	bdl	bdl	bdl
Sc_2O_3	bdl	bdl	bdl	bdl	bdl	bdl	bdl	bdl	bdl	bdl	bdl	bdl	bdl	bdl	bdl	bdl	bdl	bdl	0.03	bdl
ThO_2	bdl	bdl	bdl	bdl	bdl	bdl	bdl	bdl	bdl	bdl	0.04	0.06	bdl	bdl	bdl	0.04	bdl	bdl	bdl	bdl
UO_2	bdl	bdl	bdl	bdl	bdl	bdl	bdl	bdl	bdl	bdl	bdl	bdl	bdl	bdl	bdl	bdl	bdl	bdl	bdl	bdl
P_2O_5	37.22	38.51	40.10	37.45	40.00	39.23	37.79	37.65	33.39	33.11	31.95	31.53	32.96	31.97	30.51	30.37	31.97	30.77	30.44	29.81
SO_3	0.14	0.10	0.06	0.15	0.05	0.06	0.07	0.12	0.10	0.08	0.12	0.14	bdl	0.06	0.16	0.16	bdl	0.08	0.07	0.10
F	2.90	3.19	3.40	3.10	3.60	3.27	3.31	3.22	3.14	3.07	3.08	3.15	3.58	3.29	3.18	2.83	3.57	2.97	3.13	2.84
Cl	0.94	0.76	0.67	0.98	0.63	0.69	0.70	0.81	0.16	0.14	0.25	0.24	0.12	0.23	0.24	0.24	0.09	0.22	0.16	0.17
$O=(F_2,Cl_2)$	-1.43	-1.52	-1.58	-1.53	-1.66	-1.53	-1.55	-1.54	-1.36	-1.32	-1.35	-1.38	-1.54	-1.44	-1.39	-1.25	-1.52	-1.30	-1.36	-1.23
TOTAL	98.22	98.76	99.09	97.98	99.04	98.81	98.84	98.99	92.18	92.13	90.79	90.40	90.69	89.09	89.16	88.82	88.89	88.96	88.36	88.63
TREO	4.97	3.58	1.30	4.56	1.49	1.97	4.09	4.52	2.96	4.13	4.22	4.48	2.38	2.81	4.52	4.24	1.39	3.79	3.18	4.67

Table B.14 Composition of coarse red apatite (in wt.%) in apatite breccia veins.

SAMPLE	517458-2-57	517458-2-58	517458-2-59	517458-2-60	517458-2-61	517458-2-62	517458-2-63	517458-2-64	517458-3-91	517458-3-92	517458-3-93	517458-3-94	517458-3-95	517458-3-96	517458-3-97
SiO_2	0.19	0.58	0.17	0.66	0.30	0.48	0.33	0.26	0.02	0.02	0.02	0.24	0.03	0.54	0.60
Al_2O_3	0.04	0.03	0.04	0.04	0.04	0.04	0.03	0.04	0.04	0.04	0.04	0.04	0.04	0.03	0.04
Na_2O	0.05	0.05	0.04	0.06	0.04	0.07	0.06	0.05	0.04	0.04	0.04	0.03	0.04	0.03	0.08
K_2O	bdl*	bdl	bdl	bdl	bdl	bdl	bdl	bdl	bdl	bdl	bdl	bdl	bdl	bdl	bdl
CaO	55.59	54.72	55.41	54.29	55.18	54.47	54.69	54.92	56.29	56.14	55.77	55.69	56.19	54.78	54.01
MgO	0.02	0.02	0.02	0.02	0.02	0.02	0.02	0.02	0.02	0.02	0.03	0.02	0.02	0.02	0.02
FeO	0.03	0.02	bdl	bdl	0.02	0.02	0.16	0.03	0.04	0.03	0.02	0.18	0.02	0.04	0.02
MnO	0.03	0.04	0.04	0.03	0.04	0.03	0.05	0.04	0.04	0.04	0.05	0.04	0.04	0.03	0.04
BaO	bdl	bdl	bdl	bdl	bdl	bdl	bdl	bdl	bdl	bdl	bdl	bdl	bdl	bdl	bdl
SrO	0.97	0.92	0.93	0.90	0.97	0.98	0.99	0.99	0.84	0.90	0.81	1.07	0.87	0.98	0.92
TiO_2	0.03	bdl	bdl	bdl	bdl	bdl	0.03	bdl	0.04	bdl	bdl	0.04	bdl	bdl	0.05
Cr_2O_3	bdl	bdl	bdl	bdl	bdl	bdl	bdl	bdl	bdl	bdl	bdl	bdl	bdl	bdl	bdl
La_2O_3	0.07	0.09	bdl	0.09	bdl	0.10	bdl	bdl	bdl	bdl	bdl	bdl	bdl	0.15	0.11
Ce_2O_3	0.20	0.61	0.17	0.59	0.31	0.44	0.35	0.34	bdl	bdl	bdl	0.20	bdl	0.50	0.53
Pr_2O_3	bdl	0.16	bdl	0.12	0.08	0.12	0.11	0.07	bdl	bdl	bdl	bdl	bdl	0.07	0.13
Nd_2O_3	0.28	0.68	0.28	0.81	0.43	0.63	0.47	0.36	bdl	bdl	bdl	0.23	bdl	0.42	0.72
Sm_2O_3	bdl	0.13	0.06	0.19	0.13	0.13	0.10	0.07	bdl	bdl	bdl	0.05	bdl	0.09	0.16
Eu_2O_3	bdl	bdl	bdl	bdl	bdl	bdl	bdl	bdl	bdl	bdl	bdl	bdl	bdl	bdl	bdl
Gd_2O_3	bdl	0.07	bdl	0.09	bdl	0.07	bdl	bdl	bdl	bdl	bdl	bdl	bdl	0.09	0.07
Tb_2O_3	bdl	bdl	bdl	bdl	bdl	bdl	bdl	bdl	bdl	bdl	bdl	bdl	bdl	bdl	bdl
Dy_2O_3	bdl	bdl	0.07	bdl	bdl	bdl	bdl	bdl	bdl	bdl	bdl	bdl	bdl	bdl	bdl
Ho_2O_3	bdl	bdl	bdl	bdl	bdl	bdl	bdl	bdl	bdl	bdl	bdl	bdl	bdl	bdl	bdl
Er_2O_3	bdl	bdl	bdl	bdl	bdl	bdl	bdl	bdl	bdl	bdl	bdl	bdl	bdl	bdl	bdl
Tm_2O_3	bdl	bdl	bdl	bdl	bdl	bdl	bdl	bdl	bdl	bdl	bdl	bdl	bdl	bdl	bdl
Yb_2O_3	bdl	bdl	bdl	bdl	bdl	bdl	bdl	bdl	bdl	bdl	bdl	bdl	bdl	bdl	bdl
Lu_2O_3	bdl	bdl	bdl	bdl	bdl	bdl	bdl	bdl	bdl	bdl	bdl	bdl	bdl	bdl	bdl
Y_2O_3	0.05	0.10	0.05	0.07	0.07	0.10	0.04	0.04	bdl	bdl	bdl	0.08	bdl	0.12	0.10
ZrO_2	0.12	0.13	0.12	0.11	0.13	0.09	0.12	0.11	0.10	0.14	0.12	0.12	0.09	0.10	0.11
HfO_2	bdl	bdl	bdl	bdl	bdl	bdl	bdl	bdl	bdl	bdl	bdl	bdl	bdl	bdl	bdl
Nb_2O_5	bdl	bdl	bdl	bdl	bdl	bdl	bdl	bdl	bdl	0.06	0.04	bdl	bdl	bdl	bdl
Sc_2O_3	bdl	bdl	bdl	bdl	bdl	bdl	bdl	bdl	bdl	bdl	bdl	bdl	bdl	bdl	bdl
ThO_2	bdl	bdl	bdl	bdl	bdl	bdl	bdl	bdl	bdl	bdl	bdl	bdl	bdl	bdl	bdl
UO_2	bdl	bdl	bdl	bdl	bdl	bdl	bdl	bdl	bdl	bdl	bdl	bdl	bdl	bdl	bdl
P_2O_5	42.10	41.33	42.14	40.95	41.54	41.56	41.79	41.80	42.20	42.13	42.28	42.00	42.01	41.32	41.05
SO_3	bdl	0.06	bdl	0.04	bdl	bdl	bdl	bdl	bdl	0.06	0.07	0.04	0.06	0.06	bdl
F	3.55	3.48	3.61	3.52	3.57	3.47	3.74	3.74	3.62	3.70	3.85	3.57	3.67	3.49	3.61
Cl	0.09	0.10	0.08	0.08	0.07	0.08	0.10	0.05	0.07	0.07	0.08	0.04	0.06	0.06	0.11
$O=(F_2,Cl_2)$	-1.52	-1.49	-1.54	-1.50	-1.52	-1.48	-1.60	-1.59	-1.54	-1.57	-1.64	-1.51	-1.56	-1.48	-1.54
TOTAL	101.87	101.80	101.70	101.17	101.41	101.44	101.58	101.35	101.83	101.83	101.60	102.17	101.59	101.44	100.94
TREO	0.60	1.84	0.63	1.97	1.02	1.60	1.06	0.88	0.00	0.00	0.00	0.56	0.00	1.43	1.83

* below detection limit

Table B.14 cont.

SAMPLE	517458-3-98	517458-3-99	517458-3-100	517458-3-101	517458-7-361	517458-7-362	517458-7-363	517458-7-364	517458-7-365	517458-7-366	517458-7-367	517458-7-368	517458-7-369	517458-7-370
SiO_2	0.05	0.08	0.57	0.18	0.04	0.12	0.03	0.29	0.05	0.56	0.80	0.77	0.50	0.66
Al_2O_3	0.04	0.04	0.04	0.04	0.05	0.06	0.05	0.05	0.05	0.05	0.04	0.04	0.04	0.05
Na_2O	0.04	0.03	0.04	0.04	0.02	0.03	bdl	0.02	0.02	0.02	bdl	bdl	0.04	0.03
K_2O	bdl	bdl	bdl	bdl	bdl	bdl	bdl	bdl	bdl	bdl	bdl	bdl	bdl	bdl
CaO	55.45	55.52	54.17	54.98	54.25	54.26	54.87	53.60	54.26	53.28	53.16	52.90	53.36	52.72
MgO	0.02	0.02	0.03	0.02	0.02	0.05	0.03	0.02	0.03	0.02	0.02	0.02	0.03	0.02
FeO	0.02	bdl	0.02	0.02	0.03	0.13	0.02	0.02	0.04	0.03	0.05	0.03	0.03	0.04
MnO	0.04	0.03	0.04	0.04	0.04	0.03	0.03	0.05	0.03	0.03	0.04	0.05	0.04	0.04
BaO	bdl	bdl	bdl	bdl	bdl	0.06	bdl	bdl	bdl	bdl	bdl	bdl	bdl	bdl
SrO	0.82	0.92	0.90	0.90	1.02	0.87	0.98	1.04	0.85	0.90	0.96	0.95	0.97	0.85
TiO_2	bdl	0.04	bdl	0.03	bdl	0.03	0.04	bdl	bdl	bdl	bdl	0.03	bdl	0.03
Cr_2O_3	bdl	bdl	bdl	bdl	bdl	bdl	bdl	bdl	bdl	bdl	bdl	bdl	bdl	bdl
La_2O_3	bdl	bdl	0.16	bdl	bdl	bdl	bdl	0.07	bdl	0.08	0.12	0.09	0.11	0.15
Ce_2O_3	bdl	0.08	0.57	0.19	bdl	bdl	bdl	0.26	bdl	0.42	0.64	0.61	0.44	0.64
Pr_2O_3	bdl	bdl	0.12	bdl	bdl	bdl	bdl	bdl	bdl	0.09	0.11	0.11	0.06	0.11
Nd_2O_3	0.07	0.11	0.55	0.18	bdl	0.07	bdl	0.33	bdl	0.60	0.83	0.78	0.58	0.73
Sm_2O_3	bdl	bdl	0.13	0.06	bdl	bdl	bdl	0.10	bdl	0.13	0.20	0.15	0.12	0.15
Eu_2O_3	bdl	bdl	bdl	bdl	bdl	bdl	bdl	bdl	bdl	bdl	bdl	bdl	bdl	bdl
Gd_2O_3	bdl	bdl	bdl	bdl	bdl	bdl	bdl	bdl	bdl	0.12	0.11	0.11	0.10	0.05
Tb_2O_3	bdl	bdl	bdl	bdl	bdl	bdl	bdl	bdl	bdl	bdl	bdl	bdl	bdl	bdl
Dy_2O_3	bdl	bdl	0.06	bdl	0.07	bdl	bdl	bdl	bdl	bdl	bdl	0.07	bdl	0.07
Ho_2O_3	bdl	bdl	bdl	bdl	bdl	bdl	bdl	0.06	bdl	bdl	bdl	bdl	bdl	bdl
Er_2O_3	bdl	bdl	bdl	bdl	bdl	bdl	bdl	bdl	bdl	bdl	bdl	bdl	bdl	bdl
Tm_2O_3	bdl	bdl	bdl	bdl	bdl	bdl	bdl	bdl	bdl	bdl	bdl	bdl	bdl	bdl
Yb_2O_3	bdl	bdl	bdl	bdl	bdl	bdl	bdl	bdl	bdl	bdl	bdl	bdl	bdl	bdl
Lu_2O_3	bdl	bdl	bdl	bdl	bdl	bdl	bdl	bdl	bdl	bdl	bdl	bdl	bdl	bdl
Y_2O_3	bdl	bdl	0.06	0.04	bdl	bdl	bdl	0.07	bdl	0.14	0.13	0.15	0.08	0.09
ZrO_2	0.10	0.13	0.14	0.11	0.12	0.12	0.12	0.11	0.13	0.10	0.13	0.14	0.08	0.11
HfO_2	bdl	bdl	bdl	bdl	bdl	bdl	bdl	bdl	bdl	bdl	bdl	bdl	bdl	bdl
Nb_2O_5	0.04	bdl	bdl	bdl	0.04	bdl	0.05	bdl	bdl	bdl	bdl	bdl	bdl	bdl
Sc_2O_3	bdl	bdl	bdl	bdl	bdl	bdl	bdl	bdl	bdl	bdl	bdl	bdl	bdl	bdl
ThO_2	bdl	bdl	bdl	bdl	bdl	bdl	bdl	bdl	bdl	bdl	bdl	0.04	bdl	bdl
UO_2	bdl	bdl	bdl	bdl	bdl	bdl	bdl	bdl	bdl	bdl	bdl	bdl	bdl	bdl
P_2O_5	42.12	42.00	40.65	42.18	41.86	41.97	42.29	41.52	41.78	40.76	40.29	41.10	41.20	40.40
SO_3	bdl	bdl	0.09	bdl	bdl	0.04	0.04	0.04	0.05	bdl	0.09	bdl	bdl	bdl
F	3.60	3.55	3.70	3.90	3.68	3.36	3.53	3.59	3.68	3.66	3.58	3.46	3.55	3.66
Cl	0.09	0.07	0.09	0.07	0.05	0.03	0.04	0.09	0.05	0.06	0.08	0.05	0.06	0.07
$O=(F_2,Cl_2)$	-1.54	-1.51	-1.58	-1.66	-1.56	-1.42	-1.50	-1.53	-1.56	-1.55	-1.52	-1.47	-1.51	-1.56
TOTAL	100.95	101.10	100.54	101.32	99.73	99.81	100.61	99.79	99.44	99.49	99.83	100.19	99.87	99.14
TREO	0.07	0.19	1.63	0.48	0.07	0.07	0.00	0.89	0.00	1.58	2.14	2.08	1.49	1.99

Table B.15 Composition of apatite of undeterminable stage (in wt.%) in apatite breccia veins.

SAMPLE	881309A-1-110	881309A-1-112	881309A-1-113	881309A-1-118	881309A-1-119	881309A-1-123	881309A-1-124	881309A-1-125	881309A-1-126	881309A-1-127	881375B-6-89	881375B-6-90	881375B-6-91	881375B-6-92	881375B-6-93	881253-1-134	881253-1-135	881253-1-136	881253-1-137
SiO_2	1.01	1.38	2.19	2.06	1.32	0.54	1.55	1.52	0.68	0.56	2.02	1.96	0.97	0.71	1.15	1.83	1.03	0.45	1.20
Al_2O_3	0.06	0.05	0.07	0.04	0.05	0.05	0.05	0.04	0.05	0.04	bdl	bdl	bdl	bdl	bdl	bdl	bdl	bdl	bdl
Na_2O	bdl*	0.02	0.04	0.02	0.03	bdl	bdl	0.03	0.03	0.02	0.19	0.21	0.08	0.08	0.08	0.04	0.05	0.03	0.03
K_2O	bdl	bdl	bdl	bdl	bdl	bdl	bdl	bdl	bdl	bdl	bdl	bdl	bdl	bdl	bdl	bdl	0.02	bdl	bdl
CaO	49.73	51.67	49.74	49.77	50.88	53.73	50.30	49.93	52.65	53.09	48.76	48.37	51.12	51.97	51.47	48.42	49.88	51.21	49.61
MgO	0.01	0.01	0.01	0.02	0.02	0.01	0.01	0.02	0.02	0.01	0.02	0.03	0.02	0.01	0.02	0.02	0.01	0.01	0.01
FeO	1.32	0.10	0.75	0.04	0.03	0.03	0.04	0.02	0.05	0.05	0.03	0.04	bdl	bdl	0.02	0.02	0.04	0.02	bdl
MnO	0.06	0.06	0.08	0.08	0.05	0.06	0.07	0.04	0.05	0.05	0.08	0.09	0.06	0.05	0.05	0.09	0.07	0.06	0.07
BaO	bdl	bdl	bdl	bdl	bdl	bdl	bdl	bdl	bdl	bdl	bdl	bdl	bdl	bdl	bdl	bdl	bdl	bdl	bdl
SrO	0.83	1.07	1.07	0.96	1.05	1.07	0.94	1.04	1.11	1.14	1.01	1.57	1.11	1.08	1.07	1.15	1.13	1.23	1.18
TiO_2	bdl	bdl	bdl	bdl	bdl	0.03	bdl	bdl	bdl	0.03	bdl	bdl	bdl	bdl	bdl	bdl	bdl	bdl	bdl
Cr_2O_3	bdl	bdl	bdl	bdl	bdl	bdl	bdl	bdl	bdl	bdl	bdl	bdl	bdl	bdl	bdl	bdl	bdl	bdl	bdl
La_2O_3	0.63	0.42	0.83	0.66	0.55	0.21	0.52	0.58	0.24	0.22	0.78	0.91	0.27	0.23	0.34	0.43	0.30	0.17	0.39
Ce_2O_3	2.01	1.63	2.73	2.62	1.73	0.62	1.93	1.98	0.87	0.75	2.22	2.26	1.12	0.83	1.39	1.74	1.04	0.52	1.33
Pr_2O_3	0.26	0.30	0.47	0.42	0.27	0.10	0.31	0.35	0.17	0.09	0.31	0.29	0.16	0.14	0.19	0.25	0.17	0.08	0.16
Nd_2O_3	1.48	1.65	2.17	2.35	1.47	0.81	1.85	1.85	0.76	0.66	1.36	1.30	0.96	0.68	1.01	1.38	0.84	0.42	1.04
Sm_2O_3	0.18	0.29	0.29	0.32	0.23	0.12	0.29	0.24	0.12	0.11	0.14	0.19	0.15	0.08	0.17	0.19	0.13	0.07	0.12
Eu_2O_3	bdl	bdl	0.06	0.07	0.08	bdl	0.06	0.07	bdl	bdl	bdl	bdl	bdl	bdl	0.05	0.06	0.07	bdl	bdl
Gd_2O_3	0.08	0.12	0.09	0.14	0.09	0.06	0.13	0.07	bdl	bdl	0.09	0.11	0.05	0.08	0.10	0.14	0.08	bdl	0.07
Tb_2O_3	bdl	bdl	bdl	bdl	bdl	bdl	bdl	bdl	bdl	bdl	bdl	bdl	0.07	bdl	bdl	bdl	bdl	bdl	bdl
Dy_2O_3	bdl	bdl	bdl	bdl	bdl	bdl	bdl	bdl	bdl	bdl	bdl	bdl	bdl	bdl	bdl	bdl	bdl	bdl	bdl
Ho_2O_3	bdl	bdl	bdl	bdl	bdl	bdl	bdl	bdl	bdl	bdl	bdl	bdl	bdl	bdl	bdl	bdl	bdl	bdl	bdl
Er_2O_3	bdl	bdl	bdl	bdl	bdl	bdl	bdl	bdl	bdl	bdl	bdl	bdl	bdl	bdl	bdl	bdl	bdl	bdl	bdl
Tm_2O_3	bdl	bdl	bdl	bdl	bdl	bdl	bdl	bdl	bdl	bdl	bdl	bdl	bdl	bdl	bdl	bdl	bdl	bdl	bdl
Yb_2O_3	bdl	bdl	bdl	bdl	bdl	bdl	bdl	bdl	bdl	bdl	bdl	bdl	bdl	bdl	bdl	bdl	bdl	bdl	bdl
Lu_2O_3	bdl	bdl	bdl	bdl	bdl	bdl	bdl	bdl	bdl	bdl	bdl	bdl	bdl	bdl	bdl	bdl	bdl	bdl	bdl
Y_2O_3	0.07	0.09	0.12	0.20	0.10	0.06	0.13	0.14	bdl	0.05	0.09	0.09	0.07	0.09	0.10	0.10	bdl	bdl	0.09
ZrO_2	0.10	0.10	0.06	0.10	0.09	0.11	0.13	0.12	0.10	0.13	0.13	0.12	0.10	0.15	0.14	0.17	0.14	0.15	0.14
HfO_2	bdl	bdl	bdl	bdl	bdl	bdl	bdl	bdl	bdl	bdl	bdl	bdl	bdl	bdl	bdl	bdl	bdl	bdl	bdl
Nb_2O_5	bdl	bdl	bdl	bdl	bdl	0.05	bdl	bdl	bdl	bdl	bdl	bdl	bdl	bdl	bdl	bdl	bdl	bdl	bdl
Sc_2O_3	bdl	bdl	bdl	bdl	bdl	bdl	bdl	bdl	bdl	bdl	bdl	bdl	bdl	bdl	bdl	bdl	bdl	bdl	bdl
ThO_2	bdl	bdl	0.11	bdl	bdl	bdl	bdl	bdl	bdl	bdl	0.13	0.09	0.06	0.04	bdl	bdl	bdl	bdl	bdl
UO_2	bdl	bdl	bdl	bdl	bdl	bdl	bdl	bdl	bdl	bdl	bdl	bdl	bdl	bdl	bdl	bdl	bdl	bdl	bdl
P_2O_5	32.69	37.69	35.45	36.09	37.79	39.16	37.62	37.35	39.38	39.21	32.43	31.79	33.41	34.21	34.34	29.28	30.11	31.85	30.47
SO_3	bdl	bdl	0.31	0.09	bdl	bdl	bdl	0.04	0.05	0.05	0.51	0.57	0.05	0.06	0.09	0.30	0.06	bdl	0.08
F	3.39	3.34	2.75	2.78	2.91	3.80	2.67	2.46	2.93	3.79	3.10	2.94	3.35	3.37	3.12	2.68	2.79	3.09	2.90
Cl	0.62	0.76	0.93	0.70	0.64	0.35	0.62	0.64	0.54	0.45	0.38	0.44	0.31	0.26	0.30	0.87	0.67	0.51	0.65
$O=(F_2,Cl_2)$	-1.57	-1.58	-1.37	-1.33	-1.37	-1.68	-1.27	-1.18	-1.35	-1.70	-1.39	-1.34	-1.48	-1.48	-1.38	-1.32	-1.33	-1.42	-1.37
TOTAL	92.96	99.19	98.96	98.21	98.02	99.28	97.94	97.35	98.44	98.81	92.42	92.06	92.01	92.64	93.83	87.82	87.29	88.46	88.20
TREO	4.70	4.51	6.76	6.79	4.53	1.97	5.20	5.27	2.16	1.88	5.01	5.17	2.86	2.13	3.35	4.28	2.62	1.27	3.21

* below detection limit

Table B.15 cont.

SAMPLE	881253-1-138	881253-1-139	881253-3-150	881253-3-151	881253-3-152	881253-3-153	881253-3-154	881253-3-155	881253-3-156	881253-3-157	517256-1-160	517256-1-161	517256-3-180	517256-3-181	517256-4-191	517256-4-192	517256-4-193	516647-3-298	516647-3-299
SiO_2	1.52	0.54	1.57	0.83	1.59	0.48	1.29	0.52	1.21	1.03	bdl	bdl	0.07	0.03	bdl	bdl	0.04	0.28	0.05
Al_2O_3	bdl	bdl	bdl	bdl	bdl	bdl	bdl	bdl	bdl	bdl	0.01	bdl	0.03	0.01	bdl	bdl	0.03	bdl	bdl
Na_2O	0.03	0.04	0.03	0.02	0.03	0.03	0.03	0.03	0.03	0.03	0.05	0.06	0.08	0.06	0.03	0.06	0.05	0.03	0.03
K_2O	bdl	bdl	bdl	bdl	bdl	bdl	bdl	bdl	bdl	bdl	bdl	bdl	bdl	bdl	bdl	bdl	bdl	bdl	bdl
CaO	49.08	51.34	48.38	49.30	46.87	50.58	47.92	50.78	49.10	48.35	52.99	53.09	51.66	52.09	52.77	51.66	52.07	52.64	53.84
MgO	0.01	0.02	0.02	0.01	0.02	0.02	0.02	bdl	0.02	0.02	0.02	0.02	0.02	0.02	0.01	0.01	0.02	0.01	0.02
FeO	0.03	bdl	bdl	0.03	bdl	0.02	bdl	bdl	0.02	bdl	0.12	0.19	1.54	0.68	0.09	0.10	0.91	bdl	0.03
MnO	0.07	0.05	0.08	0.07	0.06	0.07	0.06	0.07	0.07	0.08	0.19	0.16	0.21	0.11	0.17	0.29	0.23	0.05	0.04
BaO	bdl	bdl	bdl	bdl	bdl	bdl	bdl	bdl	bdl	bdl	bdl	bdl	bdl	bdl	bdl	bdl	bdl	bdl	bdl
SrO	1.15	1.11	1.04	1.03	1.18	1.23	1.18	1.12	1.13	1.18	bdl	0.08	0.09	bdl	bdl	0.11	bdl	0.85	0.71
TiO_2	bdl	bdl	bdl	bdl	bdl	bdl	bdl	bdl	bdl	bdl	bdl	bdl	bdl	bdl	bdl	bdl	bdl	bdl	bdl
Cr_2O_3	bdl	bdl	bdl	bdl	bdl	bdl	bdl	bdl	bdl	bdl	bdl	bdl	bdl	bdl	bdl	bdl	bdl	bdl	bdl
La_2O_3	0.48	0.17	0.48	0.25	0.42	0.13	0.35	0.17	0.27	0.29	bdl	bdl	bdl	bdl	bdl	0.08	bdl	0.07	bdl
Ce_2O_3	1.53	0.68	1.62	0.88	1.70	0.48	1.45	0.55	1.29	1.20	bdl	bdl	0.09	0.08	bdl	0.16	0.12	0.30	0.06
Pr_2O_3	0.26	0.12	0.26	0.17	0.27	0.08	0.17	0.08	0.21	0.21	bdl	bdl	bdl	bdl	bdl	bdl	bdl	bdl	bdl
Nd_2O_3	1.21	0.50	1.26	0.73	1.36	0.50	1.18	0.55	1.08	0.89	0.06	0.06	0.08	0.07	0.06	0.17	0.06	0.29	0.05
Sm_2O_3	0.19	0.07	0.21	0.08	0.18	0.07	0.17	0.11	0.15	0.14	bdl	bdl	bdl	bdl	bdl	bdl	bdl	bdl	bdl
Eu_2O_3	bdl	bdl	0.07	bdl	bdl	bdl	0.05	bdl	0.06	bdl	bdl	bdl	bdl	bdl	bdl	bdl	bdl	bdl	bdl
Gd_2O_3	0.10	0.06	0.11	0.05	0.06	0.08	0.05	bdl	0.11	0.05	0.06	0.04	bdl	bdl	bdl	bdl	bdl	0.05	bdl
Tb_2O_3	bdl	bdl	bdl	bdl	bdl	bdl	bdl	bdl	bdl	bdl	bdl	bdl	bdl	bdl	bdl	bdl	bdl	bdl	bdl
Dy_2O_3	bdl	bdl	bdl	bdl	bdl	bdl	bdl	bdl	bdl	bdl	bdl	bdl	0.04	bdl	0.06	bdl	bdl	bdl	bdl
Ho_2O_3	bdl	bdl	bdl	bdl	bdl	bdl	bdl	bdl	bdl	bdl	bdl	bdl	bdl	bdl	bdl	bdl	bdl	bdl	bdl
Er_2O_3	bdl	bdl	bdl	bdl	bdl	bdl	bdl	bdl	bdl	bdl	bdl	bdl	bdl	bdl	bdl	bdl	bdl	bdl	bdl
Tm_2O_3	bdl	bdl	bdl	bdl	bdl	bdl	bdl	bdl	bdl	bdl	bdl	bdl	bdl	bdl	bdl	bdl	bdl	bdl	bdl
Yb_2O_3	bdl	bdl	bdl	bdl	bdl	bdl	bdl	bdl	bdl	bdl	bdl	bdl	bdl	bdl	bdl	bdl	bdl	bdl	bdl
Lu_2O_3	bdl	bdl	bdl	bdl	bdl	bdl	bdl	bdl	bdl	bdl	bdl	bdl	bdl	bdl	bdl	bdl	bdl	bdl	bdl
Y_2O_3	0.13	bdl	0.13	0.09	0.13	bdl	0.11	bdl	0.12	0.09	0.09	bdl	0.10	0.07	0.06	0.08	bdl	bdl	bdl
ZrO_2	0.14	0.12	0.17	0.14	0.11	0.16	0.10	0.18	0.11	0.16	0.15	0.11	0.13	0.16	0.15	0.17	0.16	0.09	0.12
HfO_2	bdl	bdl	bdl	bdl	bdl	bdl	bdl	bdl	bdl	bdl	bdl	bdl	bdl	bdl	bdl	bdl	bdl	bdl	bdl
Nb_2O_5	bdl	bdl	bdl	bdl	bdl	bdl	bdl	bdl	bdl	bdl	bdl	bdl	bdl	bdl	bdl	bdl	bdl	bdl	bdl
Sc_2O_3	bdl	bdl	bdl	bdl	bdl	bdl	0.03	bdl	bdl	bdl	bdl	bdl	bdl	bdl	bdl	bdl	bdl	bdl	bdl
ThO_2	bdl	bdl	0.06	bdl	bdl	bdl	bdl	bdl	bdl	bdl	bdl	bdl	bdl	bdl	bdl	bdl	bdl	bdl	bdl
UO_2	bdl	bdl	bdl	bdl	bdl	bdl	bdl	bdl	bdl	bdl	bdl	bdl	bdl	bdl	bdl	bdl	bdl	bdl	bdl
P_2O_5	30.05	31.46	28.52	28.96	28.40	29.92	28.65	30.11	29.87	29.22	32.73	31.95	30.97	31.14	30.90	31.35	31.03	39.69	40.59
SO_3	0.09	bdl	0.15	0.04	0.18	bdl	0.09	0.06	0.05	0.07	bdl	bdl	bdl	bdl	bdl	bdl	bdl	0.07	0.06
F	2.82	3.35	2.73	3.02	2.71	2.98	2.85	3.08	3.05	2.99	2.99	2.89	2.74	2.81	3.12	2.36	3.23	3.03	3.33
Cl	0.64	0.51	0.76	0.54	0.56	0.47	0.56	0.46	0.53	0.55	0.32	0.44	0.43	0.29	0.19	0.26	0.29	0.07	0.05
$O=(F_2,Cl_2)$	-1.33	-1.52	-1.32	-1.39	-1.27	-1.36	-1.33	-1.40	-1.41	-1.38	-1.33	-1.32	-1.25	-1.25	-1.35	-1.05	-1.43	-1.29	-1.41
TOTAL	88.20	88.63	86.31	84.85	84.55	85.95	84.97	86.46	87.08	85.15	88.44	87.77	87.05	86.37	86.24	85.82	86.81	96.23	97.59
TREO	3.90	1.61	4.14	2.24	4.12	1.35	3.53	1.45	3.30	2.86	0.21	0.10	0.31	0.23	0.18	0.50	0.18	0.71	0.12

Table B.15 cont.

SAMPLE	516647-5-310	516647-5-311	516647-5-312	881328B-3A-256	881328B-3A-257	881328B-3A-258	881328B-7A-261	881328B-7A-262	516674-4A-281	516674-6A-288	516674-6A-289	516665A-23A-71	516665A-23A-78	516665B-2A-126	516665B-2A-127	516665B-2A-128	516665B-2A-129	516665B-14A-143
SiO_2	0.52	0.55	0.26	0.52	0.42	0.13	0.93	0.45	0.45	0.34	0.58	2.06	1.95	2.27	2.22	2.26	2.18	2.09
Al_2O_3	bdl	0.01	bdl	bdl	0.01	0.01	bdl	bdl	bdl	bdl	0.01	bdl	bdl	bdl	bdl	bdl	bdl	bdl
Na_2O	0.08	0.03	0.03	0.07	0.05	0.03	0.08	0.04	0.11	0.14	0.14	0.12	0.07	0.06	0.07	0.08	0.07	0.09
K_2O	bdl	0.02	bdl	bdl	bdl	bdl	bdl	bdl	0.01	bdl	bdl	0.03	bdl	bdl	bdl	bdl	bdl	bdl
CaO	52.32	52.58	53.48	53.00	52.61	53.21	51.69	52.81	52.30	53.14	52.26	44.44	41.74	49.23	49.24	49.04	49.47	47.42
MgO	0.02	bdl	bdl	0.02	0.02	0.02	0.02	0.02	0.02	0.02	0.01	0.02	0.01	bdl	0.01	0.01	bdl	0.01
FeO	bdl	0.03	0.02	0.03	0.03	0.03	bdl	0.02	0.18	bdl	0.02	bdl	bdl	bdl	0.02	0.02	bdl	0.02
MnO	0.05	0.04	0.05	0.03	0.03	0.02	0.03	bdl	0.06	0.05	0.07	bdl	bdl	0.06	0.06	0.06	0.05	0.05
BaO	bdl	bdl	bdl	bdl	bdl	bdl	bdl	bdl	bdl	bdl	bdl	bdl	bdl	bdl	bdl	bdl	bdl	bdl
SrO	0.91	0.64	0.63	1.24	1.04	1.03	0.98	1.15	1.33	0.93	0.95	1.27	1.19	1.25	1.29	1.19	1.28	1.26
TiO_2	bdl	bdl	bdl	bdl	bdl	bdl	bdl	bdl	bdl	bdl	bdl	bdl	bdl	bdl	bdl	bdl	bdl	bdl
Cr_2O_3	bdl	bdl	bdl	bdl	bdl	bdl	bdl	bdl	bdl	bdl	bdl	bdl	bdl	bdl	bdl	bdl	bdl	bdl
La_2O_3	0.16	0.08	0.06	bdl	0.10	bdl	0.17	bdl	0.14	0.07	0.06	0.83	0.80	0.92	0.88	0.91	0.84	0.83
Ce_2O_3	0.53	0.38	0.23	0.16	0.37	0.08	0.73	0.31	0.38	0.37	0.45	2.60	2.52	2.59	2.48	2.62	2.52	2.42
Pr_2O_3	0.09	bdl	0.05	0.09	0.09	bdl	0.13	0.08	0.10	0.06	0.10	0.33	0.33	0.35	0.37	0.35	0.35	0.32
Nd_2O_3	0.35	0.28	0.23	0.40	0.41	0.13	0.86	0.45	0.36	0.39	0.58	1.50	1.45	1.48	1.51	1.51	1.47	1.47
Sm_2O_3	0.09	0.08	bdl	0.12	0.09	0.05	0.14	0.10	0.04	0.10	0.08	0.17	0.15	0.20	0.22	0.19	0.22	0.19
Eu_2O_3	bdl	bdl	bdl	bdl	bdl	bdl	bdl	bdl	bdl	bdl	bdl	bdl	bdl	bdl	bdl	bdl	bdl	bdl
Gd_2O_3	0.05	bdl	0.04	0.10	0.05	bdl	0.09	0.07	0.04	0.05	0.08	bdl	bdl	0.08	0.12	0.14	0.09	0.05
Tb_2O_3	bdl	bdl	bdl	bdl	bdl	bdl	bdl	bdl	bdl	bdl	bdl	bdl	bdl	bdl	bdl	bdl	bdl	bdl
Dy_2O_3	bdl	bdl	bdl	0.06	0.04	0.06	bdl	0.07	bdl	bdl	0.07	bdl	bdl	bdl	bdl	0.05	bdl	bdl
Ho_2O_3	bdl	bdl	bdl	bdl	bdl	bdl	bdl	bdl	bdl	bdl	bdl	bdl	bdl	bdl	bdl	bdl	bdl	bdl
Er_2O_3	bdl	bdl	bdl	bdl	bdl	bdl	bdl	bdl	bdl	bdl	bdl	bdl	bdl	bdl	bdl	bdl	bdl	bdl
Tm_2O_3	bdl	bdl	bdl	bdl	bdl	bdl	bdl	bdl	bdl	bdl	bdl	bdl	bdl	bdl	bdl	bdl	bdl	bdl
Yb_2O_3	bdl	bdl	bdl	bdl	bdl	bdl	bdl	bdl	bdl	bdl	bdl	bdl	bdl	bdl	bdl	bdl	bdl	bdl
Lu_2O_3	bdl	bdl	bdl	bdl	bdl	bdl	bdl	bdl	bdl	bdl	bdl	bdl	bdl	bdl	bdl	bdl	bdl	bdl
Y_2O_3	bdl	bdl	bdl	0.19	0.08	0.10	0.13	0.11	bdl	0.06	0.12	0.11	0.12	0.10	0.12	0.06	0.10	0.10
ZrO_2	0.13	0.10	0.10	0.15	0.10	0.11	0.14	0.12	0.15	0.12	0.12	0.13	0.12	0.15	0.12	0.11	0.13	0.11
HfO_2	bdl	bdl	bdl	bdl	bdl	bdl	bdl	bdl	bdl	bdl	bdl	bdl	bdl	bdl	bdl	bdl	bdl	bdl
Nb_2O_5	bdl	bdl	bdl	bdl	bdl	bdl	bdl	bdl	bdl	bdl	bdl	bdl	bdl	bdl	bdl	bdl	bdl	bdl
Sc_2O_3	bdl	bdl	bdl	bdl	bdl	bdl	bdl	bdl	bdl	bdl	bdl	bdl	bdl	bdl	bdl	bdl	bdl	bdl
ThO_2	bdl	bdl	bdl	bdl	bdl	bdl	bdl	bdl	bdl	bdl	bdl	bdl	0.05	0.10	0.09	0.10	0.06	0.09
UO_2	0.03	bdl	bdl	0.03	bdl	bdl	bdl	bdl	bdl	bdl	bdl	bdl	bdl	bdl	bdl	bdl	bdl	bdl
P_2O_5	39.83	39.92	40.76	38.44	38.58	39.32	37.90	38.49	38.38	39.11	38.47	34.98	34.90	35.12	34.97	35.05	34.58	35.07
SO_3	0.51	0.09	0.05	0.12	0.06	0.07	0.12	0.04	0.24	0.13	0.20	0.27	0.26	0.25	0.20	0.22	0.24	0.21
F	3.73	3.36	3.38	3.09	2.97	3.06	2.93	3.16	3.01	3.37	3.39	3.15	2.89	3.13	3.30	3.19	3.36	3.15
Cl	0.09	0.05	0.02	0.08	0.08	0.07	0.09	0.07	0.11	0.11	0.13	0.11	0.11	0.16	0.14	0.22	0.17	0.15
$O=(F_2,Cl_2)$	-1.59	-1.43	-1.43	-1.32	-1.27	-1.30	-1.25	-1.34	-1.29	-1.44	-1.46	-1.35	-1.24	-1.36	-1.42	-1.39	-1.45	-1.36
TOTAL	97.89	96.83	97.97	96.63	95.98	96.24	95.90	96.20	96.10	97.10	96.42	90.75	87.42	96.15	96.01	95.99	95.73	93.75
TREO	1.27	0.83	0.62	1.13	1.24	0.43	2.25	1.19	1.07	1.09	1.54	5.54	5.37	5.72	5.69	5.84	5.59	5.38

Table B.16 Composition of monazite (in wt.%) in apatite breccia veins.

SAMPLE	881309A-1-116	881309A-1-117	881309A-1-128	881309A-1-129	881309A-1-130	881309A-1-131	881309A-1-132	881309A-1-133	881309A-1-134	881309A-1-138	881309A-2-139	881309A-2-140	881309A-2-141	881309A-2-142	881309A-2-143	881309A-2-144	881309A-2-145	881309A-2-146	881309A-2-147	881309A-2-148	881309A-2-149	881309A-2-150	881309A-2-151
SiO_2	1.19	1.22	0.92	2.99	3.01	2.93	2.67	0.82	1.26	1.34	0.70	1.45	1.59	2.37	1.93	1.20	0.84	0.85	1.36	1.51	1.98	1.78	1.92
Al_2O_3	0.02	bdl	0.03	bdl	bdl	bdl	bdl	0.02	0.02	0.03	0.02	0.02	0.02	0.02	0.02	0.02	0.02	bdl	0.02	0.02	0.02	0.02	0.03
Na_2O	bdl*	bdl	bdl	bdl	bdl	bdl	bdl	bdl	bdl	bdl	bdl	0.08	0.05	bdl	0.04	0.04	bdl	bdl	bdl	bdl	0.04	bdl	bdl
K_2O	bdl	bdl	bdl	bdl	bdl	bdl	bdl	bdl	bdl	bdl	bdl	bdl	bdl	bdl	bdl	bdl	bdl	bdl	bdl	bdl	bdl	bdl	bdl
CaO	1.16	0.42	0.29	0.42	0.44	0.49	0.39	0.34	0.48	0.66	0.44	0.40	0.40	0.43	0.37	0.29	0.23	0.36	0.37	0.32	0.40	0.54	0.50
MgO	0.02	0.03	0.04	bdl	0.02	0.02	0.02	0.03	0.03	0.03	0.03	0.02	0.04	0.03	0.04	0.03	0.02	0.03	0.03	0.02	0.02	0.02	0.03
FeO	0.09	0.19	0.03	bdl	0.05	0.07	0.03	0.03	0.04	0.05	0.04	0.05	0.03	0.03	bdl	0.03	0.04	0.03	bdl	bdl	bdl	bdl	bdl
MnO	bdl	bdl	0.04	bdl	bdl	bdl	bdl	0.03	bdl	bdl	bdl	bdl	bdl	bdl	bdl	bdl	bdl	bdl	bdl	bdl	bdl	bdl	bdl
BaO	bdl	bdl	bdl	bdl	bdl	bdl	bdl	bdl	bdl	bdl	bdl	bdl	bdl	bdl	bdl	bdl	bdl	bdl	bdl	bdl	bdl	0.10	bdl
SrO	0.12	bdl	bdl	0.12	0.14	0.13	0.08	bdl	bdl	0.09	bdl	0.13	0.11	0.12	0.10	0.14	0.09	0.07	0.08	0.10	0.14	0.18	0.11
TiO_2	bdl	bdl	bdl	bdl	bdl	bdl	bdl	bdl	bdl	bdl	bdl	bdl	bdl	bdl	bdl	bdl	bdl	bdl	bdl	bdl	bdl	bdl	bdl
Cr_2O_3	0.68	0.74	0.54	0.60	0.63	0.60	0.61	0.53	0.55	0.55	0.41	0.47	0.45	0.39	0.39	0.49	0.40	0.39	0.44	0.43	0.42	0.42	0.40
La_2O_3	20.63	24.23	15.26	19.72	19.65	19.65	19.85	15.92	18.63	17.19	15.28	20.20	20.01	18.65	18.93	20.47	16.29	15.41	19.84	19.87	18.80	19.17	19.21
Ce_2O_3	38.16	37.51	37.43	33.71	33.98	34.20	33.91	37.50	38.91	38.13	35.35	33.73	33.34	30.99	32.60	35.28	36.09	35.81	33.54	33.06	31.55	31.42	31.90
Pr_2O_3	4.42	3.83	5.27	3.94	3.76	3.85	4.04	5.09	4.67	4.64	5.20	4.60	4.47	4.18	4.43	4.76	4.98	5.21	4.45	4.23	4.24	4.21	4.22
Nd_2O_3	13.32	11.48	19.76	12.82	12.74	12.49	12.82	18.76	14.83	16.07	18.20	12.44	12.50	11.30	12.05	12.83	16.98	17.82	12.42	12.06	11.87	11.62	11.83
Sm_2O_3	0.79	0.62	1.54	0.75	0.82	0.87	0.84	1.40	0.89	0.99	1.41	0.79	0.73	0.66	0.70	0.63	1.13	1.28	0.72	0.75	0.73	0.73	0.71
Eu_2O_3	bdl	0.09	0.17	bdl	bdl	bdl	bdl	0.20	0.18	0.14	0.28	0.08	0.10	0.12	bdl	0.09	0.24	0.29	bdl	0.10	bdl	0.15	0.12
Gd_2O_3	0.21	0.26	0.59	0.43	0.42	0.34	0.46	0.51	0.18	0.20	bdl	bdl	bdl	bdl	bdl	bdl	bdl	bdl	bdl	bdl	bdl	bdl	bdl
Tb_2O_3	bdl	bdl	bdl	bdl	bdl	bdl	bdl	bdl	bdl	bdl	bdl	bdl	bdl	bdl	bdl	0.10	bdl	bdl	bdl	bdl	bdl	bdl	bdl
Dy_2O_3	bdl	bdl	bdl	bdl	bdl	bdl	bdl	bdl	bdl	bdl	bdl	bdl	bdl	bdl	bdl	bdl	bdl	bdl	bdl	bdl	bdl	bdl	bdl
Ho_2O_3	bdl	bdl	bdl	bdl	bdl	bdl	bdl	bdl	bdl	bdl	bdl	bdl	bdl	bdl	bdl	bdl	bdl	bdl	bdl	bdl	bdl	bdl	bdl
Er_2O_3	bdl	bdl	bdl	bdl	bdl	bdl	bdl	bdl	bdl	bdl	bdl	bdl	bdl	bdl	bdl	bdl	bdl	bdl	bdl	bdl	bdl	bdl	bdl
Tm_2O_3	bdl	bdl	bdl	bdl	bdl	bdl	bdl	bdl	bdl	bdl	bdl	bdl	bdl	bdl	bdl	bdl	bdl	bdl	bdl	bdl	bdl	bdl	bdl
Yb_2O_3	bdl	bdl	bdl	bdl	bdl	bdl	bdl	bdl	bdl	bdl	bdl	bdl	bdl	bdl	bdl	bdl	bdl	bdl	bdl	bdl	bdl	bdl	bdl
Lu_2O_3	bdl	bdl	bdl	bdl	bdl	bdl	bdl	bdl	bdl	bdl	bdl	bdl	bdl	bdl	bdl	bdl	bdl	bdl	bdl	bdl	bdl	bdl	bdl
Y_2O_3	bdl	bdl	bdl	bdl	bdl	bdl	bdl	bdl	bdl	bdl	bdl	bdl	bdl	bdl	bdl	bdl	bdl	bdl	bdl	bdl	bdl	bdl	bdl
ZrO_2	0.12	0.09	0.09	0.08	bdl	0.09	0.10	0.15	0.07	0.07	bdl	0.07	0.07	bdl	0.10	0.09	0.08	0.09	0.06	0.08	0.07	0.07	0.07
HfO_2	bdl	bdl	bdl	bdl	bdl	bdl	bdl	bdl	bdl	bdl	bdl	bdl	bdl	bdl	bdl	bdl	bdl	bdl	bdl	bdl	bdl	bdl	bdl
Nb_2O_5	bdl	bdl	bdl	bdl	bdl	bdl	bdl	bdl	bdl	bdl	bdl	bdl	bdl	bdl	bdl	bdl	bdl	bdl	bdl	bdl	bdl	bdl	bdl
Sc_2O_3	bdl	bdl	bdl	bdl	bdl	bdl	bdl	bdl	bdl	bdl	bdl	bdl	bdl	bdl	bdl	bdl	bdl	bdl	bdl	bdl	bdl	bdl	bdl
ThO_2	0.16	bdl	0.07	5.85	5.85	5.74	4.77	bdl	0.28	0.37	bdl	2.67	3.35	7.69	5.64	1.36	0.37	0.32	3.13	4.35	6.43	5.50	6.04
UO_2	bdl	bdl	bdl	0.05	0.06	bdl	bdl	bdl	bdl	bdl	bdl	bdl	bdl	bdl	0.06	bdl	bdl	bdl	bdl	bdl	bdl	0.07	bdl
P_2O_5	28.27	28.42	28.97	25.26	25.31	25.69	25.88	29.38	28.72	28.39	29.33	26.60	26.34	24.10	25.56	27.41	28.52	29.02	26.76	26.91	25.28	25.24	25.54
SO_3	1.19	1.34	0.82	1.54	1.62	1.61	1.62	0.64	1.08	1.08	0.75	0.82	0.82	0.80	1.36	0.77	0.91	0.84	1.21	1.10	0.83	1.40	1.32
F	bdl	bdl	bdl	bdl	bdl	bdl	bdl	bdl	bdl	bdl	bdl	bdl	bdl	bdl	bdl	bdl	bdl	bdl	bdl	bdl	bdl	bdl	bdl
Cl	0.04	0.04	0.05	0.03	0.04	0.04	0.04	0.05	0.04	0.05	0.06	0.09	0.08	0.06	0.05	0.08	0.05	0.05	0.03	0.04	0.08	0.05	0.03
TOTAL	110.57	110.51	111.90	108.31	108.52	108.81	108.13	111.39	110.87	110.05	107.46	104.68	104.47	101.91	104.35	106.09	107.27	107.88	104.47	104.96	102.87	102.67	103.97
TREO	77.52	78.03	80.03	71.37	71.36	71.41	71.93	79.39	78.29	77.34	75.71	71.83	71.14	65.90	68.71	74.16	75.70	75.82	70.97	70.08	67.19	67.29	67.99

* below detection limit

Table B.16 cont.

SAMPLE	881309A-2-152	881309A-2-153	881309A-2-154	881309A-2-155	881309A-2-156	881309A-2-157	881309A-2-158	881309A-2-159	881309A-2-160	881309A-2-162	881309A-3-178	881309A-3-179	881309A-3-180	881309A-3-183	881309A-3-184	881309A-4-214	881309A-4-215	881309A-4-216	881309A-4-233	881309A-4-234	881309A-5-240	881309A-5-241	881309A-5-245
SiO_2	2.33	1.87	1.46	1.27	1.01	1.26	1.02	1.65	1.24	1.44	1.89	1.96	1.71	1.28	1.89	0.83	0.91	1.45	2.13	2.91	0.92	0.84	0.91
Al_2O_3	bdl	0.02	0.02	bdl	0.02	bdl	0.02	0.02	0.02	0.02	0.02	bdl	bdl	0.02	0.02	0.02	0.05	0.02	0.02	0.02	0.02	0.02	0.02
Na_2O	bdl	bdl	bdl	bdl	bdl	0.04	bdl	bdl	bdl	bdl	bdl	bdl	bdl	bdl	bdl	bdl	bdl	bdl	bdl	bdl	bdl	0.04	bdl
K_2O	bdl	bdl	bdl	bdl	bdl	bdl	bdl	bdl	bdl	bdl	bdl	bdl	bdl	bdl	bdl	bdl	bdl	bdl	bdl	bdl	bdl	bdl	bdl
CaO	0.42	0.41	0.35	0.28	0.47	3.19	0.60	0.46	0.66	0.65	0.32	0.30	0.36	0.31	0.31	0.37	1.88	0.30	0.38	0.44	0.20	0.26	0.24
MgO	0.03	0.04	bdl	0.04	0.03	0.04	0.03	0.03	0.02	0.02	0.03	bdl	0.03	0.03	0.02	0.03	0.03	0.02	0.03	0.03	0.04	0.04	0.02
FeO	bdl	bdl	bdl	bdl	bdl	0.06	0.04	bdl	0.03	0.05	0.06	0.11	0.08	0.04	0.11	0.03	5.73	0.07	bdl	0.05	0.17	0.18	0.06
MnO	bdl	bdl	bdl	bdl	bdl	bdl	0.04	0.04	0.03	bdl	bdl	bdl	bdl	0.03	bdl	bdl	0.04	bdl	bdl	bdl	bdl	bdl	bdl
BaO	bdl	bdl	bdl	bdl	bdl	bdl	bdl	bdl	bdl	bdl	bdl	bdl	bdl	bdl	bdl	bdl	bdl	bdl	bdl	bdl	bdl	bdl	bdl
SrO	0.13	0.10	0.08	0.08	0.14	0.16	0.09	0.11	0.15	0.17	0.09	0.12	0.09	0.11	0.08	bdl	0.13	0.10	0.14	0.09	bdl	bdl	bdl
TiO_2	bdl	bdl	bdl	bdl	bdl	bdl	bdl	bdl	bdl	bdl	bdl	bdl	bdl	bdl	bdl	bdl	bdl	bdl	bdl	bdl	bdl	bdl	bdl
Cr_2O_3	0.44	0.43	0.48	0.46	0.32	0.51	0.60	0.52	0.53	0.56	0.63	0.63	0.67	0.52	0.64	0.55	0.47	0.67	0.62	0.58	0.59	0.54	0.59
La_2O_3	18.53	19.33	20.01	20.37	15.08	16.95	17.25	16.25	17.43	17.47	20.50	20.37	21.23	15.59	21.13	15.00	13.83	19.81	20.36	19.15	16.64	15.12	17.44
Ce_2O_3	31.25	32.55	33.81	34.81	35.31	35.16	37.71	37.68	37.37	37.35	35.91	35.91	36.53	37.04	36.47	37.27	33.76	36.83	35.16	33.74	38.07	37.16	37.93
Pr_2O_3	4.10	4.40	4.57	4.71	5.19	4.12	4.81	4.91	4.71	4.68	4.06	3.99	4.13	4.91	4.16	5.14	4.57	4.50	4.12	3.91	4.67	5.18	4.76
Nd_2O_3	11.58	11.95	12.46	12.66	17.54	14.95	16.81	17.52	16.74	16.56	13.66	13.38	13.47	18.90	13.35	19.63	17.88	14.79	13.42	12.86	17.87	19.28	16.98
Sm_2O_3	0.68	0.71	0.75	0.73	1.29	0.83	1.25	1.28	1.18	1.26	0.88	0.76	0.83	1.40	0.83	1.50	1.44	0.88	0.80	0.84	1.17	1.53	1.18
Eu_2O_3	0.10	bdl	0.14	bdl	0.19	0.16	0.19	0.20	0.23	0.25	0.07	0.08	bdl	0.17	bdl	0.19	0.23	bdl	bdl	0.09	0.16	0.19	0.11
Gd_2O_3	bdl	bdl	bdl	bdl	bdl	0.20	0.39	0.22	0.37	0.26	0.23	0.30	0.30	0.41	0.24	0.46	0.40	0.31	0.22	0.26	0.44	0.56	0.36
Tb_2O_3	bdl	bdl	bdl	bdl	bdl	bdl	bdl	bdl	bdl	bdl	bdl	bdl	bdl	bdl	bdl	bdl	bdl	bdl	bdl	bdl	bdl	bdl	bdl
Dy_2O_3	bdl	bdl	bdl	bdl	bdl	bdl	bdl	bdl	bdl	bdl	bdl	bdl	bdl	bdl	bdl	bdl	bdl	bdl	bdl	bdl	bdl	bdl	bdl
Ho_2O_3	bdl	bdl	bdl	bdl	bdl	bdl	bdl	bdl	bdl	bdl	bdl	bdl	bdl	bdl	bdl	bdl	bdl	bdl	bdl	bdl	bdl	bdl	bdl
Er_2O_3	bdl	bdl	bdl	bdl	bdl	bdl	bdl	bdl	bdl	bdl	bdl	bdl	bdl	bdl	bdl	bdl	bdl	bdl	bdl	bdl	bdl	bdl	bdl
Tm_2O_3	bdl	bdl	bdl	bdl	bdl	bdl	bdl	bdl	bdl	bdl	bdl	bdl	bdl	bdl	bdl	bdl	bdl	bdl	bdl	bdl	bdl	bdl	bdl
Yb_2O_3	bdl	bdl	bdl	bdl	bdl	bdl	bdl	bdl	bdl	bdl	bdl	bdl	bdl	bdl	bdl	bdl	bdl	bdl	bdl	bdl	bdl	bdl	bdl
Lu_2O_3	bdl	bdl	bdl	bdl	bdl	bdl	bdl	bdl	bdl	bdl	bdl	bdl	bdl	bdl	bdl	bdl	bdl	bdl	bdl	bdl	bdl	bdl	bdl
Y_2O_3	bdl	bdl	bdl	bdl	bdl	bdl	bdl	bdl	0.07	bdl	bdl	bdl	bdl	bdl	bdl	bdl	bdl	bdl	bdl	bdl	bdl	bdl	bdl
ZrO_2	0.08	0.09	0.09	0.10	0.08	0.12	0.09	0.12	0.11	0.11	0.07	bdl	0.09	0.10	0.09	0.06	0.08	0.08	0.08	0.07	0.06	0.06	0.10
HfO_2	bdl	bdl	bdl	bdl	bdl	bdl	bdl	bdl	bdl	bdl	bdl	bdl	bdl	bdl	bdl	bdl	bdl	bdl	bdl	bdl	bdl	bdl	bdl
Nb_2O_5	bdl	bdl	bdl	bdl	bdl	bdl	bdl	bdl	bdl	bdl	bdl	bdl	bdl	bdl	bdl	bdl	bdl	bdl	bdl	bdl	bdl	bdl	bdl
Sc_2O_3	bdl	bdl	bdl	bdl	bdl	bdl	bdl	bdl	bdl	bdl	bdl	bdl	bdl	bdl	bdl	bdl	bdl	bdl	bdl	bdl	bdl	bdl	bdl
ThO_2	7.68	5.31	2.92	1.92	0.61	1.09	bdl	0.67	0.11	0.22	2.25	2.50	1.42	0.50	1.86	bdl	bdl	1.20	3.12	5.84	0.41	0.11	bdl
UO_2	bdl	bdl	bdl	bdl	bdl	bdl	bdl	0.07	bdl	0.05	bdl	bdl	bdl	bdl	bdl	bdl	bdl	bdl	bdl	0.06	bdl	bdl	bdl
P_2O_5	24.78	25.62	26.67	27.30	27.93	29.84	29.20	28.18	29.04	28.41	26.75	26.37	27.81	28.75	27.73	29.51	27.81	28.24	26.84	25.65	28.98	29.33	29.11
SO_3	1.31	1.45	1.28	0.81	0.98	0.82	0.97	1.17	1.26	1.33	1.18	1.31	0.86	1.17	0.96	0.69	0.62	1.18	1.44	1.47	0.57	0.58	0.66
F	bdl	bdl	bdl	bdl	bdl	bdl	bdl	bdl	bdl	bdl	bdl	bdl	bdl	bdl	bdl	bdl	bdl	bdl	bdl	bdl	bdl	bdl	bdl
Cl	0.05	0.05	0.06	0.09	0.06	0.10	0.04	0.05	0.04	0.04	0.05	0.04	0.08	0.05	0.06	0.04	0.04	0.04	0.04	0.04	0.04	0.05	0.04
TOTAL	103.46	104.31	105.12	105.59	106.25	109.58	111.13	111.13	111.35	110.89	108.65	108.14	109.67	111.32	109.95	111.30	109.90	110.49	108.91	108.07	110.99	111.05	110.51
TREO	66.24	68.94	71.73	73.28	74.60	72.37	78.42	78.05	78.11	77.84	75.33	74.80	76.49	78.43	76.17	79.19	72.11	77.13	74.09	70.84	79.01	79.02	78.76

Table B.16 cont.

SAMPLE	881309A-5-247	881344-1-256	881344-1-258	881344-2-269	881344-2-270	881344-2-280	517458-8-39	517458-8-40	517458-8-41	517458-8-42	517458-8-43	517458-8-44	517458-8-48	517458-2-65	517458-2-66	517458-2-70	517458-2-71	517458-2-75	881344-3-396	881344-3-423	881375B-2-54	881375B-2-55	881375B-2-56
SiO_2	1.14	0.50	1.29	2.30	3.22	0.97	1.17	1.25	0.89	0.90	0.94	1.19	1.18	1.15	1.04	1.18	1.06	3.70	1.72	1.79	1.64	1.93	2.20
Al_2O_3	0.02	0.02	0.02	0.02	0.18	bdl	bdl	bdl	bdl	bdl	bdl	bdl	bdl	bdl	bdl	bdl	bdl	0.55	bdl	bdl	bdl	bdl	bdl
Na_2O	bdl	bdl	bdl	bdl	0.35	bdl	bdl	bdl	bdl	bdl	bdl	0.03	bdl	bdl	bdl	bdl	bdl	0.04	bdl	bdl	bdl	0.05	0.05
K_2O	bdl	bdl	bdl	bdl	bdl	bdl	bdl	bdl	bdl	bdl	bdl	bdl	bdl	bdl	bdl	bdl	bdl	bdl	bdl	bdl	bdl	bdl	bdl
CaO	0.29	0.21	0.15	0.40	0.66	0.17	0.21	0.26	0.14	0.08	0.15	0.47	0.21	0.30	0.36	0.43	0.27	1.32	0.90	1.59	0.19	0.49	0.29
MgO	0.03	0.04	0.03	0.02	0.52	0.04	0.03	bdl	0.02	0.02	0.02	bdl		0.03	bdl	0.02	bdl	0.03	0.21	bdl	0.04	bdl	0.03	0.04
FeO	0.07	0.04	0.06	0.06	0.30	0.56	0.08	0.04	0.04	0.03	bdl	0.05	0.06	0.07	0.07	0.03	0.05	1.31	0.07	3.52	0.39	0.04	0.11
MnO	bdl	bdl	bdl	bdl	bdl	bdl	0.03	bdl	bdl	bdl	bdl	bdl	bdl	0.03	bdl	0.03	0.04	0.07	bdl	0.03	bdl	bdl	bdl
BaO	bdl	bdl	bdl	bdl	bdl	bdl	bdl	bdl	bdl	bdl	bdl	bdl	bdl	bdl	bdl	bdl	bdl	0.19	bdl	0.46	bdl	bdl	bdl
SrO	0.14	bdl	bdl	bdl	0.23	bdl	bdl	bdl	0.06	bdl	0.06	0.15	0.10	bdl	bdl	bdl	bdl	0.56	bdl	0.72	0.14	bdl	bdl
TiO_2	bdl	bdl	bdl	bdl	bdl	bdl	bdl	bdl	bdl	bdl	bdl	bdl	bdl	bdl	bdl	bdl	bdl	bdl	bdl	bdl	bdl	bdl	bdl
Cr_2O_3	0.60	0.72	0.75	0.64	0.70	0.67	0.53	0.65	0.67	0.64	0.82	0.60	0.61	0.52	0.51	0.50	0.48	0.47	0.57	0.56	0.19	0.14	0.19
La_2O_3	17.74	22.20	22.64	20.09	23.30	21.32	14.00	17.15	18.46	18.22	23.77	15.75	15.56	13.00	13.51	12.79	11.56	12.58	17.39	15.96	15.27	13.78	17.87
Ce_2O_3	37.69	36.42	36.69	35.65	33.03	36.27	33.23	35.06	35.36	33.84	34.33	34.86	34.82	33.40	33.63	33.23	32.49	30.03	34.39	32.14	35.52	33.65	34.43
Pr_2O_3	4.81	4.31	4.40	4.12	3.49	4.45	4.71	4.33	4.14	4.29	3.53	4.45	4.35	4.77	4.68	4.80	4.84	3.96	3.40	3.13	3.71	3.81	3.21
Nd_2O_3	16.58	14.91	15.20	13.67	9.94	15.78	17.69	14.21	12.91	14.54	9.95	14.91	15.28	17.96	17.43	17.81	19.58	14.68	12.41	11.28	12.84	14.28	10.54
Sm_2O_3	1.16	1.06	1.08	0.98	0.54	1.22	1.54	1.21	0.87	1.21	0.53	1.14	1.30	1.60	1.45	1.67	2.08	1.17	0.92	0.85	0.83	1.31	0.69
Eu_2O_3	0.18	0.09	0.08	0.13	bdl	0.14	0.22	0.15	0.14	0.20	bdl	0.17	0.21	0.21	0.22	0.32	0.36	0.16	0.11	0.10	0.12	0.18	0.07
Gd_2O_3	0.35	0.43	0.44	0.36	0.25	0.50	0.70	0.55	0.51	0.59	0.38	0.58	0.61	0.68	0.62	0.75	0.92	0.51	1.34	1.20	0.31	0.38	0.32
Tb_2O_3	bdl	bdl	bdl	bdl	bdl	bdl	bdl	bdl	bdl	bdl	bdl	bdl	bdl	bdl	bdl	bdl	bdl	bdl	bdl	bdl	bdl	0.09	0.09
Dy_2O_3	bdl	bdl	bdl	bdl	bdl	bdl	bdl	bdl	bdl	bdl	bdl	bdl	bdl	bdl	bdl	bdl	bdl	bdl	bdl	bdl	bdl	bdl	
Ho_2O_3	bdl	bdl	bdl	bdl	bdl	bdl	bdl	bdl	bdl	bdl	bdl	bdl	bdl	bdl	bdl	bdl	bdl	bdl	bdl	bdl	bdl	bdl	
Er_2O_3	bdl	bdl	bdl	bdl	bdl	bdl	bdl	bdl	bdl	bdl	bdl	bdl	bdl	bdl	bdl	bdl	bdl	bdl	bdl	bdl	bdl	bdl	
Tm_2O_3	bdl	bdl	bdl	bdl	bdl	bdl	bdl	bdl	bdl	bdl	bdl	bdl	bdl	bdl	bdl	bdl	bdl	bdl	bdl	bdl	bdl	bdl	
Yb_2O_3	bdl	0.43	bdl	bdl	bdl	bdl	bdl	bdl	bdl	bdl	bdl	bdl	bdl	bdl	bdl	bdl	bdl	bdl	bdl	bdl	bdl	bdl	
Lu_2O_3	bdl	bdl	bdl	bdl	bdl	bdl	bdl	bdl	bdl	bdl	bdl	bdl	bdl	bdl	bdl	bdl	bdl	bdl	bdl	bdl	bdl	bdl	
Y_2O_3	0.08	bdl	bdl	bdl	bdl	0.06	bdl	bdl	bdl	bdl	bdl	bdl	bdl	bdl	bdl	bdl	0.09	bdl	bdl	bdl	bdl	bdl	0.09
ZrO_2	0.11	bdl	0.11	0.10	0.08	0.12	bdl	0.08	bdl	bdl	bdl	bdl	bdl	bdl	bdl	bdl	bdl	bdl	bdl	bdl	bdl	bdl	
HfO_2	bdl	bdl	bdl	bdl	bdl	bdl	bdl	bdl	bdl	bdl	bdl	bdl	bdl	bdl	bdl	bdl	bdl	bdl	bdl	bdl	bdl	bdl	
Nb_2O_5	bdl	bdl	bdl	bdl	bdl	bdl	bdl	bdl	bdl	bdl	bdl	bdl	bdl	bdl	bdl	bdl	bdl	bdl	bdl	bdl	bdl	bdl	
Sc_2O_3	bdl	bdl	bdl	bdl	bdl	bdl	bdl	bdl	bdl	bdl	bdl	bdl	bdl	bdl	bdl	bdl	bdl	bdl	bdl	bdl	bdl	bdl	
ThO_2	0.22	bdl	bdl	3.30	4.40	bdl	2.01	0.97	0.75	0.84	0.29	0.91	1.06	2.04	1.97	1.98	1.71	4.52	2.38	1.84	1.16	1.38	2.07
UO_2	bdl	bdl	bdl	0.06	bdl	bdl	bdl	0.06	bdl	bdl	bdl	bdl	bdl	bdl	bdl	bdl	bdl	bdl	bdl	bdl	bdl	bdl	0.07
P_2O_5	28.66	30.18	29.50	26.97	26.60	29.82	27.91	27.69	28.03	27.79	27.80	27.23	27.62	27.77	28.00	27.42	27.92	23.54	27.50	23.84	24.36	23.96	23.12
SO_3	1.06	0.56	1.09	1.04	1.14	0.93	0.21	0.82	0.58	0.37	0.74	0.78	0.74	0.46	0.34	0.44	0.49	0.48	0.73	1.15	1.17	1.12	1.34
F	bdl	bdl	bdl	bdl	bdl	bdl	bdl	bdl	bdl	bdl	bdl	bdl	bdl	bdl	bdl	bdl	bdl	bdl	bdl	bdl	0.15	0.20	0.23
Cl	0.04	0.05	0.04	0.04	0.09	0.04	0.06	0.04	0.05	0.04	0.03	0.06	0.05	0.06	0.05	0.05	0.10	0.07	0.06	0.08	0.12	0.10	0.12
TOTAL	110.95	112.13	113.57	109.95	108.99	113.05	104.31	104.50	103.63	103.59	103.35	103.31	103.81	104.01	103.88	103.43	104.05	100.11	103.86	100.25	98.03	96.82	97.01
TREO	78.59	79.83	80.53	74.99	70.55	79.74	72.08	72.65	72.39	72.89	72.50	71.85	72.14	71.63	71.55	71.38	71.92	63.10	69.96	64.65	68.61	67.48	67.31

Table B.16 cont.

SAMPLE	881375B-2-57	881375B-2-58	881375B-2-59	881375B-2-60	881375B-2-61	881375B-2-62	881375B-6-94	881375B-6-95	881375B-6-96	881011B-1-110	881011B-3-117	881011B-3-118	881011B-7-132	881011B-7-133	881253-1-140	881253-1-141	881253-2-148	881253-2-149	517256-4-195	948521-1-206	948521-1-212	948521-1-213	948521-1-214
SiO_2	2.06	2.26	2.53	3.09	2.60	1.29	1.43	1.42	1.59	1.73	1.36	1.04	0.99	2.08	1.01	1.65	1.64	2.00	0.22	1.52	1.91	1.47	1.82
Al_2O_3	bdl	bdl	bdl	bdl	bdl	bdl	bdl	bdl	bdl	bdl	bdl	bdl	bdl	bdl	bdl	bdl	bdl	bdl	bdl	bdl	bdl	bdl	bdl
Na_2O	0.04	bdl	bdl	0.07	0.05	0.06	0.05	0.07	0.05	0.09	0.06	0.05	0.04	0.04	bdl	bdl	0.04	bdl	0.05	bdl	bdl	bdl	bdl
K_2O	bdl	bdl	bdl	bdl	bdl	bdl	bdl	bdl	bdl	bdl	bdl	bdl	bdl	bdl	bdl	bdl	bdl	bdl	bdl	bdl	bdl	bdl	bdl
CaO	0.22	0.22	0.30	0.30	0.20	0.05	0.46	0.39	0.30	0.76	0.50	0.27	0.18	0.36	0.20	0.61	0.26	0.15	4.02	0.19	0.45	0.67	1.48
MgO	bdl	bdl	0.03	bdl	0.03	0.04	0.04	0.03	0.03	0.03	bdl	0.04	0.03	0.03	0.04	0.03	0.03	0.04	0.04	bdl	0.03	0.03	0.04
FeO	bdl	bdl	bdl	0.05	0.03	bdl	bdl	bdl	bdl	bdl	bdl	0.09	bdl	bdl	bdl	0.07	bdl	bdl	0.60	bdl	0.03	0.07	bdl
MnO	bdl	bdl	bdl	bdl	bdl	bdl	bdl	bdl	bdl	bdl	bdl	bdl	bdl	bdl	bdl	bdl	bdl	bdl	bdl	0.03	bdl	bdl	bdl
BaO	bdl	bdl	bdl	bdl	bdl	bdl	bdl	bdl	bdl	bdl	bdl	bdl	bdl	bdl	bdl	bdl	bdl	bdl	bdl	bdl	bdl	bdl	bdl
SrO	bdl	bdl	bdl	bdl	bdl	bdl	bdl	bdl	0.13	bdl	bdl	bdl	bdl	bdl	bdl	bdl	bdl	bdl	bdl	bdl	bdl	bdl	bdl
TiO_2	bdl	bdl	bdl	bdl	bdl	bdl	bdl	bdl	bdl	bdl	bdl	bdl	bdl	bdl	bdl	bdl	bdl	bdl	bdl	bdl	bdl	bdl	bdl
Cr_2O_3	0.21	0.23	0.21	0.20	0.20	0.22	0.15	0.17	0.14	0.18	0.25	0.22	0.24	0.27	0.20	0.22	0.23	0.19	0.11	0.23	0.20	0.22	0.23
La_2O_3	17.74	18.52	18.52	17.73	17.60	16.25	17.90	17.20	16.83	20.56	20.48	19.02	20.74	20.19	13.47	18.18	18.01	18.16	10.40	13.03	11.85	15.00	12.30
Ce_2O_3	34.12	33.71	33.44	32.45	33.39	35.62	34.72	34.92	34.31	35.08	35.03	35.92	34.66	33.62	34.76	34.76	34.56	33.94	28.57	33.86	34.03	35.87	33.84
Pr_2O_3	3.31	3.03	3.03	2.97	3.11	3.56	3.61	3.58	3.51	2.93	3.02	3.29	2.93	2.72	4.08	3.00	3.18	3.05	3.61	4.28	4.08	3.95	4.15
Nd_2O_3	10.55	10.00	9.76	9.74	10.20	12.08	10.85	11.10	11.23	10.00	9.66	10.65	9.63	9.36	15.06	10.60	10.76	10.47	16.57	15.61	16.20	13.33	15.69
Sm_2O_3	0.75	0.61	0.68	0.61	0.63	0.79	0.70	0.80	0.82	0.56	0.57	0.69	0.56	0.56	1.29	0.66	0.69	0.70	2.79	1.34	1.34	0.88	1.28
Eu_2O_3	bdl	bdl	0.07	0.12	0.10	0.09	0.08	0.12	bdl	0.16	0.11	0.09	0.07	0.12	0.23	0.16	0.09	0.11	0.20	0.18	0.30	0.07	0.21
Gd_2O_3	0.28	0.31	0.33	0.24	0.30	0.34	0.16	0.22	0.17	0.21	0.29	0.36	0.30	0.27	0.50	0.25	0.30	0.33	1.60	0.40	0.36	0.19	0.37
Tb_2O_3	bdl	bdl	bdl	0.07	bdl	0.09	0.08	bdl	0.08	bdl	bdl	bdl	0.09	bdl	bdl	bdl	bdl	bdl	0.18	0.14	0.11	0.10	0.11
Dy_2O_3	bdl	bdl	bdl	bdl	bdl	bdl	bdl	bdl	bdl	bdl	bdl	bdl	bdl	bdl	bdl	bdl	bdl	bdl	0.18	bdl	bdl	bdl	bdl
Ho_2O_3	bdl	bdl	bdl	bdl	bdl	bdl	bdl	bdl	bdl	bdl	bdl	bdl	bdl	bdl	bdl	bdl	bdl	bdl	bdl	bdl	bdl	bdl	bdl
Er_2O_3	bdl	bdl	bdl	bdl	bdl	bdl	bdl	bdl	bdl	bdl	bdl	bdl	bdl	bdl	bdl	bdl	bdl	bdl	bdl	bdl	bdl	bdl	bdl
Tm_2O_3	bdl	bdl	bdl	bdl	bdl	bdl	bdl	bdl	bdl	bdl	bdl	bdl	bdl	bdl	bdl	bdl	bdl	bdl	bdl	bdl	bdl	bdl	bdl
Yb_2O_3	bdl	bdl	bdl	bdl	bdl	bdl	bdl	bdl	bdl	bdl	bdl	bdl	bdl	bdl	bdl	bdl	bdl	bdl	bdl	bdl	bdl	bdl	bdl
Lu_2O_3	bdl	bdl	bdl	bdl	bdl	bdl	bdl	bdl	bdl	bdl	bdl	bdl	bdl	bdl	bdl	bdl	bdl	bdl	bdl	bdl	bdl	bdl	bdl
Y_2O_3	bdl	bdl	bdl	bdl	bdl	bdl	bdl	bdl	bdl	0.10	bdl	bdl	bdl	bdl	0.15	bdl	0.11	bdl	1.19	0.12	0.11	bdl	bdl
ZrO_2	bdl	bdl	bdl	0.09	bdl	bdl	bdl	bdl	bdl	bdl	bdl	bdl	bdl	bdl	bdl	bdl	bdl	bdl	bdl	bdl	bdl	bdl	bdl
HfO_2	bdl	bdl	bdl	bdl	bdl	bdl	bdl	bdl	bdl	bdl	bdl	bdl	bdl	bdl	bdl	bdl	bdl	bdl	bdl	bdl	bdl	bdl	bdl
Nb_2O_5	bdl	bdl	bdl	bdl	bdl	bdl	bdl	bdl	bdl	bdl	bdl	bdl	bdl	bdl	bdl	bdl	bdl	bdl	bdl	bdl	bdl	bdl	bdl
Sc_2O_3	bdl	bdl	bdl	bdl	bdl	bdl	bdl	bdl	bdl	bdl	bdl	bdl	bdl	bdl	bdl	bdl	bdl	bdl	bdl	bdl	bdl	bdl	bdl
ThO_2	2.13	2.58	3.22	4.76	3.80	0.87	0.73	0.57	1.41	1.18	0.38	0.13	bdl	2.23	0.35	1.39	1.28	1.93	bdl	1.40	2.12	1.45	1.77
UO_2	0.10	bdl	0.07	0.11	0.11	bdl	bdl	bdl	bdl	bdl	bdl	bdl	bdl	bdl	bdl	bdl	bdl	bdl	bdl	bdl	bdl	bdl	bdl
P_2O_5	23.06	22.55	21.83	21.14	23.00	24.65	24.38	24.84	24.81	24.00	23.17	23.23	22.37	21.12	22.96	21.50	21.21	20.91	23.77	28.81	27.49	28.33	27.19
SO_3	1.09	1.20	1.44	1.21	1.19	0.77	1.02	1.19	1.19	1.21	0.94	0.68	0.73	1.14	0.76	0.96	1.25	1.22	bdl	0.75	0.92	0.62	0.92
F	0.18	0.25	0.14	0.20	0.17	0.25	0.14	0.22	0.23	0.20	0.15	0.19	0.17	0.11	0.17	0.19	0.18	0.16	0.24	0.21	0.26	0.17	0.31
Cl	0.09	0.07	0.06	0.09	0.08	0.05	0.07	0.05	0.05	0.05	0.05	0.05	0.04	0.05	0.07	0.06	0.05	0.04	0.09	0.06	0.07	0.05	0.06
TOTAL	95.82	95.44	95.57	95.14	96.70	96.96	96.48	96.81	96.77	98.96	95.93	95.94	93.67	94.21	95.20	94.20	93.80	93.32	94.32	102.06	101.74	102.39	101.62
TREO	66.74	66.19	65.82	63.93	65.33	68.83	68.09	67.95	66.95	69.61	69.17	70.02	68.98	66.84	69.54	67.62	67.70	66.76	65.30	68.97	68.38	69.39	67.95

Table B.16 cont.

SAMPLE	516665A-5A-82	516665A-9A-93	516665A-9A-94	516665B-26A-164	516665B-18A-167	516665B-T-2A-174	516665B-T-2A-176	516665B-T-6A-178	516665B-T-4A-185	516658-14A-194	516658-14A-195	516658-1A-197	516658-1A-198	516658-1A-199	516658-2A-200	516658-2A-201	516658-6A-202	516658-9A-203	516658-9A-204	516658-9A-206	516658-9A-207	516658-9A-208
SiO_2	3.57	3.88	2.20	1.98	2.37	1.88	1.32	2.36	4.56	1.79	1.10	1.30	1.43	1.52	1.32	1.19	1.01	1.42	1.27	1.58	1.55	1.82
Al_2O_3	bdl	bdl	bdl	bdl	bdl	bdl	bdl	bdl	bdl	bdl	bdl	bdl	bdl	bdl	bdl	bdl	bdl	bdl	bdl	bdl	bdl	bdl
Na_2O	0.04	bdl	bdl	0.05	0.05	0.04	0.04	0.05	0.07	0.07	0.06	0.05	0.04	0.03	0.03	0.06	0.05	0.05	0.06	0.05	0.04	0.06
K_2O	bdl	bdl	bdl	bdl	bdl	bdl	bdl	bdl	bdl	bdl	bdl	bdl	bdl	bdl	bdl	bdl	bdl	bdl	bdl	bdl	bdl	bdl
CaO	1.04	0.72	0.50	0.66	0.63	0.98	0.53	0.33	0.96	0.92	0.52	0.43	0.37	0.76	0.47	0.46	1.51	0.73	0.44	0.54	1.65	0.57
MgO	bdl	bdl	bdl	0.03	0.03	bdl	bdl	bdl	bdl	0.05	0.03	0.03	0.02	0.02	0.02	bdl	0.05	0.03	bdl	bdl	0.09	0.03
FeO	bdl	bdl	bdl	bdl	bdl	bdl	bdl	bdl	bdl	0.63	bdl	bdl	bdl	bdl	bdl	bdl	0.41	bdl	bdl	bdl	0.86	bdl
MnO	0.05	bdl	bdl	bdl	bdl	bdl	bdl	bdl	bdl	bdl	bdl	bdl	bdl	bdl	bdl	bdl	bdl	bdl	bdl	bdl	bdl	bdl
BaO	0.35	bdl	bdl	bdl	bdl	bdl	bdl	bdl	0.20	bdl	bdl	bdl	bdl	bdl	bdl	bdl	bdl	bdl	bdl	bdl	bdl	bdl
SrO	0.36	bdl	0.15	bdl	bdl	bdl	bdl	bdl	bdl	0.21	bdl	bdl	bdl	bdl	bdl	0.12	0.11	0.16	0.19	bdl	0.37	bdl
TiO_2	bdl	bdl	bdl	bdl	bdl	bdl	bdl	bdl	bdl	bdl	bdl	bdl	bdl	bdl	bdl	bdl	bdl	bdl	bdl	bdl	bdl	bdl
Cr_2O_3	0.18	0.22	0.17	0.25	0.18	0.27	0.26	0.19	0.20	0.20	0.25	0.21	0.23	0.22	0.25	0.26	0.16	0.22	0.20	0.23	0.15	0.25
La_2O_3	20.82	19.88	20.94	20.07	22.16	23.72	21.06	16.91	20.19	19.87	20.39	19.34	20.14	21.38	23.34	23.77	16.54	17.69	17.89	21.67	17.36	22.01
Ce_2O_3	29.85	30.99	33.70	35.04	33.23	33.88	35.19	33.59	29.12	34.88	36.16	35.48	35.27	35.15	35.16	34.48	33.41	36.00	36.05	34.64	32.65	34.20
Pr_2O_3	2.51	2.55	2.76	3.07	2.71	2.58	3.12	3.37	2.39	3.07	3.09	3.15	3.18	2.93	2.75	2.74	3.55	3.55	3.46	2.99	3.24	2.77
Nd_2O_3	7.73	7.46	8.82	9.11	8.02	7.51	9.36	11.85	6.94	9.12	9.71	10.34	10.03	8.88	8.05	7.76	13.19	11.25	10.96	8.68	11.42	8.36
Sm_2O_3	0.49	0.41	0.51	0.51	0.44	0.41	0.58	0.84	0.38	0.51	0.49	0.63	0.56	0.48	0.45	0.45	1.40	0.76	0.72	0.45	1.03	0.45
Eu_2O_3	bdl	bdl	0.10	0.08	0.06	0.08	0.06	0.16	bdl	0.08	0.09	0.07	0.10	bdl	bdl	bdl	0.29	0.13	0.13	bdl	0.16	bdl
Gd_2O_3	0.23	0.13	0.10	0.17	0.15	0.18	0.17	0.25	0.14	0.13	0.12	0.06	0.23	0.11	0.16	0.18	0.56	0.12	0.22	0.08	0.39	0.10
Tb_2O_3	0.07	bdl	0.08	0.09	0.07	0.08	0.07	0.08	bdl	bdl	0.08	0.08	0.07	0.09	0.09	0.08	0.06	0.07	0.07	0.09	bdl	0.07
Dy_2O_3	bdl	bdl	bdl	bdl	bdl	bdl	bdl	bdl	bdl	bdl	bdl	bdl	bdl	bdl	bdl	bdl	bdl	bdl	bdl	bdl	bdl	bdl
Ho_2O_3	bdl	bdl	bdl	bdl	bdl	bdl	bdl	bdl	bdl	bdl	bdl	bdl	bdl	bdl	bdl	bdl	bdl	bdl	bdl	bdl	bdl	bdl
Er_2O_3	bdl	bdl	bdl	bdl	bdl	bdl	bdl	bdl	bdl	bdl	bdl	bdl	bdl	bdl	bdl	bdl	bdl	bdl	bdl	bdl	bdl	bdl
Tm_2O_3	bdl	bdl	bdl	bdl	bdl	bdl	bdl	bdl	bdl	bdl	bdl	bdl	bdl	bdl	bdl	bdl	bdl	bdl	bdl	bdl	bdl	bdl
Yb_2O_3	bdl	bdl	bdl	bdl	bdl	bdl	bdl	bdl	bdl	bdl	bdl	bdl	bdl	bdl	bdl	bdl	bdl	bdl	bdl	bdl	bdl	bdl
Lu_2O_3	bdl	bdl	bdl	bdl	bdl	bdl	bdl	bdl	bdl	bdl	bdl	bdl	bdl	bdl	bdl	bdl	bdl	bdl	bdl	bdl	bdl	bdl
Y_2O_3	bdl	bdl	bdl	bdl	bdl	bdl	bdl	bdl	bdl	bdl	bdl	bdl	bdl	bdl	bdl	bdl	0.28	bdl	bdl	bdl	bdl	bdl
ZrO_2	0.06	0.10	0.13	0.14	0.08	0.10	0.10	0.09	0.09	0.09	0.10	0.10	0.10	0.12	0.13	0.12	0.07	0.15	0.10	0.08	bdl	0.10
HfO_2	bdl	bdl	bdl	bdl	bdl	bdl	bdl	bdl	bdl	bdl	bdl	bdl	bdl	bdl	bdl	bdl	bdl	bdl	bdl	bdl	bdl	bdl
Nb_2O_5	bdl	bdl	bdl	bdl	bdl	bdl	bdl	bdl	bdl	bdl	bdl	bdl	bdl	bdl	bdl	bdl	bdl	bdl	bdl	bdl	bdl	bdl
Sc_2O_3	bdl	bdl	bdl	bdl	bdl	bdl	bdl	bdl	bdl	bdl	bdl	bdl	bdl	bdl	bdl	bdl	bdl	bdl	bdl	bdl	bdl	bdl
ThO_2	6.37	8.22	2.80	1.21	3.27	1.24	0.67	3.15	10.20	1.36	bdl	0.57	0.78	1.10	bdl	bdl	0.39	0.16	0.17	1.38	1.24	1.68
UO_2	0.08	0.05	bdl	bdl	bdl	bdl	bdl	bdl	0.06	bdl	bdl	bdl	bdl	bdl	bdl	bdl	bdl	bdl	bdl	bdl	bdl	bdl
P_2O_5	23.33	23.69	26.17	26.25	26.08	27.33	27.88	26.07	23.05	23.85	27.78	27.26	27.36	27.26	27.23	27.47	17.65	27.11	27.40	27.10	18.74	26.80
SO_3	1.10	0.98	1.24	1.22	1.02	1.31	0.79	1.04	1.07	1.04	0.67	0.86	0.82	0.84	0.97	0.95	0.58	1.23	0.95	0.70	0.86	0.85
F	0.27	0.26	0.37	0.30	0.23	0.30	0.34	0.27	0.32	0.49	0.35	0.33	0.35	0.33	0.30	0.32	1.07	0.30	0.31	0.32	1.31	0.27
Cl	0.06	0.04	0.03	0.04	0.04	0.04	0.04	0.05	0.04	0.09	0.05	0.04	0.05	0.04	0.04	0.03	0.18	0.05	0.04	0.04	0.06	0.04
TOTAL	98.43	99.45	100.62	100.14	100.70	101.80	101.43	100.53	99.84	98.23	100.87	100.18	100.96	101.11	100.63	100.28	92.05	101.06	100.50	100.47	92.59	100.31
TREO	61.70	61.41	67.01	68.14	66.84	68.44	69.61	67.05	59.17	67.66	70.12	69.15	69.58	69.02	69.99	69.46	69.28	69.59	69.50	68.59	66.25	67.96

Table B.17 Composition of thorite (in wt.%) in apatite breccia veins.

SAMPLE	881309A-1-135	881309A-3-174	881309A-3-175	881309A-3-176	881309A-3-177	881309A-3-43	881309A-3-44	881309A-3-45	881309A-3-46	881309A-3-47	881309A-3-48	881309A-3-49	881309A-3-50	881309A-4-217	881309A-4-218	881309A-4-219	881309A-4-220	881309A-4-221	881309A-4-222	881309A-X-92
SiO_2	13.65	17.25	15.68	18.37	18.11	15.10	16.48	16.02	15.91	16.44	14.40	15.18	16.13	19.85	11.97	16.50	13.38	15.59	18.11	16.19
Al_2O_3	0.03	bdl	bdl	bdl	bdl	bdl	bdl	0.02	0.02	bdl	0.02	bdl	bdl	bdl	0.05	bdl	0.02	bdl	bdl	0.03
Na_2O	bdl*	bdl	bdl	bdl	bdl	bdl	bdl	bdl	bdl	bdl	bdl	bdl	bdl	bdl	bdl	bdl	bdl	bdl	bdl	bdl
K_2O	bdl	bdl	bdl	bdl	bdl	bdl	bdl	bdl	bdl	bdl	bdl	bdl	bdl	bdl	bdl	bdl	bdl	bdl	bdl	bdl
CaO	1.55	1.30	1.98	1.51	1.56	2.02	1.40	1.44	1.30	1.38	0.99	1.47	1.54	0.55	2.44	0.67	0.64	1.03	0.79	1.20
MgO	0.03	0.04	0.11	0.07	0.07	0.11	0.03	0.05	0.04	0.04	0.02	0.03	0.04	bdl	0.07	bdl	0.02	bdl	bdl	0.03
FeO	2.54	3.65	0.71	3.00	2.85	4.71	6.03	4.05	3.62	4.18	10.62	4.06	4.31	3.08	6.31	2.44	2.14	3.47	2.81	4.14
MnO	bdl	bdl	bdl	bdl	bdl	bdl	bdl	0.04	bdl	bdl	0.03	0.11	bdl	bdl	0.19	bdl	bdl	bdl	bdl	bdl
BaO	3.09	3.44	1.42	2.15	2.35	3.93	3.23	3.43	3.71	3.70	2.26	3.47	3.79	1.23	8.12	1.38	1.90	2.93	1.32	5.22
SrO	0.30	0.13	0.07	0.10	0.08	0.13	0.08	0.14	0.15	0.16	bdl	0.17	0.25	bdl	0.34	0.06	0.06	0.14	0.06	0.28
TiO_2	bdl	bdl	bdl	bdl	bdl	bdl	bdl	bdl	bdl	bdl	bdl	bdl	bdl	bdl	bdl	bdl	bdl	bdl	bdl	bdl
Cr_2O_3	bdl	bdl	bdl	bdl	bdl	bdl	bdl	bdl	bdl	bdl	bdl	bdl	bdl	bdl	bdl	bdl	bdl	bdl	bdl	bdl
La_2O_3	1.63	bdl	bdl	bdl	bdl	0.33	bdl	bdl	bdl	bdl	bdl	bdl	bdl	bdl	bdl	bdl	bdl	bdl	bdl	bdl
Ce_2O_3	4.35	1.87	2.20	1.75	2.21	1.60	1.66	1.96	1.83	1.63	2.21	1.80	1.61	1.63	1.93	2.14	2.02	1.96	2.11	1.47
Pr_2O_3	0.61	0.38	0.41	0.31	0.32	0.22	0.30	0.38	0.33	0.26	0.44	0.27	0.25	0.28	0.20	0.38	0.33	0.27	0.31	0.15
Nd_2O_3	3.01	2.58	2.84	2.26	2.78	1.34	2.62	2.80	2.69	2.56	3.16	2.81	2.59	2.80	1.90	3.19	3.05	2.66	3.07	1.73
Sm_2O_3	1.11	1.30	1.61	1.16	1.51	0.72	1.48	1.68	1.56	1.48	1.79	1.61	1.37	1.62	0.64	1.70	1.52	1.49	1.63	0.86
Eu_2O_3	0.25	0.30	0.42	0.25	0.48	0.10	0.40	0.54	0.51	0.50	0.68	0.51	0.46	0.62	0.11	0.53	0.42	0.56	0.53	0.12
Gd_2O_3	0.93	1.28	1.53	1.07	1.39	0.67	1.56	1.86	1.69	1.57	1.82	1.79	1.57	1.57	0.36	1.66	1.36	1.34	1.43	0.67
Tb_2O_3	bdl	bdl	bdl	bdl	bdl	bdl	0.10	0.13	bdl	0.09	0.14	0.10	bdl	bdl	bdl	bdl	bdl	bdl	bdl	bdl
Dy_2O_3	0.57	0.67	0.94	0.62	0.76	0.38	0.92	1.02	0.99	0.89	0.99	1.06	0.86	0.75	0.12	0.74	0.64	0.73	0.75	0.40
Ho_2O_3	bdl	bdl	bdl	bdl	bdl	bdl	bdl	bdl	bdl	bdl	bdl	bdl	bdl	bdl	bdl	bdl	bdl	bdl	bdl	bdl
Er_2O_3	bdl	0.14	0.17	bdl	0.14	bdl	0.11	0.12	0.10	0.10	0.19	0.18	bdl	bdl	bdl	bdl	bdl	bdl	bdl	bdl
Tm_2O_3	bdl	bdl	bdl	bdl	bdl	bdl	bdl	bdl	bdl	bdl	bdl	bdl	bdl	bdl	bdl	bdl	bdl	bdl	bdl	bdl
Yb_2O_3	bdl	bdl	bdl	bdl	bdl	bdl	bdl	bdl	bdl	bdl	bdl	bdl	bdl	bdl	bdl	bdl	bdl	bdl	bdl	bdl
Lu_2O_3	bdl	bdl	bdl	bdl	bdl	bdl	bdl	bdl	bdl	bdl	bdl	bdl	bdl	bdl	bdl	bdl	bdl	bdl	bdl	bdl
Y_2O_3	2.23	2.59	3.10	2.26	2.80	0.52	2.91	3.52	3.40	3.16	3.48	3.53	3.35	3.22	0.58	3.32	3.08	3.11	3.35	1.88
ZrO_2	1.31	2.56	1.23	3.63	1.76	bdl	bdl	bdl	bdl	bdl	bdl	bdl	0.11	0.09	0.07	0.19	0.15	0.33	0.27	4.34
HfO_2	bdl	bdl	bdl	bdl	bdl	bdl	bdl	bdl	bdl	bdl	bdl	bdl	bdl	bdl	bdl	bdl	bdl	bdl	bdl	bdl
Nb_2O_5	bdl	bdl	bdl	bdl	bdl	bdl	bdl	bdl	bdl	bdl	bdl	bdl	bdl	bdl	bdl	bdl	bdl	bdl	bdl	bdl
Sc_2O_3	bdl	bdl	bdl	bdl	bdl	bdl	bdl	bdl	bdl	bdl	bdl	bdl	bdl	bdl	bdl	bdl	bdl	bdl	bdl	bdl
ThO_2	47.94	47.78	52.65	47.22	48.22	41.62	46.13	48.14	48.67	46.97	43.33	47.49	46.70	48.34	39.88	47.60	42.07	46.94	47.47	41.83
UO_2	0.22	bdl	bdl	bdl	bdl	bdl	0.10	bdl	bdl	bdl	bdl	bdl	bdl	0.23	bdl	0.23	0.31	bdl	0.33	bdl
P_2O_5	5.05	3.50	4.54	2.95	3.66	4.55	3.97	4.60	4.33	4.05	3.98	4.61	4.09	2.60	3.15	3.47	3.15	3.35	3.03	2.63
SO_3	0.10	0.61	0.15	0.29	0.31	bdl	0.28	bdl	0.07	0.10	bdl	bdl	bdl	bdl	0.12	bdl	3.28	0.06	bdl	0.47
F	bdl	bdl	bdl	bdl	bdl	bdl	bdl	bdl	bdl	bdl	bdl	bdl	bdl	bdl	bdl	bdl	bdl	bdl	bdl	bdl
Cl	0.14	bdl	bdl	bdl	bdl	bdl	bdl	bdl	bdl	bdl	bdl	bdl	bdl	bdl	bdl	bdl	bdl	bdl	bdl	bdl
TOTAL	90.62	91.36	91.75	88.98	91.36	78.05	89.82	91.92	90.90	89.27	90.53	90.25	89.03	88.46	78.53	86.20	79.53	85.95	87.37	83.64
TREO	14.69	11.10	13.21	9.67	12.39	5.89	12.07	14.00	13.10	12.24	14.88	13.66	12.07	12.49	5.84	13.67	12.41	12.12	13.18	7.28

* below detection limit

Table B.17 cont.

SAMPLE	881309A-X-93	881309A-X-94	881309A-X-95	881309A-X-96	881309A-X-98	881309A-X-99	881309A-X-100	881309A-X-101	517458-8-36	517458-8-37	517458-8-38	517458-8-47	881187-11-767	881011B-1-104	881011B-1-105	881011B-1-106	881011B-1-107	881011B-1-108	881011B-1-109
SiO_2	16.39	17.52	13.94	12.47	16.52	21.91	18.06	18.01	9.27	14.83	15.53	14.83	21.28	17.27	20.11	17.65	14.61	19.12	18.68
Al_2O_3	0.03	0.07	bdl	bdl	bdl	0.08	0.02	0.03	bdl	0.65	0.21	0.15	3.65	bdl	bdl	bdl	bdl	bdl	bdl
Na_2O	bdl	bdl	bdl	bdl	bdl	bdl	bdl	bdl	bdl	0.04	bdl	bdl	bdl	bdl	bdl	bdl	bdl	bdl	bdl
K_2O	bdl	bdl	bdl	bdl	bdl	bdl	bdl	bdl	bdl	0.03	bdl	bdl	bdl	bdl	bdl	bdl	bdl	bdl	bdl
CaO	1.20	1.22	1.72	1.32	1.62	2.31	2.31	2.36	1.60	2.11	2.34	2.00	0.64	1.74	1.91	2.53	2.16	1.53	1.74
MgO	0.03	0.04	0.10	0.06	0.05	0.22	0.17	0.19	bdl	0.60	0.20	0.18	5.55	bdl	0.03	0.08	0.04	0.07	0.06
FeO	4.06	4.32	0.79	18.27	1.87	1.39	0.83	0.74	0.16	2.15	0.34	0.36	5.37	7.06	8.10	3.03	1.53	3.16	2.97
MnO	bdl	bdl	bdl	0.15	bdl	0.18	0.05	0.04	bdl	bdl	bdl	bdl	0.33	bdl	bdl	bdl	bdl	0.08	bdl
BaO	4.83	6.71	0.84	0.88	1.68	2.12	1.75	1.70	0.60	0.89	0.67	0.66	0.52	4.31	3.42	1.60	1.16	3.24	3.23
SrO	0.18	0.14	0.07	bdl	bdl	0.14	0.10	0.12	bdl	0.67	0.13	0.13	bdl	bdl	bdl	bdl	bdl	bdl	bdl
TiO_2	bdl	bdl	bdl	bdl	bdl	bdl	bdl	bdl	bdl	bdl	bdl	bdl	bdl	bdl	bdl	bdl	bdl	bdl	bdl
Cr_2O_3	bdl	bdl	bdl	bdl	bdl	bdl	bdl	bdl	bdl	bdl	bdl	bdl	bdl	bdl	bdl	bdl	bdl	bdl	bdl
La_2O_3	bdl	bdl	bdl	0.10	bdl	0.15	0.11	0.12	bdl	0.42	0.14	0.15	bdl	0.24	0.18	0.32	0.27	0.23	0.29
Ce_2O_3	1.46	1.47	2.00	1.96	1.87	1.34	1.51	1.62	0.90	2.02	1.34	1.34	1.87	1.38	1.10	1.67	1.47	1.76	1.72
Pr_2O_3	0.21	0.16	0.25	0.25	0.25	0.19	0.21	0.20	0.21	0.36	0.38	0.29	0.26	0.22	0.16	0.27	0.23	0.26	0.26
Nd_2O_3	1.85	1.79	2.86	2.40	2.29	1.51	1.75	1.94	2.45	3.17	3.32	3.28	2.64	1.84	1.73	2.70	2.43	2.18	2.29
Sm_2O_3	0.88	0.82	1.42	1.21	1.15	0.92	0.91	1.05	2.03	1.99	2.40	2.41	0.95	0.73	0.70	1.14	1.08	1.16	1.10
Eu_2O_3	0.16	0.18	0.37	0.32	0.34	0.29	0.30	0.28	0.33	0.37	0.54	0.56	0.26	0.19	0.19	0.42	0.29	0.35	0.32
Gd_2O_3	0.82	0.83	1.51	1.20	1.01	0.92	1.00	1.07	2.79	2.69	3.17	3.12	0.88	0.66	0.59	0.97	0.88	0.91	0.90
Tb_2O_3	bdl	bdl	bdl	0.18	bdl	0.13	bdl	bdl	bdl	0.16	0.22	0.22	bdl	bdl	bdl	bdl	bdl	bdl	bdl
Dy_2O_3	0.39	0.49	0.73	0.70	0.57	0.73	0.80	0.81	1.58	1.55	1.77	1.77	0.45	0.11	bdl	0.26	0.31	0.26	0.34
Ho_2O_3	bdl	bdl	bdl	bdl	bdl	bdl	bdl	bdl	0.12	0.22	0.29	0.38	0.11	bdl	bdl	bdl	bdl	bdl	bdl
Er_2O_3	bdl	bdl	bdl	0.18	bdl	0.28	0.16	0.24	0.19	0.18	0.30	0.28	bdl	bdl	bdl	bdl	bdl	bdl	bdl
Tm_2O_3	bdl	bdl	bdl	bdl	bdl	bdl	bdl	bdl	bdl	bdl	bdl	bdl	bdl	bdl	bdl	bdl	bdl	bdl	bdl
Yb_2O_3	bdl	bdl	bdl	bdl	bdl	0.15	bdl	bdl	bdl	bdl	bdl	bdl	bdl	bdl	bdl	bdl	bdl	bdl	bdl
Lu_2O_3	bdl	bdl	bdl	bdl	bdl	bdl	bdl	bdl	bdl	bdl	bdl	bdl	bdl	bdl	bdl	bdl	bdl	bdl	bdl
Y_2O_3	1.94	1.71	3.38	2.44	1.95	3.36	3.31	3.49	3.56	4.30	4.92	4.79	1.99	1.09	0.93	1.39	1.45	1.58	1.64
ZrO_2	4.31	3.70	0.23	0.79	2.36	28.39	15.64	12.40	bdl	bdl	bdl	bdl	bdl	bdl	bdl	bdl	bdl	bdl	bdl
HfO_2	bdl	bdl	bdl	bdl	bdl	bdl	bdl	bdl	bdl	bdl	bdl	bdl	bdl	bdl	bdl	bdl	bdl	bdl	bdl
Nb_2O_5	bdl	bdl	bdl	bdl	bdl	bdl	bdl	bdl	bdl	bdl	bdl	bdl	bdl	bdl	bdl	bdl	bdl	bdl	bdl
Sc_2O_3	bdl	bdl	bdl	bdl	bdl	bdl	bdl	bdl	bdl	bdl	bdl	bdl	bdl	bdl	bdl	bdl	bdl	bdl	bdl
ThO_2	43.78	40.65	54.37	42.64	48.02	24.56	40.23	44.95	43.33	40.98	50.23	52.11	37.89	44.87	42.91	53.74	54.89	50.10	50.54
UO_2	bdl	bdl	bdl	bdl	bdl	0.06	bdl	0.06	1.66	4.91	2.51	1.28	0.25	bdl	bdl	bdl	bdl	bdl	bdl
P_2O_5	2.68	2.50	4.19	3.48	3.25	1.56	2.55	2.66	3.16	4.07	4.71	4.63	0.14	2.55	2.18	2.97	2.74	2.45	2.79
SO_3	0.45	1.81	0.13	0.06	0.06	bdl	bdl	bdl	0.13	0.56	bdl	0.06	bdl	bdl	bdl	0.15	bdl	bdl	bdl
F	bdl	bdl	bdl	bdl	bdl	bdl	bdl	bdl	bdl	bdl	bdl	bdl	bdl	bdl	bdl	0.11	0.07	0.09	0.13
Cl	bdl	bdl	0.03	0.03	bdl	0.04	0.02	0.02	0.09	0.05	0.12	0.14	0.03	bdl	0.01	bdl	bdl	bdl	bdl
TOTAL	85.63	86.12	88.94	91.09	84.88	92.91	91.81	94.10	74.15	89.95	95.75	95.07	85.05	84.26	84.24	90.93	85.59	88.49	88.94
TREO	7.70	7.46	12.53	10.93	9.44	9.97	10.07	10.83	14.18	17.42	18.79	18.58	9.42	6.47	5.59	9.12	8.40	8.69	8.85

Table B.18 Composition of chlorite (in wt.%) in apatite breccia veins.

SAMPLE	881309A-3-197	881309A-3-199	881309A-3-200	881344-2-273	881344-2-274	881344-2-275	881344-3-413	881344-3-414	881344-3-415	881344-3-416	881344-3-417	881344-3-425	881344-4-429	881344-4-430	881344-4-431	881344-4-436	881344-4-437
SiO_2	40.04	37.00	37.09	38.20	36.24	36.91	38.75	33.06	39.78	39.60	39.27	38.64	38.63	37.95	38.86	38.60	40.75
Al_2O_3	7.57	8.52	8.61	5.79	7.69	7.73	10.18	8.13	9.62	10.57	10.05	8.21	9.60	10.19	8.08	10.38	10.96
Na_2O	0.16	0.10	0.13	0.22	0.11	0.12	0.07	0.04	0.13	0.09	0.09	0.19	0.16	0.11	0.24	0.08	0.11
K_2O	0.19	0.12	0.13	0.06	0.03	0.04	bdl	bdl	0.03	bdl	0.03	0.06	0.07	0.03	0.14	0.02	0.03
CaO	1.18	0.84	0.80	1.17	0.87	0.95	0.43	0.41	0.64	0.40	0.44	0.83	0.63	0.40	1.09	0.33	0.36
MgO	20.79	23.74	24.34	17.41	20.39	21.27	28.01	21.85	24.58	28.47	27.76	21.05	24.05	26.44	18.62	27.97	29.64
FeO	15.84	11.96	10.29	15.48	11.45	11.80	5.96	6.22	9.11	6.90	6.21	11.11	10.04	8.13	13.89	6.81	6.75
MnO	0.23	0.32	0.25	0.11	0.08	0.08	0.09	0.07	0.06	0.08	0.07	0.07	0.06	0.07	0.09	0.09	0.08
BaO	0.29	0.20	0.07	0.19	0.17	0.13	bdl	bdl	0.15	0.06	0.06	0.24	0.11	0.07	0.23	0.06	bdl
SrO	bdl*	bdl	bdl	0.09	0.08	0.08	bdl	bdl	0.12	0.07	0.04	0.10	0.05	0.04	0.12	0.04	bdl
TiO_2	0.06	bdl	0.03	bdl	bdl	0.02	bdl	bdl	bdl	bdl	bdl	bdl	bdl	bdl	bdl	bdl	bdl
Cr_2O_3	bdl	bdl	bdl	bdl	bdl	bdl	bdl	bdl	bdl	bdl	bdl	bdl	bdl	bdl	bdl	bdl	bdl
La_2O_3	bdl	bdl	bdl	bdl	bdl	bdl	bdl	bdl	bdl	bdl	bdl	bdl	bdl	bdl	bdl	bdl	bdl
Ce_2O_3	bdl	bdl	bdl	bdl	bdl	bdl	bdl	bdl	bdl	bdl	bdl	bdl	bdl	bdl	bdl	bdl	bdl
Pr_2O_3	bdl	bdl	bdl	bdl	bdl	bdl	bdl	bdl	bdl	bdl	bdl	bdl	bdl	bdl	bdl	bdl	bdl
Nd_2O_3	bdl	bdl	bdl	bdl	bdl	bdl	bdl	bdl	bdl	bdl	bdl	bdl	bdl	bdl	bdl	bdl	bdl
Sm_2O_3	bdl	bdl	bdl	bdl	bdl	bdl	bdl	bdl	bdl	bdl	bdl	bdl	bdl	bdl	bdl	bdl	bdl
Eu_2O_3	bdl	bdl	bdl	bdl	bdl	bdl	bdl	bdl	bdl	bdl	bdl	bdl	bdl	bdl	bdl	bdl	bdl
Gd_2O_3	bdl	bdl	bdl	bdl	bdl	bdl	bdl	bdl	bdl	bdl	bdl	bdl	bdl	bdl	bdl	bdl	bdl
Tb_2O_3	0.12	bdl	0.07	0.12	0.10	0.10	bdl	bdl	0.07	bdl	bdl	0.10	bdl	bdl	0.10	bdl	bdl
Dy_2O_3	0.05	bdl	bdl	bdl	bdl	bdl	bdl	bdl	0.06	bdl	bdl	0.06	0.06	0.07	0.06	bdl	0.05
Ho_2O_3	bdl	bdl	bdl	bdl	bdl	bdl	bdl	bdl	bdl	bdl	bdl	bdl	bdl	bdl	bdl	bdl	bdl
Er_2O_3	0.07	bdl	bdl	bdl	bdl	bdl	bdl	bdl	bdl	bdl	bdl	bdl	bdl	bdl	bdl	bdl	bdl
Tm_2O_3	bdl	bdl	bdl	bdl	bdl	bdl	bdl	bdl	bdl	bdl	bdl	bdl	bdl	bdl	bdl	bdl	bdl
Yb_2O_3	bdl	bdl	bdl	bdl	bdl	bdl	bdl	bdl	bdl	bdl	bdl	bdl	bdl	bdl	bdl	bdl	bdl
Lu_2O_3	bdl	bdl	bdl	bdl	bdl	bdl	bdl	bdl	bdl	bdl	bdl	bdl	bdl	bdl	bdl	bdl	bdl
Y_2O_3	bdl	bdl	bdl	bdl	bdl	bdl	bdl	bdl	bdl	bdl	bdl	bdl	bdl	bdl	bdl	bdl	bdl
ZrO_2	bdl	bdl	bdl	bdl	bdl	bdl	bdl	bdl	bdl	bdl	bdl	bdl	bdl	bdl	bdl	bdl	bdl
HfO_2	bdl	bdl	bdl	bdl	bdl	bdl	bdl	bdl	bdl	bdl	bdl	bdl	bdl	bdl	bdl	bdl	bdl
Nb_2O_5	bdl	bdl	bdl	bdl	bdl	bdl	bdl	bdl	bdl	bdl	bdl	bdl	bdl	bdl	bdl	bdl	bdl
Sc_2O_3	bdl	bdl	bdl	bdl	bdl	bdl	bdl	bdl	bdl	bdl	bdl	bdl	bdl	bdl	bdl	bdl	bdl
ThO_2	0.09	0.09	0.06	bdl	bdl	bdl	bdl	bdl	bdl	bdl	bdl	bdl	bdl	bdl	bdl	bdl	bdl
UO_2	0.04	bdl	bdl	bdl	bdl	bdl	bdl	bdl	bdl	bdl	bdl	bdl	bdl	bdl	0.04	bdl	bdl
P_2O_5	bdl	bdl	bdl	0.04	0.04	bdl	0.04	bdl	0.05	bdl	bdl	bdl	bdl	bdl	bdl	bdl	bdl
SO_3	bdl	bdl	bdl	0.04	bdl	bdl	bdl	bdl	bdl	bdl	bdl	bdl	bdl	bdl	bdl	bdl	bdl
F	0.09	0.10	0.07	0.09	0.06	0.08	0.09	bdl	0.09	0.06	0.11	0.08	0.05	0.06	0.07	0.08	0.07
Cl	0.03	0.05	0.04	0.15	0.10	0.06	0.11	0.07	0.05	0.09	0.09	0.04	0.07	0.06	0.09	0.08	0.08
TOTAL	86.79	82.99	81.94	79.10	77.36	79.31	83.67	69.81	84.49	86.36	84.16	80.74	83.54	83.58	81.66	84.50	88.83

* below detection limit

Table B.18 cont.

SAMPLE	881344-4-438	881344-4-439	881344-4-440	881375B-3-70	881375B-3-71	881375B-4-76	881375B-4-81	881375B-4-82	881375B-5-87	881375B-5-88	881011B-1-98	881011B-1-99	881011B-1-101	881011B-1-102	881011B-3-119	881011B-3-120	881011B-3-123
SiO_2	39.44	39.31	39.46	37.54	39.47	39.31	49.88	38.24	38.81	39.50	52.57	17.32	18.21	20.14	55.09	52.98	24.87
Al_2O_3	7.66	9.74	9.98	8.94	9.97	9.42	11.24	8.75	9.88	9.54	2.26	0.81	0.91	0.77	1.51	1.18	1.00
Na_2O	0.27	0.15	0.13	0.06	0.08	0.06	0.03	0.05	0.04	0.06	0.56	0.46	0.29	0.61	0.67	0.94	0.56
K_2O	0.20	0.06	0.03	0.01	bdl	bdl	6.14	0.02	bdl	0.02	0.13	0.07	0.08	0.07	0.14	0.12	0.07
CaO	1.03	0.65	0.52	0.51	0.39	0.50	0.48	0.67	0.43	0.69	0.73	0.47	0.39	0.32	0.51	0.34	0.30
MgO	17.71	24.45	25.64	25.50	28.81	26.69	10.80	24.89	28.14	27.11	25.38	9.51	7.92	11.59	24.71	24.15	13.08
FeO	16.58	10.12	9.20	6.45	5.63	7.35	8.60	7.66	5.58	6.61	4.67	58.70	61.76	63.63	4.13	9.58	57.81
MnO	0.07	0.05	0.06	0.09	0.07	0.06	0.04	0.08	0.06	0.09	0.18	0.11	0.31	0.15	0.10	0.10	0.10
BaO	0.37	0.18	0.10	0.09	bdl	0.13	0.17	0.13	0.06	0.22	0.16	0.05	0.08	bdl	0.07	0.05	0.08
SrO	0.11	0.06	bdl	bdl	0.09	0.10	0.11	bdl	0.15	0.09	bdl	bdl	bdl	bdl	0.08	0.10	bdl
TiO_2	bdl	bdl	bdl	bdl	bdl	bdl	bdl	bdl	bdl	bdl	bdl	0.20	0.23	0.15	bdl	bdl	0.10
Cr_2O_3	bdl	bdl	bdl	bdl	bdl	bdl	bdl	bdl	bdl	bdl	bdl	bdl	bdl	bdl	bdl	bdl	bdl
La_2O_3	0.09	bdl	bdl	bdl	bdl	bdl	bdl	0.11	bdl	bdl	bdl	bdl	0.06	bdl	bdl	bdl	bdl
Ce_2O_3	0.21	bdl	bdl	bdl	bdl	bdl	bdl	0.19	bdl	bdl	bdl	bdl	bdl	bdl	bdl	bdl	bdl
Pr_2O_3	bdl	bdl	bdl	bdl	bdl	bdl	bdl	0.05	bdl	bdl	bdl	bdl	bdl	bdl	bdl	bdl	bdl
Nd_2O_3	0.07	bdl	bdl	bdl	bdl	bdl	bdl	0.06	bdl	bdl	bdl	bdl	bdl	bdl	bdl	bdl	bdl
Sm_2O_3	bdl	bdl	bdl	bdl	bdl	bdl	bdl	bdl	bdl	bdl	bdl	bdl	bdl	bdl	bdl	bdl	bdl
Eu_2O_3	bdl	bdl	bdl	bdl	bdl	bdl	bdl	bdl	bdl	bdl	bdl	bdl	bdl	bdl	bdl	bdl	bdl
Gd_2O_3	bdl	bdl	bdl	bdl	bdl	bdl	bdl	bdl	bdl	bdl	bdl	bdl	bdl	bdl	bdl	bdl	bdl
Tb_2O_3	0.11	bdl	0.07	bdl	bdl	0.05	0.07	bdl	bdl	bdl	bdl	0.54	0.59	0.55	bdl	0.08	0.53
Dy_2O_3	0.09	0.06	0.06	bdl	bdl	bdl	bdl	bdl	0.04	bdl	bdl	0.18	0.24	0.19	bdl	bdl	0.20
Ho_2O_3	bdl	bdl	bdl	bdl	bdl	bdl	bdl	bdl	bdl	bdl	bdl	bdl	bdl	bdl	bdl	bdl	bdl
Er_2O_3	bdl	bdl	bdl	bdl	bdl	bdl	bdl	bdl	bdl	bdl	bdl	0.25	0.26	0.23	bdl	bdl	0.22
Tm_2O_3	bdl	bdl	bdl	bdl	bdl	bdl	bdl	bdl	bdl	bdl	bdl	bdl	bdl	bdl	bdl	bdl	bdl
Yb_2O_3	bdl	bdl	bdl	bdl	bdl	bdl	bdl	bdl	bdl	bdl	bdl	bdl	bdl	bdl	bdl	bdl	bdl
Lu_2O_3	bdl	bdl	bdl	bdl	bdl	bdl	bdl	bdl	bdl	bdl	bdl	bdl	bdl	bdl	bdl	bdl	bdl
Y_2O_3	bdl	bdl	bdl	bdl	bdl	bdl	bdl	bdl	bdl	bdl	bdl	bdl	bdl	bdl	bdl	bdl	bdl
ZrO_2	bdl	bdl	bdl	bdl	bdl	0.08	bdl	bdl	bdl	bdl	bdl	bdl	bdl	bdl	bdl	bdl	bdl
HfO_2	bdl	bdl	bdl	bdl	bdl	bdl	bdl	bdl	bdl	bdl	bdl	bdl	bdl	bdl	bdl	bdl	bdl
Nb_2O_5	bdl	bdl	bdl	bdl	bdl	bdl	bdl	bdl	bdl	bdl	bdl	bdl	bdl	bdl	bdl	bdl	bdl
Sc_2O_3	bdl	bdl	bdl	bdl	bdl	bdl	bdl	bdl	bdl	bdl	bdl	bdl	bdl	bdl	bdl	bdl	bdl
ThO_2	bdl	bdl	bdl	bdl	bdl	bdl	bdl	bdl	bdl	bdl	0.25	bdl	0.04	0.05	0.08	0.05	bdl
UO_2	bdl	bdl	bdl	bdl	bdl	bdl	bdl	bdl	bdl	bdl	bdl	0.14	0.12	0.16	bdl	bdl	0.14
P_2O_5	bdl	bdl	bdl	bdl	bdl	bdl	0.06	0.19	bdl	bdl	bdl	bdl	0.10	0.07	bdl	bdl	bdl
SO_3	bdl	bdl	bdl	bdl	bdl	bdl	0.04	0.10	0.05	0.07	0.06	bdl	bdl	bdl	0.09	bdl	bdl
F	bdl	0.05	0.07	0.08	0.11	0.07	bdl	0.06	0.17	0.07	0.06	bdl	bdl	bdl	bdl	bdl	bdl
Cl	0.08	0.08	0.06	0.08	0.08	0.13	0.09	0.11	0.09	0.09	0.06	0.09	0.08	0.06	0.10	0.10	0.05
TOTAL	84.05	84.91	85.34	79.31	84.64	83.88	87.74	81.29	83.43	84.09	87.05	88.88	91.65	98.74	87.24	89.74	99.12

Table B.19 Composition of calcite (in wt.%) in apatite breccia veins.

SAMPLE	881309A-4-223	881309A-4-224	881309A-4-225	881309A-4-226	881309A-4-227	881309A-4-228	881309A-4-229	881344-1-259	881344-1-260	881344-2-272	881344-3-407	881344-3-408	881344-3-409	881344-3-410	881344-3-411	881344-3-412	881344-5-449
SiO_2	bdl*	bdl	bdl	bdl	bdl	bdl	bdl	bdl	bdl	bdl	bdl	bdl	bdl	bdl	bdl	0.02	0.39
Al_2O_3	bdl	bdl	bdl	bdl	bdl	bdl	bdl	bdl	bdl	bdl	bdl	bdl	bdl	bdl	bdl	bdl	0.02
Na_2O	bdl	bdl	bdl	bdl	bdl	bdl	bdl	bdl	bdl	bdl	bdl	bdl	bdl	bdl	bdl	bdl	bdl
K_2O	bdl	bdl	bdl	bdl	bdl	bdl	bdl	bdl	bdl	bdl	bdl	bdl	bdl	bdl	bdl	bdl	bdl
CaO	54.72	48.76	60.06	47.48	56.62	53.63	50.70	49.34	50.62	54.91	50.70	49.69	55.00	56.15	60.07	57.30	59.89
MgO	bdl	bdl	0.02	bdl	0.03	bdl	bdl	0.04	0.11	0.19	bdl	0.10	0.13	0.07	0.03	0.13	0.26
FeO	bdl	bdl	bdl	bdl	0.04	bdl	bdl	bdl	bdl	0.39	0.10	bdl	0.02	0.05	bdl	0.03	0.62
MnO	0.24	0.16	0.42	0.33	0.55	0.70	0.37	bdl	0.46	0.74	0.60	0.26	0.98	0.87	0.15	0.96	1.05
BaO	bdl	bdl	bdl	bdl	bdl	bdl	bdl	bdl	bdl	bdl	bdl	bdl	bdl	bdl	bdl	bdl	bdl
SrO	bdl	bdl	bdl	bdl	bdl	bdl	bdl	bdl	bdl	bdl	bdl	bdl	bdl	bdl	0.04	bdl	bdl
TiO_2	bdl	bdl	bdl	bdl	bdl	bdl	bdl	bdl	bdl	bdl	bdl	bdl	bdl	bdl	bdl	bdl	bdl
Cr_2O_3	bdl	bdl	bdl	bdl	bdl	bdl	bdl	bdl	bdl	bdl	bdl	bdl	bdl	bdl	bdl	bdl	bdl
La_2O_3	bdl	bdl	bdl	bdl	bdl	bdl	bdl	bdl	bdl	bdl	bdl	bdl	bdl	bdl	bdl	bdl	bdl
Ce_2O_3	0.07	bdl	bdl	bdl	bdl	bdl	bdl	bdl	bdl	bdl	bdl	bdl	0.14	bdl	bdl	0.18	0.18
Pr_2O_3	bdl	bdl	bdl	bdl	bdl	bdl	bdl	bdl	bdl	bdl	bdl	bdl	bdl	bdl	bdl	bdl	bdl
Nd_2O_3	bdl	bdl	bdl	bdl	bdl	bdl	bdl	bdl	bdl	bdl	bdl	bdl	bdl	bdl	bdl	bdl	0.13
Sm_2O_3	bdl	bdl	bdl	bdl	bdl	bdl	bdl	bdl	bdl	bdl	bdl	bdl	bdl	bdl	bdl	bdl	bdl
Eu_2O_3	bdl	bdl	bdl	bdl	bdl	bdl	bdl	bdl	bdl	bdl	bdl	bdl	bdl	bdl	bdl	bdl	bdl
Gd_2O_3	bdl	bdl	bdl	bdl	bdl	bdl	bdl	bdl	bdl	bdl	bdl	bdl	bdl	bdl	bdl	bdl	bdl
Tb_2O_3	bdl	bdl	bdl	bdl	bdl	bdl	bdl	bdl	bdl	bdl	bdl	bdl	bdl	bdl	bdl	bdl	bdl
Dy_2O_3	bdl	bdl	bdl	bdl	bdl	bdl	bdl	bdl	bdl	bdl	bdl	bdl	0.10	bdl	bdl	0.08	0.09
Ho_2O_3	bdl	bdl	bdl	bdl	bdl	bdl	bdl	bdl	bdl	bdl	bdl	bdl	bdl	bdl	bdl	bdl	bdl
Er_2O_3	bdl	bdl	bdl	bdl	bdl	bdl	bdl	bdl	bdl	bdl	bdl	bdl	bdl	bdl	bdl	bdl	bdl
Tm_2O_3	bdl	bdl	bdl	bdl	bdl	bdl	bdl	bdl	bdl	bdl	bdl	bdl	bdl	bdl	bdl	bdl	bdl
Yb_2O_3	bdl	bdl	bdl	bdl	bdl	bdl	bdl	bdl	bdl	bdl	bdl	bdl	bdl	bdl	bdl	bdl	bdl
Lu_2O_3	bdl	bdl	bdl	bdl	bdl	bdl	bdl	bdl	bdl	bdl	bdl	bdl	bdl	bdl	bdl	bdl	bdl
Y_2O_3	bdl	bdl	bdl	bdl	bdl	bdl	bdl	bdl	bdl	bdl	bdl	bdl	bdl	bdl	bdl	bdl	bdl
ZrO_2	bdl	bdl	bdl	bdl	bdl	bdl	bdl	bdl	bdl	bdl	bdl	bdl	bdl	bdl	bdl	bdl	bdl
HfO_2	bdl	bdl	bdl	bdl	bdl	bdl	bdl	bdl	bdl	bdl	bdl	bdl	bdl	bdl	bdl	bdl	bdl
Nb_2O_5	bdl	bdl	bdl	bdl	bdl	bdl	bdl	bdl	bdl	bdl	bdl	bdl	bdl	bdl	bdl	bdl	bdl
Sc_2O_3	bdl	bdl	bdl	bdl	bdl	bdl	bdl	bdl	bdl	bdl	bdl	bdl	bdl	bdl	bdl	bdl	bdl
ThO_2	bdl	bdl	bdl	bdl	bdl	bdl	bdl	bdl	bdl	bdl	bdl	bdl	bdl	bdl	bdl	bdl	bdl
UO_2	bdl	bdl	bdl	bdl	bdl	bdl	bdl	bdl	bdl	bdl	bdl	bdl	bdl	bdl	bdl	bdl	bdl
P_2O_5	bdl	bdl	bdl	bdl	bdl	bdl	bdl	bdl	bdl	bdl	bdl	bdl	bdl	bdl	bdl	0.04	bdl
SO_3	bdl	bdl	bdl	bdl	bdl	bdl	bdl	0.37	0.26	0.48	0.07	0.22	0.25	0.37	bdl	0.15	0.18
F	bdl	bdl	bdl	bdl	bdl	bdl	bdl	bdl	bdl	bdl	bdl	bdl	bdl	0.12	bdl	0.16	0.16
Cl	bdl	bdl	bdl	bdl	bdl	bdl	bdl	bdl	bdl	bdl	bdl	bdl	bdl	bdl	bdl	bdl	bdl
TOTAL	55.03	48.89	60.51	47.80	57.25	54.33	51.06	49.76	51.45	56.71	51.47	50.25	56.59	57.58	60.27	58.98	62.90

* below detection limit

Table B.19 cont.

SAMPLE	881344-5-450	881344-5-451	881344-5-452	881375B-4-74	881375B-5-83	881375B-5-84	881375B-5-85	881375B-5-86	881011B-1-97	881011B-3-121	881011B-3-122	881253-2-142	948521-1-205	948521-1-207	948521-1-215	948521-1-216
SiO_2	bdl	bdl	bdl	bdl	bdl	bdl	bdl	bdl	0.29	3.23	1.57	bdl	bdl	bdl	bdl	bdl
Al_2O_3	bdl	bdl	bdl	bdl	bdl	bdl	bdl	bdl	bdl	0.11	bdl	bdl	bdl	bdl	bdl	bdl
Na_2O	bdl	bdl	bdl	bdl	bdl	bdl	bdl	bdl	bdl	bdl	bdl	bdl	bdl	bdl	bdl	bdl
K_2O	bdl	bdl	bdl	bdl	bdl	bdl	bdl	bdl	bdl	bdl	bdl	bdl	bdl	bdl	bdl	bdl
CaO	55.42	58.42	59.11	52.97	53.41	53.12	52.47	58.60	52.90	51.20	51.21	46.10	50.72	51.53	50.61	52.08
MgO	0.06	0.04	0.09	0.04	0.07	0.04	0.08	0.09	0.75	1.46	2.97	0.82	0.19	0.02	bdl	0.17
FeO	0.14	bdl	0.41	bdl	bdl	bdl	bdl	bdl	0.31	1.57	0.54	0.11	0.20	0.11	bdl	0.21
MnO	1.08	0.06	0.07	0.40	bdl	0.16	bdl	bdl	0.12	0.18	0.35	0.42	0.38	0.48	bdl	0.51
BaO	bdl	bdl	bdl	bdl	bdl	bdl	bdl	bdl	bdl	bdl	bdl	bdl	bdl	bdl	bdl	bdl
SrO	bdl	bdl	bdl	bdl	0.21	0.17	0.28	0.22	bdl	bdl	0.09	bdl	1.19	0.80	bdl	0.91
TiO_2	bdl	bdl	bdl	bdl	bdl	bdl	bdl	bdl	bdl	bdl	bdl	bdl	bdl	bdl	bdl	bdl
Cr_2O_3	bdl	bdl	bdl	bdl	bdl	bdl	bdl	bdl	bdl	bdl	bdl	bdl	bdl	bdl	bdl	bdl
La_2O_3	bdl	bdl	bdl	bdl	bdl	bdl	0.10	bdl	0.11	0.16	0.12	0.06	bdl	bdl	bdl	bdl
Ce_2O_3	0.07	bdl	bdl	bdl	bdl	bdl	bdl	bdl	0.15	0.37	0.27	0.21	bdl	bdl	bdl	bdl
Pr_2O_3	bdl	bdl	bdl	bdl	bdl	bdl	bdl	bdl	bdl	bdl	bdl	bdl	bdl	bdl	bdl	bdl
Nd_2O_3	bdl	bdl	bdl	bdl	bdl	bdl	bdl	bdl	bdl	0.12	0.10	bdl	bdl	bdl	bdl	bdl
Sm_2O_3	bdl	bdl	bdl	bdl	bdl	bdl	bdl	bdl	bdl	bdl	bdl	bdl	bdl	bdl	bdl	bdl
Eu_2O_3	bdl	bdl	bdl	bdl	bdl	bdl	bdl	bdl	bdl	bdl	bdl	bdl	bdl	bdl	bdl	bdl
Gd_2O_3	bdl	bdl	bdl	bdl	bdl	bdl	bdl	bdl	bdl	bdl	bdl	bdl	bdl	bdl	bdl	bdl
Tb_2O_3	bdl	bdl	bdl	bdl	bdl	bdl	bdl	bdl	bdl	bdl	bdl	bdl	bdl	bdl	bdl	bdl
Dy_2O_3	0.08	bdl	bdl	bdl	bdl	bdl	bdl	bdl	bdl	bdl	bdl	bdl	bdl	bdl	bdl	bdl
Ho_2O_3	bdl	bdl	bdl	bdl	bdl	bdl	bdl	bdl	bdl	bdl	bdl	bdl	bdl	bdl	bdl	bdl
Er_2O_3	bdl	bdl	bdl	bdl	bdl	bdl	bdl	bdl	bdl	bdl	bdl	bdl	bdl	bdl	bdl	bdl
Tm_2O_3	bdl	bdl	bdl	bdl	bdl	bdl	bdl	bdl	bdl	bdl	bdl	bdl	bdl	bdl	bdl	bdl
Yb_2O_3	bdl	bdl	bdl	bdl	bdl	bdl	bdl	bdl	bdl	bdl	bdl	bdl	bdl	bdl	bdl	bdl
Lu_2O_3	bdl	bdl	bdl	bdl	bdl	bdl	bdl	bdl	bdl	bdl	bdl	bdl	bdl	bdl	bdl	bdl
Y_2O_3	bdl	bdl	bdl	bdl	bdl	bdl	bdl	bdl	bdl	bdl	bdl	bdl	bdl	bdl	bdl	bdl
ZrO_2	bdl	bdl	bdl	bdl	bdl	bdl	bdl	bdl	bdl	bdl	bdl	bdl	bdl	bdl	bdl	bdl
HfO_2	bdl	bdl	bdl	bdl	bdl	bdl	bdl	bdl	bdl	bdl	bdl	bdl	bdl	bdl	bdl	bdl
Nb_2O_5	bdl	bdl	bdl	bdl	bdl	bdl	bdl	bdl	bdl	bdl	bdl	bdl	bdl	bdl	bdl	bdl
Sc_2O_3	bdl	bdl	bdl	bdl	bdl	bdl	bdl	bdl	bdl	bdl	bdl	bdl	bdl	bdl	bdl	bdl
ThO_2	bdl	bdl	bdl	bdl	bdl	bdl	bdl	bdl	bdl	bdl	bdl	bdl	bdl	bdl	bdl	bdl
UO_2	bdl	bdl	bdl	bdl	bdl	bdl	bdl	bdl	bdl	bdl	bdl	bdl	bdl	bdl	bdl	bdl
P_2O_5	bdl	bdl	bdl	bdl	bdl	bdl	bdl	bdl	bdl	0.08	bdl	bdl	bdl	bdl	bdl	bdl
SO_3	0.13	bdl	0.20	0.17	bdl	bdl	bdl	bdl	0.44	0.20	0.21	0.24	bdl	bdl	bdl	bdl
F	0.10	bdl	bdl	0.10	0.07	0.08	0.11	0.10	0.06	0.07	0.11	0.10	0.07	bdl	bdl	bdl
Cl	bdl	bdl	bdl	bdl	bdl	bdl	bdl	bdl	bdl	bdl	bdl	bdl	bdl	bdl	bdl	bdl
TOTAL	57.02	58.52	59.89	53.65	53.73	53.54	52.98	58.97	55.08	58.71	57.51	48.01	52.72	52.94	50.60	53.87

Table B.20 Composition of barite (in wt.%) in apatite breccia veins.

SAMPLE	881344-1-257	516665A-5A-84	516665A-26A-86	516665A-9A-90	516665A-21A-95	516665A-21A-97	516665A-21A-98	516665A-12A-100	516665A-12A-101	516665A-12B-105	516665A-19A-106	516665A-19A-111	516665A-20A-116	516665A-14A-120	516665A-14A-121	516665B-16A-150	516665B-18A-166	516665B-T-6A-177	516665B-T-6A-179	516665B-T-3A-189	516658-1A-196
SiO_2	0.16	0.03	bdl	0.02	bdl	bdl	bdl	bdl	bdl	bdl	3.13	bdl	0.11	bdl	bdl	bdl	1.29	bdl	bdl	0.07	0.02
Al_2O_3	0.93	0.83	0.88	0.76	0.83	0.83	0.82	0.87	0.73	0.86	0.83	1.02	0.63	0.68	0.64	0.94	0.68	0.87	0.88	0.93	0.89
Na_2O	0.24	0.18	0.18	0.15	0.17	0.16	0.17	0.21	0.17	0.22	0.15	0.21	0.13	0.15	0.13	0.22	0.14	0.18	0.20	0.23	0.24
K_2O	0.04	bdl	bdl	bdl	bdl	bdl	bdl	bdl	bdl	bdl	bdl	bdl	bdl	bdl	bdl	bdl	bdl	bdl	bdl	0.02	bdl
CaO	bdl*	1.08	0.71	0.83	0.62	0.57	0.61	0.32	0.65	0.59	1.14	1.06	1.34	0.16	0.15	0.72	1.32	0.24	0.27	1.04	3.37
MgO	0.03	bdl	bdl	bdl	bdl	bdl	bdl	bdl	bdl	bdl	0.24	bdl	bdl	bdl	bdl	bdl	bdl	bdl	bdl	0.06	bdl
FeO	0.65	bdl	bdl	bdl	bdl	bdl	bdl	bdl	bdl	bdl	bdl	bdl	bdl	bdl	bdl	bdl	0.05	bdl	bdl	bdl	bdl
MnO	bdl	bdl	bdl	bdl	bdl	bdl	bdl	bdl	bdl	bdl	bdl	bdl	bdl	bdl	bdl	bdl	bdl	bdl	bdl	bdl	bdl
BaO	63.49	57.82	59.57	53.15	56.00	56.40	57.76	60.02	52.61	58.60	51.78	64.18	44.80	50.29	49.22	60.51	50.13	58.68	59.35	60.96	59.38
SrO	0.90	6.08	4.91	12.03	9.05	8.98	9.55	5.06	12.17	6.29	6.69	bdl	13.79	15.36	16.40	2.95	7.45	4.41	3.88	2.02	bdl
TiO_2	0.51	0.46	0.47	0.39	0.42	0.45	0.46	0.48	0.41	0.48	0.39	0.54	0.32	0.40	0.41	0.50	0.29	0.50	0.48	0.52	0.49
Cr_2O_3	bdl	bdl	bdl	bdl	bdl	bdl	bdl	bdl	bdl	bdl	bdl	bdl	bdl	bdl	bdl	bdl	bdl	bdl	bdl	bdl	bdl
La_2O_3	bdl	bdl	bdl	bdl	bdl	bdl	bdl	bdl	bdl	bdl	bdl	bdl	2.26	bdl	bdl	0.09	2.44	bdl	bdl	bdl	bdl
Ce_2O_3	0.12	0.07	0.13	0.17	0.16	0.17	0.07	bdl	bdl	bdl	5.13	0.12	1.00	bdl	bdl	0.08	1.49	bdl	bdl	bdl	0.10
Pr_2O_3	bdl	bdl	bdl	bdl	bdl	bdl	bdl	bdl	bdl	bdl	bdl	bdl	0.71	bdl	bdl	bdl	1.01	bdl	bdl	bdl	bdl
Nd_2O_3	bdl	bdl	bdl	bdl	bdl	bdl	bdl	bdl	0.06	bdl	0.41	bdl	2.75	bdl	bdl	0.13	3.69	bdl	bdl	bdl	0.10
Sm_2O_3	bdl	bdl	bdl	bdl	bdl	bdl	bdl	bdl	bdl	bdl	0.25	bdl	0.16	bdl	bdl	bdl	0.31	bdl	bdl	bdl	bdl
Eu_2O_3	bdl	bdl	bdl	bdl	bdl	bdl	bdl	bdl	bdl	bdl	0.06	bdl	bdl	bdl	bdl	bdl	0.08	bdl	bdl	bdl	bdl
Gd_2O_3	bdl	bdl	bdl	bdl	bdl	bdl	bdl	bdl	bdl	bdl	0.23	bdl	bdl	bdl	bdl	bdl	0.13	bdl	bdl	bdl	bdl
Tb_2O_3	bdl	bdl	bdl	bdl	bdl	bdl	bdl	bdl	bdl	bdl	bdl	bdl	bdl	bdl	bdl	bdl	bdl	bdl	bdl	bdl	bdl
Dy_2O_3	bdl	bdl	bdl	bdl	bdl	bdl	bdl	bdl	bdl	bdl	bdl	bdl	bdl	bdl	bdl	bdl	bdl	bdl	bdl	bdl	bdl
Ho_2O_3	bdl	bdl	bdl	bdl	bdl	bdl	bdl	bdl	bdl	bdl	bdl	bdl	bdl	bdl	bdl	bdl	bdl	bdl	bdl	bdl	bdl
Er_2O_3	bdl	bdl	bdl	bdl	bdl	bdl	bdl	bdl	bdl	bdl	bdl	bdl	bdl	bdl	bdl	bdl	bdl	bdl	bdl	bdl	bdl
Tm_2O_3	bdl	bdl	bdl	bdl	bdl	bdl	bdl	bdl	bdl	bdl	bdl	bdl	bdl	bdl	bdl	bdl	bdl	bdl	bdl	bdl	bdl
Yb_2O_3	0.48	bdl	bdl	bdl	bdl	bdl	bdl	bdl	bdl	bdl	bdl	bdl	bdl	bdl	bdl	bdl	bdl	bdl	bdl	bdl	bdl
Lu_2O_3	bdl	bdl	bdl	bdl	bdl	bdl	bdl	bdl	bdl	bdl	bdl	bdl	bdl	bdl	bdl	bdl	bdl	bdl	bdl	bdl	bdl
Y_2O_3	bdl	bdl	bdl	bdl	bdl	bdl	bdl	bdl	bdl	bdl	0.19	bdl	bdl	bdl	bdl	bdl	bdl	bdl	bdl	bdl	bdl
ZrO_2	bdl	bdl	bdl	bdl	bdl	bdl	bdl	bdl	bdl	bdl	bdl	bdl	bdl	bdl	bdl	bdl	bdl	bdl	bdl	bdl	bdl
HfO_2	bdl	bdl	bdl	bdl	bdl	bdl	bdl	bdl	bdl	bdl	bdl	bdl	bdl	bdl	bdl	bdl	bdl	bdl	bdl	bdl	bdl
Nb_2O_5	bdl	bdl	bdl	bdl	bdl	bdl	bdl	bdl	bdl	bdl	bdl	bdl	bdl	bdl	bdl	bdl	bdl	bdl	bdl	bdl	bdl
Sc_2O_3	bdl	bdl	bdl	bdl	bdl	bdl	bdl	bdl	bdl	bdl	bdl	bdl	bdl	bdl	bdl	bdl	bdl	bdl	bdl	bdl	bdl
ThO_2	bdl	bdl	bdl	bdl	bdl	bdl	bdl	bdl	bdl	bdl	bdl	bdl	bdl	bdl	bdl	bdl	bdl	bdl	bdl	bdl	bdl
UO_2	bdl	bdl	bdl	bdl	bdl	bdl	bdl	bdl	bdl	bdl	bdl	bdl	bdl	bdl	bdl	bdl	bdl	bdl	bdl	bdl	bdl
P_2O_5	bdl	0.73	0.10	0.13	bdl	0.05	0.05	0.07	0.06	0.06	0.34	0.19	0.12	0.05	0.06	0.07	0.10	bdl	bdl	0.48	1.34
SO_3	34.96	34.88	34.44	34.91	35.05	33.81	32.75	34.61	35.50	34.97	30.22	33.22	31.62	35.24	35.54	33.49	29.22	33.66	33.80	35.51	30.73
F	bdl	bdl	bdl	bdl	bdl	bdl	bdl	bdl	bdl	bdl	bdl	bdl	bdl	bdl	bdl	bdl	bdl	bdl	bdl	bdl	bdl
Cl	bdl	0.01	bdl	bdl	bdl	bdl	bdl	bdl	bdl	bdl	0.04	bdl	0.02	bdl	bdl	bdl	0.01	bdl	bdl	bdl	bdl
TOTAL	102.50	102.16	101.39	102.55	102.30	101.42	102.23	101.65	102.36	102.07	101.22	100.56	99.77	102.34	102.53	99.71	99.84	98.53	98.86	101.84	96.65

* below detection limit

Table B.21 Composition of REE-carbonates (in wt.%) in apatite breccia veins.

SAMPLE	881309A-1-136	881309A-1-137	881309A-3-181	881309A-3-182	881309A-3-185	881309A-3-186	881309A-3-187	881309A-3-188	881309A-3-189	881309A-3-190	881309A-3-194	881309A-4-204	881309A-4-207	881309A-5-246	881344-2-267	881344-2-268	881344-2-271	881344-2-277
SiO_2	0.38	0.38	0.60	1.10	0.37	0.39	0.36	0.37	0.49	0.34	0.54	0.35	0.33	0.58	0.57	0.66	0.54	0.37
Al_2O_3	bdl*	bdl	0.05	0.11	bdl	bdl	bdl	bdl	0.04	bdl	bdl	bdl	bdl	0.02	0.04	0.03	bdl	bdl
Na_2O	bdl	bdl	bdl	bdl	0.05	bdl	bdl	bdl	bdl	bdl	bdl	bdl	bdl	bdl	bdl	bdl	bdl	bdl
K_2O	bdl	bdl	bdl	bdl	bdl	bdl	bdl	bdl	bdl	bdl	bdl	bdl	bdl	bdl	bdl	bdl	bdl	bdl
CaO	2.83	2.51	1.69	1.42	1.79	2.15	1.95	2.27	2.42	2.81	1.66	1.80	2.30	2.05	1.74	1.71	1.45	1.44
MgO	0.06	0.04	0.08	0.17	0.06	0.05	0.05	0.06	bdl	0.04	0.04	0.04	0.04	0.06	0.16	0.09	0.06	0.06
FeO	0.11	0.09	2.84	5.96	0.06	0.09	0.32	0.10	5.56	0.31	0.45	0.40	0.03	0.57	0.33	0.73	0.22	0.34
MnO	0.03	bdl	bdl	bdl	bdl	bdl	bdl	bdl	bdl	bdl	bdl	bdl	bdl	bdl	bdl	bdl	0.04	bdl
BaO	bdl	bdl	bdl	bdl	bdl	bdl	bdl	bdl	0.35	bdl	bdl	bdl	bdl	bdl	bdl	bdl	bdl	bdl
SrO	0.10	0.12	0.10	0.09	bdl	bdl	bdl	bdl	0.30	0.11	0.24	0.09	0.11	0.51	0.12	0.16	0.16	0.32
TiO_2	bdl	bdl	bdl	bdl	bdl	bdl	bdl	bdl	bdl	bdl	bdl	bdl	bdl	bdl	bdl	bdl	bdl	bdl
Cr_2O_3	0.44	0.40	0.40	0.29	0.45	0.50	0.44	0.49	0.43	0.45	0.49	0.45	0.46	0.53	0.48	0.39	0.46	0.60
La_2O_3	16.78	17.08	15.96	14.00	16.96	16.77	16.23	16.83	16.13	16.17	17.22	17.52	17.39	17.68	15.00	17.04	18.42	21.54
Ce_2O_3	35.93	35.99	34.10	30.84	36.78	37.01	35.76	36.87	32.21	36.52	35.59	36.34	37.05	34.78	42.46	25.93	26.44	32.02
Pr_2O_3	5.34	5.39	4.76	4.10	5.42	5.23	4.97	5.26	4.32	5.14	5.01	5.18	5.16	5.40	4.32	6.06	7.16	5.43
Nd_2O_3	21.30	20.86	18.51	16.05	20.79	21.12	20.32	21.39	17.64	21.00	19.78	19.95	20.28	20.26	17.50	26.32	29.94	21.68
Sm_2O_3	2.07	2.09	1.59	1.29	1.86	2.01	1.95	1.98	1.45	2.02	1.79	1.66	1.73	1.72	1.65	3.09	2.33	1.94
Eu_2O_3	0.35	0.31	0.20	0.11	0.35	0.32	0.24	0.36	0.19	0.38	0.25	0.23	0.22	0.20	0.28	0.55	0.40	0.40
Gd_2O_3	0.88	0.76	0.74	0.48	0.83	0.83	0.76	0.81	0.50	0.86	0.80	0.68	0.78	0.74	0.65	1.35	1.02	0.92
Tb_2O_3	bdl	bdl	bdl	bdl	bdl	bdl	bdl	bdl	bdl	bdl	bdl	bdl	bdl	bdl	bdl	bdl	bdl	bdl
Dy_2O_3	bdl	bdl	bdl	bdl	bdl	bdl	bdl	bdl	bdl	bdl	bdl	bdl	bdl	bdl	bdl	bdl	bdl	bdl
Ho_2O_3	bdl	bdl	bdl	bdl	bdl	bdl	bdl	bdl	bdl	bdl	bdl	bdl	bdl	bdl	bdl	bdl	bdl	bdl
Er_2O_3	bdl	bdl	bdl	bdl	bdl	bdl	bdl	bdl	bdl	bdl	bdl	bdl	bdl	bdl	bdl	bdl	bdl	bdl
Tm_2O_3	bdl	bdl	bdl	bdl	bdl	bdl	bdl	bdl	bdl	bdl	bdl	bdl	bdl	bdl	bdl	bdl	bdl	bdl
Yb_2O_3	bdl	bdl	bdl	bdl	bdl	bdl	bdl	bdl	bdl	bdl	bdl	bdl	bdl	bdl	bdl	bdl	bdl	bdl
Lu_2O_3	bdl	bdl	bdl	bdl	bdl	bdl	bdl	bdl	bdl	bdl	bdl	bdl	bdl	bdl	bdl	bdl	bdl	bdl
Y_2O_3	0.36	0.37	0.26	0.24	0.33	0.32	0.32	0.35	0.09	0.28	0.31	0.24	0.21	0.22	0.33	0.61	0.49	0.31
ZrO_2	bdl	bdl	bdl	bdl	bdl	bdl	bdl	bdl	bdl	bdl	bdl	bdl	bdl	bdl	bdl	bdl	bdl	bdl
HfO_2	bdl	bdl	bdl	bdl	bdl	bdl	bdl	bdl	bdl	bdl	bdl	bdl	bdl	bdl	bdl	bdl	bdl	bdl
Nb_2O_5	bdl	bdl	bdl	bdl	bdl	bdl	bdl	bdl	bdl	bdl	bdl	bdl	bdl	bdl	bdl	bdl	bdl	bdl
Sc_2O_3	bdl	bdl	bdl	bdl	bdl	bdl	bdl	bdl	bdl	bdl	bdl	bdl	bdl	bdl	bdl	bdl	bdl	bdl
ThO_2	bdl	bdl	0.75	0.60	bdl	bdl	bdl	bdl	bdl	bdl	bdl	bdl	bdl	0.25	bdl	0.51	bdl	bdl
UO_2	bdl	bdl	bdl	bdl	bdl	bdl	bdl	bdl	bdl	bdl	bdl	bdl	bdl	bdl	bdl	bdl	bdl	bdl
P_2O_5	bdl	0.14	0.07	0.05	bdl	bdl	bdl	bdl	bdl	bdl	bdl	bdl	bdl	0.06	0.12	0.21	0.12	bdl
SO_3	bdl	bdl	0.14	bdl	0.08	bdl	bdl	0.07	bdl	0.07	0.08	0.07	bdl	0.72	bdl	0.17	bdl	0.08
F	bdl	bdl	bdl	bdl	bdl	bdl	bdl	bdl	bdl	bdl	bdl	bdl	bdl	bdl	bdl	bdl	bdl	bdl
Cl	0.24	0.21	0.28	0.28	0.23	0.25	0.23	0.24	0.13	0.23	0.18	0.21	0.25	0.17	0.12	0.15	0.14	0.13
TOTAL	87.16	86.69	83.05	77.12	86.36	86.98	83.85	87.41	82.22	86.68	84.38	85.15	86.29	86.48	85.84	85.72	89.36	87.54
TREO	83.02	82.85	76.11	67.10	83.33	83.60	80.55	83.86	72.53	82.37	80.74	81.81	82.81	80.99	82.19	80.96	86.21	84.23

* below detection limit

Table B.21 cont.

SAMPLE	881344-2-279	881375B-3-72	881375B-3-73	881375B-7-197	881375B-7-198	881253-2-145	881253-2-147	881319-1-272	881319-3-279	517458-8-45	517458-8-46	517458-2-77	881309A-3-195	881309A-4-205	881309A-4-206	517256-3-189	517256-3-190	517256-4-194
SiO_2	0.67	0.34	0.74	0.32	0.46	0.96	0.41	1.25	1.39	1.02	1.15	0.49	0.59	0.88	0.60	0.39	1.89	0.62
Al_2O_3	0.02	bdl	0.05	bdl	bdl	bdl	bdl	0.41	0.43	0.14	0.32	bdl	0.04	0.03	0.03	0.04	1.23	0.15
Na_2O	bdl	0.05	bdl	bdl	0.05	0.06	bdl	0.08	0.08	bdl	bdl	bdl	bdl	bdl	bdl	0.05	bdl	0.11
K_2O	bdl	bdl	bdl	bdl	bdl	bdl	bdl	bdl	bdl	bdl	bdl	bdl	bdl	bdl	bdl	bdl	bdl	bdl
CaO	1.96	0.73	0.76	0.76	0.99	1.11	0.87	1.15	1.68	1.85	2.67	4.26	16.25	17.58	16.98	17.26	17.57	17.96
MgO	0.11	0.06	0.27	bdl	0.07	0.43	0.08	0.20	0.12	0.32	0.51	0.10	0.07	0.03	0.03	0.04	1.06	0.16
FeO	0.84	0.16	0.37	0.19	0.30	1.72	0.85	0.60	0.81	0.79	0.50	0.07	2.74	4.00	5.92	1.80	1.34	1.63
MnO	bdl	bdl	bdl	bdl	bdl	bdl	bdl	bdl	0.04	bdl	0.05	bdl	bdl	bdl	bdl	bdl	bdl	bdl
BaO	bdl	bdl	bdl	bdl	bdl	bdl	bdl	bdl	bdl	bdl	bdl	bdl	bdl	bdl	bdl	bdl	bdl	bdl
SrO	0.26	bdl	0.15	bdl	0.18	bdl	bdl	bdl	bdl	0.26	0.39	0.08	0.21	0.09	0.08	bdl	bdl	bdl
TiO_2	bdl	bdl	bdl	bdl	bdl	bdl	bdl	bdl	bdl	bdl	bdl	bdl	bdl	bdl	bdl	bdl	bdl	bdl
Cr_2O_3	0.49	0.12	0.09	0.05	0.12	0.15	0.22	0.13	0.14	0.40	0.46	0.45	0.22	0.33	0.38	bdl	bdl	bdl
La_2O_3	18.69	19.97	19.01	16.28	19.07	10.88	2.95	13.29	12.75	12.26	14.22	13.05	9.42	14.43	15.91	11.66	12.64	11.39
Ce_2O_3	34.97	34.64	34.51	28.73	34.84	35.91	56.52	31.89	32.04	28.04	30.38	31.32	26.47	22.69	18.57	18.87	17.29	19.60
Pr_2O_3	4.69	3.50	3.54	2.86	3.61	4.15	1.13	4.20	4.54	4.31	4.46	4.90	2.84	3.55	3.82	2.40	2.75	2.78
Nd_2O_3	18.04	12.19	12.08	10.69	13.29	20.38	8.05	19.50	20.17	19.44	19.67	21.41	12.88	12.84	14.52	9.57	10.34	10.47
Sm_2O_3	1.68	0.95	0.97	0.83	1.11	1.91	2.39	2.51	2.12	2.34	2.29	2.44	1.71	0.89	1.17	1.08	1.18	1.27
Eu_2O_3	0.23	0.11	0.16	0.16	0.20	0.32	0.58	0.47	0.30	0.49	0.51	0.48	0.22	bdl	0.11	0.24	0.21	0.27
Gd_2O_3	0.76	0.47	0.49	0.44	0.50	0.69	1.63	0.98	0.66	1.20	1.30	1.13	0.74	0.38	0.50	0.70	0.74	0.83
Tb_2O_3	bdl	bdl	bdl	bdl	bdl	bdl	0.15	bdl	bdl	bdl	bdl	bdl	bdl	bdl	bdl	bdl	bdl	bdl
Dy_2O_3	bdl	bdl	bdl	bdl	bdl	bdl	bdl	bdl	bdl	bdl	bdl	bdl	bdl	bdl	bdl	bdl	bdl	bdl
Ho_2O_3	bdl	bdl	bdl	bdl	bdl	bdl	bdl	bdl	bdl	bdl	bdl	bdl	bdl	bdl	bdl	bdl	bdl	bdl
Er_2O_3	bdl	bdl	bdl	bdl	bdl	bdl	bdl	bdl	bdl	bdl	bdl	bdl	bdl	bdl	bdl	bdl	bdl	bdl
Tm_2O_3	bdl	bdl	bdl	bdl	bdl	bdl	bdl	bdl	bdl	bdl	bdl	bdl	bdl	bdl	bdl	bdl	bdl	bdl
Yb_2O_3	bdl	bdl	bdl	bdl	bdl	bdl	bdl	bdl	bdl	bdl	bdl	bdl	bdl	bdl	bdl	bdl	bdl	bdl
Lu_2O_3	bdl	bdl	bdl	bdl	bdl	bdl	bdl	bdl	bdl	bdl	bdl	bdl	bdl	bdl	bdl	bdl	bdl	bdl
Y_2O_3	0.21	0.21	0.24	0.12	0.31	0.29	0.76	0.27	0.23	0.24	0.27	0.25	0.48	0.11	0.24	0.84	0.72	0.83
ZrO_2	bdl	bdl	bdl	bdl	bdl	bdl	bdl	bdl	bdl	bdl	bdl	bdl	bdl	bdl	bdl	bdl	bdl	bdl
HfO_2	bdl	bdl	bdl	bdl	bdl	bdl	bdl	bdl	bdl	bdl	bdl	bdl	bdl	bdl	bdl	bdl	bdl	bdl
Nb_2O_5	bdl	bdl	bdl	bdl	bdl	bdl	bdl	bdl	bdl	bdl	bdl	bdl	bdl	bdl	bdl	bdl	bdl	bdl
Sc_2O_3	bdl	bdl	bdl	bdl	bdl	bdl	bdl	bdl	bdl	bdl	bdl	bdl	bdl	bdl	bdl	bdl	bdl	bdl
ThO_2	bdl	bdl	bdl	bdl	bdl	bdl	bdl	bdl	bdl	bdl	bdl	bdl	bdl	0.17	0.18	0.18	0.12	0.85
UO_2	bdl	bdl	bdl	bdl	bdl	bdl	bdl	bdl	bdl	bdl	bdl	bdl	bdl	bdl	bdl	bdl	bdl	bdl
P_2O_5	bdl	0.15	bdl	bdl	bdl	bdl	0.19	bdl	bdl	bdl	0.10	0.09	0.90	bdl	bdl	bdl	bdl	1.00
SO_3	0.16	bdl	bdl	bdl	bdl	bdl	bdl	bdl	0.09	bdl	bdl	bdl	0.09	bdl	bdl	0.82	bdl	bdl
F	bdl	1.53	1.66	1.69	1.65	1.50	0.84	1.14	1.54	0.59	0.68	0.22	0.88	0.94	1.36	2.82	2.82	3.07
Cl	0.16	0.12	0.14	0.11	0.14	0.24	0.18	0.23	0.31	0.36	0.37	0.20	0.05	0.11	0.13	0.08	0.05	0.15
TOTAL	83.89	74.63	74.49	62.49	76.16	80.02	77.42	77.78	78.70	73.72	79.93	80.79	76.41	78.62	79.91	67.63	70.75	71.81
TREO	79.26	72.04	70.99	60.11	72.93	74.52	74.16	73.11	72.80	68.33	73.12	74.98	54.76	54.89	54.83	45.36	45.87	47.44

Table B.22 Composition of REE-Sr-carbonate and strontianite (in wt.%) in apatite breccia veins.

SAMPLE	517458-8-49	517458-8-50	517458-8-51	948521-1-220	948521-1-221	948521-2-224	948521-2-225	948521-5-252	517458-8-53	517458-8-54	517458-8-55	517458-8-56	881375A-2A-240	881375A-2A-241
SiO_2	0.22	0.22	0.22	0.28	0.33	0.21	0.52	0.17	0.08	0.07	0.09	0.08	0.08	0.10
Al_2O_3	bdl*	bdl	bdl	bdl	bdl	bdl	0.03	bdl	bdl	bdl	bdl	bdl	bdl	bdl
Na_2O	bdl	bdl	bdl	bdl	bdl	bdl	bdl	bdl	bdl	bdl	bdl	bdl	bdl	bdl
K_2O	bdl	bdl	bdl	bdl	bdl	bdl	bdl	bdl	bdl	bdl	bdl	bdl	bdl	bdl
CaO	1.53	1.44	1.48	1.84	1.74	1.95	2.09	1.36	0.73	3.38	0.81	0.95	1.71	1.66
MgO	0.03	0.02	0.02	0.06	0.11	0.04	0.12	bdl	bdl	bdl	bdl	bdl	bdl	bdl
FeO	bdl	bdl	bdl	bdl	bdl	bdl	0.04	bdl	bdl	bdl	bdl	bdl	bdl	0.07
MnO	bdl	bdl	bdl	bdl	bdl	bdl	bdl	bdl	bdl	bdl	bdl	bdl	bdl	bdl
BaO	bdl	bdl	bdl	bdl	bdl	bdl	bdl	bdl	bdl	bdl	bdl	bdl	bdl	bdl
SrO	17.72	16.01	13.57	20.03	20.09	20.33	22.49	17.37	64.38	62.23	64.69	64.23	77.13	76.89
TiO_2	bdl	bdl	bdl	bdl	bdl	bdl	0.05	bdl	bdl	bdl	bdl	bdl	bdl	bdl
Cr_2O_3	0.31	0.32	0.34	bdl	bdl	bdl	bdl	0.08	bdl	bdl	bdl	bdl	bdl	bdl
La_2O_3	10.17	10.81	11.40	11.71	11.25	12.94	10.88	15.37	bdl	bdl	bdl	0.10	bdl	bdl
Ce_2O_3	26.44	26.21	26.70	24.23	24.23	25.55	22.84	29.64	0.08	bdl	0.12	0.12	bdl	bdl
Pr_2O_3	3.75	3.68	3.97	2.76	2.79	2.56	2.69	2.47	bdl	bdl	bdl	bdl	bdl	bdl
Nd_2O_3	12.95	13.34	13.70	10.61	10.70	8.63	10.35	6.87	bdl	bdl	bdl	bdl	bdl	bdl
Sm_2O_3	1.03	1.07	1.12	0.96	1.02	0.42	1.22	0.17	bdl	bdl	bdl	bdl	bdl	bdl
Eu_2O_3	bdl	0.10	bdl	0.12	0.15	bdl	0.20	bdl	bdl	bdl	bdl	bdl	bdl	bdl
Gd_2O_3	0.49	0.48	0.60	0.35	0.44	0.20	0.58	0.17	bdl	bdl	bdl	bdl	bdl	bdl
Tb_2O_3	bdl	bdl	bdl	bdl	bdl	bdl	bdl	bdl	bdl	bdl	bdl	bdl	bdl	bdl
Dy_2O_3	bdl	bdl	bdl	bdl	bdl	bdl	bdl	bdl	bdl	bdl	bdl	bdl	bdl	bdl
Ho_2O_3	bdl	bdl	bdl	bdl	bdl	bdl	bdl	bdl	bdl	bdl	bdl	bdl	bdl	bdl
Er_2O_3	bdl	bdl	bdl	bdl	bdl	bdl	bdl	bdl	bdl	bdl	bdl	bdl	bdl	bdl
Tm_2O_3	bdl	bdl	bdl	bdl	bdl	bdl	bdl	bdl	bdl	bdl	bdl	bdl	bdl	bdl
Yb_2O_3	bdl	bdl	bdl	bdl	bdl	bdl	bdl	bdl	bdl	bdl	bdl	bdl	bdl	bdl
Lu_2O_3	bdl	bdl	bdl	bdl	bdl	bdl	bdl	bdl	bdl	bdl	bdl	bdl	bdl	bdl
Y_2O_3	bdl	bdl	bdl	bdl	bdl	bdl	0.23	bdl	bdl	bdl	bdl	bdl	bdl	bdl
ZrO_2	bdl	bdl	bdl	bdl	bdl	bdl	bdl	bdl	bdl	bdl	bdl	bdl	bdl	0.08
HfO_2	bdl	bdl	bdl	bdl	bdl	bdl	bdl	bdl	bdl	bdl	bdl	bdl	bdl	bdl
Nb_2O_5	bdl	bdl	bdl	bdl	bdl	bdl	bdl	bdl	bdl	bdl	bdl	bdl	bdl	bdl
Sc_2O_3	bdl	bdl	bdl	bdl	bdl	bdl	bdl	bdl	bdl	bdl	bdl	bdl	bdl	bdl
ThO_2	bdl	bdl	bdl	0.20	0.31	bdl	bdl	bdl	bdl	bdl	bdl	bdl	bdl	bdl
UO_2	bdl	bdl	bdl	bdl	bdl	bdl	bdl	bdl	bdl	bdl	bdl	bdl	bdl	bdl
P_2O_5	bdl	bdl	bdl	bdl	bdl	bdl	bdl	bdl	bdl	bdl	bdl	bdl	bdl	bdl
SO_3	bdl	bdl	bdl	bdl	bdl	bdl	bdl	bdl	bdl	bdl	bdl	bdl	bdl	bdl
F	bdl	bdl	bdl	0.46	0.58	0.28	0.90	0.16	bdl	bdl	bdl	bdl	bdl	bdl
Cl	0.04	0.04	0.04	0.05	0.05	0.04	0.04	0.02	bdl	bdl	bdl	bdl	bdl	bdl
TOTAL	74.66	73.71	73.14	73.46	73.53	73.02	74.88	73.79	65.27	65.68	65.70	65.47	78.92	78.80
TREO	54.82	55.68	57.48	50.74	50.58	50.30	48.98	54.69						

* below detection limit

Table B.23 Composition of late allanite (in wt.%) in quartz-carbonate veins.

SAMPLE	517458-2-67	517458-2-68	517458-2-72	517458-2-74	517458-2-76	517458-2-78	517458-2-79	517458-2-81	517458-2-82	517458-2-83	517458-3-102	517458-3-103	517458-3-104	517458-3-105	517458-3-106	517458-3-107	517458-3-108	517458-3-109	517458-3-113	517458-3-114	517458-3-115	517458-3-117	517458-3-118	517458-3-119	517458-3-120	517458-3-121
SiO_2	30.68	31.61	28.42	29.68	28.28	28.34	28.31	30.00	27.63	29.42	29.34	31.17	28.85	31.17	28.91	31.27	31.04	32.21	31.26	29.74	32.47	35.04	32.13	33.20	30.05	30.25
Al_2O_3	15.24	15.38	9.15	11.42	7.98	7.51	8.59	11.68	11.06	11.40	10.15	14.99	7.60	15.09	8.31	14.90	15.43	16.89	16.17	12.03	14.69	16.54	16.83	17.35	12.67	11.01
Na_2O	0.02	bdl	0.07	0.13	0.07	0.21	0.15	bdl	0.09	0.13	bdl	0.13	bdl	0.10	bdl	0.10	0.14	0.11	0.15	0.15	0.13	0.05	0.13	0.09	0.11	0.09
K_2O	bdl*	bdl	bdl	bdl	bdl	bdl	bdl	bdl	bdl	bdl	bdl	bdl	bdl	bdl	bdl	bdl	bdl	bdl	bdl	bdl	0.04	0.04	0.03	0.02	bdl	bdl
CaO	12.97	12.65	10.16	11.36	9.46	8.86	9.10	10.09	14.49	10.12	10.08	11.68	9.19	11.34	9.55	12.10	10.94	12.84	10.87	10.13	9.74	9.33	9.54	12.15	10.56	9.87
MgO	0.73	0.18	0.69	0.54	0.76	0.73	0.82	1.16	0.82	0.76	0.39	0.60	0.49	0.49	0.47	0.50	0.68	0.50	0.56	0.77	0.51	0.47	0.54	0.43	0.44	0.44
FeO	14.43	15.72	16.37	14.08	18.55	18.88	18.74	16.94	13.91	15.27	20.10	13.35	22.51	12.11	21.66	12.78	11.31	11.12	10.11	14.92	11.07	8.82	8.94	10.67	14.34	18.13
MnO	0.33	0.38	0.70	0.67	0.50	0.77	0.74	0.43	0.49	0.69	0.69	0.69	0.64	0.70	0.76	0.62	0.80	0.63	0.84	0.62	0.77	0.86	1.01	0.89	0.60	0.69
BaO	bdl	bdl	bdl	bdl	bdl	bdl	bdl	bdl	bdl	bdl	bdl	bdl	bdl	bdl	bdl	0.06	bdl	bdl	0.06	bdl	1.10	1.94	0.07	bdl	bdl	bdl
SrO	1.90	2.42	0.32	0.61	0.24	0.20	0.18	0.19	0.55	0.39	0.20	0.88	bdl	0.99	0.06	0.87	0.92	1.21	1.09	0.47	1.22	1.49	1.07	1.58	0.67	0.27
TiO_2	bdl	bdl	0.53	0.38	0.58	0.25	0.28	0.04	0.13	0.11	bdl	0.14	0.06	0.15	bdl	0.33	0.21	0.17	0.20	0.10	0.27	0.23	0.14	0.14	0.12	0.05
Cr_2O_3	0.11	0.08	0.20	0.14	0.22	0.22	0.22	0.16	0.09	0.13	0.14	0.10	0.21	0.06	0.18	0.08	0.06	0.08	0.07	0.16	0.10	0.06	0.09	0.09	0.11	0.15
La_2O_3	3.62	3.40	5.87	4.75	5.98	5.59	5.82	4.98	3.59	4.31	4.89	3.36	6.07	3.31	6.04	3.39	3.71	2.97	3.96	4.89	3.94	2.46	3.78	2.93	4.11	4.91
Ce_2O_3	9.45	8.86	13.83	12.11	14.21	14.37	14.09	13.19	10.31	11.86	12.49	9.00	14.17	9.02	14.14	8.75	9.38	7.45	9.59	11.62	9.39	6.52	10.28	7.60	10.41	12.33
Pr_2O_3	1.26	1.28	1.71	1.63	1.72	1.79	1.69	1.87	1.51	1.79	1.91	1.36	1.68	1.36	1.72	1.25	1.23	1.05	1.31	1.63	1.23	1.02	1.39	1.05	1.62	1.69
Nd_2O_3	4.36	4.76	5.06	4.95	5.19	5.70	5.26	6.24	5.66	6.37	7.01	5.93	5.55	5.95	5.61	4.83	5.11	4.21	4.72	5.95	4.61	3.86	5.32	4.28	6.54	5.96
Sm_2O_3	0.39	0.46	0.30	0.33	0.31	0.40	0.39	0.51	0.47	0.60	0.70	0.67	0.36	0.72	0.36	0.51	0.53	0.51	0.44	0.45	0.44	0.50	0.59	0.49	0.76	0.50
Eu_2O_3	bdl	bdl	bdl	bdl	bdl	bdl	bdl	bdl	bdl	bdl	bdl	bdl	bdl	0.11	bdl	bdl	bdl	0.08	bdl	bdl	bdl	bdl	bdl	0.10	0.15	bdl
Gd_2O_3	0.09	0.17	0.13	0.14	0.16	0.17	0.10	0.13	0.21	0.20	0.21	0.27	0.13	0.29	0.14	0.23	0.17	0.23	0.17	0.18	0.18	0.21	0.21	0.15	0.37	0.18
Tb_2O_3	0.10	0.10	0.15	0.07	0.10	bdl	bdl	0.10	bdl	0.08	0.13	bdl	0.14	bdl	0.16	0.07	bdl	bdl	bdl	0.08	bdl	bdl	bdl	bdl	bdl	0.11
Dy_2O_3	bdl	bdl	bdl	bdl	bdl	bdl	bdl	bdl	bdl	bdl	bdl	bdl	bdl	bdl	bdl	bdl	bdl	bdl	bdl	bdl	bdl	bdl	bdl	bdl	bdl	
Ho_2O_3	bdl	bdl	bdl	bdl	bdl	bdl	bdl	bdl	bdl	bdl	bdl	bdl	bdl	bdl	bdl	bdl	bdl	bdl	bdl	bdl	bdl	bdl	bdl	bdl	bdl	
Er_2O_3	bdl	bdl	bdl	bdl	bdl	bdl	bdl	bdl	bdl	bdl	bdl	bdl	bdl	bdl	bdl	bdl	bdl	bdl	bdl	bdl	bdl	bdl	bdl	bdl	bdl	
Tm_2O_3	bdl	bdl	bdl	bdl	bdl	bdl	bdl	bdl	bdl	bdl	bdl	bdl	bdl	bdl	bdl	bdl	bdl	bdl	bdl	bdl	bdl	bdl	bdl	bdl	bdl	
Yb_2O_3	bdl	bdl	bdl	bdl	bdl	bdl	bdl	bdl	bdl	bdl	bdl	bdl	bdl	bdl	bdl	bdl	bdl	bdl	bdl	bdl	bdl	bdl	bdl	bdl	bdl	
Lu_2O_3	bdl	bdl	bdl	bdl	bdl	bdl	bdl	bdl	bdl	bdl	bdl	bdl	bdl	bdl	bdl	bdl	bdl	bdl	bdl	bdl	bdl	bdl	bdl	bdl	bdl	
Y_2O_3	bdl	bdl	bdl	bdl	bdl	bdl	bdl	bdl	bdl	bdl	bdl	bdl	bdl	0.07	bdl	bdl	bdl	bdl	bdl	bdl	bdl	bdl	0.08	bdl	bdl	
ZrO_2	bdl	bdl	bdl	bdl	bdl	bdl	bdl	bdl	bdl	bdl	bdl	bdl	bdl	bdl	bdl	bdl	bdl	bdl	bdl	bdl	bdl	bdl	bdl	bdl	bdl	
HfO_2	bdl	bdl	bdl	bdl	bdl	bdl	bdl	bdl	bdl	bdl	bdl	bdl	bdl	bdl	bdl	bdl	bdl	bdl	bdl	bdl	bdl	bdl	bdl	bdl	bdl	
Nb_2O_5	bdl	bdl	bdl	bdl	bdl	bdl	bdl	bdl	bdl	bdl	bdl	bdl	bdl	bdl	bdl	bdl	bdl	bdl	bdl	bdl	bdl	bdl	bdl	bdl	bdl	
Sc_2O_3	bdl	bdl	bdl	bdl	bdl	bdl	bdl	bdl	bdl	bdl	bdl	bdl	bdl	bdl	bdl	bdl	bdl	bdl	bdl	bdl	bdl	bdl	bdl	bdl	bdl	
ThO_2	bdl	bdl	0.14	0.29	0.11	0.11	0.05	bdl	0.19	0.15	bdl	0.09	bdl	0.25	bdl	0.40	0.34	0.40	0.38	0.28	0.59	0.76	0.43	0.44	0.33	0.09
UO_2	bdl	bdl	bdl	bdl	bdl	bdl	bdl	bdl	bdl	bdl	bdl	bdl	bdl	bdl	bdl	bdl	bdl	bdl	bdl	bdl	bdl	bdl	bdl	bdl	bdl	
P_2O_5	0.64	0.15	bdl	0.06	bdl	0.06	0.05	0.07	2.12	bdl	0.10	bdl	bdl	bdl	0.15	bdl	bdl	bdl	bdl	bdl	bdl	bdl	bdl	bdl	bdl	
SO_3	0.05	bdl	bdl	bdl	bdl	0.06	bdl	bdl	bdl	bdl	bdl	bdl	bdl	0.07	bdl	0.07	bdl	0.07	0.05	bdl	0.04	bdl	0.11	0.05	bdl	0.05
F	bdl	bdl	bdl	bdl	bdl	bdl	bdl	bdl	bdl	bdl	bdl	bdl	bdl	bdl	bdl	bdl	bdl	bdl	bdl	bdl	bdl	bdl	bdl	bdl	bdl	
Cl	0.04	0.03	0.74	0.96	0.62	0.36	0.31	0.13	0.71	0.45	0.01	0.46	0.02	0.39	0.02	0.50	0.53	0.36	0.47	0.69	0.24	0.06	0.23	0.37	0.42	0.33
TOTAL	96.40	97.63	94.38	94.10	94.92	94.51	94.82	97.89	93.87	94.13	98.54	94.76	97.66	93.65	98.23	93.51	92.41	93.03	92.37	94.71	92.69	90.23	92.89	93.99	94.30	97.04
TREO	19.26	19.04	27.05	23.98	27.67	28.03	27.35	27.02	21.75	25.22	27.35	20.59	28.09	20.82	28.18	19.03	20.12	16.51	20.20	24.80	19.78	14.56	21.64	16.62	23.97	25.69

* below detection limit

Table B.23 cont.

SAMPLE	517458-3-122	517458-3-123	517458-3-124	517458-3-125	517458-3-126	517458-3-129	517458-3-130	517458-3-131	517458-3-134	517458-3-135	517458-3-136	517458-3-161	517458-3-163	517458-3-164	517458-3-165	517458-3-166	517458-3-167	517458-3-168	517458-3-169	517458-3-170	517458-3-171	517458-3-172	517458-3-173	517458-3-174	517458-3-178	517458-3-179
SiO_2	30.43	29.32	30.43	33.52	28.88	31.68	29.61	30.66	34.13	34.61	32.15	21.82	28.49	34.02	35.00	35.64	35.60	34.48	32.62	27.72	28.27	32.36	30.46	24.40	29.55	33.69
Al_2O_3	13.31	11.72	13.54	13.69	11.47	13.30	11.82	14.01	14.04	15.51	16.04	9.42	12.29	15.09	15.37	15.67	16.24	15.14	15.55	12.21	12.56	13.85	12.34	10.22	13.01	15.15
Na_2O	0.09	0.13	0.11	0.07	0.04	0.23	bdl	0.12	0.03	0.06	0.13	bdl	0.03	0.03	0.05	0.02	0.05	bdl	0.10	0.04	bdl	0.03	bdl	bdl	bdl	0.02
K_2O	bdl	bdl	bdl	0.05	0.04	0.10	bdl	0.02	0.02	0.02	0.04	0.04	0.12	0.02	bdl	bdl	0.04	bdl	0.05	0.07	0.06	0.10	0.36	0.11	0.05	0.02
CaO	10.79	10.50	10.58	8.00	8.10	9.48	7.17	9.62	7.20	8.32	9.00	3.82	5.91	6.98	7.01	7.10	7.31	7.12	7.84	5.22	4.88	5.76	4.49	4.92	5.84	7.27
MgO	0.65	0.79	0.58	0.64	0.46	0.71	0.40	0.59	1.03	1.11	0.93	2.03	0.93	0.84	0.64	0.53	0.53	0.45	0.47	2.07	2.33	3.73	4.06	1.39	1.59	0.46
FeO	13.39	14.14	13.39	10.68	10.64	12.88	8.13	11.79	8.54	10.02	9.57	5.44	6.87	7.97	7.64	7.87	8.21	8.01	9.95	6.00	6.34	8.10	10.85	5.65	6.28	7.99
MnO	0.59	0.64	0.61	0.84	0.82	0.70	0.84	0.73	0.90	0.94	0.81	0.46	0.66	0.83	0.84	0.82	0.83	0.84	0.79	0.62	0.60	0.77	0.70	0.57	0.68	0.86
BaO	bdl	bdl	0.09	1.89	1.89	0.81	2.97	0.49	2.90	1.86	0.53	1.90	2.36	2.22	2.60	2.53	1.80	2.55	0.95	2.25	2.03	2.22	2.47	2.17	2.41	2.07
SrO	0.59	0.54	0.79	1.10	1.16	0.72	1.60	0.90	1.87	1.33	0.96	0.96	3.36	1.30	1.55	1.05	0.91	1.00	0.96	4.41	3.73	1.78	0.92	1.13	3.49	1.02
TiO_2	0.23	0.20	0.21	0.35	0.37	0.38	0.49	0.35	0.40	0.29	0.29	0.11	0.24	0.35	0.36	0.42	0.37	0.40	0.39	0.22	0.21	0.28	0.24	0.23	0.27	0.36
Cr_2O_3	0.12	0.17	0.11	0.13	0.07	0.14	0.05	0.10	0.07	0.07	0.10	0.06	0.10	0.13	0.11	0.09	0.09	0.09	0.11	0.14	0.10	0.08	0.07	0.18	0.13	0.10
La_2O_3	4.23	5.59	4.57	3.62	3.53	4.29	2.97	4.45	2.69	3.16	3.74	5.66	4.64	3.75	3.75	3.64	4.16	3.51	4.36	5.28	5.08	3.50	2.85	5.83	4.74	3.67
Ce_2O_3	10.90	12.26	10.83	9.02	8.93	10.74	7.72	10.60	6.88	7.43	9.65	15.30	12.26	9.40	9.75	9.16	9.94	9.11	10.80	13.70	13.66	8.79	7.08	15.05	12.54	9.22
Pr_2O_3	1.50	1.67	1.51	1.22	1.22	1.48	1.07	1.48	0.95	1.00	1.30	2.10	1.65	1.21	1.31	1.24	1.36	1.34	1.58	1.89	1.77	1.08	0.96	2.19	1.75	1.28
Nd_2O_3	5.83	5.28	5.23	4.66	4.67	5.46	3.93	5.21	3.60	3.71	4.94	8.63	5.64	4.37	4.54	4.19	4.77	4.24	5.35	6.25	5.97	3.96	3.41	8.56	5.57	4.44
Sm_2O_3	0.52	0.39	0.51	0.44	0.46	0.51	0.39	0.47	0.40	0.42	0.57	0.87	0.49	0.43	0.46	0.45	0.50	0.45	0.54	0.48	0.45	0.32	0.33	0.79	0.47	0.44
Eu_2O_3	bdl	bdl	bdl	bdl	bdl	bdl	bdl	bdl	0.07	bdl	bdl	0.10	bdl	bdl	bdl	bdl	0.06	bdl	bdl	bdl	bdl	bdl	bdl	0.09	bdl	bdl
Gd_2O_3	0.15	0.14	0.11	0.27	0.15	0.18	0.12	0.27	0.12	0.18	0.21	0.26	0.19	0.17	0.16	0.18	0.16	0.19	0.17	0.12	0.15	0.12	bdl	0.27	0.14	0.17
Tb_2O_3	0.07	bdl	bdl	bdl	bdl	bdl	bdl	bdl	bdl	bdl	bdl	bdl	bdl	bdl	bdl	bdl	bdl	bdl	bdl	bdl	bdl	bdl	bdl	bdl	bdl	bdl
Dy_2O_3	bdl	bdl	bdl	bdl	bdl	bdl	bdl	bdl	bdl	bdl	bdl	bdl	bdl	bdl	bdl	bdl	bdl	bdl	bdl	bdl	bdl	bdl	bdl	bdl	bdl	bdl
Ho_2O_3	bdl	bdl	bdl	bdl	bdl	bdl	bdl	bdl	bdl	bdl	bdl	bdl	bdl	bdl	bdl	bdl	bdl	bdl	bdl	bdl	bdl	bdl	bdl	bdl	bdl	bdl
Er_2O_3	bdl	bdl	bdl	bdl	bdl	bdl	bdl	bdl	bdl	bdl	bdl	bdl	bdl	bdl	bdl	bdl	bdl	bdl	bdl	bdl	bdl	bdl	bdl	bdl	bdl	bdl
Tm_2O_3	bdl	bdl	bdl	bdl	bdl	bdl	bdl	bdl	bdl	bdl	bdl	bdl	bdl	bdl	bdl	bdl	bdl	bdl	bdl	bdl	bdl	bdl	bdl	bdl	bdl	bdl
Yb_2O_3	bdl	bdl	bdl	bdl	bdl	bdl	bdl	bdl	bdl	bdl	bdl	bdl	bdl	bdl	bdl	bdl	bdl	bdl	bdl	bdl	bdl	bdl	bdl	bdl	bdl	bdl
Lu_2O_3	bdl	bdl	bdl	bdl	bdl	bdl	bdl	bdl	bdl	bdl	bdl	bdl	bdl	bdl	bdl	bdl	bdl	bdl	bdl	bdl	bdl	bdl	bdl	bdl	bdl	bdl
Y_2O_3	bdl	bdl	bdl	0.06	bdl	bdl	bdl	bdl	0.07	bdl	0.06	0.07	bdl	bdl	bdl	bdl	bdl	bdl	bdl	bdl	bdl	0.06	bdl	bdl	bdl	bdl
ZrO_2	bdl	bdl	bdl	bdl	bdl	bdl	bdl	bdl	bdl	bdl	bdl	bdl	bdl	bdl	bdl	bdl	bdl	bdl	bdl	bdl	bdl	bdl	bdl	bdl	bdl	bdl
HfO_2	bdl	bdl	bdl	bdl	bdl	bdl	bdl	bdl	bdl	bdl	bdl	bdl	bdl	bdl	bdl	bdl	bdl	bdl	bdl	bdl	bdl	bdl	bdl	bdl	bdl	bdl
Nb_2O_5	bdl	bdl	bdl	bdl	bdl	bdl	bdl	bdl	bdl	bdl	bdl	bdl	bdl	bdl	bdl	bdl	bdl	bdl	bdl	bdl	bdl	bdl	bdl	bdl	bdl	bdl
Sc_2O_3	bdl	bdl	bdl	bdl	bdl	bdl	bdl	bdl	bdl	bdl	bdl	bdl	bdl	bdl	bdl	bdl	bdl	bdl	bdl	bdl	bdl	bdl	bdl	bdl	bdl	bdl
ThO_2	0.36	0.31	0.36	0.79	0.90	0.54	1.19	0.49	1.27	0.77	0.61	1.00	0.47	0.39	0.43	0.43	0.40	0.47	0.37	0.33	0.39	0.40	0.27	0.62	0.55	0.41
UO_2	bdl	bdl	bdl	bdl	bdl	bdl	bdl	bdl	bdl	bdl	bdl	bdl	bdl	bdl	bdl	bdl	bdl	bdl	bdl	bdl	bdl	bdl	bdl	bdl	bdl	bdl
P_2O_5	bdl	bdl	bdl	bdl	bdl	bdl	bdl	bdl	bdl	bdl	bdl	bdl	bdl	bdl	bdl	bdl	bdl	bdl	bdl	bdl	bdl	bdl	bdl	bdl	bdl	bdl
SO_3	bdl	0.06	0.05	bdl	bdl	0.13	bdl	0.08	bdl	bdl	bdl	bdl	bdl	bdl	bdl	bdl	bdl	bdl	bdl	bdl	bdl	bdl	bdl	bdl	bdl	bdl
F	bdl	bdl	bdl	bdl	bdl	bdl	bdl	bdl	bdl	bdl	bdl	0.75	bdl	bdl	bdl	bdl	bdl	bdl	bdl	bdl	bdl	bdl	bdl	0.15	bdl	bdl
Cl	0.64	0.74	0.43	0.06	0.17	0.35	0.07	0.32	0.07	0.08	0.26	0.03	0.04	0.02	0.02	0.02	0.04	0.03	0.06	0.03	0.03	0.03	0.02	0.04	0.02	0.03
TOTAL	94.24	94.41	93.97	91.08	83.94	94.74	80.52	92.68	87.21	90.88	91.83	80.49	86.73	89.53	91.58	91.04	93.38	89.42	92.99	89.03	88.61	87.31	81.85	84.49	89.08	88.68
TREO	23.20	25.32	22.77	19.29	18.97	22.67	16.19	22.47	14.77	15.91	20.47	32.99	24.88	19.34	19.97	18.85	20.96	18.85	22.80	27.72	27.08	17.84	14.63	32.79	25.21	19.22

Table B.23 cont.

SAMPLE	517458-3-180	517458-3-181	517458-3-182	517458-3-183	517458-3-184	517458-3-185	517458-3-186	517458-3-187	517458-3-188	517458-3-189	517458-3-190	517458-3-191	517458-3-192	517458-3-193	517458-3-194	517458-3-195	517458-3-196	517458-3-198	517458-3-199	517458-3-200	517458-3-201	517458-3-202	517458-3-203	517458-3-204	517458-3-205	517458-3-206
SiO_2	24.97	37.89	25.23	34.36	36.00	33.83	35.79	32.72	34.88	33.38	31.31	31.57	35.55	35.86	35.60	28.61	32.28	24.38	27.09	33.50	29.93	34.35	29.50	32.94	29.61	34.28
Al_2O_3	11.11	15.05	11.36	14.87	15.60	14.43	14.79	13.47	16.21	14.72	15.15	15.26	15.52	15.61	15.55	12.55	14.51	10.97	12.14	14.35	12.97	14.94	12.07	14.28	12.50	14.84
Na_2O	bdl	0.03	0.02	0.04	bdl	bdl	bdl	bdl	0.07	0.02	0.08	0.10	0.03	bdl	bdl	bdl	0.18	bdl	0.02	0.10	0.03	0.06	0.13	0.16	0.06	0.03
K_2O	bdl	0.71	0.07	0.09	0.08	0.13	0.26	0.40	0.05	0.02	0.04	0.03	0.05	0.07	0.05	0.07	0.04	bdl	bdl	0.07	0.03	0.05	bdl	0.03	0.06	0.03
CaO	5.62	4.10	4.81	6.10	5.99	5.07	4.82	5.13	7.44	7.19	7.45	8.15	7.01	6.89	6.87	5.71	9.89	5.42	5.66	6.78	6.56	7.02	10.34	9.35	8.55	7.18
MgO	0.55	4.19	1.70	2.08	4.22	5.34	5.35	2.73	0.51	0.48	0.47	0.52	0.71	1.07	1.44	1.30	0.94	0.42	0.37	0.44	0.49	0.42	0.66	0.85	1.16	0.45
FeO	5.27	12.47	5.05	8.11	8.58	8.68	9.88	10.38	8.69	7.84	9.41	10.37	8.32	8.04	7.93	6.25	12.50	4.84	5.23	7.14	6.32	7.26	15.00	13.11	12.23	7.46
MnO	0.59	0.68	0.50	0.75	0.77	0.72	0.72	0.70	0.82	0.84	0.79	0.82	0.82	0.84	0.83	0.66	0.52	0.55	0.61	0.82	0.74	0.84	0.53	0.70	0.69	0.86
BaO	2.33	2.57	1.95	2.45	2.27	2.03	2.24	2.62	1.47	2.36	0.88	0.37	2.47	2.48	2.52	2.41	0.44	2.34	2.76	3.25	2.97	3.12	bdl	0.45	0.98	2.92
SrO	4.87	0.60	5.16	1.87	1.09	1.68	1.52	1.38	0.91	0.95	0.94	0.90	1.02	0.99	1.07	3.75	0.91	5.26	4.68	1.19	2.80	1.14	0.52	0.62	0.72	1.01
TiO_2	0.24	0.20	0.19	0.31	0.30	0.24	0.24	0.26	0.33	0.39	0.32	0.33	0.38	0.37	0.36	0.26	0.17	0.22	0.25	0.41	0.34	0.43	0.20	0.17	0.25	0.43
Cr_2O_3	0.11	bdl	0.11	0.07	0.05	0.05	0.07	0.04	0.10	0.11	0.08	0.10	0.09	0.07	0.08	0.12	0.13	0.13	0.14	0.06	0.10	0.07	0.14	0.14	0.12	0.09
La_2O_3	5.61	1.53	5.63	3.47	2.85	2.89	2.74	2.68	4.17	3.53	4.31	4.42	3.66	3.47	3.43	4.72	4.38	5.76	5.29	3.21	4.17	3.24	4.99	4.68	4.12	3.22
Ce_2O_3	15.05	4.14	14.72	9.52	7.40	7.96	7.09	7.28	10.48	9.26	10.70	11.24	9.36	9.03	8.71	12.90	11.23	15.82	14.52	8.64	11.24	8.43	11.92	11.48	10.71	8.63
Pr_2O_3	1.96	0.55	1.98	1.28	1.05	1.03	0.91	0.97	1.40	1.31	1.52	1.56	1.28	1.23	1.26	1.81	1.65	2.12	1.88	1.16	1.67	1.11	1.62	1.67	1.50	1.22
Nd_2O_3	6.36	1.84	6.28	4.32	3.51	3.52	3.18	3.18	5.01	4.34	5.29	5.54	4.43	4.36	4.21	5.59	5.85	6.81	6.26	3.93	5.17	3.99	5.57	5.70	5.31	3.95
Sm_2O_3	0.47	0.20	0.43	0.42	0.39	0.33	0.27	0.29	0.54	0.46	0.51	0.56	0.47	0.47	0.44	0.48	0.47	0.50	0.50	0.39	0.50	0.40	0.46	0.49	0.48	0.45
Eu_2O_3	bdl	bdl	bdl	bdl	bdl	bdl	bdl	bdl	bdl	bdl	0.08	bdl	bdl	bdl	bdl	bdl	bdl	bdl	bdl	bdl	bdl	bdl	bdl	bdl	bdl	bdl
Gd_2O_3	0.10	bdl	0.17	0.10	0.08	0.07	0.10	0.07	0.16	0.11	0.18	0.16	0.11	0.18	0.14	0.12	0.15	0.09	bdl	0.12	0.15	0.08	0.20	0.15	0.15	0.13
Tb_2O_3	bdl	bdl	bdl	bdl	bdl	bdl	bdl	bdl	bdl	bdl	bdl	bdl	bdl	bdl	bdl	bdl	bdl	bdl	bdl	bdl	bdl	bdl	bdl	0.07	bdl	bdl
Dy_2O_3	bdl	bdl	bdl	bdl	bdl	bdl	bdl	bdl	bdl	bdl	bdl	bdl	bdl	bdl	bdl	bdl	bdl	bdl	bdl	bdl	bdl	bdl	bdl	bdl	bdl	bdl
Ho_2O_3	bdl	bdl	bdl	bdl	bdl	bdl	bdl	bdl	bdl	bdl	bdl	bdl	bdl	bdl	bdl	bdl	bdl	bdl	bdl	bdl	bdl	bdl	bdl	bdl	bdl	bdl
Er_2O_3	bdl	bdl	bdl	bdl	bdl	bdl	bdl	bdl	bdl	bdl	bdl	bdl	bdl	bdl	bdl	bdl	bdl	bdl	bdl	bdl	bdl	bdl	bdl	bdl	bdl	bdl
Tm_2O_3	bdl	bdl	bdl	bdl	bdl	bdl	bdl	bdl	bdl	bdl	bdl	bdl	bdl	bdl	bdl	bdl	bdl	bdl	bdl	bdl	bdl	bdl	bdl	bdl	bdl	bdl
Yb_2O_3	bdl	bdl	bdl	bdl	bdl	bdl	bdl	bdl	bdl	bdl	bdl	bdl	bdl	bdl	bdl	bdl	bdl	bdl	bdl	bdl	bdl	bdl	bdl	bdl	bdl	bdl
Lu_2O_3	bdl	bdl	bdl	bdl	bdl	bdl	bdl	bdl	bdl	bdl	bdl	bdl	bdl	bdl	bdl	bdl	bdl	bdl	bdl	bdl	bdl	bdl	bdl	bdl	bdl	bdl
Y_2O_3	0.07	bdl	bdl	bdl	bdl	bdl	bdl	bdl	0.06	0.10	0.13	0.06	bdl	bdl	bdl	0.06	bdl	bdl	bdl	bdl	bdl	0.06	bdl	bdl	bdl	bdl
ZrO_2	bdl	bdl	bdl	bdl	bdl	bdl	bdl	bdl	bdl	bdl	bdl	bdl	bdl	bdl	bdl	bdl	bdl	bdl	bdl	bdl	bdl	bdl	bdl	bdl	bdl	bdl
HfO_2	bdl	bdl	bdl	bdl	bdl	bdl	bdl	bdl	bdl	bdl	bdl	bdl	bdl	bdl	bdl	bdl	bdl	bdl	bdl	bdl	bdl	bdl	bdl	bdl	bdl	bdl
Nb_2O_5	bdl	bdl	bdl	bdl	bdl	bdl	bdl	bdl	bdl	bdl	bdl	bdl	bdl	bdl	bdl	bdl	bdl	bdl	bdl	bdl	bdl	bdl	bdl	bdl	bdl	bdl
Sc_2O_3	bdl	bdl	bdl	bdl	bdl	bdl	bdl	bdl	bdl	bdl	bdl	bdl	bdl	bdl	bdl	bdl	bdl	bdl	bdl	bdl	bdl	bdl	bdl	bdl	bdl	bdl
ThO_2	0.40	0.23	0.74	0.45	0.42	0.37	0.36	0.51	0.47	0.51	0.41	0.39	0.63	0.59	0.62	1.01	0.37	0.54	0.59	0.69	0.79	0.71	0.29	0.42	0.41	0.72
UO_2	bdl	bdl	bdl	bdl	bdl	bdl	bdl	bdl	bdl	bdl	bdl	bdl	bdl	bdl	bdl	bdl	bdl	bdl	bdl	bdl	bdl	bdl	bdl	bdl	bdl	bdl
P_2O_5	bdl	bdl	bdl	bdl	bdl	bdl	bdl	bdl	bdl	bdl	bdl	bdl	bdl	bdl	bdl	bdl	bdl	bdl	bdl	bdl	bdl	bdl	bdl	bdl	bdl	bdl
SO_3	bdl	bdl	bdl	bdl	bdl	bdl	bdl	bdl	bdl	bdl	0.08	0.18	bdl	bdl	bdl	bdl	bdl	bdl	bdl	bdl	bdl	bdl	bdl	0.04	bdl	bdl
F	bdl	bdl	bdl	bdl	bdl	bdl	bdl	bdl	bdl	bdl	bdl	bdl	bdl	bdl	bdl	bdl	bdl	bdl	bdl	bdl	bdl	bdl	bdl	bdl	bdl	bdl
Cl	0.03	bdl	0.02	0.02	0.03	0.03	0.02	0.02	0.04	0.03	0.06	0.08	0.04	0.02	0.03	0.02	0.53	0.02	0.01	0.02	0.02	0.02	0.75	0.46	0.36	0.02
TOTAL	85.70	86.98	86.14	90.70	90.67	88.39	90.33	84.84	93.77	87.95	90.15	92.68	91.92	91.62	91.13	88.40	97.00	86.19	88.00	86.26	86.98	87.75	94.70	97.87	89.91	87.91
TREO	29.61	8.27	29.22	19.11	15.27	15.80	14.28	14.48	21.81	19.10	22.71	23.54	19.30	18.73	18.19	25.69	23.73	31.11	28.44	17.45	22.90	17.32	24.76	24.24	22.27	17.60

Table B.23 cont.

SAMPLE	517458-3-207	517458-3-208	517458-3-209	517458-3-210	517458-3-211	517458-3-212	517458-3-213	517458-3-214	517458-3-215	517458-3-216	517458-3-218	517458-3-219	517458-3-222	517458-3-223	517458-3-224	517458-3-225	517458-3-226	517458-3-227	517458-3-228	517458-3-229	517458-3-230	517458-3-231	517458-3-232	517458-3-233	517458-3-234	517458-3-235
SiO_2	32.47	34.72	32.51	35.04	33.43	29.62	29.13	32.60	34.43	35.12	32.49	32.47	30.37	27.67	25.45	26.30	33.71	29.92	26.29	29.50	35.09	30.23	32.89	35.88	35.56	32.63
Al_2O_3	15.54	15.08	14.90	15.78	14.83	11.76	10.82	14.83	15.33	15.42	14.13	14.54	13.19	12.47	11.84	11.75	16.13	13.06	11.52	13.09	15.02	12.18	13.50	14.46	15.33	15.45
Na_2O	0.09	0.07	0.06	0.07	bdl	0.13	0.10	0.03	0.05	0.02	0.04	0.05	0.02	0.03	0.05	0.04	0.10	0.03	bdl	0.05	0.06	bdl	bdl	0.03	0.05	0.11
K_2O	0.04	0.05	0.05	0.07	0.05	bdl	bdl	0.08	0.04	0.08	0.19	0.08	0.13	0.03	bdl	bdl	0.04	0.02	bdl	bdl	0.23	0.35	0.30	0.43	0.03	0.04
CaO	7.51	6.89	7.24	6.84	7.42	10.07	9.76	4.87	7.20	5.46	4.89	5.76	5.45	5.76	5.45	5.39	7.30	6.40	5.82	6.06	5.91	4.05	4.13	4.17	6.79	7.64
MgO	0.50	0.59	0.74	2.29	0.60	0.73	0.77	5.66	1.58	7.42	5.21	4.29	3.20	1.46	0.49	0.59	3.46	0.71	0.43	0.98	4.07	4.90	8.30	7.19	1.13	0.48
FeO	9.85	7.53	8.77	8.25	8.51	15.29	16.14	7.55	7.65	7.75	7.32	7.18	6.60	5.44	4.52	4.59	8.81	5.66	4.94	5.45	8.59	7.65	8.13	9.12	7.05	8.42
MnO	0.79	0.82	0.81	0.79	0.83	0.54	0.52	0.69	0.80	0.77	0.65	0.70	0.64	0.65	0.58	0.58	0.80	0.70	0.63	0.67	0.73	0.57	0.63	0.67	0.81	0.83
BaO	0.80	2.97	1.46	1.90	2.03	bdl	bdl	1.41	1.75	1.85	1.77	1.76	2.01	1.90	1.82	1.78	1.10	2.27	1.99	1.97	1.80	1.91	1.99	2.13	2.25	0.82
SrO	0.93	1.03	1.01	0.83	1.01	0.47	0.43	1.71	1.18	1.32	2.10	2.08	2.88	3.45	5.07	4.69	1.01	2.88	4.16	3.39	1.10	2.80	2.30	1.37	1.17	0.84
TiO_2	0.34	0.37	0.36	0.34	0.38	0.12	0.09	0.22	0.30	0.28	0.24	0.24	0.26	0.23	0.20	0.23	0.29	0.30	0.23	0.28	0.26	0.17	0.19	0.22	0.37	0.37
Cr_2O_3	0.10	0.07	0.11	0.07	0.08	0.16	0.15	0.05	0.07	0.07	0.09	0.06	0.10	0.10	0.14	0.10	0.06	0.10	0.10	0.09	0.06	bdl	0.10	0.08	0.07	0.12
La_2O_3	4.60	3.25	3.99	3.57	3.87	5.47	5.65	2.61	3.20	2.59	3.21	3.38	3.93	4.43	5.42	5.20	2.94	4.02	4.98	4.49	2.64	3.14	2.90	2.18	3.12	4.21
Ce_2O_3	11.13	8.60	9.92	9.35	9.76	12.35	12.96	7.74	8.81	7.66	9.21	9.54	11.45	13.18	15.62	15.02	8.31	11.83	14.48	12.91	7.79	9.23	8.86	6.54	8.86	11.07
Pr_2O_3	1.52	1.19	1.48	1.28	1.41	1.61	1.68	0.86	1.03	0.82	1.00	0.98	1.30	1.43	1.72	1.60	0.94	1.24	1.54	1.43	0.92	0.99	0.95	0.79	0.95	1.21
Nd_2O_3	5.41	3.90	4.91	4.51	4.77	5.63	5.62	3.71	4.42	3.44	4.08	4.39	4.84	5.76	6.82	6.25	3.94	5.37	6.30	5.67	3.65	3.88	3.85	3.01	4.15	5.28
Sm_2O_3	0.58	0.42	0.44	0.41	0.54	0.45	0.32	0.29	0.45	0.31	0.32	0.39	0.39	0.43	0.53	0.44	0.40	0.44	0.49	0.44	0.36	0.26	0.29	0.20	0.45	0.49
Eu_2O_3	bdl	bdl	bdl	bdl	bdl	bdl	bdl	bdl	bdl	0.07	bdl	bdl	bdl	bdl	bdl	bdl	bdl	bdl	bdl	bdl	bdl	bdl	bdl	bdl	bdl	0.07
Gd_2O_3	0.25	0.10	0.11	0.12	0.12	0.10	0.07	0.35	0.55	0.41	0.50	0.51	0.49	0.57	0.74	0.62	0.44	0.62	0.66	0.60	0.32	0.32	0.44	0.35	0.47	0.55
Tb_2O_3	bdl	bdl	bdl	bdl	bdl	0.07	0.08	bdl	bdl	bdl	bdl	bdl	bdl	bdl	bdl	bdl	bdl	bdl	bdl	bdl	bdl	bdl	bdl	bdl	bdl	bdl
Dy_2O_3	bdl	bdl	bdl	bdl	bdl	bdl	bdl	0.07	bdl	bdl	0.08	0.09	bdl	bdl	bdl	bdl	0.08	bdl	bdl	bdl	0.14	bdl	0.10	0.17	0.11	0.11
Ho_2O_3	bdl	bdl	bdl	bdl	bdl	bdl	bdl	bdl	bdl	bdl	bdl	bdl	bdl	bdl	bdl	bdl	bdl	bdl	bdl	bdl	bdl	bdl	bdl	bdl	bdl	bdl
Er_2O_3	bdl	bdl	bdl	bdl	bdl	bdl	bdl	bdl	bdl	bdl	bdl	bdl	bdl	bdl	bdl	bdl	bdl	bdl	bdl	bdl	bdl	bdl	bdl	bdl	bdl	bdl
Tm_2O_3	bdl	bdl	bdl	bdl	bdl	bdl	bdl	bdl	bdl	bdl	bdl	bdl	bdl	bdl	bdl	bdl	bdl	bdl	bdl	bdl	bdl	bdl	bdl	bdl	bdl	bdl
Yb_2O_3	bdl	bdl	bdl	bdl	bdl	bdl	bdl	bdl	bdl	bdl	bdl	bdl	bdl	bdl	bdl	bdl	bdl	bdl	bdl	bdl	bdl	bdl	bdl	bdl	bdl	bdl
Lu_2O_3	bdl	bdl	bdl	bdl	bdl	bdl	bdl	bdl	bdl	bdl	bdl	bdl	bdl	bdl	bdl	bdl	bdl	bdl	bdl	bdl	bdl	bdl	bdl	bdl	bdl	bdl
Y_2O_3	0.08	bdl	0.09	0.08	0.08	bdl	bdl	bdl	0.08	bdl	bdl	bdl	bdl	bdl	bdl	bdl	bdl	bdl	bdl	bdl	bdl	bdl	bdl	bdl	bdl	0.11
ZrO_2	bdl	bdl	bdl	bdl	bdl	bdl	bdl	bdl	bdl	bdl	bdl	bdl	bdl	bdl	bdl	bdl	bdl	bdl	bdl	bdl	bdl	bdl	bdl	bdl	bdl	bdl
HfO_2	bdl	bdl	bdl	bdl	bdl	bdl	bdl	bdl	bdl	bdl	bdl	bdl	bdl	bdl	bdl	bdl	bdl	bdl	bdl	bdl	bdl	bdl	bdl	bdl	bdl	bdl
Nb_2O_5	bdl	bdl	bdl	bdl	bdl	bdl	bdl	bdl	bdl	bdl	bdl	bdl	bdl	bdl	bdl	bdl	bdl	bdl	bdl	bdl	bdl	bdl	bdl	bdl	bdl	bdl
Sc_2O_3	bdl	bdl	bdl	bdl	bdl	bdl	bdl	bdl	bdl	bdl	bdl	bdl	bdl	bdl	bdl	bdl	bdl	bdl	bdl	bdl	bdl	bdl	bdl	bdl	bdl	bdl
ThO_2	0.61	0.70	0.66	0.62	0.65	0.23	0.28	0.34	0.46	0.35	0.31	0.31	0.37	0.32	0.31	0.28	0.35	0.49	0.40	0.40	0.43	0.30	0.29	0.35	0.51	0.43
UO_2	bdl	bdl	bdl	bdl	bdl	bdl	bdl	bdl	bdl	bdl	bdl	bdl	bdl	bdl	bdl	bdl	bdl	bdl	bdl	bdl	bdl	bdl	bdl	bdl	bdl	bdl
P_2O_5	bdl	bdl	bdl	bdl	bdl	bdl	bdl	bdl	bdl	bdl	bdl	bdl	bdl	bdl	bdl	bdl	bdl	bdl	bdl	bdl	bdl	bdl	bdl	bdl	bdl	bdl
SO_3	0.12	bdl	bdl	bdl	bdl	bdl	bdl	bdl	bdl	bdl	bdl	bdl	bdl	bdl	bdl	bdl	bdl	bdl	bdl	bdl	bdl	bdl	bdl	bdl	bdl	0.10
F	bdl	bdl	bdl	bdl	bdl	bdl	bdl	bdl	bdl	bdl	bdl	bdl	bdl	bdl	bdl	bdl	bdl	bdl	bdl	bdl	bdl	bdl	bdl	bdl	bdl	bdl
Cl	0.06	0.03	0.06	0.05	0.05	0.72	0.63	0.03	0.07	0.03	0.03	0.04	0.03	0.03	0.03	0.02	0.08	0.02	0.03	0.03	0.04	0.02	0.02	0.02	0.03	0.09
TOTAL	93.29	88.38	89.66	92.25	90.42	95.37	95.07	85.68	89.43	91.26	87.86	88.83	87.66	85.33	86.81	85.47	90.28	86.07	85.00	87.49	89.21	82.95	90.14	89.34	89.22	91.44
TREO	23.56	17.45	20.94	19.33	20.55	25.69	26.39	15.63	18.54	15.30	18.42	19.28	22.41	25.80	30.85	29.13	17.04	23.52	28.45	25.53	15.83	17.82	17.38	13.23	18.09	23.09

Table B.23 cont.

SAMPLE	517458-3-236	517458-3-237	517458-3-238	517458-3-239	517458-3-241	517458-3-242	517458-3-243	517458-3-244	517458-3-246	517458-3-247	517458-3-248	517458-3-249	517458-3-250	517458-3-251	517458-3-254	517458-3-255	517458-3-256	517458-3-257	517458-3-258	517458-3-259	517458-3-260	517458-3-261	517458-3-264	517458-3-265	517458-3-266	517458-3-268
SiO_2	32.54	33.36	33.32	29.67	36.50	31.74	35.38	33.32	24.92	32.19	34.87	36.79	33.54	35.58	30.22	32.01	32.28	32.89	35.18	30.70	30.47	34.81	30.84	32.19	32.91	33.51
Al_2O_3	15.18	14.88	14.50	13.16	15.55	13.67	15.85	15.71	11.15	12.98	14.54	15.06	13.58	14.27	13.33	14.98	14.24	14.08	15.16	12.94	13.59	15.25	13.21	14.71	14.64	14.58
Na_2O	0.11	0.08	0.06	bdl	0.05	0.04	0.09	0.10	0.05	0.07	0.08	0.11	0.05	0.06	0.03	0.12	0.13	0.03	0.04	0.11	0.03	0.05	0.16	0.09	0.10	0.04
K_2O	0.03	0.06	0.12	0.10	0.22	0.08	0.04	0.04	bdl	0.98	0.37	0.54	0.42	0.59	0.07	0.02	bdl	0.04	0.04	0.02	0.07	0.13	bdl	0.03	0.05	0.05
CaO	7.45	6.59	5.49	4.43	4.30	6.05	7.19	7.43	5.22	3.11	4.80	5.01	3.48	3.54	6.26	8.97	8.77	6.44	6.97	8.43	4.95	5.58	9.81	7.83	7.96	6.48
MgO	0.55	0.99	4.49	5.22	9.19	2.29	1.30	0.49	0.56	3.29	5.71	3.17	7.08	6.14	0.85	0.55	0.55	1.71	0.62	0.69	4.73	6.47	0.83	0.80	0.65	0.45
FeO	8.57	7.45	7.32	6.30	8.15	6.93	7.66	8.18	4.44	9.78	7.67	8.73	9.54	9.99	6.15	9.63	10.46	6.83	6.69	10.31	6.35	7.63	11.88	8.64	8.75	6.39
MnO	0.82	0.79	0.70	0.61	0.76	0.74	0.84	0.83	0.53	0.48	0.67	0.72	0.70	0.72	0.73	0.89	0.75	0.82	0.85	0.79	0.65	0.82	0.58	0.76	0.75	0.86
BaO	0.85	1.59	2.11	1.82	1.72	2.08	1.70	0.97	1.88	2.38	1.92	2.37	1.91	2.17	1.91	0.17	0.40	2.43	2.40	0.74	1.54	1.87	0.08	0.75	1.12	2.42
SrO	0.96	1.40	1.95	3.30	0.69	2.29	0.86	0.91	5.29	3.06	1.78	0.78	0.45	0.46	2.67	0.81	0.83	1.52	0.97	1.04	0.81	0.72	0.71	0.97	1.02	1.01
TiO_2	0.38	0.32	0.29	0.19	0.28	0.29	0.37	0.32	0.22	0.20	0.23	0.27	0.18	0.20	0.30	0.36	0.29	0.35	0.36	0.27	0.20	0.30	0.30	0.34	0.39	0.44
Cr_2O_3	0.09	0.08	0.09	0.09	bdl	0.06	0.09	0.12	0.14	bdl	0.05	bdl	bdl	bdl	0.09	0.12	0.09	0.08	0.09	0.11	0.09	0.07	0.12	0.06	0.08	0.06
La_2O_3	4.28	3.75	3.07	3.45	1.59	3.55	3.40	4.00	5.51	2.60	2.64	1.88	1.21	1.28	4.26	4.32	4.07	3.13	3.06	4.25	4.35	2.38	4.52	4.03	3.94	3.26
Ce_2O_3	11.21	10.63	9.21	10.67	4.43	10.09	9.48	10.87	15.97	8.00	7.58	5.78	3.57	3.78	12.17	11.41	10.68	9.17	8.86	11.44	11.45	6.83	11.25	10.63	10.41	9.08
Pr_2O_3	1.29	1.24	0.93	1.13	0.47	1.15	1.15	1.27	1.80	0.89	0.82	0.67	0.36	0.41	1.35	1.33	1.34	1.02	0.93	1.33	1.37	0.79	1.22	1.16	1.25	1.09
Nd_2O_3	5.30	4.98	4.28	4.73	2.28	4.56	4.37	5.11	6.65	3.41	3.58	2.60	1.57	1.60	5.42	5.62	5.23	4.20	4.05	5.45	6.37	3.13	5.32	4.96	4.96	4.34
Sm_2O_3	0.52	0.49	0.39	0.41	0.23	0.43	0.47	0.56	0.48	0.28	0.27	0.26	0.15	0.12	0.47	0.53	0.53	0.42	0.41	0.47	0.65	0.32	0.45	0.47	0.46	0.41
Eu_2O_3	0.07	bdl	bdl	bdl	bdl	bdl	bdl	bdl	bdl	bdl	bdl	bdl	bdl	bdl	bdl	bdl	bdl	bdl	bdl	bdl	bdl	bdl	bdl	bdl	bdl	bdl
Gd_2O_3	0.59	0.62	0.51	0.53	0.23	0.45	0.53	0.59	0.66	0.31	0.39	0.29	0.16	0.14	0.55	0.58	0.50	0.44	0.43	0.58	0.67	0.36	0.52	0.38	0.48	0.51
Tb_2O_3	bdl	bdl	bdl	bdl	bdl	bdl	bdl	bdl	bdl	bdl	bdl	bdl	bdl	bdl	bdl	bdl	bdl	bdl	bdl	bdl	bdl	bdl	bdl	bdl	bdl	bdl
Dy_2O_3	0.08	0.10	0.11	bdl	0.16	bdl	0.12	bdl	bdl	bdl	0.07	0.16	0.12	0.07	bdl	bdl	0.11	0.07	0.10	bdl	bdl	0.13	bdl	bdl	0.09	0.07
Ho_2O_3	bdl	bdl	bdl	bdl	bdl	bdl	bdl	bdl	bdl	bdl	bdl	bdl	bdl	bdl	bdl	bdl	bdl	bdl	bdl	bdl	bdl	bdl	bdl	bdl	bdl	bdl
Er_2O_3	bdl	bdl	bdl	bdl	bdl	bdl	bdl	bdl	bdl	bdl	bdl	bdl	bdl	bdl	bdl	bdl	bdl	bdl	bdl	bdl	bdl	bdl	bdl	bdl	bdl	bdl
Tm_2O_3	bdl	bdl	bdl	bdl	bdl	bdl	bdl	bdl	bdl	bdl	bdl	bdl	bdl	bdl	bdl	bdl	bdl	bdl	bdl	bdl	bdl	bdl	bdl	bdl	bdl	bdl
Yb_2O_3	bdl	bdl	bdl	bdl	bdl	bdl	bdl	bdl	bdl	bdl	bdl	bdl	bdl	bdl	bdl	bdl	bdl	bdl	bdl	bdl	bdl	bdl	bdl	bdl	bdl	bdl
Lu_2O_3	bdl	bdl	bdl	bdl	bdl	bdl	bdl	bdl	bdl	bdl	bdl	bdl	bdl	bdl	bdl	bdl	bdl	bdl	bdl	bdl	bdl	bdl	bdl	bdl	bdl	bdl
Y_2O_3	0.08	0.08	bdl	bdl	bdl	bdl	bdl	0.08	bdl	bdl	bdl	bdl	bdl	bdl	0.13	0.06	bdl	bdl	bdl	bdl	bdl	bdl	bdl	bdl	bdl	0.08
ZrO_2	bdl	bdl	bdl	bdl	bdl	bdl	bdl	bdl	bdl	bdl	bdl	bdl	bdl	bdl	bdl	bdl	bdl	bdl	bdl	bdl	bdl	bdl	bdl	bdl	bdl	bdl
HfO_2	bdl	bdl	bdl	bdl	bdl	bdl	bdl	bdl	bdl	bdl	bdl	bdl	bdl	bdl	bdl	bdl	bdl	bdl	bdl	bdl	bdl	bdl	bdl	bdl	bdl	bdl
Nb_2O_5	bdl	bdl	bdl	bdl	bdl	bdl	bdl	bdl	bdl	bdl	bdl	bdl	bdl	bdl	bdl	bdl	bdl	bdl	bdl	bdl	bdl	bdl	bdl	bdl	bdl	bdl
Sc_2O_3	bdl	bdl	bdl	bdl	bdl	bdl	bdl	bdl	bdl	bdl	bdl	bdl	bdl	bdl	bdl	bdl	bdl	bdl	bdl	bdl	bdl	bdl	bdl	bdl	bdl	bdl
ThO_2	0.42	0.49	0.52	0.56	0.52	0.49	0.46	0.46	0.40	0.39	0.47	0.44	0.19	0.34	0.49	0.45	0.52	0.67	0.71	0.49	0.70	0.55	0.38	0.58	0.67	0.68
UO_2	bdl	bdl	bdl	bdl	bdl	bdl	bdl	bdl	bdl	bdl	bdl	bdl	bdl	bdl	bdl	bdl	bdl	bdl	bdl	bdl	bdl	bdl	bdl	bdl	bdl	bdl
P_2O_5	bdl	bdl	bdl	bdl	bdl	bdl	bdl	bdl	bdl	bdl	bdl	bdl	bdl	bdl	bdl	bdl	bdl	bdl	bdl	bdl	bdl	bdl	bdl	bdl	bdl	bdl
SO_3	0.08	bdl	bdl	bdl	bdl	bdl	bdl	0.06	bdl	bdl	bdl	bdl	bdl	bdl	bdl	0.07	bdl	bdl	bdl	bdl	bdl	bdl	bdl	0.05	bdl	bdl
F	bdl	bdl	bdl	bdl	bdl	bdl	bdl	bdl	bdl	bdl	bdl	bdl	bdl	bdl	bdl	bdl	bdl	bdl	bdl	bdl	bdl	bdl	bdl	bdl	bdl	bdl
Cl	0.08	0.05	0.03	0.03	0.02	0.04	0.07	0.07	0.02	0.02	0.04	0.02	0.02	0.02	0.03	0.25	0.28	0.02	0.02	0.28	0.06	0.03	0.51	0.17	0.21	0.02
TOTAL	91.51	90.00	89.49	86.42	87.33	87.03	91.41	91.46	85.88	84.42	88.54	85.65	78.28	81.47	87.48	93.19	91.99	86.33	87.93	90.38	89.09	88.22	92.59	89.57	90.82	85.82
TREO	23.34	21.81	18.50	20.93	9.39	20.23	19.53	22.39	31.06	15.48	15.34	11.65	7.14	7.41	24.23	23.79	22.45	18.45	17.84	23.52	24.86	13.95	23.30	21.64	21.58	18.76

Table B.23 cont.

SAMPLE	517458-3-269	517458-3-270	517458-3-271	517458-3-272	517458-3-273	517458-3-274	517458-3-275	517458-3-276	517458-3-277	517458-3-278	517458-3-279	517458-3-280	517458-3-281	517458-3-282	517458-3-283	517458-3-284	517458-3-285	517458-3-286	517458-3-288	517458-3-289	517458-3-291	517458-3-292	517458-3-293	517458-3-294	517458-3-295	517458-3-296
SiO_2	34.02	33.46	30.97	30.95	32.66	32.54	34.56	31.97	32.36	32.85	32.18	34.65	32.04	33.96	34.94	31.31	29.13	33.15	29.31	33.72	33.27	34.27	34.50	33.75	34.13	32.32
Al_2O_3	15.81	15.63	13.20	13.43	15.51	14.15	15.98	13.23	13.97	14.27	13.83	15.55	14.61	15.43	15.45	14.67	12.55	14.40	12.72	15.41	16.33	16.22	15.64	15.18	16.09	15.23
Na_2O	0.11	0.14	0.18	0.15	0.11	0.08	0.05	0.11	0.13	0.08	0.09	0.05	0.09	0.07	0.12	0.05	0.06	0.04	0.09	0.10	0.12	0.08	0.07	0.10	0.08	0.05
K_2O	0.05	0.05	bdl	bdl	0.05	0.06	0.07	0.09	0.10	0.08	0.11	0.05	0.07	0.08	0.12	0.08	0.07	0.05	0.17	0.15	0.05	0.10	0.11	0.08	0.06	0.10
CaO	7.49	8.28	9.59	9.77	7.74	7.67	6.10	6.50	7.58	6.44	6.23	6.77	6.32	6.74	6.21	12.23	6.19	6.62	2.87	5.82	8.46	6.87	6.84	6.93	8.10	6.46
MgO	1.91	0.68	0.80	0.61	0.51	0.44	0.58	0.40	1.14	0.47	0.94	0.51	2.68	0.99	2.33	1.60	0.56	0.71	7.82	5.15	0.45	2.14	1.28	2.74	0.38	1.22
FeO	8.29	8.52	11.92	11.40	8.53	9.09	7.36	5.67	7.49	5.58	5.77	6.47	6.56	6.80	6.93	8.44	5.55	6.00	6.51	6.84	7.81	7.15	7.22	7.60	8.29	7.19
MnO	0.82	0.82	0.59	0.64	0.79	0.70	0.70	0.89	0.83	0.84	0.82	0.83	0.77	0.87	0.90	0.54	0.77	0.86	0.64	0.79	0.79	0.79	0.82	0.72	0.73	0.80
BaO	0.90	0.87	0.08	0.06	0.58	1.31	1.43	3.20	2.44	3.03	2.95	2.18	1.72	1.88	2.26	1.47	2.87	2.61	1.22	1.63	1.05	1.66	1.86	1.55	1.41	1.55
SrO	0.94	0.83	0.62	0.76	0.90	1.00	0.93	1.30	1.05	1.38	1.47	1.16	2.17	1.37	0.90	1.60	2.23	1.37	0.43	0.85	1.15	0.93	0.99	1.07	1.15	1.04
TiO_2	0.34	0.38	0.34	0.39	0.42	0.41	0.42	0.44	0.37	0.39	0.37	0.35	0.27	0.32	0.31	0.15	0.31	0.33	0.09	0.25	0.26	0.27	0.26	0.20	0.19	0.14
Cr_2O_3	0.09	0.11	0.08	0.12	0.10	0.09	0.09	0.06	0.09	0.07	0.05	0.09	0.07	0.10	0.08	bdl	0.06	0.05	bdl	0.08	0.12	0.08	0.09	0.08	0.09	0.07
La_2O_3	3.95	4.01	4.58	4.50	4.24	3.86	3.53	2.46	3.28	2.97	2.72	3.46	3.76	3.57	2.64	2.51	3.32	3.12	1.28	2.98	3.74	3.10	3.06	3.32	3.33	2.80
Ce_2O_3	10.53	10.42	11.41	11.53	11.18	10.56	10.01	7.56	8.78	8.79	8.15	9.65	10.67	10.24	7.72	6.89	10.36	9.43	3.81	8.49	9.95	8.54	8.64	8.18	9.04	8.05
Pr_2O_3	1.26	1.19	1.31	1.24	1.20	1.20	1.10	0.93	0.98	1.05	0.92	1.14	1.29	1.26	0.83	0.74	1.16	1.06	0.38	1.00	1.21	1.01	1.01	0.99	1.07	0.89
Nd_2O_3	4.98	4.93	5.50	5.61	5.16	5.09	5.14	3.83	4.21	4.52	3.84	4.86	4.83	4.92	3.83	3.29	4.83	4.26	1.79	4.23	4.85	4.35	4.51	4.37	4.76	4.42
Sm_2O_3	0.47	0.48	0.48	0.48	0.50	0.46	0.59	0.38	0.42	0.50	0.35	0.51	0.49	0.51	0.39	0.28	0.47	0.44	0.12	0.45	0.48	0.47	0.54	0.46	0.57	0.48
Eu_2O_3	bdl	bdl	bdl	bdl	bdl	bdl	0.06	bdl	bdl	bdl	bdl	bdl	bdl	bdl	bdl	bdl	bdl	bdl	bdl	bdl	bdl	0.08	0.07	bdl	0.08	0.09
Gd_2O_3	0.49	0.59	0.51	0.49	0.47	0.53	0.52	0.38	0.46	0.51	0.34	0.54	0.52	0.53	0.41	0.38	0.53	0.42	0.07	0.47	0.52	0.46	0.43	0.39	0.58	0.40
Tb_2O_3	bdl	bdl	bdl	bdl	bdl	bdl	bdl	bdl	bdl	bdl	bdl	bdl	bdl	bdl	bdl	bdl	bdl	bdl	bdl	bdl	bdl	bdl	bdl	bdl	bdl	bdl
Dy_2O_3	0.10	0.09	bdl	bdl	bdl	0.09	0.08	bdl	bdl	bdl	0.08	0.12	bdl	0.08	0.07	bdl	bdl	0.13	0.06	0.11	0.14	0.08	0.11	0.10	0.08	0.09
Ho_2O_3	bdl	bdl	bdl	bdl	bdl	bdl	bdl	bdl	bdl	bdl	bdl	bdl	bdl	bdl	bdl	bdl	bdl	bdl	bdl	bdl	bdl	bdl	bdl	bdl	bdl	bdl
Er_2O_3	bdl	bdl	bdl	bdl	bdl	bdl	bdl	bdl	bdl	bdl	bdl	bdl	bdl	bdl	bdl	bdl	bdl	bdl	bdl	bdl	bdl	bdl	bdl	bdl	bdl	bdl
Tm_2O_3	bdl	bdl	bdl	bdl	bdl	bdl	bdl	bdl	bdl	bdl	bdl	bdl	bdl	bdl	bdl	bdl	bdl	bdl	bdl	bdl	bdl	bdl	bdl	bdl	bdl	bdl
Yb_2O_3	bdl	bdl	bdl	bdl	bdl	bdl	bdl	bdl	bdl	bdl	bdl	bdl	bdl	bdl	bdl	bdl	bdl	bdl	bdl	bdl	bdl	bdl	bdl	bdl	bdl	bdl
Lu_2O_3	bdl	bdl	bdl	bdl	bdl	bdl	bdl	bdl	bdl	bdl	bdl	bdl	bdl	bdl	bdl	bdl	bdl	bdl	bdl	bdl	bdl	bdl	bdl	bdl	bdl	bdl
Y_2O_3	0.08	0.06	bdl	0.07	0.06	bdl	0.10	bdl	0.07	bdl	0.06	bdl	bdl	bdl	bdl	bdl	bdl	bdl	bdl	bdl	0.12	0.06	bdl	0.06	0.07	0.06
ZrO_2	bdl	bdl	bdl	bdl	bdl	bdl	bdl	bdl	bdl	bdl	bdl	bdl	bdl	bdl	bdl	bdl	bdl	bdl	bdl	bdl	bdl	bdl	bdl	bdl	bdl	bdl
HfO_2	bdl	bdl	bdl	bdl	bdl	bdl	bdl	bdl	bdl	bdl	bdl	bdl	bdl	bdl	bdl	bdl	bdl	bdl	bdl	bdl	bdl	bdl	bdl	bdl	bdl	bdl
Nb_2O_5	bdl	bdl	bdl	bdl	bdl	bdl	bdl	bdl	bdl	bdl	bdl	bdl	bdl	bdl	bdl	bdl	bdl	bdl	bdl	bdl	bdl	bdl	bdl	bdl	bdl	bdl
Sc_2O_3	bdl	bdl	bdl	bdl	bdl	bdl	bdl	bdl	bdl	bdl	bdl	bdl	bdl	bdl	bdl	bdl	bdl	bdl	bdl	bdl	bdl	bdl	bdl	bdl	bdl	0.04
ThO_2	0.54	0.60	0.37	0.37	0.62	0.68	0.91	1.20	0.81	1.01	0.72	0.56	0.46	0.58	0.53	0.72	0.66	0.60	0.22	0.36	0.38	0.68	0.84	0.73	0.71	0.74
UO_2	bdl	bdl	bdl	bdl	bdl	bdl	bdl	bdl	bdl	bdl	bdl	bdl	bdl	bdl	bdl	bdl	bdl	bdl	bdl	bdl	bdl	bdl	bdl	bdl	bdl	bdl
P_2O_5	bdl	bdl	bdl	bdl	bdl	bdl	bdl	bdl	bdl	bdl	bdl	bdl	bdl	bdl	bdl	bdl	bdl	bdl	0.06	bdl	bdl	bdl	bdl	bdl	bdl	bdl
SO_3	0.04	bdl	bdl	bdl	0.07	bdl	0.09	bdl	bdl	bdl	bdl	bdl	bdl	bdl	bdl	bdl	bdl	bdl	bdl	bdl	bdl	bdl	0.05	0.15	0.08	0.09
F	bdl	bdl	bdl	bdl	bdl	bdl	bdl	bdl	bdl	bdl	bdl	bdl	bdl	bdl	bdl	bdl	bdl	bdl	bdl	bdl	bdl	bdl	bdl	bdl	bdl	bdl
Cl	0.16	0.22	0.50	0.48	0.20	0.12	0.03	0.02	0.03	0.03	0.02	0.03	0.07	0.04	0.04	0.03	0.02	0.02	0.13	0.04	0.11	0.06	0.06	0.07	0.13	0.04
TOTAL	93.34	92.29	92.91	92.95	91.54	90.11	90.44	80.60	86.58	84.84	82.01	89.53	89.44	90.32	86.97	86.98	81.71	85.65	69.77	88.90	91.33	89.46	88.99	88.79	91.14	84.36
TREO	21.86	21.76	23.78	23.91	22.81	21.79	21.14	15.53	18.20	18.34	16.46	20.28	21.56	21.12	15.89	14.09	20.67	18.85	7.51	17.73	21.02	18.16	18.37	17.87	19.57	17.30

Table B.23 cont.

SAMPLE	517458-3-297	517458-3-298	517458-3-299	517458-3-300	517458-3-301	517458-3-302	517458-3-304	517458-3-305	517458-3-306	517458-3-307	517458-3-308	517458-3-309	517458-3-310	517458-3-311	517458-3-312	517458-3-313	517458-3-314	517458-3-315	517458-3-316	517458-3-317	517458-3-318	517458-3-319	517458-3-320	517458-3-321	517458-3-322	517458-3-325
SiO_2	32.83	30.15	36.72	32.18	32.59	33.60	34.14	31.28	35.03	33.90	34.18	33.59	32.63	32.45	30.96	30.87	33.67	33.19	32.93	33.25	32.78	33.38	35.97	34.82	25.80	31.10
Al_2O_3	14.75	13.23	17.15	14.17	14.74	16.01	16.19	14.08	16.08	15.94	16.18	16.10	16.91	16.82	14.92	13.91	16.63	17.41	17.44	17.59	14.55	16.98	16.36	15.36	11.13	13.48
Na_2O	0.03	0.02	0.08	0.03	0.03	0.09	0.04	bdl	0.05	0.06	0.06	0.06	0.11	0.14	bdl	0.12	0.08	0.14	0.12	0.13	0.10	0.09	0.06	0.05	0.03	0.10
K_2O	0.42	0.12	0.09	0.17	0.07	0.07	0.09	0.05	0.07	0.05	0.05	0.06	0.03	0.02	bdl	bdl	bdl	bdl	bdl	bdl	0.04	0.02	bdl	bdl	bdl	bdl
CaO	3.30	5.92	6.59	6.46	6.56	7.07	6.32	6.37	6.75	7.07	7.05	6.78	8.80	10.74	12.45	11.32	8.83	11.99	12.98	12.61	7.93	10.38	7.84	7.41	6.12	9.24
MgO	7.65	1.75	1.13	1.34	0.38	1.01	1.17	0.32	0.42	0.58	0.41	0.36	0.47	0.43	0.31	0.52	1.68	0.46	0.47	0.49	0.71	0.60	1.63	1.74	1.33	0.54
FeO	5.89	6.25	7.18	6.83	6.06	7.59	7.06	6.15	6.89	7.52	6.99	7.41	8.31	8.75	12.58	12.59	7.87	9.89	10.30	9.92	7.14	9.39	7.94	7.30	5.07	7.01
MnO	0.59	0.72	0.78	0.80	0.82	0.72	0.77	0.79	0.83	0.77	0.82	0.67	0.89	0.81	0.61	0.64	0.85	0.68	0.58	0.62	0.91	0.76	0.90	0.90	0.69	0.82
BaO	1.45	2.14	1.73	2.12	2.32	1.25	1.63	2.36	1.74	1.47	1.51	1.42	0.07	0.16	bdl	bdl	1.15	bdl	0.14	bdl	2.22	0.99	1.93	2.07	1.95	2.09
SrO	0.72	0.94	1.01	0.97	1.08	1.00	1.03	1.00	1.06	1.05	1.00	1.16	1.25	1.28	1.13	0.84	1.26	1.31	1.55	1.44	1.45	1.51	1.34	1.31	5.18	2.65
TiO_2	0.07	0.21	0.19	0.19	0.17	0.16	0.13	0.18	0.18	0.16	0.18	0.18	0.16	0.16	0.04	0.17	0.13	0.21	0.16	0.15	0.29	0.15	0.24	0.29	0.27	0.34
Cr_2O_3	bdl	0.06	0.08	0.08	0.08	0.07	0.09	bdl	0.07	0.06	0.08	0.05	0.06	0.05	0.11	0.09	0.04	0.06	0.07	0.05	0.06	0.05	0.05	0.05	0.12	0.08
La_2O_3	2.73	3.48	3.33	3.01	3.55	3.35	3.31	3.03	3.47	3.33	3.37	3.44	3.50	2.95	4.73	3.92	2.79	3.02	2.65	2.67	2.17	2.31	2.32	2.26	4.88	3.31
Ce_2O_3	7.76	9.82	9.11	8.36	9.92	9.30	9.21	8.95	9.80	9.69	9.69	9.65	9.59	8.33	9.85	9.81	7.64	7.73	7.07	7.25	6.98	6.62	6.57	6.66	14.57	9.25
Pr_2O_3	0.86	1.09	1.09	0.98	1.23	1.04	1.09	1.10	1.17	1.18	1.15	1.04	1.15	1.02	1.03	1.23	0.96	0.92	0.92	0.82	0.81	0.82	0.85	0.78	1.70	1.03
Nd_2O_3	4.43	5.16	4.97	4.27	5.51	5.11	5.07	4.75	5.05	5.15	5.23	5.18	5.39	4.64	4.67	5.53	4.09	4.13	4.13	4.18	3.71	4.05	3.49	3.56	6.55	4.55
Sm_2O_3	0.42	0.50	0.59	0.50	0.60	0.53	0.53	0.50	0.57	0.57	0.60	0.55	0.58	0.53	0.46	0.63	0.52	0.43	0.51	0.44	0.43	0.46	0.44	0.43	0.60	0.52
Eu_2O_3	bdl	0.08	0.12	bdl	0.09	0.09	0.09	bdl	bdl	bdl	0.08	bdl	0.07	0.06	0.09	0.22	0.08	bdl	0.08	0.08	0.07	0.11	bdl	bdl	bdl	bdl
Gd_2O_3	0.34	0.43	0.49	0.39	0.53	0.48	0.52	0.47	0.55	0.50	0.58	0.46	0.51	0.36	0.45	0.58	0.42	0.42	0.42	0.38	0.38	0.38	0.34	0.38	0.70	0.48
Tb_2O_3	bdl	bdl	bdl	bdl	bdl	bdl	bdl	bdl	bdl	bdl	bdl	bdl	bdl	bdl	bdl	0.07	bdl	bdl	bdl	bdl	bdl	bdl	bdl	bdl	bdl	bdl
Dy_2O_3	bdl	bdl	bdl	bdl	bdl	0.12	0.09	0.07	bdl	0.10	bdl	bdl	bdl	0.09	0.11	0.11	0.16	bdl	0.08	0.10	0.10	0.07	0.15	0.16	bdl	0.12
Ho_2O_3	bdl	bdl	bdl	bdl	bdl	bdl	bdl	bdl	bdl	bdl	bdl	bdl	bdl	bdl	bdl	bdl	bdl	bdl	bdl	bdl	bdl	bdl	bdl	bdl	bdl	bdl
Er_2O_3	bdl	bdl	bdl	bdl	bdl	bdl	bdl	bdl	bdl	bdl	bdl	bdl	bdl	bdl	bdl	bdl	bdl	bdl	bdl	bdl	bdl	bdl	bdl	bdl	bdl	bdl
Tm_2O_3	bdl	bdl	bdl	bdl	bdl	bdl	bdl	bdl	bdl	bdl	bdl	bdl	bdl	bdl	bdl	bdl	bdl	bdl	bdl	bdl	bdl	bdl	bdl	bdl	bdl	bdl
Yb_2O_3	bdl	bdl	bdl	bdl	bdl	bdl	bdl	bdl	bdl	bdl	bdl	bdl	bdl	bdl	bdl	bdl	bdl	bdl	bdl	bdl	bdl	bdl	bdl	bdl	bdl	bdl
Lu_2O_3	bdl	bdl	bdl	bdl	bdl	bdl	bdl	bdl	bdl	bdl	bdl	bdl	bdl	bdl	bdl	bdl	bdl	bdl	bdl	bdl	bdl	bdl	bdl	bdl	bdl	bdl
Y_2O_3	bdl	bdl	0.09	0.06	bdl	0.10	0.06	0.08	0.11	0.11	0.08	0.11	0.12	0.08	bdl	bdl	0.08	0.05	bdl	bdl	0.07	0.09	0.10	0.09	0.07	bdl
ZrO_2	bdl	bdl	bdl	bdl	bdl	bdl	bdl	bdl	bdl	bdl	bdl	bdl	bdl	bdl	bdl	bdl	bdl	bdl	bdl	bdl	bdl	bdl	bdl	bdl	bdl	bdl
HfO_2	bdl	bdl	bdl	bdl	bdl	bdl	bdl	bdl	bdl	bdl	bdl	bdl	bdl	bdl	bdl	bdl	bdl	bdl	bdl	bdl	bdl	bdl	bdl	bdl	bdl	bdl
Nb_2O_5	bdl	bdl	bdl	bdl	bdl	bdl	bdl	bdl	bdl	bdl	bdl	bdl	bdl	bdl	bdl	bdl	bdl	bdl	bdl	bdl	bdl	bdl	bdl	bdl	bdl	bdl
Sc_2O_3	bdl	bdl	bdl	0.03	bdl	bdl	bdl	bdl	bdl	0.03	bdl	bdl	bdl	bdl	bdl	bdl	bdl	bdl	bdl	bdl	0.04	bdl	0.04	0.05	bdl	bdl
ThO_2	0.60	0.83	0.87	0.76	1.01	0.71	0.74	0.91	0.75	0.71	0.73	0.77	0.47	0.48	bdl	0.12	0.52	0.24	0.13	0.20	1.12	0.57	0.88	0.96	1.52	1.18
UO_2	bdl	bdl	bdl	bdl	bdl	bdl	bdl	bdl	bdl	bdl	bdl	bdl	bdl	bdl	bdl	bdl	bdl	bdl	bdl	bdl	bdl	bdl	bdl	bdl	bdl	bdl
P_2O_5	bdl	bdl	bdl	bdl	bdl	bdl	bdl	bdl	bdl	bdl	bdl	bdl	bdl	bdl	bdl	bdl	bdl	bdl	bdl	bdl	bdl	bdl	bdl	bdl	bdl	1.92
SO_3	bdl	bdl	0.06	bdl	bdl	0.06	0.09	bdl	0.06	bdl	0.08	0.08	0.13	0.09	bdl	0.05	bdl	bdl	bdl	bdl	bdl	0.05	bdl	bdl	bdl	bdl
F	0.35	bdl	bdl	bdl	bdl	bdl	bdl	bdl	bdl	bdl	bdl	bdl	bdl	bdl	bdl	bdl	bdl	bdl	bdl	bdl	bdl	bdl	bdl	bdl	bdl	bdl
Cl	0.04	0.04	0.06	0.05	0.05	0.10	0.04	0.04	0.04	0.06	0.06	0.05	0.13	0.37	0.06	0.52	0.10	0.33	0.37	0.40	0.06	0.07	0.06	0.08	0.06	0.06
TOTAL	85.09	82.94	93.48	83.73	87.40	89.59	89.51	82.47	90.72	90.06	90.15	89.15	91.31	90.72	94.54	93.73	89.52	92.54	93.03	92.67	84.10	89.87	89.49	86.69	88.33	89.86
TREO	16.55	20.56	19.79	17.58	21.44	20.12	19.98	18.95	20.72	20.64	20.78	20.43	20.91	18.06	21.40	22.10	16.72	16.71	15.86	15.91	14.71	14.90	14.27	14.32	29.07	19.27

Table B.23 cont.

SAMPLE	517458-3-327	517458-3-328	517458-3-329	517458-3-330	517458-3-333	517458-3-334	517458-3-335	517458-3-336	517458-3-338	517458-3-339	517458-3-340	517458-3-341	517458-3-342	517458-3-343	517458-4-344	517458-4-345	517458-4-346	517458-4-347	517458-4-348	517458-4-349	517458-4-350	517458-4-351	517458-4-352	517458-4-354	517458-4-355	517458-4-356
SiO_2	30.98	28.75	33.17	32.89	33.29	32.45	32.43	32.99	35.68	32.69	35.52	35.83	35.52	33.92	32.78	33.02	32.79	33.15	33.33	35.76	29.14	33.36	33.71	28.00	27.80	28.15
Al_2O_3	13.57	12.66	17.93	17.42	17.93	17.42	16.93	17.61	16.20	16.21	16.39	16.31	16.21	18.15	17.40	17.40	17.78	17.83	16.80	16.06	13.07	15.52	17.65	12.04	12.29	12.19
Na_2O	0.03	0.06	0.13	0.09	0.12	0.12	0.13	0.12	0.03	0.06	0.07	0.04	0.09	0.10	0.11	0.09	0.15	0.11	0.11	bdl	0.10	0.04	0.09	bdl	bdl	bdl
K_2O	bdl	bdl	bdl	bdl	bdl	bdl	bdl	bdl	bdl	bdl	0.03	0.04	0.06	0.02	0.03	0.03	0.03	bdl	0.02	0.03	0.13	0.05	0.07	bdl	bdl	0.03
CaO	7.11	6.05	10.84	11.38	12.72	8.32	11.28	9.94	7.53	8.48	8.55	8.78	8.98	11.06	8.78	8.51	9.46	13.33	8.01	6.42	6.34	5.24	7.37	5.88	5.46	5.05
MgO	0.95	2.38	0.62	0.82	0.52	0.52	0.54	0.54	0.76	0.46	0.58	0.75	0.41	0.34	0.47	0.71	0.62	0.38	0.82	1.11	0.32	4.72	0.39	0.51	0.49	1.50
FeO	6.83	6.31	8.64	9.30	10.12	7.67	9.44	8.02	6.39	6.93	7.15	7.45	7.12	9.00	7.76	8.11	7.68	10.33	7.93	5.54	5.24	5.20	7.14	4.71	4.19	4.35
MnO	0.86	0.78	0.91	0.62	0.58	0.84	0.72	0.87	0.90	0.88	0.78	0.80	0.80	0.59	0.83	0.78	0.83	0.50	0.87	0.76	0.75	0.66	0.71	0.67	0.59	0.55
BaO	2.15	1.93	0.09	0.50	0.22	bdl	0.10	bdl	2.47	1.40	2.18	2.30	2.44	0.58	bdl	0.13	bdl	bdl	0.81	2.78	3.28	2.03	1.00	2.94	2.84	2.44
SrO	2.68	3.74	1.49	1.57	1.51	0.93	1.21	0.93	1.37	1.15	1.60	1.67	1.68	1.59	1.33	1.36	1.33	1.41	0.95	1.11	1.18	1.78	1.28	4.01	4.35	4.73
TiO_2	0.25	0.17	0.11	0.15	0.13	0.08	0.13	0.11	0.21	0.15	0.21	0.25	0.26	0.11	0.11	0.14	0.11	0.12	0.09	0.21	0.18	0.15	0.15	0.15	0.14	0.12
Cr_2O_3	0.08	0.11	bdl	0.04	0.04	0.09	0.05	0.09	bdl	0.05	0.05	bdl	0.05	bdl	0.07	0.06	0.09	bdl	0.07	0.05	bdl	bdl	0.06	0.05	0.05	0.09
La_2O_3	2.89	3.99	2.80	2.20	2.24	3.78	2.92	3.57	2.23	2.86	2.07	1.89	2.06	2.37	3.64	3.45	3.33	2.27	3.80	2.66	2.40	2.77	3.29	3.58	4.14	4.46
Ce_2O_3	8.91	11.64	7.34	6.25	6.52	10.96	7.89	9.87	6.81	7.91	5.78	5.38	5.51	6.51	9.65	9.09	9.42	6.40	10.03	7.32	7.08	8.20	9.17	10.47	12.24	12.47
Pr_2O_3	1.08	1.31	0.97	0.74	0.84	1.20	0.89	1.16	0.86	0.95	0.74	0.68	0.61	0.70	1.10	1.07	1.18	0.80	1.20	0.85	0.75	0.95	1.09	1.23	1.46	1.49
Nd_2O_3	4.55	5.50	4.38	3.77	4.08	5.32	4.43	5.25	3.80	4.28	3.19	2.84	2.96	3.59	5.31	5.19	5.28	3.68	5.40	3.90	3.48	4.23	4.97	5.46	6.12	6.25
Sm_2O_3	0.48	0.55	0.51	0.47	0.49	0.57	0.50	0.59	0.44	0.51	0.43	0.37	0.33	0.42	0.54	0.59	0.57	0.40	0.56	0.46	0.35	0.43	0.54	0.56	0.58	0.62
Eu_2O_3	0.07	bdl	0.07	0.08	0.09	0.10	0.08	0.09	0.06	0.08	bdl	bdl	bdl	0.07	0.07	0.06	0.07	bdl	bdl	bdl	bdl	bdl	bdl	bdl	0.09	0.08
Gd_2O_3	0.41	0.63	0.43	0.39	0.35	0.52	0.43	0.51	0.34	0.42	0.40	0.31	0.36	0.31	0.51	0.50	0.52	0.39	0.52	0.39	0.35	0.34	0.47	0.45	0.55	0.55
Tb_2O_3	bdl	bdl	bdl	bdl	bdl	bdl	bdl	bdl	bdl	bdl	bdl	bdl	bdl	bdl	bdl	bdl	bdl	bdl	bdl	bdl	bdl	bdl	bdl	bdl	bdl	bdl
Dy_2O_3	0.15	0.09	0.15	0.10	0.08	0.09	0.14	0.08	0.12	0.08	0.18	0.14	0.14	0.10	0.11	0.09	bdl	0.07	0.07	0.13	bdl	bdl	bdl	bdl	bdl	bdl
Ho_2O_3	bdl	bdl	bdl	bdl	bdl	bdl	bdl	bdl	bdl	bdl	bdl	bdl	bdl	bdl	bdl	bdl	bdl	bdl	bdl	bdl	bdl	bdl	bdl	bdl	bdl	bdl
Er_2O_3	bdl	bdl	bdl	bdl	bdl	bdl	bdl	bdl	bdl	bdl	bdl	bdl	bdl	bdl	bdl	bdl	bdl	bdl	bdl	bdl	bdl	bdl	bdl	bdl	bdl	bdl
Tm_2O_3	bdl	bdl	bdl	bdl	bdl	bdl	bdl	bdl	bdl	bdl	bdl	bdl	bdl	bdl	bdl	bdl	bdl	bdl	bdl	bdl	bdl	bdl	bdl	bdl	bdl	bdl
Yb_2O_3	bdl	bdl	bdl	bdl	bdl	bdl	bdl	bdl	bdl	bdl	bdl	bdl	bdl	bdl	bdl	bdl	bdl	bdl	bdl	bdl	bdl	bdl	bdl	bdl	bdl	bdl
Lu_2O_3	bdl	bdl	bdl	bdl	bdl	bdl	bdl	bdl	bdl	bdl	bdl	bdl	bdl	bdl	bdl	bdl	bdl	bdl	bdl	bdl	bdl	bdl	bdl	bdl	bdl	bdl
Y_2O_3	0.09	0.11	0.06	bdl	bdl	0.06	bdl	0.08	0.11	0.08	0.10	0.08	bdl	0.10	0.07	0.07	0.09	bdl	0.06	0.08	bdl	0.10	0.12	bdl	bdl	bdl
ZrO_2	bdl	bdl	bdl	bdl	bdl	bdl	bdl	bdl	bdl	bdl	bdl	bdl	bdl	bdl	bdl	bdl	bdl	bdl	bdl	bdl	bdl	bdl	bdl	bdl	bdl	bdl
HfO_2	bdl	bdl	bdl	bdl	bdl	bdl	bdl	bdl	bdl	bdl	bdl	bdl	bdl	bdl	bdl	bdl	bdl	bdl	bdl	bdl	bdl	bdl	bdl	bdl	bdl	bdl
Nb_2O_5	bdl	bdl	bdl	bdl	bdl	bdl	bdl	bdl	bdl	bdl	bdl	bdl	bdl	bdl	bdl	bdl	bdl	bdl	bdl	bdl	bdl	bdl	bdl	bdl	bdl	bdl
Sc_2O_3	0.05	bdl	bdl	bdl	bdl	bdl	bdl	bdl	bdl	0.03	0.05	0.05	0.08	0.06	bdl	bdl	bdl	bdl	bdl	0.03	bdl	bdl	0.03	bdl	bdl	bdl
ThO_2	1.35	2.45	0.36	0.38	0.30	0.41	0.38	0.42	1.02	0.75	1.00	0.99	0.97	0.46	0.31	0.32	0.30	0.21	0.18	0.70	0.96	1.14	0.68	1.20	0.90	0.87
UO_2	bdl	bdl	bdl	bdl	bdl	bdl	bdl	bdl	bdl	bdl	bdl	bdl	bdl	bdl	bdl	bdl	bdl	bdl	bdl	bdl	bdl	bdl	bdl	bdl	bdl	bdl
P_2O_5	bdl	bdl	bdl	bdl	bdl	bdl	0.05	bdl	bdl	bdl	bdl	bdl	0.04	bdl	bdl	bdl	bdl	bdl	bdl	bdl	bdl	bdl	bdl	bdl	bdl	0.06
SO_3	bdl	bdl	0.07	bdl	0.07	0.27	0.05	bdl	bdl	bdl	bdl	bdl	bdl	0.05	0.28	0.16	0.19	0.05	0.10	bdl	bdl	bdl	0.18	bdl	bdl	bdl
F	bdl	bdl	bdl	bdl	bdl	bdl	bdl	bdl	bdl	bdl	bdl	bdl	bdl	bdl	bdl	bdl	bdl	bdl	bdl	bdl	bdl	bdl	bdl	bdl	bdl	bdl
Cl	0.06	0.05	0.14	0.17	0.32	0.07	0.32	0.20	0.05	0.06	0.05	0.06	0.05	0.19	0.07	0.05	0.13	0.42	0.07	0.02	0.06	0.03	0.04	0.04	0.04	0.05
TOTAL	85.58	89.27	91.20	89.29	92.48	91.76	90.97	93.00	87.37	86.45	87.10	86.99	86.74	90.35	91.31	90.98	91.94	91.76	91.79	86.38	75.15	86.94	90.17	81.95	84.30	86.10
TREO	18.63	23.83	16.72	14.00	14.69	22.60	17.28	21.21	14.77	17.17	12.91	11.68	11.98	14.18	21.00	20.12	20.47	14.00	21.63	15.79	14.42	17.03	19.64	21.75	25.17	25.94

Table B.23 cont.

SAMPLE	517458-4-357	517458-4-358	517458-7-371	517458-7-372	517458-7-373	517458-7-374	517458-7-375	517458-7-376	517458-7-377	517458-7-378	517458-7-379	517458-7-380	517458-7-381	517458-7-382	517458-7-383	517458-7-384	517458-7-385	517458-7-386	517458-7-387	948521-1-208	948521-1-209	948521-2-222	948521-2-223	881319-3-278
SiO_2	31.57	36.18	29.85	29.52	31.71	33.81	33.25	33.17	33.75	31.84	33.13	26.51	28.72	34.24	27.71	33.82	30.86	31.28	32.32	33.40	24.52	32.37	35.49	32.56
Al_2O_3	13.60	16.27	11.53	10.49	15.22	15.78	16.79	17.37	17.42	15.63	16.31	10.11	12.35	13.60	11.16	13.63	12.22	14.41	15.07	16.87	11.22	16.15	18.63	13.28
Na_2O	0.03	0.04	0.08	0.07	0.08	0.09	0.14	0.09	0.09	0.10	0.09	0.02	0.06	0.08	0.03	0.10	0.09	0.09	0.09	bdl	bdl	bdl	bdl	0.30
K_2O	0.04	0.07	bdl	bdl	bdl	0.02	bdl	bdl	bdl	bdl	bdl	0.04	0.03	0.04	0.03	0.03	bdl	bdl	bdl	bdl	bdl	bdl	bdl	0.03
CaO	6.05	6.61	9.89	9.56	12.49	9.73	13.33	12.46	12.56	11.70	11.48	6.09	7.47	6.89	6.35	7.57	9.53	10.70	10.23	13.20	12.12	11.54	14.60	9.65
MgO	1.12	0.86	0.88	0.75	0.42	0.62	0.32	0.38	0.46	0.55	0.60	0.60	0.41	1.06	0.60	0.68	0.59	0.50	0.47	0.08	0.02	0.14	0.32	1.04
FeO	5.46	7.44	13.26	14.34	11.25	8.84	10.00	8.65	9.43	10.57	9.55	6.09	6.11	8.07	6.32	8.51	11.87	11.27	9.55	12.19	10.83	12.56	12.18	13.05
MnO	0.73	0.75	0.44	0.50	0.47	0.71	0.39	0.62	0.52	0.56	0.60	0.68	0.77	0.85	0.77	0.85	0.53	0.56	0.72	0.60	0.47	0.20	0.16	0.77
BaO	3.02	2.57	bdl	bdl	bdl	1.20	0.18	0.39	0.46	bdl	0.49	2.63	2.36	2.04	2.15	2.34	0.50	0.12	0.47	0.12	bdl	bdl	bdl	bdl
SrO	2.44	1.39	0.34	0.26	0.98	1.32	1.49	1.53	1.47	0.92	1.33	3.69	3.01	1.04	1.00	0.95	0.82	1.02	1.06	2.64	3.08	1.48	1.15	0.44
TiO_2	0.18	0.21	0.09	0.07	0.14	0.23	0.23	0.16	0.19	0.20	0.25	0.50	0.34	0.47	0.40	0.35	0.26	0.27	0.25	bdl	bdl	bdl	bdl	0.03
Cr_2O_3	0.09	0.05	0.13	0.11	0.07	0.05	0.04	0.04	0.07	0.10	bdl	0.11	0.09	0.11	0.08	0.09	0.13	0.06	0.08	bdl	bdl	bdl	bdl	bdl
La_2O_3	3.38	2.72	4.91	4.46	2.96	2.35	2.45	2.19	2.34	3.31	2.57	4.10	3.51	3.46	4.15	3.14	4.77	4.18	3.56	4.60	3.85	4.13	2.59	4.50
Ce_2O_3	9.13	7.59	13.22	13.07	8.77	8.08	7.17	6.87	6.62	9.30	7.51	13.07	11.50	9.67	11.54	8.85	11.26	9.98	9.31	8.06	8.16	9.22	6.86	11.28
Pr_2O_3	1.05	0.84	1.49	1.58	1.22	1.09	0.89	0.85	0.88	1.14	0.97	1.55	1.39	1.12	1.50	1.09	1.23	1.12	1.05	0.74	0.56	0.93	0.89	1.30
Nd_2O_3	4.88	4.03	6.06	6.46	5.30	4.88	4.14	4.23	3.82	5.28	4.45	6.07	5.59	4.63	6.34	4.70	5.21	4.89	4.56	2.68	2.23	3.22	3.70	5.00
Sm_2O_3	0.54	0.48	0.45	0.53	0.64	0.55	0.40	0.52	0.41	0.48	0.47	0.52	0.59	0.47	0.58	0.43	0.44	0.45	0.45	0.19	bdl	0.23	0.40	0.44
Eu_2O_3	bdl	0.08	bdl	bdl	bdl	bdl	bdl	0.11	0.08	0.11	bdl	bdl	0.06	bdl	bdl	bdl	bdl	bdl	bdl	bdl	bdl	bdl	bdl	0.07
Gd_2O_3	0.50	0.39	0.53	0.50	0.48	0.48	0.38	0.40	0.42	0.45	0.35	0.58	0.54	0.45	0.66	0.49	0.58	0.42	0.47	bdl	bdl	0.08	0.14	0.15
Tb_2O_3	bdl	bdl	bdl	0.08	bdl	bdl	bdl	bdl	bdl	bdl	bdl	bdl	bdl	bdl	bdl	bdl	bdl	bdl	bdl	0.13	0.09	0.12	0.09	0.12
Dy_2O_3	bdl	bdl	bdl	bdl	bdl	0.12	bdl	0.08	0.08	bdl	0.08	bdl	bdl	0.11	0.08	0.10	bdl	bdl	0.13	bdl	bdl	bdl	bdl	bdl
Ho_2O_3	bdl	bdl	bdl	bdl	bdl	bdl	bdl	bdl	bdl	bdl	bdl	bdl	bdl	bdl	bdl	bdl	bdl	bdl	bdl	bdl	bdl	bdl	bdl	bdl
Er_2O_3	bdl	bdl	bdl	bdl	bdl	bdl	bdl	bdl	bdl	bdl	bdl	bdl	bdl	bdl	bdl	bdl	bdl	bdl	bdl	bdl	bdl	bdl	bdl	bdl
Tm_2O_3	bdl	bdl	bdl	bdl	bdl	bdl	bdl	bdl	bdl	bdl	bdl	bdl	bdl	bdl	bdl	bdl	bdl	bdl	bdl	bdl	bdl	bdl	bdl	bdl
Yb_2O_3	bdl	bdl	bdl	bdl	bdl	bdl	bdl	bdl	bdl	bdl	bdl	bdl	bdl	bdl	bdl	bdl	bdl	bdl	bdl	bdl	bdl	bdl	bdl	bdl
Lu_2O_3	bdl	bdl	bdl	bdl	bdl	bdl	bdl	bdl	bdl	bdl	bdl	bdl	bdl	bdl	bdl	bdl	bdl	bdl	bdl	bdl	bdl	bdl	bdl	bdl
Y_2O_3	bdl	bdl	bdl	bdl	bdl	bdl	bdl	bdl	bdl	bdl	bdl	bdl	0.07	bdl	bdl	bdl	bdl	0.06	bdl	bdl	0.08	bdl	bdl	bdl
ZrO_2	bdl	bdl	bdl	bdl	bdl	bdl	bdl	bdl	bdl	bdl	bdl	bdl	bdl	bdl	bdl	bdl	bdl	bdl	bdl	bdl	bdl	bdl	bdl	bdl
HfO_2	bdl	bdl	bdl	bdl	bdl	bdl	bdl	bdl	bdl	bdl	bdl	bdl	bdl	bdl	bdl	bdl	bdl	bdl	bdl	bdl	bdl	bdl	bdl	bdl
Nb_2O_5	bdl	bdl	bdl	bdl	bdl	bdl	bdl	bdl	bdl	bdl	bdl	bdl	bdl	bdl	bdl	bdl	bdl	bdl	bdl	bdl	bdl	bdl	bdl	bdl
Sc_2O_3	bdl	bdl	bdl	bdl	bdl	bdl	bdl	bdl	bdl	bdl	bdl	bdl	bdl	bdl	bdl	bdl	bdl	bdl	bdl	bdl	bdl	bdl	bdl	bdl
ThO_2	0.88	0.80	0.10	0.13	0.20	0.60	0.36	0.46	0.31	0.40	0.31	1.16	1.13	0.86	1.09	0.76	0.46	0.27	0.45	bdl	bdl	bdl	bdl	bdl
UO_2	bdl	bdl	bdl	bdl	bdl	bdl	bdl	bdl	bdl	bdl	bdl	bdl	bdl	bdl	bdl	bdl	bdl	bdl	bdl	bdl	bdl	0.78	bdl	bdl
P_2O_5	bdl	bdl	bdl	bdl	bdl	bdl	bdl	bdl	bdl	bdl	bdl	bdl	bdl	bdl	bdl	bdl	bdl	bdl	bdl	bdl	0.16	bdl	bdl	bdl
SO_3	bdl	bdl	bdl	bdl	bdl	bdl	0.04	0.11	bdl	0.05	bdl	bdl	bdl	bdl	bdl	0.22	0.07	0.09	0.06	bdl	bdl	bdl	bdl	bdl
F	bdl	bdl	bdl	bdl	bdl	bdl	bdl	bdl	bdl	bdl	bdl	bdl	bdl	bdl	bdl	bdl	bdl	bdl	bdl	bdl	bdl	bdl	bdl	bdl
Cl	0.04	0.04	0.62	0.51	0.57	0.14	0.58	0.31	0.33	0.36	0.29	0.07	0.09	0.06	0.11	0.11	0.31	0.33	0.27	0.08	0.10	0.06	0.04	0.46
TOTAL	84.72	89.40	93.71	92.87	92.84	90.66	92.42	90.90	91.62	92.95	90.78	84.18	86.18	89.29	82.63	88.78	91.66	91.99	90.56	95.56	77.48	93.21	97.23	94.37
TREO	19.48	16.13	26.66	26.67	19.36	17.56	15.43	15.25	14.65	20.07	16.40	25.89	23.25	19.91	24.85	18.81	23.49	21.08	19.54	16.41	14.97	17.95	14.68	22.86

Table B.24 Composition of hyalophane, potassium feldspar and albite (in wt.%) in hyalophane-bearing pegmatites.

SAMPLE	881319-1-265	881319-1-266	881319-1-273	881319-3-275	517256-2-170	517256-2-173	881319-1-267	881319-1-268	517256-2-171	517256-2-172	517256-2-174	881319-1-269	881319-1-270	881319-1-271	881319-1-274	881319-3-277
SiO_2	57.77	57.03	59.23	55.63	65.78	67.45	60.82	61.47	70.37	69.66	69.75	68.50	68.72	68.38	68.84	69.74
Al_2O_3	21.36	21.74	20.87	22.17	18.37	18.13	19.92	19.90	19.29	19.17	18.86	19.93	21.05	20.54	20.21	20.81
Na_2O	1.62	1.79	1.47	1.52	0.87	0.02	0.95	1.03	9.47	9.52	9.56	10.45	9.40	10.51	10.10	9.63
K_2O	10.09	9.79	11.05	9.17	14.15	14.88	12.75	12.40	0.06	0.05	0.03	0.07	0.11	0.05	0.07	0.37
CaO	0.03	0.05	0.07	0.04	0.07	0.04	0.02	0.02	0.11	0.19	0.07	0.73	1.43	1.02	0.76	0.86
MgO	bdl*	bdl	bdl	bdl	bdl	bdl	bdl	bdl	bdl	bdl	bdl	bdl	bdl	bdl	bdl	0.02
FeO	0.04	0.03	0.36	0.02	0.02	0.08	0.04	0.03	0.05	0.06	0.12	0.03	0.04	0.03	0.02	0.19
MnO	bdl	bdl	bdl	bdl	bdl	bdl	bdl	bdl	bdl	bdl	bdl	bdl	bdl	bdl	bdl	bdl
BaO	7.81	8.47	6.00	9.87	0.44	0.05	4.78	4.80	bdl	bdl	bdl	bdl	bdl	bdl	bdl	bdl
SrO	2.46	2.27	1.86	2.71	0.23	bdl	1.06	1.11	0.10	0.16	0.11	0.49	0.83	0.54	0.55	0.53
TiO_2	0.06	0.06	0.05	0.06	bdl	bdl	0.05	0.03	bdl	bdl	bdl	bdl	bdl	bdl	bdl	bdl
Cr_2O_3	bdl	bdl	bdl	bdl	bdl	bdl	bdl	bdl	bdl	bdl	bdl	bdl	bdl	bdl	bdl	bdl
La_2O_3	bdl	bdl	bdl	bdl	bdl	bdl	bdl	bdl	bdl	bdl	bdl	bdl	bdl	bdl	bdl	bdl
Ce_2O_3	bdl	bdl	bdl	bdl	bdl	bdl	bdl	bdl	bdl	bdl	bdl	bdl	bdl	bdl	bdl	bdl
Pr_2O_3	bdl	bdl	bdl	bdl	bdl	bdl	bdl	bdl	bdl	bdl	bdl	bdl	bdl	bdl	bdl	bdl
Nd_2O_3	bdl	bdl	bdl	bdl	bdl	bdl	bdl	bdl	bdl	bdl	bdl	bdl	bdl	bdl	bdl	bdl
Sm_2O_3	bdl	bdl	bdl	bdl	bdl	bdl	bdl	bdl	bdl	bdl	bdl	bdl	bdl	bdl	bdl	bdl
Eu_2O_3	bdl	bdl	bdl	bdl	bdl	bdl	bdl	bdl	bdl	bdl	bdl	bdl	bdl	bdl	bdl	bdl
Gd_2O_3	bdl	bdl	bdl	bdl	bdl	bdl	bdl	bdl	bdl	bdl	bdl	bdl	bdl	bdl	bdl	bdl
Tb_2O_3	bdl	bdl	bdl	bdl	bdl	bdl	bdl	bdl	bdl	bdl	bdl	bdl	bdl	bdl	bdl	bdl
Dy_2O_3	bdl	bdl	bdl	bdl	bdl	bdl	bdl	bdl	bdl	bdl	bdl	bdl	bdl	bdl	bdl	bdl
Ho_2O_3	bdl	bdl	bdl	bdl	bdl	bdl	bdl	bdl	bdl	bdl	bdl	bdl	bdl	bdl	bdl	bdl
Er_2O_3	bdl	bdl	bdl	bdl	bdl	bdl	bdl	bdl	bdl	bdl	bdl	bdl	bdl	bdl	bdl	bdl
Tm_2O_3	bdl	bdl	bdl	bdl	bdl	bdl	bdl	bdl	bdl	bdl	bdl	bdl	bdl	bdl	bdl	bdl
Yb_2O_3	bdl	bdl	bdl	bdl	bdl	bdl	bdl	bdl	bdl	bdl	bdl	bdl	bdl	bdl	bdl	bdl
Lu_2O_3	bdl	bdl	bdl	bdl	bdl	bdl	bdl	bdl	bdl	bdl	bdl	bdl	bdl	bdl	bdl	bdl
Y_2O_3	bdl	bdl	0.07	bdl	bdl	bdl	bdl	bdl	bdl	0.07	bdl	bdl	bdl	bdl	bdl	bdl
ZrO_2	bdl	bdl	bdl	bdl	bdl	bdl	bdl	bdl	bdl	bdl	bdl	bdl	bdl	bdl	bdl	bdl
HfO_2	bdl	bdl	bdl	bdl	bdl	bdl	bdl	bdl	bdl	bdl	bdl	bdl	bdl	bdl	bdl	bdl
Nb_2O_5	bdl	bdl	bdl	bdl	bdl	bdl	bdl	bdl	bdl	bdl	bdl	bdl	bdl	bdl	bdl	bdl
Sc_2O_3	bdl	bdl	bdl	bdl	bdl	bdl	bdl	bdl	bdl	bdl	bdl	bdl	bdl	bdl	bdl	bdl
ThO_2	bdl	bdl	bdl	bdl	bdl	bdl	bdl	bdl	bdl	bdl	bdl	bdl	bdl	bdl	bdl	bdl
UO_2	bdl	bdl	bdl	bdl	bdl	bdl	bdl	bdl	bdl	bdl	bdl	bdl	bdl	bdl	bdl	bdl
P_2O_5	bdl	bdl	bdl	bdl	bdl	bdl	bdl	bdl	bdl	bdl	bdl	bdl	bdl	bdl	bdl	bdl
SO_3	bdl	bdl	bdl	bdl	0.04	bdl	bdl	bdl	bdl	bdl	bdl	bdl	bdl	bdl	bdl	bdl
F	bdl	bdl	bdl	bdl	bdl	bdl	bdl	bdl	bdl	bdl	bdl	bdl	bdl	bdl	bdl	bdl
Cl	bdl	bdl	bdl	bdl	bdl	bdl	bdl	bdl	bdl	bdl	bdl	bdl	0.01	bdl	bdl	bdl
TOTAL	101.23	101.24	101.02	101.19	99.98	100.63	100.40	100.79	99.45	98.87	98.48	100.19	101.60	101.06	100.54	102.13

* below detection limit

Table B.25 Average and range of detection limits (99% confidence level) for electron microprobe analyses.

Element	Average	Minimum	Maximum
Si	0.006	0.004	0.009
Al	0.006	0.002	0.012
Na	0.016	0.009	0.028
K	0.014	0.009	0.021
Ca	0.014	0.010	0.023
Mg	0.008	0.004	0.014
Fe	0.016	0.011	0.024
Mn	0.017	0.012	0.026
Ba	0.052	0.036	0.079
Sr	0.052	0.028	0.125
Ti	0.018	0.012	0.027
Cr	0.024	0.017	0.035
La	0.054	0.034	0.093
Ce	0.052	0.036	0.079
Pr	0.051	0.031	0.076
Nd	0.053	0.035	0.084
Sm	0.045	0.031	0.068
Eu	0.048	0.033	0.069
Gd	0.048	0.030	0.072
Tb	0.055	0.033	0.081
Dy	0.053	0.030	0.079
Ho	0.055	0.033	0.079
Er	0.057	0.034	0.085
Tm	0.058	0.033	0.088
Yb	0.050	0.034	0.083
Lu	0.059	0.036	0.089
Y	0.045	0.027	0.079
Zr	0.040	0.025	0.071
Hf	0.058	0.040	0.077
Nb	0.035	0.022	0.054
Sc	0.017	0.011	0.029
Th	0.039	0.027	0.055
U	0.039	0.026	0.056
P	0.019	0.011	0.043
S	0.017	0.011	0.025
F	0.069	0.034	0.244
Cl	0.008	0.006	0.012

APPENDIX C.

ADDITIONAL DATA FOR LASER ABLATION ICP-MS ANALYSIS

Table C.1 Discordant U-Pb isotopic data for zircon from the Hoidas Lake REE deposit.

Sample	^{207}Pb/^{235}U	2σ	^{206}Pb/^{238}U	2σ	error correlation	^{207}Pb/^{206}Pb	2σ	^{207}Pb/^{235}U age (Ma)	2σ	^{206}Pb/^{238}U age (Ma)	2σ	^{207}Pb/^{206}Pb age (Ma)	2σ
881339-3	8.119	0.120	0.3943	0.0045	0.6583	0.1492	0.0011	2244	13	2142	21	2337	8
881339-7	7.638	0.140	0.3767	0.0060	0.5433	0.1471	0.0011	2190	18	2062	29	2310	8
881339-11	7.287	0.100	0.3645	0.0041	0.7398	0.1446	0.0009	2148	13	2003	19	2283	7
881339-13	5.336	0.130	0.2697	0.0055	0.9287	0.1433	0.0010	1875	20	1539	28	2268	9
881339-14	9.322	0.140	0.4468	0.0050	0.8284	0.1512	0.0010	2370	13	2381	22	2359	8
881339-16	9.359	0.130	0.4473	0.0047	0.8098	0.1519	0.0010	2373	12	2383	21	2366	6
881339-17	9.232	0.130	0.4443	0.0047	0.6969	0.1503	0.0010	2361	13	2370	21	2350	7
881339-18	9.224	0.120	0.4397	0.0044	0.5804	0.1521	0.0010	2360	12	2349	20	2370	8
881339-19	4.394	0.100	0.2702	0.0051	0.8008	0.1181	0.0009	1713	18	1542	25	1927	10
881339-20	3.584	0.062	0.2265	0.0035	0.7129	0.1147	0.0008	1546	15	1316	19	1878	7
881339-22	3.759	0.110	0.2331	0.0062	0.8480	0.1170	0.0008	1584	21	1350	32	1914	8
881339-24	5.689	0.078	0.3516	0.0037	0.5329	0.1177	0.0008	1930	12	1943	17	1925	7
881339-26	5.728	0.078	0.3544	0.0038	0.6378	0.1177	0.0008	1935	12	1956	18	1921	7
881339-28	5.683	0.076	0.3543	0.0037	0.6277	0.1168	0.0008	1929	12	1955	18	1907	6
881339-29	5.624	0.077	0.3502	0.0036	0.5672	0.1171	0.0008	1920	12	1935	17	1916	7
881339-30	5.674	0.076	0.3532	0.0036	0.4653	0.1171	0.0008	1927	12	1950	17	1913	7
881339-31	9.335	0.130	0.4505	0.0049	0.7578	0.1510	0.0010	2371	13	2397	22	2360	6
881339-33	9.088	0.120	0.4432	0.0046	0.6923	0.1496	0.0010	2347	12	2366	21	2341	7
881179-1	6.075	0.092	0.3524	0.0038	0.7212	0.1259	0.0010	1988	13	1946	18	2043	10
881179-2	6.066	0.093	0.3457	0.0037	0.3476	0.1279	0.0013	1985	13	1914	18	2070	16
881179-3	6.967	0.095	0.3841	0.0041	0.4172	0.1322	0.0010	2107	12	2095	19	2129	8
881179-4	7.191	0.100	0.3836	0.0042	0.6789	0.1367	0.0010	2135	13	2093	20	2187	9
881179-5	8.670	0.190	0.4139	0.0052	0.9053	0.1516	0.0021	2302	22	2232	24	2363	23
881179-6	6.500	0.093	0.3783	0.0039	0.2848	0.1247	0.0011	2046	13	2068	18	2021	10
881179-7	6.098	0.094	0.3428	0.0045	0.5057	0.1291	0.0009	1990	14	1900	22	2084	8
881179-8	7.107	0.120	0.3602	0.0041	0.5710	0.1435	0.0016	2125	15	1984	20	2268	18
881179-9	5.859	0.093	0.3261	0.0041	0.6586	0.1297	0.0009	1956	15	1820	20	2095	9
881179-10	7.091	0.110	0.3739	0.0045	0.8724	0.1369	0.0010	2122	14	2047	21	2191	9
881179-11	7.493	0.100	0.3827	0.0042	0.5683	0.1419	0.0010	2172	13	2089	20	2248	7
881179-12	6.732	0.160	0.3743	0.0045	0.6554	0.1301	0.0020	2077	17	2052	21	2097	18
881179-13	6.001	0.084	0.3255	0.0034	0.5715	0.1332	0.0010	1976	12	1816	17	2143	9
881179-14	5.154	0.150	0.3000	0.0067	0.7445	0.1244	0.0015	1844	31	1691	34	2019	22
881179-17	7.670	0.100	0.3909	0.0041	0.6659	0.1414	0.0010	2193	12	2127	19	2245	7
881179-18	8.813	0.130	0.4285	0.0047	0.5221	0.1481	0.0011	2319	13	2299	21	2323	8
881179-20	7.630	0.290	0.3767	0.0067	0.9691	0.1437	0.0030	2171	32	2059	31	2266	34
881179-22	6.695	0.120	0.3425	0.0055	0.8825	0.1410	0.0010	2071	15	1898	26	2239	9
881179-23	8.323	0.130	0.4085	0.0050	0.8813	0.1468	0.0011	2266	15	2208	23	2310	11
881179-24	5.777	0.083	0.3470	0.0039	0.7304	0.1199	0.0009	1943	13	1920	19	1951	8
881179-25	7.374	0.100	0.3843	0.0040	0.4265	0.1385	0.0011	2157	13	2096	19	2209	8
881179-26	8.780	0.260	0.4075	0.0049	0.8868	0.1538	0.0032	2301	24	2203	23	2375	31
881179-27	8.352	0.110	0.4124	0.0043	0.4476	0.1463	0.0011	2270	12	2226	20	2300	8
881179-29	8.597	0.120	0.4213	0.0044	0.5790	0.1471	0.0011	2296	13	2266	20	2310	8

Table C.1 cont.

Sample	^{207}Pb/^{235}U	2σ	^{206}Pb/^{238}U	2σ	error correlation	^{207}Pb/^{206}Pb	2σ	^{207}Pb/^{235}U age (Ma)	2σ	^{206}Pb/^{238}U age (Ma)	2σ	^{207}Pb/^{206}Pb age (Ma)	2σ
881179-30	7.812	0.110	0.3954	0.0042	0.5793	0.1427	0.0010	2209	12	2148	19	2260	7
881179-31	8.366	0.110	0.4142	0.0044	0.5945	0.1453	0.0010	2271	12	2234	20	2291	7
881179-32	8.140	0.130	0.4053	0.0048	0.8582	0.1446	0.0011	2246	14	2193	22	2285	9
881179-33	7.411	0.110	0.3799	0.0040	0.7131	0.1407	0.0011	2162	14	2076	19	2237	13
881179-35	9.283	0.130	0.4323	0.0045	0.7002	0.1547	0.0010	2366	12	2316	20	2398	7
881179-36	9.203	0.120	0.4394	0.0046	0.7212	0.1510	0.0010	2358	12	2348	21	2359	6
881179-37	9.730	0.190	0.4427	0.0051	0.8322	0.1578	0.0016	2408	18	2362	23	2431	17
881179-38	9.255	0.120	0.4390	0.0047	0.6935	0.1526	0.0010	2363	12	2346	21	2373	5
881179-40	5.848	0.110	0.3408	0.0040	0.8352	0.1244	0.0012	1954	16	1890	19	2019	16
881179-42	6.200	0.220	0.3466	0.0044	0.8747	0.1301	0.0037	1986	25	1918	21	2055	41
881179-T-4	5.582	0.110	0.3324	0.0050	0.8139	0.1220	0.0005	1913	17	1850	24	1986	4
881179-T-5	7.506	0.150	0.3924	0.0056	0.6145	0.1395	0.0004	2174	17	2134	26	2219	4
881179-T-6	7.807	0.150	0.4031	0.0058	0.6745	0.1408	0.0005	2209	18	2183	27	2239	4
881179-T-7	7.257	0.140	0.3800	0.0056	0.8886	0.1387	0.0004	2143	18	2077	26	2210	3
881179-T-8	5.685	0.110	0.3465	0.0050	0.5424	0.1197	0.0005	1929	17	1918	24	1954	5
881179-T-10	5.693	0.110	0.3443	0.0050	0.6795	0.1202	0.0004	1931	17	1907	24	1957	3
881179-T-12	7.059	0.140	0.3778	0.0056	0.6395	0.1359	0.0006	2118	17	2066	26	2171	5
881179-T-13	5.668	0.110	0.3400	0.0049	0.4533	0.1206	0.0005	1926	17	1887	24	1963	5
881179-T-14	5.478	0.260	0.3372	0.0082	0.3536	0.1175	0.0018	1897	26	1873	32	1917	19
881187-10	9.102	0.180	0.4479	0.0065	0.6158	0.1474	0.0006	2349	18	2386	29	2317	4
881187-11	8.835	0.170	0.4283	0.0062	0.7376	0.1497	0.0006	2321	18	2298	28	2342	4
881187-13	9.168	0.180	0.4500	0.0065	0.4968	0.1484	0.0008	2354	18	2395	29	2329	5
881187-14	9.116	0.180	0.4460	0.0065	0.4782	0.1488	0.0008	2349	18	2377	29	2332	6
881187-16	8.848	0.170	0.4366	0.0065	0.7153	0.1465	0.0005	2323	18	2335	29	2309	4
881187-17	9.173	0.180	0.4509	0.0066	0.7635	0.1476	0.0006	2355	18	2399	29	2317	4
881187-18	8.935	0.180	0.4411	0.0065	0.6670	0.1466	0.0007	2331	18	2356	29	2306	5
881187-19	8.842	0.180	0.4285	0.0062	0.6591	0.1489	0.0006	2321	18	2299	28	2333	4
881187-20	8.459	0.170	0.4198	0.0061	0.4784	0.1452	0.0007	2282	18	2260	28	2289	5
881187-21	9.462	0.190	0.4527	0.0066	0.4614	0.1511	0.0007	2383	18	2408	29	2360	4
881187-22	9.411	0.190	0.4520	0.0066	0.6120	0.1502	0.0006	2379	18	2404	29	2348	5
881187-23	9.381	0.190	0.4489	0.0065	0.4202	0.1511	0.0007	2376	18	2390	29	2359	5
881187-24	8.941	0.180	0.4328	0.0065	0.2661	0.1492	0.0007	2331	18	2318	30	2335	5
881187-25	8.872	0.180	0.4237	0.0062	0.7834	0.1517	0.0005	2325	18	2277	28	2367	3
881187-26	7.861	0.160	0.3958	0.0059	0.7767	0.1452	0.0007	2216	18	2149	27	2289	6
881187-27	8.576	0.170	0.4168	0.0060	0.7642	0.1495	0.0004	2294	18	2246	27	2341	3
881187-28	8.853	0.180	0.4288	0.0063	0.7064	0.1499	0.0005	2323	19	2300	28	2345	4
881187-29	9.359	0.190	0.4517	0.0067	0.7223	0.1510	0.0006	2374	19	2403	30	2354	4
881178-1	8.329	0.160	0.4168	0.0060	0.5997	0.1450	0.0006	2267	18	2246	27	2287	4
881178-2	8.231	0.160	0.4016	0.0058	0.6120	0.1490	0.0006	2256	18	2177	27	2334	5
881178-3	8.993	0.190	0.4327	0.0064	0.7622	0.1512	0.0013	2334	18	2319	29	2351	9
881178-4	9.105	0.200	0.4356	0.0063	0.3709	0.1513	0.0013	2349	18	2331	28	2361	12
881178-7	8.840	0.170	0.4258	0.0062	0.7570	0.1501	0.0005	2322	18	2286	28	2348	3

Table C.2 Discordant U-Pb isotopic data for titanite from the Hoidas Lake REE deposit.

Sample	$^{207}Pb/^{235}U$	2σ	$^{206}Pb/^{238}U$	2σ	error correlation	$^{207}Pb/^{206}Pb$	2σ	$^{207}Pb/^{235}U$ age (Ma)	2σ	$^{206}Pb/^{238}U$ age (Ma)	2σ	$^{207}Pb/^{206}Pb$ age (Ma)	2σ
881179-T-1	5.240	0.130	0.3306	0.0047	0.6850	0.1116	0.0023	1852	22	1840	23	1824	35
881179-T-2	4.819	0.140	0.3083	0.0058	0.5460	0.1118	0.0019	1786	23	1732	29	1822	32
881179-T-4	5.170	0.160	0.3178	0.0048	0.6544	0.1157	0.0032	1852	25	1779	23	1889	47
881179-T-5	5.183	0.150	0.3233	0.0057	0.5358	0.1140	0.0022	1855	26	1805	28	1863	36
881179-T-6	5.671	0.100	0.3403	0.0039	0.6243	0.1191	0.0020	1927	16	1888	19	1949	27
881179-T-9	4.481	0.170	0.2915	0.0039	0.5878	0.1099	0.0034	1730	31	1649	19	1791	55
881179-T-10	5.369	0.120	0.3310	0.0042	0.6997	0.1161	0.0020	1878	19	1843	21	1895	30
881179-T-11	5.560	0.120	0.3421	0.0041	0.2139	0.1169	0.0019	1906	17	1896	19	1909	29
881179-T-12	5.130	0.220	0.2959	0.0089	0.8318	0.1228	0.0028	1837	36	1667	44	1988	42
881179-T-13	4.634	0.180	0.2904	0.0048	0.4655	0.1132	0.0028	1754	33	1643	24	1857	46
881179-T-14	5.033	0.130	0.3201	0.0045	0.5650	0.1141	0.0018	1824	22	1790	22	1869	29
881339-1	5.155	0.082	0.3289	0.0033	0.4534	0.1133	0.0016	1845	14	1833	16	1849	24
881339-2	5.450	0.150	0.3263	0.0043	0.8236	0.1179	0.0021	1890	24	1820	21	1918	33
881339-3	5.150	0.079	0.3276	0.0038	0.5888	0.1137	0.0013	1846	13	1827	18	1864	21
881339-4	5.010	0.110	0.3187	0.0043	0.5872	0.1130	0.0015	1820	18	1783	21	1847	25
881339-5	4.980	0.073	0.3205	0.0047	0.7119	0.1127	0.0011	1816	12	1792	23	1845	18
881339-6	5.037	0.078	0.3217	0.0050	0.5931	0.1135	0.0009	1825	13	1799	25	1857	14
881339-7	5.400	0.150	0.3294	0.0070	0.5290	0.1165	0.0018	1883	23	1835	34	1901	28
881339-8	4.744	0.090	0.3053	0.0073	0.7127	0.1108	0.0014	1775	16	1717	36	1822	24
881339-9	5.186	0.120	0.3286	0.0048	0.5580	0.1154	0.0014	1850	19	1832	24	1885	21
881339-11	5.098	0.120	0.3251	0.0048	0.6181	0.1145	0.0018	1836	20	1814	23	1870	28
881339-15	5.188	0.064	0.3291	0.0043	0.4466	0.1141	0.0011	1850	11	1834	21	1864	17
881339-18	4.733	0.110	0.3061	0.0037	0.6626	0.1118	0.0017	1774	18	1721	18	1830	27
881339-20	4.981	0.150	0.3217	0.0048	0.6101	0.1127	0.0018	1817	25	1798	24	1843	29
881339-22	4.839	0.090	0.3078	0.0075	0.3936	0.1118	0.0018	1788	16	1731	37	1824	29
881187-5	5.207	0.110	0.3283	0.0044	0.6586	0.1163	0.0018	1854	19	1831	22	1898	29
881187-8	5.273	0.190	0.3291	0.0045	0.5219	0.1169	0.0028	1865	31	1835	22	1904	43
881187-11	5.395	0.160	0.3400	0.0050	0.4482	0.1161	0.0018	1885	27	1887	24	1899	29
881187-14	5.483	0.180	0.3418	0.0050	0.3634	0.1168	0.0022	1899	29	1896	23	1907	33
881187-15	5.569	0.120	0.3432	0.0049	0.6298	0.1182	0.0016	1912	19	1902	24	1930	25
881187-18	4.470	0.190	0.2949	0.0056	0.4240	0.1096	0.0039	1722	28	1665	26	1785	46
881187-20	5.508	0.610	0.3429	0.0150	0.5742	0.1165	0.0076	1902	63	1901	64	1902	57
881187-22	5.560	0.460	0.3455	0.0120	0.5700	0.1173	0.0071	1913	49	1913	39	1915	45
881187-23	5.354	0.430	0.3382	0.0086	0.5958	0.1155	0.0049	1877	45	1877	34	1886	41

Table C.3 Discordant U-Pb isotopic data for monazite from the Hoidas Lake REE deposit.

Sample	^{207}Pb/^{235}U	2σ	^{206}Pb/^{238}U	2σ	error correlation	^{207}Pb/^{206}Pb	2σ	^{207}Pb/^{235}U age (Ma)	2σ	^{206}Pb/^{238}U age (Ma)	2σ	^{207}Pb/^{206}Pb age (Ma)	2σ
881253-1	5.321	0.077	0.3458	0.0051	0.4308	0.1115	0.0023	1871	12	1916	25	1819	23
881253-3	5.289	0.066	0.3443	0.0050	0.3496	0.1106	0.0022	1867	11	1907	24	1813	24
881253-5	5.286	0.071	0.3453	0.0051	0.5092	0.1112	0.0022	1866	11	1912	24	1818	21
881253-8	5.340	0.210	0.3318	0.0095	0.6488	0.1159	0.0031	1874	29	1846	45	1913	31
881253-9	5.227	0.072	0.3397	0.0051	0.4751	0.1113	0.0022	1857	12	1885	25	1819	22
881253-10	5.270	0.075	0.3441	0.0049	0.4265	0.1111	0.0023	1865	12	1906	24	1811	22
881253-11	5.288	0.065	0.3406	0.0048	0.3544	0.1120	0.0022	1866	10	1890	23	1831	21
881253-12	5.127	0.075	0.3367	0.0050	0.4231	0.1099	0.0023	1843	13	1871	25	1806	23
881253-13	4.940	0.130	0.3223	0.0082	0.8815	0.1108	0.0022	1813	25	1800	41	1820	24
881253-15	5.245	0.071	0.3383	0.0051	0.4347	0.1118	0.0022	1859	12	1878	24	1830	21
881253-16	5.272	0.076	0.3410	0.0051	0.4599	0.1119	0.0022	1866	12	1891	24	1826	23
881253-17	5.257	0.067	0.3385	0.0050	0.4746	0.1115	0.0022	1863	11	1879	24	1827	22
881253-18	5.206	0.076	0.3378	0.0051	0.2628	0.1115	0.0023	1853	12	1876	24	1816	25
881253-19	5.289	0.082	0.3422	0.0052	0.3574	0.1114	0.0024	1865	13	1897	25	1827	22
881253-20	5.238	0.072	0.3411	0.0051	0.5295	0.1111	0.0022	1859	12	1892	24	1817	22
881253-22	5.137	0.070	0.3365	0.0051	0.2714	0.1098	0.0023	1842	12	1869	24	1798	25
881253-23	5.233	0.081	0.3372	0.0053	0.4386	0.1120	0.0024	1858	13	1873	26	1827	21
881253-26	5.491	0.085	0.3478	0.0055	0.3782	0.1118	0.0025	1899	13	1924	26	1829	20
881253-27	5.267	0.087	0.3382	0.0051	0.2551	0.1109	0.0025	1864	14	1878	25	1810	24
881253-28	5.225	0.068	0.3251	0.0050	0.5588	0.1146	0.0023	1856	11	1814	24	1875	21
881253-29	5.515	0.072	0.3500	0.0052	0.4772	0.1115	0.0022	1903	11	1934	25	1824	21
881253-30	5.505	0.073	0.3502	0.0051	0.4753	0.1109	0.0022	1902	11	1935	24	1822	20
881253-31	5.573	0.075	0.3519	0.0052	0.5863	0.1118	0.0022	1912	12	1944	25	1825	21
881253-32	5.405	0.073	0.3455	0.0050	0.4699	0.1111	0.0022	1886	12	1914	24	1816	21
881253-33	5.352	0.071	0.3419	0.0051	0.3898	0.1105	0.0022	1877	11	1896	25	1808	26
881253-34	5.237	0.081	0.3374	0.0052	0.2101	0.1100	0.0025	1858	13	1874	25	1809	23
881253-37	5.500	0.120	0.3542	0.0061	0.3156	0.1092	0.0028	1902	18	1954	29	1785	29
881253-38	5.449	0.089	0.3512	0.0058	0.2000	0.1104	0.0026	1892	14	1940	28	1816	25
881350B-1	5.157	0.230	0.3348	0.0120	0.6301	0.1105	0.0026	1844	31	1864	54	1805	30
881350B-2	5.180	0.075	0.3373	0.0051	0.5297	0.1094	0.0022	1849	12	1873	25	1785	22
881350B-3	5.156	0.092	0.3359	0.0057	0.2880	0.1097	0.0023	1844	15	1867	27	1801	21
881350B-4	5.222	0.072	0.3387	0.0052	0.3940	0.1096	0.0023	1856	12	1880	25	1796	18
881350B-5	5.147	0.078	0.3359	0.0053	0.3979	0.1095	0.0023	1844	13	1867	26	1786	24
881350B-6	5.384	0.087	0.3467	0.0055	0.3618	0.1100	0.0025	1882	14	1920	26	1804	24
881350B-11	5.145	0.096	0.3333	0.0071	0.4603	0.1100	0.0025	1845	15	1854	35	1796	25
881350B-12	5.268	0.081	0.3431	0.0052	0.4415	0.1095	0.0023	1863	13	1901	25	1794	23
881350B-13	5.493	0.087	0.3524	0.0058	0.5401	0.1114	0.0024	1899	14	1946	28	1824	24
881350B-15	5.304	0.079	0.3415	0.0054	0.3507	0.1111	0.0024	1869	13	1893	26	1811	21
881350B-16	5.322	0.076	0.3529	0.0054	0.4788	0.1078	0.0022	1871	12	1948	26	1766	22
881350B-17	5.314	0.078	0.3508	0.0054	0.6023	0.1089	0.0022	1871	12	1938	26	1787	21
881350B-18	5.184	0.081	0.3367	0.0050	0.1388	0.1102	0.0025	1849	13	1871	24	1805	22
881350B-19	5.542	0.091	0.3498	0.0055	0.3351	0.1130	0.0026	1905	14	1933	26	1849	27
881350B-20	5.223	0.080	0.3448	0.0055	0.5661	0.1085	0.0023	1860	13	1909	26	1781	23
881350B-21	5.442	0.081	0.3593	0.0056	0.5479	0.1102	0.0023	1890	13	1980	26	1795	21
881350B-22	5.253	0.076	0.3524	0.0054	0.4034	0.1084	0.0022	1862	13	1946	26	1778	25
881350B-23	5.369	0.098	0.3473	0.0055	0.3199	0.1123	0.0027	1879	15	1923	26	1832	24
881350B-24	5.564	0.100	0.3665	0.0061	0.1457	0.1099	0.0027	1910	17	2014	28	1783	27
881350B-25	5.188	0.077	0.3437	0.0054	0.2161	0.1100	0.0025	1849	13	1906	26	1810	24
881350B-26	5.397	0.082	0.3579	0.0055	0.3408	0.1099	0.0024	1884	13	1972	26	1790	24
881350B-27	5.110	0.078	0.3424	0.0056	0.5879	0.1089	0.0022	1837	13	1898	27	1782	24

APPENDIX D.
COPYRIGHT PERMISSIONS

The permission letters and copyright information of the following papers:

Pandur, K., Kontak, D.J., and Ansdell, K.M. (2014) Hydrothermal evolution in the Hoidas Lake vein-type REE deposit, Saskatchewan, Canada: Constraints from fluid inclusion microthermometry and evaporate mound analysis. *Canadian Mineralogist* **52**, 717-744, DOI: 10.3749/canmin.1400005.

Pandur, K., Ansdell, K.M., and Kontak, D.J. (2015) Graphic-textured inclusions in apatite: Evidence for pegmatitic growth in a REE-enriched carbonatitic system. *Geology* **43**, 547-550.

are included in the following pages.

Mineralogical Association of Canada
Association minéralogique du Canada

17 April 2015

Krisztina Pandur
University of Saskatchewan
Saskatoon, Saskatchewan
Canada

Dear Krisztina,

Permission is granted for your use of the following paper, published in the August 2014 issue of Canadian Mineralogist, in your thesis at the University of Saskatchewan:

Pandur, K., Kontak, D.J., and Ansdell, K.M. (2014) Hydrothermal evolution in the Hoidas Lake vein-type REE deposit, Saskatchewan, Canada: Constraints from fluid inclusion microthermometry and evaporate mound analysis. Canadian Mineralogist 52(4), 717-744.

Proper citation of where the paper was originally published is all that is required.

Best regards,

Mackenzie Parker

Managing Editor
The Canadian Mineralogist

490, rue de la Couronne, Québec, QC G1K 9A9 Tel.: (418) 653-0333 Fax: (418) 653-0777 office@mineralogicalassociation.ca
www.mineralogicalassociation.ca

THE CANADIAN MINERALOGIST 52/4

TRANSFER OF COPYRIGHT AGREEMENT

Author(s) Name(s) Pandur, K., Kontak, D.J., and Ansdell, K.M.

Title of Article Hydrothermal evolution in the Hoidas Lake vein-type REE deposit, Saskatchewan, Canada: Constraints from fluid inclusion microthermometry and evaporate mound analysis

Volume: 52 Part: 4 Publication Date: August 2014 Pages: 717–744

I hereby assign and transfer to the Mineralogical Association of Canada copyright (and all rights associated with it) to the article listed above. Where applicable, I have the consent of each author to this transfer. I further confirm that this article has not been published previously elsewhere, nor is it under consideration by any other publication.

Name Printed or Typed: Krisztina Pandur

Title:

Signature: Date: 2015. 04. 24.

Address in Full

Institution University of Saskatchewan

Department: Department of Geological Sciences

Address: 114 Science Place

City: Saskatoon State: SK Zip: S7N 5E2

Country: Canada

Phone: +1 306 241 4788 Fax:

E-mail: krisztinapandurkp@gmail.com

Signed form must be returned prior to publication to: (may be faxed or scanned and emailed)

Johanne Caron, Mineralogical Association of Canada
490, rue de la Couronne, Québec, (QC) G1K 9A9 CANADA
Phone : (1) 418-653-0333, Fax: (1) 418-653-0777
E-mail address : jcaron@mineralogicalassociation.ca

THE GEOLOGICAL SOCIETY
OF AMERICA®

SCIENCE ▪ STEWARDSHIP ▪ SERVICE

16 April 2015

Krisztina Pandur
University of Saskatchewan
Saskatoon, Saskatchewan
Canada

Dear Krisztina,
Permission is granted for your use of the following paper, accepted for publication in *Geology* on 14 April 2015, in your thesis at the University of Saskatchewan.

Pandur, K., Ansdell, K.M., and Kontak, D.J., in press, Graphic-textured inclusions in apatite: Evidence for pegmatitic growth in a REE-enriched carbonatitic system: Geology, doi: 10.1130/G36613.1.

Proper citation of where the paper was originally published is all that is required. (From the *Geology* masthead: "Individual scientists are hereby granted permission, without fees or further requests to GSA, to use a single figure, a single table, and/or a brief paragraph of text in other subsequent works and to make unlimited photocopies of items in this journal for noncommercial use in classrooms to further education and science. In addition, an author has the right to use his or her article or a portion of the article in a thesis or dissertation without requesting permission from GSA, provided the bibliographic citation and the GSA copyright credit line are given on the appropriate pages."

Best regards,

Jeanette Hammann
Director, GSA Publications
(303) 357-1048
jhammann@geosociety.org

3300 Penrose Place, P.O. Box 9140, Boulder, Colorado 80301–9140, USA

Tel +1.303.357.1000 ▪ Toll Free +1.800.472.1988 ▪ Fax +1.303.357.1070 ▪ www.geosociety.org

TRANSFER of COPYRIGHT to GSA for JOURNAL ARTICLES

GEOLOGICAL SOCIETY OF AMERICA

Return completed form to: Editorial Asst., GSA Editorial Dept., PO 9140, Boulder, CO 80301-9140, USA Fax: 303-357-1073

MS Number: G-36613 : ☐ *GSA Bulletin* ☒ *Geology*

Title of your paper: GRAPHIC-TEXTURED INCLUSIONS IN APATITE: EVIDENCE FOR PEGMATITIC GROWTH IN A REE-ENRICHED CARBONATITIC SYSTEM

Author(s): KRISZTINA PANDUR,
KEVIN M. ANSDELL
DANIEL J. KONTAK

At least one author (the senior author) must sign this form, although all authors are encouraged to do so. Please type or print the name beside each signature. If the article was commissioned by an individual or organization other than the author, or was written as part of the duties of an employee, then this permission must be signed by an authorized representative of the commissioning organization or employer. Please read the explanations on the back side of this sheet.

COPYRIGHT AGREEMENT

I/we own the copyright, and have the consent and permission of each author to transfer copyright, of the article referenced above. I hereby assign and transfer to The Geological Society of America, Inc. full copyright and all rights under it, including, but not limited to, all rights for publication in paper, electronic, and facsimile formats, and for electronic capture, reproduction, and licensing in all formats, in whole or in part, now and in perpetuity, in the original and all derivative works. I affirm that this article has not been published previously elsewhere, nor is it under active consideration for publication at this time by any other publisher. I understand that I may not publish this paper by any means, including on any World Wide Web site, without prior written permission from the Geological Society of America.

Signature

Institution Name: UNIVERSITY OF SASKATCHEWAN

Street Address: 114 SCIENCE PLACE

Name (printed or typed): KRISZTINA PANDUR

City: SASKATOON State: SK ZIP: S7N 5E2

Date: APRIL 07, 2015

Country: CANADA

CERTIFICATION OF U.S. GOVERNMENT WORKS

*(Sign this section **only if** __ALL__ authors were U.S. Government employees at the time the work was prepared. Any privately employed authors should sign above. Please read the reverse side carefully.)*

I certify that the article referenced above was prepared solely by U.S. Government employees as part of their official duties and therefore legally cannot be copyrighted. I confirm that this article has not been published previously elsewhere and that it is not under consideration by any other publisher.

Signature

Institution Name

Name (printed or typed)

Street Address

Date

City State ZIP Country

WE CANNOT PUBLISH YOUR PAPER WITHOUT THIS FORM – PLEASE RETURN IT PROMPTLY

GSA cannot publish any works without a completed copyright-transfer agreement. Authors of manuscripts subject to Crown copyright, *i.e.,* those that are prepared solely by official employees of the governments of the United Kingdom, Canada, Australia, New Zealand, or other members of the Commonwealth, should contact GSA for an alternate copyright transfer form.

INFORMATION CONCERNING YOUR COPYRIGHT AGREEMENT

Introduction

Copyright Law and modern technology dictate that the Geological Society of America (GSA) obtain full copyright transfers on all articles we publish in our journals and books. This does not alter the long-standing relationship of trust between GSA and its authors, nor does it change the traditional philosophy behind our practice of copyrighting our journals and books.

GSA's copyright philosophy recognizes (1) that authors should be able to: present their works orally, and freely use "fair-use" items (figures, tables, and brief extracts) of their material in their future works; (2) that GSA needs to disseminate scholarly works as broadly as possible; (3) that individual scientists should be free to utilize GSA's material for limited educational uses such as in the classroom; and (4) that we need to insure the integrity of our publications in the face of technology that make unauthorized distribution of data inviting.

Important Limitation—Pre-publication, by the author or others, by any means whatsoever of the material covered by this agreement is prohibited prior to publication by the GSA. This prohibition includes, but is not limited to, publication electronically via the Internet or on any World Wide Web site, or in print. Re-publication of the material by the author or others after publication by the GSA is subject to the terms of this agreement and of the statements detailed in the masthead of each publication. When in doubt, request permission from GSA Copyright Permissions.

Works prepared by independent authors—Under this agreement, authors retain all proprietary rights other than copyright, such as patent rights. GSA hereby grants to the authors of this work the right to present the material orally; the right to reproduce "fair use" items such as figures, tables, and extracts, properly cited, in their future works without further permission from GSA, and to use the material for certain purposes that advance science and education. To ensure the broadest dissemination of your work in GSA publications, we require all non-U.S. Government employees to transfer copyright to us. This permits us to publish our journals and books in all formats (including paper, microform, and electronic media), to grant permission to abstracting and indexing services that wish to include titles, authors, abstracts, etc., from our publications, and to grant permission for photocopying beyond the narrow limits defined in the law, such as for classroom use and other scientific purposes, for licensed inter-library services; for commercial purposes where deemed appropriate, including use in future works by other authors.

Works prepared only by U.S. Government Employees—Work prepared *only* by U.S. Government employees in their official capacities is not subject to copyright in the U.S. Works prepared by these authors are *generally* considered to be in the public domain, where they may be freely copied, republished, and redistributed. In order for the work to be placed in the public domain, *all authors* of the paper must be official U.S. Government employees.

Works prepared by both official U.S. Government employees and privately employed persons—In instances where authorship consists of *both* U.S. Government employees and privately employed individuals, we require at least one privately employed author to transfer copyright to GSA. This provides the best protection and makes possible the broadest dissemination of the science.

Works prepared by privately employed persons in the course of their job—Privately employed authors who have written articles in their official capacities as employees (other than U.S. Government employees) should transfer copyright to GSA on our form. The author's employer retains the same rights as individual authors, as noted above. This category will usually include employees of state and local governments and agencies who prepare works in their official capacities.

Works supported by U.S. Government grants or contracts—Authors who publish works specifically supported by a U.S. Government grant or contract are requested to transfer copyright to GSA. This permits broad dissemination of the work while recognizing the U.S. Government's prior license to use the work for noncommercial purposes.

Copyright exchange between GSA & the Treatise on Invertebrate Paleontology—Authors should be aware that a special relationship exists between GSA and the *Treatise on Invertebrate Paleontology* at the University of Kansas that permits reproduction of fair-use items (figures, tables, and extracts), properly cited, by one organization in the publications of the other without requesting permission. This applies only if the material was "original" within the respective publication, not "by permission" from another source—check the citation to be sure. If it was by permission, or for more than fair-use portions, permission should be requested.

Please sign the applicable part of the form on the reverse side and return it *promptly* to GSA. We cannot guarantee publication nor begin the production process until this signed form has been received. Help us expedite the publication of your paper with your immediate response. If you have any questions, please contact the Editorial Department, (303) 357-1048, geology@geosociety.org.